K. Gupta
Editor

IUTAM Bookseries

IUTAM Symposium on Emerging Trends in Rotor Dynamics

Proceedings of the IUTAM Symposium on Emerging Trends in Rotor Dynamics, held in New Delhi, India, March 23 - March 26, 2009

Springer

IUTAM Symposium on Emerging Trends in Rotor Dynamics

IUTAM BOOKSERIES
Volume 25

Aims and Scope of the Series

The IUTAM Bookseries publishes the proceedings of IUTAM symposia under the auspices of the IUTAM Board.

For other titles published in this series, go to
http:www.springer.com/series/7695

K. Gupta
Editor

IUTAM Symposium on Emerging Trends in Rotor Dynamics

Proceedings of the IUTAM Symposium on Emerging Trends in Rotor Dynamics, held in New Delhi, India, March 23 – March 26, 2009

Springer

Editor
K. Gupta
Department of Mechanical Engineering
Indian Institute of Technology
Hauz Khas
110016 New Delhi
India
kgupta@mech.iitd.ac.in

ISSN 1875-3507 e-ISSN 1875-3493
ISBN 978-94-007-0019-2 e-ISBN 978-94-007-0020-8
DOI 10.1007/978-94-007-0020-8
Springer Dordrecht Heidelberg London New York

Library of Congress Control Number: 2010938474

Foreword

Rotors represent a very important part in many machines, devices and plants, and give rise to engineering and design challenges. While some problems in rotor dynamics nowadays can be considered as solved, new problems have emerged from the broad utilisation, but also from the frequent need to increase the operating range, the rotational speed, the load or the power of rotating machinery. New solutions for increasing demands are needed and this emphasizes the importance of rotor dynamics and its status as a cutting edge field of research.

This IUTAM-Symposium was especially devoted to emerging and new trends in rotor dynamics. As one can see from the many interesting contributions in this volume, there are new approaches, ideas and solutions developed for the old and for the new challenges in rotor dynamics. It is widely accepted that rotor unbalance must not be considered as the single cause to initiate large vibrations. Attention has to be paid to rotor instability due to destabilizing effects by seals and bearings, which may lead to dangerous self-excited vibrations. To understand the underlying mechanisms and predict the dynamic behaviour, efforts are made by considering internal resonances, thermal and other effects. Powerful computers have become very important tools for engineers and researchers in this context, but are still pushed to their limits when, e.g. seals are treated by CFD methods. This is also an example for the virtues of experimental research, which is still important for studying certain effects, to verify numerical results and to initiate further investigations.

It is also evident from the included papers that the non-linear analysis of rotor systems has become essential, and will be so even more in the future. Whether friction has to be considered in bladed disks, cracks are to be detected in shafts, or rotor rubbing is studied, non-linear models have to be used and analysed accordingly. Last but not least, active vibration control of rotors by various means is becoming more and more important and will supplement conventional passive methods in the future.

It is my pleasure to congratulate the authors on their valuable contributions as well as to thank the symposium chairman and his colleagues for organizing this forward-looking IUTAM-Symposium and for making the proceedings available to the scientific community.

Prague, Czech Republic *Aleš Tondl*

Preface

Rotor dynamics is an important branch of dynamics that deals with behavior of rotating machines ranging from very large systems like the power plant rotors i.e., turbogenerators, to very small systems like a tiny dentist's drill, with variety of rotors such as the pumps, compressors, steam/gas turbines, motors, turbopumps etc. as used for example in process industry, falling in between. Speeds of these rotors vary in a large range from, may be a few hundred RPM to more than hundred thousand RPM. Complex system of rotating shaft(s) depending upon their specific requirements, are supported on different types of bearings e.g., the rolling element bearings, different kinds of fluid film bearings, foil and gas bearings, magnetic bearings etc. The present day rotors are much lighter, handle a large amount of energy and fluid mass, operate at much higher speeds, and therefore are most susceptible to vibration and instability problems. These have given rise to variety of interesting physical phenomena, some of which are fairly well understood today (for example the oil whirl/whip), while some are subject of continued investigation (fluid-structure interaction, various forms of instability, nonlinear and parametric effects, chaotic behaviour etc.). Research in rotor dynamics started more than one hundred years back. The progress of research in early years was slow. However, with the availability of larger computing power and the versatile measurement technologies, research in all aspects of rotor dynamics has accelerated over the past several decades. The demand from industry for light weight, high performance and reliable rotor-bearing systems is the driving force for research, and the new developments in the field of rotor dynamics.

The history and development of the subject of Rotor Dynamics is an interesting one. Early research with the first analysis of a spinning shaft by Rankine (1869) followed by the work of several researchers during the period of late 19^{th} century and the early 20^{th} century, clearly indicates that the researchers of that time struggled with deficient mathematical models, with an inadequate understanding of 'whirling/critical speed(s)', and were ceased with a practical question, whether or not a rotor could operate in a stable mode above these speed(s). Once these questions got addressed and the basic mathematical models were fairly well established and understood (Jeffcott 1919), research driven by the needs of a rapidly expanding industry progressed at an exponential rate.

That brings us to two important questions, (i) what have we achieved till now in terms of research in Rotor Dynamics and (ii) where are we heading to? An attempt was made to address these questions in a special session of nearly 3 hours duration, devoted to an open discussion on 'Emerging Trends in Rotor Dynamics'. All the participants representing 21 countries (including India) shared their views. The first question pertains to identifying important milestones in the development of the area of Rotor Dynamics. The second question is an attempt to peep into the future. There was convergence of view that the future research has to be directed towards development of intelligent/smart rotor systems which will be extremely robust and ultra-reliable. This would require further research on diagnostic and prognostic aspects. To develop a better understanding of various phenomena in rotor systems, future research would require a highly interdisciplinary approach to account for the interactions of the rotor with the surrounding fluid medium and the support structure. Considerable electronics would be inbuilt into the next generation rotor systems; a new term '*rotortronics*' was coined during discussion to represent such rotor systems as a class distinct from '*mechatronic*' systems of today. No doubt, the long term requirements from industry will set the direction of future research, for example the development of micro rotors.

The preparations for the present symposium actually started as far back as in August 2006, after the first communication was received from IUTAM informing us about the acceptance of our proposal to organize the symposium. It was indeed a proud moment for us, particularly noting that the last IUTAM symposium on Dynamics of Rotors was held 35 years back in 1974 at Lyngby, Denmark; which was organized by Prof. Niordson, the Scientific Committee comprising of Professors Bishop, Crandall, Dimentberg, Tondl, and Ziegler. There were 87 participants from 18 countries.

The Scientific Committee comprising of Professors Nicolo Bachschmid from Italy, D.H. van Campen from The Netherlands, David Ewins from UK, Yukio Ishida from Japan, Chong-Won Lee from South Korea, Richard Markert from Germany, Agnes Muszynska from USA, Nalinaksh Vyas, Narinder Gupta and K. Gupta (Chairman) from India, was constituted. It undertook the most important task of finalizing the list of invited (keynote) speakers through mutual discussions extending over a period of more than a year. Finally 33 speakers accepted the invitation, out of which 31 speakers participated in the Symposium and delivered their keynote lectures of 30 minutes duration each. To encourage wider participation, the Scientific Committee also decided upon a format under which 40 poster papers were selected for presentation in two poster sessions. Finally 33 poster papers were presented. The authors of the poster papers were given an opportunity to make a presentation of 5–7 minutes duration before the display of their papers in a conventional poster session. Total of 45 papers are selected for the Symposium proceedings after a rigorous review of all the papers. This comprises of 30 invited (keynote) papers and 15 poster papers.

Presented papers on various important aspects of rotor dynamics, could be broadly classified as:

Modelling and general aspects
Developments in bearings
Turbomachine blades
Vibration control strategies
Nonlinear dynamics
Fault diagnostics and condition monitoring
Cracked rotors

The symposium aimed at bringing together, leading researchers from all over the world to share their research experiences, and more importantly to set up the directions for future research in rotor dynamics. I have no hesitation in stating that the above objective was more than duly achieved.

The breakup of 36 participants from 20 countries other than India is given below:

Australia – 1, Austria – 1, Brazil – 1, China – 2, Czech Republic – 1, Denmark – 1, Egypt – 1, France – 1, Germany – 6, Greece – 1, Israel – 1, Italy – 3, Japan – 1, Korea – 1, Lithuania – 2, Poland – 3, Sweden – 1, Switzerland – 1, UK – 3 and USA – 4.

In addition to this, there were 50 delegates from India representing Indian industry, academia, and R&D laboratories.

An important highlight of the symposium was an open session to discuss 'Emerging Trends in Rotor Dynamics Research' all over the world. The session was chaired by Prof. Gordon Kirk, and after his opening remarks, he invited several speakers to initiate the discussion. This was followed by an intense discussion on Emerging Trends in Rotor Dynamics.

First and foremost, I wish to thank Indian National Science Academy (INSA) for making this symposium possible by submitting and presenting our proposal to IUTAM Bureau. I also wish to thank the various agencies in India namely, the Council of Scientific and Industrial Research (CSIR), All India Council for Technical Education (AICTE), Indian Space Research Organization (ISRO), Bharat Heavy Electricals Ltd. (BHEL), the Triveni Engineering and Industries Ltd., Indian Institute of Technology (IIT) Kanpur, Altair Engineering India, and ANSYS India, for providing financial support towards the organization of symposium.

I am grateful to my colleagues and associates, in particular to our Director and Patron of the Symposium, Prof. Surendra Prasad, the Head of Mechanical Engineering, Prof. J.P. Subrahmanyam, members of organizing committee, Professors Chandra Shakher, S.P.Singh, S.K. Saha, Sudipto Mukherjee, Drs. A. K. Singh, S.V. Modak, J.K. Dutt, H. Hirani, and organizing secretary Dr. A.K. Darpe, for their continuous support throughout the period of organization of the Symposium. The prompt advice and guidance received throughout from Prof. J.S. Rao, who also agreed to be the co-patron of the symposium, is gratefully acknowledged. Thanks are also due to Mr. K. N. Madhu of Vibration Research Laboratory, staff of various sections and units of the Institute, and all the student volunteers, for their untiring efforts.

I am particularly grateful to all the members of the Scientific Committee for providing support and valuable guidance on all important matters beginning with the finalization of the format of the symposium, then the list of invited speakers, and in the end the organization of symposium sessions. Finally I wish to thank all the invited speakers who delivered their keynote lectures, and all participants and authors for their efforts in contributing the papers to the symposium, and all reviewers for their invaluable help in selection of papers for the symposium proceedings.

New Delhi, March 2010 K. Gupta

Welcome address by Professor Surendra Prasad, Director, Indian Institute of Technology (IIT) Delhi

Distinguished delegates and participants of IUTAM, chief guest Professor D.V. Singh, distinguished faculty colleagues, friends, ladies and gentlemen;

It is a matter of great pleasure for me to welcome you to IIT Delhi, on this very significant occasion of the organization of this IUTAM meeting on Rotor Dynamics, being held for the first time in India. I know how hard my good friend and colleague, Professor Kshitij Gupta from the Department of Mechanical Engineering, Professor N.K.Gupta, Emeritus Chair Professor in the Department of Applied Mechanics, and an esteemed mentor and senior ex-colleague of IIT Delhi, Professor J.S. Rao, have worked together with many other colleagues from India, to bring this meeting to New Delhi, and hence to IIT Delhi. On behalf of the entire Institute Community, I extend my thanks and greetings to the organizers of this meeting for giving us the privilege to host a galaxy of eminent individuals and scientists in our lovely campus.

All of us are aware of the high standards of the meetings of ICSU in general, and IUTAM in particular. These meetings are outstanding events with high scientific impact, and we are proud that with the efforts of our colleagues we have been able to hold this meeting in our campus. Like many other similar meetings that we hold in our campus every year, this too will be an occasion for our students and faculty to savor the scholarship of international experts, while also using this opportunity to develop international linkages for collaborative research.

Rotor dynamics is an important area not only for research in academic Institutions, but also for the Industry. Rotors find application in practically all machinery, and in all types of industries. Often a rotor forms a critical component of these machines and plants. Several catastrophic accidents, for example in power plants, in all parts of the world triggered by failures in rotors have been reported in published literature.

Traditionally rotor dynamics has been an area of active research in several departments and centers (Mechanical Engineering, Applied Mechanics, and Industrial Tribology Machine Dynamics and Maintenance Engineering Centre ITMMEC) of IIT Delhi, for the past several decades. There has been considerable interaction with power sector on problems of vibrations and rotor dynamics. BHEL, a major

manufacturing industry for power plant equipment in India, has created a Chair in IIT Delhi with an objective to provide an impetus to research in the area of rotor dynamics. It is just befitting that this prestigious symposium on Rotor Dynamics is being held at IIT Delhi, with the primary objective to have on a single platform, leading researchers from all over the world to share their experiences and to set the directions for future research.

As a host of this important meeting, it is my privilege to share some thoughts with our distinguished guests today about IIT Delhi. But before that, it would be appropriate to tell our distinguished Guests something about the IIT system. The idea of Indian Institutes of Technology was born even as the country was achieving its freedom from centuries of foreign rule, and was turned into a reality soon after Independence. Our first Prime Minister, Pundit Jawahar Lal Nehru, strongly believed in the power of Science and Technology to transform the country's fortunes, and therefore supported this initiative enthusiastically with a dream to see these Institutes come up to the international level and serve the country in its march towards prosperity. IIT Delhi was the fifth such Institute to come up in 1963, although our Institute was born a little earlier as the College of Engineering and Technology in 1961. In this brief history of 50 years, IIT Delhi has indeed come a long way and we have not only successfully established our presence in the international arena, but have been ranked amongst the top 50 technological universities by the Times Higher Education Supplement, and other international rankings. The IIT system has recently expanded from a system of seven Institutes, to one of 15, in view of the high demand for quality education in science and technology in the country.

Let me now briefly tell you a little about IIT Delhi, but instead of giving you data and statistics, which you can find on our website, I would like to talk about the three pillars on which we stand and which, in some sense, also represent our core strengths.

First and foremost, IIT Delhi stands for free thinking. We aspire to be known as a place where exploration of truth and knowledge is pursued earnestly, where young people can be freed from the presumptions and prejudices with which they were raised, freed by the power of ideas to pursue their own path in life - a place where our students feel inspired to develop an approach towards life and profession that brings dignity and honor to human affairs. So, while we share the universal dreams of all great research universities of the world and wish to be known as a place where science, technology, humanities and management, are pursued at their frontiers to bring benefit to the society and mankind, we equally wish to try to be a place where the mind becomes free in the true sense of freedom spoken of by the poet Laureate Rabindra Nath Tagore.

Second, IIT Delhi stands for scholarship and learning. Needless to say that our faculty, who are selected and rewarded for these virtues, and our students who are amongst the best that any institution can wish for, make it easy for us to pursue these goals.

Third, IIT Delhi stands for a value system which recognizes the important challenges which our planet and society face today – the challenges of energy security, environment, climate change and in our part of the world, the challenges of inequity,

poverty and lack of access to basic amenities and quality education. No doubt some of these challenges have surfaced as a result of indiscriminate use of technology and human greed. But we believe that the answer to these ills lies not in less, but more technology, and of course, more scientific and value-based management of human affairs, which would make it possible for mankind to work its way towards sustainable development and growth, rather than the unsustainable and chaotic growth of the last few decades with its dire consequences.

Ladies and gentlemen, I hope this brief introduction about IIT Delhi will be useful to you. I do hope that you will find not only the scientific deliberations of this meeting to be useful, but also that you will make many friends in this part of the world.

Welcome address by Professor Narinder K. Gupta, Member IUTAM Bureau, and Vice-President INSA, IIT Delhi

The Chief Guest Prof. D. V. Singh, Prof. Surendra Prasad, Director IIT Delhi, Prof. J. S. Rao, Prof. J. P. Subrahmanyam, Prof. K. Gupta, Chairman of the Symposium, distinguished delegates, ladies and gentlemen;

On behalf of the Indian National Science Academy (INSA) and International Union of Theoretical and Applied Mechanics (IUTAM), I am delighted in welcoming you all to this important IUTAM symposium on Emerging Trends in Rotor Dynamics.

This symposium is special in many ways and leaves its imprint in the process of our (Indian) participation in IUTAM activities. IUTAM is one of the adhering bodies of ICSU, the International Council of Science, formerly called International Council of Scientific Unions.

ICSU, was founded in 1931 to promote international scientific activities in different branches of science and applications for the benefit of humanity. Its membership consists of National Scientific bodies and also International Scientific Unions. Wide spectrum of scientific expertise drawn from such membership allows ICSU to address major international, interdisciplinary issues which requires participation of scientists from various disciplines and various countries. India has been its member right from its inception and has been participating in its various programmes actively over the years. Prof. M. G. K. Menon and Prof. G. Mehta, both past Presidents of INSA, have been Presidents of ICSU during 1989–1995 and 2006–2008 respectively.

IUTAM came in to being in 1946 with the aim of promoting development of mechanics, both theoretical and applied, in various ways which include forming linkages between scientists and holding congresses and symposia. Its plan seems to have been initiated by ICSU. The history of conferences which made IUTAM possible dates back to 1922 – with the one organized by von Karman at Innsbruck. Conferences thereafter were organised every four years till 1938 (in Zurich (1926), Stockholm (1930), Cambridge UK (1934), and Cambridge USA (1938)). Then there

was a disruption due to the world war. The first congress of IUTAM was held in 1948, and INDIA became member of IUTAM in 1950. Till 1949, there were only 3 adhering bodies. Today IUTAM has nearly 450 members representing 55 countries and 18 affiliated organizations.

Mechanics in India in those years had found its place as an important discipline by itself. There were major initiatives for bringing together scientists working in various disciplines of Mechanics and for promoting Mechanics in its various forms. Indian Society of Theoretical and Applied Mechanics (ISTAM) came in to being in 1955 through the efforts of Prof. B. R. Seth of IIT Kharagpur. The first congress of ISTAM was held in the November of 1955 in IIT Kharagpur under the Presidentship of Prof. K. S. Krishnan, renowned Physicist, who had worked with Prof. C. V. Raman. Prof. B. R. Seth was its first Secretary, who later became its President in 1964. Since then, ISTAM has been holding its annual congresses every year and over the years it has been contributing to the cause of Mechanics. Prof. Seth represented India in the IUTAM during the early years.

From 1968, Indian National Science Academy (INSA) was given the responsibility of representing India in ICSU and its adhering bodies. INSA has thus been responsible for representing India in IUTAM. National committees were formed which are expected to establish close linkages with the international unions and with the scientists and professional bodies within the country. IUTAM national committees over the years have been constituted which encourage the participation of Indian Scientists in IUTAM Congresses and promote Mechanics through Symposia, Workshops and Congresses within the country. Prof. Roddam Narasimha, has been representing India and has been member of the IUTAM Bureau in the past.

Our societies and institutions have been holding National and International conferences and symposia on various areas of Mechanics in India with great success, and participation from within the country and abroad has been quite good. However, in the last 6 decades of our association with IUTAM, we have yet not organized any quadrennial congress of IUTAM in India. Though in the past we have organized IUTAM Symposia/ workshops in India, but their total number has relatively been not as much.

Prof. D. V. Singh our Chief Guest today, has been associated with ICSU bodies for almost three decades. We have lately been making efforts in enhancing our participation in IUTAM activities. Prof. K. Gupta worked out the proposal for the present Symposium on Emerging Trends in Rotor Dynamics. Soon there were more proposals from other parts of India. Fortunately we were able to present four proposals over two IUTAM meetings and three of them were approved – this symposium is one of those.

Therefore, personally and on behalf of INSA and IUTAM, I thank the Director Prof. Surendra Prasad and Prof. K. Gupta for making this symposium possible to be held in the Indian Institute of Technology Delhi. The ball is set rolling and we do hope that such symposia on various specializations of Mechanics will henceforth be held in IIT Delhi or other parts of the country every year. I must specially thank Prof. D. V. Singh and Prof. J. S. Rao for being with us on this occasion.

Today, we have nearly 36 distinguished scientists from 20 countries, and several distinguished researchers from India. I am conscious that organizing an event of this magnitude is not very easy. Prof K. Gupta and his colleagues have certainly done a splendid job.

I end by wishing you all a very pleasant and memorable stay, and with the hope that the symposium is a big success.

Address by the Chief Guest, Professor D. V. Singh

Professor Surendra Prasad, Prof. J. S. Rao, Prof. N. K. Gupta, Prof. J. P. Subrahmanyam, Prof. Kshitij Gupta, Distinguished Delegates, Ladies and Gentlemen:

I consider it my privilege and pleasure to be invited to the IUTAM Symposium on "Emerging Trends in Rotor Dynamics". I would like to compliment IIT-Delhi for hosting this IUTAM Symposium, which has attracted leading researchers in the field of rotor dynamics from twenty countries. Hosting a IUTAM Symposium is an honour and a recognition of the high standing of the Institute in the subject of the Symposium.

Recalling the history of IUTAM Symposium, Prof. N. K. Gupta pointed out that the first IUTAM Symposium was held in the year 1922 in Denmark. Prof. Kshitij Gupta mentioned that the first IUTAM Symposium on Rotor Dynamics was held thirty five years ago. I have found that the best glimpses of history of a subject area can be had in the prefaces of books.

I would like to share with you a few pieces of history of rotatory motion. By the middle of the eighteenth century the dynamics of translation of bodies took much of the form it now has. But the scientists of the day did not quite know how to treat general cases of rotation. They recognized that "there was some thing about rotation, either its mechanical laws or just its mathematical description, which some how made the rotation problem of a higher order of difficulty. We now know that problem is in mathematics and not in physics". The problem is still with us when dynamics of complex multibody systems, within which rotation of one or more of its parts occurs, is to be analysed and understood.

The history of rotor dynamics shows interplay of theory and practice. Supercritical speeds of spinning shafts attracted attention of scientists since the middle of the 19^{th} Century. I am referring to the analytical work of Rankine (1869) and experimental work of (Carl Gustav) De Laval (1889), and of Dunkerley (1895). Kerr published his work in 1916 showing evidence of a second critical speed.

Commissioned by the Royal Society of London to resolve the conflict between theory and practice, Henry Jeffcott published a paper, now considered a classic, in the *Philosophical Magazine* in 1919 in which he confirmed the existence of stable supercritical speeds. August Föppl had earlier published much the same conclusions in 1895, but history largely ignored his work.

Post Jeffcott and until the start of the Second World War II, a lot of work in the area of instabilities and modeling techniques was done culminating in the work of Prohl and Myklestad which led to the Transfer Matrix Method (TMM) for analyzing rotors. Now of course FEM is generally used for rotor dynamics analysis.

The rotor-bearing systems of modern rotating machines have interesting and challenging complexities. The challenging nature of rotor dynamics problems have attracted many scientists and engineers whose investigations have contributed to the impressive progress in the study of rotating systems. With the advancement in high-speed machinery and increase in their power/ weight ratio, the determination of the rotor dynamic characteristics through reliable mathematical models have become more important. The advancement in modern instrumentation and computational capabilities has helped in implementing simulation techniques of these complex models. Modern machinery must fulfill increasing demands concerning durability as well as safety requirements. On-line condition monitoring strategies are becoming increasingly commonplace in a bigger range of systems.

Rotors are often prone to mechanical vibrations, which may lead to machine failure. Correction is only possible when proper and accurate diagnosis is obtained through understanding of rotor operation and all of the potential malfunctions that may occur. Mathematical modeling, in particular modal modeling, is key to understanding the observed phenomena through measured data and for predicting and preventing failure.

Rotor dynamics considerations that are important to successful design or troubleshooting of a turbomachine include bearings, fluid seals, rotor geometry configuration, and rotor environment, which affect system behaviour and can be computationally handled for system analysis.

Rotating machines, depending on their environment, could be subjected to fluid-structure interactions, electromagnetic forces and pressure fields, which result in complicated vibration patterns that are to be resolved to distinguish the physical attributes of the machines.

The unsteady and non-linear approaches allow simulation of dynamic response of various systems. So it is possible to create calculation based diagnostic algorithms without numerous expensive specific experiments.

Recent developments in microfabrication techniques permit production of complex geometries and micro scale systems. Many researchers have been working on the development of devices such as micro electric motors, micro turbines, micro pumps, micro reaction wheels, micro gyroscopic sensors and micro spindles. These systems require high speed rotating parts to achieve the same performances as in macro level. Classical rotor dynamic modeling approaches are not sufficient for micro systems due to various effects becoming crucial in small scale, such as viscous forces, which are more important at small scale. Heat transfer is another important aspect since micro devices operate in a much smaller design space than do large-scale machines. The high angular speeds require un-traditional levitation systems for low friction operation. More accurate dynamic analysis tools are needed for the design of micro systems with high speed rotating parts considering multi-physical effects and to tackle the problems of rotor dynamics such as imbalance and eccentricity.

One of the critical technology areas is aircraft engine design and engine rotor dynamics. Improvements of engine dynamics models and their validation continue to be subjects of research, where the needs are to predict dynamic performance to produce lighter, more efficient engines, through the development stage, where more rapid resolution of problems will contribute to reduced time and cost for manufacture and reduction of maintenance cost.

In rotor dynamics problems, often empirical and intuitive methods are risky and can be avoided since predictions of rotor dynamics analysis are quite accurate if accurate values of machine parameters are used in the mathematical model. These predictions some time are contradictory to intuition and disprove them. For example, damping in the rotor of a turbomachine can produce a violently unstable whirling motion at high speeds.

Commercial softwares are now available for advanced modeling and simulation of all kinds of bearings (foil bearings, hydrostatic bearings, hydrodynamic bearings, magnetic bearings and rolling element bearings), seals (labyrinth, honeycomb, and damping seals), and rotor dynamics design and analysis. Evaluations can be completed quickly using advanced steady-state and time transient solutions as part of their bearing, seal, and vibration analysis codes. Advanced Nonlinear software solutions (e.g., ADINA, Nastran) enable analysis of models with nonlinearity from contacting parts, material nonlinearities and geometric nonlinearities (large deformations).

With reference to modern computer models, Dara Childs could be quoted, “the quality of predictions from a computer code has more to do with the soundness of the basic model and the physical insight of the analyst. Superior algorithms or computer codes will not cure bad models or a lack of engineering judgment.”

Though the knowledge and understanding of rotor dynamics and stability have steadily increased through the years, much more work is needed to fully understand the dynamics profile of high speed rotors.

In the above context, the importance of research in rotor dynamics becomes much more to meet the needs of the machines of the future for industries, power plants, Space and Defense.

I have scanned the abstracts of the papers to be presented in the Symposium, which were sent to me by Prof. K. Gupta. These papers offer the excitement of the current research being done by the experts in the area in several countries that are represented here. I am sure that the Symposium will be highly successful in achieving its objectives and the deliberations of leading experts in the field of Rotor Dynamics will be very fruitful.

With my best wishes for the success of the Symposium, it is my privilege to inaugurate this IUTAM Symposium.

Thank you.

List of Speakers

Keynote Lectures

Jan-Olov Aidanpää Division of Computer Aided Design, Lulea University of Technology, Lulea, S-971-87, SWEDEN, Jan-Olov.Aidanpaa@ltu.se

Nicolò Bachschmid Dipartimento di Meccanica Politecnico di Milano, Via La Masa, 34, I-20156 Milano, ITALY, nicolo.bachschmid@polimi.it

V. Barzdaitis Kaunas University of Technology, Dept. of Engineering Mechanics, Donelaičio St.73, Kaunas, LT-44244, LITHUANIA, vytautas.barzdaitis@ktu.lt

Izhak Bucher Dynamics Laboratory, Mechanical Engineering, Technion Israel Institute of Technology, Haifa 32000, ISRAEL, izhak.bucher@gmail.com

Katia Lucchesi Cavalca Department of Mechanical Design Unicamp, Postal Box 6122, 13083-970 Campinas, SP, BRAZIL, katia@fem.unicamp.br

Horst Ecker Institute of Mechanics and Mechatronics, Technische Universität Wien, Wiedner HauptstraX e 8-10/E325, Karlsplatz 13 | A-1040 Wien, Vienna, AUSTRIA, horst.ecker@tuwien.ac.at

D.J. Ewins Dept. of Mechanical Engineering, Imperial College London, Centre of Vibration Engineering, London SW7 2BX, UK, d.ewins@imperial.ac.uk

G. Genta Mechatronics Laboratory, Politecnico di Torino –, Corso Duca degli Abruzzi, 24 - 10129 Torino, ITALY, giancarlo.genta@polito.it

Zdzislaw Gosiewski Dept. of Mechanical Engineering, Bialystok Technical University, ul. Wiejska 45C, 15-351 Białystok, POLAND, gosiewski@pb.bialystok.pl

Yukio Ishida Department of Electronic-Mechanical Engineering, Nagoya University, Furo-cho, Chikusa-ku, Nagoya 464-8603, JAPAN, ishida@nuem.nagoya-u.ac.jp

Georges Jacquet-Richardet Laboratoire de Dynamique des, Machines et des Structures, INSA Lyon,Villeurbanne, FRANCE, Georges.Jacquet@insa-lyon.fr

Jan Kiciński Institute of Fluid-Flow Machinery PASci, 80-952 Gdansk, Fiszera 14 Str., POLAND, kic@imp.gda.pl

R. Gordon Kirk Mechanical Engineering (0238), Virginia Tech., Blacksburg, VA 24061, USA, gokirk@vt.edu

Chong-Won Lee Dept. of Mechanical Engineering, KAIST, Yuseong-gu, Daejeon 305-701, REPUBLIC OF KOREA, cwlee@kaist.ac.kr

Robert Liebich Department of Engineering Design and Product Reliability, Berlin Institute of Technology, Fakulty V - Sekr. H66, Strasse des 17. Juni 135, 10623 Berlin, GERMANY, robert.liebich@tu-berlin.de

E. Malenovský Brno University of Technology, Technicka 2, 616 69 Brno, CZECH REPUBLIC, malenovsky@fme.vutbr.cz

C. Nataraj Dept. of Mechanical Engineering, Villanova University, Villanova, PA 19085, USA, c.nataraj@villanova.edu

C.A. Papadopoulos Machine Design Laboratory, Department of Mechanical Engineering and Aeronautics, University of Patras, Patras-26504, GREECE, chris.papadopoulos@mech.upatras.gr

P. Pennacchi Dipartimento di Meccanica, Politecnico di Milano, Campus Bovisa, Via La Masa 34, I-20158 Milano, ITALY, paolo.pennacchi@polimi.it

E.P. Petrov Mechanical Engineering Department, Imperial College London, South Kensington Campus, London SW7 2AZ, U.K., y.petrov@imperial.ac.uk

R.B. Randall School of Mechanical & Manufacturing Engineering, UNSW, Sydney, NSW 2052, AUSTRALIA, b.randall@unsw.edu.au

J.S. Rao Altair Engineering (India), Mercury 2B Block, 5th Floor, Prestige Tech Park, Sarjapur Marathhalli, Bangalore 560 087, INDIA, js.rao@altair.com

Ilmar F. Santos MEK – Dept. of Mechanical Engineering, DTU- Tech. University of Denmark, Nils Koppels Allé, Building 404, Lyngby 2800, DENMARK, ifs@mek.dtu.dk

Gerhard Schweitzer Mechatronics Consulting, Lindenbergstrasse 18 A, CH-8700 Kuesnacht, SWITZERLAND, g.schweitzer@ggaweb.ch

A.S. Sekhar Dept. of Mechanical Engineering, Indian Institute of Technology Madras, Chennai, INDIA, as_sekher@iitm.ac.in

A. El-Shafei Dept. of Mechanical Design & Production, Cairo University, 12316 Giza, EGYPT, elshafei@ritec-eg.com

Alok Sinha Mechanical Engineering Department, The Pennsylvania State University, 330 Reber Building, University Park, PA 16802, USA, axs22@psu.edu

R. Tiwari Dept. of Mechanical Engineering, Indian Institute of Technology Guwahati, Guwahati, 781039, INDIA, rtiwari@iitg.ernet.in

Heinz Ulbrich Institute of Applied Mechanics, TU Muenchen, Boltzmannstr. 15, 85748 Garching GERMANY, ulbrich@amm.mw.tu-muenchen.de

Nalinaksh S. Vyas Dept. of Mechanical Engineering, Indian Institute of Technology Kanpur, UP-208016, INDIA, vyas@iitk.ac.in

Poster Papers

T.S. Aravindhan MSC Software, Geometric Limited, RMZ NXT Campus, 1a unit, 101 & 102 First Floor, Whitefield Road, Sonehalli Village, Near SAP Labs, Bangalore- 560066, INDIA, aravindhan.ts@gmail.com

J. Sharana Basavaraja Dept. of Mechanical Engineering, B. M. S. College of Engineering, Bangalore – 560019, INDIA, khinaresh@gmail.com

Skylab Bhore Zanskar Hostel, WD-5, IIT Delhi, Hauz Khas, New Delhi- 110016, INDIA, skylab2000@rediffmail.com

Aydin Boyaci Institut für Technische Mechanik, Universität Karlsruhe (TH), Kaiserstraße 12, 76131 Karlsruhe, GERMANY, boyaci@itm.uni-karlsruhe.de

Ashish K. Darpe Department of Mechanical Engineering, Indian Institute of Technology Delhi, Hauz Khas, New Delhi – 110016, INDIA, akdarpe@mech.iitd.ac.in

J.K. Dutt Department of Mechanical Engineering, IIT Delhi, Hauz Khas, New Delhi -110016, INDIA, jkdutt@yahoo.co.in

Felix Fritz Institut für Technische Mechanik, Universität Karlsruhe, Kaiserstr. 10, Geb. 10.23, Raum 205.2, 76131 Karlsruhe, GERMANY, fritz@itm.uni-karlsruhe.de

G. Genta Mechatronics Laboratory, Politecnico di Torino –, Corso Duca degli Abruzzi, 24 - 10129 Torino, ITALY, giancarlo.genta@polito.it

S.S. Goilkar PS-75, 'C' Wing, Tulsi Quarters, Hill Side, IIT Campus, IIT Bombay, Powai, Mumbai- 400076, ssgoilkar@gmail.com

T.C. Gupta Department of Mechanical Engineering, National Institute of Technology, Jaipur, INDIA, tcgmnit@gmail.com

Qingkai Han School of Mechanical Engineering and Automation, Northeastern University, Shenyang, Liaoning Province, 110004, P. R. CHINA, qhan@mail.neu.edu.cn

S.P. Harsha Mechanical & Industrial Engineering Department, Indian Institute of Technology Roorkee – 247667, INDIA, spharsha@yahoo.com

Angello Innocent ICGS Savitribai Phule, C/O coastguard Dist. Head quarter No. 3, Panambur, Mangalore-575010, INDIA, angello_mani@rediffmail.com

Rakesh Kamra 410 YP Marg B.E.G & Center, Roorkee-247667, INDIA, karmapme@iitr.ernet.in

Zbigniew Kozanecki Institute of Turbomachinery, Technical University of Lodz, 219/223 Wolczanska str., 93-005 Lodz, POLAND, zkozan@p.lodz.pl

Chandan Kumar Dept. of mechanical Engineering, Sant Longowal Institute of Engineering and Technology, Longowal-148106, Punjab, INDIA, chandan_rit@yahoo.com

M. Santhosh Kumar ANSYS Software Pvt Ltd, # 1302 Jeevan Bhima, Nagar Main Road, Bangalore-560008, INDIA, Santhoshkumar.M@ansys.com

V. Satish Kumar Reprocessing Plant Design Division, Reprocessing Group, IGCAR, Kalpakkam, Tamil Nadu, INDIA, vsatish@igcar.gov.in

S.K. Laha Mechanical Engineering Department, Indian Institute of Technology Guwahati-781039, INDIA, swarup@iitg.ernet.in

R.J. Lalwani Dept. Of Mechanical Engineering, Skyline Institute of Engineering and Technology, Greater Noida,UP–201306, INDIA, drlalwani@yahoo.com

Arghya Nandi Dept. of Mechanical Engineering, Jadhavpur University, Kolkata, 700032, INDIA, arghyan@yahoo.com

C. Nataraj Dept. of Mechanical Engineering, Villanova University, Villanova, PA 19085, USA, c.nataraj@villanova.edu

Atul Nath ABRO Technologies Pvt. Ltd., 12, Scindia House, Second Floor, Connaught Circus, New Delhi – 110001, INDIA, atul_nath@yahoo.com

T.V.V.L. Narsimha Rao Mechanical Group, Birla Institute of Technology and Science, Pilani, Pilani 333 031, INDIA, tvvlnrao@bits-pilani.ac.in

Sumant Neogy Dept. of Mechanical Engineering, Jadhavpur University, Kolkata, 700032, INDIA, am_sneogy@hotmail.com

B.M. Nikhil TATA motors, Pimpri, Pune, Maharashtra, INDIA, nikhil.maruthi@gmail.com

Saranu Ravikumar Mechanical Engineering Department, Bapatla Engineering College, Bapatla, Guntur (dist), Andhrapradesh, 52210, INDIA, ravikumar.saranu@gmail.com

Rishi Relan Dept. of Mechanical Engineering, Indian Institute of Technology, Delhi, New Delhi -110016, INDIA, rishirelan@yahoo.co.in

S.K. Singh Dept. of Mechanical Engineering, Indian Institute of Technology Guwahati, 781039, INDIA, s.sachin@iitg.ernet.in

Jyoti K. Sinha School of Mechanical, Aerospace and Civil Engineering (MACE) B3, Pariser Building, Sackville Street, The University of Manchester, P.O.Box 88, Manchester M60 1QD, UK, Jyoti.Sinha@manchester.ac.uk

G.N.D.S. Sudhakar Room No. 2015, Krishna Hostel, IIT Madras, Chennai-60003, INDIA, sudhakar.gantasala@gmail.com

Mayank Tiwari GE John F. Welch Technology Center, Sy. No. 152, Hoodi Village, Export Promotion Ind. Park, Phase 2, Whitefield Road, Bangalore - 560 066, INDIA, mayank.tiwari@geind.ge.com

S. Verma Dept. of Mechanical Engineering, DCR University of Science & Technology, Murthal-131039, INDIA, sureshc30@yahoo.co.in

Members of Scientific Committee

Nicolò Bachschmid Dipartimento di Meccanica, Politecnico di Milano, Via La Masa, 34, I-20156 Milano, ITALY, nicolo.bachschmid@polimi.it

Dick H. van Campen Dept. of Mechanical Engineering, Eindhoven University of Technology, P.O. Box 513, 5600 MB Eindhoven, The Netherlands, D.H.v.Campen@tue.nl

D.J. Ewins Dept. of Mechanical Engineering, Imperial College London, Centre of Vibration Engineering, London SW7 2BX, UK, d.ewins@imperial.ac.uk

K. Gupta Mechanical Engineering Department, Indian Institute of Technology Delhi, New Delhi 110016, INDIA, kgupta@mech.iitd.ernet.in

Narinder K. Gupta Applied Mechanics Department, Indian Institute of Technology Delhi, New Delhi 110016, INDIA, nkgupta@am.iitd.ernet.in

Yukio Ishida Department of Electronic-Mechanical Engineering, Nagoya University Furo-cho, Chikusa-ku, Nagoya 464-8603, JAPAN, ishida@nuem.nagoya-u.ac.jp

Chong-Won Lee Dept. of Mechanical Engineering, KAIST, Yuseong-gu, Daejeon 305-701, REPUBLIC OF KOREA, cwlee@kaist.ac.kr

Richard Markert Institute of Mechanics, AG II, Darmstadt University of Technology, Hochschulstrasse 1, 64289 Darmstadt, GERMANY, markert@sdy.tu-darmstadt.de

Agnes Muszyńska A.M. Consulting, P.O. Box 792, Minden, NV 89423, USA, agnesm@charter.net

Nalinaksh S. Vyas Dept. of Mechanical Engineering, Indian Institute of Technology Kanpur, UP-208016, INDIA, vyas@iitk.ac.in

Contents

Rotordynamics Research: Current Interests and Future Directions

R. Gordon Kirk

Abstract The level of understanding of machinery dynamics is higher today than was ever thought possible 35 years ago. In fact, a major source of excitation was overlooked and thought to be coming from aerodynamic excitation forces in centrifugal compressors. The evaluation of instability mechanisms has advanced to the point that standard procedures are currently being proposed for all petrochemical rotating machinery. While this all sounds so fine, a closer look reveals that much more work is necessary to fully understand the machinery being built today and the advanced technology machinery that will be needed in future years. Most major universities are not interested in machinery dynamics research due to the low level of funding that the machinery OEMs and users have come to expect for such research programs. If this trend continues, it will eventually be left to industry to self-teach and advance the knowledge required to produce the necessary rotating machinery. This paper will address the most interesting results from the author's current research efforts in two different areas. First, a key area of research for the past 25 years has been the proper prediction of labyrinth seal excitation in centrifugal compressors. Second, for the past 15 years, the fluid film bearing thermally induced synchronous instability has been the most interesting and widespread source of a new excitation mechanism for modern machinery. A summary of results and future requirements for each of these areas will be discussed in the conclusions and recommendations.

Keywords Labyrinth · Seals · Stability · Thermal instability · Rotordynamics

1 Introduction

The analysis of full scale rotor bearing systems has slowly advanced over the last six decades. The computation of the undamped critical speed of turbine rotors was outlined by Prohl [1] in the mid 1940s and awaited the digital computer to speed

R.G. Kirk (✉)
Mechanical Engineering Department, Virginia Tech., Blacksburg, VA 24061, USA
e-mail: gokirk@vt.edu

K. Gupta (ed.), *IUTAM Symposium on Emerging Trends in Rotor Dynamics*,
IUTAM Bookseries 25, DOI 10.1007/978-94-007-0020-8_1,

up the hand calculations that were initially used. Bearing stability [2] and rotor balancing [3] were some of the topics of discussion in the 1950s. In the 1960s it was a challenge to have proper bearing characteristics for analysis and many bearing designs required interpolation from tables or charts. This was the decade that the tilting bearing was introduced [4] thus allowing higher operating speeds for new centrifugal compressors. It was also the decade that computer generated elliptic response resulting from rotor imbalance was first realized [5]. The concept of rotor stability for simple reduced rotor models was the current state of the art [6]. The mechanism for instability of turbine rotors was introduced by Alford [7]. Soon thereafter, this allowed for a procedure to estimate the instability threshold speed of centrifugal compressors by re-defining the basic equation parameters in terms of a centrifugal compressor stage, rather than the axial turbine stage studied by Alford. The concept of aerodynamic excitation was to be used until the early 1980s and in fact is still used today, together with more advanced analysis of seal excitation, to evaluate centrifugal compressor stability. It also became possible in the 1960s to monitor the shaft relative to the bearing pedestal motion by using non-contact eddy current probes developed by Don Bently, now known and used world-wide in most all critical path rotating machinery.

In the 1970s refined bearing and oil seal analysis became common and the ability to compute the rotor bearing dynamic stability was introduced [8–11], allowing computation of damped critical speed and stability for total rotor-bearing-support systems. The transfer matrix method was used for undamped critical speeds, forced response and stability computation. However, it must be noted that Ruhl and Booker [8] presented results by both finite element theory and transfer matrix methods. In the 1980s the analysis of gas labyrinth seals was finally possible [12, 13]. In fact, a major source of excitation had been overlooked and thought to be coming from aerodynamic excitation forces in centrifugal compressors. The evaluation of instability mechanisms has advanced to the point that standard procedures are currently being proposed for all petrochemical rotating machinery. The use of gas face seals to replace oil ring seals, the combination of a tilting pad bearing plus oil film damper, swirl breaks on labyrinth seals and selective use of honeycomb seals have made it possible to build very stable equipment [14]. Personal computer for FEA [15], together with the transfer matrix programs [16] have been used since 2002 for instruction in the Introduction to Rotor Dynamics graduate, course taught by the author, at Virginia Tech.

While the previous literature review would seem to indicate that all problems are resolved, a closer look reveals that much more work is necessary to fully understand the machinery being built today and the advanced technology machinery that will be needed in future years. Most major universities are not interested in machinery dynamics research due to the low level of funding that the machinery OEMs and users have come to expect for such research programs. Industry sponsored research groups for rotating machinery were started at the University of Virginia in 1972, Texas A&M in 1981, and Virginia Tech in 1985. These groups have generated many students and computer analysis capabilities for industry to apply to their machinery. The current funding levels are, however, too low to have sustained research

where the expected research grants are expected to be in millions, not thousands of dollars per faculty member involved. This paper will address recent results from the author's current research efforts concerning labyrinth seal excitation in centrifugal compressors and fluid film bearing thermally induced synchronous instability. The future requirements for each of these areas will be discussed in the closing remarks.

2 Labyrinth Seal Excitation

2.1 Background

The analytical methods for analysis of gas labyrinth seals employing bulk flow models were developed in the early 1980s [12, 13] to estimate the dynamic instability of rotor bearing systems including the influence of the gas labyrinth seals. These methods continue to be used in the industrial compressor industry and have made it possible for engineers to solve complex field problems and also to design new high performance stable rotating machinery. The bulk flow programs can be run on a personal computer with standard memory. They do require the proper calibration to have the analysis predictions match the experimental results. Recent progress of computer analysis makes it possible to apply commercial CFD programs for predicting the leakage flow, detailed velocity and pressure fields and the calculation of the stiffness and damping of machinery gas labyrinth seals. With this progress, the personal computer has the required speed and memory for a 3D analysis of a multi-tooth labyrinth seal in addition to the actual geometry of the entrance leak path. Rhode et al. [17, 18], Ishii et al. [19] and Kwanka et al. [20] calculated the rotordynamic force of gas labyrinth seals using the CFD programs they developed. Moore [21] used SCISEAL, a CFD code specially developed for the analysis of the seals, and compared the results with experiment results and the bulk flow programs. Hirano et al. [22] have presented results for a low speed steam turbine seal including the entry leak path and also an isolated centrifugal compressor eye seal. The evaluation of the leak path flow down the cover or back side of the higher speed centrifugal impeller was not solved at that time due to convergence problems in the solver. The time required to have a single converged solution can vary from hours to weeks in the worst case. The extended solution time points to a major problem in the application of CFD analysis to the complicated geometry of an otherwise simple sealing geometry. The past eight years have been spent working on advances in the analysis of gas labyrinth seals. The major portion of this work was solved using ANSYS-TASCFlow 2.12.1 [23]. The progress to date has been documented in several papers [24–28] and a brief summary of the major results will be discussed in the following section.

2.2 Summary of Prior Work

A typical centrifugal compressor labyrinth seal configuration that has been previously used for calculation of both bulk flow and CFD analysis results [13, 22] is shown in Fig. 1. This figure shows a shaft seal labyrinth, an eye seal labyrinth and a balance drum seal labyrinth. For centrifugal compressors the balance piston is the potential source of the largest excitation mechanism. For CFD evaluation, the large number of teeth on the typical balance piston or balance drum makes it more demanding regarding the memory required to conduct the study. Hence, most CFD work to date has used the impeller eye seal for research studies. The last stage eye seal, just prior to the balance drum is also a major concern due the gas pressure, the diameter and the swirling leakage flow coming from the tip of the impeller. The eye seal geometry consists of a smooth rotor surface and a stator with teeth. The calculations assumed the working fluid to be an ideal gas, the flow to be turbulent and the k-ε model was used for turbulence effects. The swirl at the inlet to the seal is most easily assumed to be zero. The seal force in the tangential direction by TASCFlow is close to those by the bulk flow program (DYNLAB), though there is some difference for the results in the radial direction. The predicted seal forces by TASCFlow are smaller than those by DYNLAB. It means that TASCFlow gives a more stabilizing result compared to the bulk flow solution by DYNLAB.

The former results were similar to other reported comparison of DYNLAB to CFD results for a seal without the leak path channel flow [21, 22]. More details of the research for the normal speed eye labyrinth seal can be found in Kirk and Guo [24]. Initial attempts to include the gas leak path geometry were not successful due to lack of convergence with the grids selected for evaluation. The isolated seal results were very instructive and the comparison to bulk flow analysis indicated

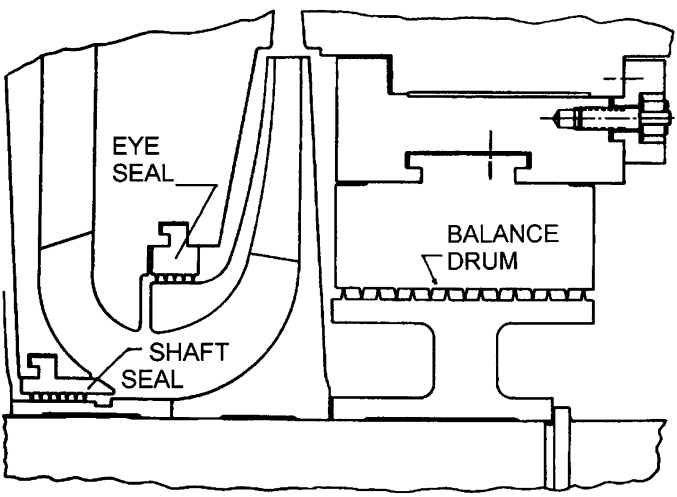

Fig. 1 Typical compressor labyrinth configuration

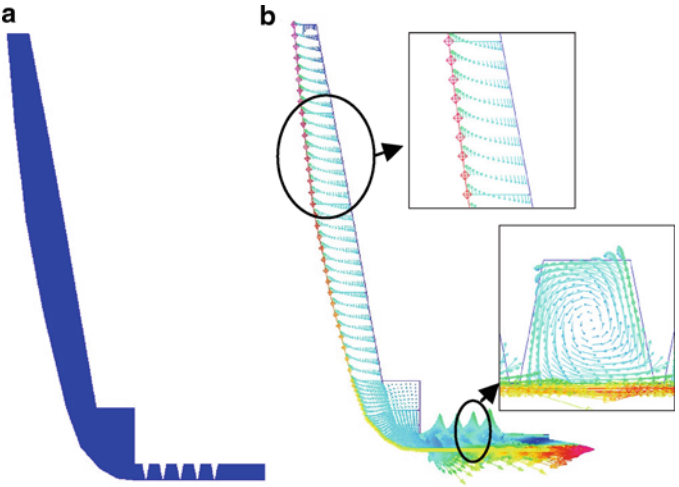

Fig. 2 **(a)** Leak path geometry for the normal speed eye seal. **(b)** Vector plot for the normal speed compressor eye seal, results shown are from Kirk and Guo [24]

that the results were conservative and likely suitable for design analysis of high pressure compressors. The ability to predict the inlet swirl of a seal is however, essential for an accurate prediction of rotor system stability. The bulk flow analysis program used for these comparison studies has an automated calculation of the swirl increase or decrease, depending on geometry of the leak path [13, 16], and this is the central issue for comparison in current and future planned research. The seal geometry of interest was a leak path geometry (see Fig. 2a) similar to that from the impeller tip to the eye seal as shown in Fig. 1. The leak path vector plot (see Fig. 2b) shows the predicted complex swirling flows and resulting jet flow under the tips of the labyrinth teeth. The chamber flow was similar to the isolated seal results of a previous study [22], as would be expected. The leak path or channel region indicates a division of the leaking flow and the reverse pumping region of the channel. About 60% of the channel has the leaking flow field and the remainder is the reverse pumping flow field. This is contrary to the assumed bulk flow simulation where the disk is assumed to be the surface resisting the leakage flow. This result makes it very clear that the disk friction is not what is resisting the inward flow field, rather a liquid interface. This concept has resulted in a modified approach to the analysis of the inlet swirl using the bulk flow solution.

The correct prediction of stiffness and damping is very much dependent on the inlet swirl and the swirl in each chamber of the seal. The swirl ratio results of several different models were calculated for the bulk flow analysis and compared to the CFD prediction from TASCFlow. The variation of the bulk flow results resulted from the modification of the leak path geometry but more importantly, the assumed disk friction coefficients. By reducing the disk surface friction effect, the correct swirl velocity can be nearly matched [24].

These results are for a condition of zero inlet swirl ratio at the tip of the impeller. While the zero inlet swirl is not realistic for a real impeller leakage flow, it can be computed more easily and compared to the same inlet condition for the bulk flow calculation. This then gives a good estimation of what friction effect to use to allow a better match to the CFD results for swirl velocity.

The evaluation of a small high speed centrifugal compressor seals is of increasing interest as the application of gas bearing technology to turbocharger type designs are being evaluated for new applications. The same bulk flow analysis can be used for these seals and the concerns are for the accuracy of the leakage flows and the seal inlet swirl prediction for these designs. The size is much smaller for a typical operating speed of 100,000 RPM (10,466.7 rad/s). The results for such a seal were compared to the bulk flow analysis for similar geometry conditions [25]. The leakage prediction from TASCFlow and the prediction from the bulk flow analysis show good agreement for this high speed seal design, with a maximum of 0.8% difference for the bulk flow results. The pressure drop was in very good agreement and it was possible to improve the match of the swirl ratio by using variation in friction factors in the inlet region and the labyrinth seal chambers.

To investigate the influence of entry channel geometry on the performance of labyrinth seals, a centrifugal compressor eye seal with various entry channel configurations was considered, as shown in Fig. 3. It was discovered that the average swirl was larger for the converging case and smaller for the diverging case at the early part of the entry leak path from the impeller tip, which was the result expected. However, this result switches at about 30% of the leak path and the diverging channel actually displays the larger average swirl pattern and the converging channel case becomes smaller. This is opposite to the original expectation that the converging channel would cause an increase in the tangential swirling velocity due to the converging path. To explain this phenomenon, the tangential velocity plots and velocity vector profiles were examined. From enlarged subplots of velocity vector of the partial entry channel it is observed that the reverse pumping flow decreases when the entry channel changes from the converging, to uniform, and then, to diverging profile.

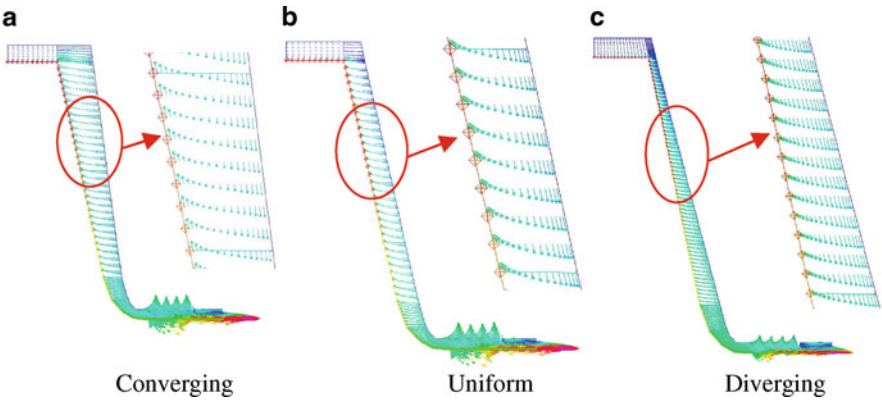

Fig. 3 Velocity vector plots for different inlet channel geometry **(a)** converging **(b)** uniform **(c)** diverging, results from Kirk and Guo [26]

The original bulk flow analysis was developed using the Yamada friction factors (turbulence factors [13]), with the added ability to modify each chamber for either rotor or stator friction factor. In addition, a general global correction factor was also provided to calibrate the results to actual field data or more detailed analysis results.

For the direct comparison between the CFD and bulk flow calculations, the cases with the same tip clearance by both CFD and the bulk flow methods were calculated [26]. In the CFD simulations, the entry swirl was assumed to be zero at the very beginning of the grid inlet. In order to make a reasonable comparison, the bulk flow calculations of either normal disk friction or modified disk friction models use the CFD swirl velocity ratio at the impeller tip as the bulk flow initial swirl ratio condition. For the case having the 1x base clearance, the modified calculations by the bulk flow method were closer to the CFD results. For the initial region of the entry channel, the two results are closer than in the remaining region. In the region of the seal chambers and entry channel near it, the bulk flow overestimates the swirl level, which means that the bulk flow gives a more pessimistic estimate than does the CFD calculation. This fact matches with the conclusions indicated in previous publications [24–28].

3 Synchronous Thermal Instability

In the mid 1990s the concept of a synchronous thermal instability was not well known but the papers by Morton [29,30] generated interest in trying to use this concept to solve a number of machinery field problems. Originally it seemed unlikely to be a candidate for any normal machine since the source of the instability was a fluid-film bearing heating of the shaft in other than a uniform manner. For a well balanced rotor, it seemed impossible that this could be considered seriously, by anyone. In the midst of trying to solve a test stand vibration, a very interesting thing happened. The typical procedure to conduct a stability or forced response analysis of an existing machine design, is to find the bearing characteristics without great concern for the details, such as operating eccentricity. In the midst of trying to confirm why the analysis indicated no critical speed while the machine had a large increase in amplitude of synchronous response, it became evident that the bearings were very lightly loaded and running at very low eccentricity. This condition made it easier to imagine the shaft vibrating with the same hot spot on the journal due to the centered orbit. A modification to load the bearing more eccentric solved the problem and allowed the first documented case for this author [31, 32], of what would become known as the Morton Effect. Just after this study, more and more machinery experts were telling of machines having a similar vibration. A design tool was needed and the initial Morton design program was developed to predict the onset of this problem for overhung machines or normal beam machines with overhung couplings or stages [33, 34]. The original program further developed and improved into the program VTMAP [35]. The program was applied to numerous test stand machines to predict the problems and implement the design changes.

A recent case was a turbine gearbox pinion vibration problem. The desire initially was to determine if the VT-MAP program can predict the known instability in a 28 MW gear pinion rotor. The bearings were a five pad design and load on pivot had been selected by the designers for no load condition and between pivot for full load. The thermal stability analysis evaluates an equivalent overhang mass with a journal orbit predicted by the linear forced response analysis. The temperature across the journal for steady state conditions is then computed and the thermal bow calculated. The thermal imbalance is added to the static imbalance and compared to the instability boundary for this specific machine. The program VT-MAP 3.0 was utilized to automate these calculations. The results of the analysis for this pinion, as shown in Fig. 4, indicate the pinion would become unstable at 12,130 rpm, below the design speed of 13,425 rpm. The test trial weight used for the analysis was a level equal to the old API balance specification. This imbalance is about 1/3 of the balance level used by the OEM in their model of the pinion. The criteria used in this analysis for a problem to occur, is when the thermal imbalance causes the resultant imbalance to increase by more than 50% from the initial cold imbalance level. For this pinion rotor, in the as-is condition and at no load, the instability is predicted to occur below the design speed. The response from Turbine OEM was "I have read your report and we understood the analysis results represent well the actual phenomena. In the 28MW project the instability occurred at the speed of 12800rpm." This is one of several machines over the past ten years that have proven to be accurate predictions of the thermal instability.

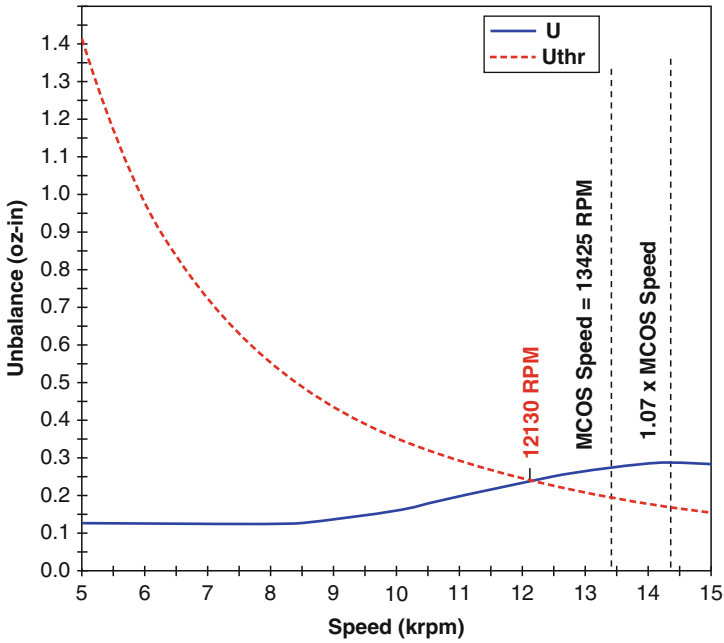

Fig. 4 Thermal synchronous instability prediction by VT-MAP

4 Conclusions

The following conclusions can be stated from the research summarized in this paper:

1. A general purpose CFD code can be used to simulate the flow of complex geometry labyrinth seals.
2. The bulk flow program gives a pessimistic prediction of the destabilizing forces for the conditions under investigation.
3. It is possible to adjust the friction factors of the bulk flow analysis to match more closely the CFD predictions.
4. For the seal model with entry channel, the fluid in the channel regions can have both leaking flow and recirculation flow, which is not usually considered by the bulk flow programs.
5. The CFD simulation shows that the diverging width channel geometry will generate a higher level of seal inlet average swirl ratio than does the uniform width channel condition, while the CFD simulation shows that the converging width channel geometry will generate a lower level of seal inlet average swirl ratio than does the uniform width channel condition.
6. The pinion for the 28 MW turbine was predicted to be unstable at 12,130 rpm from a Morton thermal instability. The actual instability occurred at 12,800 rpm.

5 Recommendations

This paper has summarized the major emphasis of the author's research for the past decade. The labyrinth seal analysis has been automated into a user friendly LabyXL program [36] but the greater needs are in further comparison and calibration to additional CFD solutions for different seal designs and comparison to any available experimental data that is deemed reliable. New gas seal designs will likely take advantage of both mechanical and aerodynamic swirl brakes. It may also be possible to use inlet leak path geometry and enhanced surface friction to reduce the inlet swirl. The further evaluation of thermal synchronous instability is currently being developed at Virginia Tech for both overhung massive rotor sections and also between bearing stages or rotor sections. The goal is a design tool to allow proper design audits to prevent test stand and field problems related to thermal bending of shafting resulting from steady non-uniform journal temperatures.

Acknowledgements The author is thankful to his current and former students who have been involved in the research work discussed in this paper, especially Toshio Hirano, Dr. Zenglin Guo and Dr. Avinash Balbahadur. Thanks are also given to the Virginia Tech Rotordynamics Industry Affiliates Group who have sponsored the majority of this research, with special thanks to Dr. John Nicholas, John Fulton, John Platt, Fred Evans and Dr. Ed Memmott.

References

1. Prohl, M.A.: A general method for calculating critical speeds of flexible rotors. J. Appl. Mech. ASME **67**, A-142–A-148 (1959)
2. Hori, Y.: A theory of oil whip. J. Appl. Mech., Trans. ASME **26**(2), 189–198 (1959)
3. Goodmann, T.P.: A least-squares method for computing balance correction. J. Eng. Ind., Trans. ASME, Ser. B **86**(3), 273–279 (1964)
4. Lund, J.W.: Spring and damping coefficients for the tilting pad journal bearing. Trans. ASLE **7**, 342–352 (1964)
5. Lund, J.W.: Rotor-Bearing Dynamics Technology. Part V, AFAPL-TR-65-45, Aero Propulsion Lab. Wright-Patterson Air Force Base, Dayton, Ohio, May (1965)
6. Gunter, E.J.: Dynamic stability of rotor-bearing systems. NASA SP-113 (1966)
7. Alford, J.S.: Protecting turbomachinery from self-excited rotor whirl. ASME, J.Eng. Power, Ser. A **87**(4), 333–344 (1965)
8. Ruhl, R.L., Booker, J.F.: A finite element model for distributed parameter turborotor systems. ASME, J. Eng. Ind., Ser. B 128–132 (1972)
9. Lund, J.W.: Stability and damped critical speeds of a flexible rotor in fluid-film bearings. ASME J. Eng. Ind., Ser. B **96**(2), 509–517 (1974)
10. Bansal, P.N., Kirk, R.G.: Stability and damped critical speeds of rotor-bearing systems. ASME J. Eng. Ind. **97**(B4), 1325–1332 (1975)
11. Kirk, R.G.: Stability and damped critical speeds: how to calculate and interpret the results. CAGI Tech. Dig. **12**(2), 375–383 (1980)
12. Iwatsubo, T.: Evaluation of instability forces of labyrinth seals in turbines or compressors. In: Proceedings of Rotordynamic Instability Problems in High Performance Turbomachinery, NASA CP-2133, pp. 139–167. Texas A & M University — (1980)
13. Kirk, R.G.: A method for calculating labyrinth seal inlet swirl velocity. ASME J. Vib. Acous. **112**(3), 380–383 (1990)
14. Memmott, E.A.: Stability of centrifugal compressors by applications of tilt pad seals, damper bearings, and shunt holes. In: IMechE, 5th International Conference on Vibrations in Rotating Machinery, pp. 99–106. Bath, — 7–10 Sept. 1992
15. Gunter, E.J., Chen, W.J.: DyRoBeS© - Dynamics of Rotor Bearing Systems User's Manual. RODYN Vibration Analysis, Inc., Charlottesville, VA (2000)
16. Kirk, R.G., Raju, K.V.S., Ramesh, K.: PC-based analysis of turbomachinery vibration. Shock and Vib. Dig. **31**(6), 449–454 (1999)
17. Rhode, D.L., Hensel, S.J., Guidry, M.J.: Labyrinth seal rotordynamic forces using a three-dimensional Navier-Stokes code. ASME J. Tribol. **114**, 683–689 (1992)
18. Rhode, D.L., Hensel, S.J., Guidry, M.J.: Three-dimensional computations of rotordynamic force distribution in a labyrinth seal. STLE Tribol. Trans. **36**(3), 461–469 (1993)
19. Ishii, E., Kato, C., Kikuchi, K., Ueyama, Y.: Prediction of rotordynamic forces in a labyrinth seal based on three-dimensional turbulent flow computation. JSME Int. J., Ser. C **40**(4), 743–748 (1997)
20. Kwanka, K., Sobotzik, J., Nordmann, R.: Dynamic coefficients of labyrinth gas seals: a comparison of experimental results and numerical calculations. ASME International Gas Turbine and Aeroengine Congress & Exhibition, 2000-GT-403 (2000)
21. Moore, J.J.: Three-dimensional CFD rotordynamic analysis of gas labyrinth seals. J. Vib. and Acous., Trans. ASME **125**(3), 427–433 (2003)
22. Hirano, T., Guo, Z., Kirk, R.G.: Application of CFD analysis for rotating machinery, Part 2: labyrinth seal analysis. ASME J. Eng. Gas Turb. and Power **127**(4), 820–826 (2005)
23. ANSYS: TASCflow 2.12.1 Documentation (2003)
24. Kirk, R.G., Guo, Z.: Calibration of labyrinth seal bulk flow design analysis prediction to cfd simulation results. In: Proceedings of IMechE Eighth International Conference on Vibrations in Rotating Machinery, Swansea 3-12 (2004). (The definitive version is available at www.wileyinterscience.com)

25. Kirk, R.G., Guo, Z.: Labyrinth seal forces for a high speed centrifugal impeller eye seal. In: Proceedings of 7th IFToMM-Conference on Rotor Dynamics, Vienna, Austria (2006)
26. Kirk, R.G., Guo, Z.: Influence of leak path friction on labyrinth seal inlet swirl. Tribol. Trans. **52**(2), 139–145 (2009)
27. Guo, Z., Kirk, R.G.: CFD evaluation of turbomachinery secondary flow leak path and labyrinth seal entry swirl. In: Proceedings of ISCORMA-3, Cleveland, Ohio (2005)
28. Kirk, R.G., Guo, Z.: Leak path geometry influence on labyrinth seal inlet swirl velocity ratio. In: BHR 19th International Conference on Fluid Sealing, Poitiers, France (2007)
29. deJongh, F.M., Morton, P.G.: The synchronous instability of a compressor rotor due to bearing journal differential heating. ASME paper, 94-GT-35 (1994)
30. Keogh, P.S., Morton, P.G.: The dynamic nature of rotor thermal bending due to unsteady lubricant shearing within bearing. Proc. Royal Soc. London, Ser. A **445**, 273–290 (1994)
31. Faulkner, H.B., Strong, W.F., Kirk, R.G.: Thermally induced synchronous instability of a radial inflow overhung turbine, part I. In: Proceedings of ASME Design Engineering Technical Conferences, DETC97/VIB-4063, Sacramento (1997)
32. Faulkner, H.B., Strong, W.F., Kirk, R.G.: Thermally induced synchronous instability of a radial inflow overhung turbine, part II. In: Proceedings of ASME Design Engineering Technical Conferences, DETC97/VIB-4174, Sacramento (1997)
33. Balbahadur, A.C., Kirk, R.G.: Part I – Theoretical model for a synchronous thermal instability operating in overhung rotors. In: Proceedings of IFToMM, Sixth International Conference on Rotor Dynamics, Sydney, Australia (2002)
34. Balbahadur, A.C., Kirk, R.G.: Part II – Case studies for a synchronous thermal instability operating in overhung rotors. In: Proceedings of IFToMM, Sixth International Conference on Rotor Dynamics, Sydney, Australia (2002)
35. Kirk, R.G., Guo, Z., Balbahadur, A.C.: Synchronous thermal instability prediction for overhung rotor. In: Proceedings of 32nd Turbomachinery Symposium, Houston (2003)
36. Mehta, R.: Labyrinth Seal Preprocessor and Post-Processor Design and Parametric Study. Master's Thesis, Virginia Tech, May (2008)

Optimized Life Using Frequency and Time Domain Approaches

J.S. Rao

Abstract Life estimation of mechanical components has been practiced for quite some time. There are two approaches available: (1) use the response in time domain and do a cycle counting and (2) determine the response in frequency domain and use a cumulative damage calculation to cross the resonance. These two methods apparently look different and generally not connected. Here we examine these methods and their applicability in determining life of mechanical components and find their suitability for different applications. We will also discuss their common aspects and state their relative advantages and disadvantages.

Keywords Lifing · Time domain · Cycle counting · Frequency domain · Optimized life

1 Introduction

All mechanical components are subjected to alternating forces and fatigue is essentially due to the resulting alternating stresses; Wöhler [1] conducted earliest tests to define S-N diagrams. The influence of mean stress component is presented in Goodman diagrams [2]. Bagci [3] proposed a fourth order relation which is shown to give good results for ductile materials. S-N diagrams and mean stress diagrams are combined to define fatigue failure surface under elastic conditions, see Rao [4]. The fatigue failure surface defined thus is applicable when the stress field is entirely in the elastic region.

Ludwik [5] and Hollomon [6] defined the stress–strain relation in plastic region, $\sigma = K\varepsilon^n$ where K is the strength coefficient and n is strength exponent. For globally elastic and locally plastic structures, Neuber [7] hypothesis is used for relating the nominal and local cyclic stresses and strains, e.g., [8, 9]. For fatigue loading,

J.S. Rao (✉)
Altair Engineering India, Prestige Tech Park, Bangalore 560 087, India
e-mail: js.rao@altair.com

K. Gupta (ed.), *IUTAM Symposium on Emerging Trends in Rotor Dynamics*,
IUTAM Bookseries 25, DOI 10.1007/978-94-007-0020-8_2,

using fatigue stress concentration factor K_f, local stress and strain ranges are related to nominal stress range

$$\Delta\varepsilon\Delta\sigma = \left(K_f \Delta S\right)^2 / E \tag{1}$$

Socie et al. [10] suggest that K_f can be taken to be the theoretical stress concentration factor. Based on Basquin [11] for endurance and Manson [12] and Coffin [13] works, we have a life relation for crack initiation given by

$$\frac{1}{2}\Delta\varepsilon = \frac{1}{E}\sigma_f{}'(2N_i)^b + \varepsilon_f{}'(2N_i)^c \tag{2}$$

Palmgren [14] and Miner [15] gave linear cumulative damage law and Marco and Starkey [16] gave nonlinear damage rule based on the stress amplitude. For other nonlinear relations, see Rao et al. [17]. For details on these aspects, reference may be made to Collins [18] and Rao [19].

Lifing of mechanical components from cumulative damage can be broadly classified into two categories.

1. Components subjected to relatively low alternating stresses that lead to large life in terms of number of cycles of loading; typically the alternating stresses under these conditions arise out of forced vibration from several sources that produce no resonant conditions; usually cycle counting methods in time domain can be adopted for this purpose. The method of lifing can be termed *Time Domain Method*.
2. Components subjected to resonances lead to large alternating stresses; typically such conditions occur during start up and shut down conditions or a given mission of operation when the component crosses several critical speeds. The alternating stresses can then be high because of resonance and correspondingly the life cycles will also be low. The stress values increase rapidly near resonance in a pure harmonic manner while crossing a critical speed and also fall rapidly to nominal values. Lifing is then done for pure harmonic alternating stresses over a mean stress and this lifing can be termed *Frequency Domain Method.* These two methods are discussed as follows.

2 Time Domain

For complex load, stress or strain time histories a cycle counting method is developed by Dowling [20]. He proposed several cycle counting methods: (1) Peak Count, (2) Peak between Mean Crossing Count, (3) Level Crossing Count, (4) Fatigue Meter Count, (5) Range Count, and (6) Range Mean Count.

Each of the above methods are shown to be deficient in some respect or other by Dowling and two additional methods are proposed, viz., Range Pair Method and Rain Flow Method.

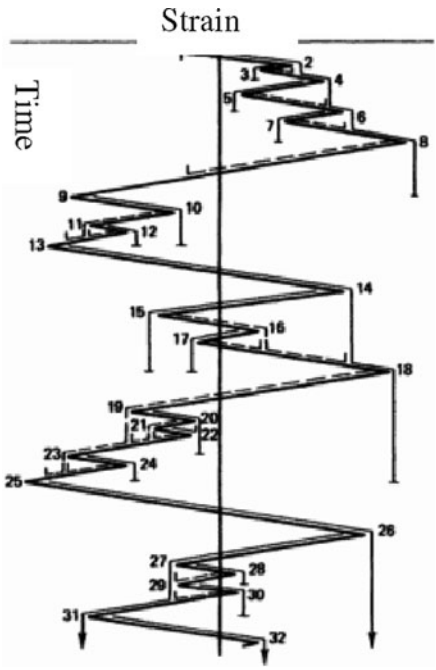

Fig. 1 Range pair cycle counting

Range Pair Method is illustrated in Fig. 1. A strain range is counted as a cycle if it can be paired with a subsequent straining of equal magnitude in the opposite direction. The counted ranges are marked with solid lines and the paired ranges with dashed lines.

The Rain Flow Cycle Counting Method illustrated in Fig. 2 is more widely used than any other method. The lines connecting strain peaks are imagined to be a series of Pagoda roofs. Rules are imposed on rain dropping down these roofs so that cycles and half cycles are defined.

Rainflow begins successively at the inside of each strain peak and is allowed to drop down and continue except that, if it initiates at a minimum, it must stop when it comes opposite a minimum more negative than the minimum from which it initiated. Let us begin at peak 1 in Fig. 2 and stop opposite peak 9, peak 9 being more negative than peak 1. A half cycle is counted between peaks 1 and 8. Similarly if the rain flow initiates at a maximum, it is stopped when it comes opposite a maximum more positive than the maximum from which it is initiated. If we begin at peak 2 and stop opposite peak 4, we count a half cycle between peaks 2 and 3. Every part of the strain time history is counted once only. We can also build from Rain Flow Cycle counting method the stress strain hysteresis loops and thus account for all cycles of loading accurately.

This type of rain flow cycle counting is adopted in many codes, e.g., Altair HyperWorks Fatigue Process Manager [21].

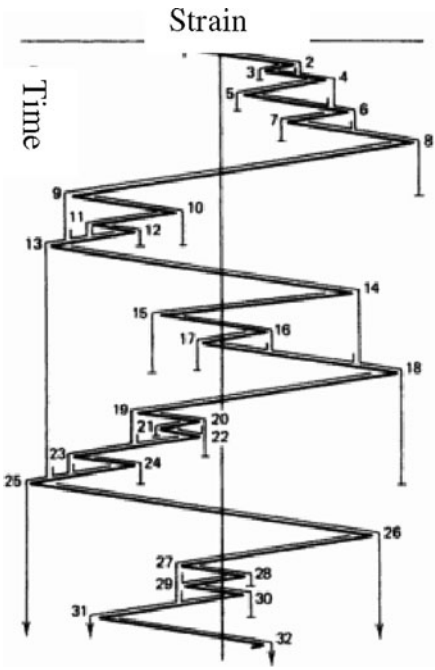

Fig. 2 Rain flow cycle counting

2.1 Some Observations on Time Domain Method

Complex time domain patterns usually mean that the alternating stresses are not at resonance but caused by several excitation frequencies, as in automotive drive train with excitations arising out of engine harmonics, gear mesh from several gear trains in the transmission unit, road excitations … Also in these applications, the natural frequencies are relatively high compared to excitation frequencies from engine speed and harmonics. Traditionally automotive drive train developers resort to laboratory or road tests and the strain signals collected in time domain can be used to make an approximate estimate of life of the structural parts.

In order to obtain correct estimates of life, we need to make first several corrections on the specimen material properties before applying them to the measured time domain signals. They can be size effect, surface finish effect, stress concentration effect, reliability factor … The signals can be measured at a suitable location but not on actual stress raiser locations. Complex time domain signals mean long life and predictions with low level stresses become difficult and compare with test values. Nevertheless, the time domain cycle counting methods are employed in determining the life.

Other disadvantages in time domain method for lifing include:

1. Cycle counting method does not recognize the frequency, it is only the number of cycles that matter.

2. Lifing is made by counting cycles irrespective of the order of application of stress whether it is increasing or decreasing with cycles (or time).
3. Since the frequency is not recognized, the life is given in terms of number of cycles of load rather than hours or days.
4. Frequency plays important role in the response of flexible structures yielding dynamically magnified values near resonant conditions; though time domain signals can be processed in frequency domain, this is not the practice as the data collected can be huge and one has no idea whether there is resonance in the response or not.
5. All the cycles whether the stress amplitudes are large or small are to be included in cycle counting; for each cycle, the mean and range are to be calculated and its damage is to be determined.

As a design tool the time domain method has several limitations listed below.

1. Analytical design produces stress response with several harmonics; only some harmonics or modal components with large amplitudes contribute to the damage – time domain analysis does not recognize this.
2. Damping plays significant role and is rarely viscous in nature. Material damping is always nonlinear and depends on strained condition in the structure. In addition bolted or fabricated joints may have friction between interfacial surfaces. Usually transient analysis to determine the response in time domain or conventional steady state analysis can use only linear damping model.
3. Time domain analysis cannot easily identify the deficiencies in the design.

3 Frequency Domain

Frequency domain methods are now gaining wide applications in aerospace and automotive fields amongst others. They are useful both at the design and test stages. They can be broadly classified into two approaches, viz., (1) when a structural component goes through a critical speed suffering damage and (2) when the structure experiences continuous complex response as considered in time domain analysis.

3.1 Structural Components Crossing Critical Speeds

The first step in this analysis is to determine damping. The damping model in a rotating structure is first obtained experimentally, Rao et al. [22]; their test rig is shown in Fig. 3. They used electromagnets in place of nozzles and thus provide excitation.

The test results are quantified as shown in Fig. 4, which allowed the development of a nonlinear damping model with the equivalent viscous damping expressed as a function of strain amplitude at a reference point in a given mode of vibration at a given speed of rotation.

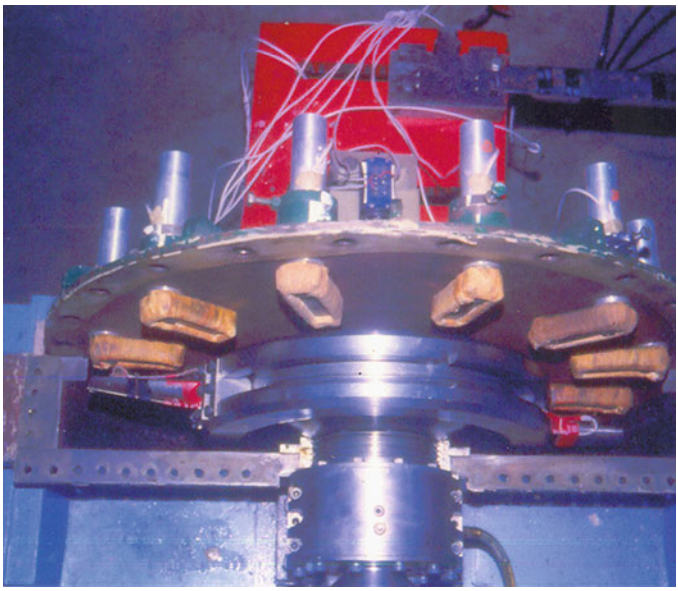

Fig. 3 Blade test rig for damping [22]

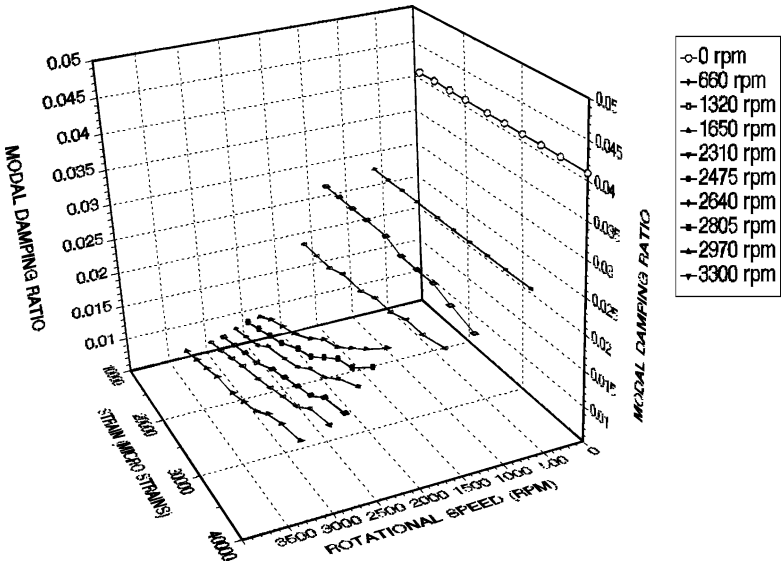

Fig. 4 Nonlinear damping model [22]

Rao and Saldanha [23] developed an analytical procedure using Lazan's hysteresis law [24] to determine such a nonlinear model with material damping. From hysteresis tests with specimens loaded under tension with stress σ, Lazan correlated the damping energy D through hysteresis area to give

$$D = J\left(\frac{\sigma}{\sigma_e}\right)^n \tag{3}$$

where J and n are material constants and σ_e is fatigue strength. If we consider the FE model of a structure, in this case, a bladed disk with each of the element as a test specimen, the total damping energy D_0 (Nm), loss factor η and equivalent viscous damping C (N-s/m) and damping ratio ξ in a given mode of free vibration be obtained from

$$D_0 = \int_0^v D dv; \eta = \frac{D_0}{2\pi W_0}; C = \frac{\eta K}{\omega}; \xi = \frac{C_e}{2\sqrt{Km}} \tag{4}$$

where v is the volume, W_0 is the potential energy in the mode, ω is the natural frequency (rad/s) and K is the modal stiffness (N/m). We can start with an orthonormal mode and choose a convenient reference point to determine the material damping as a function of reference strain amplitude. For increased strain amplitudes the orthonormal reference strain amplitudes, stress and strain energy are multiplied by a factor F to obtain the equivalent viscous damping C_e at various strain amplitudes as given in Eq. (5).

$$\varepsilon' = \varepsilon F; {W_0}' = W_0 \times F^2; \eta' = \frac{{D_0}'}{2\pi {W_0}'}; C_e' = \frac{\eta' K}{\omega_n} F^2; \xi' = \frac{C_e}{2\sqrt{Km}} F^2 \tag{5}$$

A plot of equivalent viscous damping ratio as a function of reference strain amplitude in the chosen mode of vibration defines the nonlinear material damping model. Figure 5 shows a typical material damping model in the first two modes of vibration of a blade rotating at 200 rpm.

3.2 Friction Damping

The friction damping characteristic is obtained by determining the transient response due to an impulse excitation at a suitable point on the blade to simulate the desired mode of vibration and assessing the decay curve. With the help of transient response we can obtain a nonlinear friction damping model of the blade as shown in Fig. 6. Likewise, a combined material and friction damping model can also be developed.

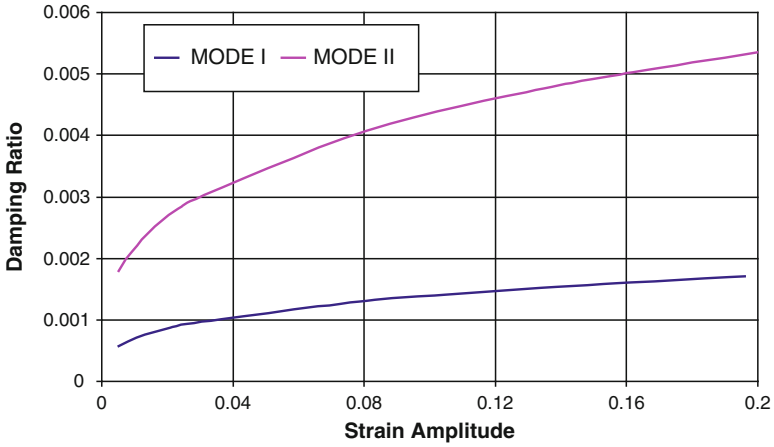

Fig. 5 Material damping model

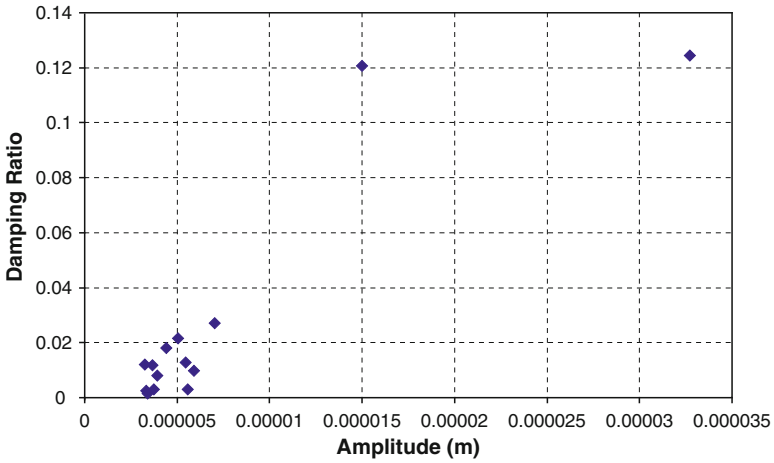

Fig. 6 Friction damping model

3.3 Identification of Critical Speed

Fatigue damage occurs whenever a structure goes through a resonance with the running speed or its harmonics coinciding with any of the natural frequencies. First the natural frequencies are determined as a function of speed and a Campbell diagram is plotted. From the Campbell diagram the critical speeds are identified. When a structure goes through this resonance, large stresses result in and fatigue damage will be predominant here. A typical Campbell diagram and critical speeds are shown in Fig. 7 along with stress response at one critical speed.

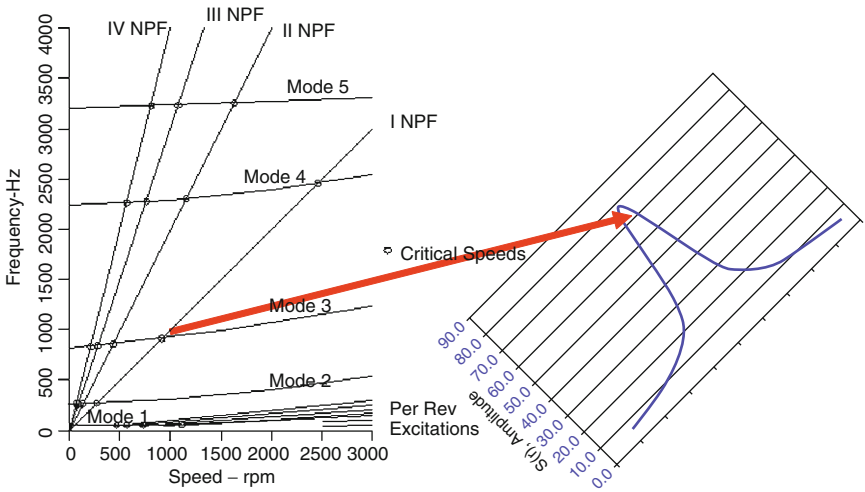

Fig. 7 Resonant response at one of the critical speeds on Campbell diagram

3.4 Resonant Response

This is best determined from fundamental modal properties rather than performing a forced vibration analysis at resonance. The damping is so small in structures, resonance is very sharp and it is difficult to make the excitation frequency and natural frequency coincide. Resonant response is best determined by using quality factor $Q = 1/2\xi$, see Rao and Gupta [25]. Treating the unsteady pressure field or excitation force as steady, steady state response is first determined and multiplied by the quality factor.

The damping ratio is however not known. The damping model developed is highly nonlinear and therefore we need to develop a procedure to handle this damping model. Rao and Vyas [26] developed an iterative procedure for this purpose. Through this procedure one determines the exact resonant stress amplitude through a critical speed.

Once the resonant stress is determined, it is a matter of using modal dynamic magnifier relation [25] given by

$$H(\omega) = \frac{1}{\sqrt{(1-r^2)^2 + (2\xi r)^2}} \tag{6}$$

where r is frequency ratio ω/p. This procedure is developed in Rao et al. [27, 28] *BLADE* that operates on *HyperWorks* platform now called *Altair TurboManager*.

3.5 Cumulative Damage Through Resonance

The stress response before and after resonance and above endurance limit at each critical speed is divided into several steps and a linear [14, 15] or nonlinear cumulative damage [16, 17] is adopted to determine the damage fraction while crossing each critical. Knowing the acceleration with which the blade passes the resonance, each step through resonance is considered with the stress amplitude and the elapsed number of cycles in that step time period. Cumulative damage is then estimated to reach resonance and return to stress levels below fatigue limit. Since the application of stress levels may play a significant role a nonlinear rule is recommended. It is found that decreasing stress from resonant value to fatigue limit consumes more cycles of life; further while the machine is shut down, these damages could be different because acceleration rates will be different. It may be noted that the acceleration through resonance may affect the resonant amplitude as well as speed at which resonance takes place and this may be incorporated in determining the resonant stress, see Rao et al. [27]. The total damage fractions for each start up and shut down operation can be next obtained to give the life in terms of start ups. *TurboManager* is developed to determine this life in frequency domain.

3.6 Example of Propeller Shaft Life in Frequency Domain

Consider the case of simulation of a drive train of an automobile given in Rao et al. [29] and shown in Fig. 8. The drive train has several rotating components operating at different speeds at any given instant depending on which sets of gears are participating in the transmission. Each of the transmission units may contain several

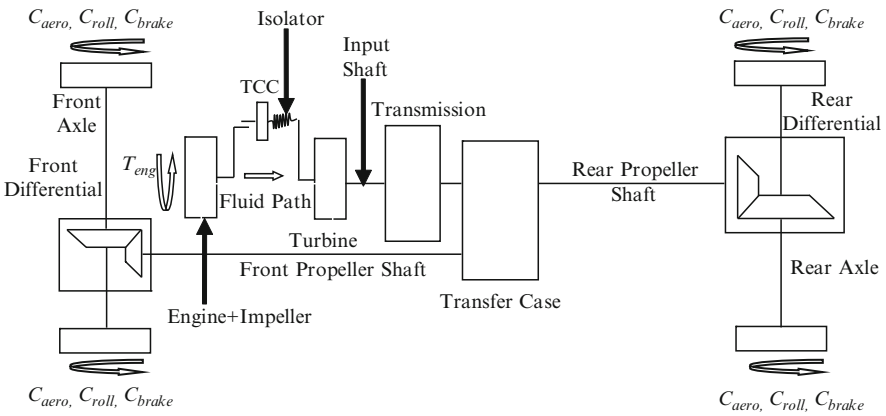

Fig. 8 Drive train model [29]

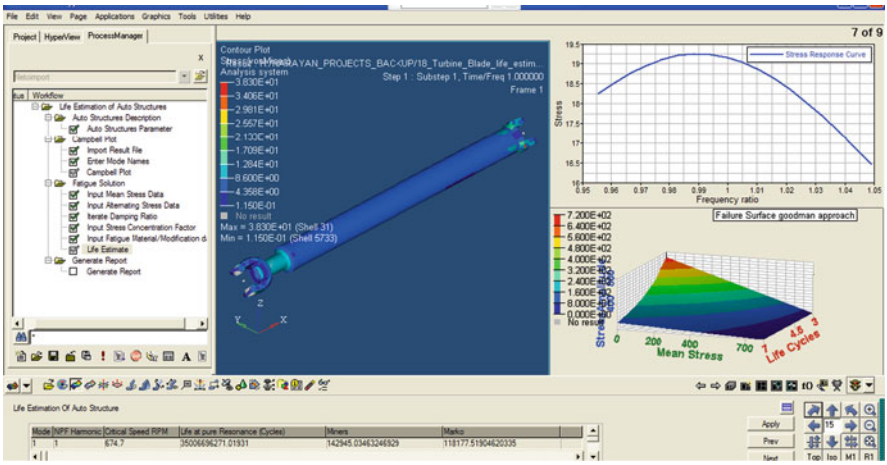

Fig. 9 Stress response and fatigue failure surface

flexible elements transmitting the torque from the engine. The mean torque provides the mean stresses and can be determined from simulation. Maximum value of stress in the propeller shaft of such a train is 28 MPa.

One of the modes of vibration of the drive train in III Mode torsion is 44.98 Hz at engine speed 674.7 rpm [29]. The drive train in Fig. 8 incorporates damping in torque converter and other elements which is fairly larger than the material damping and therefore no material damping is estimated. The alternating stress range at the stress raiser at this speed is found to be 38.3 MPa [30]. The resonant response is then obtained as given in Fig. 9. Using fatigue strength modification factors with the material properties as described in Rao et al. [27], the fatigue failure surface is also shown in Fig. 9.

For stress level above the fatigue limit, assuming a constant stress operation at resonance the life cycles are 3.5×10^{11}, whereas with ten steps in each rise and fall of stress, linear cumulative damage gives 142,945 and non linear cumulative damage gives 118,177 crossings at 674.7 rpm for life.

4 Lifing and Optimization

While lifing technologies have improved providing accurate simulation as discussed above, the next question a designer has – How can I get more life out of this structure within the available constraints? Typically stress raiser locations in any structure give stress concentrations that may be unacceptable and as local plastic conditions are reached under extreme loading the local strains control the life. To get optimum life, a shape optimization in the vicinity of stress raiser can be made to minimize the

stress concentration or minimize the local strain under local plastic conditions. The best shape to give more life is achieved in earlier days through tests and now we can perform a shape optimization and increase life through simulation.

A typical rotating blade [31] under a given unsteady pressure field has its fundamental mode at 344.5 Hz at the operating speed 8,500 rpm Under self excited vibration from low back pressure under power generation well below rated value, life of the blade was predicted from *Blade* [28] as 101.592 minutes.

The blade root experiences a local plastic region. It should be noted that stress in the plastic region does not decrease significantly as the material is yielding, however we can reduce the strain and increase life. Figure 10 shows the space in which we can allow the shape to be altered consistent with manufacturing and design constraints.

Rao and Suresh [32] adopted an optimization using *HyperStudy* [33] and the range of variables given in Table 1. The optimization can be achieved either using elastic or elasto-plastic analysis.

The optimized shapes at 8,500 rpm from *HyperStudy* are given in Table 2.

The maximum stress at stress raiser decreased marginally from 768 to 746 MPa by 22 MPa (2.86%) from baseline elasto-plastic analysis for 8,500 rpm; however the peak plastic strain reduced from 0.0153 to 0.01126 by 26.4%. This is the major advantage in optimization for a blade root shape.

With the optimized shape, the life of the blade estimated by *Altair TurboManager* at 344.51 Hz, increases to 420.9 minutes which is 4.14 times the base line value of 101.592 minutes.

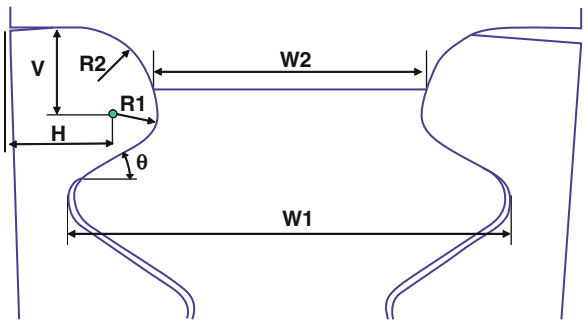

Fig. 10 Shape variables for optimization

Table 1 Shape variable definitions

Min value (mm)	Max value (mm)
W1 = 22.17	W1 = 25.76
W2 = 13.65	W2 = 13.86
R1 = 1.70, H = 5.67,	R1 = 2.14, H = 4.85,
V = 4.13, R2 = 4.0	V = 4.06, R2 = 3.37
$\theta = 29.86°$	$\theta = 16.25°$

Table 2 Optimized configurations under elastic and elasto plastic analyses

Optimized shape (mm) 8,500 rpm – Elastic	Optimized Shape (mm) 8,500 rpm – EP
W1 = 25.43	W1 = 25.48
W2 = 13.86	W2 = 13.82
R1 = 1.89, H = 5.17,	R1 = 2.08, H = 4.96,
V = 4.01, R2 = 4.0	V = 4.07, R2 = 4.0
$\theta = 16.50°$	$\theta = 17.15°$

5 Concluding Remarks

Lifing techniques in time domain and frequency domain are discussed and the advantages of frequency domain method for advanced structures are highlighted.

A special feature in today's technologies is the ability to analytically determine a nonlinear damping model of a rotating structure that enables an accurate estimation of resonant stress at a critical speed. This analytical development allows a true simulation and faster turn around design cycle time.

Optimization techniques are now increasingly employed to minimize stress concentration factors under elastic conditions or minimize local strains for globally elastic but locally plastic structures considering design constraints. A shape optimization thus performed gives the best possible life.

The lifing and optimization procedures together reduce testing costs and bring an accurate solution to advanced structures in getting maximum life.

Acknowledgements The author is thankful to many of his colleagues who performed variety of lifing and optimization problems in Altair India and in IIT Delhi.

References

1. Wöhler, A.: Versuche űber die Festigkeit der Eisenbahnwagen-Achsen. Zeitschrift fűr Bauwesen (1860)
2. Heywood, R.B.: Designing Against Fatigue. Chapman and Hall (1962)
3. Bagci, C.: Fatigue design of machine elements using Bagci line defining the fatigue failure surface line (mean stress diagram). Mechanism and Machine Theory **16**, 339 (1997)
4. Rao, J.S.: Turbomachine Blade Vibration. John Wiley, 1991 and New Age International (1997)
5. Ludwik, P.: Elemente der technologischen mechanik. Springer (1909)
6. Hollomon, J.H.: Tensile deformation. Trans. Am. Inst. Min. Metall. Eng. **162**, 268 (1945)
7. Neuber, H.: Theory of stress concentration for shear-strained prismatical bodies with arbitrary nonlinear stress-strain law. J. Appl. Mech. **8**, 544 (1961)
8. Topper, T.H., Wetzel, R.M., Morrow, J.D.: Neuber's rule applied to fatigue of notched specimens. J. Mater. **4**(1), 200 (1969)
9. Impellizzeri, L.F.: Cumulative damage analysis in structural fatigue, effects of environment and complex load history on fatigue life. STP-462, ASTM, 40 (1970)
10. Socie, D.F., Dowling, N.E., Kurath, P.: Fatigue life estimation of notched members. Proc. 15th Symp. Frac. Mech., STP **833**, 284 (1984)

11. Basquin, O.H.: The experimental law of endurance tests. Proc. ASTM **10**, 625 (1910)
12. Manson, S.S.: Behavior of Materials Under Constant Thermal Stress. Heat Transfer Symposium, University of Michigan, Engineering Research Institute, p. 9 (1953)
13. Coffin, L.F., Jr: A study of the effects of cyclic thermal stresses on a ductile material. Trans. ASME **76**, 931 (1954)
14. Palmgren, A.: Die lebensdauer von kugellagern. ZVDI **68**, 339 (1924)
15. Miner, M.A.: Cumulative damage in fatigue. Trans. ASME, J. Appl. Mech. **67**, A159 (1945)
16. Marco, S.M., Starkey, W.L.: A concept of fatigue damage. Trans. ASME **76**, 627 (1954)
17. Rao, J.S., Pathak, A., Chawla, A.: Blade life – a comparison by cumulative damage theories. J. Eng. Gas Turb. and Power **123**(4), 886 (2001)
18. Collins, J.A.: Failure of Materials in Mechanical Design. John Wiley (1993)
19. Rao, J.S.: Turbine Blade Life Estimation. Alpha Science, UK (2001)
20. Dowling, N.E.: Fatigue failure predictions for complicated stress-strain histories. J. Mater. **7**(1), 71–87 (1972)
21. Altair HyperWorks 9.0 Fatigue Process Manager FMP
22. Rao, J.S., Vyas, N.S., Gupta, K.: Blade damping measurement in a spin rig with nozzle passing excitation simulated by electromagnets. Shock & Vib. Bull. **56**(Pt 2), 109 (1986)
23. Rao, J.S., Saldanha, A.: Turbomachine blade damping. J. Sound and Vib. **262**(3), 731 (2003)
24. Lazan, B.J.: Damping of Materials and Members in Structural Mechanics. Pergamon Press (1968)
25. Rao, J.S., Gupta, K.: Theory and Practice of Mechanical Vibration. John Wiley (1984)
26. Rao, J.S., Vyas, N.S.: Determination of blade stresses under constant speed and transient conditions with nonlinear damping. J. Eng. Gas Turb. and Power, Trans ASME **118**(2), 424 (1996)
27. Rao, J.S., Narayan, R., Ranjith, M.C.: Lifing of Turbomachinery Blades – A Process Driven Approach. GT2008-50231, ASME Turbo Expo 2008, Berlin, Germany, 9–13 June 2008
28. Rao, J.S., Narayan, R., Ranjith, M.C., Rejin, R.: Blade lifing with material and friction damping. The future of gas turbine technology, 4th International Conference, Brussels, Belgium, 15–16 October 2008
29. Rao, J.S., Mahadevappa, V., Dey, P., Rajeshwar, B., Kumar, H.: Automotive driveline simulation. International Conference on CAE, IIT, Madras, 13–15 December 2007
30. Rao, J.S., Narayan, R.: Lifing of Automobile Structures and Drive Trains in Frequency Domain. Automotive Symposium India (ASI), Mumbai, Global Automotive Management Council, Michigan, USA, 4–5 February 2009
31. Rao, J.S., Peraiah, K.C., Singh, U.K.: Estimation of dynamic stresses in last stage steam turbine blades under reverse flow conditions. Advances in Vibration Engineering, J. Vib. Inst. India **8**(1), 71 (2009)
32. Rao, J.S., Suresh, S.: Blade root shape optimization. The Future of Gas Turbine Technology, 3rd International Conference, Brussels, October (2006)
33. Altair HyperStudy: User's Manual v7.0. Troy, MI (2003)

Dynamic Modeling of Rotors: A Modal Approach

G. Genta

Abstract Dynamic modeling of rotors is usually performed under the assumption that the rotating parts of the machine are axially symmetrical, while the non-rotating ones may have no particular symmetry properties. The rotor model, based on the FEM, can be reduced in modal form and then assembled in the FEM model of the stator of the machine. Different rotors, rotating at different speeds, can be assembled on the same stator, even if the rotors are not coaxial.

The rotor need not to be axially symmetrical, a cyclic symmetry of order 3 or higher being required. Modal modeling of rotors is dealt with in detail, and an example shows the effects of modal truncation on the precision of the results for a rotor with substantial gyroscopic and non-rotating damping effects. The algorithms are here developed for 1-D and $1^1/_2$-D beamlike rotors models but generalization to full 3-D modeling is possible.

Keywords Rotordynamics · FEM modeling · Modal component synthesis

1 Introduction

The dynamic study of rotating machines is mostly performed by modeling the rotor (and often also the stator) as a "beamlike" object, i.e., by resorting to one-dimensional (1-D) models. If the flexibility of the discs and even of the blades (in turbomachinery) must be accounted for, models in which the displacements of discs and blades are expressed as Fourier series in the angle can be devised. This approach is usually referred to as one-and-one-half dimensional ($1^1/_2$-D) [1–3]. The DYNROT FEM code, for instance, operates in this way [4]. In this case also the stator must be modeled using a 1-D (or a $1^1/_2$-D) approach.

The difficulties of using a full three dimensional approach, as that described in Geradin and Kill [5], are linked with a possible lack of symmetry of both

G. Genta (✉)
Politecnico di Torino, Department of Mechanics, Corso Duca degli Abruzzi 24,
10129 Torino, Italy
e-mail: giancarlo.genta@polito.it

K. Gupta (ed.), *IUTAM Symposium on Emerging Trends in Rotor Dynamics*,
IUTAM Bookseries 25, DOI 10.1007/978-94-007-0020-8_3,

the rotor and the stator. In particular, the latter can hardly be assumed as an axisymmetric body. The presence of a non axisymmetric stator compels to study the dynamics of the system in a reference frame fixed to it, usually an inertial frame. If the rotor is not axially symmetrical, the equations of motion are not time-invariant, even if in constant speed operation their coefficients are periodic in time with a period equal to half the period of rotation [1]. Actually, axial symmetry is not required: it is sufficient that the rotor has a cyclic symmetry of order 3 or higher [6].

A possible approach to the study of a complex rotating machine, made of one or more rotors and a stator, is to resort to the FEM, coupled to Component Mode Synthesis (CMS), as described first by Craig and Bampton in 1968 [7]. Codes like ARDS by NASA Lewis Research Center, XLTRC by Texas A&M University, Dynamics R4 by Alfa-Tranzit and Samcef by Samtech, operate in this way. Some of them have a 1-D formulation, others are fully 3-D or allow mixing the two approaches for different parts of the machine.

Each rotor can be reduced to a superelement by assuming as boundary degrees of freedom those corresponding to the generalized forces exerted by the devices connecting it to the other parts of the machine (bearings, dampers, seals, etc.) and as internal degrees of freedom all the others. Modal analysis can thus be performed constraining the rotor in correspondence to the boundary degrees of freedom and neglecting rotation, damping and centrifugal stiffening.

This does not detract from the precision of the results and if all modes are retained the same results obtained without modal synthesis are reached. However, the number of modes needed to reach a satisfactory solution may be large.

Cyclic symmetry causes the modes to be of three types [6, 8, 9]:

1. Modes in which all sectors displace in an identical way. They are related to zero-order axial, torsional or radial extensional modes of disc-type structures. They do not exhibit degeneracy, resulting in distinct eigenfrequencies.
2. Modes in which all substructures displace in an identical way, but with a phasing of 180° from each other. They can exist only if the symmetry order m is even and have the same properties as those of the first type.
3. Modes exhibiting a two-fold degeneracy. The corresponding eigenfrequencies come in pairs with identical values, like in axi-symmetric structures. A mode of this type can be rotated by any angle about the symmetry axis (i.e., the spin axis), and the result is still an eigenvector with the same eigenvalue.

If the rotation axes of the rotors are all parallel and the stator is such that axial and radial forces applied in correspondence to the thrust bearings and torsional moments applied to the rotors produce uncoupled deformations, it is possible to study separately axial and torsional vibrations, coupled to the modes of type 1 (and possibly 2) and lateral vibration coupled to modes of type 3. In the most general case, the stator couples all the rotor modes.

In case the system has a nonlinear behavior, nonlinearities are often concentrated in the bearings, dampers and seals, while the rotors are linear. The modal approach allows thus to reduce the size of the problem, a thing that in nonlinear dynamics is even more important than in linear dynamics.

2 Analysis

The aim of the present work is that of showing a general approach to converting the 1-D and $1^1/_2$-D rotor model obtained using the complex coordinates approach (for instance using the DYNROT code) to a "rotor superelement" through the application of component element synthesis.

2.1 Generalized Coordinates

The complex displacements and rotations involved in flexural behavior are

$$r = u_x + iu_y,\ \phi = \phi_y - i\,\phi_x \tag{1}$$

where u_x, u_y, ϕ_x and ϕ_y are the nodal displacements and rotations.

The axial displacement u_z and the torsional rotation φ_z must then be added. Each node has thus two real plus two complex degrees of freedom.

In case of $1^1/_2$-D modeling, some nodes are not located on the rotation axis and the number of degrees of freedom is higher. Depending on the exact formulation of the node [2–4], the number of degrees of freedom spans from four to five complex degrees of freedom for bending behavior plus three to four real degrees of freedom for axial and torsional behavior. Axial and torsional dynamics are coupled when the blades are twisted or set at an angle with respect to the axial direction.

Component element synthesis is at its best where the system is complex, with a number of rotors, running possibly at different speeds and possibly spinning about axes which are neither coincident nor parallel, and a complex stator. Codes based on complex coordinates like DYNROT cannot be used directly in this case.

Since the stator is modeled using standard finite elements, the rotor superelement obtained through component mode synthesis must be described in terms of real coordinates, at least at its boundary nodes, while the internal degrees of freedom of each rotor can be expressed using any kind of coordinates. The stator itself can be reduced using the component mode synthesis, by dealing with the degrees of freedom of the nodes that are connected to the rotor(s) and those at which the stator is supported as boundary degrees of freedom and using modal coordinates for all internal nodes. This is however immaterial for what follows: here the stator is assumed to be a general FEM model of any kind, provided that its interface with the rotor is made of nodes whose degrees of freedom are the displacements in the direction of the reference axes of the "global" reference frame.

Each rotor has its own "element" reference frame $x_i\,y_i\,z_i$ (with z_i axis along the spin axis) and its own (constant) spin speed Ω_i. A number k_i of boundary nodes are defined. The displacements in x_i and y_i directions are related to radial bearings, dampers and possibly seals, while displacements in z_i direction are related to thrust bearings, dampers or seals. This approach is redundant, since a boundary node can be constrained in just one or two directions: by reasoning in terms of boundary

degrees of freedom and not of boundary nodes a smaller model can be obtained. This would however preclude the possibility of studying cases in which the reference frame of the rotor is skew with respect to the global reference frame.

The boundary degrees of freedom of the ith rotor are thus $3k_i$.

This approach, mainly justified by the need of matching the "beamlike" structure of the rotor with the solid elements modeling of the stator, has its advantages and as well its drawback. A clear advantage is that of allowing to use the complex-coordinates formulation for the rotor without bothering about the sign conventions for rotational coordinates in the yz plane that are inconsistent with the usual ones and do not allow to use standard rotation matrices.

The main drawback is that no torque can be applied on the rotor at the interface points. For the lateral dynamics of the rotor this means that the bearing can be modeled as compliant supports but not as compliant clamps, which is fairly realistic. If bearings that can transfer bending moments are used, like preloaded packs of ball bearings, it is always possible to model them as at least two connections located at a certain distance, which in most cases is even more realistic.

The impossibility of constraining the rotation of a boundary node leads to the impossibility of constraining the rotors against rotation. In most cases this is not a problem: a rotor is usually not constrained in rotation to the stator of the machine. It can receive a driving or braking torque: this torque can be modeled as such on the rotor and the corresponding reaction can be modeled as forces on the stator, following the actual layout. If there are several rotors, they can be constrained to each other in rotation, using rigid or elastic constraints to model gear wheels, chains, belts or any other transmission device. Since this involves only torsional dynamics, that in most cases is uncoupled, there is no problem in introducing this effect. It is also possible to account for the bending loads due to meshing gears or belts.

2.2 Formulation of the Rotor Model

The model for the lateral behavior of the ith rotor can be written as [1]

$$\mathbf{M}_b\ddot{\mathbf{q}}_b + (\mathbf{C}_b + i\,\Omega\mathbf{G}_b)\,\dot{\mathbf{q}}_b + \left(\mathbf{K}_b + \Omega^2\mathbf{K}_{b\Omega} + i\,\Omega\mathbf{C}_b\right)\,\mathbf{q}_b = \mathbf{F}_b(t), \qquad (2)$$

where subscripts i for all matrices and vectors have been dropped. All matrices are real and symmetric, while the vectors of the generalized coordinates and forces are complex, with the real and imaginary parts referring to the xz and the yz planes respectively. The generalized coordinates of each node are those defined in Eq. (1).

Matrix $\mathbf{C}_b$ is a rotating damping matrix, but there is no non-rotating matrix since there is no stator element included in this model.

The model for the torsional and axial behavior, that may be coupled owing to the presence of blades, is

$$\mathbf{M}_{ta}\ddot{\mathbf{q}}_{ta} + \mathbf{C}_{ta}\dot{\mathbf{q}}_{ta} + \left(\mathbf{K}_{ta} + \Omega^2\mathbf{K}_{ta\Omega}\right)\mathbf{q}_{ta} = \mathbf{F}_{ta}(t)\,. \tag{3}$$

Here the generalized coordinates of the nodes are u_z and ϕ_z and all matrices and vectors are real.

3 Modal Reduction

3.1 First Approach

In the first approach Eq. (2) is first transformed from complex to real coordinates by doubling the number of equations

$$\begin{bmatrix} \mathbf{M}_x & \mathbf{0} \\ \mathbf{0} & \mathbf{M}_y \end{bmatrix} \begin{Bmatrix} \ddot{\mathbf{x}}_b \\ \ddot{\mathbf{y}}_b \end{Bmatrix} + \left(\begin{bmatrix} \mathbf{C}_x & \mathbf{0} \\ \mathbf{0} & \mathbf{C}_y \end{bmatrix} + \Omega \begin{bmatrix} \mathbf{0} & \mathbf{G}_{xy} \\ -\mathbf{G}_{yx} & \mathbf{0} \end{bmatrix} \right) \begin{Bmatrix} \dot{\mathbf{x}}_b \\ \dot{\mathbf{y}}_b \end{Bmatrix}$$
$$+ \begin{bmatrix} \mathbf{K}_x & \mathbf{0} \\ \mathbf{0} & \mathbf{K}_y \end{bmatrix} + \left(\Omega^2 \begin{bmatrix} \mathbf{K}_{x\Omega} & \mathbf{0} \\ \mathbf{0} & \mathbf{K}_{y\Omega} \end{bmatrix} + \Omega \begin{bmatrix} \mathbf{0} & \mathbf{C}_{xy} \\ -\mathbf{C}_{yx} & \mathbf{0} \end{bmatrix} \right) \begin{Bmatrix} \mathbf{x}_b \\ \mathbf{y}_b \end{Bmatrix} = \begin{Bmatrix} \mathbf{F}_{xb}(t) \\ \mathbf{F}_{yb}(t) \end{Bmatrix} \tag{4}$$

- Matrices $\mathbf{M}_x$, $\mathbf{C}_x$, $\mathbf{K}_x$ and $\mathbf{K}_{x\Omega}$ coincide with matrices $\mathbf{M}_b$, $\mathbf{C}_b$, $\mathbf{K}_b$ and $\mathbf{K}_{b\Omega}$ respectively.
- Matrices $\mathbf{M}_y$, $\mathbf{C}_y$, $\mathbf{K}_y$ and $\mathbf{K}_{y\Omega}$ coincide with matrices $\mathbf{M}_b$, $\mathbf{C}_b$, $\mathbf{K}_b$ and $\mathbf{K}_{b\Omega}$ with all terms with subscripts that add to an odd number changed in sign.
- Matrices $\mathbf{G}_{xy}$ and $\mathbf{C}_{xy}$ coincide with matrices $\mathbf{G}_b$ and $\mathbf{C}_b$ with all even columns changed in sign.
- Matrices $\mathbf{G}_{yx}$ and $\mathbf{C}_{yx}$ coincide with matrices $\mathbf{G}_b$ and $\mathbf{C}_b$ with all even rows changed in sign.
- Vectors $\mathbf{x}_b$ and $\mathbf{F}_{xb}(t)$ coincide with the real part of vectors $\mathbf{q}_b$ and $\mathbf{F}_b(t)$.
- Vectors $\mathbf{y}_b$ and $\mathbf{F}_{yb}(t)$ coincide with the imaginary part of vectors $\mathbf{q}_b$ and $\mathbf{F}_b(t)$, with all even terms changed in sign.

At this point the order of rows and columns of all matrices and vectors is changed, listing first the translational coordinates of the boundary nodes, then all other coordinates. The coordinates in $\mathbf{x}_b$ and $\mathbf{y}_b$ are mixed at this point, so that their order is that usually considered. Actually, this is needed only for boundary nodes, while the generalized coordinates for internal nodes can retain their original order (first *xz*, then *yz* plane). The axial and torsional behavior can be integrated with the bending behavior at this level, but since it is uncoupled, modal reduction can be performed separately to reduce the size of the eigenproblem.

Using subscript 1 for the boundary degrees of freedom and subscript 2 for internal degrees of freedom, it thus follows

$$\begin{bmatrix} \mathbf{M}_1 & \mathbf{M}_{12} \\ \mathbf{M}_{21} & \mathbf{M}_2 \end{bmatrix} \begin{Bmatrix} \ddot{\mathbf{x}}_1 \\ \ddot{\mathbf{x}}_2 \end{Bmatrix} + \left(\begin{bmatrix} \mathbf{C}_1 & \mathbf{C}_{12} \\ \mathbf{C}_{21} & \mathbf{C}_2 \end{bmatrix} + \Omega \begin{bmatrix} \mathbf{G}_1 & \mathbf{G}_{12} \\ \mathbf{G}_{21} & \mathbf{G}_2 \end{bmatrix} \right) \begin{Bmatrix} \dot{\mathbf{x}}_1 \\ \dot{\mathbf{x}}_2 \end{Bmatrix}$$
$$+ \begin{bmatrix} \mathbf{K}_1 & \mathbf{K}_{12} \\ \mathbf{K}_{21} & \mathbf{K}_2 \end{bmatrix} + \left(\Omega^2 \begin{bmatrix} \mathbf{K}_{1\Omega} & \mathbf{K}_{12\Omega} \\ \mathbf{K}_{21\Omega} & \mathbf{K}_{2\Omega} \end{bmatrix} + \Omega \begin{bmatrix} \mathbf{C}_1 & \mathbf{C}_{12} \\ \mathbf{C}_{21} & \mathbf{C}_2 \end{bmatrix} \right) \begin{Bmatrix} \mathbf{x}_1 \\ \mathbf{x}_2 \end{Bmatrix} = \begin{Bmatrix} \mathbf{F}_{1b}(t) \\ \mathbf{F}_{2b}(t) \end{Bmatrix} \tag{5}$$

where the overall gyroscopic and rotating damping matrices are skew-symmetric.

Mode component synthesis is applied at this point. The eigenvector matrix Φ of the MK system whose mass and stiffness matrices are $\mathbf{M}_2$ and $\mathbf{K}_2$ is computed.

Owing to axial symmetry, all flexural modes exhibit a two-fold degeneracy. As a consequence, the eigenvectors are not said to lie in either *xz* or *yz* planes, since any linear combination of the two modes with any given eigenvector is itself a mode. This however is not a reason of concern, except for possible numerical problems it might cause. A reduced eigenvector matrix $\boldsymbol{\phi}^*$, in which only a number of modes (usually those with the lowest eigenfrequencies) are retained, is used to perform modal reduction. Since they come in pairs, the number of flexural modes must be even. The transformation matrix is the usual one [10]

$$\Psi = \begin{bmatrix} \mathbf{I} & \mathbf{0} \\ -\mathbf{K}_{22}^{-1}\mathbf{K}_{21} & \Phi^* \end{bmatrix}, \tag{6}$$

and the reduced matrices and force vector are

$$\mathbf{M}^* = \boldsymbol{\Psi}^T \mathbf{M} \boldsymbol{\Psi}, \quad \mathbf{G}^* = \boldsymbol{\Psi}^T \mathbf{G} \boldsymbol{\Psi}, \quad \mathbf{C}^* = \boldsymbol{\Psi}^T \mathbf{C} \boldsymbol{\Psi}, \quad \mathbf{K}^* = \boldsymbol{\Psi}^T \mathbf{K} \boldsymbol{\Psi},$$
$$\mathbf{K}_\Omega^* = \boldsymbol{\Psi}^T \mathbf{K}_\Omega \boldsymbol{\Psi}, \quad \mathbf{C}_r^* = \boldsymbol{\Psi}^T \mathbf{C}_r \boldsymbol{\Psi}, \quad \mathbf{f}^* = \boldsymbol{\Psi}^T \mathbf{f}. \tag{7}$$

If the torsional and axial matrices were not assembled earlier, they can be reduced at this point and then assembled to the bending matrices.

3.2 Second Approach

Modal reduction can be performed before passing from complex to real coordinates. The procedure is the same as seen above, but now the partitioned matrices in an equation having the same structure as Eq. (5) are built starting from the matrices in Eq. (7). In this case the complex coordinates $\mathbf{q}_1$ are the complex displacements of the boundary nodes, while $\mathbf{q}_2$ are the complex displacements and rotations of the internal nodes. All matrices are symmetrical and their size is half the size of the corresponding matrices in the previous approach. The eigenvectors of the MK eigenproblem have no degeneracy and this can help simplifying the problem and avoiding numerical problems.

Once matrices $\mathbf{M}^*$, $\mathbf{K}^*$, etc. have been obtained, it is possible to pass to real coordinates

$$\begin{bmatrix} \mathbf{M}^* & \mathbf{0} \\ \mathbf{0} & \mathbf{M}^* \end{bmatrix} \begin{Bmatrix} \ddot{\mathbf{x}}_b \\ \ddot{\mathbf{y}}_b \end{Bmatrix} + \left(\begin{bmatrix} \mathbf{C}^* & \mathbf{0} \\ \mathbf{0} & \mathbf{C}^* \end{bmatrix} + \Omega \begin{bmatrix} \mathbf{0} & \mathbf{G}^* \\ -\mathbf{G}^* & \mathbf{0} \end{bmatrix} \right) \begin{Bmatrix} \dot{\mathbf{x}}_b \\ \dot{\mathbf{y}}_b \end{Bmatrix}$$

$$\begin{bmatrix} \mathbf{K}^* & \mathbf{0} \\ \mathbf{0} & \mathbf{K}^* \end{bmatrix} + \left(\Omega^2 \begin{bmatrix} \mathbf{K}^*_\Omega & \mathbf{0} \\ \mathbf{0} & \mathbf{K}^*_\Omega \end{bmatrix} + \Omega \begin{bmatrix} \mathbf{0} & \mathbf{C}^* \\ -\mathbf{C}^* & \mathbf{0} \end{bmatrix} \right) \begin{Bmatrix} \mathbf{x}_b \\ \mathbf{y}_b \end{Bmatrix} = \begin{Bmatrix} \mathbf{F}^*_{xb}\ (t) \\ \mathbf{F}^*_{yb}\ (t) \end{Bmatrix} \quad (8)$$

where now $\mathbf{x}_b$ and $\mathbf{y}_b$ are vectors containing only translational coordinates (for the first few rows) and modal coordinates (the remaining rows). Since no sign problem is involved for translational coordinates, there is no need for sign changes.

4 The Rotor Superelement

Once the reduced matrices of the rotor have been obtained, the final order of the degrees of freedom is:

- A number $3n$ displacement degrees of freedom (u_x, u_y and u_z) for the n boundary nodes, ordered in subsequent groups, one for each node.
- A number m of modal coordinates for bending (in the two planes), axial and torsional (or coupled axial-torsional) modes. The number of modes used for bending in the two planes must be the same, but bending, axial and torsional modes may differ in number.

If the rotors are linked together torsionally, it is possible to insert a number of boundary degrees of freedom for torsional behavior between the degrees of freedom of the first group and those of the second. In the case such a connection is performed using gear wheels, belts, etc., with a gear ratio different from unity, suitable equivalent inertia and stiffness for torsional motion must be used since the start of the computation. These torsional boundary degrees of freedom must be assembled in a suitable way, following the layout of the system, but this assembling procedure does not need rotation.

The rotation matrix for the superelement has the structure

$$\mathbf{R} = \begin{bmatrix} \mathbf{R}' & \ldots & \mathbf{0} & \mathbf{0} \\ \ldots & \ldots & \ldots & \ldots \\ \mathbf{0} & \ldots & \mathbf{R}' & \mathbf{0} \\ \mathbf{0} & \ldots & \mathbf{0} & \mathbf{I} \end{bmatrix} \quad (9)$$

where the 3×3 matrices are the n identical rotation matrices needed to rotate the displacements of the boundary nodes and $\mathbf{I}$ is an identity matrix of order m (modal coordinates do not need to be rotated). If some torsional degrees of freedom are assembled, the corresponding rows and columns contain an identity matrix.

5 Example

To evaluate the precision attainable with the present approach for a rotor modeled using the $1^1/_2$-D approach, the rotor of a turbomolecular pump will be studied. The sketch of the model, built using the DYNROT code, is shown in Fig. 1.

The rotor is made by a shaft, on which an electric motor and the magnetic bearings are assembled, plus a bell-shaped part carrying 12 discs, eight of which bladed. The model is made by 124 elements (74 beam, 14 disc, 15 blade, 13 beam-disc transition, 8 disc-blade transition elements), connecting 108 nodes. The total number of complex degrees of freedom involved in the lateral behavior is 339.

Since the example is meant to evaluate the errors introduced by modal reduction in a single rotor, the axial, torsional and bending behavior are assumed to be uncoupled.

The boundary nodes are the third node at the left, where the axial constraint is applied (actually the constraint should be applied to the disc of the axial bearing, but the present model required that constraint are applied to a node connected to a beam element) and the two nodes where there are the radial bearings (shown as springs in Fig. 1). This amounts to assuming that the sensor-actuator pairs of the bearings are co-located, but this issue has no importance for the aim of the present example. The number of the boundary degrees of freedom is thus nine.

The stator thus reduces to an axial spring applied to the first boundary node and two radial springs applied to the following two. A low value of the stiffness is assumed, namely 10^6 N/m, also because in this way the shapes of the constrained modes are quite different from the actual mode shapes of the system, maximizing the errors due to modal reduction.

The Campbell diagram related to the bending modes was first computed using the standard DYNROT routine. The result is reported in Fig. 2 (dashed lines).

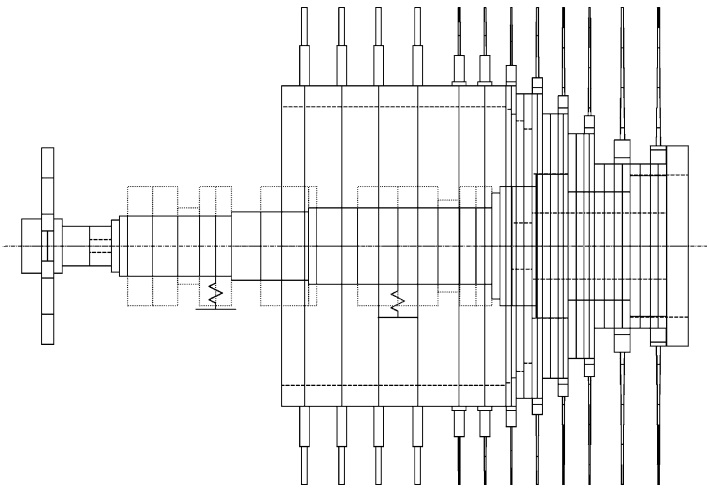

Fig. 1 FEM model of the rotor of a turbomolecular pump

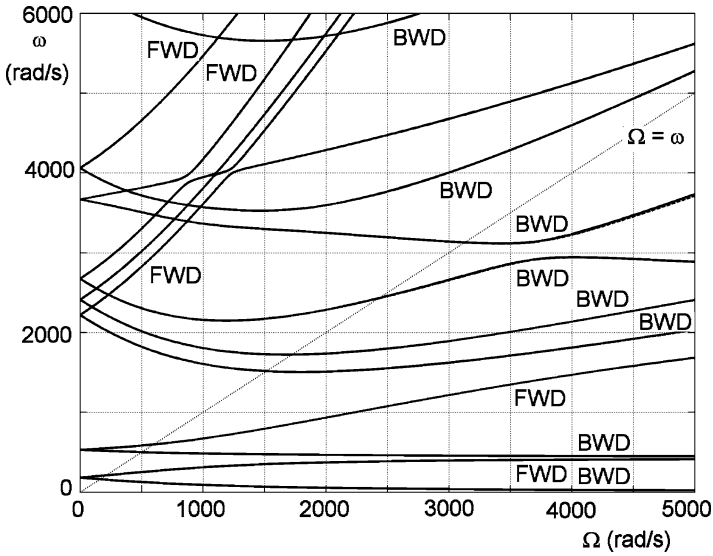

Fig. 2 Campbell diagram obtained from the nonmodal computation (dashed lines) and the modal computation with 50 modes (full lines)

The computation has then been repeated extracting all matrices from the DYNROT code and applying the procedure referred above as "second approach", retaining 50 modes from the complex model. The total number of degrees of freedom for the flexural problem is thus 106 (six boundary plus 100 modal degrees of freedom). The result is reported in Fig. 2 (full lines).

The two approaches yield the same results, within the thickness of the line. From the Campbell diagram it is clear that both the gyroscopic and the centrifugal stiffening effects are quite large, particularly in the modes 3, 4, 5 and 7 (forward and backward, even if there is an exchange between the mode 6 and 7). These modes are clearly disc-blades modes: the backward modes first decrease their frequency (gyroscopic effect), to increase it at a higher speed (centrifugal stiffening).

The forward modes increase sharply, due to both effects, and remain subcritical even at high speed (explaining why blade damping is always stabilizing).

These results are quite obvious, since 50 modes is quite a large number, and their interest is just showing that no error (larger than 0.02%) was introduced in the implementation of the procedure. The largest errors are those of modes 5 BWD and 7 BWD, which at 5,000 rad/s are of 0.17% and 0.54% respectively.

The computation was repeated using 5 modes. The total number of degrees of freedom for the flexural problem is 16 (6 boundary plus 10 modal). The result is reported in Fig. 3, together with the results of the nonmodal computation.

At low speed the accuracy with which the first 5 forward and 5 backward modes is obtained is remarkable. With increasing speed gyroscopic and centrifugal stiffening effects cause the lower modes to be mostly backward and the precision

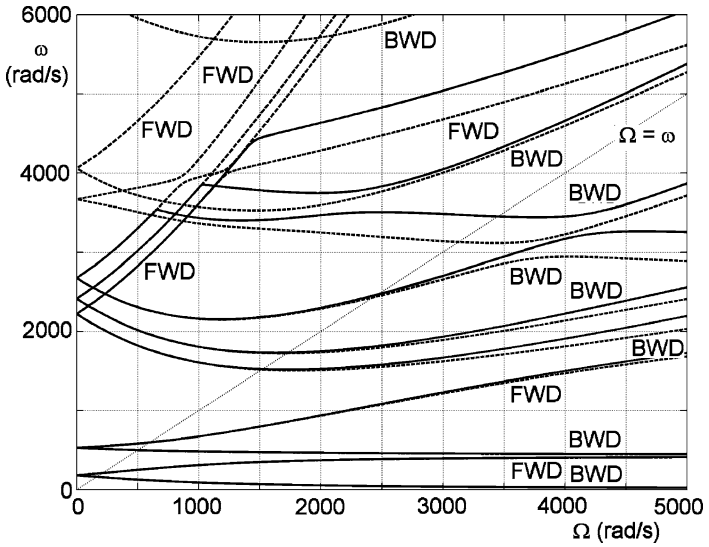

Fig. 3 Campbell diagram obtained from the nonmodal computation (dashed lines) and the modal computation with five modes (full lines)

decreases. The errors (expressed as %) at 5,000 rad/s are reported in the second line of the table below. The errors obtained using 10 modes (a total of 26 degrees of freedom) are reported in the third line of the same table.

Mode	1 BWD	1 FWD	2 BWD	2 FWD	3 BWD	4 BWD	5 BWD	6 BWD	7 WD	3 FWD
Error	0.044	0.020	0.020	2.60	7.41	5.80	11.46	4.03	1.96	7.22
Error	0.014	0.015	0.011	0.97	7.28	5.23	1.014	3.57	1.82	2.23

The presence of blades inclined with respect to the axial direction causes the axial and torsional behavior to couple. The total number of torsional and axial degrees of freedom is 289. Again the computation was performed using the nonmodal procedure and the modal one, obtaining errors on the first 10 natural frequencies smaller than 0.01%.

The analysis was then performed using 10 modes, i.e., a total of 13 degrees of freedom (3 boundary and 10 modal). The result is reported in Fig. 4 (full lines), compared with those obtained using the nonmodal approach (dashed lines).

The errors (expressed as percentages) for the first 10 modes (note the first mode has a natural frequency equal to 0, since the system is torsionally not constrained) at the maximum speed (5,000 rad/s) are reported in the table on the next page (second line). Except for the tenth mode, the errors are quite small.

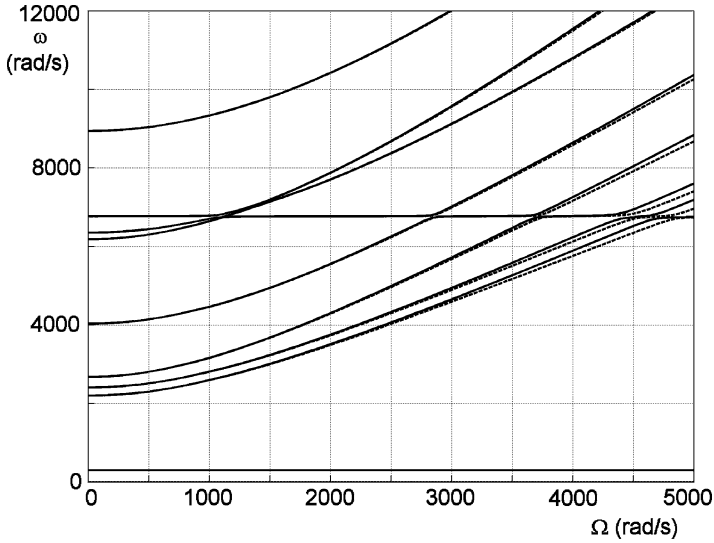

Fig. 4 Campbell diagram for the coupled torsional-axial dynamics obtained from the nonmodal computation (dashed lines) and the modal computation with ten modes (full lines)

Mode	1	2	3	4	5	6	7	8	9	10
Error	0	0.01	0.13	3.28	2.66	1.88	1.07	0.39	1.22	18.56
Error	0	0.01	6.51	9.04	19.38	19.50	–	–	–	–

Repeating the computation with just five modes, the errors are still acceptable for the lowest order modes (last line of the same table).

6 Conclusions

The component mode synthesis allows to reduce each rotor of a generic machine to a single superelement, with a number of boundary degrees of freedom equal to three times the number of boundary nodes plus a number of internal degrees of freedom equal to the number of the modes considered.

The present paper shows that this approach is possible even when the rotor is modeled using a number of complex degrees of freedom for the flexural behavior and of real degrees of freedom for the (possibly coupled) axial and torsional behavior. True axial symmetry of the rotor is not required, since cyclic symmetry is sufficient to write time-invariant equations of motion in an inertial reference frame. The stator can be modeled using any kind of finite elements and need not to have any symmetry property.

An example showed that a small number of modes is sufficient for modeling accurately even rotors with large gyroscopic and centrifugal stiffening effects.

The paper deals with rotors modeled using the 1-D and the $1^1/_2$-D approaches, but the same approach can be used for general 3-D models.

References

1. Genta, G.: Dynamics of Rotating Systems. Springer, New York (2005)
2. Genta, G., Tonoli, A.: A harmonic finite element for the analysis of flexural, torsional and axial rotordynamic behavior of discs. J. Sound and Vib. **196**(1), 19–43 (1996)
3. Genta, G., Tonoli, A. A harmonic finite element for the analysis of flexural, torsional and axial rotordynamic behavior of bladed arrays. J. Sound and Vib. **207**(5), 693–720 (1997)
4. Genta, G.: DYNROT Handbook. Department of mechanics, Politecnico di Torino, Torino, November (2000)
5. Geradin, M., Kill, N.: A new approach to finite element modelling of rotors. Eng. Comput. 52–64 (1984)
6. Genta, G., Silvagni, M.: Some Considerations on Cyclic Symmetry in Rotordynamics. ISCORMA-3, Cleveland, September (2005)
7. Craig, R.R., Bampton, M.C.C.: Coupling of substructures for dynamic analyses. AIAA J. **6**(7) 1313–1319 (1968)
8. Jacquet-Richardet, G., Ferraris, G., Rieutord, P.: Frequencies and modes of rotating flexible bladed disc-shaft assemblies: a global cyclic symmetry approach. J. Sound Vib. **191**(5), 901–915 (1996)
9. Thomas, D.L.: Dynamics of rotationally periodic structures. Int. J. Numer. Meth. Eng. **14**, 81–102 (1997)
10. Genta, G.: Vibration Dynamics and Control. Springer, New York (2008)

Evolution of Frequency-Speed Diagram in Rotating Machinery

Chong-Won Lee

Abstract Frequency-speed diagram, often known as Campbell diagram that has long been an important tool in the design and operation of rotating machinery plots most of time the imaginary part of eigenvalues and the incomplete, but useful, frequency information of probable external disturbances, which is known as excitation order lines. Thus, from such diagrams drawn for rotating machines, engineers can understand which modes are likely to be excited by the excitation sources of interest, which speed regions are safe for operation, and so on.

In this paper, the pros and cons of the conventional frequency-speed diagram are discussed in relation to the desired rotordynamic properties. And, then is introduced how frequency-speed diagram has been evolved in the past in order to improve the original diagram by adding missing rotordynamic properties.

Keywords Frequency-speed diagram · Campbell diagram · Lee diagram · Strong and weak modes · Infinity norm of directional frequency response functions

1 Introduction

Rotating machines nowadays are designed such that they can be safely operated beyond or passing through many critical speeds. Rotating machinery consists of many structural elements such as shaft, disk, blade, bearing/seal/damper, casing and foundation. Not only each machine structure reveals its own local dynamic characteristics, but the whole machine as an assemblage of part structures also reveals global dynamic characteristics. The dynamic properties of most common interest in rotating machinery typically include the critical speeds, stability of modes and forced response. The critical speeds of a rotor are defined as the rotational speeds at which the speed-dependent modal (natural) frequencies, rigid or flex-

C.-W. Lee (✉)
Center for Noise and Vibration Control, Department of Mechanical Engineering, KAIST, Daejeon, Korea
e-mail: cwlee@kaist.ac.kr

K. Gupta (ed.), *IUTAM Symposium on Emerging Trends in Rotor Dynamics*, IUTAM Bookseries 25, DOI 10.1007/978-94-007-0020-8_4,

ible, intersect with the order lines associated with possible excitation sources of paramount interest.

Perhaps one of the most convenient and elegant graphical presentations for predicting critical speeds is known as the Campbell diagram, which was introduced by Campbell in 1924 in a study of circumferential waves in turbine disks [1, 2]. He believed that "one of the most important features in the design and manufacture of a steam turbine is the elimination of the possibility of vibration occurrence at the various natural frequencies of its disk wheels and buckets." It is often referred to as the whirl speed chart (map) [3], frequency-speed diagram, natural frequency-speed map, damped natural frequency map, interference map, and frequency interference diagram, where the whirl speeds, or equivalently the modal frequencies, and the order lines of possible excitation forces are plotted against the rotational speed. Campbell diagram is helpful for design and practice engineers to judge on the margin of safe operation in the design as well as field operation processes. The Campbell diagram has been popularly adopted in the design of rotors with bladed disks such as turbines and fans, where the blade natural frequencies and the excitation order lines associated with the blade passing frequency and the integer multiples are easily identified [4,5]. However, its usage is limited in the sense that it does not provide practice engineers with the essential information such as the stability and forced response of the actual rotor system, particularly when the system possesses both stationary and rotating asymmetry. In other words, it does not tell us about which critical speeds have to be considered seriously in design and operation – the severity of the rotor response at each critical speed. For the critical speeds of an isotropic rotor system associated with unbalance excitation, the backward whirl speeds are traditionally indicated by broken lines, in order to indicate the less importance of the backward critical speeds in the unbalance response of the isotropic rotor system [6].

In this paper, we discuss the essence of the Campbell diagram that was invented early 1920s and how the frequency-speed diagram has evolved since then.

2 Campbell Diagram

The Campbell diagram, the earliest version of frequency-speed diagram, basically uses only the imaginary part of eigenvalues (modal frequencies) against the varying rotational speed, while the real part of eigenvalues and thus the stability of modes are missing. Moreover, the eigenvectors associated with modes were not of a concern at all. Figure 1 shows the Campbell diagram for a steam turbine [1] developed by Campbell in 1924. The diagram plots all possible modal frequencies of the rotating turbine disk associated with forward and backward traveling waves with up to six nodal diameters, along with the synchronous excitation and higher order lines. The intersections between the excitation order lines and the modal frequencies are identified by circles of different size for convenience, requiring a full knowledge of rotating disk vibration. The large, medium and small circles indicate the critical, minor and sub-minor resonant speeds, which were determined in accordance to the severity of excitation order lines and the importance of modes. Although

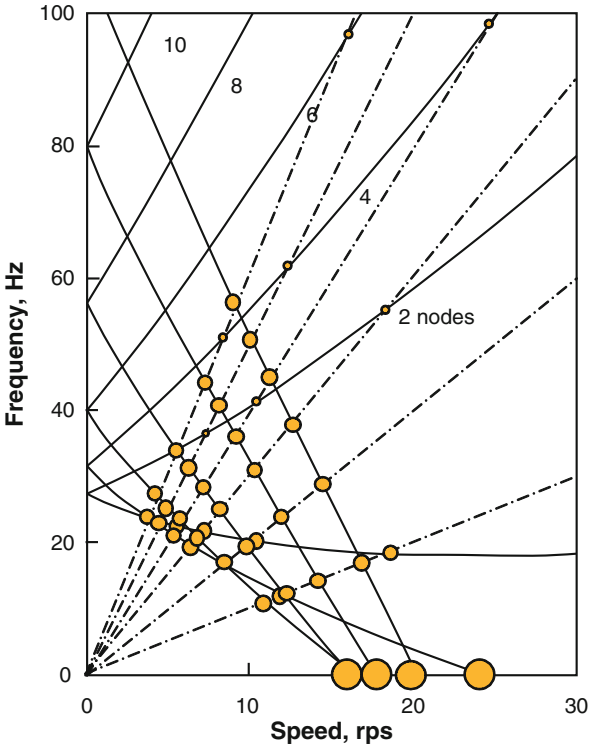

Fig. 1 Original frequency-speed diagram by Campbell for steam turbine [1]

the Campbell diagram successfully identifies the importance of resonant speeds by careful investigation of the cause of the intersections, the diagram is over-crowded with possible resonant speeds, so that design of steam turbines is like walking into a mine field. In summary, the Campbell diagram is useful in design and operation of a rotating machine, in the sense that all possible resonant speeds are readily identified. However, it does not provide the information on modal stability and systematic way of judging the severity of resonant speeds.

3 Enhanced Frequency-Speed Diagrams

One method of accommodating the stability information, which has been well adopted by many researchers in the past, is simply to add the information of the modal damping as well as frequency for each mode in the Campbell diagram, or to draw Root Loci with the rotational speed varied [7]. Root Loci technique, which is basically a polar plot of complex eigenvalues with the rotational speed varied, has been extensively adopted in the control area for a long time. Figure 2 is the typical Root Loci plot [8] where the real (modal damping) as well as imaginary parts of

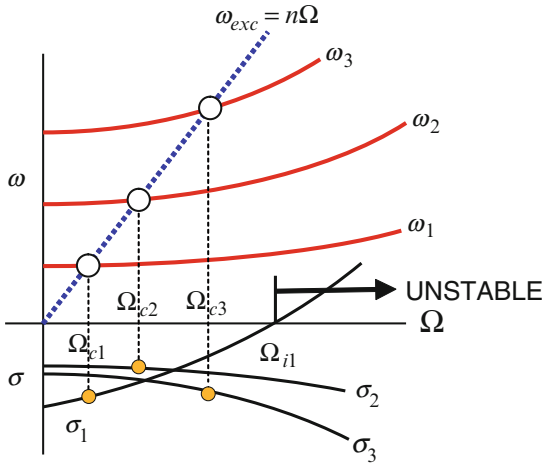

Fig. 2 Whirl speed map

eigenvalues are plotted against the rotational speed, so that not only the (relative) stability of the possible resonant speeds is easily identified but the absolute stable speed region is detected. The stability of each mode can be addressed based on the added information on modal damping, but as the number of modes increases, the additional information complicates the understanding of the plot, obscuring the essence of information.

As the rotor system configuration becomes complicated as in the case of bladed turbine wheels, the corresponding whirl speed charts are often over-crowded with many sub-system natural frequencies and order lines, resulting in many intersections. However, not all the intersections may be engaged with possible resonances, when each order line is associated with a particular mode. Singh [9] introduced a method of reducing the number of meaningful intersections by using the relation between the order lines and the mode shapes of bladed turbine wheels. However, his method still lacks the information of modal damping and forced response at the critical speeds.

4 Separation of Forward and Backward Modes

Frequency-speed diagram or whirl speed chart is the plot of modal frequencies (damped natural frequencies) against the rotational speed. Such diagram has traditionally been plotted in three different ways in the past. The most popular way is to plot the diagram only in the first quadrant defined by the positive rotational speed as the abscissa and the absolute modal frequencies as the ordinate as shown in Fig. 3a. Natural frequencies of non-rotating structures are taken as positive quantities in the structural vibration area with no confusion. However, the natural frequencies associated with forward and backward modes of rotating shafts and disks can have

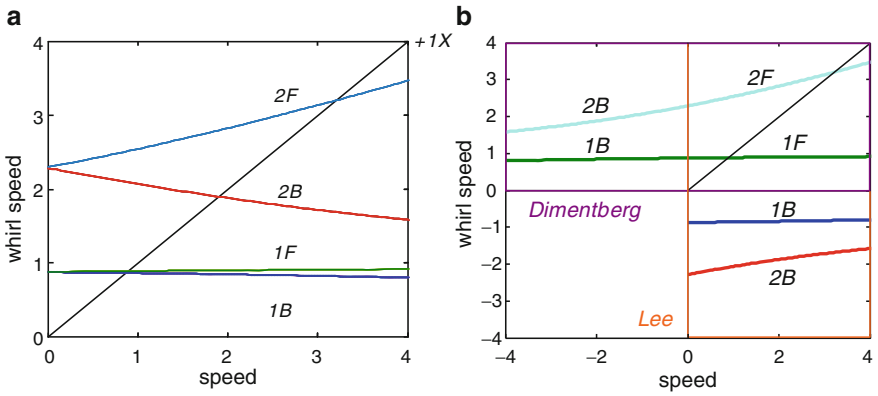

Fig. 3 **(a)** Single and **(b)** two-quadrant plotting methods for frequency-speed diagram

different signs for clear understanding of physical phenomena. Thus, when they are plotted in the first quadrant only, the diagram would be crowded with backward and forward modes, and/or their complex conjugate modes, as shown in Figs. 1 and 4. Figure 4 shows the Campbell diagram for a twin spool jet engine, where solid and broken lines indicate forward and backward whirl modes, respectively [4,6]. Broken lines are often used to identify the backward modes from the forward modes that are considered to be more important in contribution to forced response of the rotor at critical speeds. The problems with the single quadrant plot for frequency-speed diagram are:

1. There is no systematic way of identifying forward and backward modes other than experienced judgment.
2. There exist too many intersections of modes with excitation order lines, meaning that there are many possibilities of excessive resonant vibration, which is normally not true.
3. It becomes almost impossible to understand the plot with over-crowded modes, when the rotor model becomes more complicated and realistic.

In order to resolve the complexity of the diagram, Dimentberg [3] extensively adopted the frequency-speed diagram plotted in the first and second quadrants, so that the forward and backward modes can be shown separately in the first and second quadrants, respectively, as shown in Fig. 3b. Although it takes some caution to understand what is meant by negative rotational speed in the plot, all forward and backward modal frequencies can take positive values. The most recent method is to use the first and fourth quadrants for the frequency-speed diagram [10], with no allowance of the negative rotational speed. The modal frequencies can freely take positive or negative values, and, the forward and backward modes are completely separated as in Dimentberg [3]. In conclusion, the two quadrant plots are much simpler and more convenient to use, yet giving more physical insight into the directivity of modes, than the conventional single quadrant plot.

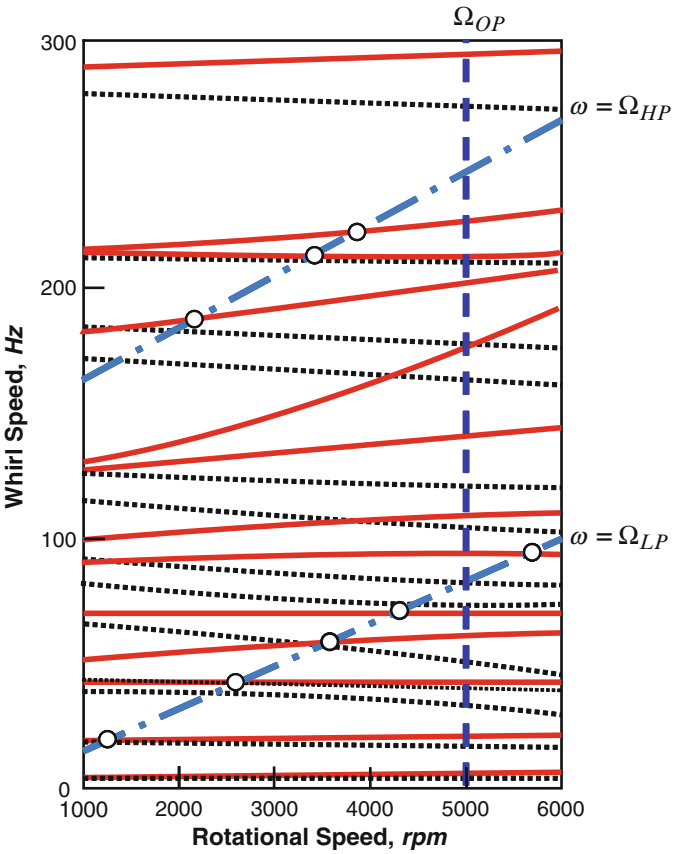

Fig. 4 Campbell diagram for twin spool jet engine: solid and broken lines indicate forward and backward whirl modes, respectively. $\Omega_{HP} = 1.25\Omega_{LP} + 146(Hz)$ [6]

5 Modal Analysis and Commercial Software

In general, a rotor-bearing system has two main parts, rotor and stator. According to the non-axisymmetric properties of the rotor and stator parts, a rotor-bearing system may be classified into four types [10, 11]: (1) *isotropic* (symmetric) rotor system, when both the rotor and the stator are axi-symmetric; (2) *anisotropic* rotor system, when the rotor is axi-symmetric but the stator is not (stationary asymmetry); (3) *asymmetric* rotor system when the stator is axi-symmetric but the rotor is not (rotating asymmetry); (4) *general* rotor when neither the rotor nor the stator is axi-symmetric (both stationary and rotating asymmetry).

Modal analysis of the isotropic [10], anisotropic [10, 12, 13] and asymmetric linear rotor systems [11], which are essentially formulated as a time-invariant linear system, has been well developed. But, the modal analysis of general rotor systems,

which is characterized by the presence of periodically time-varying parameters [14, 15], has recently been conducted, using both the Floquet theory [16] and the modulation coordinate technique [17].

Although commercial FEM codes such as NASTRAN have been widely used for structural vibration analysis since a couple of decades ago, they often have limitations in applications and users' access to intermediate data. For example, they can calculate the frequency-speed diagram for isotropic, anisotropic and asymmetric rotors, but they cannot handle general rotors with both stationary and rotating asymmetry and they have limitations in utilizing the right and left eigenvectors. SAMCEF and ANSYS, which have recently been available in the market for rotordynamic analysis, have the same limitations in applications and intermediate data access for further analysis. So far, any commercial codes are not capable of rotordynamic analysis for general rotors characterized by both stationary and rotating asymmetry, because the modal analysis method for general rotors have not been available until a couple of years ago.

6 New Whirl Speed Chart

Modal damping certainly has to do with the relative stability of mode. Presence of modes with positive damping at a rotational speed indicates the unstable free response of the rotor at that speed, the response becoming large as far as the linearity assumption allows. Modes of light damping contribute more to the transient response than modes of heavy damping. However, it is not completely correct to say that modes of light damping contribute more to the steady-state response than modes of heavy damping. In fact, the magnification factor near the modal frequency for the harmonic response is inversely proportional to modal damping, but the response is also proportional to the residue that is a product of the modal and adjoint vectors as well as the force itself. Thus, the modal vector, whose importance is often forgotten, should be accounted whenever the severity of the response is addressed [18]. Based on the modal analysis of general rotor systems, the rigorous norm analysis of modal vectors has recently been carried out [18], in order to represent the strength of modes in the complex coordinate system. Based on the modal vector norm strength, the method classifies the modes into two groups: strong and weak modes. The frequency-diagram incorporated with modal strength certainly enhances the Campbell diagram in the sense that the importance of modes are systematically and clearly identified in the diagram so that the severity of the resonant vibrations which are expected from the intersections with possible excitation lines of any order can be readily evaluated. The Campbell diagram incorporated with modal strength uses all available sources in predicting the possible resonances, but it fails in direct indication of the stability of modes in the diagram.

In order to resolve the stability issue with the diagram incorporated with modal strength, a new method is recently proposed, based on calculation of the infinity norms of the four directional frequency response matrices [10, 16] defined in the

complex coordinates, which are referred to as Lee diagram [19]. Lee diagram not only utilizes all available information in predicting possible resonances with associated modal strength, but also they classify all modes into four different groups: modes of symmetry, anisotropy, asymmetry and coupled asymmetry. Lee diagram is functions of the frequency and the rotational speed, which can be used as a powerful and effective tool in selecting only a few important possible resonances for design and operation of rotors in practice, from, otherwise, too many possible ones. The features of Lee diagram are:

1. Lee diagram, consisting of the four plots, $L_{11}(\omega, \Omega)$, $L_{12}(\omega, \Omega)$, $L_{21}(\omega, \Omega)$ and $L_{22}(\omega, \Omega)$, clearly identifies the important modes as well as resonances of a general rotor system with either the weak rotating and stationary asymmetry or the strong skew-symmetric coupled system matrices.
2. $L_{11}(\omega, \Omega)$ readily differentiates the original (strong) modes from the complex conjugate (weak) modes.
3. $L_{12}(\omega, \Omega)$, $L_{21}(\omega, \Omega)$, and $L_{22}(\omega, \Omega)$ are useful in identifying the weak modes of less importance associated with the stationary asymmetry, the rotating asymmetry and the coupled asymmetry of the rotor, respectively.
4. Lee diagram can be used as a powerful design tool for rotating machinery, particularly for FEM based rotor models in their design phase.
5. Among others, $L_{11}(\omega, \Omega)$ alone is far superior in prediction of occurrence of possible resonances of the rotor to the conventional Campbell diagram, because it identifies the modes of paramount importance in design and operation of rotating machines.

7 Illustrative Examples

The first example is a two-pole generator [19]. The commercial two-pole generator has asymmetry in the rotating part because there are many slots in the rotor for coil windings. Moreover, three journal bearings, of which bearing properties are strongly dependent upon the rotational speed, have anisotropy. The two-pole generator is modeled by finite elements of Rayleigh's beam and the coil windings are modeled by additional point masses. Figure 5a shows the conventional Campbell diagram drawn from 1,000 to 3,960 rpm. As there are numerous modes in the Campbell diagram, it may mislead us to a wrong judgment that it is almost impossible to operate the generator near at 3,600 rpm without a chance of resonance. Instead, the significance of resonances can be evaluated by modal strength as shown in Fig. 5b. Primary strong modes are distinguished from numerous weak modes by their modal strength (intensity level in the figure). However, the Campbell diagram only with modal strength is very conservative in the sense that it exaggerates the role of primary strong modes, because it still lacks the information of the damping and the input to output relation of the generator.

Figure 6 plots Lee diagram for the two-pole generator [19]. Figure 6a shows $L_{11}(\omega, \Omega)$, which represents symmetric property. The plot is the most important

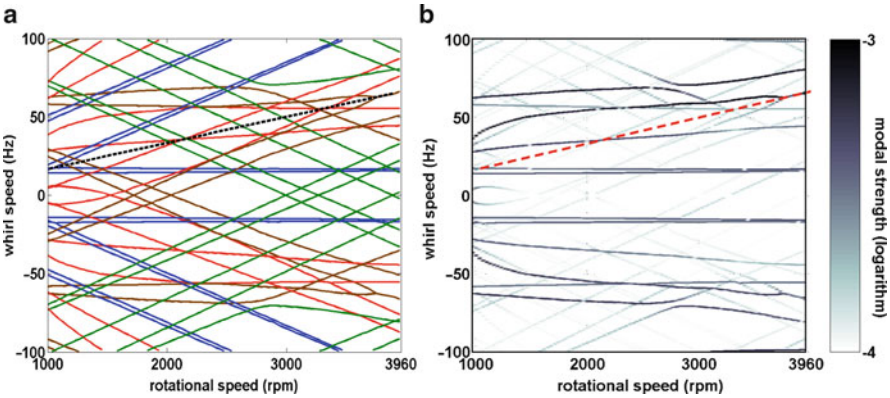

Fig. 5 **(a)** Conventional Campbell diagram and **(b)** Campbell diagram incorporated with modal strength for two-pole generator [18, 19]

to evaluate the possible contribution of modes to forced responses because the symmetric property is generally much larger than the anisotropic and asymmetric property. From the plot of $L_{11}(\omega, \Omega)$, it can be concluded that only the first translatory modes near at ± 20 Hz play an important role in the predicted forced response, although the generator system has many other strong modes, as seen in Fig. 5b. Because the other strong modes except the first translatory modes are heavily damped by the three journal bearings of large damping, the potential contributions of those modes to forced responses remain insignificant, compared with the first translatory modes. Note that other strong modes near at ± 60 Hz may also have a little, if not significant, contribution to the forced responses. The magnitude of $L_{12}(\omega, \Omega)$ is similar to that of $L_{11}(\omega, \Omega)$. It means that the system possesses a relatively large amount of anisotropy in the journal bearing properties. The weak modes in $L_{21}(\omega, \Omega)$ that do not appear in $L_{11}(\omega, \Omega)$ and $L_{12}(\omega, \Omega)$ become visible, but they have small magnitudes compared with $L_{12}(\omega, \Omega)$ (see the use of two different scales). It is because the asymmetry of the two-pole generator is relatively small, compared to the journal bearing anisotropy. From the plots of $L_{11}(\omega, \Omega)$ and $L_{21}(\omega, \Omega)$, we can identify the possibility of excessive unbalance and transient response in the narrow speed region centered at about 1,050 rpm, due to the presence of asymmetry in the generator rotor. The anisotropy-asymmetry coupled modes are well identified from $L_{22}(\omega, \Omega)$ in Fig. 6d.

Now let us consider a commercial gas turbine shown in Fig. 7. For the FEM modeling of the gas turbine, the rotating part and the two bearings are assumed to be symmetric, so that the whole rotor model becomes an isotropic rotor. Figure 8 compares the Lee diagram with the Campbell diagram [20] for the gas turbine. The Campbell diagram is not too complicated in this case, because the dominant modes are the typical translatory, conical and the first and second bending modes. Thus, it is quite straightforward to identify the backward modes for an isotropic rotor, which are less important than the forward modes in determination of critical speeds from

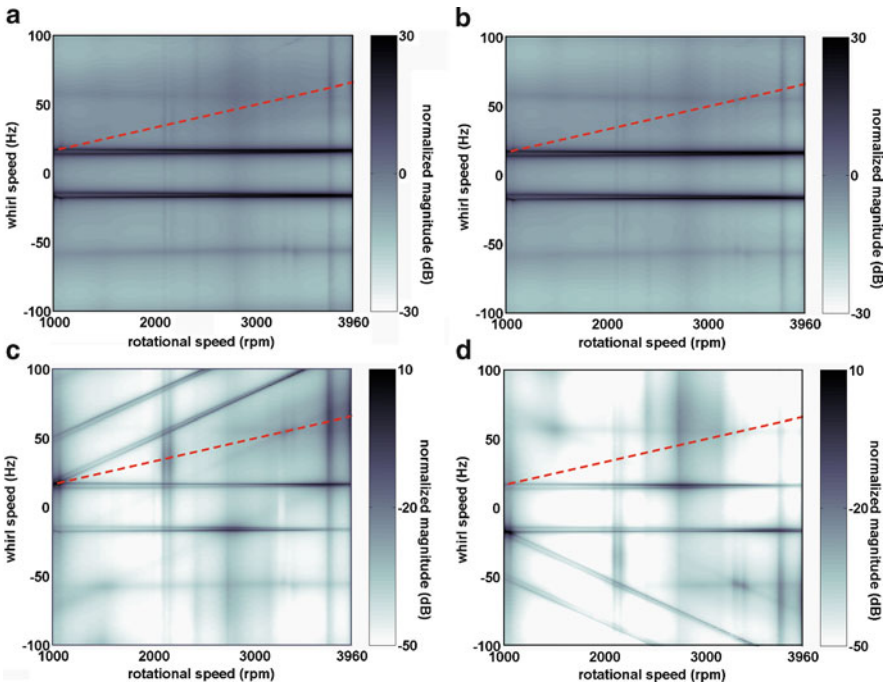

Fig. 6 Lee diagram (upper bound) for two-pole generator: **(a)** $L_{11}(\omega, \Omega)$ **(b)** $L_{12}(\omega, \Omega)$ **(c)** $L_{21}(\omega, \Omega)$ and **(d)** $L_{22}(\omega, \Omega)$ [19]

Fig. 7 Gas turbine model

both diagrams. However, in comparison with the Campbell diagram, the Lee diagram, $L_{11}(\omega, \Omega)$, systematically identifies the backward modes and indicates the modes of importance by the grey-level scale. Note that, for an isotropic rotor, the other three plots than $L_{11}(\omega, \Omega)$ always vanish.

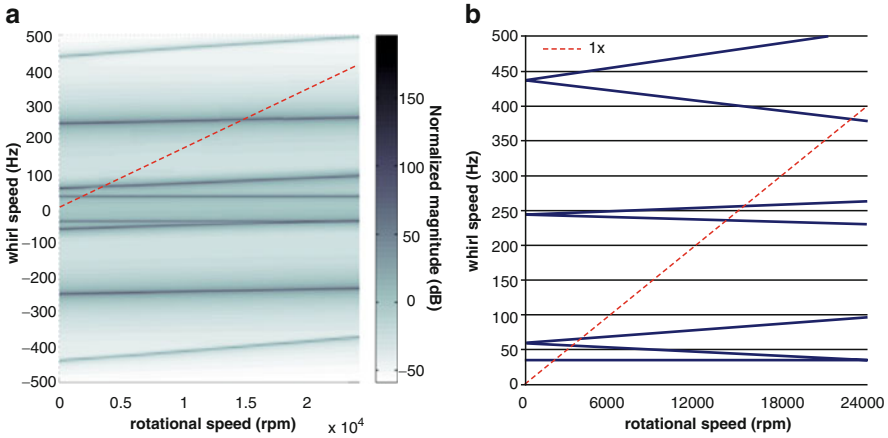

Fig. 8 **(a)** Lee and **(b)** Campbell diagrams for the gas turbine [20]

Table 1 Comparison of diagrams in usage of available information [19]

	Re(λ)	Im(λ)	Modal vector	Excitation
Campbell diagram	X	O	X	Order lines
Root Locus	O	O	X	X
SAFE	X	O	No. of nodal diameters	Order lines
Campbell diagram with modal strength	X	O	Modal vector norm	Order lines
Lee diagram	O	O	Residue matrix norm	Order lines

8 Conclusions

Table 1 summarizes and compares the five different diagrams in terms of information usage. The classical Campbell diagram essentially plots only the imaginary part of eigenvalues against the rotational speed, along with the excitation order lines, lacking the knowledge of stability and strength of modes. Root locus plot extensively utilizes the stability of modes, but it lacks the information of modal strength and possible resonances. SAFE attempts to remove irrelevant modes to possible resonant vibrations, but it also lacks the information on stability and strength of the relevant modes. The Campbell diagram incorporated with modal strength better identifies the modes of importance than the previous diagrams, but it lacks the information on stability of modes and input-output relation.

Finally, the Lee diagram successfully utilizes all available useful information not only on the modal parameters but the input-output relation. Lee diagram is an excellent design tool for rotating machines, particularly for FEM based rotor models with strong skew-symmetric coupled system matrices and weak anisotropy

and asymmetry. It can identify the modes of symmetry, rotating and stationary asymmetry, and extract only a few critical resonances out of the, otherwise, over-crowed ones without a measure of priority as in the Campbell diagram.

Acknowledgment The author is grateful to Doosan Heavy Industries and Construction Co. Ltd., for the financial support of the research. This work was also supported by the Brain Korea 21 project.

References

1. Campbell, W.E.: The Protection of steam turbine disk wheels from axial vibration. Trans. ASME, **46**, 31–160 (1924)
2. Crandall, S.H.: Rotordynamics. In: Kliemann, W., Namachchivaya, N.S. (eds.) Nonlinear Dynamics and Stochastic Mechanics, CRC Press, Boca Raton (1995)
3. Dimentberg, F.M.: Flexural Vibrations of Rotating Shafts. Butterworths, London (1961)
4. Rao, J.S.: Turbomachine Blade Vibration. Wiley Eastern LTD., New Delhi (1991)
5. Irretier, H.: Free and force vibrations of turbine blades. In: Rieger, N.F. (ed.) Rotordynamics 2: Problems in Turbomachinery, Springer-Verlag (1988)
6. Lalanne, M., Ferraris, G.: Rotordynamics Prediction in Engineering. John Wiley & Sons (1990)
7. Bently, D.E.: Fundamentals of Rotating Machinery Diagnostics. Bently Pressurized Bearing Press (2002)
8. Nelson, H.D., Crandall, S.H.: Analytic prediction of rotordynamic response. In: Ehrich, F.F. (ed.) Handbook of Rotordynamics), McGraw-Hill Inc (1992)
9. Singh MP.: SAFE Technology Report ST 16. Dresser-Rand Company (1984)
10. Lee, C.W.: Vibration Analysis of Rotors, Kluwer Academic Publishers (1993)
11. Lee, C.W., Lee, S.K.: An efficient complex modal testing theory for asymmetric rotor systems: use of unidirectional excitation method. J. Sound Vib. **206**(3), 327–328 (1997)
12. Bucher, I., Ewins, D.J.: Modal analysis and testing of rotating structures. Philos. Trans. R. Soc. London A **359**, 61–96 (2000)
13. Nordmann, R.: Identification of modal parameters of an elastic rotor with oil film bearings. ASME J. Vib. Acous., Stress and Reliability in Design **106**, 107–112 (1984)
14. Genta, B.: Whirling of unsymmetrical rotors: a finite element approach based on complex coordinates. J. Sound Vib. **124**, 27–53 (1988)
15. Ardayfio, D., Frohrib, D.A.: Instability of an asymmetric rotor with asymmetric shaft mounted on symmetric elastic supports. ASME J. Eng. Ind. **98**, 1161–1165 (1976)
16. Lee, C.W., Han, D.J., Suh, J.H., Hong, S.W.: Modal analysis of periodically time-varying linear rotor systems. J. Sound Vib. **303**, 553–574 (2007)
17. Suh, J.H., Hong, S.W., Lee, C.W.: Modal analysis of asymmetric rotor system with isotropic stator using modulated coordinates. J. Sound Vib. **284**, 651–671 (2005)
18. Lee, C.W., Han, D.J.: Strength of modes in rotating machinery. J. Sound Vib. **313**, 268–289 (2007)
19. Lee, C.W., Seo, Y.H.: Enhanced Campbell diagram with the concept of h-infinity in rotating machinery: Lee diagram. ASME J. Appl. Mech. **77**, 021012-1-021012-12 (2010)
20. Chung, H.J.: Dynamic Analysis of the Small-Size Gas Turbine Engine Rotor using Commercial s/w and its Limitations. M.S. thesis, KAIST, February (2009)

Developments in Rotor Dynamical Modeling of Hydropower Units

J.-O. Aidanpää, R.K. Gustavsson, N.L.P. Lundström, M. Karlsson, Y. Calleecharan, M.L. Nässelqvist, M. Karlberg, and U. Lundin

Abstract During the last century the hydropower units have been developed from a few megawatts per unit, up to several hundreds megawatts per unit. Over the years the operating conditions have also been changed from the ones that the machines were originally designed. These changes will significantly affect the lifespan of the machines. The hydropower plants are in general old, and large-scale revisions will be performed in the coming years. This implies that new components with new materials and design will be installed to the old machines. To reduce the risk of failures it is essential that better methods for rotor dynamical simulations are developed. In this paper our research on electromagnetic-rotor interaction is summarized. Results are presented on new rotor models in connection with stability, excitation sources for backward/forward whirling and the occurrence of a tangential force.

Keywords Hydropower · Rotor · Dynamic · Magnetic pull · UMP · Stability

1 Introduction

In many countries, hydropower plants were built in the twentieth century on a regulated energy market, where the units served as base load. Nowadays, hydroelectric generation is frequently used to serve as intermittent load on a deregulated market. In the future, hydropower units are expected to more frequently complement other renewable sources, e.g., windpower. This will lead to more frequent starts and stops of the hydroelectric units, which will influence the lifetime of the machine

J.-O. Aidanpää (✉), R.K. Gustavsson, N.L.P. Lundström, M. Karlsson, Y. Calleecharan, M.L.Nässelqvist, and M. Karlberg
Department of Applied Physics and Mechanical Engineering, Luleå University of Technology, 971 87 Luleå, Sweden
e-mail: Jan-Olov.Aidanpaa@ltu.se

U. Lundin
Ångström Laboratory, Uppsala University, SE 751 21 Uppsala, Sweden

K. Gupta (ed.), *IUTAM Symposium on Emerging Trends in Rotor Dynamics*,
IUTAM Bookseries 25, DOI 10.1007/978-94-007-0020-8_5,

components. Development in rotor dynamical modelling and analysis is therefore essential in order to avoid failures. In 2006, the Swedish Hydropower Centre (SVC) was established as a competence centre for education and research within the field of hydropower. The most important tasks for SVC are to create high quality long-term competence at selected universities and to establish close co-operation between industries, universities and authorities. Luleå University of Technology was selected to develop the hydropower competence in rotor dynamics. We have worked in this area since 2001 with main focus has been electromagnetic interaction. We have also worked with measurement technique, turbine contact, bearing analysis and fluid-rotor interaction.

This paper summarizes our work on rotor interaction with the magnetic field. An off-centred rotor in a generator results in asymmetry in the air gap. The rotor will be affected by forces due to the asymmetrical magnetic field around the air gap. To determine the forces due to the asymmetrical magnetic field, the magnetic flux density must be determined in the whole air gap region around the rotor. The determination of magnetic forces has been carried out for more than a century. Early papers by Behrend [1], Gray [2] and Robinson [3] suggested linear equations for magnetic pull. Covo [4] and Ohishi et al. [5] considered the saturation of the magnetic core to improve the magnetic pull equations. Früchtenicht et al. [6] observed the existence of two electromechanical force components (one radial and one tangential) when the rotor of an asynchronous induction motor performs a circular motion. Over the past decade, the finite element method has been used to calculate electromagnetic forces. Arrkio et al. [7] solved the magnetic field for cage induction motors using time-stepping finite element analysis to numerically determine a parametric electromagnetic force. Holopainen et al. [8] continued the work and used the parametric force to study a rotor dynamical system. Laiho et al. [9] coupled a finite element code for rotor dynamic with a finite element code for electromagnetic field, in order to simulate the whole system continuously. Most papers published regarding unbalanced magnetic pull concern asynchronous motors. In this paper some important results from our research on electromagnetic rotor interaction on large synchronous generators are presented [10–16]. The results come from our cooperation together with Uppsala University who have competence in electromagnetic simulations and analysis of hydropower generators. With SVC as the link to industry, the cooperation between academia and industry will eventually lead to more reliable machines being designed in the future.

2 Magnetic Pull Force

The electromagnetic pulling force acting on the generator rotor depends on the asymmetry in the air gap between the rotor and stator. In a perfectly symmetrical machine the radial pulling forces should add up to zero. However, all practical generators have some degree of asymmetry in the air gap. A common example of

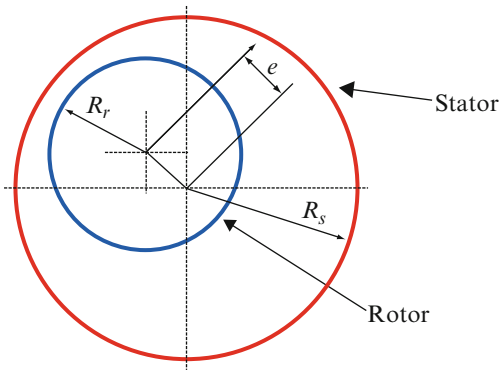

Fig. 1 Schematic diagram of the air-gap with an eccentric rotor

asymmetry is when the rotor centre and stator centre do not coincide with each other. The relative eccentricity is defined as:

$$\varepsilon = e/\Delta R \tag{1}$$

where e is the radial displacement of the rotor centre and the average air gap ΔR is the radial clearance between the inner radius of the stator R_s and the outer radius of the rotor R_r. A schematic diagram depicting rotor eccentricity is shown in Fig. 1.

Belmans et al. [17] have shown that in a three-phase electrical machine having an arbitrary number of poles, the magnetic pulling force is composed of a constant part and an alternating part. Hydropower generators usually have many poles and they operate as synchronous machines. This implies that the alternating magnetic pulling force is negligible in comparison to the constant magnetic pulling force. The expression for the value of the constant unbalanced magnetic pulling force f_e, for a rotor parallel to the stator was found from the integration of the horizontal and vertical projection of the Maxwell stress over the rotor surface. The mean value of the magnetic pulling force can be expressed as:

$$f_e = \frac{\mu_0 S_s^2 R_s^3 h\pi}{2p^2 \Delta R^2} \frac{\varepsilon}{\sqrt{(1-\varepsilon^2)^3}} \tag{2}$$

where S_s is the stator linear current density, p is the number of pole pairs, h is the length of the rotor and μ_0 is the permeability of free space. Equation (2) shows that the magnetic pulling force is a non-linear function of the air-gap eccentricity which makes the magnetic pulling force to destabilize the rotor system with increasing rotor eccentricity.

The air gap eccentricity can be divided in two categories: stator eccentricity and rotor eccentricity. In the case of stator eccentricity the rotor will be in a fixed position relative to the stator under a constant magnetic pulling force. This means that the smallest air gap will be in a same position during the rotation of the shaft. A characteristic for the rotor eccentricity is that the rotor will whirl around the centre

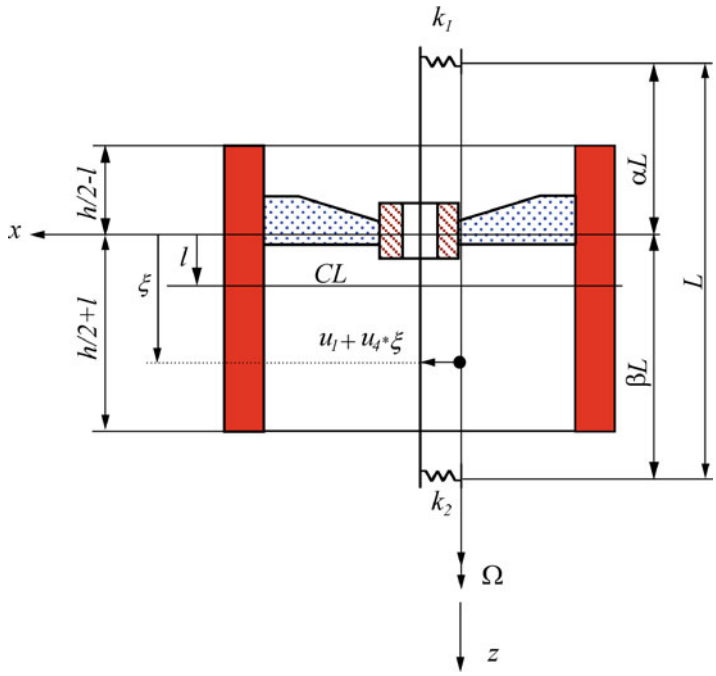

Fig. 2 Generator rotor displaced a distance $u_1 + u_4\xi$ from the generator vertical axis of symmetry

line of the rotor in an orbit. However, the most common case of eccentricity is a combination of stator and rotor eccentricity where the rotor centre will whirl around a fixed position in the stator bore with the angular speed of rotation.

The generator eccentricity causes a disturbance in the magnetic field, which results in a pulling force and torque acting on the generator spider hub. The magnetic force f_e depends on the rotor displacement $u_1(x$ – displ.), $u_2(y$ – displ.), on the inclination of the rotor $u_3(x$ – rot.), $u_4(y$ – rot.), and on the distance l between the generator spider hub and the geometrical centre of the generator rim, Fig. 2. The inclination of the rotor is assumed to be small which gives the cosine of inclination angle to be approximately equal to unity and the sine of the angle to be the angle itself.

The magnetic pulling force acting on a unit length of the rotor rim has been obtained by dividing the magnetic pulling force in Eq. (2) by the length h of the rotor rim. By assembling the constants in Eq. (2) into the term k_e, the equation can be rewritten for a load element as

$$df_e = \frac{k_e u_r(\xi)}{h\sqrt{\left(1-\left(\frac{u_r(\xi)}{\Delta R}\right)^2\right)^3}} \tag{3}$$

where $d\xi$ is the length of the element in the axial direction. The magnetic pulling force for a rotor not parallel to the stator can be obtained by substituting the rotor displacements $u_r(\xi)$ in Eq. (3) with a function for the rotor displacement at a specific distance (ξ) from the rotor hub. The magnetic pulling force in the x-direction can be found by substituting the rotor displacement $u_r(\xi)$ in Eq. (3) with $u_{r_1}(\xi) = u_1 - u_4\xi$, and by substituting $u_{r_2}(\xi) = u_2 - u_3\xi$ in the y-direction. Integration of Eq. (3) over the rotor height h from the centre of the rotor hub gives

$$\left.\begin{aligned} f_{ei} = \frac{K_e}{h} \int_{-\frac{h}{2}+l}^{\frac{h}{2}+l} \frac{u_{r_i}}{\sqrt{\left(1-\left(\frac{u_{r_i}}{\Delta R}\right)^2\right)^3}} d\xi \approx \\ \frac{k_e}{h} \int_{-\frac{h}{2}+l}^{\frac{h}{2}+l} u_{r_i}\left(1+\frac{3}{2}\left(\frac{u_{r_i}}{\Delta R}\right)^2+\frac{15}{8}\left(\frac{u_{r_i}}{\Delta R}\right)^4 \frac{35}{16}\left(\frac{u_{r_i}}{\Delta R}\right)^6+\frac{315}{64}\left(\frac{u_{r_i}}{\Delta R}\right)^8\right) d\xi \end{aligned}\right\} \text{for } i=1,2 \tag{4}$$

The torque acting on the generator spider hub depends on the vertical position l of the rotor rim, on the rotor displacements u_1, u_2 and on the inclinations u_3, u_4 of the rotor. The torque on the rotor hub due to the magnetic pulling force (as acting on a rotor element $d\xi$ at a distance ξ from the rotor hub) can be found by calculating the torque from the magnetic pulling force acting on the rotor rim. Furthermore, the torque around the x coordinate axis can be formulated by substituting the displacements $u_r(\xi)$ in Eq. (2) with $u_{r\,3}(\xi) = -u_2 + u_3\xi$ and the torque around the y coordinate axis can be formulated by the substitution of $u_{r\,4}(\xi) = u_1 + u_4\xi$. Multiplication of Eq. (2) with ξ and integration over the rotor height h from the centre of the rotor hub gives Eq. (5).

$$\left.\begin{aligned} f_{ei} = \frac{K_e}{h} \int_{-\frac{h}{2}+l}^{\frac{h}{2}+l} \frac{u_{r_i}\xi}{\sqrt{\left(1-\left(\frac{u_{r_i}}{\Delta R}\right)^2\right)^3}} d\xi \approx \\ \frac{k_e}{h} \int_{-\frac{h}{2}+l}^{\frac{h}{2}+l} \xi u_{r_i}\left(1+\frac{3}{2}\left(\frac{u_{r_i}}{\Delta R}\right)^2+\frac{15}{8}\left(\frac{u_{r_i}}{\Delta R}\right)^4 \frac{35}{16}\left(\frac{u_{r_i}}{\Delta R}\right)^6+\frac{315}{64}\left(\frac{u_{r_i}}{\Delta R}\right)^8\right) d\xi \end{aligned}\right\} \text{for } i=3,4 \tag{5}$$

The usual way of calculating the influence of magnetic pull on a generator rotor is to apply a radial pulling force at the generator-spider hub. However a tangential magnetic pulling force which is perpendicular to the radial magnetic pulling force can also appear in a hydropower generator. In Gustavsson and Aidanpää [11], the presence and the influence that a tangential magnetic pulling force has on rotor stability has been investigated for a specific rotor configuration. A description of the tangential magnetic pulling force is found in Sect. 5.

The non-linear magnetic force and moment acting on the rotor hub are described in Eqs. (4) and (5). However, in many cases it is sufficient to use a linear model for the magnetic pulling force. A linear model of the magnetic pulling force which acts on the rotor can be achieved by using the linear part in Eqs. (4) and (5).

3 Stability due to Magnetic Pull

The equation of motion for the generator rotor model shown in Fig. 2, including the effects of the magnetic pull and that of the displacement of the generator rim from the spider hinge line, can be written in matrix form as

$$\mathbf{M}\ddot{\mathbf{u}} + (\Omega\mathbf{G} + \mathbf{C})\,\dot{\mathbf{u}} + \mathbf{K}\mathbf{u} = \mathbf{f_e}(\mathbf{u}) \tag{6}$$

In the linear case the electromagnetic force vector $\mathbf{f_e}(\mathbf{u})$ will be a stiffness matrix and the eigenvalue problem can be solved directly. In the non-linear case, the static eccentricity is solved by first defining a state vector $\mathbf{U} = \left\{\mathbf{u}\ \dot{\mathbf{u}}\right\}^T$ and rewriting Eq. (6) in state vector form. The stationary point $\mathbf{U_s}$ can be found by setting the time derivatives equal to zero. This stationary point is the rotor position at operating conditions. The Jacobian matrix $\mathbf{J}$ evaluated at the stationary point $\mathbf{U_s}$ can be found and the complex eigenvalues λ solved. These eigenvalues can be expressed in the general form

$$\lambda = -\tau + i\,\omega \tag{7}$$

where τ is the decay rate and ω is the damped natural frequency of each eigenvalue. The system is asymptotically stable if all eigenvalues have positive decay rates. In Fig. 3, the stability is shown for a hydropower generator using the parameters from Table 1.

The left figure of Fig. 3 shows a case with the linear electromagnetic force while the right figure pertains to a nonlinear case for the same machine. It is obvious that there is a large difference between the two models. It is to be noted that the stable regions are coloured white in the left figure while they are coloured black in the

Table 1 Dimensions and parameters used in the calculations for Fig. 3

	Item	Value	Unit
E	Young's modules	$2.0{\cdot}10^{11}$	$\mathrm{N/m^2}$
m	Mass of the rotor	336,000	kg
Jp	Polar moment of inertia	$5.3{\cdot}10^{6}$	$\mathrm{kg\,m^2}$
Jt	Transverse moment of inertia	$3.3{\cdot}10^{6}$	$\mathrm{kg\,m^2}$
L	Length of shaft	6.5	m
H	Length of rotor	3	m
k_M	Magnetic stiffness	$331{\cdot}10^{6}$	N/m
I	Moment of inertia	0.0201	$\mathrm{m^4}$
k_1	Bearing stiffness	$7{\cdot}10^{8}$	N/m
k_2	Bearing stiffness	$7{\cdot}10^{8}$	N/m

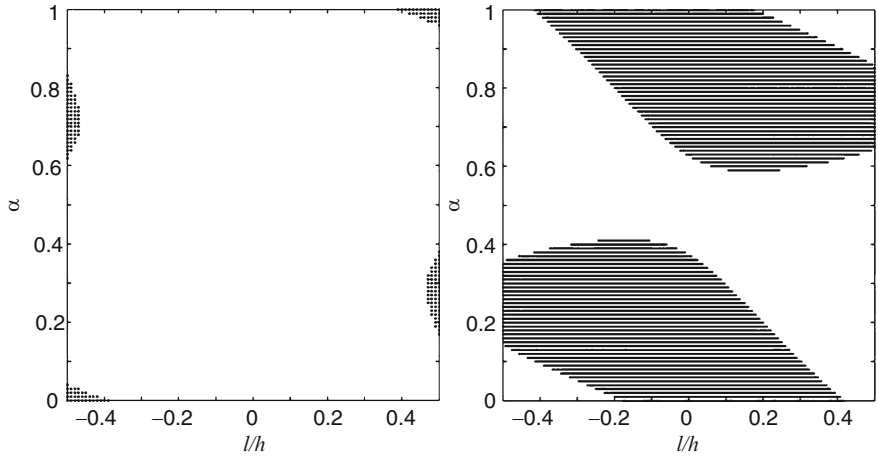

Fig. 3 Stable regions as function of generator position α and generator rotor offset l/h. Stability region (white) for a linear magnetic stiffness k_M (*left*). Stable region (black) for stator displacement of 7% of the air-gap (*right*)

right figure in Fig. 3. The main reason is that in the nonlinear case the stability is sensitive to the initial stator displacement.

4 Influence of Shape Deviations

Hydropower generators normally have a large radius combined with a small air gap. Most of the machines are old and therefore several imperfections exist due to material quality, tooling and uneven temperature distribution. All these effects result in shape deviations of the rotor and stator rim. Figure 4 shows the geometry of the generator model, having an arbitrary non-circular shaped rotor and stator. The generator is treated as a balanced Jeffcott or Laval rotor having length l_0, mass γ and stiffness k of the generator axis. The rotor rotates at a constant counterclockwise angular speed ω. Point C_s gives the location of the bearings while point C_r is the centre of rotation of the rotor. In Fig. 4, the coordinate system has the origin at C_s, r is the rotor radius, and s is the stator radius.

Let r_0 and s_0 be the average radius of the rotor and the stator respectively. An arbitrary non-circular shape can be described by adding a Fourier series of cosine terms to the rotor radius, r and the stator radius, s as follows

$$r = r_0(z) + \sum_{n=1}^{\infty} \delta_n^r(z) \cos n(\phi + \alpha_n^r(z)) \tag{8}$$

$$s = s_0(z) + \sum_{m=1}^{\infty} \delta_m^s(z) \cos m(\phi + \alpha_m^s(z)) \tag{9}$$

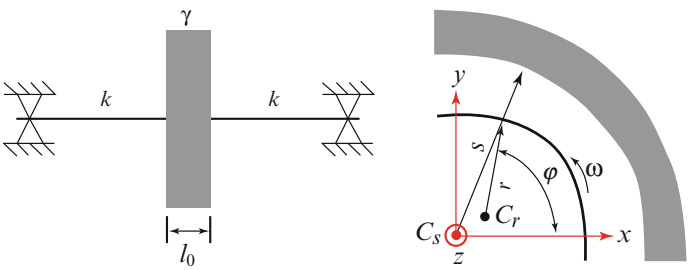

Fig. 4 The Jeffcott rotor (*left*). The cross-section of the generator (*right*)

where

$$\delta_n^r \geq 0, \quad \delta_m^s \geq 0, \quad \sum_{n=1}^{\infty} \delta_n^r(z) + \sum_{m=1}^{\infty} \delta_m^s(z) < g_0(z) \tag{10}$$

Here, $g_0 = s_0 - r_0$ is the average air-gap, δ_n^r and δ_m^s are referred to as the rotor and stator perturbation parameters, while α_n^r and α_m^s are the corresponding phase angles. To simplify notations, it is subsequently assumed in the following discussion that $\delta_n^r = \delta_m^s = 0$ for all $m, n \in N$, if nothing else is mentioned. N is here the set of all natural numbers. The case $\delta_1^r > 0$ and $\delta_1^s > 0$ will correspond to rotor eccentricity and stator eccentricity respectively. Since dynamic eccentricity is normally small compared to the dimensions of the generator, it is assumed that the perturbed air gap (g) is

$$g = g_0(z) + \sum_{m=1}^{\infty} \delta_m^s(z) \cos m(\phi + \alpha_m^s(z)) - \sum_{n=1}^{\infty} \delta_n^r(z) \cos n(\phi + \alpha_n^r(z) - \omega t) \\ -x \cos \phi - y \sin \phi \tag{11}$$

where (x, y) gives the position of C_r. Forces on the rotor can be found by using the principal of virtual work on the potential energy stored in the air gap, see Lundström and Aidanpää [12, 15]. The total forces in the x- and y-direction can then be expressed as

$$f_x = \frac{1}{2\mu_0} \int_0^{2\pi} \int_0^{l_0} \frac{B_0(z)^2 g_0(z)^2 u_0(z)}{g(x, y, z, t, \phi)^2} \cos \phi \, dz \, d\phi$$

$$f_y = \frac{1}{2\mu_0} \int_0^{2\pi} \int_0^{l_0} \frac{B_0(z)^2 g_0(z)^2 u_0(z)}{g(x, y, z, t, \phi)^2} \sin \phi \, dz \, d\phi \tag{12}$$

Here B_0 is the uniformly distributed magnetic flux density (B-field) for a perfect circular geometry i.e., $g = g_0$ and $u_0 = (r_0 + s_0)/2$. Equation (12) gives the UMP (unbalanced magnetic pull) for a rotor with shape deviations. UMP is a magnetic

force caused by a nonuniform air gap due to eccentricity or shape deviations in the air gap. Analysis of this force model has resulted in two theorems where the first one is a theorem about stable equilibrium of the rotor, see Lundström and Aidanpää [12]. By using a Taylor series expansion of Eq. (12), the second theorem about angular frequency and amplitude of the UMP is proved. Let θ be the average value of the angular frequency of the UMP and define $\psi = \theta/\omega$

Theorem. *Assume a shape perturbed generator of which one rotor perturbation parameter, δ_n^r, and one stator perturbation parameter, δ_m^s are dominating such that*

$$|x| + |y| + \sum_{\substack{i=1 \\ i\neq m}}^{\infty} \delta_i^s + \sum_{\substack{i=1 \\ i\neq n}}^{\infty} \delta_i^r << (\delta_n^r)^q + (\delta_m^s)^q \tag{13}$$

is satisfied for $q = 1, 2, \ldots, q'$. Then, for shape deviations with mn-combinations on the lines $(q-j)m - jn = \pm 1$, where $j = 0, 1, 2, \ldots, q$ and $q = 1, 2, \ldots, q'$, the UMP has the following properties:

1. *The average angular velocity satisfies $\psi = \mp j\, n$.*
2. *The amplitude will be proportional to $\left(\delta_n^r\right)^j \left(\delta_m^s\right)^{q-j}$*
3. *For mn-combinations outside the lines for all $q = 1, 2, ..., q'$, the UMP is zero.*

A proof can be found in Lundström and Aidanpää [15]. Results of the average angular frequency from the theorem are illustrated in Table 2 for $m, n \in [1, 10]$.

5 Tangential Forces

Unbalanced magnetic forces (UMP) arise in the generator when the air gap is smaller in one region, compared to the symmetrical case. Thus, the magnetic pull force from the region with a small air gap is larger than from the region with a large air gap. This net unbalanced force acts in the direction of the smallest air gap. In this paper, the consequence of this UMP on stability and whirling frequency is shown. Table 2 shows that different whirling frequencies, backward as well as

Table 2 Whirl frequency ψ due to shape deviations $m, n \in [1, 10]$

M:n	1	2	3	4	5	6	7
1	+1	+2	+3	+4	+5	+6	+7
2	+1	x	+3	x	+5	x	+7
3	+1	−2	x	+4	−5	x	+7
4	+1	x	−3	x	+5	x	−7
5	+1	−4	+6	−4	x	+6	−14
6	+1	x	x	x	−5	x	+7
7	+1	−6	−6	+8	+15	−6	x

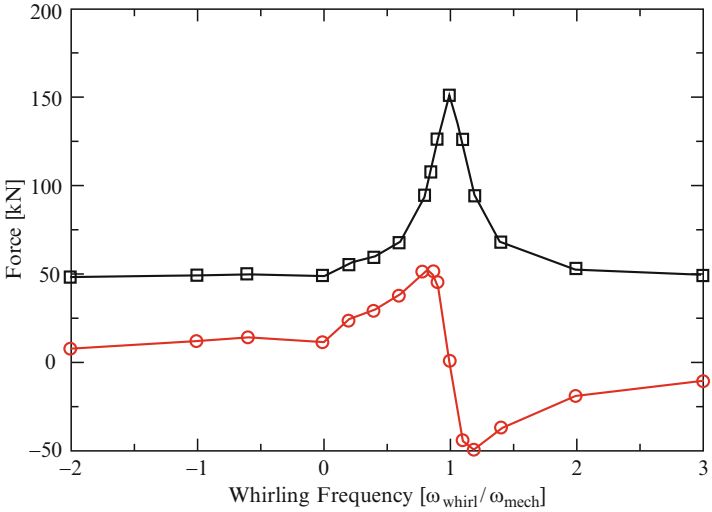

Fig. 5 Radial and tangential electromagnetic forces for 20% eccentricity and different whirling frequencies

forward whirling, can occur in large synchronous generators due to deviations in the generator shape.

The presence of damper windings in the case of an eccentric rotor/stator configuration gives a reaction magnetomotive force that lags the main flux and introduces a force-component perpendicular to the smallest air gap, denoted by the tangential component below. Saturation also affects the forces. The side with the smaller air gap length saturates and decreases the flux density in the air gap, reducing the UMP. In Fig. 5, the whirling dependent forces are shown for a hydropower generator.

The change in electromagnetic force due to the induced current in the damper windings has recently been documented in several publications, see e.g., Lundin and Wolfbrandt [16] and Burakov and Arkkio [18]. At synchronous whirl (when the whirling and mechanical frequencies are the same) the rotor always shows the same pole to the smallest air gap and, thus, the damper windings are not subjected to any changing magnetic field and no current is induced in them. It is these currents which damp the amplitude of the UMP and introduce the tangential component. During asynchronous whirl with constant eccentricity, the pole pointing to the smallest air gap will vary since the frequency of the whirling and the mechanical frequency do not coincide, hence the damper windings are subjected to a change in the magnetic field and the currents are induced in the windings. In the design of generators, this tangential force is not considered today. Therefore it is important to determine these forces and evaluate the dynamical consequences which will allow reliable machines to be built in the future.

6 Conclusions

Better models of the electromagnetic interaction in hydropower rotors are essential in order to meet the new demands on the machines. In this paper, the development in dynamical modelling of the electromagnetic interaction in hydropower rotors is summarized. From the results it is clear that nonlinear stability analysis, shape deviations in the air gap and whirling dependent electromagnetic forces needs to be considered in order to build reliable machines in the future.

Acknowledgment The research presented in this paper has been carried out with funding by Elforsk AB and the Swedish Energy Agency through their joint Elektra programme and as a part of Swedish Hydropower Centre - SVC' (www.svc.nu). SVC has been established by the Swedish Energy Agency, Elforsk and Svenska Kraftnäat together with Luleå University of Technology, The Royal Institute of Technology, Chalmers University of Technology and Uppsala University.

References

1. Behrend, B.A.: On the mechanical force in dynamos caused by magnetic attraction. AIEE **17**, 617 (1900)
2. Gray, A. Electrical Machine Design. McGraw-Hill Book Company Inc., New York, pp. 498–500 (1926)
3. Robinson, R.C.: The calculation of unbalanced magnetic pull in synchronous and induction motors. Electr. Eng. **62**, 620–624 (1943)
4. Covo, A.: Unbalanced magnetic pull in induction motors with eccentric rotors. Trans. AIEE **73**(III), 1421–1425 (1954)
5. Ohishi, H., et al.: Radial magnetic pull in salient poles machines. IEEE Trans. Energ. Convers. **EC-2**, 3 (1987)
6. Früchtenicht, J., et al.: Exzentrizitätsfelder als Ursache von Laufinstabilitäten bei Asynchronmaschinen. Teil I und II. Arch. Elektrotech. **65**, 271–292 (1982)
7. Arrkio, A., et al.: Electromagnetic force on a whirling cage rotor. IEE Proc. Electr. Power Appl. **147**(5), 353–360 (2000)
8. Holopainen, T.P., et al.: Electromagnetic circulatory forces and rotordynamic instability in electric machines. In: Proceedings of the 6th International Conference on Rotor Dynamics, vol. 1, pp. 446–463. University of New South Wales, Sydney, Australia (2002)
9. Laiho, A.N., et al.: Structural finite element modeling of electromechanical interaction in rotordynamics of electrical machines. In: Proceedings of ASME International Design Engineering Technology Conferences & Computers and Information in Engineering Conference, Long Beach, California USA, September 24–28 (2005)
10. Gustavsson, R.K., Aidanpää, J.-O.: The influence of magnetic pull on the stability of generator rotors. In: The 10th of International Symposium on Transport Phenomena and Dynamics of Rotating Machinery, Honolulu, Hawaii (2004)
11. Gustavsson, R.K., Aidanpää, J.-O.: The influence of nonlinear magnetic pull on hydropower generator rotors. J. Sound Vib. **297**(3–5), 551–562 (2006)
12. Lundström, N., Aidanpää, J.-O.: Dynamic consequences of electromagnetic pull due to deviations in the generator shape. J. Sound Vib. **301**(1–2), 207–225 (2007)
13. Karlsson, M., Aidanpää, J.-O.: Dynamic Behaviour in a Hydro power Rotor System due to the Influence of Generator Shape and Fluid Dynamics. PWE2005, ASME Power, Chicago, Illinois, 5–7 April 2005
14. Karlsson, M., et al.: Rotor dynamic analysis of an eccentric hydropower generator with damper winding for reactive load. J. Appl. Mech. **74**,1178–1186 (2007)

15. Lundström, N., Aidanpää, J.-O.: Whirling frequencies and amplitudes due to deviations in generator shape. Int. J. Non-Linear Mech. **43**(9), 933–940 (2008)
16. Lundin, U., Wolfbrandt, A.: Method for modelling time dependent non-uniform rotor/stator configurations in electrical machines. IEEE Trans. Magn. **45**(7), 2976–2980 (2009)
17. Belmans, R., et al.: Unbalanced magnetic pull and homopolar flux in three phase induction motors with eccentric rotors. In: Proceedings, International Conference on Electrical Machines-Design and Application, Budapest, pp. 916–921 (1982)
18. Burakov, A., Arkkio, A.: Comparison of the unbalanced magnetic pull mitigation by the parallel paths in the stator and rotor windings. IEEE Trans. Magn., In Press (2008)

Control-Oriented Approach to the Rotor Dynamics

Zdzisław Gosiewski

Abstract A new procedure of the design of rotor vibration control system is presented in the paper. It bases on the decoupling of the rotating system into smaller subsystems to find the dynamical phenomena responsible for rotor instability or pour vibration damping. The procedure is shown in an example of the control system for a simple three-mode model of torsional/lateral rotor vibrations. The root locus method was used to find influences between different vibration modes. It leads to the explanation which intersections of torsional and lateral natural frequency maps are unstable and why. Vibration analysis with help of the control theory methods indicates such control procedures which amplify the stabilizing mechanisms in the rotor dynamics. We are able to find the solutions which also lead to the energy saving control laws. In the case of lateral vibrations there were considered four control strategies. These strategies were compared to indicate an optimal one.

Keywords Coupled vibrations · Rotor · Root locus · Control

1 Introduction

Deep analysis of the control plant brings many useful information for the designer of the control system. The analysis is also important in the design of active vibration control system. The coupling of different dynamical phenomena in rotating machinery leads to unstable vibrations. Usually, the coupling effects are caused by some parameters. Angular speed or rotor unbalance in some applications are such parameters which change in the wide range. The problem is to find for which angular speeds we have unstable torsional/lateral vibrations. Usually, the unstable regions are in the vicinity of angular speeds where maps of natural frequencies for both dynamical systems cross each other.

Z. Gosiewski (✉)
Department of Mechanical Engineering, Bialystok Technical University,
ul. Wiejska 45C, 15-351 Białystok, Poland
e-mail: gosiewski@pb.bialystok.pl

K. Gupta (ed.), *IUTAM Symposium on Emerging Trends in Rotor Dynamics*,
IUTAM Bookseries 25, DOI 10.1007/978-94-007-0020-8_6,

There are two main aims of the vibration control systems: the system stabilization and the increase of the vibration damping [1]. The modal control of flexible structures is usually applied [2]. The modal control is a global one, while the sensors and actuators are located at specific points. In control-oriented modeling it is important to find input-output relations among these points [3]. So simpler the model of the plant, simpler is the control design. The disadvantages of modal approach are particularly well seen in the case of the rotor vibration control. The coupled vibrations are often met in the rotordynamics and small changes of the value of the coupling parameters can lead to the unstable behavior of the rotating machinery. So it is important to divide dynamical system into smaller subsystems and to find which parameters are responsible for the coupling of the subsystems and the system instability. Such vibration analysis can indicate what one should do to design the energy saving control system. We use three-mode rotor model to show how to do it.

All considerations are illustrated by the results of the computer simulations.

2 Mathematical Model

The physical model of flexible rotor is shown in Fig. 1. The model consists of a rigid disc and a massless flexible shaft. The static unbalanced disc is located in the center of the shaft. The shaft is driven with angular speed Ω which can be slowly changed in the range 0–30,000 rpm (0–3,140 rad/s). The disc has mass m and inertia momentum I_o. We assume that flexibilities of the shaft in both directions: ξ, η, are: k_1, k_2, respectively. The torsional flexibility coefficient is k_t.

Lagrange's equations were used to obtain the motion equations of the rotor. The set of three nonlinear motion equations with periodic time-varying coefficients was obtained where: $x_s = x – e\cos(\gamma + \delta)$, $y_s = y + e\sin(\gamma + \delta)$ are coordinates of the disc mass centre S in inertial coordinate system XYZ, while: $\xi = x\cos\gamma + y\sin\gamma$,

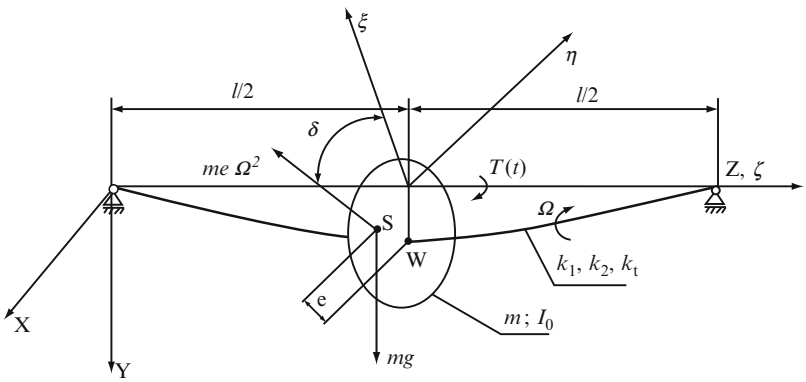

Fig. 1 Physical model of the anisotropic rotor

$\eta = -x\sin\gamma + y\cos\gamma$ are co-ordinates of the disc geometrical centre W in rotating co-ordinate system $\xi\eta z$, which rotates with rotor angular speed Ω. Furthermore: γ – is the angle of the shaft twist, e – is the eccentricity (distance) of rotor mass centre S from its geometrical centre W, while δ – is the angle between unbalance vector and axis ξ, b_z – coefficient of external damping, b_w – coefficient of internal damping, b_t– coefficient of torsional damping.

After linearization the rotor model in rotating co-ordinates is as follows:

$$\begin{aligned}
&\ddot{\xi} - 2\Omega\dot{\eta} - \Omega^2\xi + 2h_z(\dot{\xi} - \Omega\eta) + 2h_w\dot{\xi} + \omega_1^2\xi + e\Omega^2\sin\delta\phi - 2e\Omega\cos\delta\dot{\phi} \\
&\quad -e\sin\delta\ddot{\phi} = e\Omega^2\cos\delta + g\sin\Omega t, \\
&\ddot{\eta} + 2\Omega\dot{\xi} - \Omega^2\eta + 2h_z(\dot{\eta} + \Omega\xi) + 2h_w\dot{\eta} + \omega_2^2\eta + e\Omega^2\cos\delta\phi - 2e\Omega\sin\delta\dot{\phi} \\
&\quad +e\cos\delta\ddot{\phi} = e\Omega^2\sin\delta + g\cos\Omega t, \\
&\ddot{\phi} + 2h_t\dot{\phi} + \mathrm{Re}\Omega^2\phi + \mu^2\phi + R\omega_1^2\sin\delta\xi - R\omega_2^2\cos\delta\eta = -Rg\cos(\Omega t + \delta).
\end{aligned} \tag{1}$$

where: $\Omega_1^2 = \frac{k_1}{m}$, $\Omega_2^2 = \frac{k_2}{m}$, $\mu^2 = \frac{k_t}{I_0}$, $R = \frac{me}{I_0}$, $h_t = \frac{b_t}{2I_o}$, $h_z = \frac{b_z}{2m}$, $h_w = \frac{b_w}{2m}$

Equations in rotating coordinates (1) have constant coefficients. Therefore, the calculations of unstable ranges of angular speed will be much simple in opposition to the analysis of the equations in non-rotating coordinates.

3 Classical Analysis of Free Torsional/Lateral Rotor Vibrations

When we use Laplace transform and omit external excitations the differential equations (1) will be changed to the algebraic form:

$$\begin{bmatrix} A_{1d}(s) & -B_d(s) & -D(s) \\ B_d(s) & A_{2d}(s) & -F(s) \\ -H(s) & -K(s) & C(s) \end{bmatrix} \begin{bmatrix} \xi \\ \eta \\ \phi \end{bmatrix} = \begin{bmatrix} 0 \\ 0 \\ 0 \end{bmatrix}, \tag{2}$$

where:

$$\begin{aligned}
&A_{1d}(s) = s^2 + 2(h_z + h_w)s + \omega_1^2 - \Omega^2, A_{2d}(s) = s^2 + 2(h_z + h_w)s + \omega_2^2 - \Omega^2, \\
&C(s) = s^2 + 2h_t s + \mathrm{Re}\Omega^2 + \mu^2,\ D(s) = -e(\Omega^2\sin\delta - 2\Omega s\cos\delta - s^2\sin\delta), \\
&F(s) = e(\Omega^2\cos\delta + 2\Omega s\sin\delta - s^2\cos\delta),\ H(s) = -R\omega_2^2\sin\delta, \\
&K(s) = R\omega_1^2\cos\delta
\end{aligned} \tag{3}$$

The roots (poles) of the characteristic equation (Fig. 2) have been calculated in function of rotor speed Ω for the following parameters: $\omega_1 = 900\,\mathrm{rad/s}$, $\omega_2 = 1,000\,\mathrm{rad/s}$, $\omega_t = 1,500\,\mathrm{rad/s}$, $R_h = 0.01$, $h_z = h_w = 0.04\Omega_1$, $h_t = 0.02\omega_t$, $\rho = 30°$.

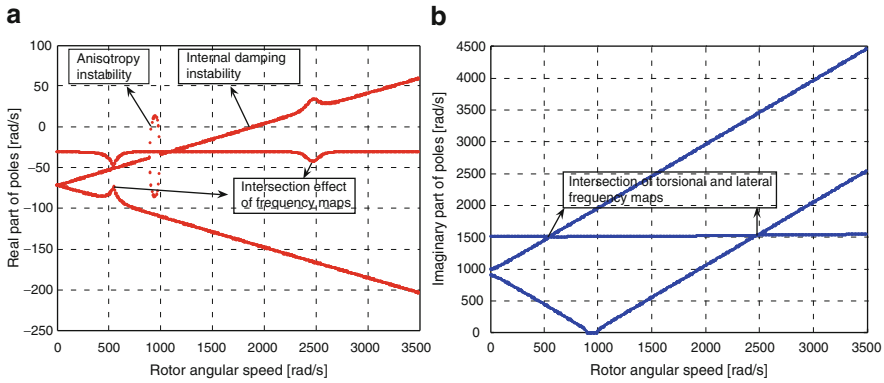

Fig. 2 Map of real part **(a)** and imaginary part **(b)** of characteristic equation roots (poles) for the torsional/lateral vibrations of the rotor with anisotropic flexibility

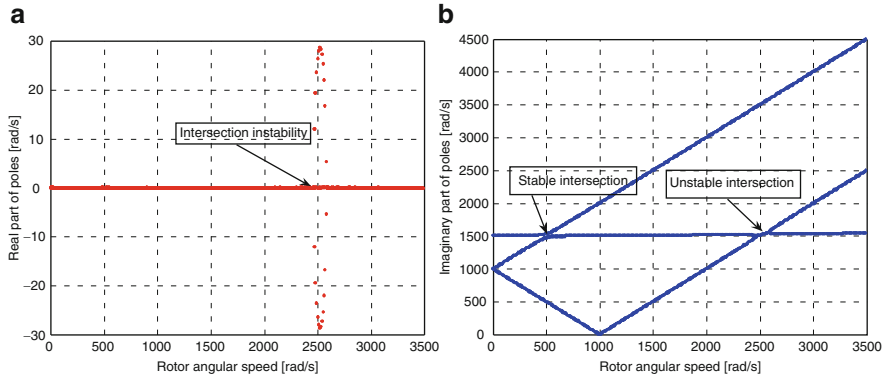

Fig. 3 Map of real part **(a)** and imaginary part **(b)** of characteristic equation roots (poles) for the udamped torsional/lateral vibrations of the rotor with isotropic flexibility

In the case of undamped torsional/lateral vibrations and isotropic flexibility ($\omega_1 = \omega_2 = 1,000\,\text{rad/s}$) the roots of the characteristic equation in the considered range of rotor speeds are shown in Fig. 3.

In the upper right quarter of the natural frequency map (Fig. 3b) we can notice three crossings of the natural frequency lines. Two intersections are in spots where torsional map meets lateral map: $\Omega \cong \mu_z - (\omega_1 + \omega_2)/2, \Omega \cong \mu_z + (\omega_1 + \omega_2)/2$. The third crossing is in the vicinity of the frequency $\Omega \cong (\omega_1 + \omega_2)/2$ where the natural frequencies of lateral vibrations in two perpendicular directions η, ξ approach each other. In the vicinity of two crossings there are unstable ranges of the rotor speeds Ω. The problem is: why some of the intersections are stable while others not?

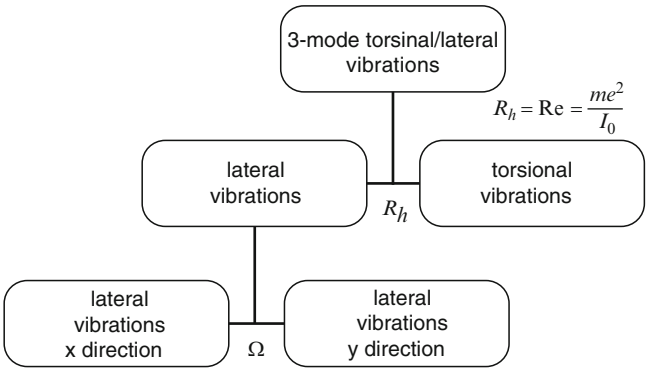

Fig. 4 Coupling parameters in considered rotor model

In the case of undamped isotropic system the inspection of the equations (1) leads to conclusion that the particular subsystems are coupled by two particular parameters: rotor unbalance R_h and rotor angular speed Ω as it is shown in Fig. 4.

4 Control Theory Approach to the Vibration Analysis

4.1 Undamped Free Vibrations of Isotropic Rotor

We neglect the damping and assume a rotor with isotropic flexibility $\Omega = \Omega_1 = \Omega_2 = 1,000\,\mathrm{rad/s}$. The mathematical model (2) can be presented in the form of block scheme, given in Fig. 5.

It is a dynamical system with feedback loop very well known from control theory, where particular transfer functions have the form:

$$G_1(s) = \frac{\xi(s)}{\varphi(s)} = \frac{B(s)F(s) + A(s)D(s)}{A^2(s) + B^2(s)}; G_2(s) = \frac{\eta(s)}{\varphi(s)} = \frac{A(s)F(s) - B(s)D(s)}{A^2(s) + B^2(s)};$$
$$G_3(s) = \frac{\varphi(s)}{\xi(s)} = \frac{H(s)}{C(s)}; \qquad G_4(s) = \frac{\varphi(s)}{\eta(s)} = \frac{K(s)}{C(s)}. \tag{4}$$

We break the feedback loop in the place indicated by tildes to obtain open-loop system. The open-loop transfer function has the form:

$$G_o(s) = \frac{-R_h\omega^2\{s^4 + s^2(3\Omega^2 + \omega^2) - (\omega^2 - \Omega^2)\Omega^2\}}{\{s^4 + 2s^2(\omega^2 - \Omega^2) + (\omega^2 - \Omega^2)^2\}(s^2 + \mu_z^2)} = R_h G_r(s) \tag{5}$$

In the Evans method, we will consider rotor unbalance parameter R_h as a gain which changes from zero to the infinity. Transfer function (5) has negative sign. It means a positive feedback – the rotor unbalance destabilizes the rotor motion.

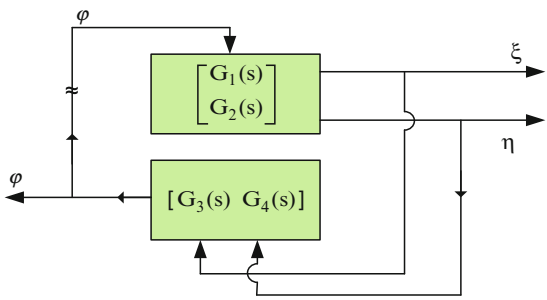

Fig. 5 Block scheme of the torsional/lateral vibrations of the flexible rotor

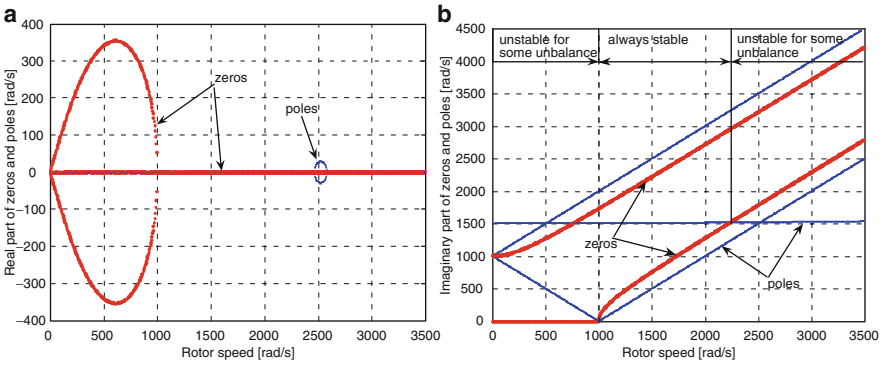

Fig. 6 The ranges of angular speeds destabilized by rotor unbalance. Real parts **(a)** and imaginary parts **(b)** of zeros in the transfer function $G_r(s)$ versus rotor angular speed Ω drown as bold lines. Slim lines show the poles of the transfer function $G_r(s)$

For R_h increasing from zero to the infinity the open-loop poles move towards zeros of the same open-loop transfer function $G_\mathrm{r}(s)$ (5). If the number of poles is bigger then the number of zeros the other poles escape to the infinity along asymptotes which start from the central point in the complex plane.

It means that zeros of the open-loop transfer function should play important role in the analysis of the dynamic behavior of the coupled vibrations. The real and imaginary part of transfer function zeros and poles are presented in Fig. 6.

When all zeros and poles of transfer function are purely imaginary the root locus plot moves along imaginary axis. In this case each pole has its interlacing zero which is a target for locus line. Two biggest poles move to infinity along imaginary axis. Such rotor is completely stable for all values of unbalance R_h.

Such harmony is destroyed when rotor angular speed cross value 2,250 rad/s (see Fig. 6). For angular speeds $\Omega > 2,250\,\mathrm{rad/s}$ the alteration of poles and zeros is replaced by close neighborhood of two poles. To reach open-loop zeros the locus lines are forced to make a circle. The circle enters the positive side of the complex plane. It means the motion becomes unstable for some values of unbalance. By analysis of the pole and zero values the ranges of unstable vibrations (Fig. 6) can be indicated. In first range (to 1,000 rad/s) the instability is connected with positive value

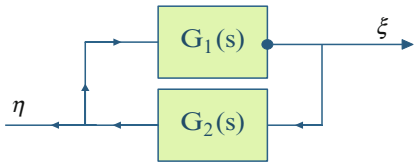

Fig. 7 The block scheme of rotor lateral vibrations

of the real part of two zeros of the open-loop transfer function. In second range of the unstable rotor angular speeds the alternating pole-zero pattern [4] is destroyed. The neighborhood of two zeros and two poles is a simple way to detect the unstable behavior of the system. The closer these are to the crossing point on natural frequency maps, the smaller value of unbalance is needed to trigger the instability in both ranges.

4.2 Damped Lateral Vibrations of Anisotropic Rotor

Now, we will consider free damped lateral vibrations of an anisotropic rotor. We separate two perpendicular directions of the rotor lateral vibrations. The block scheme of the system is shown in Fig. 7.

The open-loop transfer function is as follows:

$$G_{od}(s) = G_{1d}(s)G_{2d}(s), \tag{6}$$

where: $G_{1d}(s) = \frac{B(s)}{A_{1d}(s)}$; $G_{2d}(s) = \frac{-B(s)}{A_{2d}(s)}$. Finally, we have:

$$G_{od}(s) = \frac{4\Omega^2(s+h_z)^2}{[s^2+2(h_z+h_w)s+\omega_1^2-\Omega^2][s^2+2(h_z+h_w)s+\omega_2^2-\Omega^2]} = R_d G_{rd}(s) \tag{7}$$

The open-loop system is unstable for: $\Omega > \omega_1$ while closed-loop system [2] is stable also in the range $\omega_2 < \Omega < \omega_1(h_w + h_z)/h_w$. To find mechanism which extends the range of stable rotor speeds the Evans method is again used. We assume that rotor rotation is a cause of this mechanism so we introduce an artificial Evans' gain in the form: $R_D = 4\Omega^2$. It is evident that (7) has positive sign; it means the negative feedback. It can be deduced that angular speed stabilizes the rotor motion.

5 Control of Damped Lateral Vibrations of Anisotropic Rotor

The control forces f_ξ, f_η were added to rotor movement Eqs. (12). Let us consider the equations of lateral vibrations of the anisotropic rotor in an input-output form convenient to design the control law:

$$\mathbf{Y}_r(s) = \mathbf{G}_r(s)\mathbf{F}_r(s), \tag{8}$$

where:

$$\mathbf{Y}_r(s) = \begin{bmatrix} \xi(s) \\ \eta(s) \end{bmatrix}, \quad \mathbf{G}_r(s) = \frac{1}{D_{op}} \begin{bmatrix} A_{2d}(s) & B_d(s) \\ -B_d(s) & A_{1d}(s) \end{bmatrix}, \quad \mathbf{F}_r(s) = \begin{bmatrix} f_\xi(s) \\ f_\eta(s) \end{bmatrix}, \tag{9}$$

and D_{op} is plant characteristic equation. The control forces can be written as functions of measurement signals. These relationships are called control law:

$$\mathbf{F}_r(s) = -\mathbf{K}_r(s)\mathbf{Y}_r(s). \tag{10}$$

The characteristic equation of the closed-loop system is given by:

$$\det[\mathbf{I} + \mathbf{G}_r(s)\mathbf{K}_r(s)] = 0. \tag{11}$$

The Eq. (10) describes the control law in rotating coordinate system. In practice, the rotor vibrations are controlled in non-rotating inertial coordinate system. Thus, we introduce the transformation matrix between coordinates of rotating and non-rotating coordinate systems:

$$\begin{bmatrix} \xi(t) \\ \eta(t) \end{bmatrix} = \begin{bmatrix} \sin \Omega t & \cos \Omega t \\ -\cos \Omega t & \sin \Omega t \end{bmatrix} \begin{bmatrix} x(t) \\ y(t) \end{bmatrix}, \tag{12}$$

that is: $\mathbf{Y}_r(t) = \mathbf{T}\mathbf{Y}(t)$. The non-rotating control forces are $\mathbf{F}_r(t) = \mathbf{T}\mathbf{F}(t)$.

Finally, the control law in non-rotating coordinate system is $\mathbf{F}(s) = -\mathbf{K}(s)\mathbf{Y}(s)$, where the gain parameter of controller can be obtained from relation:

$$\mathbf{K}(s) = \mathbf{T}^T \mathbf{K}_r(s)\mathbf{T} \tag{13}$$

So the control law can be calculated in rotating coordinate system (which is advantageous in case of parametric vibrations) and then transformed to the inertial coordinate system.

6 Chosen Strategies of Rotor Lateral Vibration Control

After reanalysis of above analysis, we will try to improve lateral performance of the closed-loop system by:

– additional external damping,

$$\mathbf{K}_{r1}(s) = k_1 s \begin{bmatrix} 1 & 0 \\ 0 & 1 \end{bmatrix}, \tag{14}$$

– additional gyroscopic effect,

$$\mathbf{K}_{r2}(s) = \begin{bmatrix} 0 & -k_2 s \\ k_2 s & 0 \end{bmatrix}. \tag{15}$$

– change of system direct stiffness,

$$\mathbf{K}_{r3}(s) = -\begin{bmatrix} k_{31} & 0 \\ 0 & k_{32} \end{bmatrix}, \tag{16}$$

– change of system tangential stiffness.

$$\mathbf{K}_{r4}(s) = \begin{bmatrix} 0 & -k_4 \\ k_4 & 0 \end{bmatrix}. \tag{17}$$

For the control plant with parameters: $\omega_1 = 900\,\text{rad/s}$, $\omega_2 = 1,000\,\text{rad/s}$, $R_\text{h} = 0.01$, $h_\text{z} = h_\text{w} = 0.04\omega_1$, we have calculated such gain coefficients of controllers which bring the closed-loop system to the stability limit. The values of gain on the stability border for different rotor angular speeds Ω are called the critical coefficients. Such coefficients are shown in Fig. 8.

Only controllers $\mathbf{K}_{r3}, \mathbf{K}_{r4}$ are able to stabilize rotor motion in full range of the considered angular speeds. The cross change of system stiffness by $\mathbf{K}_{r4}$ controller significantly reduces the critical gains in comparison with the $\mathbf{K}_{r3}$ controller.

To compare different control systems we have taken into account the power consumption by amplifiers. The closed-loop systems with controllers $\mathbf{K}_{r2}$ i $\mathbf{K}_{r4}$ are

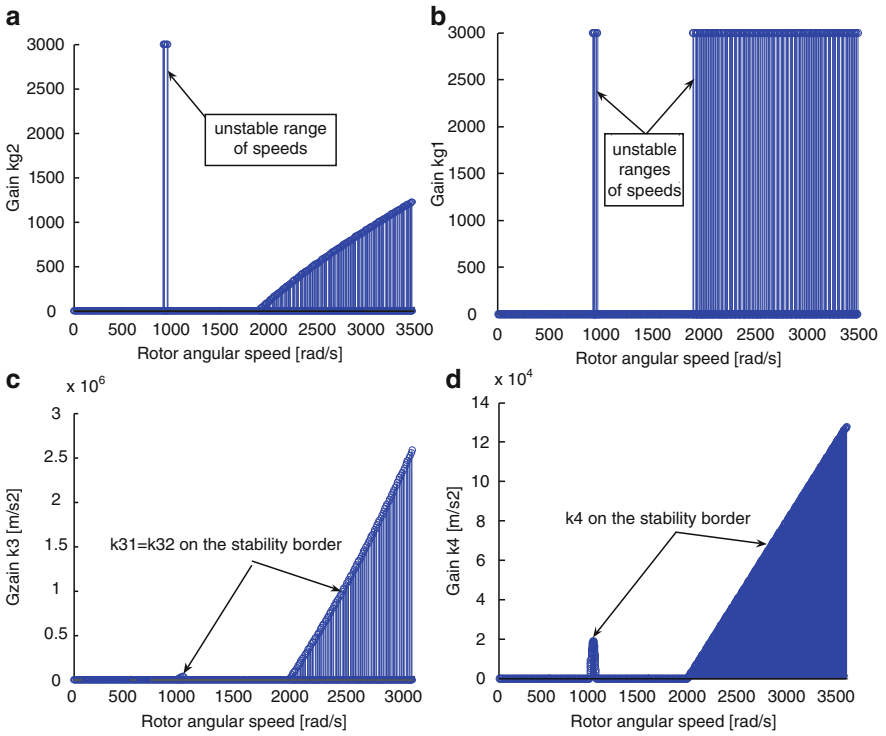

Fig. 8 Critical gain coefficients: **(a)** k_1, **(b)** k_2, **(c)** k_3, and **(d)** k_4, for rotor angular speed Ω from 0 to 3,500 rad/s

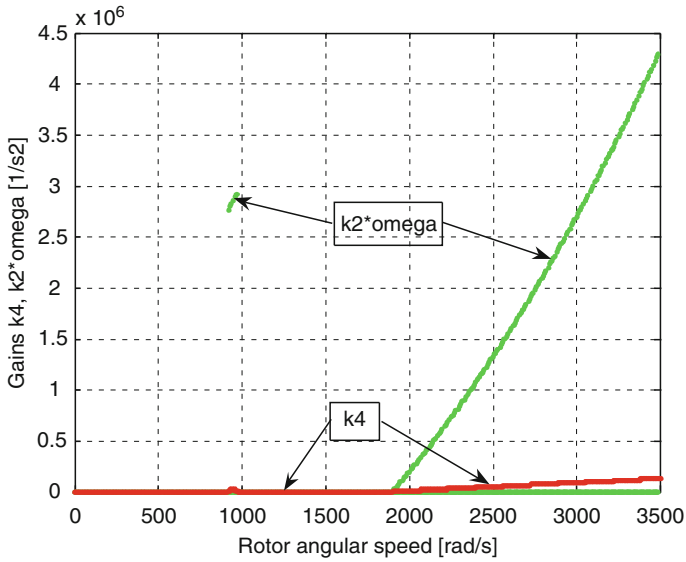

Fig. 9 The comparison of two critical gain parameters of the control system

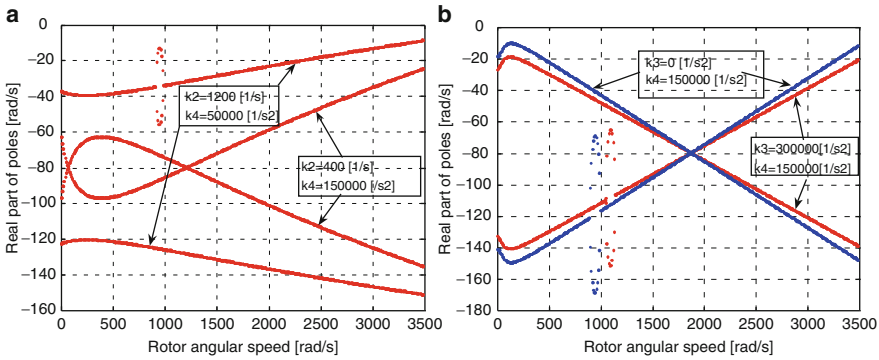

Fig. 10 Influence of different combinations of elementary controllers on the real parts of the closed-loop system poles

the most interesting. In the case of $\mathbf{K}_{r2}$ controller the gain coefficient has dimension of velocity while in the case of $\mathbf{K}_{r4}$ controller the gain coefficient has dimension of acceleration. The main rotor vibration velocity is connected with angular speed Ω. Therefore, to compare control forces the gain k_2 is multiplied by rotor angular speed Ω. The comparison of critical gain parameters for the $\mathbf{K}_{r2}$ i $\mathbf{K}_{r4}$ controllers is shown in Fig. 9. The $\mathbf{K}_{r4}$ closed-loop system is definitely the best one.

Unfortunately, the $\mathbf{K}_{r4}$ controller has poor transient response for some angular speeds. Therefore the elementary control laws are combined in more complex laws. According to Fig. 10 the best damping of the considered systems is for the control law with gain matrix $\mathbf{K}_{r5}$, where:

$$\mathbf{K}_{r5} = \begin{bmatrix} 0 & -400s - 150000 \\ 400s + 150000 & 0 \end{bmatrix}. \tag{18}$$

7 Control of Full Torsional/Lateral Model

Presently, the controller $\mathbf{K}_{r5}$ will be joined to the full model of the rotor torsional/lateral vibrations (Fig. 11). Its influence on the dynamic behaviour of the closed-loop system will be checked.

First we consider problem in classical way. The input/output model of the torsional/lateral plant (2) has the form:

$$\begin{bmatrix} \xi(s) \\ \eta(s) \end{bmatrix} = \frac{1}{\Delta} \begin{bmatrix} A_{2d}C - FK & B_dC + DK \\ -B_dC + FH & A_{1d}C - DH \end{bmatrix} \begin{bmatrix} f_\xi(s) \\ f_\eta(s) \end{bmatrix}, \tag{19}$$

where Δ is characteristic equation and f_ξ, f_η are control forces from Eqs. (8).

The poles of the closed-loop system are presented in Fig. 12. The system is stable in all range of considered rotor angular speed. The relative vibration damping considered as a relation of real and imaginary parts of poles decreases together with rotor speed because real parts of poles connected with uncontrolled torsional vibrations are almost constants. The controller influences the both imaginary and real parts of the poles. The maximal decrease of the negative real part of some poles moves together with the intersection of frequency maps for torsional and lateral vibrations from 2,500 (open-loop system) to 2,770 rad/s (closed-loop system).

It is much more interesting to carry out the closed loop system analysis in another way – by manipulation of the block scheme. According to Fig. 11 the control forces are defined as:

$$\mathbf{F}_r(s) = \begin{bmatrix} f_\xi(s) \\ f_\eta(s) \end{bmatrix} = -\begin{bmatrix} 0 & -k \\ k & 0 \end{bmatrix} \begin{bmatrix} \xi(s) \\ \eta(s) \end{bmatrix} + \begin{bmatrix} D(s) \\ F(s) \end{bmatrix} \phi(s), \tag{20}$$

where $k = k_2 s + k_4$.

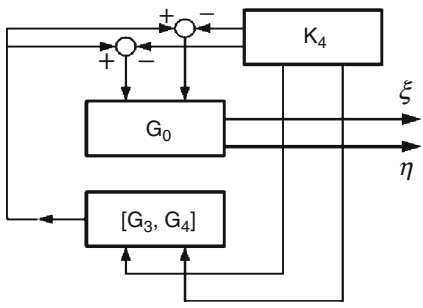

Fig. 11 Block scheme of the considered model for the rotor with active control of the lateral vibrations

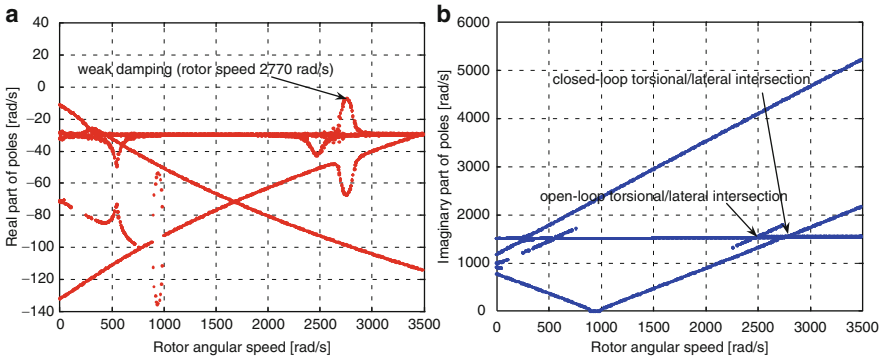

Fig. 12 Real **(a)** and imaginary **(b)** parts of the poles in closed-loop system in the rotor speed range 0–3,500 rad/s

The above input forces are introduced to the lateral vibrations model to obtain the relations between the torsional and lateral vibrations in the closed loop system:

$$\frac{1}{D_{op}}\begin{bmatrix} D_{op}+Bk & -A_2k \\ A_1k & D_{op}+Bk \end{bmatrix}\begin{bmatrix}\xi \\ \eta\end{bmatrix} = \frac{1}{D_{op}}\begin{bmatrix} A_{2d} & B_d \\ -B_d & A_{1d}\end{bmatrix}\begin{bmatrix} D \\ F\end{bmatrix}\phi \tag{21}$$

Using above relation, we can find the transfer functions between the lateral vibrations and torsional vibrations in the following form:

$$\begin{bmatrix}\xi \\ \eta\end{bmatrix} = \frac{1}{D_{op}D_{cl}}\begin{bmatrix}(D_{op}+Bk)(A_2D+BF)-A_1k(A_1F-BD) \\ A_2k(A_2D+BF)+(D_{op}+Bk)(A_1F-BD)\end{bmatrix}\phi, \tag{22}$$

where D_{cl} is the characteristic polynomial of the closed-loop system designed to control lateral vibrations.

In case of the minimal realization of the transfer functions the polynomial D_{op} from the denominator should be compensated by the same polynomial in the numerator. The above considerations lead to the reduced scheme (Fig. 5). Only the transfer functions $G_1(s)$,$G_2(s)$ were replaced by transfer functions $G_{1c}(s)$, $G_{2c}(s)$:

$$G_{1c} = \frac{(D_{op}+Bk)(A_2D+BF)-A_1k(A_1F-BD)}{D_{op}D_{cl}},$$
$$G_{2c} = \frac{A_2k(A_2D+BF)+(D_{op}+Bk)(A_1F-BD)}{D_{op}D_{cl}}. \tag{23}$$

It means that full analysis of the system dynamics can be carried out according to procedure shown in Sect. 4.

8 Summary

The full analysis of the rotor torsional/lateral vibrations is much simpler when we can divide the system into smaller subsystems. In this case the calculations are simplified and we have deep insight into mechanisms leading to good or bed behaviour of the rotor motion. It is particularly important in the case of the rotor working in the wide range of the angular speeds. Turbo jet engines and flywheels are such rotors. For the vibration analysis the methods known from control theory was applied. In the paper it is Evans method. As well some other control methods can also be used for the vibration analysis.

The proposed approach was verified in the paper on the simple three-mode rotor model (Jeffcott model). The torsional vibrations were separated from lateral vibrations and a feedback among subsystems was established. The subsystems are coupled by rotor unbalance and Evans method allows us to show the critical values of the unbalance which destabilize rotor motion for different angular speeds. The lateral vibrations are stabilized by angular speed and using again Evans method it is possible to find how large a value of the rotor speed is sufficient to stabilize rotor motion.

Such analysis of the rotor vibrations appeared very useful for the choice of the control strategy. It indicated such control procedures which amplify the positive (stabilizing) mechanisms in the rotor dynamics. Such procedures can also lead to the energy saving control laws. In the case of lateral vibrations there were considered four control strategies. And these strategies were compared to indicate optimal one. We hope that the decomposition will also be useful in the diagnostic systems.

References

1. Gosiewski, Z.: Control-oriented modeling and control of rotor vibration. Acta Mech. Autom. 2(2), Bialystok (2008)
2. Gosiewski, Z., Muszyńska, A.: Dynamika maszyn wirnikowych (Dynamics of Rotating Machinery). Publishing Office of WSInż, Koszalin (1992)
3. Kaczorek, T.: Teoria sterowania i systemów (Theory of Control and Systems). Wydawnictwo Naukowe PWN (1993)
4. Preumont, A.: Vibration Control of Active Structures: An Introduction. Kluwer Academic Publishers, Dordrecht (2002)

New Approach to the Analysis of the Dynamics Behavior of a Fluid Structure Interaction

E. Malenovský, F. Pochyly, and L. Pohanka

Abstract This contribution is focused on the analysis of dynamic behavior of an elastic body moving in liquid. This paper presents a new approach to the solution that allows the separation of the structure and liquid from each other. The approach is based on the expansion of the solution into a series of eigenshapes of vibration. In addition, a new type of boundary conditions is presented that allows modal analysis and calculates the steady state or unsteady response. It is however necessary to perform some computational and experimental testing to verify this approach which is new. The cantilever beam vertically submerged in water was chosen as a test set up to represent a rotor. In the paper, some comparisons of computational and experimental analyses are presented. For this case a specific programme was created in MATLAB, where the curvilinear co-ordinates were chosen. The Bézier body was chosen for the description of the geometrical configuration and also for the approximation of the solution. For the experimental verification, a cantilever beam submerged under water was chosen.

Keywords Fluid structure interaction · Finite element method · Modal added mass · Modal added damping · Experimental analysis

1 Introduction

The interaction between shaft and surroundings has an influence on the dynamic behavior of hydraulic rotor systems, e.g., in water turbines and pumps the interaction has a substantial influence on the frequency modal behavior. Computational analysis using commercial solvers, e.g., ANSYS or FLUENT, is very time consuming. Mostly it is necessary to have two types of meshes: the first is applied on the structure and the second is used for liquid. If the fluid-structure interaction is included, it makes the system equations nonlinear.

E. Malenovský (✉), F. Pochyly, and L. Pohanka
Brno University of Technology, Faculty of Mechanical Engineering,
Technicka 2, Brno, 616 69, Czech Republic
e-mail: malenovsky@fme.vutbr.cz

K. Gupta (ed.), *IUTAM Symposium on Emerging Trends in Rotor Dynamics*,
IUTAM Bookseries 25, DOI 10.1007/978-94-007-0020-8_7,

This contribution presents a new approach to the solution that allows the separation of the structure and liquid from each other. This approach is based on the expansion of the solution into a series of eigenmodes of vibration. A new algorithm for the solution was needed which is presented. The first step of solving the coupled problem is to perform the analysis of the individual structure, in this case the shaft. The frequency modal behavior is a result of this solution. In the general case, when large displacement and strain are considered, the chosen shaft position is an input parameter. The second step of the solution provides the analysis of the individual liquid system. Boundary conditions in places where interaction occurs are dependant on the chosen mode of vibration. The input parameter is the chosen boundary, which again depends on the chosen mode of vibration. The results from this step are the velocity and pressure fields. The last computational step is the analysis of the structure which includes the influence of liquid. In the form of added mass, damping and stiffness matrices, the effect of liquid system on the structure is included. These matrices for finite elements are calculated based on the liquid system analysis; consequently depend on the known velocity and pressure fields. It is necessary to perform some computational and experimental testing, because this approach to the solution is new. The cantilever beam submerged in water was chosen as a test rig. Some comparisons between computational and experimental analyses are presented.

A solution to the problem of a fluid – elastic structure interaction belongs to the most difficult category in mechanics. There are three basic tasks. The first is the eigenvalue problem; the second is the solution of steady state response under the harmonic (periodic) excitation and the third one is solution of the unsteady state response. These approaches are standard features of commercial programme packages such as ANSYS, FLUENT [1] etc. The Problem of fluid structure interaction needs a different approach to computational modeling. Generally, it has bad numerical stability and is very time consuming. Scientists are exploring various ideas to achieve better numerical stability and reduce the computation time. Because the presented method and algorithm is totally new, it is very difficult to find some relevant literature references. The authors are not aware of any publication where the application of modal transformation in fluid interaction with structure is presented. For this reason, literature references are focused only on the overview of the most used methods. The authors believe that this presented new approach will be less time consuming and will have better numerical stability. A general overview of the methods to the computational modeling is presented by Pochyly and Malenovský [2], Malenovský and Pochyly [3], Stein et al. [4], Axisa and Antuncs [5], Levy and Wilkinson [6], Legay and Kölke [7], Sigrist et al. [8] and Antoci et al. [9]. The general approach to the analysis of coupled vibrations of a beam that is submerged in a liquid is presented by Pochyly and Malenovský [10] and Malenovský and Pochyly [11], including an overview of methods of computational modeling. The main goal of the authors is to find a suitable algorithm for separating an elastic structure and fluid from each other. This means that for practical applications, firstly the analysis of separated fluid with given boundary conditions is performed. The second step provides the analysis of dynamic behavior of an elastic structure, including added

effects of fluid. Next goal of the authors is to propose algorithms for the analysis of motion for an elastic structure in fluid using the commercial programme codes. The methodology is based on the expansion into the series of eigenmodes of vibration. It means that the fluid does not have an expressive influence on the mode of vibration of an individual structure, but has influence only on the eigenvalues. It is possible to address the problem using this assumption and assume large deformations of the structure. For this configuration, the added effects of fluid are calculated.

2 Mathematical Model for Fluid Analysis

The Navier–Stokes and continuity equations are the fundamental equations for the analysis

$$\rho\frac{\partial c_i}{\partial t} - \eta\frac{\partial^2 c_i}{\partial x_j \partial x_j} + \frac{\partial p}{\partial x_i} = 0,\ \rho\frac{\partial c_i}{\partial x_i} = 0 \tag{1}$$

where η is dynamic viscosity, ρ is density, c_i is velocity, p is pressure, and $x_i (i = 1 - 3)$ is Cartesian co-ordinate. The boundary conditions for a real fluid are such that on a given point on the surface, the velocity of the structure and the fluid are the same

$$c_i = v_i^{\bullet} \tag{2}$$

where v_i is the displacement of the structure. The main aim of the authors is to find a suitable algorithm, using which it should be possible to exclude the unknown structure velocity from the boundary conditions. It is possible to achieve this by using the following transformation relations (this transformation is in detail described by Malenovský and Pochyly [3])

$$c_i = \int_0^t \alpha_{ik}(t-\tau)v_k^{\bullet}(\tau)d\tau, \quad p = \int_0^t \beta_k(t-\tau)v_k^{\bullet}(\tau)d\tau \tag{3}$$

where α_{ik} is the velocity function, β_k is pressure function, t, τ is time. Previously, this approach was applied for the analysis of rigid body, such as for journal bearings or squeeze film dampers. Equation (3) is in principle the modal transformation with the possibility of mutual separation of elastic structure and fluid from each other. Some results of several years of research are presented as a summary by Pochyly and Malenovský [2] and Malenovský and Pochyly [3]. This contribution is focused on the analysis of an elastic structure. The solution is based on an expansion into a series of eigenmodes of vibration. It is possible to write the following expression for the displacement of an elastic structure

$$v_i(z,t) = \sum_{k=1}^{\infty} w_{ik}(z)q_k(t) \tag{4}$$

where w_{ik} is the ith deformation parameter of the structure for the kth mode of vibration, and q_k is a time function. The new boundary conditions for the kth mode of vibration have the form

$$\int_0^t \alpha_{ik}(t-\tau)q_k^{\bullet}(\tau)d\tau = w_{ik}(z)q_k^{\bullet}(t) \tag{5}$$

After including the boundary conditions, the Navier–Stokes and continuity equations for one mode of vibration, will have the matrix form

$$\mathbf{A}\boldsymbol{\alpha}^{\bullet} + \mathbf{B}\boldsymbol{\alpha} + \mathbf{C}\boldsymbol{\beta} = \mathbf{f}_a\delta^{\bullet} + \mathbf{f}_b\delta, \quad \mathbf{D}\boldsymbol{\alpha} = \mathbf{f}_d\delta \tag{6}$$

where $\delta, \delta^{\bullet}$ are the Dirac function and its time derivative respectively. When the shaft rotation is included, the right side depends also on the Heaviside function. However in the present study, rotation of shaft is not included. These equations are solved using the Laplace transformation. Then, the resulting solution has the form

$$\boldsymbol{\alpha} = (\mathbf{W}\mathbf{f}_a + \mathbf{Z}\mathbf{f}_d)\delta - \boldsymbol{\varepsilon}^{\bullet} \tag{7}$$

$$\boldsymbol{\beta} = \mathbf{V}(\mathbf{D}\mathbf{A}^{+}\mathbf{f}_a - \mathbf{f}_d)\delta^{\bullet} + \mathbf{V}\mathbf{D}\mathbf{A}^{+}[\mathbf{f}_b - \mathbf{B}(\mathbf{W}\mathbf{f}_a + \mathbf{Z}\mathbf{f}_d)]\delta + \mathbf{V}\mathbf{D}\mathbf{A}^{+}\mathbf{B}\boldsymbol{\varepsilon}^{\bullet} \tag{8}$$

where some matrices have the form $\mathbf{V} = (\mathbf{D}\mathbf{A}^{+}\mathbf{C})^{+}$, $\mathbf{W} = \mathbf{A}^{+} - \mathbf{A}^{+}\mathbf{C}[\mathbf{V}(\mathbf{D}\mathbf{A}^{+})]$, $\mathbf{Z} = \mathbf{A}^{+}\mathbf{C}\mathbf{V}$, $\mathbf{U} = \{\mathbf{A}^{+} - \mathbf{A}^{+}\mathbf{C}[\mathbf{V}(\mathbf{D}\mathbf{A}^{+})]\}\mathbf{B}$. The unknowns $\boldsymbol{\varepsilon}$ and $\boldsymbol{\varepsilon}^{\bullet}$ are determined from Eq. (9)

$$\boldsymbol{\varepsilon}^{\bullet} + \mathbf{W}\mathbf{B}\boldsymbol{\varepsilon} = -\mathbf{W}[\mathbf{f}_b - \mathbf{B}(\mathbf{W}\mathbf{f}_a + \mathbf{Z}\mathbf{f}_d)]h \tag{9}$$

Here h is the Heaviside function. If $\boldsymbol{\varepsilon}^{\bullet}$ is neglected for the velocity and pressure field, it is possible to write

$$\boldsymbol{\alpha} = \boldsymbol{\alpha}_1\delta, \quad \boldsymbol{\beta} = \boldsymbol{\beta}_1\delta^{\bullet} + \boldsymbol{\beta}_2\delta \tag{10}$$

The force from the liquid that impacts the element of structure with area S_e, in normal direction n_i, is given by the expression

$$f_i = -\int_{S_e} p n_i dS_e + \eta \int_{S_e} \frac{\partial c_i}{\partial x_j} n_j dS_e \tag{11}$$

According to Eqs. (3) and (10) the velocity and pressure are

$$c_i = \alpha_{1ij}v_j^{\bullet}, \quad p = \beta_{1j}v_j^{\bullet\bullet} + \beta_{2j}v_j^{\bullet} \tag{12}$$

The solution for application of the Finite Element Method and with respect to the separation of the liquid and structure from each other is presented by Pochyly and Malenovský [10]. It is possible to derive, using Eqs. (11), (4) and (12), the expression for local finite element mass and damping matrices of the added effects from liquid in the form

$$m_{ij} = \int_{S_e} u_i \beta_{1l} w_{jl}^{-1} dS_e, \quad b_{ij} = \int_{S_e} u_i \left[\beta_{2l} + \eta \left(\frac{\partial \alpha_{1ml}}{\partial x_n} + \frac{\partial \alpha_{1nl}}{\partial x_m} \right) \right] w_{jl}^{-1} dS_e \tag{13}$$

where u_i is the base function. Rotation of the shaft has influence on the damping and mainly on the added stiffness, especially for small radial gap. The general algorithm for numerical analysis is as follows:

1. The whole range in frequency or time domain is divided into a finite number of steps.
2. The modal behavior analysis of individual continuum (without liquid) for a finite number of steps of geometry configuration is created.
3. The analysis of an individual liquid with boundary conditions which are given by the chosen eigenmode of vibration is performed. This step is repeated until the finite number of eigenvalues is achieved. The velocity and pressure fields are obtained for each step and a given continuum position.
4. On behalf of the velocity and pressure field on the continuum surface, the added matrices of liquid influence are calculated. In addition, the global added modal matrices for a given mode of vibration and given vibrating position of continuum are arranged (this step depends on parameter, which is selected for shape of vibration and corresponding positions).

Interpolation of the analysis of individual continuum, including the global matrices from the analysis of an individual liquid (step 4), is used during the numerical solution.

3 Model Sample

The model exercise is a cantilever beam vertically submerged in water (as shown schematically in Fig. 1). This model was chosen for the possibility of comparing it with the experiment. The experimental equipment consists of a cantilever steel tube 17.85/16.85 mm (beam) of length of 1,100 mm that is vertically submerged into a liquid, in this case in water. The tube was enclosed in a cylindrical vessel filled with water. The five cylinders (1–5) were manufactured with diameters: 40, 50, 70, 100 and 220 mm (with gaps 2.5, 7.5, 17.5, 32.5 and 82.5 mm). Acrylic glass was chosen for the material of the vessels. A transparent material was chosen to visually control the water level in which the beam is submersed. The harmonic exciter type Brüel & Kjaer 4824 was chosen, whereas a suitable point on the upper part of the beam was chosen for excitation. The exciter was freely–hanged, whereas the moving part of the exciter was fixed to the excited beam near the fixed end of the beam. The direction of excitation was not changed during the experiment and vibration amplitude was maintained constant during all the experiments. Two acceleration sensors Brüel & Kjaer 4374 were chosen for recording the data of the vibrating beam. These were glued to the inner surface of the beam near the free end, before the tube was plugged. Both, the modal damping and eigenfrequency of the submersed beam in

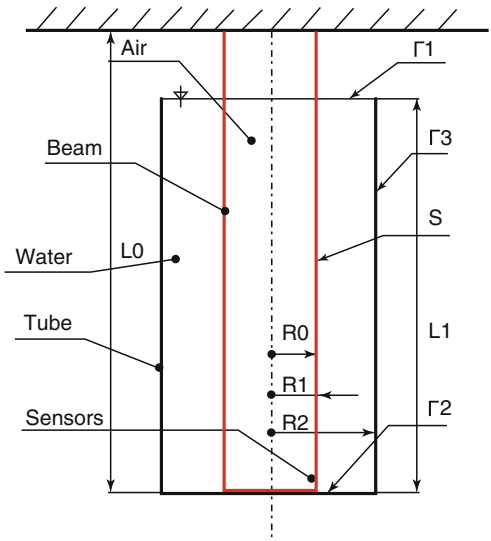

Fig. 1 Scheme of cantilever beam

water was evaluated during the first experiment. On the whole, 11 measurements were carried out with the height of water varying from 0 to 1,000 mm with a step of 100 mm. For the first mode of vibration a frequency with bandwidth 8–25 Hz was chosen and 60–135 Hz for the second mode. Frequency of excitation in both modes was varied linearly i.e., at a constant rate. The time for increasing the frequency from minimum to maximum value was chosen as 128 s for the first mode and 64 s for the second mode. From the time dependant acceleration (path through resonant state) the eigenfrequencyand damping were evaluated. The system Brüel & Kjaer HW – 3,560D Pulse and Brüel & Kjaer SW – 7,700 Pulse Labshop was used for recording the data and numerical treatment of accelerations. Time dependant acceleration is shown in Fig. 2. From the maximum amplitude, the eigenfrequency was determined. Based on the frequency bandwidth near the resonance peak, the modal damping for a given mode of vibration was determined. Figures 3 and 4 present the comparison of eigenfrequency from theory and experiment for the first and second modes of vibration respectively. Based on this experiment (path through the resonant state) it is very difficult to evaluate damping, because it is evaluated from the bandwidth of resonant state. It is necessary to assume for this approach of damping evaluation, that the dynamic system is linear and damping is viscous. However, none of these assumptions are valid. Despite that, this approach was chosen for the evaluation of damping. From this evaluation, qualitative and quantitative differences were evident in comparison of theoretical and experimental values. Relatively good agreement was seen in eigenfrequencies. But in the modal damping, substantial difference between computational and experimental values is observed.

Therefore a second experimental method was chosen for evaluating the eigenfrequencies and damping coefficient. This method was based on the static deflection from static equilibrium position and eigenfrequency and damping were

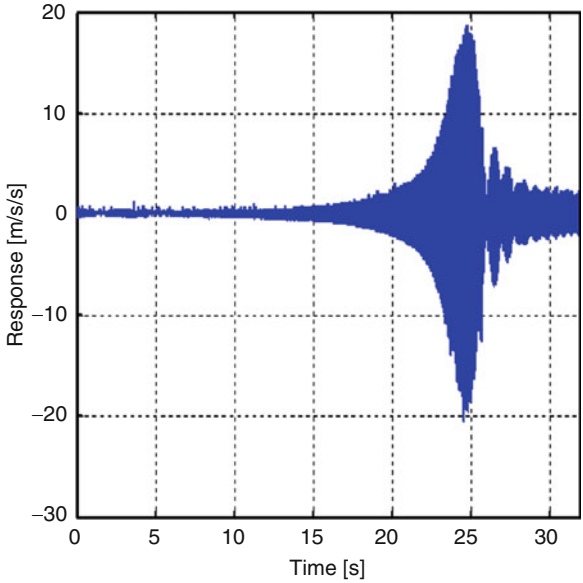

Fig. 2 Time dependent acceleration

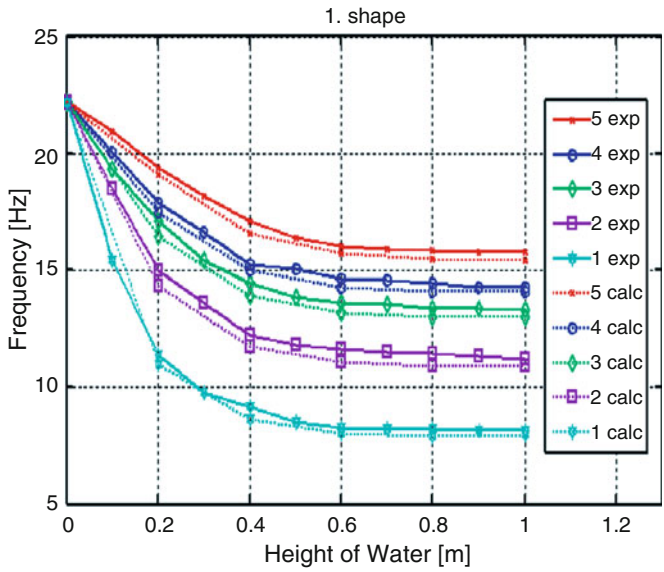

Fig. 3 Comparison for the first shape

evaluated from free damped vibration. For this experiment it was necessary to modify the experimental equipment. Deflection of the tube was provided mechanically on the free end of the inner tube. For this purpose an orifice was drilled on

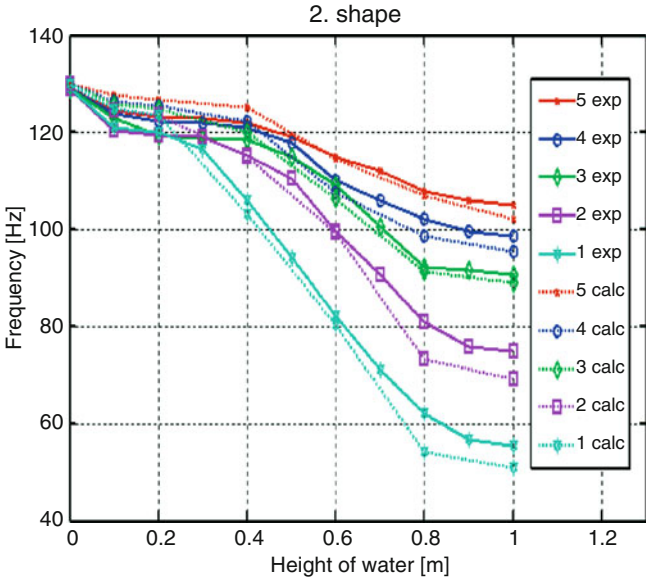

Fig. 4 Comparison for the second shape

the outer tube and a wire was inserted. Using this wire, the inner tube was deflected from the static equilibrium position. This arrangement is shown in Fig. 5. From the free damped vibration the eigenfrequency and damping coefficient were evaluated. Time dependence of acceleration for each configuration is evident from Fig. 6. There are no substantial differences in the eigenfrequencies, which are evaluated from the path through the resonant state and from the free damped vibration. For the evaluation of the damping it is possible tochoose more methods. It may be noted, that this dynamic system is nonlinear. When the displacements are small and the beam vibrates around the static equilibrium position, the system can be assumed to be close to linear. The damping coefficient was evaluated from the two amplitudes and finite number of periods from each other as per the approach presented by Ver and Beranek [12]. According to point of excitation (free end of beam), it was possible to evaluate the damping only for the first mode of vibration. Therefore the damping for the second mode of vibration is not presented. Figure 7 presents the comparison of the damping coefficient determined using the computational and experimental methods. Smaller damping is observed for the case of large diameters. From the comparison, it is evident that for higher levels of liquid, damping determined from experiment is less than from computation. This fact indicates that this dynamic system is nonlinear. In addition, gravity can have some influence, which was not included in the computational model. Furthermore it is evident from this experiment, that the results have higher uncertainty, which produce some variance of damping. This fact can be partially eliminated by conducting more experiments, but due to paucity of time this was not possible.

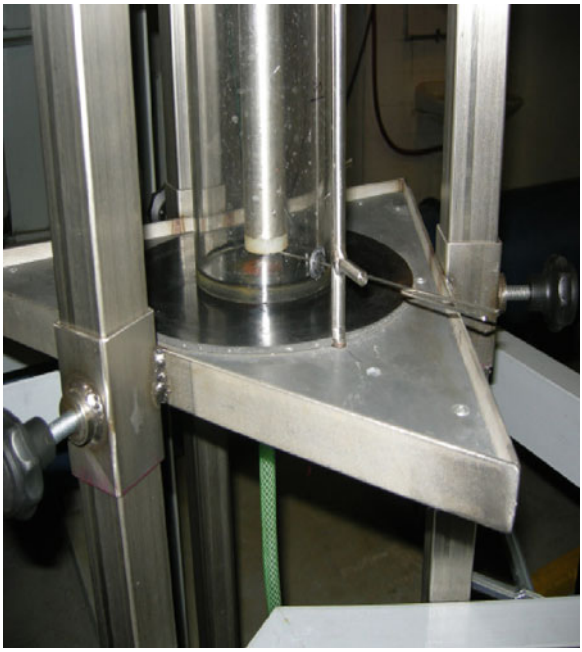

Fig. 5 Test equipment for the deflection

The computational analysis was provided for the cases of liquid at a height from 0 to 1,000 mm with a step of 200 mm curvilinear coordinates are used for the software. For the solution of the Navier–Stokes equation, the Finite Volume Method is used and for the continuity equation, the Finite Difference Method is used. This combination was chosen to achieve the best numerical stability of the numerical solution. It may be noted that all possible combinations between both methods were tested. Also, it is necessary to note, that both methods are used as collocations. The Bézier body is used for the approximation of the geometrical configuration as well as for the approximation of velocity and pressure solution. The following conclusions are evident from the comparison of the experimental and numerical analysis:

1. Good agreement between the experiment and numerical solution is evident for the dependency of eigenvalue on the height of water.
2. For both modes of vibration, a little but lower value for the numerical solution are evident. It may be due to the influence of the acceleration and amplitude of force of excitation on the complex eigenvalues (both, damping coefficient and eigenfrequency of system). It was evident from experimental analysis, that the eigenfrequency in the two directions is a little different and both are bounded.

From the comparison of damping it is evident that lower damping is evaluated from experiment. It can be caused by such factors as the approximations in computational model, nonlinearity of the system, effect of gravity, mismatch of boundary conditions for the numerical solution and experiment etc.

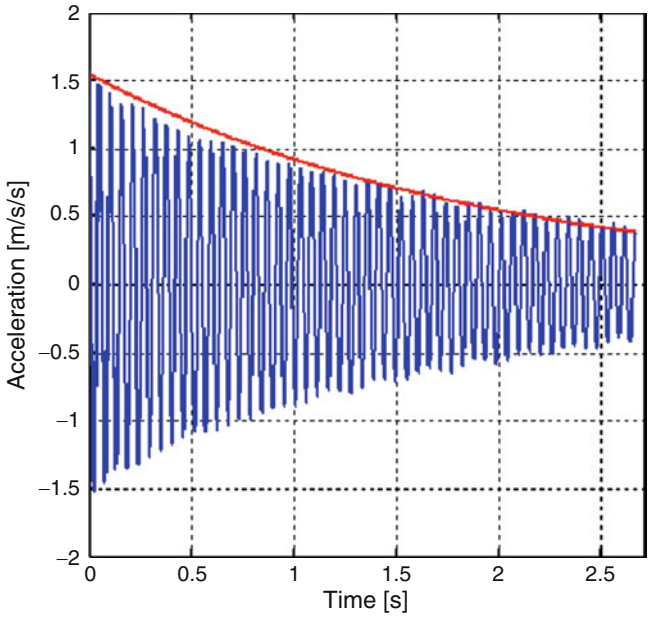

Fig. 6 Response of free damped vibration

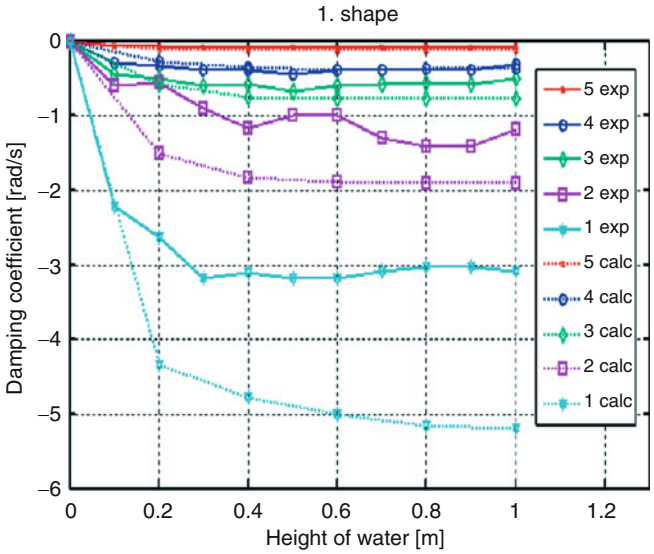

Fig. 7 Comparison of damping

4 Conclusion

This contribution presents a new mathematical model and algorithm to the solution of the interaction between an elastic structure and liquid. It is possible to use the presented approach for the solution and also for a continuum with large displacement and large constraints. It may be noted, that the presented mathematical and computational model can be executed using the systems ANSYS and FLUENT. It is necessary to compare the presented method and algorithm with the other approaches that are presently used. This is the main goal for forthcoming research activity. Present approach can be easily implemented for the analysis of the rotor dynamic systems, where the fluid-structure interaction occurs.

Acknowledgment This research is sponsored by grant GACR No. 101/09/1716.

References

1. FLUENT 6.2 Documentation: PDF Manual. Lebanon (NH), Fluent. Inc. (2005)
2. Pochyly, F., Malenovský, E.: Computational modeling of additional effects during fluid film interaction with structures in time and frequency domains. In: Eighth International Conference on Flow – Induced Vibration, Paris, France, 6–9 July 2004
3. Malenovský, E., Pochyly, F.: The computational modeling of frequency dependent additional effects during fluid film interaction with structures. In: Eighth International Conference on Vibrations in Rotating Machinery, Swansea, United Kingdom, 6–9 September 2004
4. Stein, K., Tezduyar, T., Benney, R.: Mesh moving techniques for fluid – structure interaction with large displacement. J. Appl. Mech. **70**(1), 58–63 (2003)
5. Axisa, F., Antuncs, J.: Modelling of Mechanical Systems: Fluid – Structure Interaction. Elsevier (2007)
6. Levy, S., Wilkinson, J.P.D.: The Component Element Method in Dynamics with Application to Earthquake and Vehicle Engineering. McGraw-Hill Inc (1976)
7. Legay, A., Kölke, A.: An enriched space – time finite element method for fluid – structure interaction – Part I, Prescribed structural displacement III. In: European Conference on Computational Mechanics Solids, Structures and Coupled Problems in Engineering, Lisbon, Portugal, 5–9 June 2006
8. Sigrist, J.F., Melot, V., Laine, C., Peseux, B.: Numerical simulation of fluid structure problem by coupling fluid finite volume and structure finite element or modal approach. In: Eighth International Conference on Flow Induced Vibrations, Paris, France, 6–9 July 2004
9. Antoci, C., Gallati, N., Sibilla, S.: Numerical simulation of fluid next term–structure previous term interaction next term by SPH. Sci. Direct Comput. Struct. **85**, 879–890 (2007)
10. Pochyly, F., Malenovský, E.: New mathematical and computational model of fluid – structure interaction using FEM. In: Nineth International Conference Flow Induced Vibration, Prague, Czech Republic, 30 June–3 July 2008
11. Malenovský, E., Pochyly, F.: New approach to the analysis of dynamic behavior of rotor dynamic systems in hydraulic machines. In: Tenth International Conference on the Theory of Machines and Mechanisms, Liberec, Czech Republic, 2–4 September 2008
12. Ver, I., Beranek, L.: Noise and Vibration Control Engineering, Principles and Applications. Wiley (2005)

On the Analysis of Rotor-Bearing-Foundation Systems

Katia Lucchesi Cavalca and Eduardo Paiva Okabe

Abstract This work presents a methodology to analyse the influence of the foundation or supporting structure on the rotor-bearings system. A frequency response analysis of the complete system was accomplished by considering physical co-ordinates for the rotor-bearings system and principal co-ordinates for the foundation. The mathematical procedure applied a modal approach to the supporting structure, using modal parameters of generalised mass, damping ratio and natural frequency, which were calculated from the frequency response functions (FRF) of an actual structure. Convergence of the method was verified and the effect of the flexible foundation on the complete system response was analysed. A new formulation for the Mixed Co-ordinates method was presented to evaluate the influence of the supporting structure on the directional response of a rotor. An analysis of the directional frequency response function (dFRF) of the complete system was accomplished considering directional co-ordinates for the rotor-bearings system and principal co-ordinates for the foundation. These results were compared to the conventional FRF procedure.

Keywords Flexible structures · Mixed co-ordinates · Modal parameters · Complex modal analysis

1 Introduction

The current power generation system is broadly supported by hydroelectric and thermoelectric plants. These plants are usually composed of several rotating machines, and it is necessary to predict their behaviour under several conditions of operation. In order to improve the knowledge about rotating machines, several methods have been developed and validated in experimental test-rigs, supplying more

K.L. Cavalca (✉) and E.P. Okabe
Laboratory of Rotating Machinery, Faculty of Mechanical Engineering,
University of Campinas, UNICAMP 13083-970, Campinas, SP, Brazil
e-mail: katia@fem.unicamp.br

K. Gupta (ed.), *IUTAM Symposium on Emerging Trends in Rotor Dynamics*,
IUTAM Bookseries 25, DOI 10.1007/978-94-007-0020-8_8,

complete models for their main components. Part of the rotor-bearings systems simulations has not considered the foundation effect, or it has incorporated this structure through models of highly complex numerical solutions, depending on the physical configuration of the actual supporting structure. Consequently, special attention has been given to the significant influence of the foundation on the dynamic response of the rotor as well as on its operational modes.

Weber [1] extended the transfer matrix method to simulate the foundation behaviour on a rotor system and the influence of the supporting structure on the rotor was demonstrated. In the following decade, with the introduction of the elasticity theory in the analysis of the structures behaviour, the solution to the interaction problem assumed a highly complex form.

Gasch [2] used an experimental approach including the foundation effects through its dynamic stiffness matrices, obtained from the inversion of the sum of the receptance matrix of the horizontal and vertical displacements. Other studies introduced this concept by taking into account measurements on hydrodynamic bearings [3] and bearing pedestals influence [4], as well as studies of oil-film instability and foundation dynamics [5].

From 1980 to 1990, an expressive number of new proposed models contained a foundation modal modelling, used to determine its influence on the critical speeds of the shaft. Again, an innovative contribution by Gasch et al. [6] to the rotor dynamics field proposes a classical solution to the analysis of the complete rotor-bearings-foundation-soil model. Bachschmid et al. [7] tested experimentally the foundation structure of 660 MW turbo-generator, composed by a reinforced concrete structure embedded in a sand soil by long pillars. The soil flexibility was represented by a stiffness coefficient added to the connection points between the structure and soil, however, it turned out to be improper in representing the behaviour of the actual structure.

Buckles et al. [8] discussed the presence of new critical rotational speeds in the system response when considering the dynamic effect of the foundation. In this case, these critical speeds were related to natural frequencies of the foundation, and the interaction between the resonance regions of rotor and foundation. Consequently, special attention was drawn to the significant influence of the foundation on the rotor dynamic response and operational modes [9, 10].

Feng et al. [11] proposed a combination of finite elements and transfer matrix to add the foundation effect to rotor simulation, as an alternative to the finite elements method or the mechanical impedance technique. Krämer [12] used the dynamic stiffness matrix to consider the foundation effects. He emphasized that including these effects is particularly important on the analysis of large size rotating machinery and high production volume rotating machinery. Cavalca [9] proposed a mixed co-ordinates solution where the model was theoretical for rotor and bearings (hydrodynamics in this case) and experimental for supporting structure.

Experimental methodologies have been applied to the study of the dynamic behaviour of structures and mechanical systems [13], which enabled the analysis of mixed modes to rotor-structure systems. Edwards et al. [14] presented an experimental technique applied to the unbalance and support parameters identification of

rotor-bearings-foundation systems using a rotor run-down. Bachschmid et al. [15] proposed an unbalance identification method applied to a 320 MW steam turbo-generator. The foundation was represented by a modal model coupled to a rotor through the mixed co-ordinates method, improving the unbalance identification.

Cavalca et al. [16] extended the study of 2002, with a more detailed investigation into the influence of support structure on rotor dynamics. The method of mixed co-ordinates was verified experimentally with good results on natural frequencies prediction, although the amplitudes presented a lower correlation.

In this work, the method of the Mixed Co-ordinates is presented, and applied to analyse the behaviour of the rotor-support-foundation system and the interactions among these components. An experimental model of the foundation is obtained by modal approach, making possible the identification of its modal parameters and the prediction of its behaviour. In this case, a few mode shapes of the structure can be selected to be used inside the complete system. The main contribution of this work is to propose a combined theoretical-experimental model for the rotor-supports-structure system. The theoretical is for the rotor and the supports (hydrodynamic bearings in this case) and the experimental for the support structure. The difficulty in modelling some actual structures rises when we have concrete structures with immersed metal parts, as the skids in turbomachinery bearing assemblies. In these cases, the complexity to model the boundary conditions increases with the non-linearity involved in the interface between parts of different materials.

2 Theoretical Model

The mathematical modelling of the complete rotor-bearings-foundation system considers two subsystems [17]: rotor-bearings and foundation. The complete system response is obtained by joining both subsystems dynamic responses. The support structure (foundation) model is described as a function of the most significant mode shapes in the rotor operation range. In this analysis, modal analysis techniques were applied on experimental data to determine the support structure parameters (modal mass, stiffness and damping).

A mathematical method was developed to simulate a complete system. The mixed co-ordinates method represents the displacement vector of the structure connection nodes as independent variables using a modal approach [9]. This transformation is applied on a mixed co-ordinates vector, physical co-ordinates for the rotor and modal co-ordinates for the foundation, which describes the complete system behaviour.

According to Cavalca [9], to solve the motion equation of the complete system, it is necessary to establish the relation between physical and principal co-ordinates:

$$\{x_f\} = [\Phi] \cdot \{q\} \tag{1}$$

Here $\{x_f\}$ is the physical co-ordinates vector of the foundation, $\{q\}$ is the generalized (modal) co-ordinates vector, and $[\Phi]$ is the modal matrix (eigenvectors).

Using Eq. (1) the foundation mechanical impedance matrix in modal co-ordinates can be obtained without the inversion of the flexibility matrix.

Neglecting the oil film inertia, the equation of the rotor-bearings subsystem becomes:

$$\begin{bmatrix} [M_R] & [0] \\ [0] & [0] \end{bmatrix} \begin{Bmatrix} \{\ddot{x}_r\} \\ \{\ddot{x}_m\} \end{Bmatrix} + \begin{bmatrix} [R_R]+[R_{rr}] & [R_{rm}] \\ [R_{mr}] & [R_{mm}] \end{bmatrix} \begin{Bmatrix} \{\dot{x}_r\} \\ \{\dot{x}_m\} \end{Bmatrix} + \begin{bmatrix} [K_R]+[K_{rr}] & [K_{rm}] \\ [K_{mr}] & [K_{mm}] \end{bmatrix} \begin{Bmatrix} \{x_r\} \\ \{x_m\} \end{Bmatrix} = \begin{Bmatrix} \{F_0\} \\ \{0\} \end{Bmatrix} + \begin{Bmatrix} \{0\} \\ \{F_f\} \end{Bmatrix} \tag{2}$$

Here $\{\ddot{x}_r\}, \{\dot{x}_r\}, \{x_r\}$ are the acceleration, velocity and displacement vectors of the rotor; $\{\ddot{x}_m\}, \{\dot{x}_m\}, \{x_m\}$ are the acceleration, velocity and displacement vectors of the bearings; $[M_R], [R_R], [K_R]$ are the mass, damping, stiffness matrices of the rotor; $[R_{rr}], [R_{rm}], [R_{mr}], [R_{mm}]$ are the linear damping coefficient matrices of the oil film; $[K_{rr}], [K_{rm}], [K_{mr}], [K_{mm}]$ are the linear stiffness coefficient matrices of the oil film; $\{F_0\}$ is the force due to rotor unbalance; $\{F_f\}$ is the force transmitted to the foundation.

A third equation is necessary to solve the linear system of equations, because the number of unknown variables ($\{x_r\}, \{x_m\}$ and $\{F_f\}$) is larger than the number of equations. The forces transmitted through the oil film on the rotor-foundation interface $\{F_f\}$ are determined through the modal approach of the Eq. (3).

Using the foundation motion equation in modal co-ordinates:

$$[m_f] \cdot \{\ddot{q}\} + [r_f] \cdot \{\dot{q}\} + [k_f] \cdot \{q\} = -[\Phi]^T \{F_f\} \tag{3}$$

where $[m_f]$ is the modal mass matrix; $[r_f]$ is the modal damping matrix; $[k_f]$ is the modal stiffness matrix; $[\Phi]^T$ is the transposed modal matrix.

The foundation forces, transmitted by the oil film of the bearings, can also be written as:

$$[R_{mr}]\{\dot{x}_r\} + [R_{mm}]\{\dot{x}_m\} + [K_{mr}]\{x_r\} + [K_{mm}]\{x_m\} = \{F_f\} \tag{4}$$

Replacing Eq. (4) in Eq. (3):

$$[m_f]\{\ddot{q}\} + [r_f]\{\dot{q}\} + [k_f]\{q\} = -[\Phi]^T \cdot ([R_{mr}]\{\dot{x}_r\} + [R_{mm}]\{\dot{x}_m\} + [K_{mr}]\{x_r\} + [K_{mm}]\{x_m\}) \tag{5}$$

The modal shapes are independent, and then the matrices, which contain the modal parameters determined through the modal analysis methods, are diagonal. Expressing the foundation dynamic behaviour through its bearing connecting nodes, the bearing nodes $\{x_m\}$ become the connection foundation nodes $\{x_f\}$.

After the determination of the foundation forces, the equation of the complete system is obtained replacing these forces obtained by Eq. (5) into Eq. (2), and using the modal approach of Eq. (1):

$$\begin{bmatrix} [M_R] & [0] \\ [0] & [m_f] \end{bmatrix} \cdot \begin{Bmatrix} \{\ddot{x}_r\} \\ \{\ddot{q}\} \end{Bmatrix} + \begin{bmatrix} [R_R]+[R_{rr}] & [R_{rm}][\Phi] \\ [\Phi]^T[R_{mr}] & [r_f]+[\Phi]^T[R_{mm}][\Phi] \end{bmatrix} \begin{Bmatrix} \{\dot{x}_r\} \\ \{\dot{q}\} \end{Bmatrix} + \begin{bmatrix} [K_R]+[K_{rr}] & [K_{rm}][\Phi] \\ [\Phi]^T[K_{mr}] & [k_f]+[\Phi]^T[K_{mm}][\Phi] \end{bmatrix} \begin{Bmatrix} \{x_r\} \\ \{q\} \end{Bmatrix} = \begin{Bmatrix} \{F_o\} \\ \{0\} \end{Bmatrix} \tag{6}$$

The support structure can be represented only by its most significant modes, in the analysed frequency range, independent of the degrees of freedom of the connection points (bearings).

This procedure is valid for orthogonal mode shapes that transform mass and the stiffness matrices of the foundation into diagonal matrices.

The method presented here uses the mechanical impedance matrix of the foundation in principal co-ordinates, based on the modal approach to the system response by a linear combination of the vibration modes of the system. As the only external excitation force considered in the model is the unbalance force, the modes that influence the rotor response must be inside its operational frequency range. Therefore, using this approach, the number of identified modes does not need to be equal to the number of degrees of freedom associated with the bearings. Consequently, the modal co-ordinates associated to the contributing modes will take place in the whole matrix of the system, substituting the bearings degrees of freedom connected to the structure.

In order to apply the complex modal analysis technique to develop the new mixed co-ordinates method to the whole rotating system, a simple rotor supported by flexible bearings was modelled in complex co-ordinates. The physical response of the rotor, in the yz plane (transversal to the rotor shaft), needs to be related to the forward and backward components of the system response. For that reason, the solution to an unbalance external excitation force $\{F_o\}$ is considered at the frequency of rotation Ω, as given by Eq. (7):

$$\{F_o\} = \{f_o\}\, e^{j\Omega t} \tag{7}$$

where j is the imaginary constant $\left(\sqrt{-1}\right)$ and t is the time. The system response presents the same behaviour of the excitation force, and the perpendicular co-ordinates can be described on the complex plane as rotating vectors:

$$\{y\} = \{y_{re} + jy_{im}\}\, e^{j\Omega t} \text{ and } \{z\} = \{z_{re} + jz_{im}\}\, e^{j\Omega t} \tag{8}$$

where y_{re} and z_{re} are the real components, and y_{im} and z_{im} are the imaginary components of the rotating vectors. Equation (9) can be developed as follows:

$$\begin{aligned} \{y\} &= \{(y_{re} + jy_{im})\,(\cos\Omega t + j\,\sin\Omega t)\} \\ &= \{(y_{re}\cos\Omega t - y_{im}\sin\Omega t) + j\,(y_{im}\cos\Omega t + y_{re}\sin\Omega t)\} \\ \{z\} &= \{(z_{re} + jz_{im})\,(\cos\Omega t + j\,\sin\Omega t)\} \\ &= \{(z_{re}\cos\Omega t - z_{im}\sin\Omega t) + j\,(z_{im}\cos\Omega t + z_{re}\sin\Omega t)\} \end{aligned} \tag{9}$$

It is important to point out that the imaginary part is related to the rotation of the vectors $\{y\}$ and $\{z\}$, while the real part corresponds to the physical co-ordinates that can actually be measured.

Now, the same system response is represented by the directional forward and backward components:

$$\{p\} = \{f\}\, e^{j\Omega t} + \{b\}\, e^{-j\Omega t} \tag{10}$$

where $\{f\} = \{f_{re} + jf_{im}\}\, e^{j\Omega t}$ and $\{b\} = \{b_{re} + jb_{im}\}\, e^{-j\Omega t}$

$$\begin{aligned}
\{f\} &= \{(f_{re} + jf_{im})\,(\cos\Omega t + j\,\sin\Omega t)\} \\
&= \{(f_{re}\cos\Omega t - f_{im}\sin\Omega t) + j\,(f_{im}\cos\Omega t + f_{re}\sin\Omega t)\} \\
\{b\} &= \{(b_{re} + jb_{im})\,(\cos\Omega t - j\,\sin\Omega t)\} \\
&= \{(b_{re}\cos\Omega t + b_{im}\sin\Omega t) + j\,(b_{im}\cos\Omega t - b_{re}\sin\Omega t)\}
\end{aligned} \tag{11}$$

Comparing Eqs. (9) and (11), the real part of x co-ordinate corresponds to the real part of the directional response, while the real part of y co-ordinate corresponds to the imaginary part of the directional response:

$$\begin{aligned}
(y_{re}\cos\Omega t - y_{im}\sin\Omega t) &= (f_{re}\cos\Omega t - f_{im}\sin\Omega t + b_{re}\cos\Omega t + b_{im}\sin\Omega t) \\
(z_{re}\cos\Omega t - z_{im}\sin\Omega t) &= (f_{im}\cos\Omega t + f_{re}\sin\Omega t + b_{im}\cos\Omega t - b_{re}\sin\Omega t)
\end{aligned} \tag{12}$$

Arranging the terms in $\cos\Omega t$ and $\sin\Omega t$ in Eq. (12), the relation between physical and directional co-ordinates is obtained:

$$\begin{cases} y_{re} = f_{re} + b_{re} \\ z_{re} = f_{im} + b_{im} \\ -y_{im} = -f_{im} + b_{im} \\ -z_{im} = f_{re} - b_{re} \end{cases} \text{or} \quad \begin{matrix} f_{re} = (y_{re} - z_{im})/2 \\ f_{im} = (z_{re} + y_{im})/2 \\ b_{re} = (z_{im} + y_{re})/2 \\ b_{im} = -(y_{im} - z_{re})/2 \end{matrix} \tag{13}$$

The systems of Eqs. (13) lead to a transformation from physical co-ordinates y and z to directional co-ordinates f (forward) and b (backward), as it can be seen in Lee [18].

Defining, hence, the transformation matrix $[A]$ so that:

$$\begin{Bmatrix} f \\ \bar{b} \end{Bmatrix} = [A]^{-1} \begin{Bmatrix} y \\ z \end{Bmatrix}\ ;\ \begin{Bmatrix} y \\ z \end{Bmatrix} = [A] \begin{Bmatrix} f \\ \bar{b} \end{Bmatrix} \tag{14}$$

where $\bar{b}$ is the complex conjugate of b.

The transformation matrix $[A]$ and its inverse can be expressed as:

$$[A] = \begin{bmatrix} 1 & 1 \\ -j & j \end{bmatrix};\ [A]^{-1} = \begin{bmatrix} 1/2 & j/2 \\ 1/2 & -j/2 \end{bmatrix} \tag{15}$$

Translational and angular co-ordinates of each node of the beam element can be transformed using the following equations:

$$\{x_r\} = [T_A]\{p\}; \quad \{p\} = [T_A]^{-1}\{x_r\} \tag{16}$$

where the vectors $\{x_r\}$ and $\{p\}$, and the matrices $[\mathrm{T_A}]$ and $[\mathrm{T_A}]^{-1}$ can be defined as follows:

$$\{x_r\} = \begin{Bmatrix} y_i \\ z_i \\ \alpha_i \\ \beta_i \end{Bmatrix}; \{p\} = \begin{Bmatrix} f_i \\ \bar{b}_i \\ \gamma_i \\ \bar{\eta}_i \end{Bmatrix}; [T_A] = \begin{bmatrix} [A] & [0] \\ [0] & [A] \end{bmatrix}; [T_A]^{-1} = \begin{bmatrix} [A]^{-1} & [0] \\ [0] & [A]^{-1} \end{bmatrix} \tag{17}$$

Here y_i and z_i are the displacement co-ordinates of the ith node, α_i and β_i are the angular co-ordinates of the ith node, f_i and b_i are the directional co-ordinates of the ith node, γ_i and η_i are the angular directional co-ordinates of the ith node.

The transformation from modal to physical co-ordinates expressed by Eq. (1) is applied to transform modal to directional co-ordinates [18], and Eq. (1) becomes:

$$\{p\} = [T_A]^{-1}[\Phi]\{q\} \tag{18}$$

Matrices of mass, stiffness and damping of rotor and bearings must be converted from physical cartesian co-ordinates to directional ones. Using the transformation matrices of Eqs. (17) and (18), it is possible to rewrite Eq. (6) and replace physical co-ordinates by directional ones:

$$\begin{bmatrix} [M_P] & [0] \\ [0] & [m_f] \end{bmatrix} \begin{Bmatrix} \{\ddot{p}\} \\ \{\ddot{q}\} \end{Bmatrix} + \begin{bmatrix} [R_P] + [R_{pp}] & [R_{pf}][T_A]^{-1}[\Phi] \\ [\Phi]^T[R_{mr}][T_A] & [r_f] + [\Phi]^T[R_{mm}][\Phi] \end{bmatrix} \begin{Bmatrix} \{\dot{p}\} \\ \{\dot{q}\} \end{Bmatrix}$$
$$+ \begin{bmatrix} [K_P] + [K_{pp}] & [K_{pf}][T_A]^{-1}[\Phi] \\ [\Phi]^T[K_{mr}][T_A] & [r_f] + [\Phi]^T[K_{mm}][\Phi] \end{bmatrix} \begin{Bmatrix} \{p\} \\ \{q\} \end{Bmatrix} = \begin{Bmatrix} \{F_p\} \\ \{0\} \end{Bmatrix} \tag{19}$$

Here $\{\ddot{p}\}, \{\dot{p}\}, \{p\}$ are the acceleration, velocity and displacement vectors of the rotor in directional co-ordinates; $\{\ddot{q}\}, \{\dot{q}\}, \{q\}$ are the acceleration, velocity and displacement vectors of the support structure in modal co-ordinates; $[M_P], [R_P], [K_P]$ are the mass, damping, stiffness matrices of the shaft in directional co-ordinates; $[R_{pp}], [R_{pf}]$ are the linear damping coefficient matrices of the oil film in directional co-ordinates; $[R_{mr}], [R_{mm}]$ are the linear damping coefficient matrices of the oil film in physical co-ordinates; $[K_{pp}], [K_{pf}]$ are the linear stiffness coefficient matrices of the oil film in directional co-ordinates; $[K_{mr}], [K_{mm}]$ are the linear stiffness coefficient matrices of the oil film in physical co-ordinates; $\{F_p\}$ is the force due to rotor unbalance in directional co-ordinates; $[T_A]$ is the transformation matrix from directional to physical co-ordinates.

Equation (19) relates to directional and modal co-ordinates, which refers to rotor and foundation movements. An interesting feature of Eq. (19), as in Eq. (6),

is that the rotor model, in physical or directional co-ordinates, did not affect the foundation model in (uncoupled) principal co-ordinates (m_f, r_f, k_f). The bearings coefficients, instead, were partially affected due to the connection between rotor and structure.

3 Test-Rig Modelling

The test rig was modelled to be numerically simulated. The shaft of the rotor was modelled by finite element method using beam elements with circular cross sections. The shaft was composed of 32 elements containing 33 nodes, and supported by two hydrodynamic cylindrical bearings, located at nodes 2 and 32 of the shaft, which were connected to the foundation by nodes 34 and 35 (Fig. 1). The rotor shaft had a length of 600 mm and 12 mm of diameter. The bearing journal had a diameter of 31 mm and length of 20 mm, which gave a L/D ratio equal to 0.64, close to the 0.5 ratio of short bearings. A mass (disk) of 2.3 kg was attached in the shaft mid span to reduce gyroscopic effects.

Damping and stiffness coefficients of hydrodynamic bearings were calculated using the finite difference method, considering a finite bearing model. The synchronous response of the rotor was used to obtain the rotor unbalance response, including, through the mixed co-ordinates method, the foundation effect. The simulation was performed in a range from 0 to 50 Hz.

4 Experimental Set-up

The support structure tested (Fig. 2) was composed by a metallic base borne by ten columns. To determine its modal parameters the first step was the experimental measurement of its frequency response function (FRF), generating a Gaussian white noise through the data acquisition device. This signal was amplified and sent to the shaker, which excited the structure on the driving point. A force transducer was attached to the stinger end to measure the force applied to the structure, and an accelerometer was added to the driving point to measure the structure response. Both acceleration and force measurements were conditioned and sent to data acquisition board, using a sample rate from 2 to 5 kHz, and a total sample time from 100 to

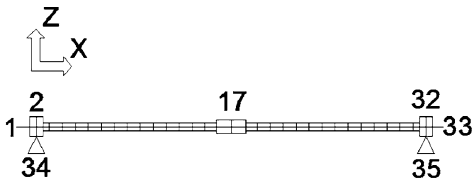

Fig. 1 Finite element model of the rotor

Fig. 2 Experimental set-up

200 seconds. The digital data were processed by the same program which generated the excitation signal. This data processing involved a digital filtering, resampling, overlapping and windowing which depended on the experimental requirements. The frequency response function (FRF) was calculated through the autocorrelation and cross correlation between force and acceleration, this calculation also yielded the coherence which was used to determine the quality of the acquired data.

The FRF was calculated with frequency resolution from 0.1 to 0.5 Hz, using from 25 to 200 averages. The finest resolution (0.1 Hz) was applied to analyze light damping modes, increasing the number of points available in the resonance region, therefore improving the modal analysis [19].

5 Results

The first step was the analysis of the mixed co-ordinates method convergence applying Eq. (6) for physical co-ordinates. As it was based on the fact that only the most significant modes of the supporting structure can represent this element in the model of the complete rotor-bearings-foundation system, a numerical simulation was carried out considering different number of identified modes of the foundation. Figure 3 shows the shaft response in bearing 2 (located at node 32).

A natural frequency was observed at 23 Hz in y-direction and 24 Hz in z-direction when no foundation effects were present (rigid foundation).

The sequence of Figs. 4a to 4c shows successively the influence of a flexible foundation, when represented by the most significant vibration modes.

In this case, the convergence could be observed for 2, 6, 12, 16 and 20 modes.

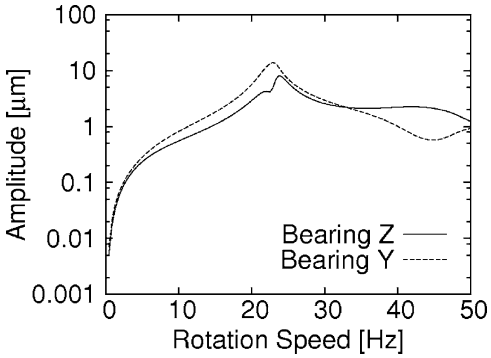

Fig. 3 Amplitude of vibration of the shaft at bearing 2 – no foundation effect

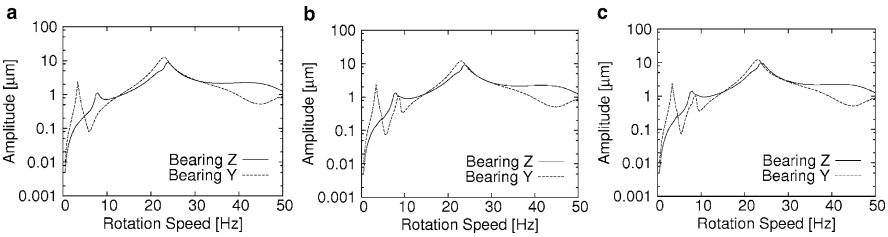

Fig. 4 Amplitude of vibration of the shaft at bearing 2 – flexible foundation: **(a)** two vibration modes; **(b)** six vibration modes; **(c)** 12; 16 and 20 vibration modes

New peaks of amplitude appeared in the frequencies around 3 and 8 Hz in y-direction, as well as around 7 Hz in z-direction, due to the flexible foundation effects on the rotor-bearing system.

It was important to highlight that, in this case, the solution converged for 12 modes, because the frequency response of the rotor did not present considerable changes when the number of modes of the foundation increased. The same behaviour could be observed in the phase plotting.

The same rotating system was simulated according to Eq. (19), initially considering no foundation effects, as shown in Fig. 5. Some similarity can be observed between the behaviour of the forward response in Fig. 5 and the y-direction response in Fig. 3, as well as in the backward response (Fig. 5) and the z-direction response (Fig. 3). However, only Fig. 5 brings the information about forward and backward motion.

The natural frequencies of the complete system, in this case, were all in forward motion. Moreover, comparing Figs. 5 and 6, it was possible to see that the rotor interaction with a flexible foundation reduces the frequency range of backward motion. The rotor motion is dominated by the backward motion in the range of 2.5 to 22 Hz approximately, being in forward motion in the rest of the frequency domain. When a flexible foundation effect was considered in the directional mixed co-ordinates method (Fig. 6), taking into account 20 vibration modes of the supporting structure, the backward motion of the shaft in the bearing 2 changed to a frequency interval from 10 to 20 Hz.

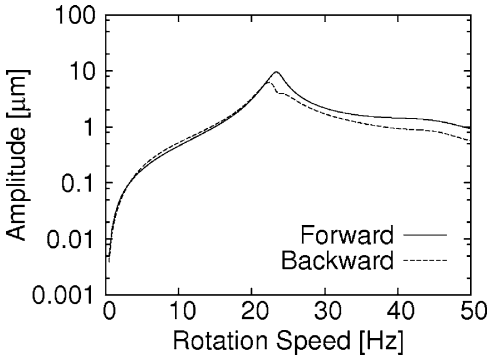

Fig. 5 Amplitude of vibration of the shaft at bearing 2 (directional response) – no foundation effect

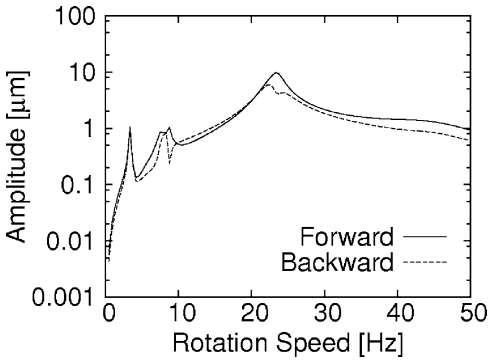

Fig. 6 Amplitude of vibration of the shaft at bearing 2 (directional response) – flexible foundation: 20 vibration modes

6 Conclusions

This work presents a methodology to solve a mathematical representation of rotor-bearings systems with a significant effect of the foundation structure flexibility. The model presented a satisfactory convergence, which reinforces that a supporting structure can be represented by selecting only its most significant modes. The connecting points (bearings) were the main concern in the modal analysis, because the forces between rotor and structure are transmitted through these nodes.

The proposed method allows one to work with an arbitrary number of identified vibration modes, even if there are less or more modes than degrees of freedom associated with the supports (bearings). The predominance of the most significant modes of the foundation can be observed within the operation range of the system, checking the convergence of the system dynamic behaviour.

The new formulation for the mixed co-ordinates method can be applied to analyse the forward and backward motion in the operation frequency domain of the rotor, and the simulation results showed the importance of considering this new approach to analyse the rotor dynamics under the influence of flexible supporting structure.

Acknowledgements The authors would like to thank FAPESP and CNPq for the financial support for this work, and LAMAR team for the technical support. The authors also would like to acknowledge the invaluable contribution of professors Hans Ingo Weber and Nicoló Bachschmid to their scientific education in the rotor dynamics field.

References

1. Weber, H.: Über das gemeinsame Schwingungsverhalten von Welle und Fundament bei Turbinenanlagen. VDI-Berichte **48**, 55–62 (1961)
2. Gasch, R.: Vibration of large turbo-rotors in fluid-film bearings on an elastic foundation. J. Sound Vib. **47**(1), 53–73 (1976)
3. Morton, P.G.: Measurement of the dynamic characteristics of a large sleeve bearing. J. Lubr. Technol. **93**(1), 143–155 (1971)
4. Nicholas, J.C., Barret, L.E.: The effect of support flexibility on critical speed prediction. ASLE Trans. **29**(3), 329–338 (1986)
5. Vance, J.M., Murphy, B.T., Tripp, H.A.: Critical speeds of rotating machinery: computer predictions vs experimental measurements. Part I: The rotor-mass elastic model. ASME paper VIB85RD-142 1–8 (1985)
6. Gasch, R., Maurer, S., Sarfeld, W.: Soil influence on unbalance response and stability of a simple rotor-foundation system. J. Sound Vib. **93**(4), 549–566 (1984)
7. Bachschmid, N., Bernante, R., Frigeri, C.: Dynamic analysis of a 660 MW turbogenerator foundation. In: International Conference Rotordynamic Problems in Power Plants, International Federation for the Promotion of Mechanism and Machine Science, Rome, pp. 151–161 (1982)
8. Buckles, J.R., Rouch, K.E., Baker, J.R.: Modeling support effects – finite element and experimental modal methods. In: Proceedings of the International Gas Turbine and Aeroengine Congress & Exhibition, ASME, New York (1996)
9. Cavalca, K.L.: L'Interazione tra rotori e struttura portante: metodologie per la sua modelazione. Ph.D. Thesis (in italian), Dipartimento di Meccanica, Politecnico di Milano, p. 143 (1993)
10. Cavalcante, P.F., Cavalca, K.L.: A method to analyse the interaction between rotor-foundation systems. In: 16th International Modal Analysis Conference(IMAC98), Santa Barbara, USA (1998)
11. Feng, N., Hahn, E.J., Sestieri, A.: A combined finite element/transfer matrix approach for including foundation effects on the vibration behaviour of rotating machinery. In: Proceedings of Sixth International Conference on Vibrations in Rotating Machinery, Institution of Mechanical Engineers, Bath, pp. 529–534 (1992)
12. Krämer, E.: Dynamic of Rotor and Foundations. Springer-Verlag, Berlin, p. 383 (1993)
13. McConnell, K.G.: Vibration Testing Theory and Practice, 1st ed. John Wiley & Sons Inc., p. 605 (1995)
14. Edwards, S., Lees, A.W., Friswell, M.I.: Experimental identification of excitation and support parameters of a flexible rotor-bearings-foundation system from a single run down. J. Sound Vib. **232**(5), 963–992 (2000)
15. Bachschmid, N., Pennacchi, P., Vania, A., Gregori, L., Zanetta, G.A.: Unbalance identification in a large steam turbogenerator using model-based identification and modal foundation. In: Proceedings of Eighth International Conference on Vibrations in Rotating Machinery, Institution of Mechanical Engineers, Swansea, pp. 383–392 (2004)
16. Cavalca, K.L., Cavalcante, P.F., Okabe, E.P.: An investigation on the influence of the supporting structure on the dynamics of the rotor system. Mech. Syst. Signal Process. **19**, 157–174 (2005)
17. Weiming, L., Novak, M.: Dynamic behaviour of turbine-generator-foundation systems. Earthquake Eng. Struct. Dyn. **24**(3), 339–360 (1996)

18. Lee, C.W.: Vibration Analysis of Rotors. Kluwer Academic Publishers, Dordrecht, p. 312 (1993)
19. Okabe, E.P.: Rotor-Structure Interaction: Theoretical-Experimental Model. Ph.D. Thesis (in portuguese), Campinas, Departament of Mechanical Project, Faculty of Mechanical Engineering – Unicamp, p. 177 (2007)

A Multiple Whirls Phenomenon and Heuristic Problems in Rotor-Bearing Systems

J. Kiciński

Abstract The results of investigations of the high-speed rotor of a micro turbine being an element of the micro power plant in dispersed power engineering based on renewable energy sources are presented in the paper. The basic problem of such devices is to assure a stable rotor operation within the entire range of rotational speeds. Foil bearings and special rotor structure were applied. It turned out that the situation, in that the rotor – after loosing its stability – stabilizes again when the rotational speed increases, is possible. This is a phenomenon determined by the author as multiple whirls. Another topic discussed in the present paper is an assessment of the influence of a random character of certain input data – in this case – changes of external excitations of the system. This problem is related to the so-called heuristic models often placed in opposition to widely used algorithmic models.

Keywords Rotor dynamics · Nonlinear vibrations · Hydrodynamic instability · Heuristic problems · Computer simulation

1 Research Tools and Their Verification

The MESWIR computer code, based on nonlinear models of complex system rotor-bearings, was applied in research. Theoretical models, basic equations as well as the system itself have been presented already several times during the conferences and in publications [1–3]. Therefore MESWIR series code will not be presented here in detail. However, it is worth mentioning that the most useful feature of this system is the possibility of description of the rotor machine state both in a linear and nonlinear range by means of the same tool, thereby describing new vibration forms at transition of the stability limit. The description capability of bearings of

J. Kiciński
Institute of Fluid-Flow Machinery, Polish Academy of Sciences
Fiszera 14, 80-952 Gdansk University of Warmia and Mazury, Olsztyn Poland
e-mail: kic@imp.gda.pl

K. Gupta (ed.), *IUTAM Symposium on Emerging Trends in Rotor Dynamics*,
IUTAM Bookseries 25, DOI 10.1007/978-94-007-0020-8_9,

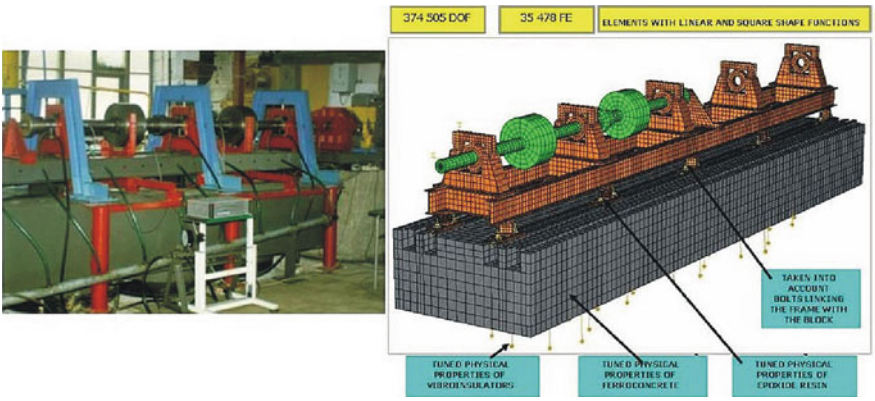

Fig. 1 Photograph of the testing stand and the FEM discretisation of rotor and supporting structure (taking into account properties of coupling elements, vibroinsulators and a concrete block [2, 9])

a complex geometry of oil clearance including foil bearings is also important. The MESWIR code was experimentally verified both at the research stand and with using real systems such as large power turbo-sets [1].

For the needs of the research, this system was coupled with commercial programs of the ABAQUS type to determine dynamic properties of the supporting structure and of the whole system. Thus, bearing and rotor characteristics (MESWIR system) as well as dynamic characteristics of supporting structure (ABAQUS system) were calculated in one iteration loop. However, this type of coupling requires additional verification of such research tools. The photograph of the testing stand operating in the diagnostics Laboratory of the Institute of Fluid-Flow Machinery, Polish Academy of Sciences (IF-FM PAS), as well as the FEM discretisation of this system together with details concerning modeling of characteristic structural nodes such as fixing bolts or vibro-insulators, are presented in Fig. 1.

This is a system of a journal of diameter $d = 0.1$ m, disc diameter $D = 0.4$ m and length $L = 3.2$ m. Experimental verification of dynamic flexibility coefficients is very complex. Obtaining a good compatibility in such systems is much more difficult and sometimes even impossible. This is illustrated in Fig. 2. The experimental data were obtained by sinusoidal excitations of subsequent supports and recording the bearing bush displacements, whereas the theoretical data constitute the results of calculations performed by means of the ABAQUS commercial software coupled with the MESWIR code. Regardless of such precise theoretical modeling of the entire system (Fig. 1), we did not manage to achieve sufficient compatibility of experimental and theoretical results, see upper diagrams in Fig. 2. After several tests, only when a crack of one of the fixing bolts was taken into account in calculations that the verification results improved, see lower diagrams in Fig. 2. It occurred, that this bolt was actually quite loose and behaved as if being cracked. This example can serve as an excellent illustration of capabilities of the model based diagnostics, since knowing the symptom we can by means of the computer analysis localize the defect.

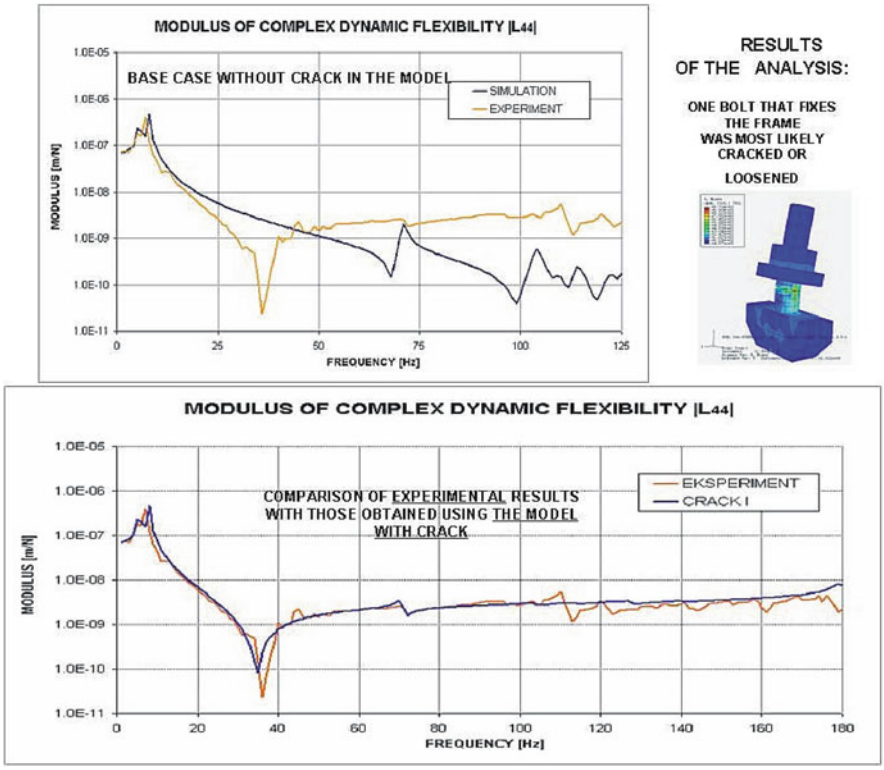

Fig. 2 Verification of dynamic flexibility coefficients for one bearing support of the system shown in Fig. 1. Experimental tests: excitations of one support by a sinusoidal exciter and measuring displacements. Theoretical investigations: calculations by the ABAQUS system coupled with the MESWIR series code. Upper diagram: calculations not taking into account any cracking (loosening). Lower diagram: calculations taking into account the crack of one bolt that fixes the frame [2,9]

Research tools prepared and verified in such a way were applied in the research constituting the basic contents of the present paper.

2 Stability Testing of High-Speed Rotors; Phenomenon of Multiple Whirls

Problems related to ecological energy generation at a small and dispersed scale have become very important in recent years. A dispersed power engineering re quires building micro power plants which means also micro turbines of a power from a few to a dozen or so kW. The idea of building micro turbines for low-boiling agents ORC, which ensures small dimensions of devices and easiness of servicing, has become attractive. Unfortunately it is obtained at the cost of a high rotational speed

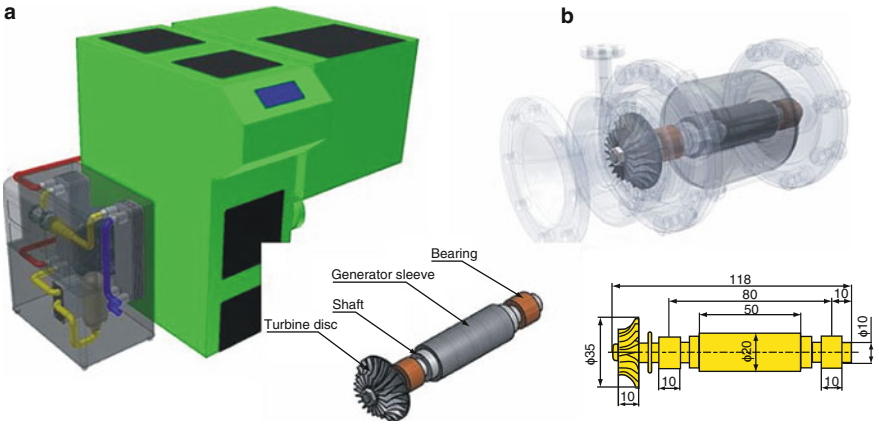

Fig. 3 Object of testing. Micro power plant **(a)** boiler and **(b)** turbine set developed in the IF-FM PAS in Gdansk of a thermal and electric power of 20 kW and 3 kW, respectively. Single-stage radial-axial turbine for low-boiling medium ORC and a rotational speed up to 100,000 rpm [4]

of the rotor, approaching 100,000 rpm. Thus, the main problem becomes ensuring the stable operation of the device within the entire rotational speed range of the rotor. These types of devices are most often coupled with boilers supplied with renewable energy sources.

A concept of such micro power plant developed in the IF-FM PAS in Gdansk is shown in Fig. 3 [4]. Essential elements of the micro turbine constitute slide bearings of special characteristics ensuring a high stability of a system. The foil bearings were chosen since – due to easiness of changing the oil clearance geometry (deformations of a membrane part of a bearing bush) – they can stabilize the system operation as the rotational speed increases.

The notion of the substitute stiffness is essential for the calculation capabilities of the MESWIR code (multiple calculations in one iteration loop).

The system assumed for testing consisted of a rotor (with one disc and a generator) placed on two foil bearings of dimensions shown in Fig. 3 (shaft diameter 10 mm). A low-boiling medium ORC was used as bearings lubricant, which significantly simplifies construction of the whole micro power plant. Typical values of the possible unbalancing of a rotor disc (as an excitation force) were assumed as well as some parametric values of damping of the foil bearing bush and supporting structure (from the material data sheets) [5–7].

The calculation results in the form of amplitude – speed characteristics within the speed range up to 100,000 rpm are presented in Fig. 4.

The attention is called to quite different operation of bearing No. 1 (at the disc) and bearing No. 2 (free end). While bearing No. 1 is stable within the entire range of rotational speeds, bearing No. 2 exhibits two characteristic zones of exceptionally high vibration amplitudes exceeding 70% of a bearing clearance.

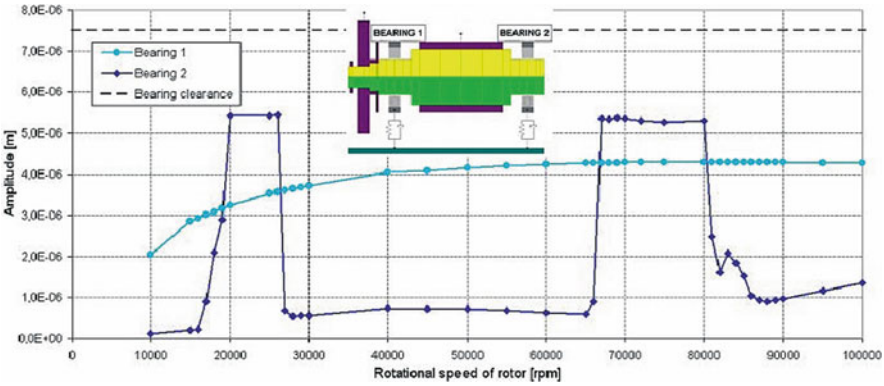

Fig. 4 Amplitude – speed characteristics of the rotor from the micro turbine (shown in Fig. 3) calculated for the relative vibrations of a journal and foil bearing bush. Illustration of the multiple whirls phenomenon in bearing No. 2 (repeated processes of formation and decaying of high amplitude zones caused by a hydrodynamic instability)

To identify this phenomenon and to exclude common resonance, the shape of relative displacement trajectories of the journal and bearing bush in these zones were analyzed. The calculation results for the first zone and after passing through it are presented in Fig. 5.

Analysis of Fig. 5 explicitly indicates that the displacement trajectory of bearing No. 2 at a rotational speed of 25,000 rpm (the first zone of high amplitudes) has features characteristic for the expanded hydrodynamic instability, the so-called "whip". The "whip" means in this case, a developed form of whirls of a lubricating medium within the lubrication clearance. This is pointed out by double shaft rotations (it means a vector of external excitations) falling to one full precession, which creates two phase markers (FM) on the trajectory. This means, that the same positions of the excitation force vectors (horizontally to the right: TAL = 0,360 and 720 degrees) correspond to different positions on the journal trajectory within the bearing clearance.

However, the most unexpected is the observation that after the system has exceeded the first zone of hydrodynamic instability (which means the first "whip") the system returns to a stable operation of bearing No. 2 (it means a typical situation, in which one phase marker on the trajectory corresponds to one rotation of the excitation vector). The situation remains a stable one up to the rotational speed of approximately 65,000 rpm. After the system has exceeded this speed, a rapid instability ("whip") occurs again followed by a subsequent calming down.

If we assume a stiff bearing bush we are unable to model the phenomenon. This allows to assume that variable deformations of the foil bearing bush (corresponding to the turbine rotational speed increase) are responsible for such a process.

The phenomenon of multiple whirls has been quite often observed in practice in large power plants. Small oil whirls were formed and then disappearing on one of the recorded bearings and this did not cause any instability of the entire system. A zone

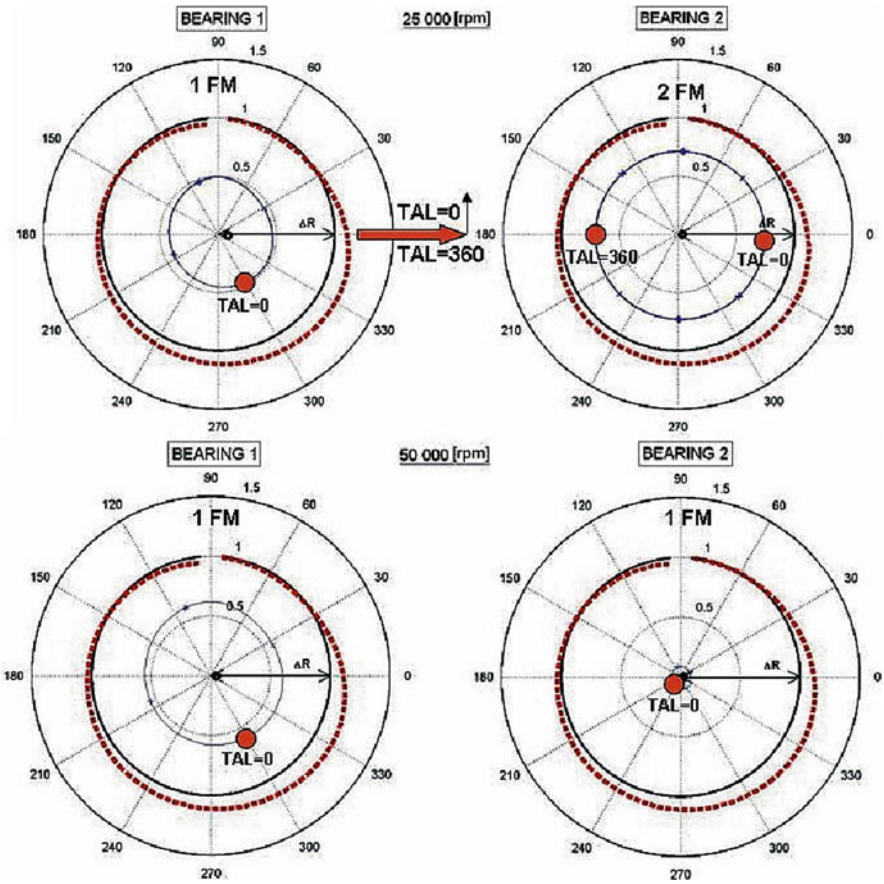

Fig. 5 Displacement trajectories of journal of bearing No. 1 and 2 calculated for the first high amplitudes zone (25,000 rpm) and in the transient period (50,000 rpm). Image of the first hydrodynamic "whip" in the trajectory – two phase markers FM (upper right-hand side trajectory). Broken red line indicates deformations of the bearing inner foil

of multiple whirls is very interesting from the point of view of the hydrodynamic pressure distribution. This is illustrated in Fig. 6.

3 Stochastic Variability of Input Data in Heuristic Modeling of Rotors

A classic, traditionally applied for many years, approach to the state modeling of various kinds of machines is the **algorithmic** approach, i.e., the one in which for the known set of input data we obtain the same, precisely repeatable, set of output data

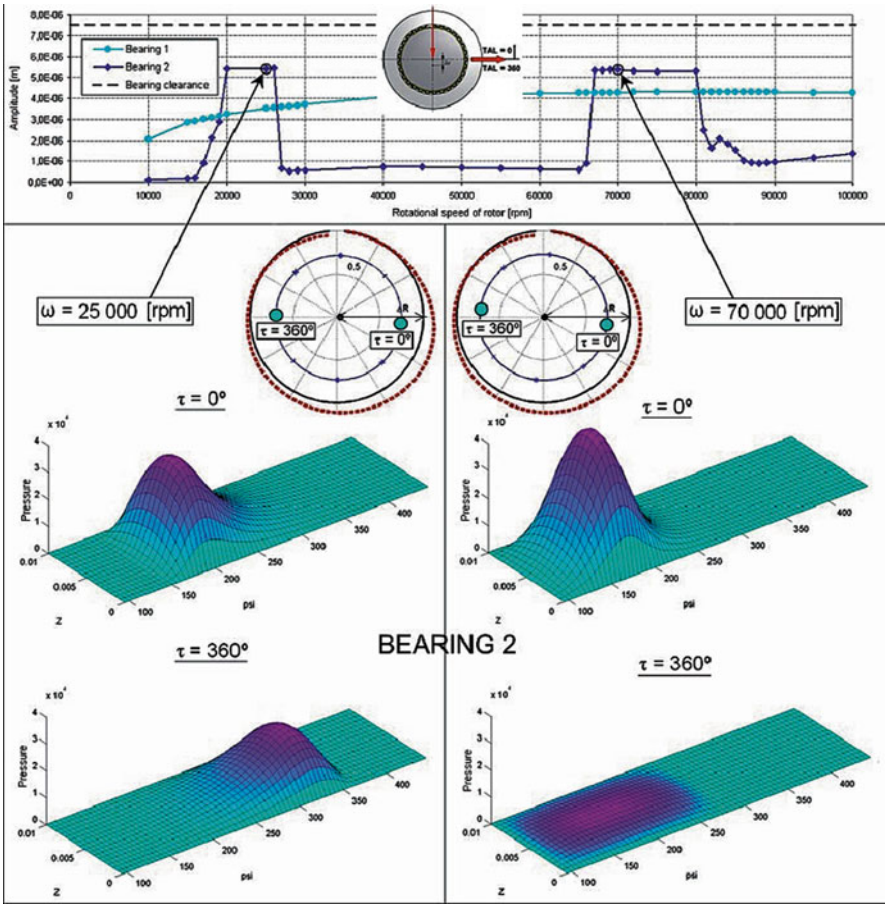

Fig. 6 Pressure distribution calculated for various positions of phase markers within a zone of multiple whirls for the same position of the excitation force vector (horizontally to the right, it means for TAL = 0 and 360 degrees)

(results). This is the obvious consequence of calculation capability of computers and the applied programs. However, this type of "traditional" research tools, often highly advanced and applicable in practice, are neither able to correct the already introduced data nor to modify the assumed model depending on external conditions during the calculation procedure being in progress.

Meanwhile natural phenomena and a human nature (and thereby objects created by it) are of a **heuristic** character, which means possible feedbacks occurring in processes, intrinsic data and the previously assumed methodology of state assessment corrections. It also means the necessity of taking into account influences of various errors and the uncertainty of input data, what is often intuitively done.

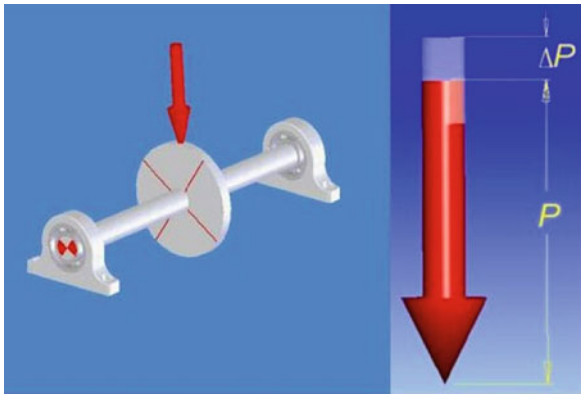

Fig. 7 Object of investigations: twin-support, symmetric rotor of a shaft diameter of 0.1 m, disc diameter 0.4 m, shaft length 1.4 m and a mass of 179 kg. Classic, cylindrical slide bearings lubricated by machine oil were used. The stochastic variability of an external excitation force within limits $+/-\Delta P = 20\%$ in proportion to the constant (basic) value P was assumed

It is worth to mention that the trial of heuristic modeling means the necessity of having highly advanced "traditional" research tools. The so called **nonlinear description** is extremely important since heuristic models are nonlinear by nature. Another substantial feature is the possibility of a smooth transition from the linear to nonlinear description applying the same research tools (the Superposition Principle cannot be used in this case). In consideration of the above, the MESWIR series code was applied in investigations. Figure 7 presents the object used in tests as well as the concept of random changes of external excitation forces acting on a rotor disc. The randomness of changes was assumed (random-number generator was applied) although within limits $+/-\Delta P$ in proportion to the basic value P. Calculations were performed for different ΔP values simulating in this way various possible situations (e.g., displacement of rotating masses, influence of magnetic fields, etc.).

External rotating excitation forces, which can randomly change within limits $+/-20\%$ in proportion to the basic value, P, was assumed for the analysis (Fig. 7). The calculation results for the rotor shaft rotational speed from 300 to 5,550 rpm are shown in Figs. 8 and 9 [8]. The trajectory of the rotor centre loaded by a constant force (basic), rotating synchronously, is shown for the comparison on the left-hand side of each figure, whereas the trajectory of the rotor loaded by randomly changing force, within limits $+/-\Delta P = 20\%$ in proportion to the basic force P, is shown on the right-hand side of the figure. Images of trajectories in co-ordinate systems related to the maximum value of bearing clearance are placed in the upper part, while images of trajectories magnified as much as possible to exhibit clearly the phenomena are shown in the lower part of the figure.

The analysis of the figure indicates that influence of randomly changing values of the external excitation force is significant in the case of small rotational speeds of the rotor. When the speed increases this influence diminishes, that can be explained by the influence of rotor inertial forces generally attenuating a time-history.

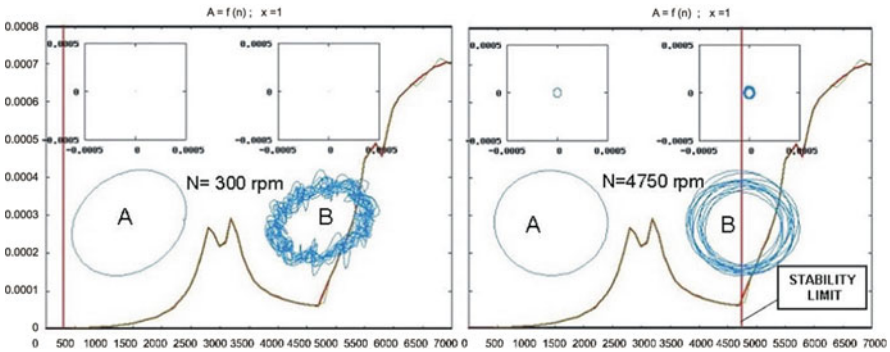

Fig. 8 Displacement trajectories of the rotor centre – within a stable operation range – calculated for the constant excitation force (basic) P (part A) and for the randomly changing – within limits $+/-\Delta P = 20\%$ (part B) shown at the background of the rotor amplitude-frequency response [8]

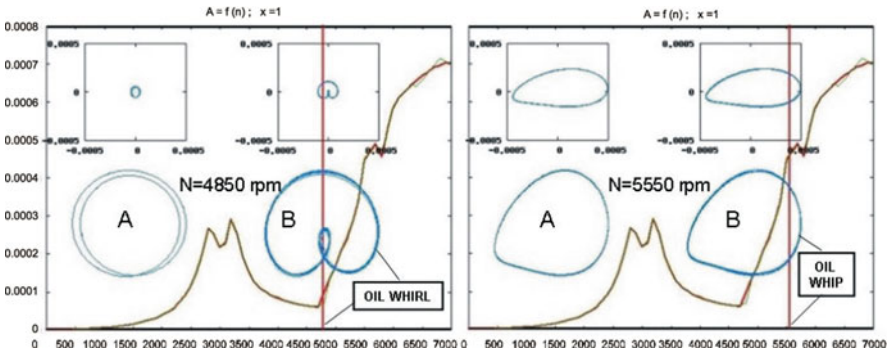

Fig. 9 Displacement trajectories of the rotor centre after the system exceeded the stability limit calculated for the constant basic force P (part A) and for the randomly changing – within limits $+/-\Delta P = 20\%$ (part B) shown at the background of the rotor amplitude-frequency response [8]

At the very stability limit a certain increase in the trajectory disturbance can be observed. However, disturbances caused by the stochastic variability of input data decay when the rotor rotational speed increases and the hydrodynamic instability develops (Fig. 9). This is rather a startling result, since it could have been expected that such perturbations – after exceeding the stability limit – would intensify the instability of the entire system since it has been already unstable. Similar conclusions were found when investigations were performed for various ΔP values and various algorithms of random excitations. Thus, a system defect in the form of the hydrodynamic instability attenuates to a certain degree the defect caused by stochastic effects of input data. It is an interesting observation resulting from the performed research.

4 Final Conclusions

The phenomenon of multiple whirls presented in the present paper, found by advanced computer simulations and performed by means of the experimentally verified own and commercial codes, requires further investigations both theoretical and experimental. Experimental investigations in this field are planned in the Gdansk Research Centre. However, they will be put into operation only after building the first prototypes of micro power plants and relevant testing stands. Currently we have only unpublished information that the similar phenomenon was recognized by means of direct measurements of vibrations at large power plants.

Preliminary considerations concerning heuristic modeling of rotors are included in the paper. In such modeling we took into account uncertainty and randomness of the calculation input data and mutual couplings. It was found that an influence of the stochastic variability of input data decreases after the system has exceeded the stability limit. This indicates that the defect of the hydrodynamic instability type can attenuate – to a certain degree – the defect in the form of a random scatter of input data.

References

1. Kicinski, J.: Rotor Dynamics. IFFM Publishers, Gdansk (2006)
2. Batko, W., Dabrowski, Z., Kicinski, J.: Nonlinear Effects in Technical Diagnostics. Publishing and Printing House of the Institute for Sustainable Technologies, Warsaw (2008)
3. Kicinski, J.: Materials and operational imperfections in rotating machinery. In: IFToMM – Seventh International Conference on Rotor Dynamics, Paper-ID 307, Vienna (2006)
4. Kiciński, J., Żywica, G., Banaszek, S., Bogulicz, M., Czoska, B.: Modelling of thermo-elastic deformations of the foil bearing bush with the application of authors' own and commercial calculation codes (in polish). Internal Report of the IF-FM PAS, no. 22/08, Gdansk (2008)
5. Agrawal, G.L.: Foil air/gas bearing technology – an overview. In: ASME International Gas Turbine & Aeroengine Congress, 97-GT-347, Orland, USA (1997)
6. Andres, L.S., Rubio, D., Kim, T.H.: Rotordynamic performance of a rotor supported on bump type foil bearings: experiments and predictions. ASME Turbo Expo, GT2006-91238, Barcelona, Spain (2006)
7. Hou, Y., Zhu, Z.H., Chen, C.Z.: Comparative test on two kinds of new compliant foil bearing for small cryogenic turbo-expander. CRYOGENICS **44**, 69–72 (2004)
8. Pietkiewicz, P., Kiciński, J., Czoska, B., Markiewicz, A.: Development of defect models – with uncertainty of input data taken into account (in polish). Internal Report IF-FM PAS, Gdansk (2008)
9. Zywica, G.: Simulation investigation of the effect of a supporting structure defect on the dynamic state of the rotor supported on slide bearings. In: ASME International Design Engineering Technical Conference, DETC2007-34415, Las Vegas (2007)

Experimental Decomposition of Vibration, Whirl and Waves in Rotating and Non-rotating Parts

I. Bucher

Abstract Modern rotating machines rotate faster than before in an attempt to produce more power while reducing weight. Rotating machines are coupled to fluids, electromagnetic forces and varying pressure fields, as a result, complicated vibration patterns can develop. In order to diagnose and understand the physical behavior of such machines, the measured vibrations need to be separated into components that indicate distinct physical phenomena. This paper deals with the separation of several types of vibrations in an attempt to diagnose and decompose the individual phenomena. The simplest decomposition isolates forward and backward whirl of shafts. Instead of performing this task in the frequency domain, in an off-line manner, a real-time decomposition that exploits a phase shifting filter is introduced here. This separation is a valuable tool to determine the isotropy of the supports and blade mistuning. An additional decomposition of the measured response isolates synchronous and non-synchronous vibrations thus highlighting the induced rotating vibrations and those coming from other sources. Yet decomposition adds the spatial dimension to the temporal, sense of whirl and frequency (or order) domains. This is accomplished by measuring along a spatial coordinate. Spatial decomposition can be achieved with an array of sensors or by continuously moving sensors.

Keywords Time-frequency decomposition · Traveling waves · Forward backward whirling · Blade mistuning

1 Introduction

Rotating machine's dynamics is composed of many components that can form a rather complicated response pattern. In order to assess the true state of a machine

I. Bucher (✉)
Dynamics Laboratory, Mechanical Engineering,
Technion Israel Institute of Technology, Haifa 32000, Israel
e-mail: izhak.bucher@gmail.com

K. Gupta (ed.), *IUTAM Symposium on Emerging Trends in Rotor Dynamics*,
IUTAM Bookseries 25, DOI 10.1007/978-94-007-0020-8_10,

and identify the physical reasons for high vibration and stress levels, researchers and manufacturers traditionally employ testing procedures. Some machines contain embedded sensors providing real time data for cases of emergency and predictive maintenance.

The industry traditionally lags behind the state-of-the-art developments where elaborate testing procedures emerge and disappear unused (e.g., Dhadwal et al. [1], Di Maio [2], Bucher et al. [3]). Indeed, shaft vibrations are often monitored in real installations (Muszynska [4]) in an attempt to detect irregular patterns and support asymmetry (Kim and Lee [5]). When the rotating structure contains disk-like components, in particular when the rotating part contains blades, the spatial, temporal and directional decomposition of the response is essential since the different vibration patterns overlap and can be inseparable.

The importance of blade vibration for assessment of the machine's health has inspired the development of tip-timing techniques (Carrington et al. [6]) and Laser tracking measurement set-ups (Di Maio [2] and Bucher et al. [3]). Tip timing techniques are relatively easy to install and therefore they became popular in industrial development sites, this is despite their deficiency and limited ability to capture the spatial dynamics of a bladed disks. Tracking laser techniques have proved informative and useful (Di Maio [2]), but they are limited to optically visible parts such as fan blades, they are expensive and they cannot be used during normal operation.

The rapid development in wireless micromechanical sensors, can speculatively, in the foreseeable future, present a line of embedded sensors that can be made an integral part of machine or a blade. Smart blades that broadcast their condition wirelessly while using the ambient vibrations to self-power their operation and to energize communications are a good candidate to fulfill the task of in-situ vibration measurements.

Some technical obstacles must be overcome before this type of sensors becomes commercially available, but, the author believes that once the usefulness of embedded sensors is demonstrated, the technological barriers can be overcome. This paper tries to make a small step in this direction.

A network or rather an array of sensors distributed along a rotating and vibrating machine can provide more refined information that the usual RMS levels and spectra provide. Indeed, a stationary array of sensors that measures disk vibrations has been employed in the past to separate response waves into traveling in co- and counter rotating components (Bucher and Ewins [7]). This method uses a stationary array of sensors, is capable of decomposing the different wavelengths as a means to diagnose discs and bladed disc vibrations. In order to compute the response in body coordinates, an elaborate, speed dependent, transformation should be employed.

Other methods present a similar decomposition for the time frequency and sense of whirl (e.g., Han and Lee [8] and Lee and Han [9]), but do not offer spatial separation. In complicated structures, the spatial separation of wavelength-related components provides a significant reduction in the complexity of the individual patterns. Spatial separation is helpful when some phenomena are hidden underneath large vibrations occurring at frequencies that are nearly identical.

The paper briefly mentions forward and backward whirling motions on a laboratory system emphasizing the ability to perform this decomposition in real time. Finally it uses a simulated disk to demonstrate combined spatial and temporal decomposition as an analysis and diagnosis tool.

2 Separation of Measured Signals in Rotating Machines

When more than one sensor is deployed on the vibrating and rotating structure, the combined data can be used to produce more informative information than the individual spectra and waterfall plots. This section briefly describes some traditional and new derivations for shaft and disk vibration decompositions from measured response data. The main purpose of these transformations is to project the measurements to the moving material frame of reference thus providing information about the actual stress levels it experiences.

2.1 Shaft Dynamics – Decomposition and Transformation

A common arrangement deploys two sensors that are fixed in space. These can measured any orbital motion of the shaft and decompose it as outlined below.

Several *standard transformations are employed in this paper. The Hilbert transform, indicated here* by $H[s(t)]$, advances all the frequencies in a measured signal $s(t)$, by 90 degrees (Hahn [10]). With this transformation one can express the forward, $s_f(t)$, and backward $s_b(t)$ whirling components of the shaft as:

$$s_f(t) = \frac{1}{2}\left(s_x(t) - H\left[s_y(t)\right]\right),\ s_b(t) = \frac{1}{2}\left(s_x(t) + H\left[s_y(t)\right]\right) \tag{1}$$

The importance of Eq. (1) is two-fold: (i) it computes the forward and backward components in real time (see IEEE [11] for the real time implementation of H[.]) and (ii) it separates the (nearly) static deformation associated synchronous part of the forward whirl, i.e., body-fixed coordinates from the backward whirl associated with oscillating stress. In fact the backward component oscillates twice per revolution, Gasch and Nordmann [12], thus exhibiting a greater threat to fatigue related failure than the forward whirl.

A second transformation that is now widespread is generally called time-frequency distribution. In rotordynamics circles the spectrum evolving with time, the waterfall, is computed by performing a Fourier transform on short segments of the data and stacking them time wise. The more advanced techniques (Cohen [13] and Han and Lee [8]) use the Wigner-Ville or the Short-Time Fourier Transform (STFT) to achieve a similar task. Normally, the speed of rotation is linearly

proportional to time, $\Omega = \alpha t$ (or the signals are re-sampled to achieve this) and thus, the time evolution of the response spectrum

$$STFT\,[s(t)] = S(\omega, t) \tag{2}$$

provides in fact the distribution of spectrum (ω, representing frequency) vs. speed. $S(\omega, \Omega)$.

It is worth noting that both the Hilbert transform and the STFT are linear operators and thus they can be applied at any order or sequence. Clearly, the STFT can be applied to Eq. (1) to obtain the time-frequency map of the forward and backward whirl.

It would seem illustrative to demonstrate Eq. (1) and Eq. (2) with genuinely measured data.

2.1.1 Experimental Demonstration of Real Time Decomposition of Shaft Vibrations

A laboratory test rig which is shown in Fig. 1 was used to acquire the data from two sensors deployed as shown in Fig. 2. The rig was accelerated until it reached some top speed and after a short dwell it was decelerated. Figure 3 shows the time measurements of the displacement sensors in the x and y directions respectively. The signals were artificially displaced to obtain better visibility. Figure 4 transforms the measured signals using Eq. (1) to obtain the forward and backward components.

It is instructive to apply the STFT to the signals in Fig. 4 to observe the effect of the real-time forward-backward decomposition. First the STFT of one of the raw signals $s_x(t)$ is shown (Fig. 5).

Applying the same transformation to $s_f(t)$ and $s_b(t)$, the following is obtained.

Figures 6 and 7, in addition to showing the synchronous X1 and higher engine orders (i.e., X2, X3,...), separate the natural frequency curves of the forward (increasing with speed) and backward (decreasing with speed), thus showing that the

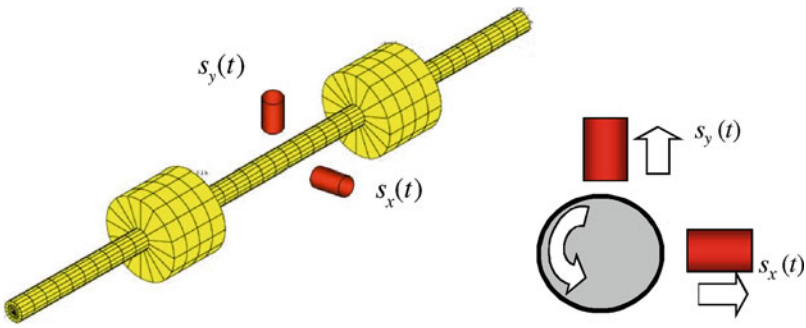

Fig. 1 Rotating shaft test rig instrumented with sensors

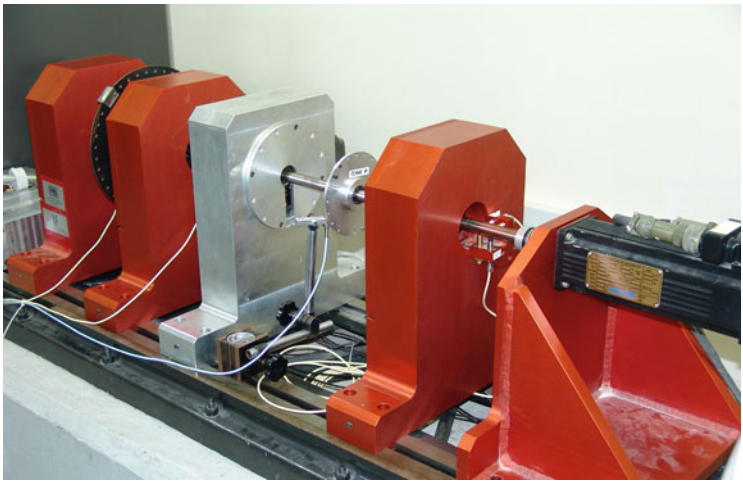

Fig. 2 Rotating shaft and two stationary sensors at right angle

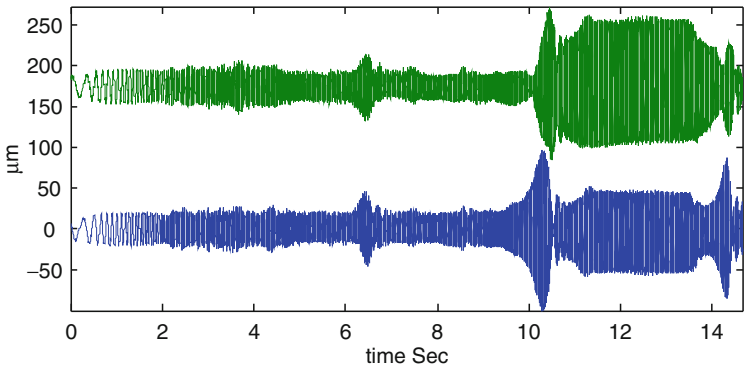

Fig. 3 Measured response, bottom: $s_x(t)$ and top: $s_y(t)$

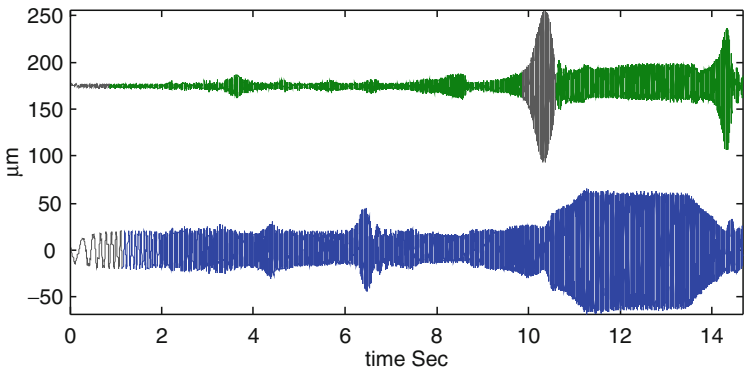

Fig. 4 The output of Eq. (1) bottom: $s_f(t)$ and top: $s_b(t)$ (signals are displaced for clarity)

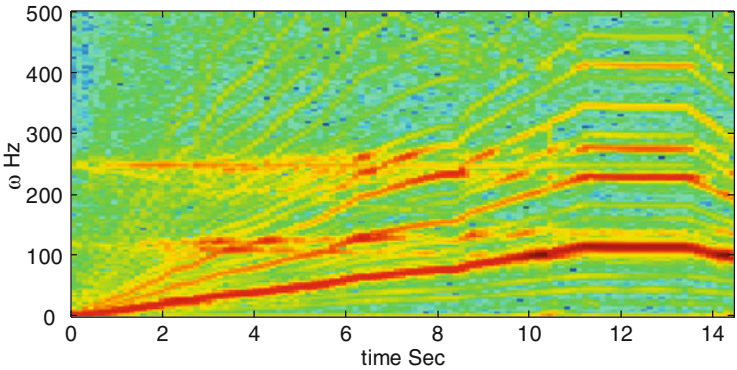

Fig. 5 STFT $S_x(\omega, t)$ of the raw

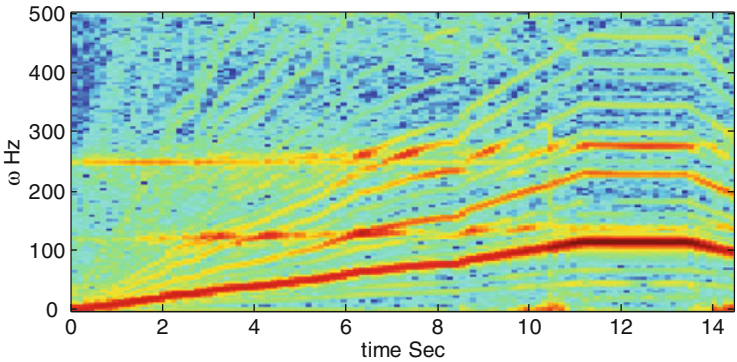

Fig. 6 STFT $S_f(\omega, t)$ of the forward whirling component

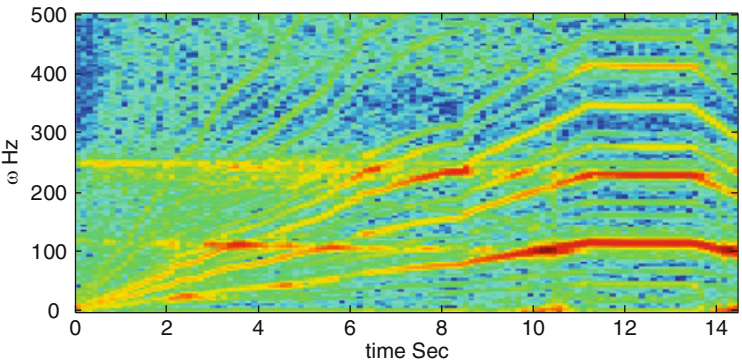

Fig. 7 STFT $S_b(\omega, t)$ of the backward whirling component

decomposition does perform what was anticipated. The decomposition offered by Eq. (1) is performed in real time contrary to traditional methods, e.g., Kim and Lee [5].

2.2 Disc and Blade Dynamics: Decomposition and Transformation

Rotating disks and bladed disks exhibit more complex dynamics than shafts. Consider, for example the response measured by an array of sensors placed near the tip of the blades, as illustrated by the model in Fig. 8.

Being cyclically symmetric, the response measured at a fixed radius r_0 will be a spatially periodic function of the angular position of each sensor, indicated by θ. Since the structure operates under time varying conditions, its response, as measured by a sensor located at (r_0, θ), can be expressed as:

$$s(\theta, t) = \sum_{n=0}^{\infty} p_n(t)\, e^{in\theta} + p_{-n}(t)\, e^{-in\theta} \tag{3}$$

Here, $p_n(t)$, $p_{-n}(t)$ represent the time evolution of the forward and backward progressing (respectively) nth nodal diameter vibration mode.

Restricting our attention to modes having N nodal diameters at most, using sensors N_s, one can approximate:

$$s(\theta, t) \approx \sum_{n=0}^{N} p_n(t)\, e^{in\theta} + p_{-n}(t)\, e^{-in\theta} \tag{4}$$

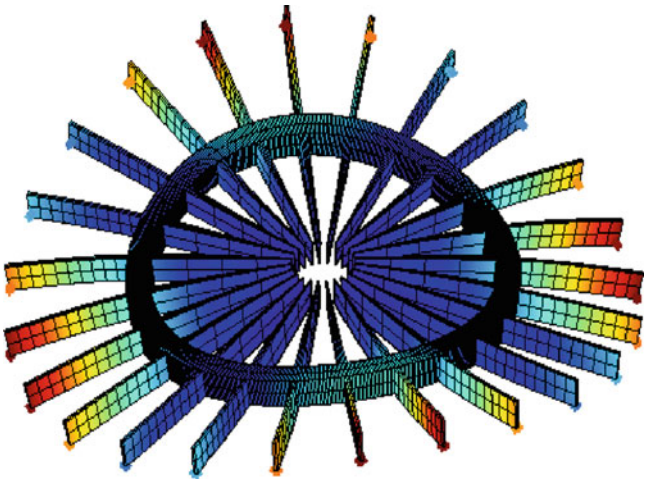

Fig. 8 Bladed disk crude model showing the embedded sensors at the tips of the blades

Now, since the sensors are spaced $\Delta\theta$ radians apart within $0 \ldots 2\pi$, the $p_n(t)$, $p_{-n}(t)$ can be computed in the frequency domain by employing a spatial Fourier transform to $s(k\Delta\theta, t), k = 0 \ldots N_s - 1$ (e.g., Bucher and Ewins [7]). In this paper we seek to obtain real-time information by simultaneously processing the entire array of sensors. Once more we employ the Hilbert transform to compute the phase shifted signal.

Denoting, $s_k(t) \triangleq s(k \cdot \Delta\theta, t)$ and its Hilbert transform $g_k(t) \triangleq H[s_k(t)]$. It can be shown (see appendix), that the real and the imaginary parts obey:

$$\begin{aligned} p_k^R(t) &\triangleq \Re \hat{S}_k(t) = \sum_{n=0}^{N-1} (s_n(t)) \cos \tfrac{2\pi}{N} kn + (g_n(t)) \sin \tfrac{2\pi}{N} kn \\ p_k^I(t) &\triangleq \Im \hat{S}_k(t) = \sum_{n=0}^{N-1} (g_n(t)) \cos \tfrac{2\pi}{N} kn - (s_n(t)) \sin \tfrac{2\pi}{N} kn \end{aligned} \tag{5}$$

It is worth mentioning that for $k > \frac{N_s}{2}$ one obtains the negative ongoing vibration wave with $p_k(t) \equiv p_{k-N_s}(t)$, and $p_k(t) \triangleq p_k^R(t) + i p_k^I(t)$.

Equation (5) computes the forward and backward ongoing wave components at every moment in time by employing linear combination of the measured signals from the entire array and their Hilbert transform. It can thus be used to form an instantaneous signal of each individual component. It will be shown below how this expression can be used to detect detuning and decompose the response into simpler components.

In order to demonstrate the method, the bladed disk in Fig. 8 was used in a simulation where the speed of rotation and hence the external excitation were varied with time. The external excitation was set-up to apply rotating forces in both standing and rotating directions thus simulating pressure fluctuations with certain spatial and temporal behavior. The bladed disk had three levels of mistuning. Level 1, no mistuning; level 2, slight mistuning; level 3, more mistuning (see Tobias and Arnold [14] and Ewins [15] for a definition of mistuning and its effect). The mistuning was simulated by adding random amount of mass to the tip of the blades.

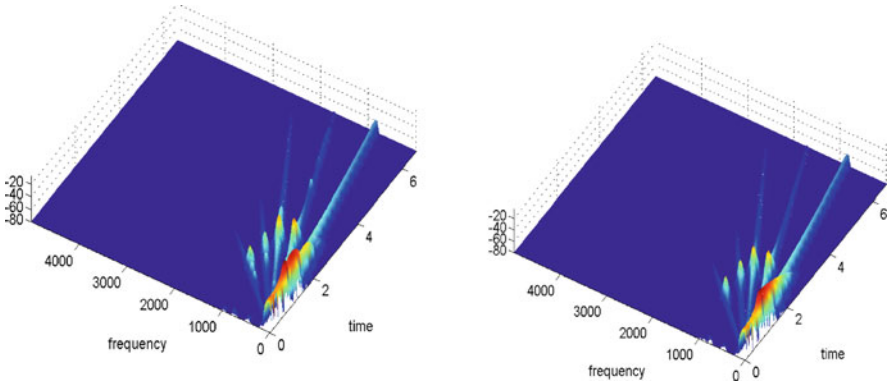

Fig. 9 Time-frequency distribution of run-up perfect and mistuned systems

A single sensor mounted on blade #1 was used to produce the STFT of level 1 and level 3 mistuning. Clearly, as can be seen in Fig. 9, the waterfall or time-frequency distribution seem identical and no indication can be made about the fact that mistuning exists.

At this stage, the decomposition presented in Eq. (5) was employed to separate the different wavelengths and plot their modulating function vs. time. Clearly, it can

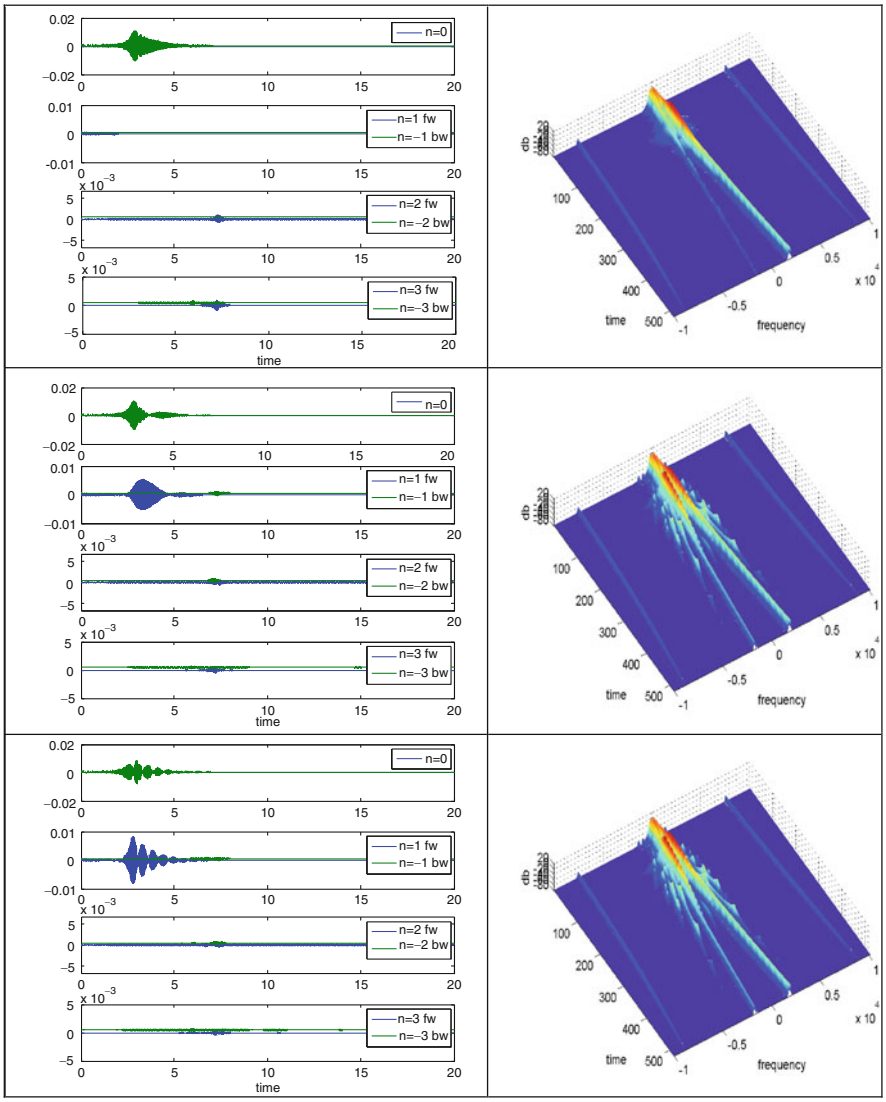

Fig. 10 Left column, decomposed time response for $p_n(t)$ and $p_{-n}(t)$ for $n = 0 \ldots 3$. Right column: STFT of $p_1(t)$ and $p_{-1}(t)$ together showing forward and backward whirl

be seen that mistuned systems' modes no longer have a single wavelength in their spatial response of individual modes. As a result, mistuning has created additional wavelength in the response.

The right column of Fig. 10 shows that standing waves (in the body fixed coordinates) become more pronounced due to mistuning.

3 Concluding Remarks

A method to combine the result of an array of sensors that is embedded in the rotating structure or fixed in a non-rotating frame of reference was presented. It has been demonstrated that the sensor of progression of whirl and waves can be decomposed in real time by computing a weighted sum of Hilbert transformed measurements. The method was demonstrated for a simple accelerating shaft in the laboratory and for a simulated bladed disk-like structure. It appears that the decomposed response that makes use of an array of sensors can potentially provide more refined information about mistuning or any emerging defect.

Acknowledgements The author is thankful to SDTools France and to Prof. Etienne Balmes who provided the code for some of the simulation studies. This research was partly supported by THE ISRAEL SCIENCE FOUNDATION (grant No. 579/04).

References

1. Dhadwal, H.S., Radzikowski, M., Strukov, D., Kurkov, A.: Real time flutter monitoring system for turbomachinery. In: Proceedings of the ASME Turbo Expo, vol. 2, pp. 799–809 (2004)
2. Di Maio, D.: SLDV technology for measurement of mistuned bladed disc vibration. Ph.D. Thesis, Imperial college, London (2007)
3. Bucher, I., Schmiechen, P., Robb, D.A., Ewins, D.J.: A laser-based measurement system for measuring the vibration on rotating discs. In: International Conference On Vibration Measurement by Laser Techniques, pp. 398–401. Ancona, Italy (1994)
4. Muszynska, A.: Forward and backward precession of a vertical anisotropically supported rotor. J. Sound Vib. **192**(1), 207–222 (1996)
5. Kim, M.E., Lee, C.W.: Use of dFRFs for identification of travelling wave modes in rotating disks. J. Vib. Acoust., Trans. ASME **120**(3), 719–726 (1998)
6. Carrington, I.B., Wright, J.R., Cooper, J.E., Dimitriadis, G.: A comparison of blade tip timing data analysis methods. Proc. Inst. Mech. Eng. **215**(G), 301–312 (2001)
7. Bucher, I., Ewins, D.J.: Multi-dimensional decomposition of time-varying vibration response signals in rotating machinery. Mech. Syst. Signal Process. **11**(4), 577–601 (1997)
8. Han, Y.S., Lee, C.W.: Directional Wigner distribution for order analysis in rotating/reciprocating machines. Mech. Syst. Signal Process. **13**(5), 723–737 (1999)
9. Lee, C.W., Han, D.J.: Strength of modes in rotating machinery. J. Sound Vib. **313**(1–2), 268–289 (2008)
10. Hahn, S.L.: On the uniqueness of the definition of the amplitude and phase of the analytic signal. Signal Process. **83**, 1815–1820 (2003)
11. IEEE: Programs for Digital Signal Processing. IEEE Press John Wiley & Sons (1997)
12. Gasch, R., Nordmann, R.: Rotordynamik. Springer (2007)

13. Cohen, L.: Time-Frequency Analysis. Prentice Hall, Englewood Cliffs, pp. 113–135 (1995)
14. Tobias, S.A., Arnold, R.N.: The influence of dynamical imperfection on the vibration of rotating disks. Proc. Inst. Mech. Eng. **171**, 666–690 (1957)
15. Ewins, D.J.: The effects of detuning upon the forced vibrations of bladed disks. J. Sound Vib. **9**, 65–79 (1969)

Appendix: Decomposition of Spatial Wavelengths

Consider the discrete Fourier transform of N sensors, distributed at a uniform angular spacing.

$$S_k(t) = \sum_{n=0}^{N-1} s_n(t)\, e^{-\frac{2\pi}{N}kn} = \sum_{n=0}^{N-1} s_n(t)\, \cos\frac{2\pi}{N}kn \\ -i\, s_n(t)\, \sin\frac{2\pi}{N}kn\,,\ k = 0 \ldots N-1 \tag{6}$$

Clearly, $S_k(t) \equiv p_k(t)$ represents the kth component with wavelength.

Now applying the Hilbert transform and adding Eq. (6), one has:

$$p_k(t) = \sum_{n=0}^{N-1} \hat{s}_n(t)\, \cos\frac{2\pi}{N}kn - i\,\hat{s}_n(t)\, \sin\frac{2\pi}{N}kn \tag{7}$$

Defining $\hat{s}_k(t) = s_k(t) + iH[s_k(t)] \triangleq s_k(t) + ig_k(t)$, one can obtain an explicit expression for the analytic signal of the k wavelength:

$$p_k(t) = \sum_{n=0}^{N-1} (s_n(t) + ig_n(t))\cos\frac{2\pi}{N}kn + (g_n(t) - i\ s_n(t))\ \sin\frac{2\pi}{N}kn \tag{8}$$

Separating real and imaginary parts, Eq. (5) is obtained.

Rotating Internal Damping in the Case of Composite Shafts

G. Jacquet-Richardet, E. Chatelet, and T. Nouri-Baranger

Abstract There is an increasing range of applications for rotors made of composite materials and operating at supercritical speeds. Design of such structures involves specific features which have to be accounted for in order to allow safe operations. A proper modeling of the mechanical characteristics of the composite is first needed. But, as far as the structure is rotating, the effect of stress stiffening and spin softening may be considered and the effect of internal damping has to be studied in order to avoid possible instability. Internal or rotating damping modeling remains an active field of research where both theoretical developments and experimental results are needed.

Keywords Rotating shaft · Composite material · Instability · Internal damping · Rotating damping

1 Introduction

Damping, coming from different sources, is one of the most difficult issues for structural dynamic predictions. Damping effects are mainly modeled using viscous and hysteretic damping. The main difference between both types of damping is that the energy dissipated per cycle by viscous damping is frequency (spin speed) dependent, whereas the energy dissipated by hysteretic damping is not. Damping associated to the non-rotating parts of the structure has a usual stabilizing effect while damping associated to rotating parts can trigger instability in supercritical ranges. Internal viscous damping is well known. Hysteretic damping is often substituted by an equivalent viscous damping for harmonic motions.

First investigations by Newkirk [1] showed that rotors may experience violent whirling at speeds above the first critical due to internal damping. Since then, many

G. Jacquet-Richardet (✉), E. Chatelet, and T. Nouri-Baranger
Université de Lyon, CNRS
INSA-Lyon, LaMCoS UMR5259 Villeurbanne F-69621, France
e-mail: Georges.Jacquet@insa-lyon.fr

K. Gupta (ed.), *IUTAM Symposium on Emerging Trends in Rotor Dynamics*,
IUTAM Bookseries 25, DOI 10.1007/978-94-007-0020-8_11,

researchers have studied the combined influence of internal (material, dry friction) and external damping (bearings...). Classical results were obtained, showing that rotor stability is improved by increasing the damping provided by the bearings, whereas increasing internal damping may reduce the instability threshold [2–4]. Genta [5] demonstrated that an error is made when considering that hysteretic rotating damping is destabilizing at any speed. Until now internal rotating damping modeling remains an up to date research area [6, 7].

Because of the specific strength and stiffness of high performance fiber reinforced materials, attempts are being made to replace metal shafts by composite ones in many applications: driveshafts for helicopters and cars, centrifugal separators, cylindrical tubes [8–10]. These materials provide advantages in terms of weight reduction and give designers the possibility of obtaining predetermined behavior by changing the arrangement of the composite layers [11, 12]. For a rotor made of composite materials, internal damping can be significant [13] due to the damping capacity of the matrix. Optimization techniques have been used in order to avoid instability, minimize the unbalanced response and maximize the stability limit speed. For composite shafts, equivalent modulus beam theory (EMBT) based on classical laminate theory, has many limitations [14], and is only valid for symmetric stacking. General homogenized beam theory (GHBT) has been developed to reduce the previous limitations [15]. The equivalent flexural moduli are in this case evaluated using the Young's modulus, shear modulus and specific damping capacity of each layer. The distance to the neutral axis and the thickness of each layer are explicitly taken into account. Shear effects are considered by evaluating the flexural warping function.

Beam based models are generally useful but may also be questionable. In the case of tubes, multilayered shell models may be needed. Finally, most of the published studies remain purely numerical and there is a lack of experimental results that may be used for a better understanding of the effect of rotating damping as well as for validation purpose [16, 17].

This paper gives first some brief descriptions of the theoretical background concerning internal damping modeling and the equations of motions. Then, applications are presented in order to illustrate and discuss specific features.

2 Equations of Motion: Composite Rotor

Most existing rheological models are based on the combination of elastic and viscous basic elements such as those of Maxwell, Hook and Kelvin-Voigt [18]. In this work, the Kelvin-Voigt model has been chosen. It consists of a spring and a damper in parallel and is commonly used for linear viscoelastic systems. The associated equations of motion of the rotor [19] are, in the rotating frame:

$$[M]\left\{\ddot{d}\right\} + [C_i + C(\Omega)]\left\{\dot{d}\right\} + [K + K_i(\Omega)]\{d\} = \{0\} \tag{1}$$

where $[M]$ represents the mass, $[C_i]$ the internal damping, $[C(\Omega)]$ includes an antisymmetric gyroscopic matrix (function of Ω speed of rotation) and a frequently asymmetric matrix owing to the characteristics of bearings, $[K]$ is the elastic stiffness matrix, and $[K_i(\Omega)]$ is the stiffness matrix associated to internal damping as well as stress stiffening and spin softening effects. $\left\{\ddot{d}\right\}$, $\left\{\dot{d}\right\}$ and $\{d\}$ are respectively nodal accelerations, velocities and displacements. The Campbell diagram and instability regions are determined from the solution of the eigenvalue problem obtained after reduction by the pseudo modal method [19]. The natural frequencies are obtained from the imaginary part and stability criterion is defined from the real part of the eigenvalues.

Considering formulations based on beam theories and dealing with homogeneous materials, the stiffness of the structure is a function of the product EI, where E is the Young's modulus and I, the inertia of the section. Similarly, dissipation due to internal damping is a function of $EI\eta$, where η is the loss factor. When considering composite rotors, two formulations may be used. The most classical one uses equivalent homogenized material approaches and leads to the Equivalent Modulus Beam Theory (EMBT). On the other hand, General Homogenized Beam Theory (GHBT) is based on a direct homogenization of the products EI and $EI\eta$. GHBT has the advantage of being valid for any laminate stacking of the rotor wall. The homogenized parameters of the rotor are derived from the strain energy and are expressed as follows [15]:

$$EI = \sum_{k=1}^{N} E^k \pi \left(\frac{{R_k}^4 - {R_{k-1}}^4}{4} \right) EI\eta = \sum_{k=1}^{N} E^k \eta^k \pi \left(\frac{{R_k}^4 - {R_{k-1}}^4}{4} \right) \quad (2)$$

$$E^k = \frac{1}{\frac{c^4}{E_l} + \frac{s^4}{E_t} + c^2 s^2 \left(\frac{1}{G_{lt}} - 2\frac{\upsilon_{tl}}{E_t} \right)} \quad (3)$$

with: E_l, E_t, υ_{tl}, G_{lt} respectively Young's moduli, Poisson's ratio and shear modulus in the orthotropic axes, $c = \cos(\theta)$, $s = \sin(\theta)$, R_k, R_{k-1} give the beginning and the end of the kth layer from the neural axis, θ is the layer orientation angle and $E^k \eta^k$ is the damped Young's modulus of layer k along the rotor axis. Damping factor η is obtained from the specific damping capacity of layers according to the longitudinal, transversal and shear directions respectively. For the effect of transverse shear, the homogenized shear modulus GS is obtained from the shear strain energy.

3 Application

Two different applications are presented and used for illustration. The first one concerns a thin wall composite shaft and the second a composite rotor with discs.

3.1 Thin Walled Composite Shaft

The application considered first is a simply supported thin-walled tube with two lateral inner discs at both ends. The shaft length is $L = 1.5\,\text{m}$, its outer diameter is $D = 0.09\,\text{m}$ and its wall thickness is $e = 7.0 \times 10^{-4}\,\text{m}$. The discs lie at a distance of $0.05\,\text{m}$ from both ends of the tube, their thickness is $3.0 \times 10^{-3}\,\text{m}$ and their inner radius is $0.0075\,\text{m}$. The shaft is made of five layers of Boron/Epoxy ($\rho = 1{,}600\,\text{kg/m}^3$, $E_1 = 3.0 \times 10^{11}\,\text{Pa}$, $E_2 = 6.2 \times 10^9\,\text{Pa}$, $G_{12} = G_{13} = G_{23} = 4.1 \times 10^9\,\text{Pa}$ and $\nu_{12} = 0.26$). The stacking sequence considered is $[0°, -30°, +30°, 0°, 90°]$, given from the inner to the outer surface of the cylinder. Mechanical damping is here neglected.

As shown in Fig. 1, only 1/12th (30°) of the whole structure is meshed using a multilayered shell element, constructed from the solid isoparametric element with 16 nodes, by applying Reissner-Mindlin hypotheses. The resulting element is geometrically characterised by 16 nodes and kinematically by eight nodes and five dof per node. A shear correction coefficient equal to 5/6 is considered and reduced integration is used to prevent shear locking.

The three first bending frequencies obtained for the structure at rest are reported in Table 1. These values are compared with those computed using ROTORINSA [19] associated with an EMBT. Differences in results are significant and can be explained by the effect of the simplifying assumptions associated with EMBT: (a) contribution of each layer independent of its radial position, this hypothesis being only valid for thin-walled shafts with symmetrical sequences, (b) longitudinal shear deformations associated with bending not considered. Critical speeds obtained with both shell and beam models are also reported. Due to stress stiffening effects, accuracy of the beam model decreases when rotation speed increases.

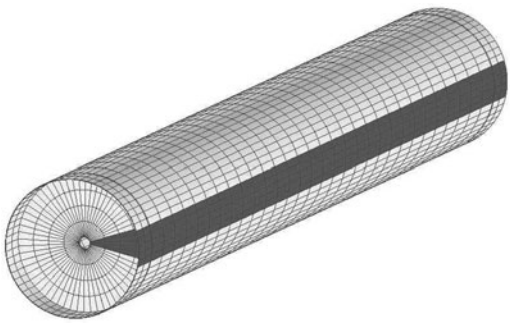

Fig. 1 Cylindrical tube. Only 1/12th of the mesh (dark) is considered by the numerical model

Table 1 Natural frequencies at rest (Hz) and first critical speeds (rpm)

Freq. at rest Rotorinsa	Freq. at rest 3D model	Δ(%)	Critical speed Rotorinsa	Critical speed 3D model	Δ(%)
508.4	475.4	6.7	31, 820	28, 570	11.4
1, 749.2	1, 446.7	18.9	116, 625	91, 660	27.2
3, 305.7	2, 564.7	24.0			

3.2 Composite Rotor with Two Discs

In order to emphasize the influence of internal damping in rotordynamic analysis, Campbell diagram and instability thresholds are determined for a rotor made of a filament wound shaft when considering different configurations of stacking sequences. The structure, proposed by Pereira and Marcio [12], is a composite shaft with two rigid steel disks supported by two bearings as shown in Fig. 2. Rotor parameters are: $L = 1.2\,\text{m},\ D = 0.096\,\text{m},\ e = 0.008\,\text{m}$, Disc: $D_i = 0.096\,\text{m},\ D_o = 0.3\,\text{m},$ h=0.05 m.

Material properties of each ply made of carbon/epoxy are summarized in Table 2 and the anisotropic bearing stiffness characteristics are: $K_{xx} = 1.10^7\,\text{N/m},\ K_{zz} = 1.10^8\,\text{N/m},\ K_{xz} = K_{zx} = 0$ (no external damping considered). The first configuration consists of 8 plies of 0.001 m thickness in a balanced and symmetric configuration $[\pm\theta^\circ]$s. Figure 3 gives the Campbell diagram obtained using GHBT. Frequencies and instabilities thresholds are in this case in very good agreement with those obtained by Pereira and Marcio [12] using EMBT. As there is no external damping, instability occurs just after the critical speed.

The same structure with different symmetrical and asymmetrical stacking sequences is then considered. When examining Table 3, the influence of stacking on the fundamental frequency as well as on the instability threshold appears clearly.

As shown in Table 4, where both results obtained from GHBT and EMBT are compared, the distance to the neutral axis contributes to the calculation of the mechanical characteristics of the rotor with GHBT but not accurately with EMBT. When using EMBT, an error up to 16% on instability threshold and 7% on the fundamental frequency is observed. The Campbell diagram associated with the second configuration considered above is presented in Fig. 4.

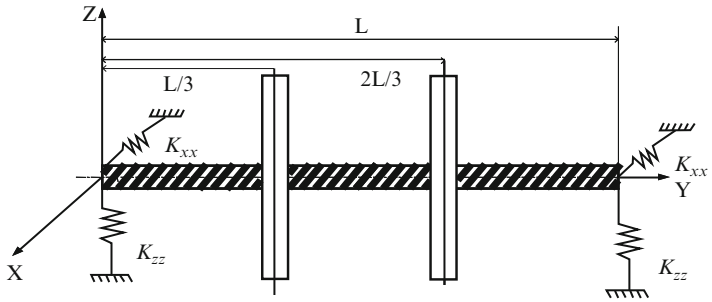

Fig. 2 Filament wound shaft with two disks

Table 2 Material data for the shaft (carbon epoxy)

E_l (GPa)	E_t (GPa)	G_{lt} (GPa)	υ_{tl}	ρ (kg/m^3)	ψ_l (%)	ψ_t (%)	ψ_{lt} (%)
172.7	7.20	3.76	0.3	1,446.2	0.45	4.22	7.05

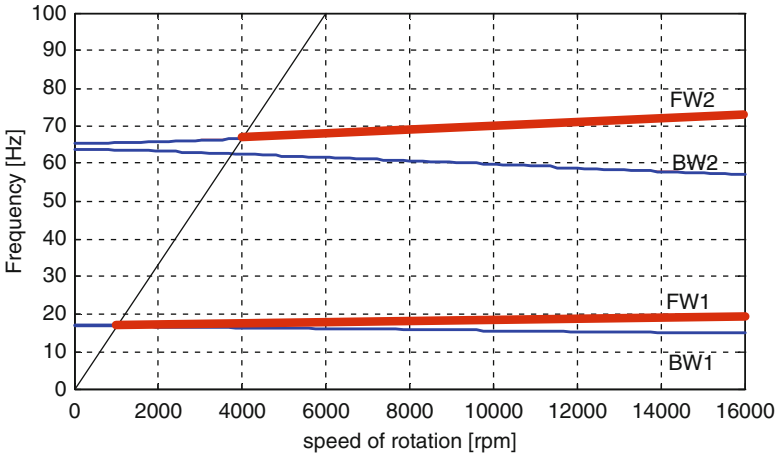

Fig. 3 Campbell diagram and instability regions for a laminate $\theta = 75°$ with anisotropic bearings (thick lines = unstable)

Table 3 Mechanical characteristics of the shaft

	Stacking sequence	Freq (Hz)	Instability threshold (rpm)
1	$[90_2, 45, 0]_S$	39.87	5, 864
2	[90,0,90,45,90,45,0,90]	40.08	5, 913
3	$[90, 45, 0_2]_S$	50.71	10, 981
4	[45,0,45,0,90,0,90,0]	51.36	11, 395

Table 4 Comparison between GHBT and EMBT. Instability threshold – first frequency

	GHBM (rpm)	EMBT (rpm)	%	GHBM (Hz)	EMBT (Hz)	%
$[90_2, 45, 0]_S$	5,864	6,956	15.7	39.87	42.76	6.7
[90, 0, 90, 45, 90, 45, 0, 90]	5,913	6,965	15.1	40.08	42.76	6.3
$[90, 45, 0_2]_S$	10,981	12,064	9.0	50.71	52.37	3.2
[45, 0, 45, 0, 90, 0, 90, 0]	11,395	12,064	5.5	51.36	52.37	2.0

Differences between configurations is up to 21% for frequencies at rest and about 47% for instability thresholds, and for different cases, not presented here, the rotor may exceed the third critical speed without generating instability. The greater the number of fibers oriented close to the longitudinal direction of the tube, the more they contribute to shaft rigidity and, consequently, higher the frequencies are. Similarly, the lower the orientation angle, the lower the internal damping due to composite materials is and, consequently, the instability occurs later.

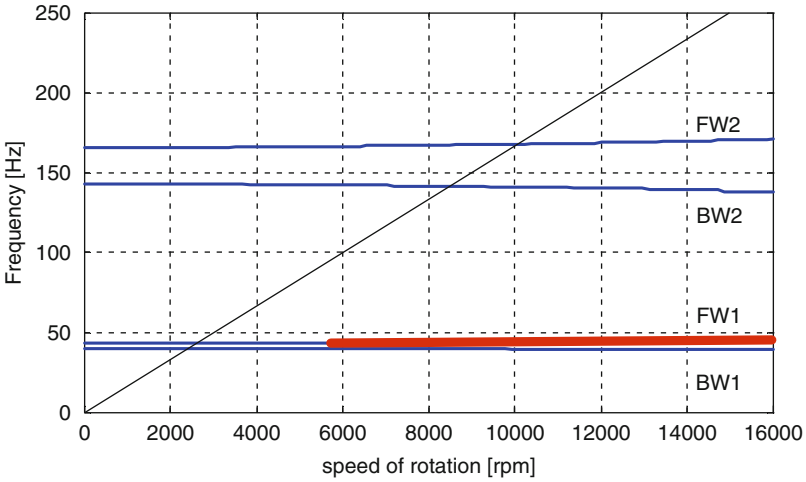

Fig. 4 Campbell diagram for configuration [90,0,90,45,90,45,0,90]

4 Experimental Analyses

An experimental set up developed at the LMA of Marseille France, shown in Fig. 5 is used for illustration and validation. The set up allows studying the stability of shafts made of different materials with various lengths ranging between 0.5 and 3 m. To allow supercritical behavior, passive dissipation is introduced at bearing level using viscoelastic supports (damping factor 3.5%). Bearings are classical ball bearings. The main characteristics of the tested rotors, made of PVC, are: Young modulus 2.2 GPa, density 1,350 kg/m^3, external radius 0.025 m, internal radius 0.0215 m, damping factor 1.25%. Isotropic bearing mass is 2.608 kg and foundation stiffness is 567×10^3 N/m.

Figure 6 shows the evolution of the computed frequencies and instability thresholds, with respect to the rotor length L. Legends are as follows: F_{csi} is ith frequency of the system; SI_i is ith associated instability threshold. The instability zone (grey) of this rotor is greater than the instability zone of rotors made of classical materials due to the material damping which is more significant for PVC (1.25% here compared to 0.2 associated to an aluminum rotor for example). Experimental results obtained at the LMA are also given. They are symbolized by a circle ◯ for the first frequency and by a star @ for the instability thresholds. Four experimental tests were performed for tubes of lengths 0.6 m, 0.8 m, 0.9 m and 1 m. The experimental instability was detected at the first critical speed. Tendencies shown by experimental results are in good agreement with theoretical results and the first frequency identified matches very well.

Observation points out two instability zones merging at a length L near 0.8 m. Within this zone the different components of the system are highly coupled. Frequencies associated to the rigid rotor with flexible bearings match frequencies of the tube supported by rigid bearings. For this particular length of rotor, bearings are

Fig. 5 Testing machine for high-speed tubes

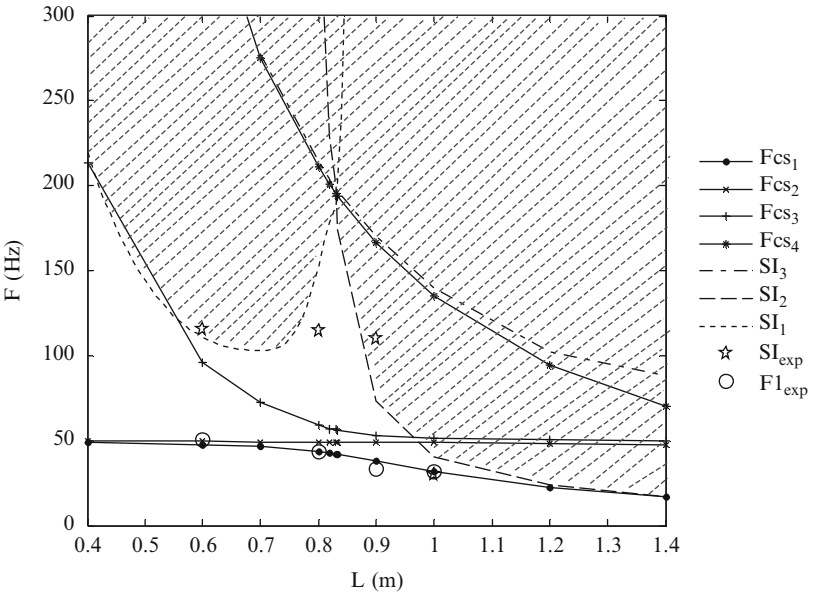

Fig. 6 PVC Tube: numerical and experimental results (dashed zone is unstable)

highly responding and then provide more external damping to the system, increasing stability. Such behavior has also been observed by Dutt and Nakra [20] who show that a proper selection of the value of support parameters can increase significantly instability threshold for a system on viscoelastic supports.

5 Conclusion

The presented paper deals with the dynamical analysis of internally damped rotating composite shafts. Usual rotordynamics modeling is based on beam theories. In this case, the General Homogenized Beam Theory is needed to avoid the main drawbacks associated with formulations that consider only symmetrical and balanced stacking sequences and do not take into account the distance of layers from the neutral axis. As already shown, those simplifications may lead to significant discrepancies in terms of frequencies and instability thresholds. The method also allows accurate characterization of the structure's internal damping, based on the specific damping capacity of each ply of the composite assembly. Another limitation illustrated here concerns the case where the rotating structure is more a tube than a shaft. In this case classical effects such as stress stiffening and spin softening shall be accounted for. Then beam theories are no more valid and shall be replaced by multilayered shell theories.

Finally an experimental set up is described and used for illustration and validation. New techniques are under development and major improvements are clearly needed to overcome the severe limitations of the classical equivalent viscous damping model. But the development of those techniques has to be clearly associated with much more fine available experimental results (transient response. . .).

Acknowledgements The authors wish to thank Pr. C. Hochard from the Laboratoire de Mécanique et d'Acoustique, UPR CNRS 7051 Marseille France and Dr O. Montagnier for providing the experimental data presented in Sect. 4.

References

1. Newkirk, B.L.: Shaft whipping. Gen. Electr. Rev. **27**(3), 169–178 (1924)
2. Genta, G.: Dynamics of Rotating Systems. Springer, New York (2005)
3. Cerminaro, A.M., Nelson, F.C.: The Effect of Viscous and Hysteretic Damping Rotor Stability. ASME TURBOEXPO, Munich, Germany (2000)
4. Sino, R., Chatelet, E., Montagnier, O., Jacquet-Richardet, G.: Dynamic Instability of Internally Damped Rotors. ASME TURBOEXPO, Montreal, Canada (2007)
5. Genta, G.: On a persistent misunderstanding of the role of hysteretic damping in rotordynamics. J. Vib. Acoust. **126**, 459–461 (2004)
6. Genta, G.: Time domain simulation of rotors with hysteretic damping. In: Nineth International Conference on Vibrations in Rotating Machinery, Exeter, pp.799–810 (2008)
7. Vatta, F., Vigliani, A.: Internal damping in rotating shafts. Mech. Mach. Theor. **43**, 1376–1384 (2008)
8. Darlow, M.S., Creonte, J.: Optimal design of composite helicopter power transmission shafts with axially varying fiber lay-up. J. Am. Helicop. Soc. **40**(2), 50–56 (1995)
9. Singh, S.P., Gupta, K.: Damping measurements in fiber reinforced composite rotors. J. Sound Vib. **211**(3), 513–520 (1998)
10. Chatelet, E., Lornage, D., Jacquet-Richardet, G.: A three-dimensional modeling of the dynamic behavior of composite rotors. Int. J. Rotating Mach. **8**(3), 185–192 (2002)
11. Bauchau, O.: Optimal design of high speed rotating graphite/epoxy shafts. J. Compo. Mater. **17**(3), 170–181 (1983)

12. Pereira, J.C., Marcio, E.S.: Evaluation and Optimization of the Instability Regions on Rotors in Wounding Shaft. II Congresso Nacional de Engenharia Mecânica, João Pessoa, Brazil (2002)
13. Wettergren, H.L., Olsson, K.O.: Dynamic instability of a rotating asymmetric shaft with internal viscous damping supported in anisotropic bearings. J. Sound Vib. **195**(1), 75–84 (1996)
14. Singh, S.P., Gupta, K.: Free damped flexural vibration analysis of composite cylindrical tubes using beam and shell theories. J. Sound Vib. **172**(2), 171–190 (1994)
15. Sino, R., Baranger, T.N., Chatelet, E., Jacquet, G.: Dynamic analysis of rotating composite shaft. Compo. Sci. Technol. **68**(2), 337–345 (2008)
16. Montagnier, O., Hochard, C.:Etude théorique et expérimentale de la dynamique des arbres de transmission supercritiques. 17ème congrès Français de Mécanique, Troyes, 29 Août-2 Septembre (2005)
17. Montagnier, O., Hochard, C.: Design of Supercritical Composite Helicopter Driveshafts: Theoretical and Experimental Study. European Conference for Aerospace Sciences (EUCASS) (2005)
18. Osinski, Z.: Damping of Vibrations. Institute of Machine Design Fundamentals, Warsaw University of Technology, Poland, A.A.balkema (1998)
19. Lalanne, M., Ferraris, G.: Rotordynamics Prediction in Engineering, 2nd edn. J. Wiley and Sons, p. 254 (1998)
20. Dutt, J.K., Nakra, B.C.: Stability of rotor systems with viscoelastic supports. J. Sound Vib. **153**(1), 89–96 (1992)

Unbalance Response Analysis of a Spinning Rotor Mounted on a Precessing Platform

Ankuran Saha, Rajesh Ghosh, Arghya Nandi, and Sumanta Neogy

Abstract The present work deals with analysis of a uniformly spinning shaft with a non-central disc mounted on a rotating (precessing) base, where the spin axis and the precession axis intersect at right angle. The motion of the rotor is such that it undergoes small elastic deformation superposed on rigid body rotation about a point. It is assumed that the shaft is axially and torsionally stiff and the disc has four degrees of freedom. Due to unbalance excitation, somewhat like a rotor on an orthotropic support, this rotor has also been found to undergo backward whirl.

Keywords Spin · Precession · Rotor · Unbalance response · Backward whirl

1 Introduction

Spinning and precessing motions of a rigid body with a constant nutation angle are frequently encountered in practice like a motor-shaft-disk system on a turntable, a helicopter rotor in pitching (in a circular path) flight, a special purpose machine tool etc. Many sophisticated analyses have been attempted for spinning, symmetric and non-symmetric shaft-disk systems on fixed base [1–5]. A general continuum formulation has also been recently reported for non-axisymmetric rotors on fixed bases [6]. It is Lin and Meng [7], who first reported on dynamics of an elastic rotor on a maneuvering support. They considered a two-degree of freedom accelerating Jeffcott rotor model primarily in a pitching aircraft. On the other hand considerable work has already been done on vibration of rotating beams (precessing but non-spinning). This has always been an important topic as turbine and compressor blades [8], flexible manipulators in robotic applications [9] etc. can also be approximately modeled as rotating beams. Xiao et al. [10] demonstrated the effect of simultaneous

A. Saha, R. Ghosh, A. Nandi (✉), and S. Neogy
Department of Mechanical Engineering, Jadavpur University,
Kolkata – 700032, India
e-mail: arghyan@yahoo.com

K. Gupta (ed.), *IUTAM Symposium on Emerging Trends in Rotor Dynamics*,
IUTAM Bookseries 25, DOI 10.1007/978-94-007-0020-8_12,

dynamic softening and stiffening in a rotating beam with a tip mass. In the present work response analysis of spinning and precessing rotor due to unbalance excitation is performed.

2 Analysis

2.1 Governing Equations of Motion

The shaft-disk system shown in Fig. 1 is spinning with a constant angular velocity Ω_s about an axis a. This axis is again precessing about the inertial Z axis with an angular velocity Ω_p. The inertial reference is represented by the coordinate system *XYZ*. The coordinate system *xyz* precesses about the axis Z with a uniform angular velocity Ω_p (Fig. 2a). The axis Z and the axis z are coincident. The reference $x'y'z'$ rotates about the axis x with an angular velocity $\Omega_s\hat{i}$. The axes x and x' are coincident ones. This reference frame $x'y'z'$ would have been the body-fitted frame had the solid been rigid. With respect to the reference $x'y'z'$ the solid has elastic deformations only. The solid undergoes a small elastic deformation superposed on the specified rigid body motion.

It is assumed that during deformation the disk remains rigid in its own plane. In undeformed condition, the vector $R\hat{i} + e\cos\Omega_s t\,\hat{j} + e\sin\Omega_s t\hat{k}$ locates the center of mass of the disk. The unit vectors $\hat{i}$, $\hat{j}$ and $\hat{k}$ are along the axes *x,y* and *z* respectively. In deformed configuration, the center has a position vector (Fig. 2b).

$$\overline{\boldsymbol{\rho}}_{\mathbf{c}} = R\hat{i} + e\cos\Omega_s t\,\hat{j} + e\sin\Omega_s t\hat{k} + u_y\hat{j} + u_z\hat{k} \tag{1}$$

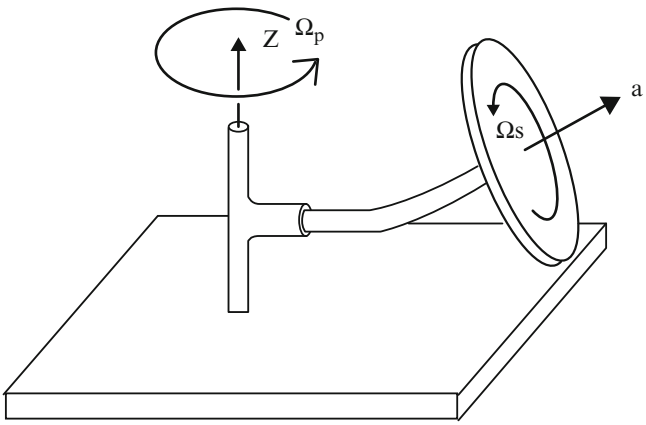

Fig. 1 A spinning and precessing rotor.

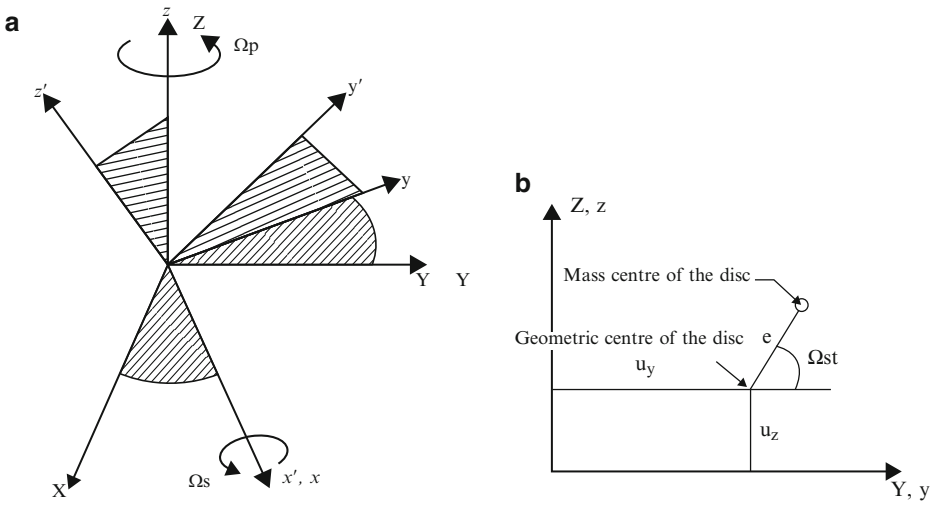

Fig. 2 **(a)** Coordinate systems fixed to inertical and rotating references **(b)** location of the centre of mass

The last two terms in the above expression define the translation of the disk due to the elastic bending. In case of no elastic rotation (slope) of the disk, the plane of the disk would have been parallel to the *y*-*z* plane.

The velocity of the centre of mass of the disk is as follows:-

$$\bar{\mathbf{v}} = \frac{d\,\bar{\rho}_c}{dt} = \left(-\Omega_p u_y - \Omega_p e\cos\Omega_s t\right)\hat{i} + \left(\frac{\partial u_y}{\partial t} - \Omega_s e\sin\Omega_s t + \Omega_p R\right)\hat{j} + \left(\frac{\partial u_z}{\partial t} + \Omega_s e\cos\Omega_s t\right)\hat{k} \tag{2}$$

The kinetic energy of translation for the disk is expressed as follows:

$$T_{trans} = \frac{1}{2}\left\{\begin{array}{c} -\Omega_p u_y - \Omega_p e\cos\Omega_s t \\ \left(\frac{\partial u_y}{\partial t} + \Omega_p R - \Omega_p e\sin\Omega_s t\right) \\ \frac{\partial u_z}{\partial t} + \Omega_s e\cos\Omega_s t \end{array}\right\}^T \begin{bmatrix} m & 0 & 0 \\ 0 & m & 0 \\ 0 & 0 & m \end{bmatrix} \left\{\begin{array}{c} -\Omega_p u_y - \Omega_p e\cos\Omega_s t \\ \left(\frac{\partial u_y}{\partial t} + \Omega_p R - \Omega_p e\sin\Omega_s t\right) \\ \frac{\partial u_z}{\partial t} + \Omega_s e\cos\Omega_s t \end{array}\right\} \tag{3}$$

The angular location of the disk can be expressed by the following consecutive rotations (Fig. 3).

Fig. 3 Rotations of the disk.

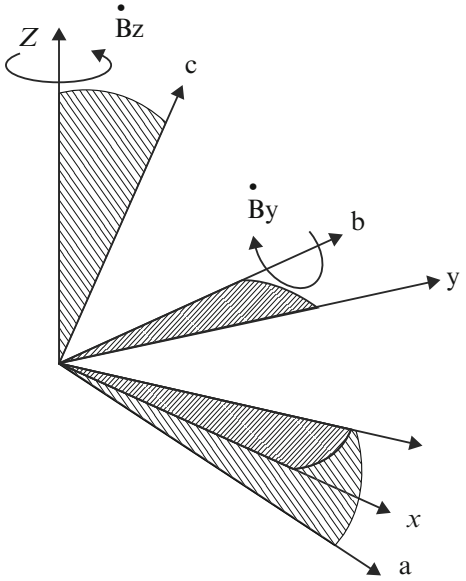

i. Rotation $\Omega_p t$ about inertial Z axis.
ii. Rotation B_z about z or Z axis. Due to this rotation the y axis rotates and becomes the b axis.
iii. Rotation B_y about the b axis. After this rotation the coordinate system abc is obtained.
iv. Rotation $\Omega_s t$ about axis a.

The elastic rotations of the disk can be described as two infinitesimal rotations B_z and B_y about the axes z and b (close to y) respectively.

Now, retaining all the terms to avoid missing out of any resulting significant term in the process, the components of the angular velocity vector can be expressed in the coordinate system abc as follows: -

$$\begin{Bmatrix}\omega_a\\ \omega_b\\ \omega_c\end{Bmatrix} = \begin{bmatrix}\cos B_y & 0 & -\sin B_y\\ 0 & 1 & 0\\ \sin B_y & 0 & \cos B_y\end{bmatrix}\begin{Bmatrix}0\\ 0\\ \Omega_p + \dot{B}_z\end{Bmatrix} + \begin{Bmatrix}\Omega_s\\ \dot{B}_y\\ 0\end{Bmatrix} = \begin{Bmatrix}-\left(\Omega_p + \dot{B}_z\right)\sin B_y + \Omega_s\\ \dot{B}_y\\ \left(\Omega_p + \dot{B}_z\right)\cos B_y\end{Bmatrix} \tag{4}$$

The rotational kinetic energy of the disk is

$$T_{rot} = \frac{1}{2}\begin{Bmatrix}\omega_a\\ \omega_b\\ \omega_c\end{Bmatrix}^T \begin{bmatrix}I_P & 0 & 0\\ 0 & I_T & 0\\ 0 & 0 & I_T\end{bmatrix}\begin{Bmatrix}\omega_a\\ \omega_b\\ \omega_c\end{Bmatrix} \tag{5}$$

The symbols I_P and I_T stand for polar and transverse mass moment of inertia respectively.

The total potential energy of the non-symmetric shaft in terms of linear and angular displacements in the spinning and precessing frame *xyz* is given by

$$V = \frac{1}{2} \begin{Bmatrix} u_y \\ u_z \\ \mathrm{B}_y \\ \mathrm{B}_z \end{Bmatrix}^T [\mathbf{K}] \begin{Bmatrix} u_y \\ u_z \\ \mathrm{B}_y \\ \mathrm{B}_z \end{Bmatrix} \tag{6}$$

$$[\mathbf{K}] = \begin{bmatrix} k_{11} & 0 & 0 & k_{14} \\ 0 & k_{22} & k_{23} & 0 \\ 0 & k_{23} & k_{33} & 0 \\ k_{14} & 0 & 0 & k_{44} \end{bmatrix} \tag{7}$$

The Lagrangian can be defined as,

$$L = T_{Trans} + T_{Rot} - V \tag{8}$$

Combining Eq. (3), Eq. (5) and Eq. (6), the Lagrange's equations of motion can be presented as follows:

$$[M]\left\{\ddot{U}\right\} + [G]\left\{\dot{U}\right\} + ([K] + [K]_1)\{U\} = \{f\} + \{f\}_{Unb} \tag{9}$$

$$[\mathbf{M}] = \begin{bmatrix} m & 0 & 0 & 0 \\ 0 & m & 0 & 0 \\ 0 & 0 & I_T & 0 \\ 0 & 0 & 0 & I_T \end{bmatrix} \tag{10a}$$

$$[\mathbf{G}] = \Omega_s \begin{bmatrix} 0 & 0 & 0 & 0 \\ 0 & 0 & 0 & 0 \\ 0 & 0 & 0 & I_P \\ 0 & 0 & -I_P & 0 \end{bmatrix} = \Omega_s I_T \begin{bmatrix} 0 & 0 & 0 & 0 \\ 0 & 0 & 0 & 0 \\ 0 & 0 & 0 & \chi \\ 0 & 0 & -\chi & 0 \end{bmatrix} \tag{10b}$$

$$[\mathbf{K}]_\mathbf{1} = \begin{bmatrix} -m\Omega_p^2 & 0 & 0 & 0 \\ 0 & 0 & 0 & 0 \\ 0 & 0 & -(I_P - I_T)\,\Omega_p^2 & 0 \\ 0 & 0 & 0 & 0 \end{bmatrix}$$

$$= \begin{bmatrix} -m\Omega_p^2 & 0 & 0 & 0 \\ 0 & 0 & 0 & 0 \\ 0 & 0 & -I_T\,(\chi - 1)\,\Omega_p^2 & 0 \\ 0 & 0 & 0 & 0 \end{bmatrix} \tag{10c}$$

$$\{\mathbf{f}\}^{\mathbf{T}} = \lfloor 0 \;\; 0 \;\; -I_P \Omega_s \Omega_p \;\; 0 \rfloor \tag{10d}$$

$$\{\mathbf{f}\}_{\mathbf{unb}}{}^{T} = \left\lfloor m\left(\Omega_p^2 + \Omega_s^2\right) e \cos \Omega_s t \;\; m\Omega_s^2 e \sin \Omega_s t \;\; 0 \;\; 0 \right\rfloor \tag{10e}$$

$$\{\mathbf{U}\}^{\mathbf{T}} = \lfloor u_y \;\; u_z \;\; B_y \;\; B_z \rfloor \tag{10f}$$

Damping terms can be included as follows to give,

$$[\mathbf{M}]\left\{\ddot{\mathbf{U}}\right\} + ([\mathbf{D}] + [\mathbf{G}])\left\{\dot{\mathbf{U}}\right\} + ([\mathbf{K}] + [\mathbf{K}]_{\mathbf{1}} + [\mathbf{K_2}])\{\mathbf{U}\} = \{\mathbf{f}\} + \{\mathbf{f}\}_{\mathbf{Unb}} \tag{11}$$

where,

$$[\mathbf{K}]_{\mathbf{2}} = \begin{bmatrix} 0 & -c_r \Omega_s & 0 & 0 \\ c_r \Omega_s & 0 & 0 & 0 \\ 0 & 0 & 0 & 0 \\ 0 & 0 & 0 & 0 \end{bmatrix} \tag{12a}$$

$$[\mathbf{D}] = \begin{bmatrix} c_n + c_r & 0 & 0 & 0 \\ 0 & c_n + c_r & 0 & 0 \\ 0 & 0 & 0 & 0 \\ 0 & 0 & 0 & 0 \end{bmatrix} \tag{12b}$$

Here the symbols c_n and c_r stand for coefficient of non-rotating and rotating (with respect to the precessing frame) damping respectively.

As an initial partial check of governing Eq. (11) one can make the precession speed Ω_p zero, which represents a rotor on a fixed base. For this case the results are available in literature and can be used for comparison.

For

$$\Omega_p = 0, [\mathbf{K}]_{\mathbf{1}} = [0] \tag{13}$$

For an undamped case and for a thin disk, all the matrices match exactly with those derived by Nelson and McVaugh [1].

3 Numerical Example

A cantilevered shaft of circular cross-section with a disc at its tip is considered for numerical simulation. The root of the shaft is connected to a motor. The shaft-disc system along with the motor is placed on a rotating base. The following numerical values are considered for the rotational speeds and the dimensions of the shaft-disc system.

Radius of the disc $R_d = 0.075m$, Thickness of the disc $t_d = 0.010m$
Mass of the disc $m_d = 1.38kg$
Moment of inertia of the disc about its diameter $I_d = 1.9408 \times 10^{-3}\, kgm^2$

Diameter of the shaft $d_s = 0.015m$, Length of the shaft $L_s = 0.400m$
Unbalance $me = 10^{-4}\, kg.m$

Percentage damping values are computed by consider critical damping coefficient $= 2 \times m_d \times \omega_n \approx 350Ns/m$. The non-rotating first natural frequency of the rotor is denoted by ω_n. A value of 5% non-rotating damping is considered in this work. It is observed that effect of precession is more prominently felt in the displacement in the y-direction. As is noted from Eq. (9) and relation (10c), precession has an effect similar to that of an orthotropic support.

This is also evident from the Campbell diagram shown in Fig. 4. For the present configuration the stiffness in the y-direction is reduced due to precession. Figure 5a shows the response of the rotor in y-direction.

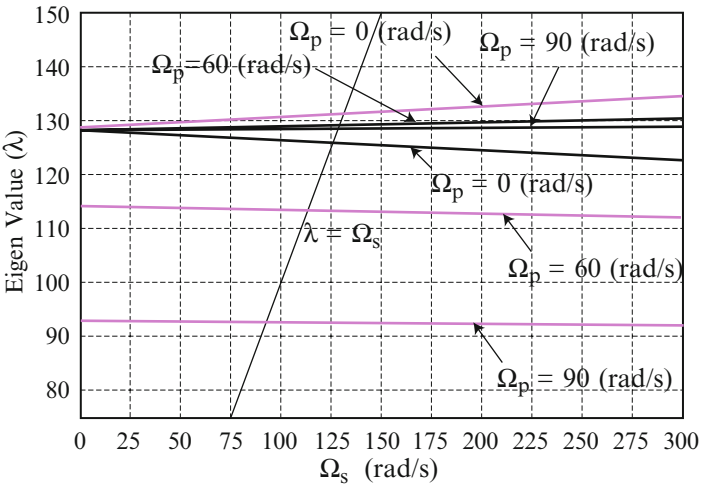

Fig. 4 Campbell diagram for the first forward and backward whirl modes

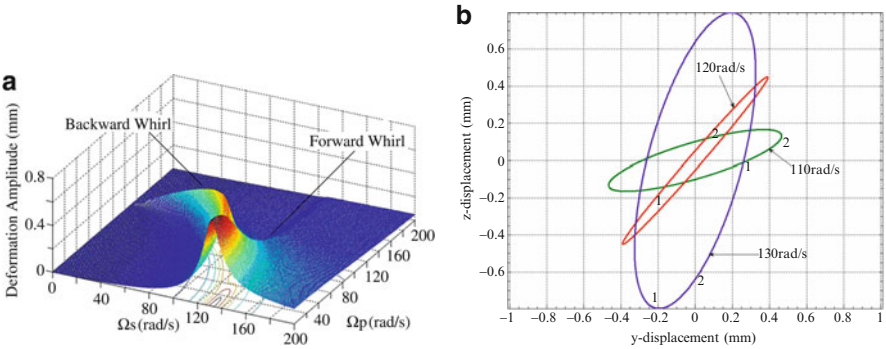

Fig. 5 **(a)** Amplitude of y-displacement for a spinning and precessing shaft. **(b)** Transition from forward to backward to forward whirl at $\Omega_p = 60rad/s$

With increase in precession speed the peak response at the first forward critical speed breaks up in two branches. At the first branch at lower spin speed the rotor whirl changes from forward to backward and then backward to forward (Fig. 5b).

4 Conclusion

In the present work the investigation centers around the effect of precession speed on unbalance response of a spinning rotor supported on a precessing base. Since such a motion introduces a negative stiffness in one direction, this rotor behaves like one on orthotropic support and exhibits backward whirl. Though simple two and four degrees of freedom models are considered here, this method can also be extended to three-dimensional rotor models.

References

1. Nelson, H.D., McVaugh, J.M.: The dynamics of rotor bearing systems using finite elements. J. Eng. Ind. **98**(2), 593–600 (1976)
2. Gmur, T.C., Rodrigues, J.D.: Shaft finite elements for rotor dynamics analysis. J. Vib. Acoust. **113**, 482–493 (1993)
3. Stephenson, R.W., Rouch, K.E.: Modeling rotating shafts using axisymmetric solid finite elements with matrix reduction. J. Vib. Acoust. **115**(1), 484–489 (1993)
4. Nandi, A., Neogy, S.: Modeling of rotors using three-dimensional solid finite elements. J. Strain Anal. Eng. **36**(4), 359–371 (2001)
5. Nandi, A., Neogy, S., Das, A.S.: Application of harmonic balance technique to finite element models of asymmetric rotors via sparse Kronecker products. J. Strain Anal. Eng. **40**, 1–9 (2005)
6. Mahadevan, P., Jog, C.S., Chatterjee, A.: Modal projections for synchronous rotor whirl. P.Roy. Soc. Lond. A. Mat. **464**, 1739–1760 (2008)
7. Lin, F., Meng, G. Study on the dynamics of a rotor in a maneuvering aircraft. J. Vib. Acoust. **125**, 324–327 (2003)
8. Genta, G.: Dynamics of Rotating Systems. Springer, Italy (2004)
9. Oguamanam, D.C.D., Arshad, M.: On the natural frequency of a flexible manipulator with a tip payload. J. Mech. Eng. Sci. **219**(11), 1199–1205 (2005)
10. Xiao, S., Chen, B., Du, Q.: On dynamic behavior of a cantilever with tip mass in centrifugal field. Mech. Base Des. Struc. **33**, 79–98 (2005)

A Simple Viscoelastic Model of Rotor-Shaft Systems

J.K. Dutt

Abstract Damping exists in every material in varying degrees; so materials in general are viscoelastic in nature. Energy storage as well as dissipation in varying degrees, accompany every time varying deformation, with the effect that stress and strain in a material get out of phase. This work presents the development of preliminary equations of motion of a simple viscoelastic rotor-shaft-system by using differential operator algebra. Sample results of stability limit of spin speed and stability limit of uniform angular acceleration at a stable spin speed are also presented. Use of operators enables one to consider linear multi-element (e.g., 3, 4 or higher elements) material model for better representation of the viscoelastic rotor continuum rather than a two-element Voigt model used generally. The primary inspiration for a multi-element model arises from the need to capture broad band spectral behaviour of materials, primarily polymers and polymer composites. Additionally such a model is generic, as with suitable choice of model parameters, the formulation may also be used to obtain the equations of motion, if a two-element (Voigt model) or a single element (purely elastic) model is used to represent the rotor material behaviour. The equations developed may be easily used to find the time response of the rotor-disc subjected to any dynamic forcing function.

Keywords Viscoelastic rotors · Multi-element rotor models · Rotor stability

1 Introduction

Viscoelastic materials store and dissipate energy simultaneously upon deformation, the frequency of which influences the energy storage and dissipation. For linear viscoelastic solids this behaviour may be represented by multi-element models, many of which are found in Bland [1]. Asnani [2] obtained the frequency dependent

J.K. Dutt
Department of Mechanical Engineering IIT Delhi, Hauz Khas
New Delhi – 110016, India
e-mail: jkrdutt@yahoo.co.in

K. Gupta (ed.), *IUTAM Symposium on Emerging Trends in Rotor Dynamics*,
IUTAM Bookseries 25, DOI 10.1007/978-94-007-0020-8_13,

storage modulus and loss factor of Poly-Vinyl-Chloride (PVC) at different temperatures and Kapur et al. [3] extracted parameters for a four-element model to represent its behaviour. Efficient energy dissipation is the primary motivation to use viscoelastic materials, such as polymers for vibration reduction and vibration control; Nakra [4] has given many such examples. Although light weight is a good advantage to use such materials for rotor-shafts, at least for cold low duty operations, yet, low elastic modulus is an impediment towards achieving high rotor speed for problems of stability. Texts by Dimentberg [5], Tondl [6] and many others used two-element Voigt model to represent the material behaviour and developed equations of motion of rotor-shaft-systems. Zorzi and Nelson [7], Ozguven and Ozkan [8], Ku [9] and many others used the two-element material model to formulate the equations of motion after discretizing the rotor continuum with finite beam elements. The above authors also proposed a combination of viscous and hysteretic damping models for structural materials like steel. In this regard, Genta [10] pointed out correct interpretation and the use of hysteretic damping model. However for frequency-dependent material properties, (storage modulus and loss factor), shown by polymers, such material models do not work well. Grybos [11] used three-element material model and studied the dynamics of a viscoelastic rotor. Roy et al. [12] reported a finite-element approach, where viscoelastic behaviour of the rotor-continuum was represented by ATF (Augmenting Thermodynamic Field). Roy [13] in his doctoral work investigated in detail different approaches to represent viscoelastic material behaviours to model the rotor continuum. This paper attempts to obtain the equations of motion of a simple rotor-shaft system in the time domain by considering a multi-element material model to represent the viscoelastic behaviour for closely investigating the dynamics of a viscoelastic rotor.

2 Analysis

Figures 1a–c show the two-element, three-element and the four-element models respectively [1]. In general, for linear viscoelastic solids, the constitutive relationship may be represented by $\sigma = E\ ()\ \varepsilon$ where σ, the instantaneous dynamic stress is obtained by operating $E\ () = (Nu\ (D)/Dn\ (D))$, a function of differential time $D \equiv (d/dt)$, on instantaneous dynamic strain ε. For the special case of linear elastic behaviour, E is a constant. Expressions of $E_\iota()$, $\iota = 2, 3, 4$ for 2, 3, and 4-element models, shown in Figs. 1a–c, are given by Eqs. (1a), (1b) and 1(c) respectively.

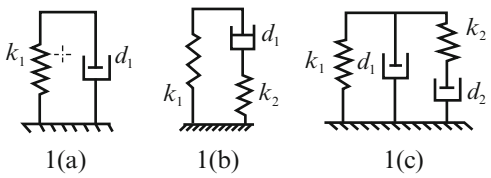

1(a) 1(b) 1(c)

Fig. 1 Two-element, Three-element and four-element models

$$E_2() = \gamma_1 + \gamma_2 D, \gamma_1 = k_1, \gamma_2 = d_1 \tag{1a}$$

$$E_3() = \frac{\gamma_1 + \gamma_2 D}{(1 + \gamma_4 D)}, \gamma_1 = k_1, \gamma_2 = d_1 + \frac{k_1 d_1}{k_2}, \gamma_4 = \frac{d_1}{k_2} \tag{1b}$$

$$E_4() = \frac{\gamma_1 + \gamma_2 D + \gamma_3 D^2}{(1 + \gamma_4 D)}, \gamma_1 = k_1, \gamma_2 = d_1 + d_2 + \frac{k_1 d_2}{k_2},$$
$$\gamma_3 = \frac{d_1 d_2}{k_2}, \gamma_4 = \frac{d_2}{k_2} \tag{1c}$$

The units of k_j, d_j $(j = 1, 2)$ above are adjusted accordingly. Expressions of E_2 () and E_3 () may be obtained from Eq. (1c) by eliminating appropriate elements.

Ghosh and Mallik [14] reported a simple classical approach to include the effect of rotor-material damping. Figure 2a drawn after following the authors, shows a displaced section of a rotor shaft and three reference frames, the "fixed frame" (x, y), spin synchronized or "spin frame" (ξ, η), and the whirl-synchronized or the "whirl frame" (r, φ), having unit vectors $(\mathrm{e_x}, \mathrm{e_y})$, $(\mathrm{e}_\xi, \mathrm{e}_\eta)$ and $(\mathrm{e_r}, \mathrm{e}_\varphi)$ respectively. These frames are attached at "O" the point of intersection of rotor-shaft section plane considered and the bearing centre-line. Figure 2b shows the bending of a differential element of the shaft in the whirl plane and the longitudinal strain ε_z at a fibre at a distance δ_1 from the neutral plane is

$$\varepsilon_z = (\delta_1 / R) = \delta_1 (\partial^2 \delta(z, t) / \partial z^2) \tag{2}$$

In the above equation, $R = (\partial^2 \delta(z, t) / \partial z^2)$ is the instantaneous radius of curvature at the section considered, where $\delta(z, t)$ is the instantaneous deflection of the rotor, at a spatial location z. From Fig. 2a the expression of instantaneous longitudinal strain at the location (r, α) may be written as

$$\varepsilon_z = (\varepsilon_z)_{\max} \left(\frac{r}{r_0} \right) \cos\alpha, \ (\varepsilon_z)_{\max} = r_0 \frac{\partial^2 \delta(z, t)}{\partial z^2} \tag{3}$$

Instantaneous longitudinal stress in the above fibre may be written as

$$\sigma_z = E_\iota() \varepsilon_z = \frac{Nu(D)}{Dn(D)} \varepsilon_z \tag{4}$$

Expressions of instantaneous bending moments M_r and M_φ may be written with the help of Eq. (3) by integrating the corresponding expressions of differential quantities over the entire cross section as

$$\begin{aligned} Dn(D)[M_r] &= \int_0^{2\pi} \int_0^{r_0} \frac{r^3}{r_0} N_u(D) \left[(\varepsilon_z)_{\max} \cos\alpha \right] (\cos\alpha) dr d\alpha \\ Dn(D)[M_\phi] &= \int_0^{2\pi} \int_0^{r_0} \frac{r^3}{r_0} N_u(D) \left[(\varepsilon_z)_{\max} \cos\alpha \right] (\sin\alpha) dr d\alpha \end{aligned} \tag{5}$$

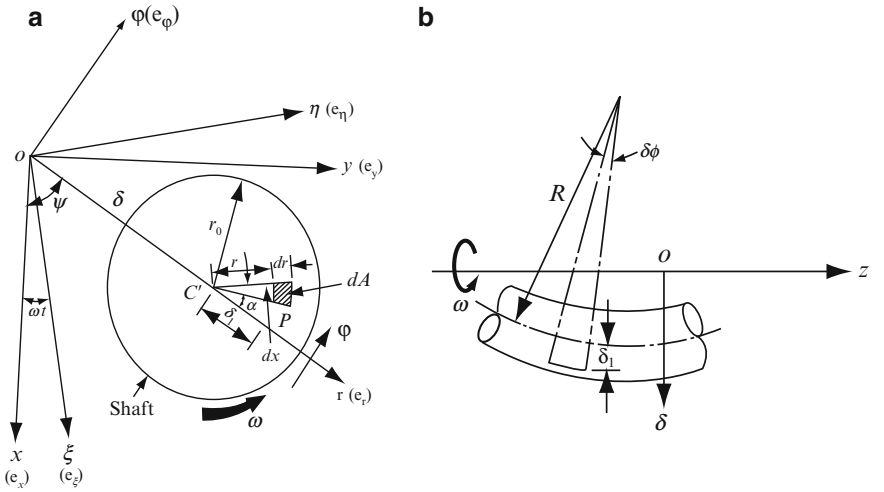

Fig. 2 **(a)** Shaft section, **(b)** differential shaft length and radius of curvature

The operator $Nu(D)$ operates only on the strain term i.e., $(\varepsilon_z)_{\max}\cos\alpha$ and not on all functions of time. Expressions of force per unit length along the r and φ directions p_{r} and p_φ respectively may be had from Eqs. (6).

$$\begin{aligned} p_r(z,t) &= \frac{-\partial^2 M_r}{\partial z^2} = \frac{-1}{Dn(D)}\frac{\partial^2}{\partial z^2}\left[\frac{I}{\pi r_0}\int_0^{2\pi} Nu(D)[(\varepsilon_z)_{\max}\cos\alpha]\cos\alpha\, d\alpha\right] \\ p_\phi(z,t) &= \frac{-\partial^2 M_\phi}{\partial z^2} = \frac{-1}{Dn(D)}\frac{\partial^2}{\partial z^2}\left[\frac{I}{\pi r_0}\int_0^{2\pi} Nu(D)[(\varepsilon_z)_{\max}\cos\alpha]\sin\alpha\, d\alpha\right] \end{aligned} \tag{6}$$

In the above, I is the diametral area moment of inertia of the shaft section. Total force acting on the shaft at a section as a result of the bending moment is obtained by integrating Eq. (6) between spatial limits. Considering simply supported end conditions and approximating $\delta(z,t)$ by its first mode shape for simplicity i.e., by $\delta(z,t) \cong \delta_c(t)\cos\left(\frac{\pi z}{L}\right)$, where $\delta_c(t)$ is the instantaneous deflection in the mid-span, and using the expression of $(\varepsilon_z)_{\max}$, the total instantaneous force acting at a rotor-section in the middle of its span along r and φ directions may be written as in Eq. (7).

$$\begin{aligned} P_r &= \frac{-1}{Dn(D)}\int_{-L/2}^{L/2}\frac{I}{\pi}(\pi/L)^4\int_0^{2\pi}[Nu(D)[\delta_c(t)\cos(\pi z/L)\cos\alpha]\cos\alpha\, d\alpha]dz \\ P_\phi &= \frac{-1}{Dn(D)}\int_{-L/2}^{L/2}\frac{I}{\pi}(\pi/L)^4\int_0^{2\pi}[Nu(D)[\delta_c(t)\cos(\pi z/L)\cos\alpha]\sin\alpha\, d\alpha]dz \end{aligned} \tag{7}$$

Expressions of P_r and P_φ for any material model may now be obtained from Eq. (7) by putting appropriate expressions of $Nu(D)$ and $Dn(D)$.

For a four-element material model, as an example, (i.e., with $Nu(D) = \gamma_1 + \gamma_2 D + \gamma_3 D^2$ and $Dn(D) = 1 + \gamma_4 D$) the expressions of P_r and P_φ are given in Eq. (8).

$$\begin{aligned} P_r &= \frac{-1}{(1+\gamma_4 D)} 2I(\pi/L)^3(\gamma_1\delta_c(t) + \gamma_2\dot{\delta}_c(t) + \gamma_3\ddot{\delta}_c(t) \\ &\quad +\gamma_3\dddot{\delta}_c(t) + \gamma_3\delta_c(t)\dot{\alpha}^2) \\ P_\phi &= \frac{-1}{(1+\gamma_4 D)} 2I(\pi/L)^3(\gamma_2\dot{\delta}_c(t)\dot{\alpha} + 2\gamma_3\dot{\delta}_c(t)\dot{\alpha} + \gamma_3\delta_c(t)\ddot{\alpha}) \end{aligned} \tag{8}$$

It may easily be verified that by putting $\gamma_1 = E,\ \gamma_2 = \mu_v,\ \gamma_3 = \gamma_4 = 0$ the operator corresponding to the two-element material model is obtained, which matches exactly with those given in equation (12.39) in Ghosh and Mallik [14]. So generalized expressions of P_r and P_φ are obtained.

Coordinate transformation may be performed to obtain the components (P_ξ, P_η) in the spin frame (ξ, η). Expressions of P_ξ and P_η are obtained as in Eq. (9) by putting in Eq. (8), $\xi_c = \delta_c(t)\cos(\psi - \omega t)$, $\eta_c = \delta_c(t)\sin(\psi - \omega t)$, $\dot{\alpha} = \omega - \dot{\psi}$, and the derivatives.

$$\begin{aligned} P_\xi &= \tfrac{-1}{(1+\gamma_4 D)} 2I(\pi/L)^3[\gamma_1\xi_c + \gamma_2\dot{\xi}_c + \gamma_3\ddot{\xi}_c] \\ P_\eta &= \tfrac{-1}{(1+\gamma_4 D)} 2I(\pi/L)^3[\gamma_1\eta_c + \gamma_2\dot{\eta}_c + \gamma_3\ddot{\eta}_c] \end{aligned} \tag{9}$$

Writing the radius vector in the spin frame, i.e., vector $\mathrm{OC} = \zeta_c = \xi_c + \iota\eta_c$, (where $\iota = \sqrt{-1}$) the expression of force $P_\zeta = P_\xi + \iota P_\eta$ is given in Eq. (10)

$$P_\zeta = \frac{-1}{(1+\gamma_4 D)} 2I(\pi/L)^3[\gamma_1\zeta_c + \gamma_2\dot{\zeta}_c + \gamma_3\ddot{\zeta}_c] \tag{10}$$

Using the expression in Eq. (10) and Newton's second law of motion, the equations of motion for free vibration of the rotor-disc placed in the middle of rotor-shaft with simply supported end conditions (as shown in Fig. 3) are obtained as in Eq. (11).

$$m_{eq}(\ddot{\zeta}_c + i2\omega\dot{\zeta}_c - \omega^2\zeta_c) - P_\zeta = 0 \tag{11}$$

In Eq. (11) m_{eq} is the equivalent mass of the disc, i.e., the disc mass plus an effect of the shaft mass which is $\cong 48.57\%$ by using Rayleigh's principle. Operating Eq. (11)

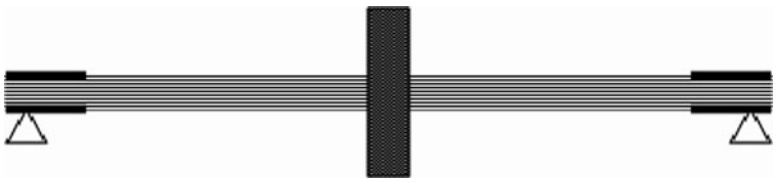

Fig. 3 The rotor-shaft system

with $(1 + \gamma_4 D)$ and transforming the same using $\zeta_c = \rho_c e^{-\iota\omega t}$ and its derivatives, the equations of motion are written in stationary frame as in Eq. (12).

$$m_{eq}\gamma_4\dddot{\rho}_c + [(m_{eq} + \beta\gamma_3) - im_{eq}\gamma_4\omega]\ddot{\rho}_c + [\beta\gamma_2 - i(2\beta\ \gamma_3\omega + m_{eq}\gamma_4\dot{\omega})]\dot{\rho}_c$$
$$+[(\beta\gamma_1 - \beta\gamma_3\omega^2 - m_{eq}\gamma_4\omega\dot{\omega}) - i(m_{eq}\dot{\omega} + m_{eq}\gamma_4\ddot{\omega} + \beta\gamma_2\omega + \beta\gamma_3\dot{\omega})]\rho_c = 0 \tag{12}$$

This equation may be used with suitable values of $\gamma_\iota[\iota = 2, 3]$ to get equations of motion of the rotor-shaft system if two- or three-element material models are used. It may be noted that Eq. (12) is a linear differential equation in terms of the complex displacement ρ_c and the material model incorporates the effect of spin speed and generally its time derivatives in the dynamics of the rotor.

This paper investigates the transient response of Eq. (12) to study the stability of the system, which is found using the Routh's criterion as used by Tondl [6] and applied by Dutt and Nakra [15]. For this, putting $\rho_c = Z\ e^{\iota\lambda t}$ in Eq. (11), the characteristic equation is obtained as in Eq. (12) and may be expressed as a polynomial in λ as written in Eq. (13). Equation (13) is rewritten as in Eq. (14).

$$-i\ m_{eq}\gamma_4\lambda^3 + [-(m_{eq} + \beta\gamma_3) + i\ m_{eq}\gamma_4\omega]\lambda^2 + [(2\beta\ \gamma_3\omega + m_{eq}\gamma_4\dot{\omega})$$
$$+i\ \beta\ \gamma_2]\lambda + [(\beta\ \gamma_1 - \beta\ \gamma_3\omega^2 - m_{eq}\gamma_4\omega\dot{\omega}) - i\ (m_{eq}\dot{\omega} + m_{eq}\gamma_4\ddot{\omega} + \beta\ \gamma_2\omega$$
$$+\beta\ \gamma_3\dot{\omega})] = 0 \tag{13}$$

$$(a_0 + i\ b_0)\lambda^3 + (a_1 + i\ b_1)\lambda^2 + (a_2 + i\ b_2)\lambda + (a_3 + i\ b_3) = 0 \tag{14}$$

Stability is found out by applying on Eq. (14), the Routh's criterion, which prescribes simultaneous satisfaction of three conditions as the polynomial is a cubic with complex coefficients. The general form of conditions is given in Eq. (15). Using these conditions, the stability limit of the spin speed and the stability limit of uniform angular acceleration at a stable spin speed are determined.

$$(-1)^n \begin{vmatrix} a_0 & a_1 & a_2 & . & . & . & a_n & 0 \\ b_0 & b_1 & b_2 & . & . & . & b_n & 0 \\ 0 & a_0 & a_1 & a_2 & . & . & a_n & 0 \\ 0 & b_0 & b_1 & b_2 & . & . & b_n & 0 \\ . & . & . & . & . & . & . & . \\ . & . & . & . & . & . & . & \\ 0 & 0 & 0 & a_0 & a_1 & a_2 & . & a_n \\ 0 & 0 & 0 & b_0 & b_1 & b_2 & . & b_n \end{vmatrix} > 0 (n = 1, 2, 3) \tag{15}$$

3 Results and Discussion

For presenting the results, a shaft of length 0.25 m and diameter 0.025 m, made of Poly-Vinyl-Chloride (PVC) of density 1,390 kg/m^3 as shown schematically in Fig. 3, is considered where a disc of mass 0.5 kg is at the mid-span. The ends

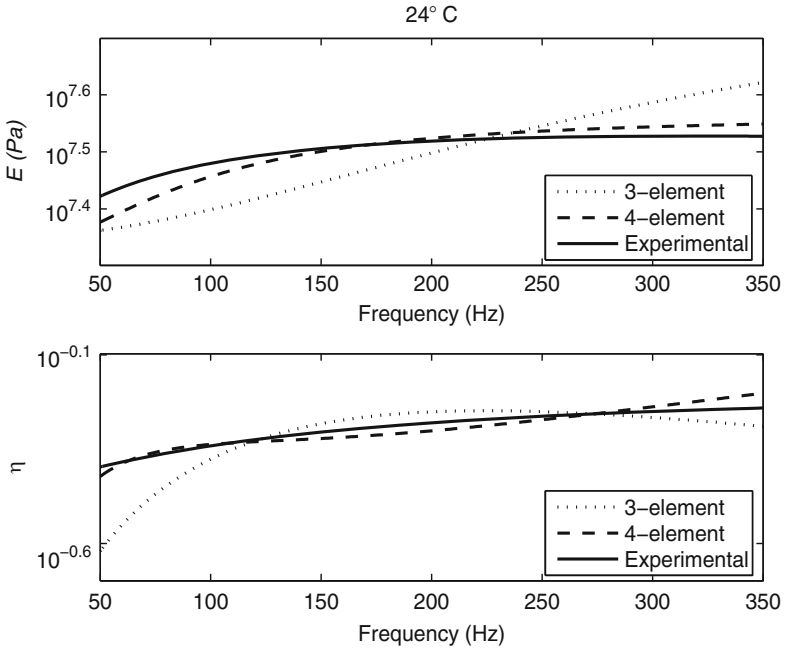

Fig. 4 E and η predicted by three and four-element models

are assumed to be supported on rolling element bearings, which are considered rigid with respect to the PVC shaft and generate simply supported boundary conditions at the ends. Frequency dependent values of storage modulus and loss factor of PVC are reported by Asnani [2] as well as by Kapur et al. [3] at different temperatures. From these, and also following Dutt and Toi [16], Roy [13] extracted both three- and four-element models by using genetic algorithm. Figure 4 shows the quality of fit between the predicted and experimentally obtained storage modulus and loss factor; the table containing the model parameters are shown at a temperature of 24°C only. It is obvious that the four-element model represents the material behaviour more accurately. For the three-element model $k_1 = 2.231\text{e}7\,\text{N/m}^2$, $k_2 = 4.3239\text{e}7\,\text{N/m}^2$, and $d = 17875\,\text{N-sec./m}^2$, whereas for the four-element model $k_1 = 2.0579\text{e}7\,\text{N/m}^2$, $k_2 = 1.6015\text{e}7\,\text{N/m}^2$, $d_1 = 8210.9\,\text{N-sec./m}^2$, $d_2 = 25614\,\text{N-sec./m}^2$.

Using these values, stability limit of the spin speed, predicted by the three-element model is 515 rpm and that by the four-element model is 494 rpm. The stability limit of uniform acceleration level is calculated and plotted in Fig. 5. The four-element model predicts a higher value of stability limit of angular acceleration than that predicted by the three-element material model. Difference of predicted values of stability limits of spin-speed and angular acceleration between the models results due to the presence of an extra damping element in four-element model, generating extra stationary as well as rotating damping forces.

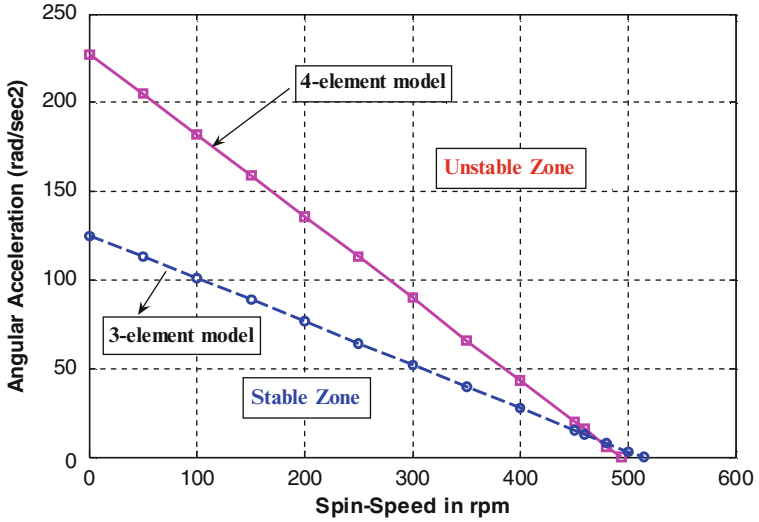

Fig. 5 Limit of angular acceleration predicted by three and four-element models

4 Conclusions

This work proposes an operator based generalized formulation of equations of motion of a simple viscoelastic rotor-shaft-system, by considering multi-element (e.g., three-element, four-element) standard viscoelastic solid model to represent frequency dependent behaviour of rotor-shaft material. Thus the time domain model enables the analysis of transient as well as steady-state behaviours. It is noted that higher orders of the model introduce the influence of higher time derivatives of spin-speed in deciding the dynamics of rotor-shaft system. Stability limit of steady angular acceleration predicted for a PVC rotor-shaft-system by using a four-element material model shows lower values compared to that predicted by three-element model. Effect of temperature should be taken in the analysis in general. Experimental verification is necessary for confirmation of these results.

Acknowledgment The author gratefully acknowledges the kind help extended by Mr. Rishi Relan, Senior Research Fellow, for preparing this paper.

References

1. Bland, D.R.: Linear Viscoelasticity. Pergamon Press, Oxford (1960)
2. Asnani, N.T.: Vibration Analysis of Multi-layered Beams with Constrained Viscoelastic Layers. Ph.D.Thesis, Indian Institute of Technology, Delhi (1971)
3. Kapur, A.D., Nakra, B.C., Chawla, D.R.: Shock response of viscoelastically damped beams. J. Sound Vib. **55**(3), 351–362 (1977)

4. Nakra, B.C.: Vibration control in machines and structures using viscoelastic damping. J. Sound Vib. **211**(3), 449–465 (1998)
5. Dimentberg, M.: Flexural Vibration of Rotating Shafts. Butterworth, London, England (1961)
6. Tondl, A.: Some Problems of Rotor Dynamics. Publishing House of Czechoslovak Academy of Sciences, Prague (1965)
7. Zorzi, E.S., Nelson, H.D.: Finite element simulation of rotor-bearing systems with internal damping. J. Eng. Power, Trans. ASME **99**, 71–76 (1977)
8. Ozguven, H.N., Ozkan, Z.L.: Whirl speeds and unbalance response of multibearing rotors using finite elements. J. Vib. Acoust. Stress Reliab. Des., Trans. ASME **106**, 72–79 (1984)
9. Ku, D.M.: Finite element analysis of whirl speeds for rotor-bearing systems with internal damping. Mech. Syst. Signal Process. **12**(5), 599–610 (1998)
10. Genta, G.: On a persistent misunderstanding of the role of hysteretic damping in rotordynamics. J. Vib. Acoust., Trans. ASME **126**, 459–461 (2004)
11. Grybos, R.: The dynamics of a viscoelastic rotor in flexible bearing. Arch. Appl. Mech., Springer Verlag **61**, 479–487 (1991)
12. Roy, H., Dutt, J.K., Datta, P.K.: Dynamics of a viscoelastic rotor shaft using augmenting thermodynamic fields—a finite element approach. Int. J. Mech. Sci. **50**, 845–853 (2008)
13. Roy, H.: Study on Dynamics of Viscoelastic Rotors: A Finite Element Approach. Ph.D. Thesis, Department of Aerospace Engineering, IIT Kharagpur (2008)
14. Ghosh, A., Mallik, A.K.: Theory of Mechanisms and Machines, 3rd edn. East West Press (1998)
15. Dutt, J.K., Nakra, B.C.: Stability of rotor systems with viscoelastic supports. J. Sound Vib. **153**(1), 89–96 (1992)
16. Dutt, J.K., Toi, T.: Rotor vibration reduction with polymeric sectors. J. Sound Vib. **262**, 769–793 (2003)

Rotor Dynamic Analysis Using ANSYS

M. Santhosh Kumar

Abstract The computer based codes for rotor dynamics evolved from tabular method, transfer matrix method and to finite element method. Recent trends in rotor dynamics analysis indicate a shift from beam to solid and shell models, which enable the classical finite element approach to be used in the design process. The application of the finite element method is a useful and important tool when the classic theory is difficult to use or apply.
The ANSYS finite element programs are used extensively in many disciplines of engineering to solve variety of problems. Over the years, ANSYS mechanical program's dynamics capabilities have evolved according to the emerging analysis needs, maturity of analysis methods and increasing computing power. The program's rotor dynamic analysis technology has developed at a rapid pace to meet the requirements of Industry. This paper is devoted to discuss the various features available in ANSYS mechanical program to study the dynamic characteristics of rotors and their supporting systems.

Keywords FEM · ANSYS · Critical speed · Campbell diagram · Stability

1 Introduction

Until recently, the industry specific rotor dynamic codes in the common practice are based on one dimensional model, historically referred to as a "Jeffcott" or "Laval" model, consisting of beam-mass–spring elements for lateral and torsional vibration based on transfer matrix method, tabular methods and finite element method. Gradually, the one dimensional rotor models came closer to the practical needs of early rotordynamicsts; but, not close enough. The distinction between disk and shaft and coupled behaviors are blurred in the typical applications like aircraft gas turbine. A more general modeling technique was needed.

M.S. Kumar
Technical Support Division ANSYS India, Bangalore, India
e-mail: Santhoshkumar.M@ansys.com

K. Gupta (ed.), *IUTAM Symposium on Emerging Trends in Rotor Dynamics*,
IUTAM Bookseries 25, DOI 10.1007/978-94-007-0020-8_14,

ANSYS mechanical program allows the mass, spring, beam, shell and the solid elements to model complex system for analysis of stress, free and forced vibration. The tendency of a rotor systems angular momentum to couple with rotations about the rotor axis is called the "gyroscopic effect" and causes the natural frequency to vary with rotor speed. The rotation effect makes formulation and solution of the system equation different from classical vibration problems. Though ANSYS code contains the basic FEA tools to carry out various investigations of rotor dynamics from the earlier days, there were no routines grouped specifically for rotor dynamic evaluations. From ANSYS Version 10, special routines are being developed for modeling, solving and interpretation of result of rotor systems to address the specific requirements of rotor dynamic industry. The various modeling solution and post processing features relevant to rotor dynamics that are available in ANSYS [1] are briefly summarized in this paper.

2 Theoretical Background

Common procedures for analyzing rotating structures in stationary reference frame are limited to structures which are axisymmetric about the axis of rotation. The stationary reference frame leads to the gyroscopic matrix added to the damping matrix. Rotating structures which are not axisymmetric about the axis of rotation or where the off-axis flexibility is important, or where the inertia or stiffness is not axisymmetric, are most easily formulated in a rotating reference frame. The rotating reference frame leads to the coriolis matrix added to the damping matrix as well as the modification of the apparent stiffness of the structure also known as spin-softening effect. The results in rotating reference frame are different from the result in stationary reference frame. For example, in the rotating reference frame the bending frequencies are offset by rotational velocity. The rotating and stationary reference frame approaches have their benefits and limitations. Table 1 below can be used to choose the best option for different applications [1].

2.1 The Fundamental Equations

The dynamic behavior of a rotor system is described by the discrete differential equation in the stationary frame of reference.

$$[M]\{\ddot{u}\} + \left([C] + \left[C_{gyr}\right]\right)\{\dot{u}\} + [K]\{u\} = \{F\} \tag{1}$$

where $[M]$ is mass matrix, $[K]$ is stiffness matrix, $[C]$ is damping matrix, and $[C_{gyr}]$ is gyroscopic matrix. ANSYS derives the gyroscopic matrix $[C_{gyr}]$, starting from the kinetic energy expression [1, 2]:

Table 1 Reference frame considerations

Stationary reference frame	Rotating reference frame
Structure must be axisymmetric about the spin axis. The stationary structure and supports (such as bearings) need not be axisymmetric.	Structure need not be axisymmetric about the spin axis. Supports need to be symmetric.
Rotating structure can be part of a stationary structure in an analysis model (such as a rotor-stator assembly).	Rotating structure must be the only part of an analysis model (such as a gas turbine engine rotor alone).
Supports more than one rotating structure spinning at different rotational speeds about different axes of rotation (such as a multi-spool rotor).	Supports only a single rotating structure.
Not applicable to static analysis	Applicable to static analysis
Supported elements: BEAM4, PIPE16, MASS21, SHELL63, BEAM188, SHELL181, BEAM189, SOLID45, SOLID95, SOLID185, SOLID186, SOLID187, SOLID272, SOLID273, SHELL281, PIPE288, and PIPE289	Supported elements: MASS21, SHELL181, PLANE182,PLANE183,SOLID185, SOLID186, SOLID187, BEAM188, BEAM189, SOLSH190, SHELL281, PIPE288, PIPE289, PLANE223, SOLID226, and SOLID227.

$$E_{mass}^{Ki} = \frac{1}{2}\begin{Bmatrix} \dot{u}_y \\ \dot{u}_z \end{Bmatrix}^T \begin{bmatrix} m & 0 \\ 0 & m \end{bmatrix} \begin{Bmatrix} \dot{u}_y \\ \dot{u}_z \end{Bmatrix} + \frac{1}{2}\begin{Bmatrix} \dot{\theta}_y \\ \dot{\theta}^z \end{Bmatrix}^T \begin{bmatrix} I_d & 0 \\ 0 & I_d \end{bmatrix} \begin{Bmatrix} \dot{\theta}_y \\ \dot{\theta}^z \end{Bmatrix} - w_x I_p \dot{\theta}_z \dot{\theta}_y \tag{2}$$

where m is mass, I_p is polar moment of inertia, I_d is diametral moment of inertia, $\grave{u}_x$ is spinning velocity about X axis, θy and θz are angular displacements about Y and Z axes respectively.

The first two terms contribute to the mass matrix of the element and the last term gives the gyroscopic matrix. For new generation elements such as SOLID185 and SHELL181 elements, the expression of the kinetic energy is:

$$E^{Gki} = -\omega_x \int_{vi} X \left(\dot{\theta}_y + \dot{\theta}_z\right) dm \tag{3}$$

The governing equation of motion in rotating frame of reference is:

$$[M]\ \{\ddot{u}_r\} + ([C] + [C_{cor}])\ \{\dot{u}_r\} + ([K] - [K_c])\ \{u_r\} = \{F\} \tag{4}$$

Coriolis force in rotating reference frame generates the damping matrix of the element as a skew symmetric matrix [1, 3],

$$[C_{cor}] = 2\int_v [N]^T\ [\omega]\ [N] \times \rho.dv \tag{5}$$

where $[N]$ is shape function matrix, $[\omega]$ is skew symmetric rotational matrix, and $[K_c]$ is global stiffness due to centrifugal force (Spin softening).

If internal damping is present in the rotating structure (proportional damping for example) or if there is localized viscous damping (as in a damper), damping forces in the rotating reference frame may be expressed as:

$$\left\{F_d'\right\} = [C]\ \{\dot{r}\} \tag{6}$$

The damping force in stationary reference frame is expressed as

$$\{F_d\} = [R]^T\ [C]\ [R]\ \{\dot{r}\} + [R]^T\ [C]\ [R]\ [\omega]^T\ \{r\} \tag{7}$$

where $\left\{\mathrm{F}_\mathrm{d}'\right\}$ and $\{\mathrm{F_d}\}$ are damping forces in the rotating and stationary reference frame; $\{r'\}$ and $\{r\}$ are the displacement vectors in the rotating and stationary reference frames; $[C]$ is the damping matrix; $[R]$ is the transformation matrix. The second term in above equation represents the effect of rotating damping. It will modify the apparent stiffness of the structure. The resulting matrix will be non-symmetric.

2.2 Supported Element Types

The computation of the gyroscopic matrix for a simple beam and mass elements was done in ANSYS many years ago. In recent versions of ANSYS, a routine has been developed to compute gyroscopic/coriolis matrix and add to the damping matrix for finite elements of different dimensionality as listed in Table 1. Also, the effects of rotary inertia, shear deformation, axial load, and internal damping have been included.

2.3 Modeling Bearings and Seals

Bearings are designed to support and to transfer pure radial loads, pure thrust loads, or a combination of the two between two parts – one rotating relative to the other. Seals are used to protect bearings from dirt and foreign matters and retain lubricants.

Bearings are not infinitely stiff, the friction and lubricant in them introduce damping. So, one can visualize rotor system rotating on a set of springs, and often springs that have stiffness that varies with speed and direction. The same is applicable for damping. Irrespective of the type of bearing, for rotor dynamic analysis purpose, all bearings need to be characterized (dynamically) by their stiffness and damping properties. Bearing coefficients can be determined from experimental data or from analytical formulae and numerical calculations or special purpose bearing performance programs. Support systems which are not well-described by these coefficients, such as magnetic bearings, are approximated.

When considering lateral vibrations in (XY) plane only, the axial coordinate can be disregarded and the position of the shaft centre at the bearing location

should be described by lateral displacements and possible rotations only. The linear constitutive equation for the bearing can be given now by a 4×4 stiffness matrix and a 4×4 damping matrix.

$$\begin{bmatrix} C_{fxx} & C_{fxy} \\ C_{fyx} & C_{fyy} \end{bmatrix} \begin{Bmatrix} \dot{u}_x \\ \dot{u}_y \end{Bmatrix} + \begin{bmatrix} K_{fxx} & K_{fxy} \\ K_{fyx} & K_{fyy} \end{bmatrix} \begin{Bmatrix} u_x \\ u_y \end{Bmatrix} = \begin{Bmatrix} F_x \\ F_y \end{Bmatrix} \tag{8}$$

Here C_f is damping coefficient and K_f stiffness coefficient.

Traditionally bearings are represented in ANSYS either by multiple COMBIN 14 elements or by a single MATRIX 27 element. But with the recent inclusion of COMBIN 214 element, radial stiffness and damping in vertical, horizontal planes and cross coupled terms can be specified by a single element. These bearing stiffness and damping coefficients can also be a function of rotor speed $C_f = C_f(\omega),\ K_f = K_f(\omega)$.

3 Free Vibration (Modal) Analysis

When components are spinning, the gyroscopic/coriolis terms introduce additional forces to the system, causing natural frequencies to split and shift up and down. These natural frequencies must be determined to predict the critical speeds where high response amplitude is expected. Running several modal analyses shows how speed affects frequency from zero rpm up to the maximum rotational velocity of the system.

Because of the inclusion of gyroscopic/coriolis matrix, the regular eigen solvers like Subspace, Block Lanczos cannot be employed. DAMP and QRDAMP complex eigen solvers available in ANSYS can be used to extract the complex eigenvalues of the rotor systems. If the damping is added to the equation of motion of free vibration

$$[M]\ \{\ddot{u}\} + [C]\ \{\dot{u}\} + [K]\ \{u\} = 0 \tag{9}$$

the behavior is expressed by complex eigenvalues and eigenvectors

$$\{u_i\} = \{\sigma_i \pm \gamma_i\, j\}\, e^{-(\sigma_i \pm \omega_i\, j)t} \tag{10}$$

In the complex conjugate pair of eigen values $(\sigma_i \pm \omega_i\, j)$, the real part σ_i represents the stability of the system and the imaginary part ω_i represents the steady-state circular frequency of the system.

The $e^{\sigma_i t}$ represents the time decay, if σ_i is negative, this indicates that the displacement amplitude will decay exponentially which denotes a stable system. On other hand if σ_i is positive, this indicates unbounded exponential growth in amplitude and leads to an unstable system.

The complex mode enables one to make clear definition of the forward whirl and the backward whirl. The whirl direction of the modes is calculated from the complex

eigenvectors. The real and imaginary parts of the displacement in two perpendicular directions normal to the axis of the rotor are collected into two vectors for each node i,

$$\{u_{1,i}\} = \begin{Bmatrix} \phi_{1,i}^{\mathrm{Re}} \\ \phi_{2,i}^{\mathrm{Re}} \\ 0 \end{Bmatrix}; \ \{u_{2,i}\} = \begin{Bmatrix} \phi_{1,i}^{\mathrm{Im}} \\ \phi_{2,i}^{\mathrm{Im}} \\ 0 \end{Bmatrix}; \tag{11}$$

The whirl direction is found from the direction of the cross product.

$$\{W\} = \{u_1\} \times \{u_2\} \tag{12}$$

The direction of vector $\{W\}$ is compared with the direction of applied rotational velocity, if the resulting vector sign is positive then ANSYS marks the mode as forward whirl and if negative the whirl is backward.

In a modal analysis with multiple load steps corresponding to different rotor speeds, ANSYS sorts the results by automatically applying a mode tracking algorithm to generate the Campbell diagram. Critical speeds are determined as intersection points between frequency curves and excitation line.

Numerical example 1: A Nelson-Vaugh rotor [2] shown in Fig. 1 was modelled using Beam 188 elements as well general axisymmetric SOLID 272 element with three Fourier terms. The comparison between reference results and ANSYS results are shown in Table 2 and Fig. 1 shows a Campbell diagram of the same model generated from ANSYS.

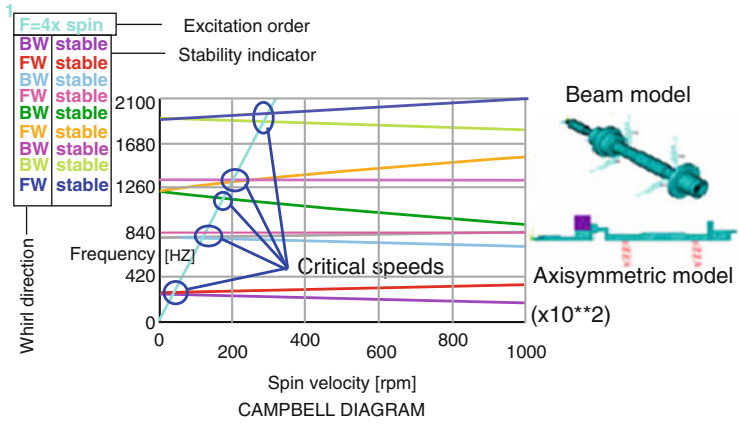

Fig. 1 Nelson-Vaugh rotor model

Table 2 Nelson-Vaugh rotor natural frequency

	Reference results	ANSYS beam model	ANSYS general axisymmetric model	Ratio beam model	Ratio axisymmetric model
Whirl speeds for excitation order (slope) = 4					
Mode 1	4, 015	4, 013.386	3, 911.15	1	0.974
Mode 2	4, 120.25	4, 116.172	4, 017.653	0.999	0.975
Mode 3	11, 989.25	12, 015.44	11, 774.622	1.002	0.982
Mode 4	12, 200	12, 227	11, 985.938	1.002	0.982
Mode 5	18, 184.25	18, 205.28	17, 445.646	1.001	0.959
Mode 6	20, 162.25	20, 127.06	19, 651.341	0.998	0.975

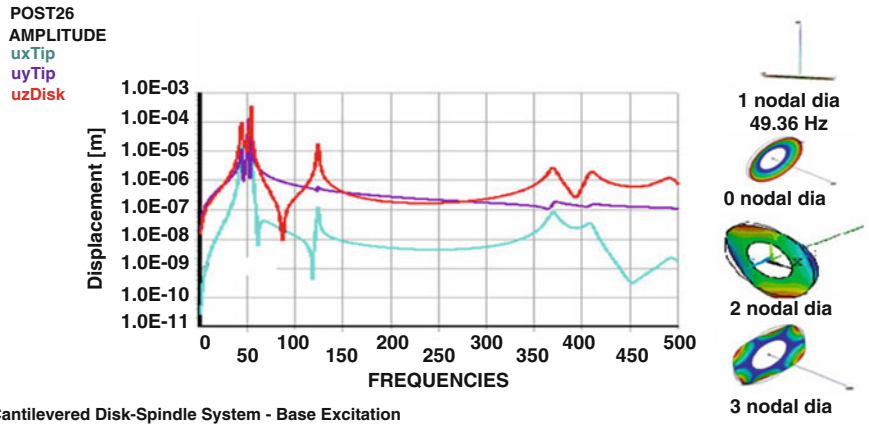

Fig. 2 Disk-spindle frequency response and mode shapes

4 Harmonic Analysis

A harmonic analysis is used to determine the frequency response of a structure to harmonically time-varying loads, such as unbalance forces, base excitations, those typically seen in rotating machinery.

Numerical example 2: A cantilevered disk-spindle system is shown in Fig. 2. The disk is fixed to the spindle with a rigid clamp and is rotating at 0.75×50 Hz. The base excitation is a harmonic acceleration along the negative Y direction, with a frequency of up to 200 Hz. The spindle is modeled using BEAM 188 elements and the disk is modeled using SHELL 181 elements. The harmonic solution was carried out using Modal Superposition techniques. The mode shape of the first nodal diameter mode shows the coupling behavior between disk and shaft. The lateral displacement amplitudes of spindle tip and axial displacement amplitude of disk are shown in Fig. 2 below.

Some forces may rotate synchronously (for example, unbalance) or asynchronously with the structure. Rather than specifying the frequency of the excitation

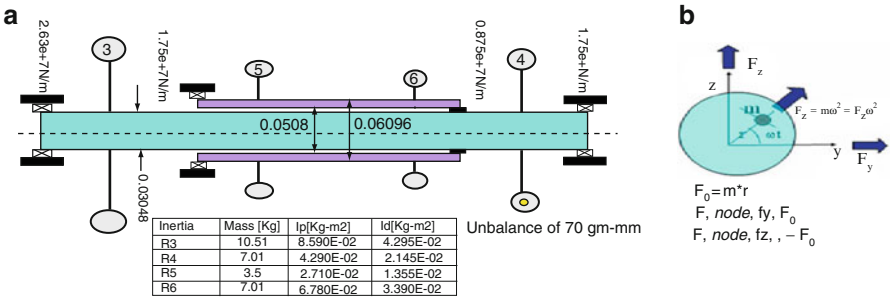

Inertia	Mass [Kg]	Ip[Kg-m2]	Id[Kg-m2]
R3	10.51	8.590E-02	4.295E-02
R4	7.01	4.290E-02	2.145E-02
R5	3.5	2.710E-02	1.355E-02
R6	7.01	6.780E-02	3.390E-02

Fig. 3 **(a)** Dual spool rotor system. **(b)** Unbalance force vector

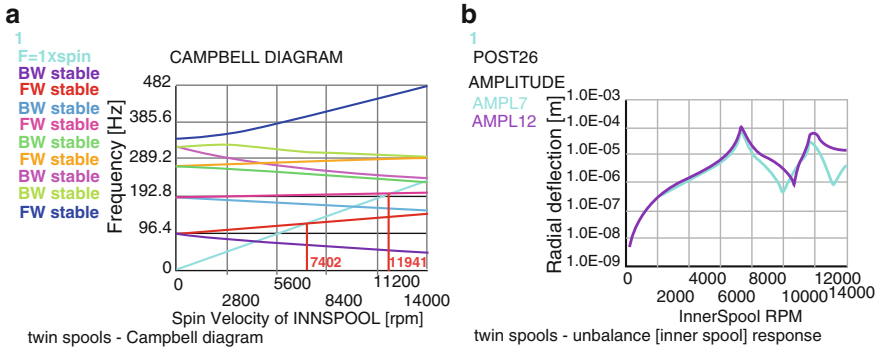

Fig. 4 **(a)** Campbell diagram of inner spool. **(b)** Frequency response plot

force, a ratio between the frequency of excitation and the frequency of the rotational velocity of the structure is specified via the SYNCHRO command.

Unbalance forces are represented on a complex plane. Unbalance force is split into real and imaginary parts. The positive real value and negative imaginary value of unbalance forces are applied along real and imaginary axes of the unbalance plane respectively, as shown in Fig. 3b.

Numerical example 3: An unbalance study of two-spool rotor shown in Fig. 3a supported on symmetric bearings was carried out. The inner spool rotates at up to 14,000 rpm and the outer spool rotates 1.5 times faster. The Campbell diagram and frequency response function are shown in Fig. 4.

5 Transient Analysis

Transient dynamic analysis technique is used to determine the dynamic response of a rotating structure under the action of any general time-dependent loads.

The direct (full) transient analysis uses the full system matrices to calculate the transient response and this facilitates the inclusion of nonlinearities such as

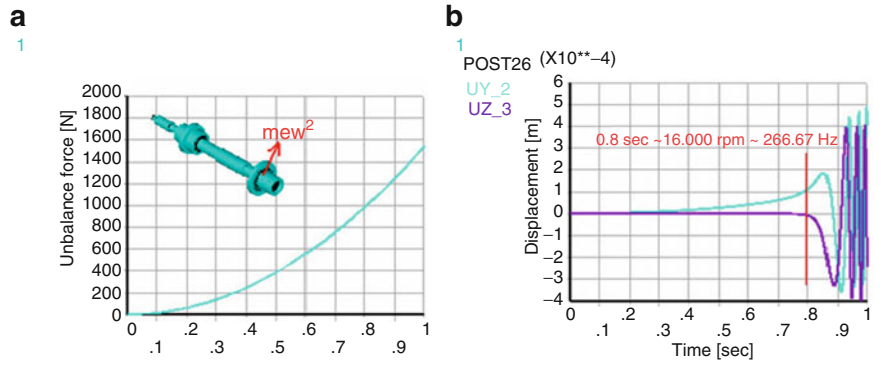

Fig. 5 **(a)** Unbalance force vs time. **(b)** Speed ramp-up response

nonlinear force deflection curve for spring elements, gap conditions, and contact elements. Alternatively the faster modal superposition transient analysis can be used to calculate response of the time varying excitations of a rotor spinning at a constant speed.

Numerical example 4: Nelson-Vaugh beam element rotor [2] shown in Fig. 1 was simulated in time-transient domain for an unbalance mass of 10 gm at 70 mm radius, when the rotor speed is ramped from 0 to 20,000 rpm in 1 sec. The unbalance response of the rotor during speed ramp is shown in Fig. 5b. One can see the magnification of lateral response near the first critical speed.

The rotor speed at different time points is used to compute imbalance forces for transient analysis. The time varying unbalance forces are computed as shown in Fig. 5a using following relations.

$$F_x(t) = mr \times \omega^2 \times (-\sin \omega t); F_y(t) = mr \times \omega^2 \times (\cos \omega t) \tag{13}$$

This requires ω to be a known function of time. The proper way to apply an imbalance force when the speed is a variable is to define both the X and Y components of force as a tabular parameter perpendicular to the rotation axis Z.

The orbital response of the rotor stations are plotted by loading the response amplitude in two directions of bending and plotting it against each other using/POST26 after the completion of solution. The ANSYS result tracking tool (NLHIST commands) enables monitoring the directional amplitudes and orbit plots online as the solution progresses as shown in Fig. 6.

6 Conclusion

Nowadays, rotordynamicsts are combining the FEM and solid modeling techniques to generate simulations that accommodate the coupled behavior of flexible disks, flexible shafts and flexible support structures into a single multidimensional model.

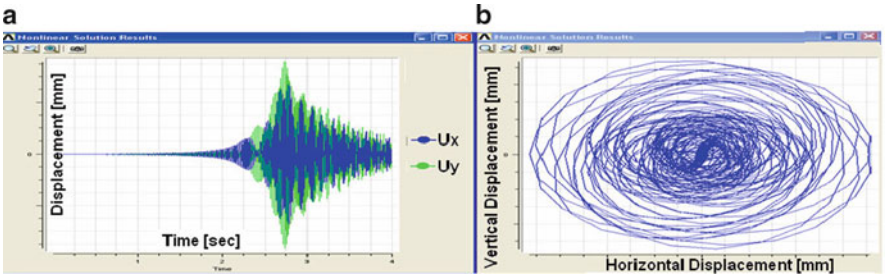

Fig. 6 **(a)** Instantaneous displacement of rotor. **(b)** Orbital motion of rotor

The ANSYS mechanical program offers comprehensive, easy-to-use rotor dynamics analysis capabilities and enables solution of large scale, complex models. The preprocessing, solution/analysis and post processing infrastructure is the common thread between the components of elements, materials, and equation solvers. This facilitates a common FEA model for both stress and rotor dynamic analysis. An integrated infrastructure, APDL customization, and the new paradigm of Workbench Simulation and Design Explorer, work together to provide tremendous simulation capabilities for rotor dynamics.

Acknowledgements Reflecting upon the effort summarized in this document, it is clear that it is the result of contributions from many people from ANSYS Inc. Aline Bely (ANSYS France) and coworkers are acknowledged with my sincere gratitude.

References

1. ANSYS Release: 12.0 Documentation & Rotor dynamics guide, ANSYS Inc. (2009)
2. Nelson, H.D., McVaugh, J.M.: The dynamics of rotor-bearing system using finite elements. J. Eng. Ind. **98**(2), 593–600 (1976)
3. Nelson, F.C.: A brief history of early rotor dynamics. Sound and Vibration **37**, 8–11 (2003)

Vibration of Rotating Bladed Discs: Mistuning, Coriolis, and Robust Design

D.J. Ewins and Y.J. Chan

Abstract Studies of the consequences of mistuning on bladed disc vibration levels have been undertaken for over 40 years and yet mistuning is still an unresolved problem for turbomachinery designers. Why is this? How have we failed to solve this problem? And what can we do now? This paper proposes a different approach which seeks to manage, rather than solve, the blade mistuning problem.

Keywords Bladed discs · Mistuning · Resonance

1 Definition of the Problem

First, we must define the Mistuned Blades problem. The essential cause of the problem is that when a bladed disc is constructed, the actual dimensions and material properties of the set of nominally-identical blades will exhibit small variations from one blade to the next. Normally, structures are expected to be robust to such inevitable manufacturing variations but the bladed disc is an exception – indeed, an extreme exception – and the consequences of these variations, referred to as "blade mistuning", can be a disproportionally large variations in resonant response levels from one blade to the next. A scatter of individual blade properties, such as mass, of the order of 2–3% can routinely lead to scatter in the resonance response peak levels of 200–300%, with the highest of these being much greater than the level which would apply to all blades if they were perfectly tuned (all identical to each other) - see Fig. 1.

D.J. Ewins (✉)
University of Bristol Faculty of Engineering, University Walk, Bristol BS8 1TR, UK
e-mail: d.ewins@imperial.ac.uk

Y.J. Chan
Imperial College London Mechanical Engineering Department
London SW7 2AZ, UK

K. Gupta (ed.), *IUTAM Symposium on Emerging Trends in Rotor Dynamics*,
IUTAM Bookseries 25, DOI 10.1007/978-94-007-0020-8_15,

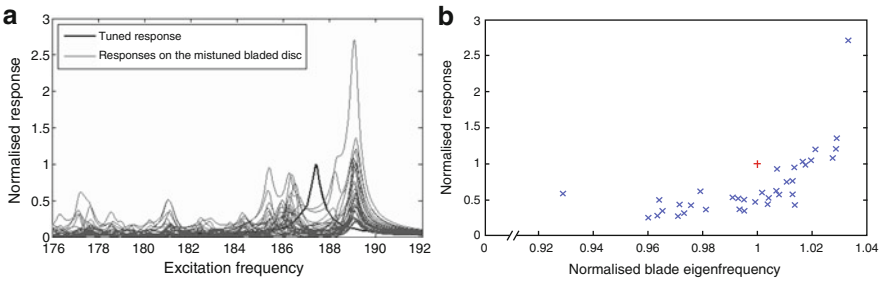

Fig. 1 **(a)** Forced response plots of individual blades on mistuned assembly. **(b)** Resonance peak amplitudes from mistuned blade set as function of individual blade mistune state

This means that normal manufacturing tolerances that are perfectly normal, and which are harmless in other contexts, can lead to wide variations in fatigue life under prolonged vibration. In contrast, when considering the other major vibration problem in turbomachine blades – that of the instabilities referred to as "flutter" – it is known that mistuning generally has a beneficial effect by raising the speed at which flutter of a bladed assembly will be initiated, thereby delaying the onset of this often destructive type of vibration. However, modern design methods are generally effective at avoiding flutter, while forced response is an inescapable feature of a running engine and cannot be avoided completely, so that designs must anticipate the vibration response levels that will be experienced in normal operation and design fatigue lives accordingly. Hence, the main concern with blade mistuning is the forced vibration response issue.

2 The Practical Problem

It is known that scatter (or "uncertainty") in blade properties leads directly to a scatter (or "variability") in the resonance forced response levels and the essential practical problem is to establish the quantitative scale of the effect and to design accordingly. The effect can be displayed graphically in plots such as that in Fig. 2a and we can superimpose this type of result for different tolerance ranges, such as in Fig. 2b. Specifically, the question is for a given scatter (pdf) of the blade properties, what will be the consequent scatter (again, as a pdf) of the resonance peak response levels of that population of blades, and this information is shown in Fig. 2c for the data shown previously in Fig. 2b. The input pdf will be bounded because of the selection/culling procedures that are applied at manufacture and/or assembly. Hence, it is supposed that the output pdf will also be bounded: thus, that there will exist a maximum value that the amplification factor can attain, and this maximum is marked on the pdf plots. We need to know that value, and the probability of encountering it and values close to it that represent the likely worst case in service to be designed against.

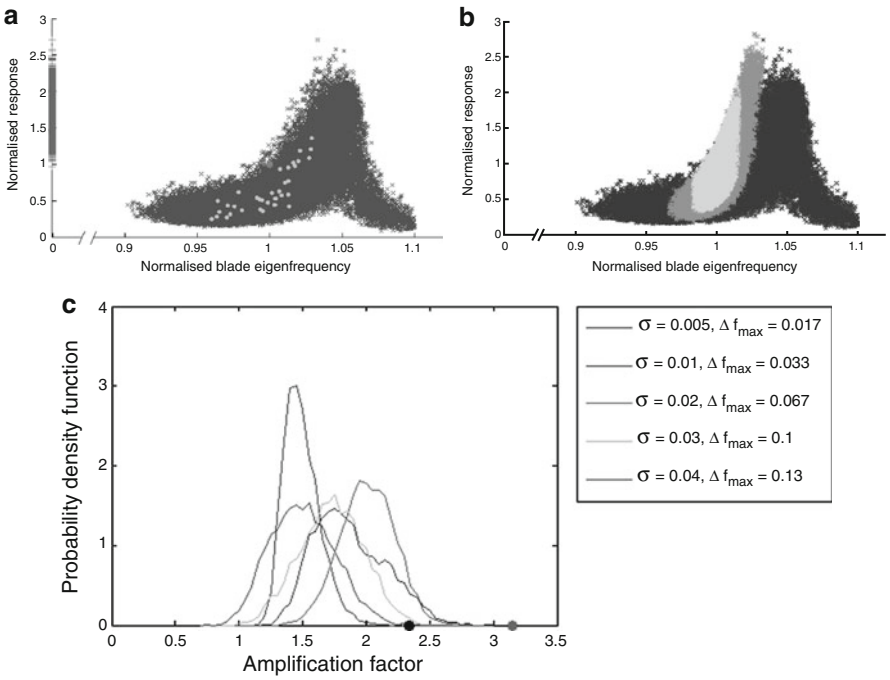

Fig. 2 **(a)** Normalised peak responses for 2,000 mistuned bladed discs. Standard deviation of normalized blade eigenfrequencies = 0.03. **(b)** Normalised peak responses for mistuned bladed discs of the same basic design. Standard deviations of blade mistune: (light grey) 0.005, (grey) 0.01, and (black) 0.03. 2,000 bladed discs are included in each cloud/pool. **(c)** Amplification factor pdfs for different blade mistune scatter. Maximum amplification factor at maximum mistune of 0.017 (black dot); all other pdfs are bounded above by the red dot

What the design engineer needs is, in essence: for a given distribution (pdf) of individual blade properties:

a. The value of the maximum response level that any blade in that population might attain, and – because that is a very rare occurrence.
b. A measure of the distribution of individual blade response levels (pdf) in order to assess the probability of the worst case being attained, and of all the higher response levels, so that a proper probabilistic design analysis can be made.

It turns out that these analyses are not simple to make, and past research has tended to seek a solution to the problem whereby the worst consequences of mistuning might somehow be avoided, or suppressed, rather than what is now proposed, to seek a strategy to manage it. In the event, no-one has succeeded in solving the problem and virtually all the 400 or so papers over the past 40 years have served only to reinforce the complexity and intractability of the problem, and the futility of seeking a magic cure – at least, so far!

3 Brief Review of Major Features from Previous Studies

Studies using the classical lumped parameter model shown in Fig. 3, and based on Dye and Henry [1], display all the essential features of mistuning: small variations in individual blade properties leading to large variations in resonance peak response amplitudes. Results with these simple models are qualitatively the same as those using more accurate physically representative models (with many more DOFs), although the latter may be used to determine specific quantitative data for specific designs. Various features found are summarized in the following paragraphs.

The basic modal structure for a bladed disc consists mostly of a set of double modes (pairs of modes with the same cyclic order/nodal diameter orthogonal to each other). When tuned, both modes of a pair have identical natural frequencies; when mistuned, the modes split into a pair with close natural frequencies (where the frequency split is of the same order as the mistune level). The characteristics of a double mode pair with increased mistune level reveal an underlying characteristic of an Amplification Factor, R, which increases from 1.0 (at the tuned state where scatter is zero) up to a maximum of about 1.28, and then falls towards 1.1 as the mistune increases even further. For more complex situations, where there are many (more than 2) modes contributing to the response, the actual extent of the mistuning effect varies from case to case but the trend is similar: as the magnitude of mistune scatter is increased from zero, the amplification factor increases steadily until reaching a peak or a plateau and the leveling off and often falling back (Fig. 4). The highest value, or peak, is generally much greater than 1.3 and has a strong dependence on blade number as well as other less tangible features such as strength of inter blade coupling.

For cases with smaller inter-blade coupling (typical for higher numbers of nodal diameters, or for systems with stiffer discs) the double mode tuned system natural frequencies tend to be closer together so that when they split because of mistuning, they quickly interact with each other, the mistuning causing a more dramatic perturbation on their frequencies and both the mode shapes and the force response plots are highly complex. In these cases, the modes quickly degenerate to become highly localised shapes and – in the limit with zero coupling (an infinitely stiff disc) – each mode shape involves just one blade at a time, with almost no amplification of response. It is in the highly complex regions between strong and zero coupling where

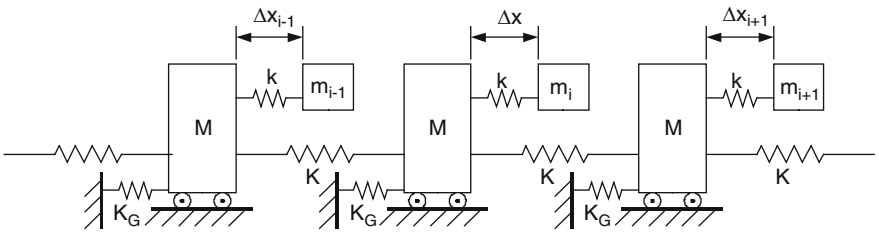

Fig. 3 Original lumped parameter bladed disc model (still) used for mistuning studies

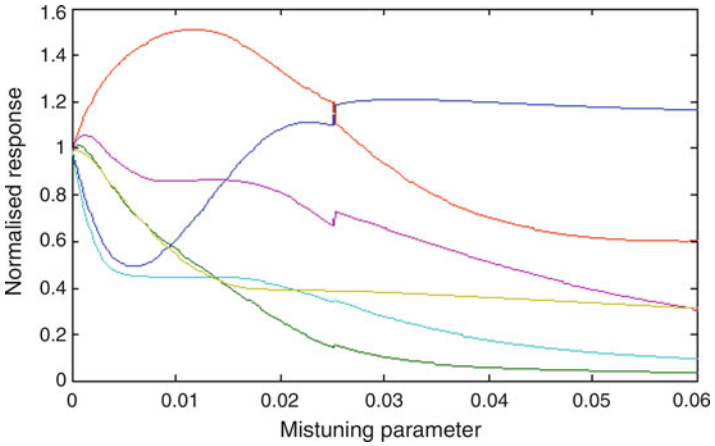

Fig. 4 Dependence of the amplification factor on mistune scatter

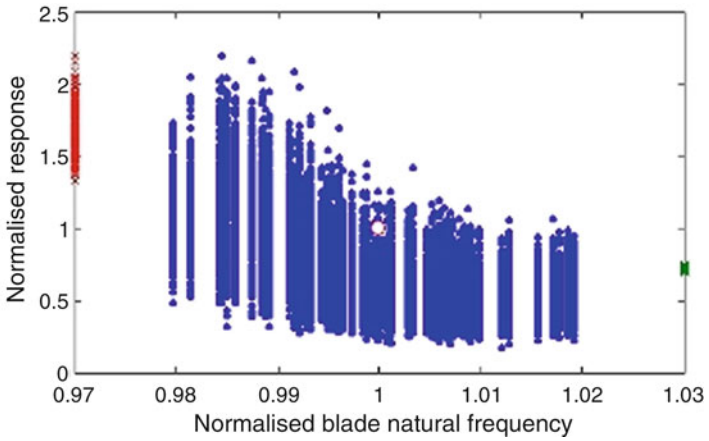

Fig. 5 Scatter plot for one set of blades re-arranged in 100 different configurations to follow

the most severe consequences of mistuning occur, leading to amplification factors which are clearly a function of blade number, and for which Whitehead's formula [2] is a useful first guide of the potential severity of mistuning. In this region where the effects are at their most acute and most complex, the only effective way to describe the magnitude of the mistuning effect is by a Monte Carlo-type of numerical exercise where literally hundreds of randomly-selected blade sets are analyzed numerically and the results superimposed on plots such as those shown in Fig. 2.

One example for a single randomly-selected set of blades which have been rearranged into different patterns (but always using the same 36 blades), is shown in Fig. 5. This result gives a strikingly similar scatter to those results obtained

from hundreds of different sets drawn from the overall population and shows that the specific arrangement of mistuned blades plays a major role in the consequences for forced response levels.

In general, it is observed that the mean level for all blades in a set drops by about 25–30% as compared with the reference (tuned system) level so that, on average, mistuning is good, overall. However, this is not true for the worst blade, and that is the only one that really matters.

Most studies find that mistuning is worse than the equivalent tuned system, in that some blades will always exhibit higher response levels than would occur in a tuned assembly subjected to the same excitation conditions. However, some published results show an overall improvement – i.e., all blades lower than the tuned system reference level [3]. If this were a general result it would be extremely useful and a solution to the blade mistune problem but it does not seem to have yet had that impact. In many cases, the comparison between tuned and mistuned conditions can be distorted if the damping is also varied from one blade to the next. This is because damping directly affects the absolute response levels of the tuned system and so comparisons between tuned and mistuned must be precise about what level of damping is used for the tuned system reference case.

4 Some Recent Developments

In this section, we review briefly some of the developments in recent years which have served to make our models and analysis of mistuned systems more accurate and more realistic. However, they have not generally provided a solution to the mistuning problem, just a more precise means of calculating how severe it is.

4.1 Coriolis Effects [4, 5]

Quite recently, it has been discovered that Coriolis effects which had previously been assumed to be second- or third-order, and therefore insignificant in practical terms, can in fact be first-order effects in the context of mistuned bladed assemblies. In simple terms, it was shown, both theoretically and by experimental validation, that in certain designs of bladed disc, Coriolis effects can result in a split in the "identical" natural frequencies which make up one double mode of a tuned system – even in the presence of zero mistune. It also turns out that the frequency splitting effect due to Coriolis, which is necessarily strongly speed-dependent, can be of the same order of magnitude as that which is brought about on the same system by realistic levels of blade mistune (see Fig. 6 for illustration). The implications of this discovery are that many previously-made calculations of mistuning effects for specific cases will be in error because of the omission of the Coriolis terms. Studies in recent research [4] show that while the inclusion of Coriolis terms in typical

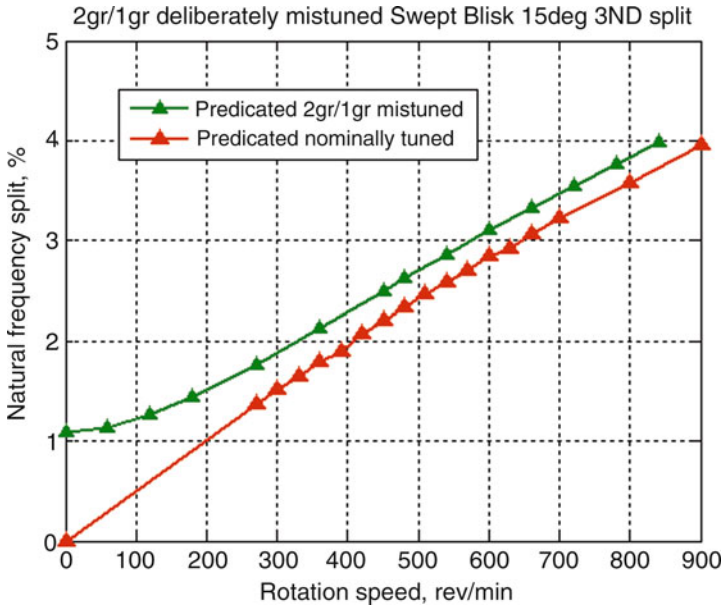

Fig. 6 Frequency split of 3ND mode with coriolis; tuned/mistuned bladed discs, lower curve is for nominally tuned case

cases does not significantly alter the bounds of the mistuning effect, it does change the specific vibration levels of individual blades and would therefore have a primary influence on attempts which might be made to compare prediction and measurement in specific cases. Such experimental data are very rare, and often inconclusive, and this effect may provide an explanation for the dearth of experimental evidence to support the many theoretical studies which have been undertaken and which are awaiting convincing validation from real measured data.

4.2 Combined Aero/Structural Effects [6–8]

Many bladed disc studies focus either on structural dynamic aspects (for mistuning due blade to blade differences, added damping devices, etc.) or on aerodynamic effects, especially for flutter, but few have included both effects simultaneously. Recently, however, there have been some mistuning studies which combine both features in the same model and while these have provided a more realistic representation of real systems, the results have been somewhat more complex to interpret. The main reason for this complication is that when considering aerodynamic mistuning – i.e., variations from blade to blade in the aerodynamics of the relevant working fluid passages – this involves a blade to blade variation in the damping as well as the inertia and/or stiffness effects. For the reason explained above, this

introduces complications in the traditional way of comparing tuned and mistuned systems, because it depends which of the various damping levels is used as the reference case in the tuned system. Nevertheless, these combined aero-structural models must become more widely used as they are closer descriptions of real systems.

4.3 Intentional Mistuning [3, 9]

Ever since mistuning appeared on the scene, and its adverse consequences appreciated, researchers have sought to find a "hair of the dog" type of antidote to it. By that we mean that ways are sought to use controlled, or intentional, mistuning in order to contain the problem within restricted bounds. The basic concept is simple: it is known from the many mistuning studies that some mistune patterns are much less aggressive in the amplification factors than are others from the same population. Indeed, as Fig. 4 shows, some arrangements of a single set of blades can have significantly lower amplification factors than slightly different patterns formed from the same set of blades. These observations lead to the conclusion that there are clearly advantageous ways to install a given set of blades, and disadvantageous ways of doing so. Perhaps, if we can master this phenomenon, we might be able to avoid the worst mistuning conditions without going to the expense of manufacturing blades to much tighter tolerances. However, there are three obstacles to this approach. The first is that the inverse problem has not been solved and the only known way to determine the optimum arrangement of a given set of blades is to compute all the possible combinations and find it empirically. Alternatively, we can follow an optimization procedure for 30 or 40 iterations and gain a significant advantage at a minimal cost. Second, it is necessary to ensure that any proposed distribution pattern is robust and that the advantage gained by its use is not immediately lost as individual blade properties change slightly with time and wear. The third drawback is again cost – the cost involved in measuring and identifying every single blade, and ensuring that it or its replacement at maintenance is of the correct tune, is probably prohibitive. Thus, we are left looking at intentional mistuning of the type where there might be, for example, two "standard" blade sets – one set with a high mean, the other with a low mean – and an associated build procedure which takes alternate high and low blades.

4.4 Determination of Specific Mistune Pattern from Bladed Disc Modes [10–12]

As interest in controlled mistuning grows, and with the widespread use of blisks, the prospect of attaining a specific mistune pattern on a bladed disc, and of maintaining that throughout a significant operating life, become both realistic and potentially attractive. For example, if it can be established that a given blisk has a mistune pattern

that means it sits well below the worst case for that design, then it is known that this unit is very unlikely to fall victim to a mistuning problem in service. Because the blades are integral with the disc, the usual uncertainties and variabilities that come with repeated loosening and tightening of the blade root/disc interface are absent and the only reason for the mistune state at build becoming different is through erosion or wear of the blade surface, and that is likely to be a slow process. Thus it may be of interest to establish the exact mistune pattern at installation and, possibly, to compute the specific mistune state of that unit (see Sect. 5 below). Of relevance here are the recently-developed methods for determining the individual blade mistune values from the blades on a blisk directly from measurement of the bladed disk assembly modes, which can be obtained from a modal test either at rest, or under rotation (see previous section).

5 A New Mistuning Strategy (NMS)

At this stage, it is appropriate to outline the proposal to **manage** rather than to **solve** the mistuning problem, and the current research project underway at Imperial College London. The NMS advocates a three-step anti-mistuning procedure at the design stage and a supplementary condition monitoring stage for blisks at production and during the operating life of these components. The essential features of this strategy, which is based on the premise that mistuning cannot be avoided, or eliminated, but can be effectively controlled by appropriate design, are as follows.

5.1 Step 1

For each case where mistuning effects could be a problem, either the upper bound response level or an upper limit with acceptable risk (such as the 99.9% probability response level) is calculated. Although the difference between the two values may be small, a 4% reduction in dynamic stress can lead to a doubled fatigue life in some superalloys [13].

Because traditional Monte Carlo-based simulations cannot provide reliable estimates for either parameter, optimization and importance sampling are introduced to find the upper bound and 99.9% probability response level respectively. Better than 95% confidence intervals of 99.9% (and even 99.99%) probability response levels can be found by importance sampling with a fraction of computational resources as compared with Monte Carlo simulations (Fig. 7).

5.2 Step 2

If necessary, seek to reduce the predicted 99.9% peak stress to the design required level by application of a series of devices, namely – (i) to strengthen the basic blade

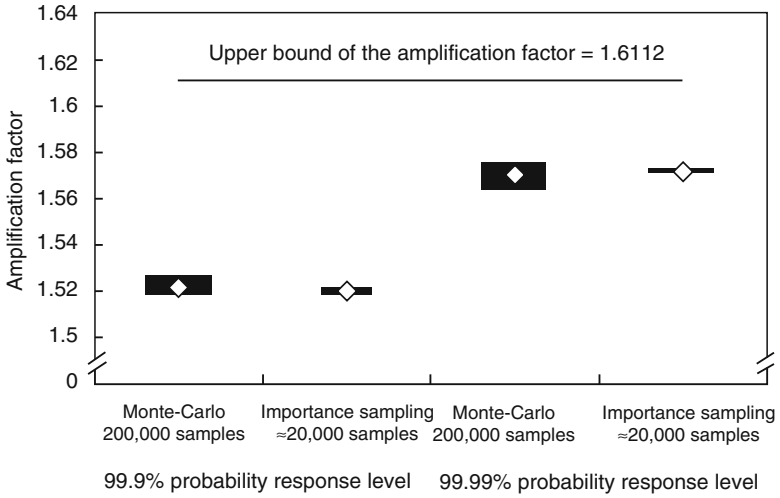

Fig. 7 Methods to assess 99.9 and 99.99% probability response levels for six-bladed disc

design so as to reduce the tuned system datum response level, (ii) modify the basic bladed disc design to change the inter-blade coupling and thus the severity of scatter magnification, and/or (iii) to add deliberate damping devices so as to lower the tuned system datum response level and, possibly, breadth of scatter of responses. Approach (i) reduces the dynamic stress in bladed discs but a handful of blades still suffer from much shorter fatigue lives than others.

Approaches (ii) and (iii) can improve the robustness of bladed discs slightly. However, the reduction of scatter from approach (iii) is generally small compared with the reduction in the tuned system datum by the increase of higher damping ratio.

If the approaches suggested above do not lower the potential worst case to an acceptable level, the mistuning patterns may need to be controlled in one of two ways, either by imposing tighter tolerances or by applying some form of intentional mistuning. Although these methods lead to much higher manufacturing costs, the upper bound or the 99% response levels can be controlled effectively. Figure 8 shows that the tolerances to be assigned depend on the bladed disc design, i.e., interblade coupling and damping: the tolerances are usually less tight if the interblade coupling or damping ratio is high. Intentional mistuning can also lower the responses of blades as shown in Fig. 9.

Through these measures, it should be possible to arrive at a design where the potential worst-case consequences of mistuning arising are taken into account at the design stage and the probability of encountering them is set at an acceptably low level.

There is an additional element in this new approach to managing mistuning which takes advantage of a number of features which are found in blisks.

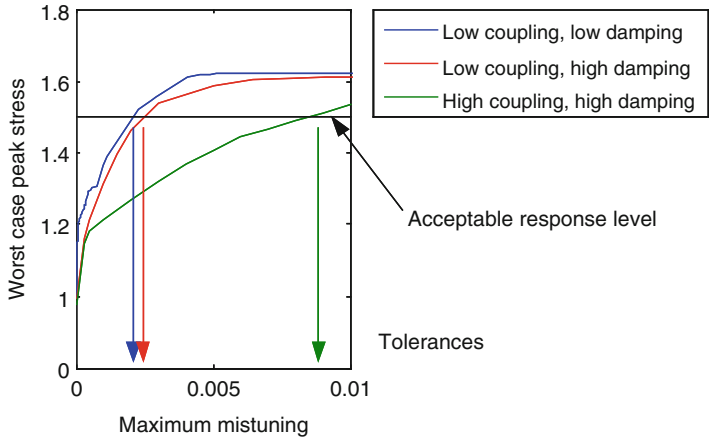

Fig. 8 Assignment of tolerances in different six-bladed disc designs given a upper limit of permissible peak stress

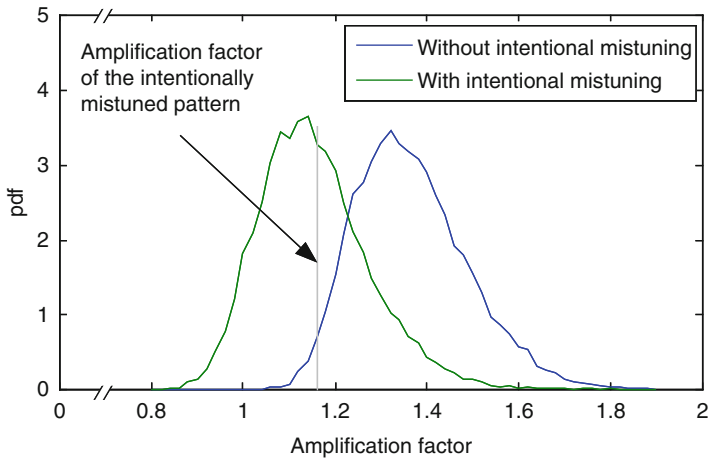

Fig. 9 Amplification factor pdfs for random and controlled mistuning

5.3 Step 3

For integrally-machined blisks: use recently-developed methods for identifying the specific mistune pattern on given blisk from measurement of the assembly modes of that blisk, together with the mathematical model used for its design, to compute the specific amplification factor for that individual unit and thereby to define its mistune vulnerability factor: e.g., the percent of the worst case response level (from the statistics of the whole population) which that specific unit will experience. Furthermore, this assessment method can be used to monitor the state of an individual unit

throughout its service life, and the evolution of its mistune characteristics can be tracked and the possibility of it moving towards a high-risk state can be identified and arrested.

6 Concluding Discussion

It is necessary to accept that mistuning is an inevitable non-robust feature of the bladed disc type of structure. Perhaps it is interesting to explore and explain why, but it is a feature that cannot be avoided. It is useful to understand the physics well enough to be able to explain the relative roles of interblade coupling, number of blades, level of damping, extent of scatter, all of which we can observe by computation but none of which have yet been explained through understanding the physics.

It should also be noted that the essential problem is deterministic, and not probabilistic, because the underlying mechanism that causes mistuning is an acute sensitivity of the forced response of the bladed disc structure to small perturbations in its properties. We need to seek a deterministic formulation of that sensitivity and how to reduce it.

For now, we must seek practical solutions by minimizing the sensitivity (even if only by trial and error), by adding more damping, and by seeking practical controlled mistune patterns, being very careful in this latter endeavor to ensure the robustness of the proposed solution (The "perfect" solution is to make all the blades identical: however, this is notoriously non-robust because slight wear causes a rapid deterioration of the mistuning problem).

References

1. Dye, R., Henry, T.: Vibration amplitudes of compressor blades resulting from scatter in blade natural frequencies. J. Eng. Power **91**, 182–188 (1969)
2. Whitehead, D.S.: Effect of mistuning on vibration of turbomachine blades induced by wakes. J. Mech. Eng. Sci. **8**, 15–21 (1966)
3. Jones, K.: Minimizing maximum modal force in mistuned bladed disk forced response. J. Turbomach., Trans. ASME **130**, 011011 (2008)
4. Nikolic, M.: New Insights into the Blade Mistuning Problem. Ph.D. Thesis, Mechanical Engineering Department, Imperial College, London (2006)
5. Nikolic, M., Petrov, E.P., Ewins, D.J.: Coriolis forces in forced response analysis of mistuned bladed disks. J. Turbomach., Trans. ASME **129**(4), 730–739 (2007)
6. Kielb, R.E., Feiner, D.M., Griffin, J.H., Miyakozawa, T.: Probabilistic analysis of mistuned bladed disks and blisks with aerodynamic and FMM structural coupling. In: Nineth National Turbine Engine HCF Conference (2004)
7. Kielb, R.E., et al. : Aerodynamic and structural coupling effects on mistuned bladed disk response. In: Tenth National Turbine Engine HCF Conference (2005)
8. Miyakozawa, T., Kielb, R.E., Hall, K.C.: The effects of aerodynamic asymmetric perturbations on forced response of bladed disks. In: Proceedings of ASME Turbo Expo: Power for land, Sea and Air (2008)

9. Lim, S., Castanier, M.P., Pierre, C.: Intentional mistuning design space reduction based on vibration energy flow in bladed disks. In: Proceedings of the ASME Turbo Expo, pp. 373–384 (2004)
10. Feiner, D.M., Griffin, J.H.: Mistuning identification of bladed disks using a fundamental mistuning model – Part I: Theory, Part II: Application. J. Turbomach., Trans. ASME **126**, 150–165 (2004)
11. Griffin, J.H., Feiner, D.M.: Determination of damping in bladed disk systems using the fundamental mistuning model. United States Patent 7,206, p. 709 (2007)
12. Laxalde, D., Thouverez, F., et al.: Mistuning identification and model updating of an industrial blisk. Int. J. Rotat. Mach., Article ID 17289, 10 (2007)
13. Reed, R.C.: The Superalloys: Fundamentals and Applications. Cambridge University Press (2006)

Modeling Geometric Mistuning of a Bladed Rotor: Modified Modal Domain Analysis

Alok Sinha and Yasharth Bhartiya

Abstract Modified Modal Domain Analysis (MMDA) is a novel method for the development of a reduced-order model of a bladed rotor with geometric mistuning. This method utilizes proper orthogonal decomposition of Coordinate Measurement Machine (CMM) data on blades' geometries, and sector analyses using ANSYS and solid modeling. In this paper, the algorithm to compute reduced-order mass and stiffness matrices from ANSYS sector analyses are provided and numerical results dealing with variations in natural frequencies and forced response are presented for different patterns of geometric mistuning.

Keywords MMDA · Geometric mistuning · Sector Analysis · Reduced order model

1 Introduction

Blade profiles of an integrally bladed rotor are manufactured by milling machines [1]. During this milling process, there are blade-to-blade variations in geometries of blades, which are known as geometric mistuning. These variations in blades' geometry cause simultaneous and dependent perturbations in mass and stiffness matrices of each blade [2]. In addition, blade-to-blade geometric variations are random in nature. It is extremely important to accurately model the effects of geometric mistuning at the design stage so that the impact of geometric mistuning on the flutter and forced response can be reliably estimated. The key to this goal is to develop an accurate reduced-order model as sector analysis cannot be performed for a mistuned bladed rotor. In this age of advanced computing, it is quite possible to model the full bladed rotor in ANSYS or NASTRAN. However, because of the stochastic nature of

A. Sinha and Y. Bhartiya
Department of Mechanical and Nuclear Engineering, The Pennsylvania State University, University Park, PA 16802, USA
e-mail: axs22@psu.edu

K. Gupta (ed.), *IUTAM Symposium on Emerging Trends in Rotor Dynamics*,
IUTAM Bookseries 25, DOI 10.1007/978-94-007-0020-8_16,

the problem, one must conduct Monte Carlo simulations to determine the statistics of response. The cost of conducting Monte Carlo simulations with finite-element models of full rotors will be prohibitive.

For the last 15 years, there has been a significant progress [3, 4] in the development of a reduced order model of a mistuned bladed disk. But, none of these techniques is able to generate a reduced-order model of a bladed rotor with geometric mistuning. The author of this paper has developed a breakthrough method [2], Modified Modal Domain Analysis (MMDA), to develop the reduced-order model in the presence of geometric mistuning. This method only requires sector analyses of certain tuned bladed disks, which are easily accomplished in ANSYS or NASTRAN. Furthermore, variations in geometry are characterized by the proper orthogonal decompositions (POD) of blades' profiles which are measured by a coordinate measurement machine (CMM). The validity of this technique has been shown for an academic rotor by comparison with results from the full rotor analysis. However, the algorithm to compute the reduced-order mass and stiffness matrices from sector analyses was not provided in the previous paper [2].

In this paper, the algorithm to compute the reduced-order mass and stiffness matrices from sector analyses is provided. Further, it is shown how a MMDA model developed on the basis of blades with specified geometry can be very easily used to perform Monte Carlo simulations of all the arrangements of blades without requiring any new finite element analysis. Numerical results from these simulations are presented.

2 Modified Modal Domain Analysis (MMDA)

A mistuned bladed-disk assembly or a bladed rotor can be described by

$$(M_t + \delta M)\ddot{\mathbf{x}} + (K_t + \delta K)\mathbf{x} = 0 \tag{1}$$

where M_t and K_t are mass and stiffness matrices of the perfectly tuned bladed rotor with each blade having the average geometry, respectively. Matrices δM and δK are deviations in mass and stiffness matrices due to mistuning. Let

$$x = \Phi y \tag{2}$$

where

$$\Phi = [\Phi_1 \ \Phi_2 \ \ldots \ \Phi_{np+1}] \tag{3}$$

Φ_1 : r tuned modes of the system with blades having the mean geometry.
Φ_ℓ : r tuned modes of the system with blades having perturbed geometry along $(\ell - 1)$th POD feature, $\ell = 2, \ldots., np + 1$.

Substituting (2) into (1), and pre-multiplying by Φ^{H}, the reduced-order model is obtained as follows:

$$M_r \ddot{y} + K_r y = 0 \tag{4}$$

where

$$K_r = \Phi^H K_t \Phi + \Phi^H \delta K \Phi \tag{5}$$

$$M_r = \Phi^H M_t \Phi + \Phi^H \delta M \Phi \tag{6}$$

To obtain reduced-order mass and stiffness matrices, $\Phi_i^H K_t \Phi_j$, $\Phi_i^H M_t \Phi_j$, $\Phi_i^H \delta K_t \Phi_j$ and $\Phi_i^H \delta M_t \Phi_j$ are to be calculated for $i = 1, 2, \ldots, np + 1$, and $j = i, i + 1, \ldots, np + 1$. Here, only algorithms to compute $\Phi_i^H M_t \Phi_j$ and $\Phi_i^H \delta M_t \Phi_j$ are presented. The procedures to compute $\Phi_i^H K_t \Phi_j$ and $\Phi_i^H \delta K_t \Phi_j$ are similar.

2.1 Computation of $\Phi_i^H M_t \Phi_j$ via ANSYS Sector Analyses

Describe the tuned mass matrix of the full rotor as follows:

$$M_t = \begin{bmatrix} M_{t,1,1} & M_{t,1,2} & \cdots & M_{t,1,n} \\ M_{t,2,1} & M_{t,2,2} & \cdots & M_{t,2,n} \\ \vdots & \vdots & \vdots & \vdots \\ M_{t,n,1} & M_{t,n,2} & \cdots & M_t, n, n \end{bmatrix} \tag{7}$$

It should be remembered that M_t will be a circulant matrix; i.e., the second block row will be obtained by shifting the first block row by one location, the third block row will be obtained by shifting the second block row by one location, and so on. Let $\varphi_{i,j,\ell}$ represent nodal displacements associated with the tuned mode for POD feature# i, sector j and the interblade phase angle $= 2\pi\ell/n$. Note that

$$\varphi_{i,j,p} = e^{\iota(j-1)\psi_p} \varphi_{i,1,p}; \iota = \sqrt{-1} \tag{8}$$

$$\psi_p = \frac{2\pi p}{n} \tag{9}$$

The $(\ell + 1, \rho + 1)$ element of $\Phi_i^H M_t \Phi_j$ is as follows:

$$\begin{aligned} &\varphi_{i,1,\ell}^H M_{t\rho}^c \varphi_{j,1,\rho} + \varphi_{i,2,\ell}^H M_{t\rho}^c \varphi_{j,2,\rho} + \cdots + \varphi_{i,n,\ell}^H M_{t\rho}^c \varphi_{j,n,\rho} \\ &= \left(1 + e^{\iota(\psi_\rho - \psi_\ell)} + \cdots + e^{\iota(n-1)(\psi_\rho - \psi_\ell)}\right) \varphi_{i,1,\ell}^H M_{t\rho}^c \varphi_{j,1,\rho} = \chi \varphi_{i,1,\ell}^H M_{t\rho}^c \varphi_{j,1,\rho} \end{aligned} \tag{10}$$

where

$$M_{t\rho}^c = M_{t,1,1} + e^{\iota\psi_\rho} M_{t,1,2} + \cdots + e^{\iota(n-1)\psi_\rho} M_{t,1,n} \tag{11a}$$

$$\chi = \frac{1 - e^{\iota n(\psi_\rho - \psi_\ell)}}{1 - e^{\iota(\psi_\rho - \psi_\ell)}} \tag{11b}$$

Let χ_R and χ_I be real and imaginary parts of χ, respectively. With $M_{t\rho}^{cR}$ and $M_{t\rho}^{cI}$ being real and imaginary parts of $M_{t\rho}^{c}$,

$$\chi M_{t\rho}^{c} = M_{t\rho}^{mcR} + \iota M_{t\rho}^{mcI} \tag{12}$$

where

$$M_{t\rho}^{mcR} = \left(\chi_R M_{t\rho}^{cR} - \chi_I M_{t\rho}^{cI}\right) \text{ and } M_{t\rho}^{mcI} = \left(\chi_I M_{t\rho}^{cR} + \chi_R M_{t\rho}^{cI}\right) \tag{13}$$

Let

$$\varphi_{j,1,\rho} = \varphi_{j,1,\rho}^{R} + \iota \varphi_{j,1,\rho}^{I} \tag{14}$$

From Eq. (10), the $(\ell+1,\ \rho+1)$ element of $\Phi_i^H M_t \Phi_j$ is expressed as follows:

$$\begin{aligned}
\chi \varphi_{i,1,\ell}^{H} M_{t\rho}^{c} \varphi_{j,1,\rho} &= \varphi_{i,1,\ell}^{H} M_{t\rho}^{mc} \varphi_{j,1,\rho} \\
&= \begin{bmatrix} \varphi_{i,1,\ell}^{R'} & \varphi_{i,1,\ell}^{I'} \end{bmatrix} \begin{bmatrix} M_{t\rho}^{mcR} & -M_{t\rho}^{mcI} \\ M_{t\rho}^{mcI} & M_{t\rho}^{mcR} \end{bmatrix} \begin{bmatrix} \varphi_{j,1,\rho}^{R} \\ \varphi_{j,1,\rho}^{I} \end{bmatrix} \\
&\quad + \iota \begin{bmatrix} -\varphi_{i,1,\ell}^{I'} & \varphi_{i,1,\ell}^{R'} \end{bmatrix} \quad \begin{bmatrix} M_{t\rho}^{mcR} & -M_{t\rho}^{mcI} \\ M_{t\rho}^{mcI} & M_{t\rho}^{mcR} \end{bmatrix} \begin{bmatrix} \varphi_{j,1,\rho}^{R} \\ \varphi_{j,1,\rho}^{I} \end{bmatrix}
\end{aligned} \tag{15}$$

From Eq. (13),

$$\begin{bmatrix} M_{t\rho}^{mcR} & -M_{t\rho}^{mcI} \\ M_{t\rho}^{mcI} & M_{t\rho}^{mcR} \end{bmatrix} = \chi_R \begin{bmatrix} M_{t\rho}^{cR} & -M_{t\rho}^{cI} \\ M_{t\rho}^{cI} & M_{t\rho}^{cR} \end{bmatrix} + \chi_I \begin{bmatrix} -M_{t\rho}^{cI} & -M_{t\rho}^{cR} \\ M_{t\rho}^{cR} & -M_{t\rho}^{cI} \end{bmatrix} \tag{16}$$

2.2 Computation of $\Phi_i^H \delta M_t \Phi_j$ via ANSYS Sector Analyses

The perturbation in the mass matrix, δM, has the block diagonal form. Therefore,

$$\Phi_i^H \delta M \Phi_j = \sum_{\ell=1}^{n} \Phi_i^H \delta M_\ell^b \Phi_j \tag{17}$$

where

$$\delta M_\ell^b = \begin{bmatrix} 0 & \cdots & 0 & \cdots & 0 \\ \cdots & \ddots & \cdots & \cdots & \cdots \\ 0 & \cdots & \delta M_\ell & \cdots & 0 \\ \cdots & \cdots & \cdots & \ddots & \cdots \\ 0 & \cdots & 0 & \cdots & 0 \end{bmatrix} \tag{18}$$

The $(\nu+1, \rho+1)$ element of $\Phi_i^H \delta M_\ell^b \Phi_j$ in Eq. (17) is as follows:

$$\varphi_{i,1,\nu}^H \delta M_\ell e^{\iota\ell(\psi_\rho-\psi_\nu)} \varphi_{j,1,\rho} = \begin{bmatrix} \varphi_{i,1,\nu}^{R'} & \varphi_{i,1,\nu}^{I'} \end{bmatrix} \begin{bmatrix} \delta M_{\ell c} & -\delta M_{\ell s} \\ \delta M_{\ell s} & \delta M_{\ell c} \end{bmatrix} \begin{bmatrix} \varphi_{j,1,\rho}^{R} \\ \varphi_{j,1,\rho}^{I} \end{bmatrix} + \iota \begin{bmatrix} -\varphi_{i,1,\nu}^{I'} & \varphi_{i,1,\nu}^{R'} \end{bmatrix} \begin{bmatrix} \delta M_{\ell c} & -\delta M_{\ell s} \\ \delta M_{\ell s} & \delta M_{\ell c} \end{bmatrix} \begin{bmatrix} \varphi_{j,1,\rho}^{R} \\ \varphi_{j,1,\rho}^{I} \end{bmatrix} \quad (19)$$

where

$$\delta M_{\ell c} = \delta M_\ell \cos(\ell(\psi_\rho - \psi_\nu)) \text{ and } \delta M_{\ell s} = \delta M_\ell \sin(\ell(\psi_\rho - \psi_\nu)) \quad (20a,b)$$

2.3 Connection with ANSYS Sector Analysis

The ANSYS code only works with real numbers [5]. It constructs two identical sectors, one for real part and another for imaginary part of the displacement. As a result, only one interblade phase angle for a repeated eigenvalue is considered. Further, the mass and stiffness matrices for a double sector are as follows:

$$\begin{bmatrix} M_{t\rho}^{cR} & -M_{t\rho}^{cI} \\ M_{t\rho}^{cI} & M_{t\rho}^{cR} \end{bmatrix} \quad \text{and} \quad \begin{bmatrix} K_{t\rho}^{cR} & -K_{t\rho}^{cI} \\ K_{t\rho}^{cI} & K_{t\rho}^{cR} \end{bmatrix} \quad (21)$$

Therefore, $M_{t\rho}^{cR}$, $M_{t\rho}^{cI}$ in Eq. (16) can be obtained directly from ANSYS mass matrices. Furthermore, eigenvectors of the double sector have exactly the form $\left[\varphi_{i,1,\ell}^{R'} \varphi_{i,1,\ell}^{I'}\right]$ and $\left[-\varphi_{i,1,\ell}^{I'} \varphi_{i,1,\ell}^{R'}\right]$ which appear in Eqs. (15) and (19).

3 Numerical Results

The bladed disk considered by Sinha [2] is again used. The number of blades is 24, and the mistuning pattern#1 [2] representing changes in uniform blades' thicknesses is studied. The factors λ for blade thickness changes are provided in Table 1 where the blade thickness $= (1+\lambda)b_0$ and b_0 is the thickness of the tuned blade. In Eq. (3), $np = 1$.

Sector analysis is performed with each blade thickness, and mass and stiffness matrices are stored. Subtracting mass and stiffness matrices of a sector having blade with the average thickness, δK_j and δM_j ($j = 1, 2, \ldots, 24$) in Eq. (18), are obtained for the implementation of MMDA.

With blade thicknesses represented in Table 1, 1,000 random permutations of the mistuning pattern are created. Using MMDA, all of these mistuned bladed disks are analyzed without needing any new finite element analysis. Using Eq. (19), Eq. (17)

Table 1 Factors λ for original pattern of blade thicknesses (geometric mistuning)

Blade 1	Blade 2	Blade 3	Blade 4	Blade 5	Blade 6	Blade 7	Blade 8
0.0051	0.0263	−0.0467	−0.0184	−0.0105	−0.0485	−0.0528	0.0372
Blade 9	Blade 10	Blade 11	Blade 12	Blade 13	Blade 14	Blade 15	Blade 16
0.0	−0.0258	0.0322	0.0093	−0.0396	0.05	0.0116	0.0492
Blade 17	Blade 18	Blade 19	Blade 20	Blade 21	Blade 22	Blade 23	Blade 24
0.0455	−0.0274	−0.0517	−0.0029	−0.0132	−0.0337	0.0199	0.0395

Table 2 Factors λ for a random permutation of original blade thicknesses

Blade 1	Blade 2	Blade 3	Blade 4	Blade 5	Blade 6	Blade 7	Blade 8
0.0492	−0.0029	−0.0517	−0.0258	0.0116	−0.0105	−0.0274	0.0051
Blade 9	Blade 10	Blade 11	Blade 12	Blade 13	Blade 14	Blade 15	Blade 16
−.0528	−0.0467	−0.0184	0.0199	0.0455	0.0372	0.0395	0.0263
Blade 17	Blade 18	Blade 19	Blade 20	Blade 21	Blade 22	Blade 23	Blade 24
0.0322	0	−0.0132	−0.0337	−0.0485	−0.0396	0.0093	0.05

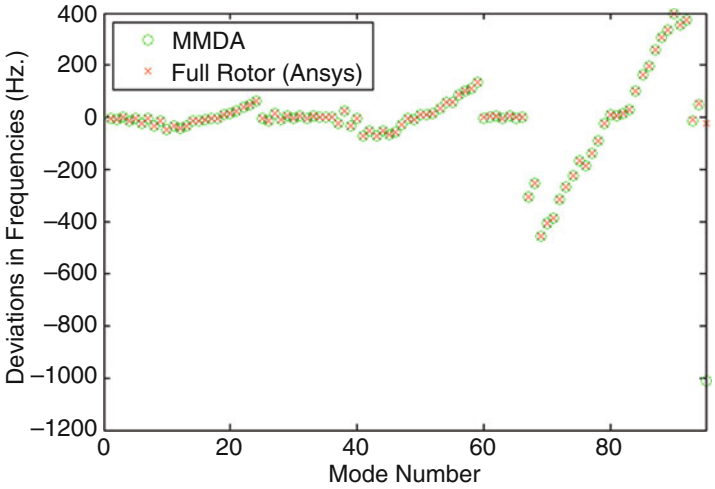

Fig. 1 MMDA results for a random permutation of original blade thicknesses

is viewed as $\varphi^H_{i,l,\nu}\delta M_\ell \varphi^H_{j,l,\rho}$ being multiplied with a weighing factor $e^{i\ell(\psi_\rho-\psi_\nu)}$ and then added. Therefore, $\varphi^H_{i,l,\nu}\delta M_\ell \varphi^H_{j,l,\rho}$ is calculated only once for each sector and then used for all permutations of the mistuning pattern. Note that the weighing factors $e^{i\ell(\psi_\rho-\psi_\nu)}$ change for different permutations. The validity of the MMDA based analysis is shown by comparison of MMDA results with full rotor results for one of the random permutations of original blade thicknesses (Table 2 and Fig. 1).

In Fig. 1, the first 24 frequencies represent the family of first bending modes of vibration of blades. The variations in these frequencies are shown in Fig. 2 for different permutations of blade thicknesses. It should be noted that the nodal diameter on the abscissa of the plot refers to the perfectly tuned system only. The histogram

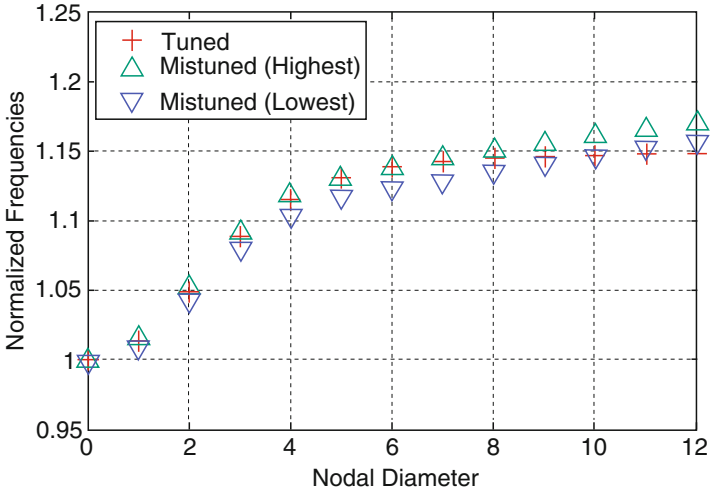

Fig. 2 Variations in first 24 mistuned natural frequencies for 1,000 permutations of mistuning pattern

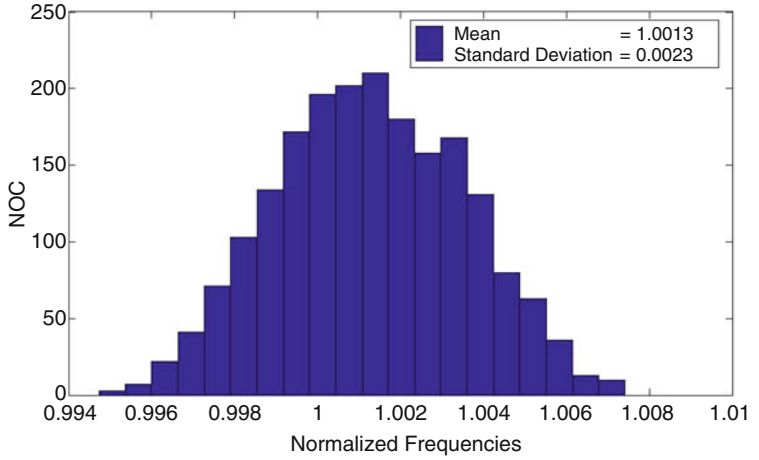

Fig. 3 Distributions of natural frequencies for nodal diameter = 9 (NOC = number of occurrences)

of variations in frequencies near the frequency of a perfectly tuned system with nodal diameter = 9 is shown in Fig. 3. The standard deviation of these frequencies is 0.0023. The histogram of the amplitude magnification with respect to tuned amplitude is shown in Fig. 4 when the nine nodal diameter forcing function is applied with the modal damping = 0.001. The standard deviation of these amplitudes is 0.0749.

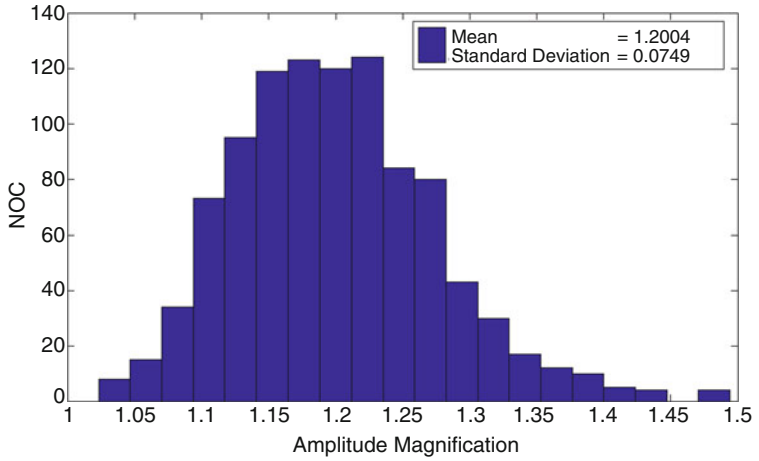

Fig. 4 Histogram of amplitude magnification (9 ND excitation, tuned modal damping = 0.001, NOC = number of occurrences)

4 Conclusions

The algorithm for MMDA has been presented. In particular, it is shown how data (mass matrices, stiffness matrices and modal vectors) from sector analyses can be used to efficiently implement MMDA. Numerical results are provided to support the fact that MMDA can be easily used to analyze the mistuned bladed disk obtained after random permutations of the original mistuning pattern. For nine nodal diameter excitation, the maximum amplitude amplification is about 1.5 with the modal damping = 0.001. The standard deviation of variations in amplitude magnifications is about 0.0749 whereas the standard deviation of corresponding mistuned natural frequencies is only 0.0023.

References

1. Sinha, A., Hall, B., Cassenti, B., Hilbert, G.: Vibratory parameters of blades from coordinate measurement machine (CMM) data. ASME J. Turbomach. **130**, 011013, January (2008) (Also GT2005–69004)
2. Sinha, A.: Reduced-order model of a bladed rotor with geometric mistuning. ASME J. Turbomach. **131**(3), 031007, July (2009) (Also GT2007–27276)
3. Yang, M.T., Griffin, J.H.: A reduced order model of mistuning using a subset of nominal system modes. ASME J. Eng. Gas Turb. Power **123**(4), 893–900 (1999)
4. Bladh, R., Castanier, M.P., Pierre, C.: Component-mode-based reduced order modeling techniques for mistuned bladed disks – Part I: Theoretical models, Part II: Application. ASME J. Eng. Gas Turb. Power **123**, 89–108 (2001)
5. ANSYS Theory Manual, 12th edn., SAS IP Inc., 15-65-15-66 (1999)

Trends in Controllable Oil Film Bearings

Ilmar F. Santos

Abstract This work gives an overview about the theoretical and experimental achievements of mechatronics applied to oil film bearings, with the aim of: controlling the lateral vibration of flexible rotating shafts; modifying bearing dynamic characteristics, as stiffness and damping properties; increasing the rotational speed ranges by improving damping and eliminating instability problems, for example, by compensating cross-coupling destabilizing effects; reducing startup torque and energy dissipation in bearings; compensating thermal effects. It is shown that such controllable bearings can act as “smart" components and be applied to rotating machines with the goal of avoiding unexpected stops of plants, performing rotordynamic tests and identifying model parameters “on site". Emphasis is given to the controllable lubrication (active lubrication) applied to different types of oil film bearings, i.e., as tilting-pad bearings, multirecess journal bearings and plain bearings.

Keywords Controllable bearings · Active lubrication · Smart bearings · Active rotor vibration control · Rotortronics · Bearing testing · Bearing parameter identification

1 Introduction

The relative maturity of many traditional technologies within different technical areas implies little or no potential for significant improvements of machine performance. Consequently, to deal with the technical challenges related to some new requirements of safety, quality, reduced weight, low vibration and noise levels, non-conventional techniques have to be introduced where the conventional ones have already reached their limits. This is especially true in the field of

I.F. Santos
MEK Ű Dept. of Mechanical Engineering, DTU- Tech. University of Denmark
Nils Koppels Allé, Lyngby 2800, DENMARK
e-mail: ifs@mek.dtu.dk

K. Gupta (ed.), *IUTAM Symposium on Emerging Trends in Rotor Dynamics*,
IUTAM Bookseries 25, DOI 10.1007/978-94-007-0020-8_17,

conventional fluid film bearings. Thus, the combination of tribology, control techniques and informatics (mechatronics) enables the development of “smart" bearings able to deal with multi-objective functions, i.e., not only the capability of supporting a rotating shaft. The synergy among different sub-areas enables balancing of various contradictory properties of integrated systems, allowing significant improvements and overcoming limitations related to conventional “passive" conventional solutions.

One of the most attractive features of mechatronics is its ability to render products “smart". Such a smart machine makes use of the built-in active control to incorporate higher performance functions. Thus, the machine may acquire higher precision and the ability for self-diagnosis, e.g., it can calibrate itself, it can give a prognosis about its future ability to operate in a satisfactory way, or about its remaining lifetime, and it can have the possibility of suggesting corrective actions which may be induced by itself. It is the mechatronic structure of the machine, the built-in control, its sensors, processors, actuators, and above all, its software, which enable these novel features. This is a way to design machines and products with higher performance, less maintenance costs, longer lifetime, and an enhanced customer attraction [37].

The development of new machine components capable of keeping low levels of machine vibrations is of fundamental importance. This claim can be easily verified by checking the number of new “passive" and “active" elements under development stages in the last two decades. Apart from the over forty years old squeeze-film damper technology [1, 24], the seal dampers [42] are one of the most important new “passive" elements. Among the “active" and “semi-active" elements (mechatronic components) one can cite: hybrid squeeze-film dampers [5], controllable squeeze film dampers using electro-rheological fluids [13, 17, 18], controllable squeeze film dampers using magneto-rheological fluids [45, 46], active hydraulic chamber systems connected to different types of bearings [2, 25, 31, 41], variable impedance hydrodynamic journal bearings using accumulators [8], piezoelectrically controlled bearings [23], combined piezoelectric-hydraulic actuators [40], actively lubricated bearings [26–28], active-controlled fluid bearings [3], magnetized journal bearings lubricated with ferro-fluids [22], disk-type electro-rheological dampers [43, 44], disk-type magneto-rheological fluid dampers [47], foil-magnetic hybrid bearings [12] and bearings composed of flexible sleeves controlled by means of hydraulic chambers [15, 39]. While active magnetic bearings have a relatively long history of development and testing, and nowadays their industrial application to rotating machines is a well-established technology, the development of new types of mechatronic components as hybrid squeeze-film dampers, controllable squeeze film dampers using electro-rheological fluids, controllable squeeze film dampers using magneto-rheological fluids, active hydraulic chamber systems connected to different types of bearings, variable impedance hydrodynamic journal bearings using accumulators, piezoelectric-controlled bearings, combined piezoelectric-hydraulic actuators, actively lubricated bearings, active-controlled fluid bearings, magnetized journal bearings lubricated with ferro-fluids, disk-type electro-rheological dampers, disk-type magneto-rheological fluid dampers, foil-magnetic hybrid bearings and bearings composed of flexible sleeves controlled by means of hydraulic chambers,

has a shorter history and is still “creeping" in different laboratories of universities and companies.

The development of journal bearings with controllable radial oil injection, or simply actively lubricated, has a history of only a little more than one decade [26]. There are obviously advantages and drawbacks when compared to active magnetic bearings, depending on the application purposes. Research activities have shown the potential of such new mechatronic devices and in this framework this work is intended to give an overview of the achievements and trends in this promising field, with special emphasis on tilting-pad bearings, multirecess hybrid bearings and plain bearings. With such controllable oil film bearings it is intended to: (a) control of the lateral vibration of flexible rotating shafts; (b) modify bearing dynamic coefficients; (c) increase the rotational speed ranges by increasing damping and eliminating instability problems, e.g., by compensating cross-coupling destabilizing effects; (d) reduce startup torque and energy dissipation in bearings; (e) compensate thermal effects; (f) develop “smart" components able to avoid unexpected plants shutdowns, perform rotordynamic tests and identify model parameters “on -site".

2 Designing and Testing Controllable Oil Film Bearings

When the hydrostatic and the hydrodynamic lubrication are simultaneously combined in a journal bearing with the aim of reducing wear between rotating and stationary parts, one refers to hybrid lubrication, which offers the advantages of both lubrication mechanisms. When part of the hydrostatic pressure is also dynamically modified by means of hydraulic control systems, one refers to active lubrication or active oil film. By the combination of fluid power, electronics and control theory, active lubrication makes simultaneously feasible the reduction of wear and the attenuation of vibration. The direct influence on the oil flow behavior in the bearing gap is achieved by machining orifices along the bearing surface or pad surface and connecting them to servo valves via pipelines. The servo valves enable changes of the fluid injection pressure directly in the bearing gap. By changing the flow characteristics through the electronic injection, one attempts to control the rotor movements, modify the stiffness and damping of the oil film or induce controllable shaft movements via calibrated oil film forces. The main advantages of the active lubricated bearing shown in Fig. 1a are: the compactness, the capability of generating high control forces, there is no need of additional backup bearings in case of control failure, since they are also able to operate passively (without control). The length of pipelines connecting the servo valves and oil film gap is significantly reduced by machining channels inside of the the bearing housing, as illustrated in details in Fig. 1b. The displacement sensors **1** and **2** capture the lateral vibrations of the rotor in the vertical and horizontal directions respectively. The accelerometer **3** mounted on the the bearing housing detects bearing housing vibrations in the horizontal direction. The servo valves **4** and **5** are used to control the pressurized oil injection. The pressurized oil flows through the channels machined inside the bearing housing, namely channels **8** and **9**, into the bearing gap by means of orifices machined in the middle of the pads. In industrial bearings such a type of orifices is normally of use

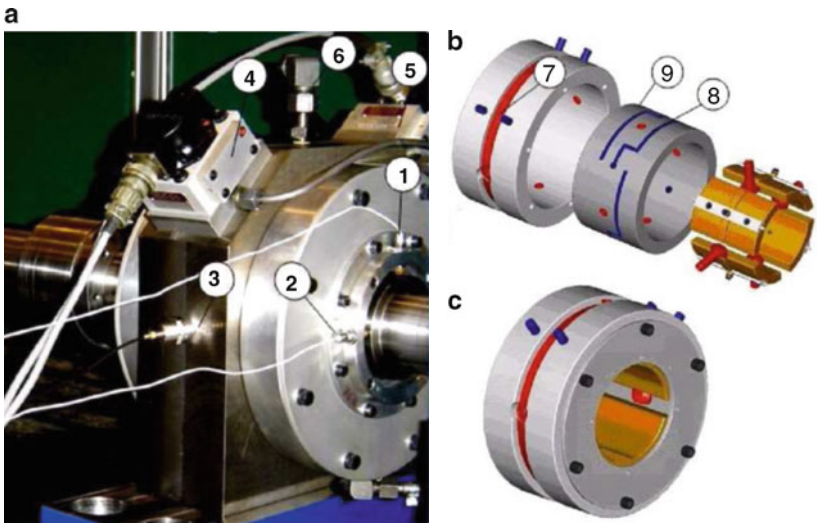

Fig. 1 Active lubricated bearing – (**a**) active lubricated bearing as a mechatronic device: **1** – displacement sensor (eddy-current) to measure rotor vibrations in the vertical direction; **2** – displacement sensor (eddy-current) to measure rotor vibrations in the horizontal direction; **3** – accelerometer to measure housing vibrations **4** and **5** – servo valves **6** – oil supply pipeline (conventional hydrodynamic lubrication); (**b**) exploded view of the bearing illustrating the channels machined inside of the housing with the aim of achieving a compact bearing: **7** channel build circumferentially to feed oil between the pads (conventional hydrodynamic lubrication); **8** and **9** – channels inside of the bearing housing connected pairwise with the the servo valves (active lubrication); (**c**) 3D-view of the bearing as a mechanical component

to hydrostatic lubrication under startup conditions. The channels **8** and **9** connected to servo valves **4** and **5** by a differential principle make possible the generation of time-dependent control forces. The pads are mounted in a load-between-pads configuration, i.e., 45° from the static loading in the vertical direction. Therefore, the oil injection will occur with an angle of 45° from the vertical or horizontal directions. Such an oil injection will be controlled using the information coming from the sensors **1**, **2**, **3** and other sensors mounted along the flexible rotating shaft. The (conventional) hydrodynamic lubrication will be always turned on. Thus, the bearing can operate passively as well as actively. The conventional hydrodynamic lubrication will be created by feeding the oil with low pressure (up to 0.2 MPa) via the pipeline connector **6** and the channel **7**. The oil will achieve the bearing gap through holes machined between the four pads. The orifices are machined 90° from each other connecting the channel **7** and the space between the four tilting-pads. A test rig was designed to experimentally evaluate the rotor-bearing performance and it is shown in Fig. 2. An electric motor **7** with speed controller and a belt transmission is used, angular velocities up to 10,000 rpm can be achieved. The rotating shaft **2** is supported at one of its ends by a ball bearing **1**. Such a shaft can behave as a rigid body or as a flexible body, depending on the frequency range and the number of rigid discs attached to its free end, close to the auxiliary bearing **4**. The active

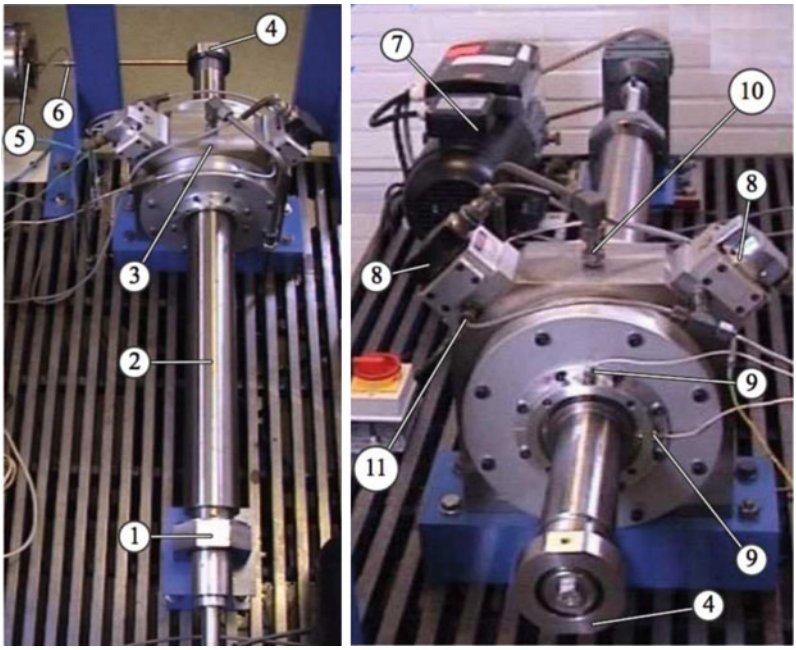

Fig. 2 Test rig to experimentally evaluate the performance of active lubricated bearings to control rigid and flexible rotating shafts: **1** – pedestal and ball bearing ; **2** – flexible shaft; **3** – active lubricated tilting-pad bearing; **4** – auxiliary bearing used as excitation and measurement station; **5** – electromagnetic shaker; **6** – force transducer; **7** – electric motor; **8** – servo valves; **9** – displacement sensors without contact (eddy-current); **10** – pipeline for low pressure injection (hydrodynamic lubrication) and **11** – pipeline for high pressure injection (active lubrication)

tilting-pad journal bearing **3** built by four pads in a load-between-pads configuration is the mechatronic device to be tested. The oil to build up the hydrodynamic lubrication is supplied through the pipelines **10**. The electronic radial oil injection (active lubrication) is built up using the two servo valves **8** as actuators, and the displacement sensors **9** are used as input signals to the controller. Accelorometers are also mounted on the auxiliary bearing **4**. Acceleration signals can also be used to define different control strategies. An excitation station built by the auxiliary bearing **4**, the electromagnetic shaker **5** and the force transducer **6** allows also dynamic testing. A hydraulic system built by a pump, accumulators, oil filters and servo valves **8** is used. A digital control unit, consisted of a PC computer with DSPACE cards and dedicated software for digital signal processing, is used to design and investigate different types of control strategies.

Active lubrication using P controllers – varying the proportional control gains while keeping the derivative gains as zero, significant modification of the stiffness coefficients is achieved, while the damping is not much altered.

Active lubrication using D controllers – varying the derivative control gains while keeping proportional gains as zero, one achieves a significant modification of the damping coefficients. The damping coefficients vary linearly as a function of the

control gains at low frequencies. Nevertheless, such a region of changes narrows with the increase of the rotating speed and frequency (synchronous coefficients). When the control voltage exceeds the linear range of the servo valve, the coefficients stop varying and remain constant in the so far achieved values. The stiffness coefficients are though not much altered by the derivative gains.

Tilting-pad journal bearings are frequently used in high speed machines with the aim of avoiding oil-whirl instabilities. They do not have significant cross-coupling effects. It means the control energy can be saved and used to increase the damping properties of the bearing instead of using it to suppress and eliminate the destabilizing cross-coupling effect. Tilting-pad bearings are though more expensive than conventional journal bearings, because they are built by extra accurately machined components, namely the pads. Multirecess journal bearings are hybrid bearings which allow a significant adjustment of the bearing stiffness. Due to their design simplicity they are cheaper than tilting-pad journal bearings. Multirecess bearings have relatively good damping characteristics in their passive form. Nevertheless, at high angular velocities the cross-coupling effect increases and affects significantly the rotor-bearing stability. The feasibility of applying multirecess journal bearings to industrial compressors is theoretically investigated in [36] and experimentally illustrated in [3, 4]. Their application to rigid rotating shafts seems to work extremely well due to strong changes of the direct stiffness and damping coefficients. Nevertheless, such a kind of bearing may not be so well suitable to control lateral movements of flexible shafts. Details will be given in Section 7.

Modifications of the direct stiffness coefficients are achieved by means of proportional as well as derivative controllers. The largest modifications of the direct stiffness are achieved by means of the proportional controllers. However, significant modifications of the direct damping coefficients are only achieved by using derivative controllers [33]. It means, that the direct damping coefficients can only be increased by means of the active lubrication, if the linear velocity of the journal center is measured or estimated. If a X-Y coupled PD controller is used, a compensation of the cross-coupling effects is possible. The significance of the modification of the bearings properties achieved by means of the active lubrication is evaluated from the behavior of the whirl frequency ratio and critical mass parameter [16]. It is possible to reduce the whirl frequency ratio and increase the critical mass parameter by properly designing a X-Y coupled PD-controller for the active lubrication system. The crossed retrofitting of the rotor linear displacements allows almost a cancelation of the cross coupling stiffness in a tiny range of proportional gain values [34]. From the point of view of control implementation in variable-speed rotating machines, an adaptive self-tuning controller with variable gains or a robust controller is necessary in order to effectively compensate the cross coupling effect.

3 Controllable Elastohydrodynamic Bearings

In [9–11] the elasticity of the sliding surfaces – the pads in the case of tilting-pad bearings – are taken into account and elasto-hydrodynamic models are created. Such models are being developed with the aim of predicting dynamic coefficients of radial

tilting-pad bearings under active elastohydrodynamic lubrication, i.e., the dynamic of the servo valves and control parameters are included into the mathematical model. Promising results are being obtained and documented in [9–11]. The possibility of applying active lubrication to deform the bearing pad and adjust the bearing preload factor is also an emerging trend in controllable fluid film bearings. Similar principle is applied to bearings composed of flexible sleeves controlled by means of hydraulic chambers [15, 39]. The main difference between the two principles is the way how the deformation of the sliding surface is achieved. In [11] the deformation is obtained with help of an appropriate distribution of the orifices along the pad surface and the controllable radial oil injection into the bearing gap.

4 Control Design Strategies

The design of feedback control laws for active lubricated bearings is not a trivial task. The active (oil film) control forces are strongly coupled to the hydrodynamic forces via the fluid continuity equation. There are different ways of designing the feedback control laws.

The first one is given by predefining the structure of the control loop, for example, by retrofitting displacement and velocity signals coming from the rotor lateral movements at the bearing location, and creating a decentralized PD controller. The gain of such feedback signals can be explicitly included into the modified Reynolds equations for active lubrication [29, 30]. By using the modified Reynolds equation and the perturbation technique damping and stiffness coefficients can be calculated as a function of the excitation frequency, Sommerfeld number and feedback control gains. Such coefficients can be introduced into rotordynamic models. Eigenvalues and eigenvectors of rotor-bearing systems can be calculated. Keeping the attention on the real part of the eigenvalues, it is possible to calculate the gains in order to obtain more stable rotor-bearing systems. Such an approach is detailed in [30, 32]. Its drawback is that only decentralized controllers can be designed. The main advantage is that the frequency-dependency of the active oil film forces is taken into account. Moreover, this approach makes feasible to elaborate tables for representing stiffness and damping coefficients as a function of Sommerfeld number, rotor eccentricity and control gains G_P and G_D. Such coefficients can be easily coupled to rotordynamic simulation programs in order to predict the dynamic behavior of rotor-bearing systems under conventional and active lubrication conditions.

Another useful approach is to decouple the active oil film forces and conventional hydrodynamic forces by using pesudo-static tests and approximate the active oil film force by a linear function of the servo valve input signal U_v. In other words, the problem is mathematically summarized by finding a linear coefficient λ that leads to $F_A = \lambda \cdot U_v$, where F_A is the active oil film force and λ is a coefficient obtained from pseudo-static tests using different values of U_v. How to obtain the coefficient λ is discussed in [20]. Such a procedure enables the design of centralized controllers based on modern control theory. Nevertheless, the results at higher

frequencies are less accurate than the results obtained via modified Reynolds equation, perturbation technique and global bearing dynamic coefficients [32]. In [21] though, such a coefficient is expressed as a function of the Sommerfeld number and the excitaiton frequency, i.e. $\lambda = \lambda(So, \omega)$, and feedback control gains are designed for attenuating vibrations of industrial gas compressor (flexible rotor-bearing system) of about 400 kg.

Another approach is to explore the nonlinear relationship between damping and stiffness coefficients and the rotor eccentricity (or equilibrium position inside of the bearing) and develop nonlinear controllers, as shown in [19]. Special attention should be paid to integral controllers which can lead to less stable rotor-bearing systems when the integral part of the controller brings the rotor back to the bearing geometric center. This leads to a reduction of the static eccentricity and, consequently, a significant reduction of the (passive) bearing damping coefficient. To achieve more stable rotor-bearing systems the integral part of the controller should not reduce the rotor eccentricity. Ideally, from the viewpoint of rotor-bearing stability the integral part should bring the rotor as close as possible to the bearing surface, increasing the static eccentricity. Nevertheless, in the case of high eccentricities, thermal effects may lead to a reduction of the (passive) damping coefficients.

5 Modification of Oil Film Dynamic Coefficients and Active Vibration Control of Rotors

One of the main advantages of incorporating the PD control gains inside of the modified Reynolds equation and obtaining the bearing coefficients using the perturbation technique is the feasibility of elaborating “Journal Bearing Tables" in the same way as presented in [16, 38], but with the fundamental difference that supply pressures and control gains shall become part of such tables. In other words, the control gains become part of the “ Controllable Journal Bearing Tables". Thus, the integration of mechanics, electronics and informatics (mechatronics) is consolidated and the limitations of bearing dynamic coefficients are overcome by introducing new design variables, as control gains and supply pressures.

Obtaining the active bearing stiffness and damping coefficients experimentally by means of identification procedures and inverse methods demands accurate calibration of the excitation systems coupled to force transducers, and the sensing systems coupled to displacement, velocity and acceleration transducers. Moreover, identification procedures are based on dynamic models which always present different levels of inaccuracy. Sensitivity and error propagation analyses are fundamental to assure a correct interpretation of experimental results. Up to now it has not been possible to identify such active bearing coefficients with appropriate accuracy to clearly validate the dependency of the active bearing coefficients on the excitation frequency and control gains. In all test setups, the non-modeled dynamics heavily influences the bearing parameters identification in different frequency ranges. However, it is possible to obtain with a good accuracy the values of damping ratio ξ of

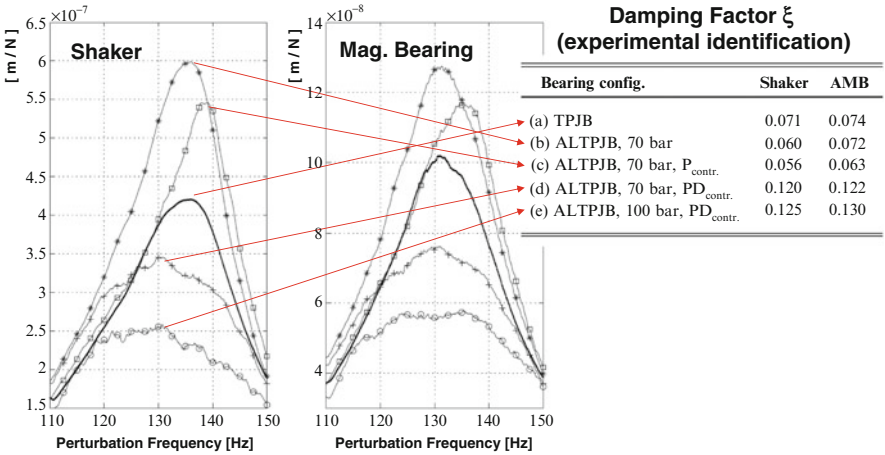

Fig. 3 Experimental results – identification of damping ratio ξ of the flexible rotor-bearing system at constant angular velocity of 1,000 rpm and different lubrication conditions using a "smart active magnetic bearing" and an electromagnetic shaker: (**a**) conventional hydrodynamics; (**b**) hybrid lubrication with $P_{inj} = 70$ bar; (**c**) active lubrication with a P-controller and supply pressure of 70 bar; (**d**) active lubrication with a PD-controller and supply pressure of 70 bar; (**e**) active lubrication with a PD-controller and supply pressure of 100 bar

a rotor-bearing system using the information around the resonance ranges, as it is illustrated in Fig. 3. Using the magnetic bearing with hall sensors carefully calibrated in [14], and an electromagnetic shaker with a force transducer attached between shaker and rotor, the identification of the system damping ratio ξ is performed. The experimental results are illustrated in Fig. 3. The rotor operates with a constant angular velocity of 1,000 rpm and the tilting-pad bearing operates under the following conditions: (a) conventional hydrodynamic lubrication; (b) hybrid lubrication with $P_{inj} = 70$ bar; (c) active lubrication with a P controller and supply pressure of 70 bar; (d) active lubrication with a PD controller and supply pressure of 70 bar; (e) active lubrication with a PD controller and supply pressure of 100 bar. A reduction of the vibration amplitudes around the resonance of the rotor-bearing system can be clearly seen. An increase in damping factor obtained via active lubrication is experimentally demonstrated and presented in the table incorporated into Fig. 3. The identification of damping ratio ξ is done with very good accuracy. The two experimental procedures are compared. Nevertheless, the identification of damping and stiffness coefficients as a function of the excitation frequency and control gains is still very poor. Research activities toward the identification of frequency-dependent coefficients are still being carried out. The feasibility of controlling lateral vibrations of flexible rotors using active lubricated bearings is experimentally proven, as shown in Fig. 3.

6 Smart Bearings – Rotordynamic Testing and Parameter Identification

When hydraulic or magnetic active forces are measured with high accuracy and displacement, acceleration and force transducers are properly adapted to the system, it is possible to develop “smart bearings" able to properly perform rotordynamic tests and aid the identification of system parameters. The characterization of active oil film forces is though a complicated task and depends on several parameters: Sommerfeld number (journal angular velocity, bearing load, oil viscosity, bearing gap, bearing dimensions), preload factors, orifice diameter and positioning over sliding surface, excitation frequency, feedback control gain, as well as on the dynamic parameters of the servo valves, i.e., their natural frequencies, damping factors and pressure-flow coefficients.

The rotor-bearing system illustrated in Fig. 4b is excited by the active oil film forces using a slow-sine sweep function as servo valve input signal. The experimental frequency response function (FRF) – estimators $H1$, $H2$ and coherence function – is illustrated in Fig. 4a. Both estimators $H1$ and $H2$ are presented and given in acceleration unit divided by volts. Good coherence is achieved between 40 and 170 Hz, as it can be seen in Fig. 4a. The feasibility of using the active lubricated bearing as a “calibrated shaker" is strongly dependent on the “active force maps" presented in Fig. 5. Such maps translate the servo valve input signal (given in volts) into values of force in Newton. In that way the functions $H1$ and $H2$ can be given in acceleration units $\mathrm{m/s^2}$ divided by Newton. Figure 5a illustrates the theoretical behavior of the active lubrication forces as a function of the excitation frequency and the amplitude of the input signal to the servo valve given in [21]. Figure 5b shows the experimental results coming from the characterization of the active lubrication forces using a quasi-static test and the determination of the coefficient λ given in [20]. As mentioned in Section 4, the conventional and active lubrication forces may be

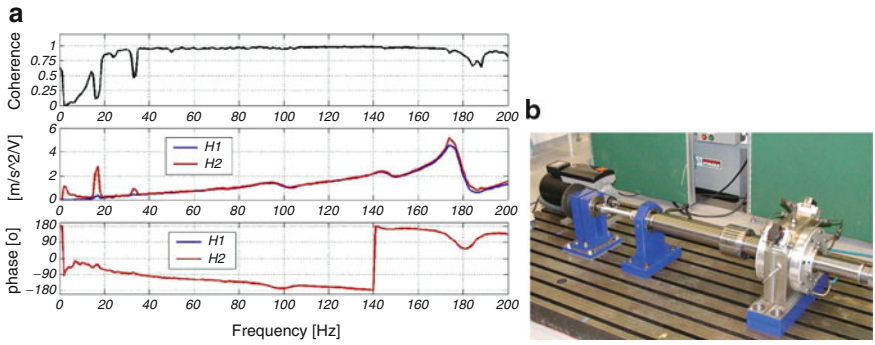

Fig. 4 Experimental results – active lubricated bearing used as shaker: (**a**) experimental frequency response function obtained via active lubrication and (**b**) flexible rotating shaft supported by an active lubricated tilting-pad journal bearing

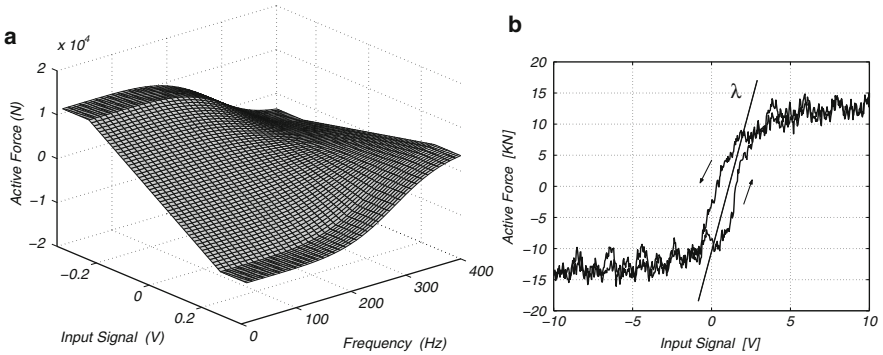

Fig. 5 Qualitative comparison of the active oil film forces and the experimental determination of the coefficient λ used to linearized the oil film active forces – (**a**) theoretical behavior of the active lubrication forces as a function of the excitation frequency and amplitude of the input signal to the servo valve; (**b**) experimental characterization of the active lubrication forces using a quasi-static test and determination of the coefficient λ

accurately decoupled using the coefficient λ, only if such a coefficient also becomes dependent on the frequency and on the Sommerfeld number, i.e., $\lambda = \lambda(So, \omega)$. It means that λ shall be estimated by a series of tests in the operational frequency range, and not only by a quasi-static test at low frequency, as it is illustrated in Fig. 5b. Moreover, the influence of hysteresis effect as a function of the excitation frequency has to be carefully investigated, aiming at correctly dealing with the nonlinear characteristics of the hydraulic control system.

7 Feasibility of Industrial Application

Active Tilting-Pad Journal Bearings – In terms of industrial application, it is important to highlight that tilting-pad bearings are the most stable among the different types of journal bearings. Normally, when vibration instabilities arise in a rotating machine supported by hydrodynamic bearings, the journal bearings are exchanged to tilting-pad bearings. If further actions shall be taken towards to improve rotor-bearing stability, control techniques can be applied to a journal bearing that already presents the best stability properties.

The feasibility of reducing lateral vibrations of an industrial gas compressor by using an active lubricated tilting-pad journal bearing is investigated in [35]. The rotating machine whose dynamics was analyzed is a gas compressor composed of five impellers, which weighs 391 kg and operates in the range of 6,942 rpm (115.7 Hz) to 10,170 rpm (169.7 Hz).

Multirecess Journal Bearings with Two Pairs of Active Pockets – In terms of industrial application, the importance of hybrid journal bearings as load support elements in high-speed turbomachinery and machine tool spindles has steadily grown

over the past years. Hybrid bearings enable high-load carrying capacity with large direct stiffness, accuracy of positioning, low friction and long life. These properties make them attractive for applications to reactor coolant pumps and precision grinder spindles. Further improvements of the rotor-bearing stability using active lubricated multirecess bearings are discussed in [36], using the same industrial gas compressor. In the special case of multirecess journal bearings, an increase of the supply pressure will necessarily lead to a simultaneous increase of the stiffness coefficients of the bearing. By increasing the stiffness of the bearings, only small relative movements between compressor shaft and bearing housing will be allowed in those nodes. This will deteriorate the capability of dissipation of vibration energy by squeezing the oil film in the bearings and will reduce the damping ratio. From the viewpoint of active lubrication applied to multirecess journal bearings with the aim of controlling lateral dynamics of flexible rotors a paradigm is reached: (a) for improving the performance of the active lubrication in such special type of bearings high values of supply pressure are needed, once the saturation of the control signals retrofitted to the servo valves limits the range in which the bearing dynamics coefficients can be modified. Nevertheless, by increasing the supply pressure the main stiffness coefficients of the bearing will also increase; (b) for reducing lateral vibrations of the flexible rotating machine it is very important to allow relative large displacements in the bearings, in order to increase the dissipation of vibration energy by squeezing the oil film. It means that it is important to keep low values of the main stiffness coefficients, which coerces into working with low values of supply pressure. With low supply pressures the efficiency of the active lubrication will be significantly reduced.

Active Lubricated Plain Bearings of Reciprocating Machines – The feasibility of applying active lubrication techniques to reciprocating machines with different sizes are investigated in [6, 7]on the system size, servo valves can be substituted by piezo-injectors in order to obtain more compact systems. Increasing the oil film thickness and reducing the rotor orbits inside of the bearings can lead to a significant reduction of friction and vibrations.

8 Concluding Remarks

One of the main advantages of incorporating the control gains inside of the modified Reynolds equation and obtaining the bearing coefficients using the perturbation technique is the feasibility of elaborating “Journal Bearing Tables" in the same way as presented in [16, 38], but with the fundamental difference that supply pressure and control gains become part of such tables. The integration of mechanics, electronics and informatics (mechatronics) allows designers to overcome the limitations of bearing dynamic coefficients by introducing new design variables.

The feasibility of compensating cross-coupling stiffness and increasing of direct damping in multi-recess journal bearings is only one of many challenges that can be overcome using controllable oil film bearings.

It is important to highlight that the required high precision calibration of the active oil film forces is a very challenging problem and, if overcame, will make feasible the utilization of such bearings as calibrated shakers, opening new possibilities of dynamic testing of rotating machines “on site" via their controllable oil film bearings.

References

1. Adiletta, G., Pietra, L.D.: The squeeze film damper over four decades of investigations. Part II: Rotordynamic analyses with rigid and flexible rotors. Shock Vibr. Digest **32**(2), 97–127 (2002)
2. Althaus, J.: Eine aktive hydraulische Lagerung für Rotorsysteme. Fortschritt-Berichte VDI, Series 11, N 154. VDI-Verlag, Germany (1991)
3. Bently, D.E., Grant, J.W., Hanifan, P.: Active controlled hydrostatic bearings for a new generation of machines. ASME/IGTI International Gas Turbine & Aeroengine Congress & Exhibition, Munich, May 8–11, 2000-GT-354 (2000)
4. Bently, D.E., Eldridge, T., Jensen, J., Mol, P.: Externally pressurized bearings allow rotor dynamic optmization. VDI-Berichte Nr. **1640**, 49–61 (2001)
5. El-Shafei, A., Hathout, J.P.: Development and control of hsfds for active control of rotor-bearing systems. ASME Trans. J. Eng. Gas Turbine Power **117**(4), 757–766 (1995)
6. Estupiñan, E.A., Santos, I.F.: Dynamic modeling of hermetic reciprocating compressors, combining multibody dynamics, finite elements method and fluid film lubrication. Int. J. Mech. **1**(4), 36–43 (2007)
7. Estupiñan, E.A., Santos, I.F.: Linking rigid multibody systems via controllable thin fluid films. Tribol. Int. **42**(10), 1478–1486 (2009)
8. Goodwin, M.J., Boroomand, T., Hooke, C.J.: Variable impedance hydrodynamic journal bearings for controlling flexible rotor vibrations. 12th Biennial ASME Conference on Vibration and Noise, Montreal, Canada, Sept 17–21: 261–267 (1989)
9. Haugaard, M.A., Santos, I.F.: Flexibility effects in tilting pad journal bearings with radial oil injection. 7th European Conference on Structural Dynamics, The Institute of Sound and Vibration Research, University of Southampton, England, Ref.E187: 1–10 (2008)
10. Haugaard, M.A., Santos, I.F.: Flexibility effects in tilting pad journal bearings with controllable radial oil injection. 13th Nordic Symposium on Tribology, Tampere, Finland, NT2008-43-4, ISBN 978-952-15-1959-8 (2008)
11. Haugaard, M.A., Santos, I.F.: Elastohydrodynamics applied to active tilting-pad journal bearings. ASME Trans J. Tribol. **132**(2), (2010), In Press (submitted)
12. Heshmat, H., Ming-Chen, H., Walton II, J.F.: On the performance of hybrid foil-magnetic bearings. ASME Trans J. Eng. Gas Turbines Power **122**(1), 73–81 (2000)
13. Jung, C.S., Choi, S.B.: Analysis of a short squeeze film damper operating with electrorheological fluids. STLE Tribol. Trans. **38**(4), 857–862 (1995)
14. Kjølhede, K., Santos, I.F.: Experimental contribution to high precision characterization of magnetic forces in active magnetic bearings. ASME Trans. J. Eng. Gas Turbine Power **129**(2), 505–510 (2007)
15. Krodkiewski, J.M., Sun, L.: Modelling of multi-bearing rotor system incorporating an active journal bearing. J. Sound Vibr. **210**(1), 215–229 (1998)
16. Lund, J.W., Thomsen, K.K.: (1978) A calculation method and data for the dynamic coefficients of oil lubricated journal bearings. In: Rhode, S.M., Allaire, P.E., Maday, C.J. (eds.) Topics in Fluid Film Bearings and Rotor Bearing System Design and Optimization, pp. 1–28. ASME, New York
17. Morishita, S., Mitsui, J.: Controllable squeeze film damper: an application of electrorheological fluid. Rotat. Mach. Vehicle Dyn. ASME DE-Vol. **35**(2), 257–262 (1991)

18. Nikolajsen, J.L., Hoque, M.S.: An electroviscous damper. Proceedings of Workshop on Rotordynamic Instability Problems i High Performance Turbomachinery, NASA Conference Publication, #3026 (1988)
19. Nicoletti, R., Santos, I.F.: Linear and non-linear control techniques applied to actively lubricated journal bearings. J. Sound Vibr. **260**(5), 927–947 (2003)
20. Nicoletti, R., Santos, I.F.: Frequency response analysis of an actively lubricated rotor/tilting-pad bearing system. ASME Trans. J. Eng. Gas Turbine Power **127**(3), 638–645 (2005)
21. Nicoletti, R., Santos, I.F.: Control system design for flexible rotors supported by actively lubricated bearings. J. Vibr. Control **14**(3), 347–374 (2008)
22. Osman, T.A., Nada, G.S., Safar, Z.S.: Static and dynamic characteristics of magnetised journal bearings lubricated with ferrofluid. Tribol. Int. **34**(6), 369–380 (2001)
23. Palazzolo, A.B., Lin, R.R., Alexander, R.M., Kascak, A.F., Montague, G.: Test and theory for piezoelectric actuator – active vibration control of rotating machinery. ASME Trans. J. Vibr. Acoust. **113**(2), 167–175 (1991)
24. Pietra, L.D., Adiletta, G.: The squeeze film damper over four decades of investigations. Part I: Characteristics and operating features. Shock Vibr. Digest **34**(1), 3–27 (2002)
25. Santos, I.F.: Aktive Kippsegmentlagerung – Theorie und Experiment. VDI – Fortschritt-Berichte; Reihe 11: Schwingungstechnik, N 189. VDI Verlag, Düsseldorf, Germany (1993)
26. Santos, I.F.: Design and evaluation of two types of active tilting pad journal bearings. In: Burrows, C.R., Keogh, P.S. (eds.) The Active Control of Vibration, pp. 79–87. Mechanical Engineering Publications Limited, London, England. ISBN 0-85298-916-4 (1993)
27. Santos, I.F.: Strategien für die Erhöhung der Dämpfungsreserve von kippsegmentgelagerten Rotorsystemen". In: Irretier, H., Nordmann, R., Springer, H. (eds.) (trans: Strategies for increasing the damping properties of rotating systems supported by tilting-pad bearings) Schwingungen in rotierenden Maschinen, vol. 3, pp. 3–12. Vieweg Verlag, Braunschweig, Germany, ISBN 3-528-06655-5 (1995)
28. Santos, I.F.: Aktive Schmierung zur Regelung von Rotorsystemen. *Schwingungen in Rotierenden Maschinen*. In: Irretier, H., Nordmann, R. (eds.) (trans: Active Lubrication for Controlling Rotating Systems), vol. 4, pp. 37–47. Springer, Braunshweig, Germany, ISBN 3-528-06908-2 (1997)
29. Santos, I.F., Russo, F.H.: Tilting-pad journal bearings with electronic radial oil injection. ASME Trans. J. Tribol. **120**(3), 583–594 (1998)
30. Santos, I.F., Scalabrin, A., Nicoletti, R.: Beitrag zur aktiven Schmierungstheorie. Schwingungen in Rotierenden Maschinen. In: Irretier, H., Nordmann, R. (eds.) (trans: Contribution to Active Lubrication Theory), vol. 5, pp. 21–30. Springer, Braunshweig, Germany, ISBN 3-528-03938-8 (2001)
31. Santos, I.F., Ulbrich, H.: Zur Anwendung von Regelungskonzepten für aktive Kippsegmentlager, ZAMM – Zeitschrift für Angewandte Mathematik und Mechanik **73**(4), 241–244 (1993)
32. Santos, I.F., Scalabrin, A.: Control system design for active lubrication with theoretical and experimental examples. ASME Trans. J. Eng. Gas Turbine Power **125**, 75–80 (2003)
33. Santos, I.F., Watanabe, F.Y.: Feasibility of influencing the dynamic film coefficients of a multirecess journal bearing by means of active hybrid lubrication. J. Brazil. Soc. Mech. Sci. Eng. **25**(2), 154–163 (2003)
34. Santos, I.F., Watanabe, F.Y.: Compensation of cross-coupling stiffness and increase of direct damping in multirecess journal bearings using active hybrid lubrication – Part I: Theory. ASME Trans. J. Tribol. **126**(1), 146–155 (2004)
35. Santos, I.F., Nicoletti, R., Scalabrin, A.: Feasibility of applying active lubrication to reduce vibration in industrial compressors. ASME Trans. J. Eng. Gas Turbine Power **126**(4), 888–894 (2004)
36. Santos, I.F., Watanabe, F.Y.: Lateral dynamics and stability analysis of a gas compressor supported by hybrid and active lubricated multirecess journal bearing. J. Brazil. Soc. Mech. Sci. Eng. **28**(4), 486–496 (2006)
37. Schweitzer, G.: Magnetic bearings as a component of smart rotating machinery. Proceedings of 5th IFToMM International Conference on Rotor Dynamics, edited by Irretier H., Nordmann R., Springer H., Darmstadt University of Technology, Germany, pp. 3–15 (1998)

38. Someya, T.: Journal Bearing Data Book. Springer, Berlin (1989)
39. Sun, L., Krodkiewski, J.M.: Experimental investigation of dynamic properties of an active journal bearing. J. Sound Vibr. **230**, 1103–1117 (2000)
40. Tang, P., Palazzolo, A., Kascak, A., Montague, G., Li, W.: Combined piezoelectric-hydraulic actuator based active vibration control for rotordynamic system. ASME Trans. J. Vibr. Acoust. **117**(3), 285–293 (1995)
41. Ulbrich, H., Althaus, J.: Actuator design for rotor control, 12th Biennial ASME Conference on Vibration and Noise, Montreal, Canada: 17–22, Sept: 17–21 (1989)
42. Vance, J.M., Li, J.: Test results of a new damper seal for vibration reduction in turbomachinery. ASME Trans. J. Eng. Gas Turbines Power **118**(4), 843–846 (1996)
43. Vance, J.M., Ying, D.: Experimental measurements of actively controlled bearing damping with an electrorheological fluid. ASME Trans. J. Eng. Gas Turbines Power **122**(2), 337–344 (2000)
44. Vance, J.M., Ying, D., Nikolajsen, J.L.: Actively controlled bearing dampers for aircraft engine applications. ASME Trans. J. Eng. Gas Turbines Power **122**(3), 466–472 (2000)
45. Zhu, C., Robb, D.A., Ewins, D.J.: A variable stiffness squeeze film damper for passing through the critical speeds of rotors. Proceeding of IMAC-19: A Conference on Structure Dynamics, vol. 2, pp. 1264–1269 (2001)
46. Zhu, C., Robb, D.A., Ewins, D.J.: A magneto-rheological fluid squeeze film damper for rotor vibration control. Proceeding of SPIE's 9th Annual International Symposium on Smart Structures and Materials, vol. 4753, pp. I: 516–522 (2002)
47. Zhu, C., Robb, D.A., Ewins, D.J.: On-off control of rotor vibration by a disk-type magneto-rheological fluid damper. Proceeding of the 9th International Symposium on Transport Phenomena and Dynamics of Rotating Machinery, Honolulu, Hawaii, February, 10–14, pp. 1–7 (2002)

Developments in Fluid Film Bearing Technology

A. El-Shafei

Abstract This paper presents some new developments in Fluid Film Bearing (FFB) technology. The phenomena of oil whirl and oil whip leading to instability in FFB supported rotors; limit the performance of rotating machinery. This paper presents some new developments that affect the instability threshold, namely the positive effect of angular misalignment on the instability threshold and related design improvements in FFB design. In addition, the concept of an integrated FFB with active magnetic bearing (AMB) is discussed with implications on improving the stability threshold, and actively controlling FFBs.

Keywords Fluid film bearings · Instability · Stability threshold · Oil whirl · Oil whip · Stable bearing design · Journal bearings · Active Magnetic bearings

1 Introduction

Fluid film bearings are the main supporting elements for many heavy rotating machinery, including high-speed high performance rotating machinery. However, the performance of rotating machinery supported by fluid film bearings are limited by the instability threshold known as oil whirl and oil whip [1]. Even though this problem has been known for nearly a century now, yet it has attracted a lot of attention. Recently Gordan Kirk [2] posed the following two questions:

1. Are there any possibilities that the rotor system transgress the threshold speed?
2. Can the rotor operate above this threshold speed?

These two questions clearly presented by Kirk are always pondered by both fluid film bearing designers and rotating machinery designers. These two questions are the motivation for this paper and the author believes that some progress towards the answer to these two questions is made here.

A. El-Shafei
Department of Mechanical Design & Production, Faculty of Engineering,
Cairo University Giza 12316, Egypt
e-mail: elshafei@ritec-eg.com

K. Gupta (ed.), *IUTAM Symposium on Emerging Trends in Rotor Dynamics*,
IUTAM Bookseries 25, DOI 10.1007/978-94-007-0020-8_18,

This paper consists basically of three parts: Part I consists of some experimental and numerical results that illustrate the effect of angular misalignment on the performance of fluid film bearings; Part II presents some possible design changes to fluid film bearings; Part III introduces the concept of an integrated fluid film bearing (FFB) and active magnetic bearing (AMB) to actively control the instability.

2 Experimental and Numerical Investigation of Misalignment

2.1 Experiments with Coupling Misalignment

While conducting some experiments on oil whirl and oil whip [3], the author and his students noticed a major effect of misalignment on the instability threshold.

The test rig which consists of a one-inch diameter rotor supporting four discs as shown in Fig. 1, and supported by two plain journal bearings was used to determine the stability threshold. The rotor was driven by an electric motor through a flexible coupling. The rotor vibration was measured by proximity probes connected to a Bently Nevada DVF-3 Tracking Filter and a Brüel and Kjaer 2515 Spectrum Analyzer.

Before starting the experiments, the rotor was first adequately balanced at the first and second critical speeds. This was a little bit difficult due to the unusual rotor configuration chosen, where three disks are overhung, and only one disk is located between the bearings. However, adequate balancing for both of the first and second modes was achieved, as shown in Fig. 2, and this balance condition was maintained throughout the experiments, except where an unbalance was purposefully introduced.

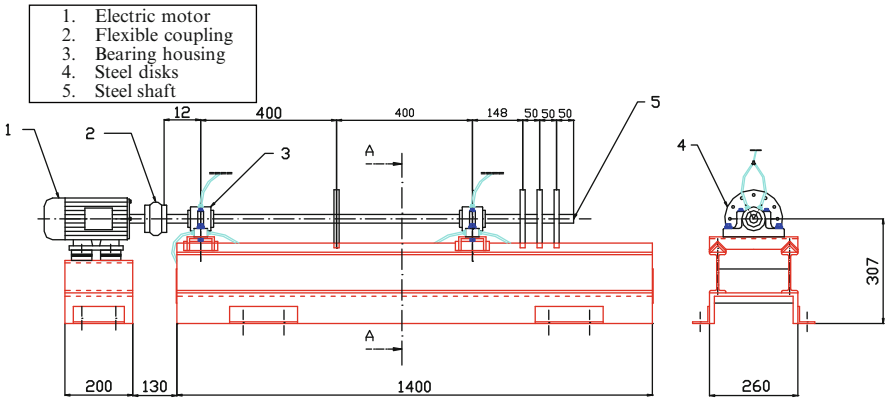

Fig. 1 Test rig

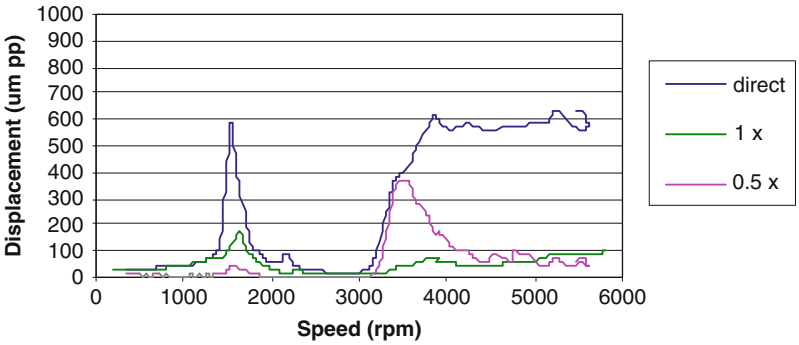

Fig. 2 Tracking data, case 1

Also before starting the experiments, the coupling connecting the drive motor to the test rig was aligned by the reverse indicator method to a parallel tolerance of 0.1 mm and an angular tolerance of 0.08°. Again, these alignment tolerances were maintained throughout the experiments, except where an angular or offset misalignment was purposefully introduced.

2.1.1 Data

Before venturing into presenting the data and explaining the results, it is appropriate to re-iterate the known definitions of oil whirl and oil whip [4]. Oil whirl is a form of instability (less severe) that occurs at little less than half the running speed ($0.49x$ in this case), which leads to the more violent oil whip when the oil whirl frequency coincides with the first critical speed [4]. The main difference lies in the fact that oil whirl is speed dependent ($0.49x$ in this case), while oil whip locks up at the first critical speed even though the rotor speed is increasing [4]. Thus, tracking the $0.49x$ component will show only the oil whirl, as well as tracking the $1x$ component will show only the usual Bodé plot with evidence of critical speeds. Plotting of the direct (unfiltered) vibration with speed will illustrate the total vibration activity measured at that location. Instead of presenting waterfall plots, which are usually used to present such experimental results, where it is sometimes difficult to extract information, presenting the results in this Bodé format, tracking different components, was chosen.

Capabilities of the measurement system were exploited, in which the DVF-3 can provide the $1x$ filtered data (showing the critical speed activity), $0.5x$ filtered (showing the oil whirl activity), as well as the direct unfiltered vibration with the speed change. A large filter bandwidth (120 cpm) for the $0.5x$ filtered data was chosen since the oil whirl in the test rig occurred at $0.49x$. Thus, filter bandwidth should be enough to capture all oil whirl activity. The direct unfiltered data contains all the spectral information. An increase in the direct vibration data that cannot be explained by either the $1x$ or $0.5x$ vibration is an indication of some other phenomena.

Since the DVF-3 cannot track a particular speed component (the first critical for oil whip), we used the direct unfiltered data as an indication of oil whip. Thus if the direct unfiltered data increased with no corresponding increase of the $0.5x$ or $1x$ components, then this is an indication of oil whip. This was confirmed by spectral plots, where the main vibration component while the rotor was operating at a high speed, was at the first critical speed and its multiples. An exception occurred while crossing the first critical speed (see, e.g., Fig. 2). Since this is transient data, and the first mode is lightly damped, the $1x$ vibration levels increased sharply, but actually the DVF-3 could not capture all the $1x$ activity in the filtered $1x$ display during fast critical speed crossing. However, the direct measurement does not have this shortcoming. Thus, only at the first critical speed, the high direct vibration is actually all $1x$.

2.1.2 Case 1

The first case to be considered is the case of a well balanced and aligned rotor, with the oil supplied at a pressure of 4 bar. Tracking data for the horizontal (x) probe are shown in Fig. 2. It can be seen that the first critical speed occurs at 1,638 rpm, while the measured second critical speed is split 3,920 rpm at the horizontal (x) probe, and 4,095 rpm at the vertical (y) probe. The onset of instability (increase of 0.5x component) was at 3,164 rpm. One can notice that the 0.5x component decreases at about 4,400 rpm, while the direct vibration is still high, indicating the persistence of oil whip. This can be seen in the spectral plot of Fig. 3.

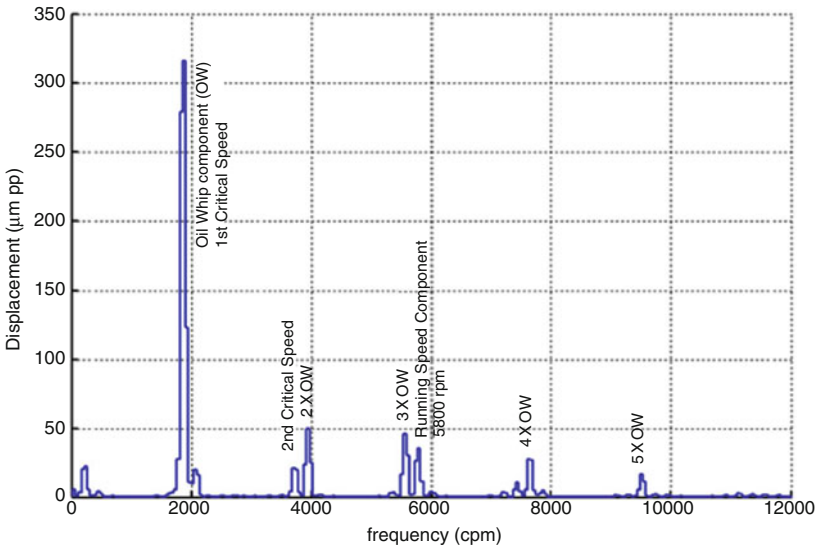

Fig. 3 Spectral data (speed 5,800 rpm), case 1

2.1.3 Case 2

Case 2 is similar to case 1, but with offset misalignment. Figure 4 shows the tracking data, with 1.85 mm offset misalignment at the coupling. The onset of instability was delayed to 3,885 rpm. The oil whirl component was obviously benign, but the oil whip became dominant at higher speeds.

2.1.4 Case 3

Case 3 is similar to case 1, but with angular misalignment. Figure 5 shows tracking data with 1° angular misalignment at the coupling. This is the most interesting case. With angular misalignment, the drive side bearing has only benign subharmonic vibration. The rotor has its smoothest behavior in this case.

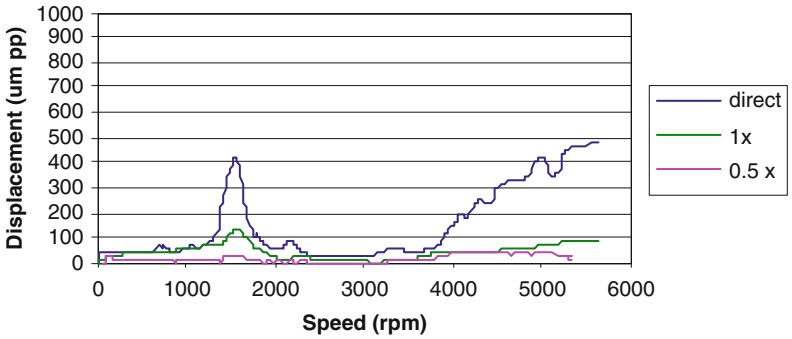

Fig. 4 Tracking data, case 2

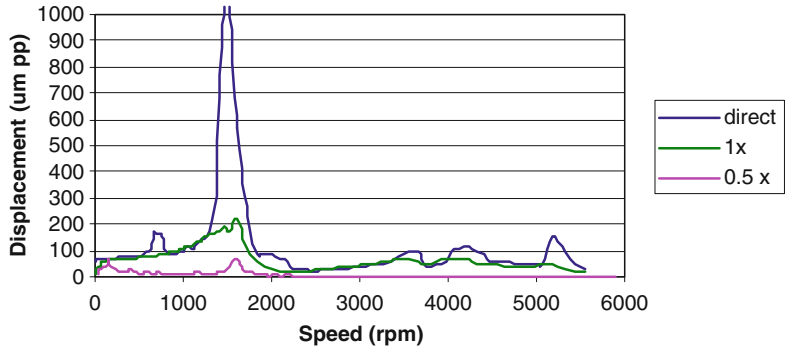

Fig. 5 Tracking data, case 3

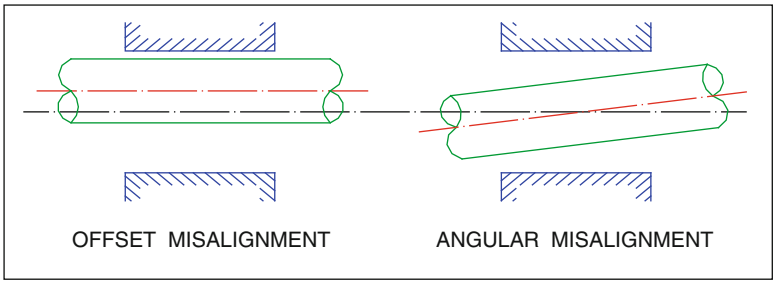

Fig. 6 Offset and angular misalignment

2.1.5 Discussion

The systematic experiments presented herein, clearly show the effect of offset misalignment and angular misalignment. These experiments clearly separate the effect of each of these conditions on bearing instability independently of each other.

The journal bearing instability is usually explained by the cross-coupled stiffness effect in the journal bearing. It is well-known that loading the bearings can improve stability characteristics of the rotor-bearing system. Bearing loading affects the stiffness characteristics of the bearing, thus increasing the threshold of instability. Bearing loading is usually taken to mean an increase in the bearing static eccentricity. This fact has led many investigators to consider offset misalignment as a means of loading bearings. Actually, in practice, this has become a common procedure to load bearings and improve stability. As an example, most vertical pumps manufacturers use the middle of three bearings to load the bearings and increase the stability threshold.

The bearing loading through static eccentricity is quite similar to the effect of offset misalignment, case 2. The separation of angular misalignment, case 3, from the offset misalignment in the presented experiments actually provides insight on their respective behavior. The difference between offset and angular misalignment is clearly illustrated in Fig. 6. Actually, the presented experimental results clearly show that angular misalignment is much more effective than offset (or parallel) misalignment in improving the stability characteristics.

2.2 Numerical Results for Bearing Misalignment

The author and his team further tried to understand these experimental results, by developing a 2D finite difference program to numerically evaluate the dynamic characteristics of journal bearings [5]. It was found that there are a total of 16 stiffness and 16 damping coefficients considering horizontal and vertical displacements and rotations. The variation of these coefficients with journal tilting (angular misalignment) is shown in Figs. 7 to 10, [5].

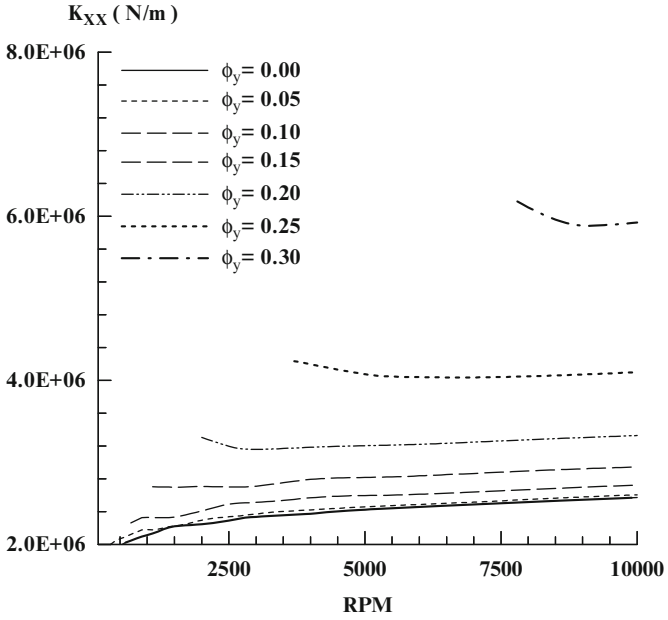

Fig. 7 Effect of varying ϕ_y on K_{xx}

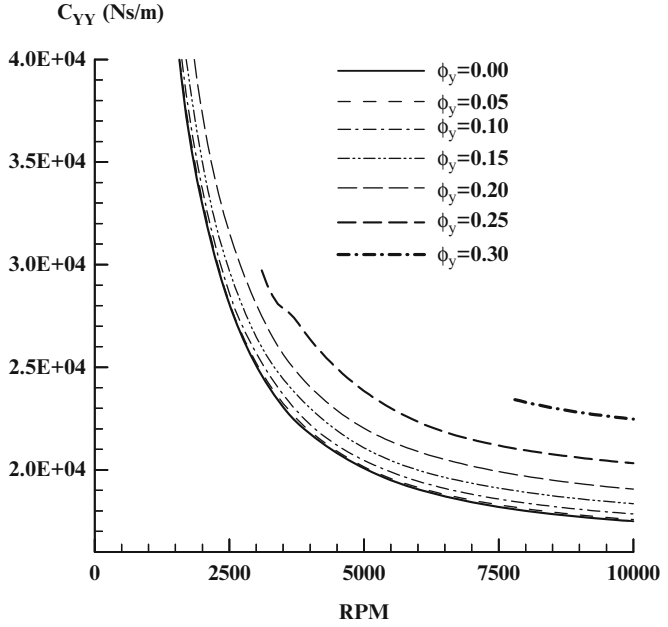

Fig. 8 Effect of varying ϕ_y on C_{yy}

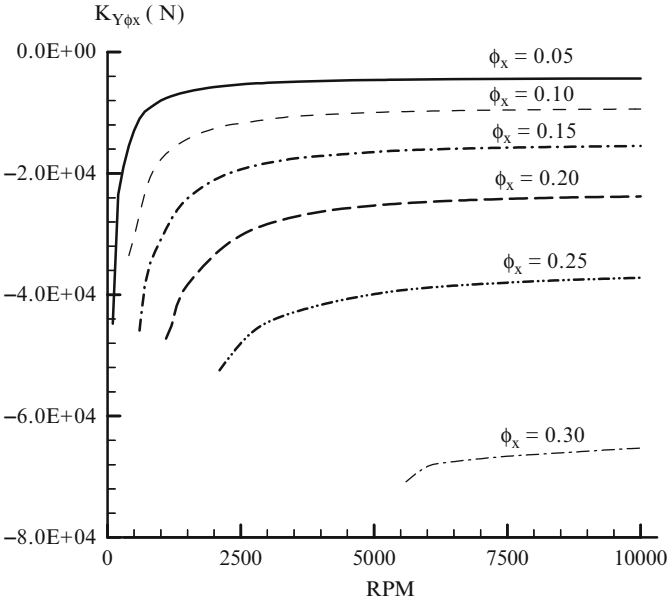

Fig. 9 Effect of varying ϕ_x on $K_{Y\phi x}$

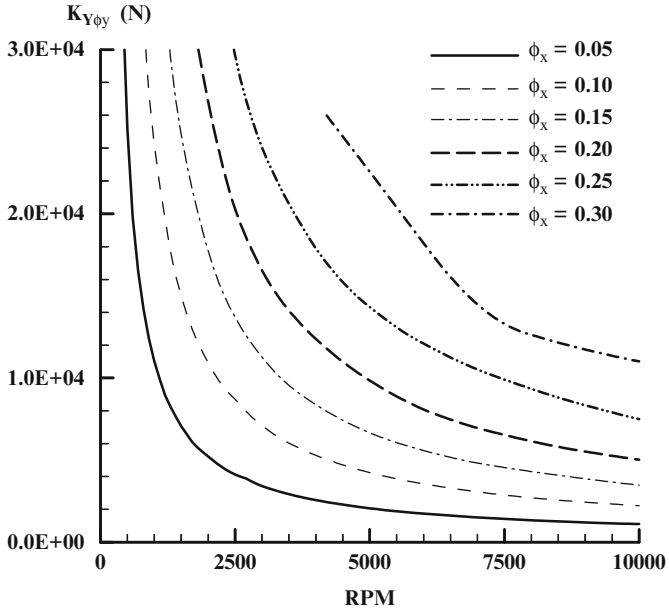

Fig. 10 Effect of varying ϕ_x on $K_{Y\phi y}$

Figure 7 illustrates the effect of varying ϕ_x and ϕ_y (the journal tilting about the x and y-axes) on the dominant K_{xx}, which can be seen to be considerable: a misalignment angle of 0.30 degrees results in a considerable increase in stiffness while Fig. 8 shows that the damping coefficient C_{yy} also increases considerably with ϕ_{yy}.

More importantly, the angular misalignment introduces substantial forces due to tilting. Figures 9 and 10 illustrate the introduction of considerable stiffness force coefficients $K_{Y\phi x}$ and $K_{Y\phi y}$ of the order of 10 kN/rad even for small tilting of 0.2 degrees [5]. Even though the moment coefficients introduced are much smaller that the force coefficients, however the large values for the force coefficients resulting from tilting should be considered by designers, as these force coefficients due to misalignment are comparable to the force coefficients due to displacements.

2.3 Experiments with Bearing Misalignment

The author decided to expand his investigation further. The experiments presented in Sect. 2.1 illustrated the effect of coupling misalignment on the instability threshold. The author and his team continued experimentation on bearing misalignment. By directly introducing the angular misalignment at the bearings [6], it was possible to investigate the effect of bearing misalignment on the instability threshold. However, to remove any coupling stiffness effect, the authors removed the flexible coupling and replaced it with a hose (see Fig. 11), and the motor-rotor alignment was maintained within tolerance. Three sets of experiments were conducted on the test rig of Fig. 1, with three different configurations as shown in Table 1. The first

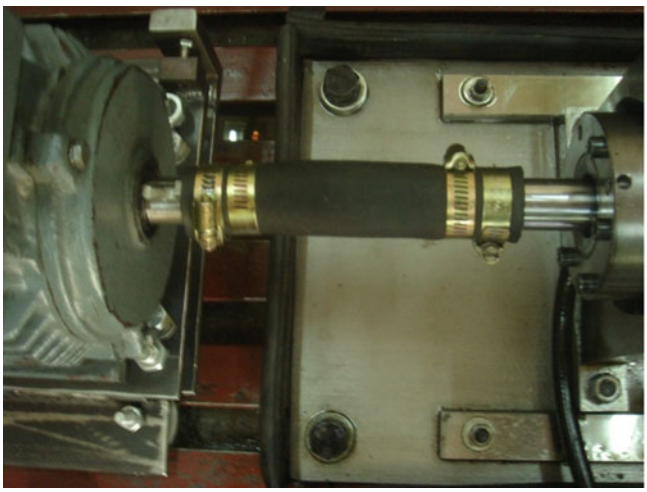

Fig. 11 Flexible coupling

Table 1 Matrix of experiments

Case	DE		NDE		Configuration
	Angle (deg)	Onset of instability (rpm)	Angle (deg)	Onset of instability (rpm)	
1	0.05	3,200	0.05	3,200	Aligned
2	0.27	3,200	0.26	3,200	Reflected
3	0.28	4,500	0.25	4,500	Parallel

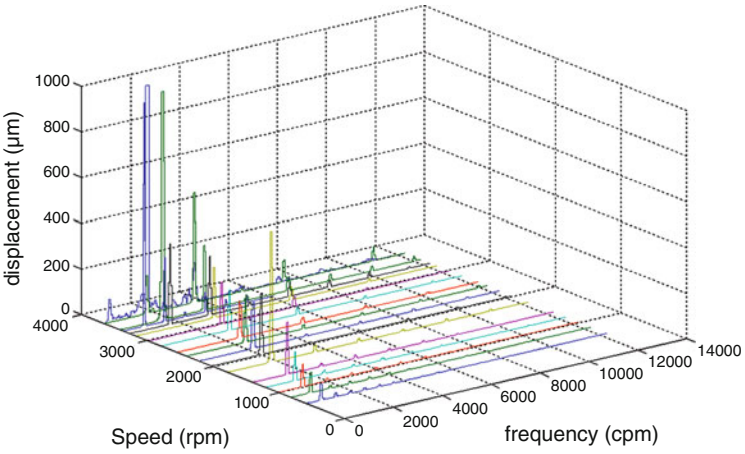

Fig. 12 Case 1 Waterfall spectrum of NDEB

set of experiments was done with aligned bearings and the onset of instability was at 3,200 rpm. The waterfall plot for the non-drive-end bearing for this case is shown in Fig. 12 illustrating the onset of instability. The second set of experiments was done with about 0.25° angular misalignment introduced at the bearings but the drive-end bearing and the non-drive-end bearing were misaligned in opposite directions. The onset of instability stayed at the same speed at 3,200 rpm. The waterfall plot for the non drive-end bearing for this case is shown in Fig. 13 illustrating the onset of instability. This case is called reflected bearing misalignment.

However, the most interesting result was obtained when, a third set of experiments were conducted, again with a 0.25° angular misalignment was introduced at the bearings, but the drive-end bearing and the non-drive-end bearing were misaligned in the same direction. This case is called parallel bearing misalignment in Table 1. The onset of instability was increased to 4,500 rpm. This is shown in Fig. 14, where the waterfall plots at the non-drive-end bearing clearly illustrates the onset of instability. This means that a 0.25° angular misalignment judiciously introduced at the bearings resulted in about a 50% increase in the stability threshold.

The above experiments conclusively illustrate that bearing angular misalignment actually improves the performance of fluid film bearings regarding the onset of instability. In addition it is clearly seen that the angular misalignment introduced interacts

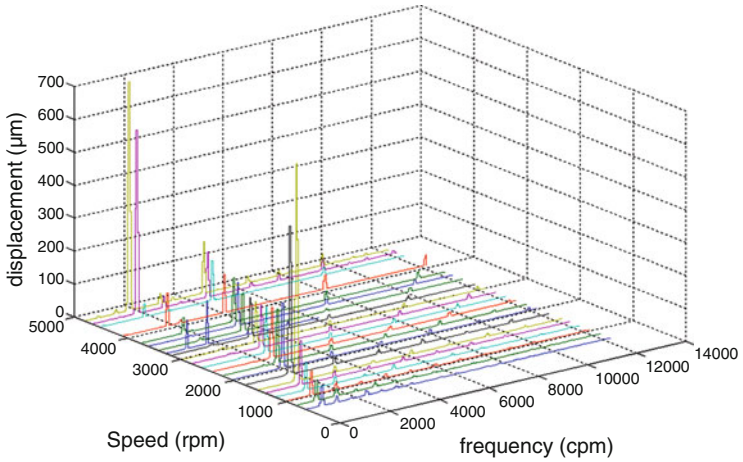

Fig. 13 Case 2 Waterfall spectrum of NDEB

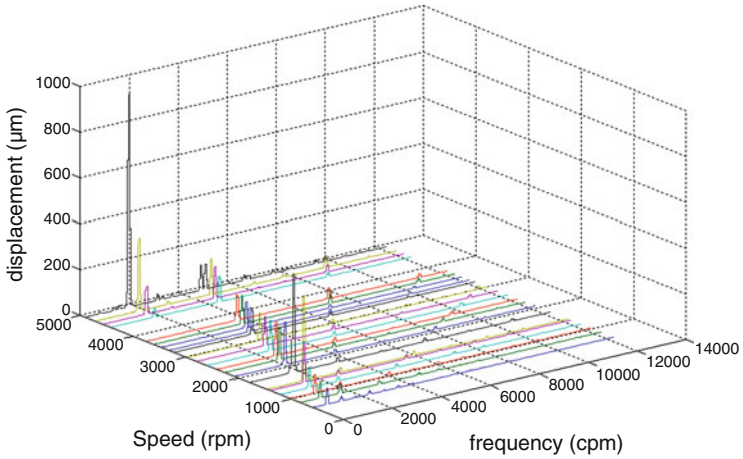

Fig. 14 Case 3 Waterfall spectrum of NDEB

with both the rotor configuration and the dynamical mode shape of the rotor, as the difference between the reflected and parallel bearing misalignment case results clearly illustrate.

The author believes that many more experiments with many more rotor//bearing configurations should be conducted to clearly understand this phenomenon, and also understand the side effects of misalignment of bearing wear and heat generated, if any.

3 Possible New Bearing Designs

Although much more work is needed to further understand the design implications of the above experiments, however the author wishes to provide an explanation for the above results. At this stage this is a conjecture rather than a theory.

In fluid film bearing design, the introduction of disturbance of the flow and pressure fields in the circumferential direction resulted in progressively better onset of instability in journal bearings through the introduction of lemon-bore bearings, pressure-dam bearings, multi-lobe bearings and finally the tilting pad bearings. However, the above experiments clearly show that by introducing angular misalignment at the bearings, this produces a significantly improved onset of instability performance.

The author thus conjures that with angular misalignment, a disturbance in the axial direction is introduced for the velocity and pressure fields resulting in this improved onset of instability. This means that by introducing a tilted pressure-dam bearing (Fig. 15), or a multi lobe bearing with tilted centers of curvature (Fig. 16), or any similar disturbance [7] can lead to an even progressively better performance of FFBs regarding the onset of instability.

The above points have to be clarified further. The author believes that by judiciously introducing a misalignment in bearings and exploiting the modal characteristics of the rotor it is possible to design fluid film bearings that can transgress the stability threshold. This requires much more work to better understand the characteristics of the instability in FFBs and the interaction of the fluid film forces with the rotor modal behavior, and the role the coupling stiffness plays in controlling the

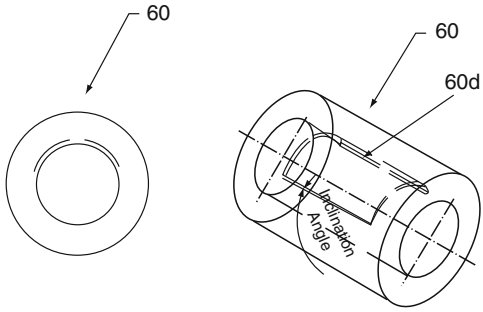

Fig. 15 Tilted pressure-dam bearing

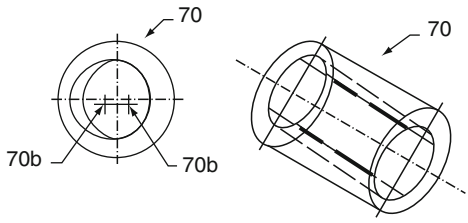

Fig. 16 Multi-lobe bearing with tilted centers of curvature

instability. The author believes that a lot more work is needed to understand these implications and a major test effort is planned by the author and his colleagues to demystify the instability problem and to clearly answer Gordon Kirk's questions introduced at the beginning of the paper. In particular we have shown here that the rotor can actually transgress the stability threshold and clearly can operate above the stability threshold by simply introducing a tilting axial disturbance in the bearing.

4 Integrated Journal and Active Magnetic Bearing

This section is about a new concept [8, 9] in load carrying and control of rotating machinery. Journal Bearings (JBs) and Active Magnetic Bearings (AMBs) are both excellent bearings for high performance rotating machinery. Actually, JBs and AMBs are two competing bearings in many markets. Both bearings' manufacturers promote their own technology. JB manufacturers promote the large load carrying capacity and high damping in JBs, while AMB manufacturers promote the controllability of the rotor system and the elimination of oil supply. However, both bearings also have their limitations. JBs are limited by the instability mechanism known as oil whirl and oil whip [2, 3], while AMBs have lower load capacity and tend to be larger for the same load.

Thus it seems natural to try to combine both bearings in a single bearing concept, where the superior load carrying capacity of JBs are to be exploited along with the controllability characteristics of AMBs that can be used to control the instability of JBs. This will result in a bearing concept with high load carrying capacity with controlled instability, and a smaller magnetic bearing that is not carrying any static load while providing the required control [9].

The author with one of his students investigated this possibility [8]. By studying an integrated JB/AMB on a Jeffcott rotor, the authors were able to show the instability of the JB (see Fig. 17) and by introducing an AMB the authors investigated three control algorithms. They were all effective, however the most efficient was with damping control (see Fig. 18).

Comparing Figs. 17 and 18, it is clearly seen that the damping controller of the integrated JB/AMB was able to eliminate the instability and allowed the rotor to operate well above the instability limit smoothly. Actually, the reduction of the orbit size at the disc location with the damping controller was 90%.

Thus the basic idea here is quite simple: rather than using the AMB as a load carrying element, the AMB is used as a controller only, resulting in a much smaller and more efficient AMB. The load carrying is done by the Journal bearings, exploiting their excellent load carrying capabilities, and the JB instability is overcome with the AMB. This results in a combined AMB/JB that exploits the advantages of each device, and eliminates the deficiencies of each bearing. The combined AMB/JB system can thus be used to carry larger loads and operate at higher speeds. If the well known capabilities of AMB control are also added to the system such as unbalance cancellation and integrating feedback, a much improved device would be developed.

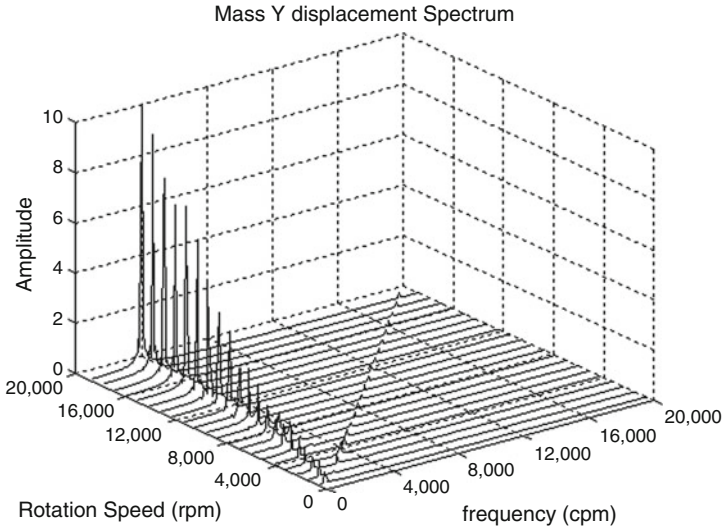

Fig. 17 Center disc "Y" displacement waterfall

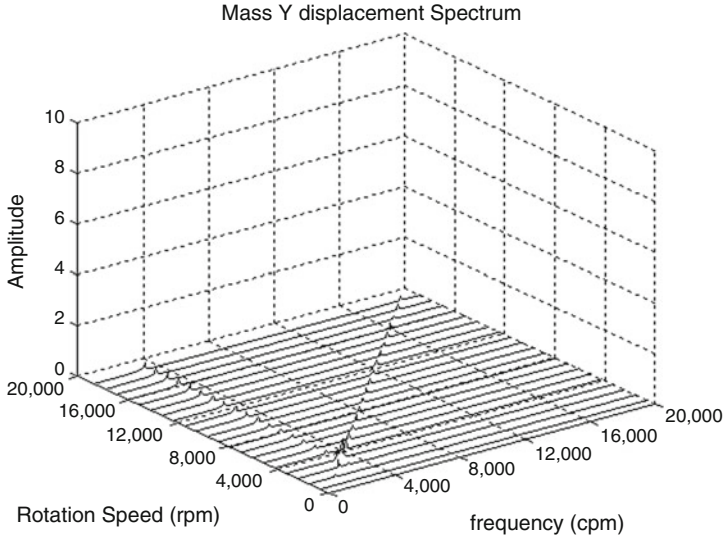

Fig. 18 Center disc "Y" displacement waterfall

5 Conclusion

This paper presented a variety of new developments in fluid film bearing technology. The basic questions posed by Prof. Kirk [2] were addressed, namely the possibility to transgress the instability in FFBs and the possibility to operate above the stability

threshold. The paper clearly presented experimental results that showed that the introduction of angular misalignment at the coupling significantly increases the speed of onset of instability, it also presented some numerical results illustrating the forces in misaligned bearings, as well as experimental results for misaligned bearings, and possible bearing designs considering axial disturbance.

Moreover the paper introduced the concept of an integrated JB/AMB and illustrated the possibility of transgressing the instability threshold effectively using a damping controller.

The above developments clearly illustrate that new FFB designs are possible that would provide better performance for high-speed high-load rotating machinery.

References

1. Newkirk, B.L., Taylor, H.D.: Shaft whipping due to oil action in journal bearings. Gen. Electr. Rev. 28, 559–568 (1925)
2. Guo, Z., Kirk, R.G.: Instability boundary for rotor-hydrodynamic bearing systems, Part I: Jeffcott rotor with external damping. ASME J. Vib. Acoust. 125(4), 417–422 (2003)
3. El-Shafei, A., Tawfick, S.H., Raafat, M.S., Aziz, G.M.: Some experiments on oil whirl and oil whip. ASME J. Eng. Gas Turb. Power 129(1), 144–153 (2007)
4. Muszynska, A.: Whirl and whip-rotor/bearing stability problems. J. Sound Vib. 110(3), 443–462 (1986)
5. Ahmed, A.M., El-Shafei, A.: Effect of misalignment on the characteristics of journal bearings. ASME J. Eng. Gas Turb. Power **130**(4), 042501-1–042501-8 (2008)
6. El-Shafei, A., Tawfick, S.H., Mokhtar, M.O.A.: Experimental investigation of the effect of misalignment on the instability of plain journal bearings. ASME/STLE 2009 International Joint Tribology Conference (IJTC2009) October 19–21, 2009, Memphis, Tennessee, USA, Paper no. IJTC2009-15057 pp. 171–173
7. El-Shafei, A.: Methods of controlling the instability in fluid film bearings, US patent application 11/147,762, publication US 2005-0275300 A1
8. El-Shafei, A., Dimitri, A.S.: Controlling journal bearing instability using active magnetic bearings. ASME J. Eng. Gas Turb. Power **132**(1), 012502-1-012502-9 (2010)
9. El-Shafei, A.: Methods of controlling the instability in fluid film bearings, US patent application 12/121,976, publication US 2008-0224556 A1

Numerical Model of the High Speed Rotors Supported on Variable Geometry Bearings

Zbigniew Kozanecki, Jan Kiciński, and Grzegorz Żywica

Abstract The reported investigations aim at developing the theoretical model of a bearing characterized by variable geometry. The method used for calculating the non-linear response to an arbitrary excitation takes into account factors characteristic of the variable bearing geometry, including friction in the supports. The article presents part of the study referring to numerical analyses oriented towards developing the model of a high-speed rotor supported on bump-foil or tilting pad bearings.

Keywords Foil bearings · Tilting pad bearings · High-speed bearings · Rotor dynamics

1 Introduction

The micro power system which is used in a small power source, of power output ranging between 1 and 20 kW, is based on the Brayton or Rankine cycle and consists of a turbine and a generator. The system requires high revolutions to generate sufficient power on the small-size turbine. The existing conventional oil-lubricated bearings reveal performance limits in these revolutions, especially when the stability of a bearing is taken into account. The development of new technologies, along with more and more common applications of non-conventional materials in machine design, provide opportunities for considering an idea to apply the working medium used in a small high-speed turbo-machine [8] as a lubricating medium for its bearings very realistic. As far as small high-speed turbo-generators are concerned, the application of bearings lubricated with a low-viscosity working medium (gas or liquid) makes it possible to increase total efficiency of the machine by several or

Z. Kozanecki (✉)
Technical University of Lodz, Wolczanska 219/223, 90-924 Lodz, Poland
e-mail: zkozan@p.lodz.pl

J. Kiciński and G. Żywica
Institute of Fluid-Flow Machinery PASci, Fiszera 14, 80-952 Gdansk, Poland

K. Gupta (ed.), *IUTAM Symposium on Emerging Trends in Rotor Dynamics*,
IUTAM Bookseries 25, DOI 10.1007/978-94-007-0020-8_19,

more percent via decreasing hydrodynamic friction losses. In machines in which the low-viscosity working gas or liquid is used, the application of hydrodynamic bearings lubricated by that working medium makes it possible:

- to increase total efficiency of the machine by several or more percent, which is done by decreasing friction losses in the bearings and by eliminating the oil system and seals connected with it;
- to simplify the design of the shaft and to reduce its length;
- to maintain absolute purity of the working medium;
- to build a "hermetic" machine without a rotating shaft end protruding outside the casing, to eliminate the mechanical gear and "working medium – atmosphere" seals in a high-frequency generator or motor integrated with the shaft.

A basic problem connected with practical application of non-conventional oil-free bearings in high-speed rotors is the reliability of machine operation in various working conditions. The materials used in such bearings have to secure:

- conditions for short, non-destructive contact of the rotating bearing journal with the bush during machine start-ups and shut-downs;
- low friction coefficient between the journal and the bush;
- corrosion resistance during the contact with the lubricating medium.

Therefore, while studying possible applications of non-conventional lubricating media, one should analyze thoroughly the dynamics of the "rotor-bearing-casing" system within the whole range of machine operation. Dynamic properties of the bearings are functions of numerous variables and their calculation may be troublesome. According to the linear theory, these properties are usually represented by a set of eight coupled dynamic coefficients, linearised around the static equilibrium position of the bearing. An assumption of small displacements of the shaft center in the closest vicinity of the equilibrium position makes it possible to simplify significantly the theoretical considerations. For the problem formulated in the above way it is necessary, however, to limit the scale of the excitation forces in order to fulfill the basic condition of small displacements around the equilibrium point. The absence of precise criteria defining the applicability range of the linear method often leads to serious errors in the dynamic analysis of the rotor-bearings system.

The development of so-called non-conventional bearings for high-speed rotors is connected with the fact that they can be often used where the application of well-known traditional bearings is not possible. The fixed geometry of the hydrodynamic bearings often leads to the unstable operation at a very high speed. A significant aspect of the bearing selected for the present investigations is to develop a theoretical model of the bearing characterized by non-rigid (compliant surface) or variable geometry. Figure 1 shows two typical designs of self-acting liquid or gas lubricated bearings characterized by variable geometry.

The two types of bearings can use gases or liquids as the working medium. Before analyzing the bearing dynamics it is necessary to find the static equilibrium position of the journal, in which the forces resulting from the pressure distribution

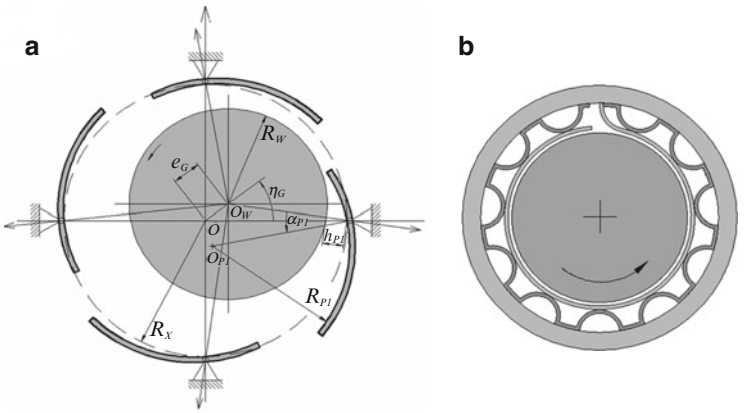

Fig. 1 Variable-geometry bearings selected for the investigation (**a**) – tilting pad bearing, (**b**) – bump foil bearing)

in the hydrodynamic (aerodynamic) film of the bearing balance the external static loading of the journal. Once the equilibrium position is found, the initial conditions for the dynamic part of the analysis are determined. The non-linear dynamic analysis of the bearings takes into account current forces existing in the film for any excitation applied, and examines the trajectory of the journal motion in such operating conditions. The above formulation of the problem requires simultaneous integration of the equations of motion for each titling pad or elastically supported bush in the bump-foil bearing and the bearing journal with the equations of pressure in the hydrodynamic film. The solution to this problem bases on the reverse problem of the dynamics of a particle, where the relations between the forces acting on the particle and the resulting motion are examined.

Thus, the solution to this problem is limited to determining the resultant force acting on the bearing journal and forces acting on each bearing titling pad or elastically supported foil at each time step. These forces are non-linear functions of the location and velocity of the journal, whose instantaneous values are used to solve the equations of motion.

The motion of tilting pads or an elastic bush generates friction forces in the elastic foil or the tilting shoe support. On the other hand, it is evident that the nature of tilting pad or elastically supported bush motion can dramatically affect dynamic characteristics of the bearing [3, 9, 10]. Therefore nonlinear modeling of dynamic properties of a variable-geometry bearing, including design characteristics of the support and the generated friction forces, becomes indispensable in high-speed bearing applications.

2 Gas Bearing Technology: Tilting Pad Bearing Model

Compressibility of the gas is an important factor which is to be taken into account in the analysis of various designs of gas bearings – of both aerodynamic and aerostatic (self-acting and externally pressurized) type. The advantages revealed by these bearings over liquid-lubricated bearings include:

- stability of the lubricant – no vaporization, cavitation, solidification, or decomposition under extreme temperatures (−260°C–1000°C),
- low friction (low viscosity), and practically no heating without contact [9, 10].

The titling pad bearing consists of independent titling pads coupled by the common mass m supported on the bearing. The calculations for an individual tilting pad are carried out in the local coordinate system, marked in Fig. 1 by the axes that connect the pivot points with the shaft center. The second, global coordinate system is immovable and is marked by the axis that connects the pivot point with the bearing center. It is assumed that the thickness of the gas film at the points of support h_{Pi} in both co-ordinate systems is the same. In order to carry out the analysis of the bearing dynamics it is necessary to find the static equilibrium position. In this shaft position the force being the geometric sum of force vectors in the films of the individual tilting pads balances the external static load of the journal. Once this position is found, the initial conditions for the dynamic part of the analysis are determined. Thus, the solution to this problem consists in determining the resultant force acting on the bearing journal and the moment acting on each bearing titling pad at each time step. These forces and moments are non-linear functions of journal location and velocity, the instantaneous values of which are used to solve the equations of motion, of the mass supported on the bearing, and of the titling pads of the bush. For the bearing with three tilting pads, assuming that the rotation of each tilting pad takes place around the axis parallel to the journal axis, the following set of differential equations should be solved at each time step:

$$\begin{array}{ll} m\ddot{x} = F_x(x, y, \dot{x}, \dot{y}, t) & J_1\ddot{\alpha_1} = MR_1(\alpha_1, \dot{\alpha}_1, x.y, \dot{x}, \dot{y}, t) \\ m\ddot{y} = F_y(x, y, \dot{x}, \dot{y}, t) & J_{i+1}\ddot{\alpha_{i+1}} = MR_{i+1}(\alpha_{i+1}, \dot{\alpha_{i+1}}, x.y, \dot{x}, \dot{y}, t) \\ & J_k\ddot{\alpha_k} = MR_k(\alpha_k, \dot{\alpha_k}, x.y, \dot{x}, \dot{y}, t) \end{array} \quad (1)$$

– journal and pad motion

$$\left\{ \begin{array}{l} \frac{\partial}{\partial\tau}(PH_1) + \Lambda\frac{\partial}{\partial\theta}(PH_1) - \frac{\partial}{\partial\theta}\left(PH_1^3\frac{\partial P}{\partial\theta}\right) - \frac{\partial}{\partial\varsigma}\left(PH_1^3\frac{\partial P}{\partial\xi}\right) = 0 \\ \frac{\partial}{\partial\tau}(PH_{i+1}) + \Lambda\frac{\partial}{\partial\theta}(PH_{i+1}) - \frac{\partial}{\partial\theta}\left(PH_{i+1}{}^3\frac{\partial P}{\partial\theta}\right) - \frac{\partial}{\partial\varsigma}\left(PH_{i+1}{}^3\frac{\partial P}{\partial\xi}\right) = 0 \\ \frac{\partial}{\partial\tau}(PH_k) + \Lambda\frac{\partial}{\partial\theta}(PH_k) - \frac{\partial}{\partial\theta}\left(PH_k^3\frac{\partial P}{\partial\theta}\right) - \frac{\partial}{\partial\varsigma}\left(PH_k^3\frac{\partial P}{\partial\xi}\right) = 0 \end{array} \right\} \quad (2)$$

– pressure distribution at each pad
where m– mass supported in the bearing, J_i – inertia of i th tilting pad, $\propto_i$ – tilting pad deflection amplitude, MR_i –tilting pad excitations,

$$\Lambda = \frac{6\mu\omega R^2}{p_a C^2},\ P = \frac{p}{p_a},\ H = \frac{h}{C},\ \tau = \frac{\omega t}{2\Lambda}$$

– compressibility number, dimensionless

A solution to the above mentioned equation set can be only obtained via numerical computations. Firstly, the examined bearing is loaded with static force components Fz_{XG} and Fz_{YG} acting along the X_G and Y_G axes of the global co-ordinate system. Forces in the bearing film balance this force, and the system is in equilibrium. At time $t = 0$, an additional arbitrary force, which can generally have a constant component and a variable component, is applied. In the global coordinate system, the following relations represent the components of the external force Fz that loads the bearing journal:

$$\left.\begin{aligned} Fz_{XG} &= F_{STXG} \\ Fz_{YG} &= F_{STYG} \end{aligned}\right\} \text{ at } t < 0 \text{ and}$$

$$\left.\begin{aligned} Fz_{XG} &= F_{STXG} + F_{OXG} + F_N \cos(\omega(t - t_O) + \phi_N) \\ Fz_{YG} &= F_{STYG} + F_{OYG} + F_N \sin(\omega(t - t_O) + \phi_N) \end{aligned}\right\} \text{ at } t \geq 0 \qquad (3)$$

where Fz_{XG}, Fz_{YG} – components of the external excitation at $t < 0$ and $t \geq 0$.

The titling pad bearing consists of three independent titling pads, coupled by the common mass m supported on the bearing. Figure 2 presents the design of a tilting pad gas bearing with various versions of a tilting shoe support.

Each design of the support adds a specific term to the pad motion equation. In order to present the effect of the pad support design on the bearing dynamic characteristics, two sample designs were selected, which were: the frictionless pivot (a) and the spherical pivot including simple Coulomb friction model (b). For each examined tilting pad, we integrate the equations of pressure, Eq. (2), with respect to time, substituting the new thickness distribution of the gas film $[H_{ij}]_I(t + \Delta t)$ resulting from the motion of the pads and the journal. After integrating the Eq. (2) for successive tilting pads we obtain instantaneous forces (F_{Xi}, F_{Yi}) resulting from the pressure in the bearing gap, and the moments M_{Ri} resulting from hydrodynamic pressure distribution which was the source of rotation of the tilting pad after Δt.

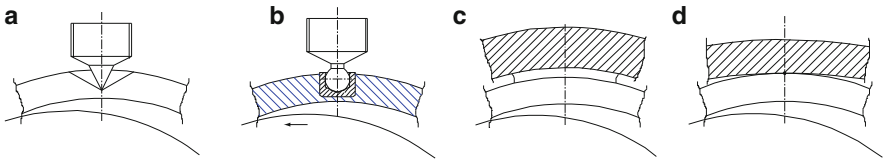

Fig. 2 Sample designs of pad supports in the high speed tilting pad bearing (**(a)** – frictionless pivot, **(b)** – spherical pivot including friction, **(c)** – elastomeric pivot, **(d)** – linear contact pivot)

$$\left.\begin{aligned} FX(t+\Delta t) &= \sum_{1}^{k} F_{Xi}(t+\Delta t)\cos((i-1)\,\gamma) \\ FY(t+\Delta t) &= \sum_{1}^{k} F_{Yi}(t+\Delta t)\sin((i-1)\,\gamma) \end{aligned}\right\} \tag{4}$$

– external excitations of the tilting pads

$$M_{Ri}(t+\Delta t) = \sum R_P\, F_{Yi}(t+\Delta t) + Mf_i \tag{5}$$

The above mentioned terms Mf_i in Eq. (5) are calculated when the friction model without hysteresis effects (Coulomb model) or that including the hysteresis effect is

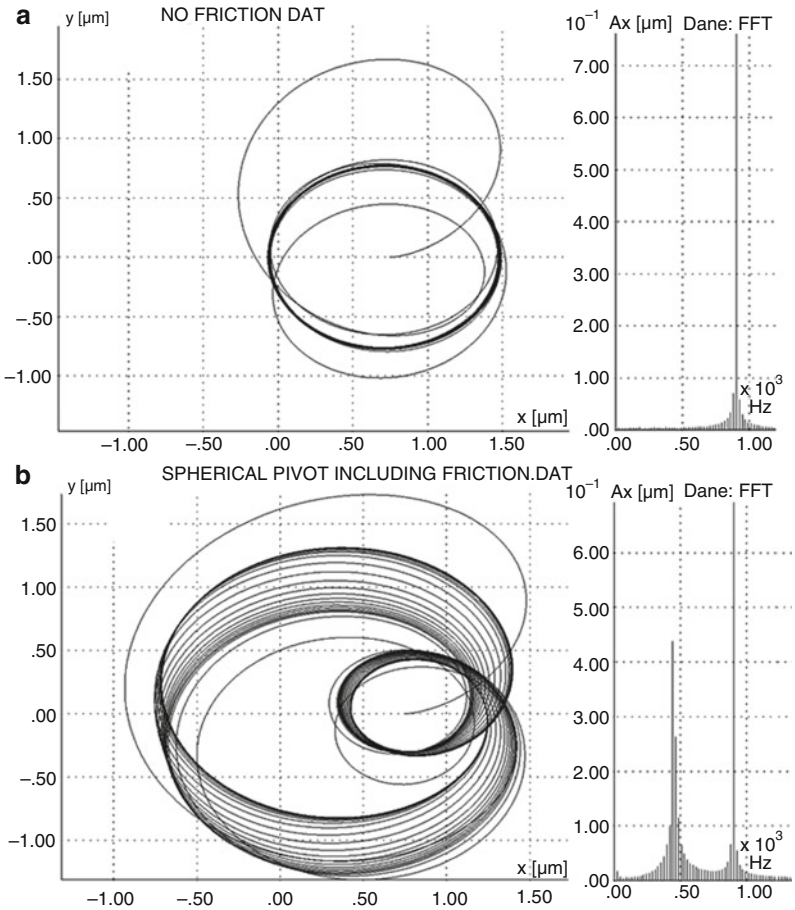

Fig. 3 Stable and unstable orbit of journal motion in the gas bearing with four ceramic pads. The journal motion is excited by the rotating synchronous force (**(a)** – frictionless pivot, **(b)** – spherical pivot including friction)

accounted for in the pad joints. A sample solution to the above equations is shown in Fig. 3 as a non-linear orbit of the journal moving in the gas bearing with four ceramic pads, and excited by the rotating synchronous force (i.e., unbalance force) at the speed of 54,000 rpm (900 Hz).

The bearing data are:
$k = 4$ (number of ceramic tilting pads)
$D = 20$ mm (journal diameter)
$L = 20$ mm (bearing length)
$C_P = 0.015$ mm (design radial clearance)
$N = 54{,}000$ rpm (rotational speed)
$\mu = 0.05$ (coefficient of the pivot friction)
$J_k = 0.122\,\text{gmm}^2$ (pad inertia)

These two presented cases refer to the same geometry of the ceramic pad bearing with frictionless pivots and with spherical pivot including Coulomb friction model. These sample results reveal crucial influence of the pad pivot design on the bearing dynamic characteristics. The calculation codes developed within the framework of those investigations were verified experimentally [10]. Good agreement between the results of the experimental investigations carried out on this machine and the theoretical results has been found.

3 Hydrodynamic Bearing Technology: Foil Bearing Model

Foil bearings have been known for many years but their modelling still faces considerable problems [1, 2]. These problems originate from the complicated structure of the bearings which, along with the elements known from classical designs of slide bearings, include a foil set (bump foil and top foil) being a key bearing component (Fig. 1). Properties of the foil set, along with those of the fluid film, determine dynamic properties of the rotor-bearing system in this type of bearing. It is obvious that modelling of foil bearings needs to take into account properties of the structural base, the lubricating film, and the interactions between them. Additionally, during the start-ups and shut-downs of the rotating machine, the journal and the top foil come into contact with each other. It is also noteworthy that the properties of materials used in the foil bearings depend on the operating temperature. Considering the above we can state that modelling the phenomena taking place in the foil bearings requires a complex thermal fluid-structure numerical analysis. The complexity of the above named problems can be a source of considerable differences between numerical calculations and experimental results [2, 4]. Nowadays, designing foil bearings requires expensive and time-consuming experiments. Reliable numerical models could make the design process easier and cheaper.

A procedure commonly used in foil bearing modelling is the following. The computer codes describing the fluid film are based on the Reynolds equation and make use of algorithms of the finite difference method or the finite volume method

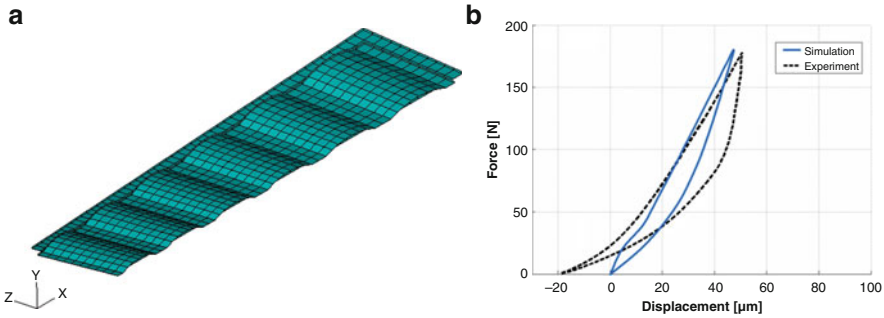

Fig. 4 Fragment of foil set ((**a**) – FEM model, (**b**) – results of verification)

[1,2,4,13]. The interaction of the foil set and the sleeve surface is usually simulated using the finite element method [2,12,13]. Some authors also propose to replace the compliant foil with a single stiffness-damping element [14]. The model of the entire foil bearing is a result of couplings between the fluid film and the compliant foil set model. Some references suggest the use of analytical formulas [11], which are significantly simplified, but in this way satisfactory results are often unattainable.

At the Institute of Fluid-Flow Machinery (IFEM) PASci in the first stage of modelling, a selected fragment of foil set was examined individually. This fragmentary model makes use of all techniques applied by authors in the final model of the entire foil bearing. Due to initial simplification of the model, quite an easy experimental verification was possible. That problem was the subject of an earlier publication [7].

The model of the structural base fragment, and the results of its verification are shown in Fig. 4, in which good conformity can be observed. A model of the structural base of the whole bearing sleeve was defined using the same modelling technique as those used for the partial model. Because of its relative small deformation, the bearing sleeve in final model was replaced with a cylindrical surface. Deformations of the foil set have a crucial impact on static and dynamic characteristics of the bearings. Therefore, a complete model of the foil set was defined in program ABAQUS [7]. Contact phenomena occurring between all bearing elements were taken into consideration. The friction coefficient was assumed equal to 0.1.

Figure 5 shows the defined model of the foil bearing structural base. This model made it possible to calculate the deformations of the top and bump foil set from pressure distributions in the bearing interspace. The dynamics of the rotor and pressure distributions inside the bearing were calculated using computer codes composing the MESWIR series [5,6], which have been worked out at IFFM PASci.

In the first step, the temperature of the fluid film was calculated using the code KINWR-D and the diathermal model of a hydrodynamic slide bearing. The temperature defines the absolute viscosity of the lubricant, a parameter which is used in the next steps of calculations. The pressure distribution in the fluid film was calculated using the code KINWIR-I-LEW, which makes use of the isothermal model. Next,

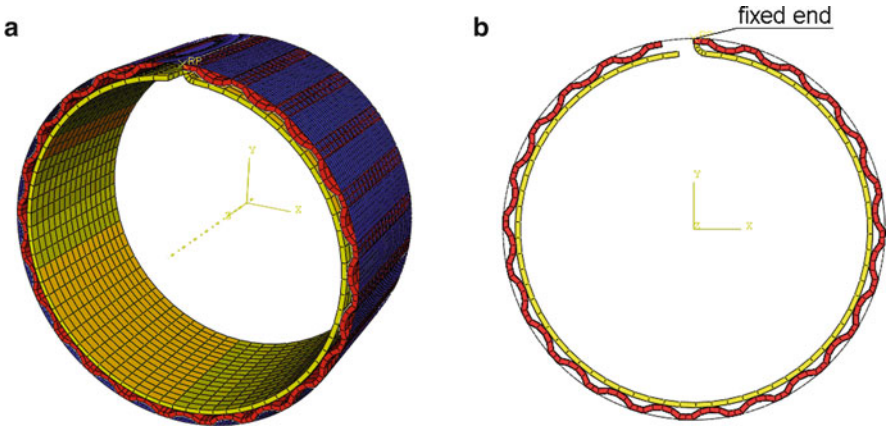

Fig. 5 FEM model of foil bearing structural base (**(a)** – isometric view, **(b)** – cross section)

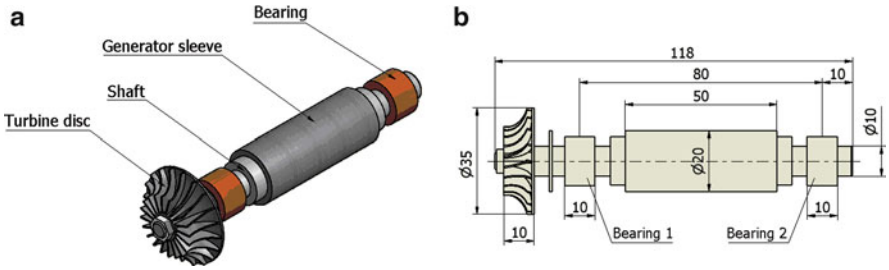

Fig. 6 Two-support shaft with two disc (**(a)** – isometric view, **(b)** – dimensions)

the pressure of the fluid film was distributed over the inner surface of the top foil. As a result of ABAQUS calculations, the modified shape of the foil set was obtained to reflect the film pressure distribution. The modified shape of the bearing interspace was introduced into the code NLDW-LEW-75-F, and the dynamic calculations of the whole rotor-bearing system were performed. In cases when condition changes were introduced (e.g., additional dynamic load appears), the shape of the foil set was determined once again, and the dynamic calculations were repeated. Using the above model of the foil bearing, the calculations for a selected rotor were performed. The dimensions of the examined rotor system are close to rotors in microturbines used in cogeneration plants. The object of investigation was a two-support shaft with two disc (a bladed disc and a generator), shown in Fig. 6.

The finite element model of the rotor-bearing system in code of MESWIR series consists of 24 Timoshenko beam elements. Sample results of calculations, having the form of relative journal-bush vibration curves are shown in Fig. 7.

Properties of the lubrication fluid were assumed for a selected low-boiling medium. The results of calculations reveal that for the analysed rotor-bearing system we can reach high rotational speed. Unfortunately, within some ranges

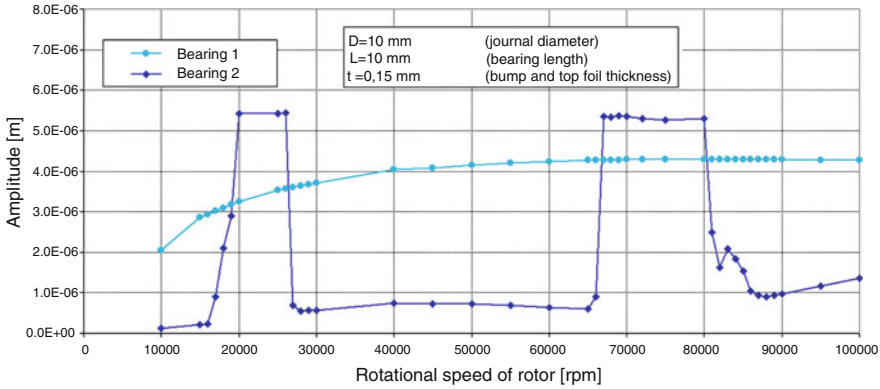

Fig. 7 Amplitudes of relative journal-bush vibrations for rotor supported on foil bearings

(close to 23,000 rpm and 74,000 rpm) we can observe remarkable increase of amplitude in bearing 2. The analysis of the vibration trajectory reveals that hydrodynamic instability appears in those ranges. Probably the origin of that instability is caused by low load of the bearing 2. It means that the analysed rotor-bearing system requires some modifications. For instance, we could change the width of the sleeve bearing or use another geometry of the bump foil and introduce additional frictional damping between the foil set by changing coating material. Using the proposed methods of calculation we are able to optimize the foil bearing design before experimental tests.

4 Conclusions

The obtained results of the theoretical analysis of the dynamics of the high speed variable geometry bearings for oil-free turbo-machines indicate that to secure correct and failure-free operation of the rotating system, one should analyze thoroughly the dynamics of the "rotor-bearing-casing" system within the whole range of machine operation. The differences between dynamic properties of the bearing with the variable geometry caused by alterations in the design of the elastic foil or tilting pad joints show crucial influence of the phenomena which normally are not included in the classical methodology.

Therefore, nonlinear modeling of dynamic properties of variable-geometry bearings, including design characteristics of the support and friction in it, becomes indispensable in high speed bearing applications.

The presented method of calculation of the non-linear response of the variable geometry bearing to any excitation takes into account the factors characteristic of the design, such as friction in the supports and the type of material used for bearing production. Experimental investigation of the machine designed and manufactured according to the methodology presented in the paper will be the subject of further investigations.

References

1. Agrawal, G.L.: Foil Air/Gas Bearing Technology – An Overview. ASME International Gas Turbine & Aeroengine Congress, Orlando (USA), 97-GT-347 (1997)
2. Andres, L.S., Rubio, D., Kim, T.H.: Rotordynamic Performance of a Rotor Supported on Bump Type Foil Bearings: Experiments and Predictions. ASME Turbo Expo, Barcelona (Spain), GT2006-91238 (2006)
3. Castelli, V., McCabe, J.T.: Transient dynamics of a tilting pad gas bearing system. ASME J. Lubr. Technol. **89**(4), 499–509 (1967)
4. Hou, Y., Zhu, Z.H., Chen, C.Z.: Comparative test on two kinds of new compliant foil bearing for small cryogenic turbo-expander. CRYOGENICS **44**, 69–72 (2004)
5. Kiciński, J.: Rotor Dynamics. IFFM PASci Publisher, Gdansk (2006)
6. Kiciński, J., Żywica, G.: Nonlinear vibration analysis in rotor-bearing systems. In: The 9th International Conference on Motion and Vibration Control (MOVIC), Munich (Germany), Paper ID-1290 (2008)
7. Kiciński, J., Żywica, G., Rządkowski, R., Drewczyński, M.: Numerical modelling of the structural layer of foil bearing. Acta Mechanica et Automatica (paper in Polish) **2**(1), 45–50 (2008)
8. Kozanecki Z, Dessornes O., et al.: Three technological bricks for a micro power generation. In: Proceedings of 5th International Workshop on Micro Technology for Power Generation and Energy Conversion Applications, Power-MEMS, Tokyo (2005)
9. Kozanecki, Z., Kazimierski, Z., Horodko, L.: Vibration of the least loaded pad of the tilting pad gas journal bearing. J. Tribol., Trans. ASME **110**, 377–380 (1988)
10. Kozanecki, Z.: Tilting pad gas journal bearing dynamics. Mach. Dyn. Probl. **23**(4), 25–38 (1999)
11. Ku, R., Heshmat, H.: Compliant foil bearing structural stiffness analysis: part I – theoretical model including strip and variable bump foil geometry. ASME J. Tribol. **114**, 394–400 (1992)
12. Lee, Y.B., et al.: Dynamic characteristics of a flexible rotor system supported by a viscoelastic foil bearing. Tribol. Int. **37**, 679–687 (2004)
13. Lez, S., Arghir, M., Frene, J.: Static and dynamic characterization of a bump-type foil bearing structure. ASME J. Tribol. **129**, 75–83 (2007)
14. Rubio, D., San Anders, L.: Bump-type foil bearing structural stiffness: experiments and predictions. ASME J. Eng. Gas Turb. Power **128**, 653–660 (2006)

Effect of Unbalance on the Dynamic Response of a Flexible Rotor Supported on Porous Oil Journal Bearings

S.K. Laha and S.K. Kakoty

Abstract The present study deals with non-dimensional dynamic analysis of a flexible rotor with a rigid disk under unbalance excitation mounted on porous oil journal bearings at the two ends. The system equation of motion is obtained by finite element formulation of Timoshenko Beam and the disk and the oil-film forces are calculated from the solution of the modified Reynolds equation simultaneously with Darcy's equation. The system equation of motion is then solved by Wilson-θ method. The effect of unbalance on the rotor-bearing system can be observed from the waterfall diagram of the rotor vibration. It has been observed that when the operating speed is low, the major cause of rotor vibration is the unbalance, but at higher operating speeds, oil-whirl phenomenon takes over as a major cause of vibration. The simulation is carried out for different rotor-bearing parameters. The method developed here can also be used to obtain journal centre trajectories and responses at different nodal points of the rotor.

Keywords Timoshenko beam · Porous hydrodynamic bearing · Unbalance response · Oil-whirl · Oil-whip

1 Introduction

Rotating machines supported on hydrodynamic journal bearings are one of the most widely used machines in engineering field. The correct prediction of the dynamic behaviour of a flexible rotor with complicated accessories is extremely essential. The hydrodynamic journal bearings supporting the rotor not only affect the critical speed and unbalance response of the rotor but also induce self-acting vibration commonly known as oil-whirl and oil-whip. Because of oil-whirl the journal centre rotates with half of the spin speed of a lightly-loaded rotor and when the spin speed

S.K. Laha (✉) and S.K. Kakoty
Mechanical Engineering Department, Indian Institute of Technology, Guwahati, Guwahati – 781039, India
e-mail: swarup@iitg.ernet.in

K. Gupta (ed.), *IUTAM Symposium on Emerging Trends in Rotor Dynamics*, IUTAM Bookseries 25, DOI 10.1007/978-94-007-0020-8_20,

reaches twice the first natural frequency of the rotor, the oil-whirl becomes equal to the shaft critical speed and at this stage severe vibration is observed which is known as oil-whip.

Porous bearing can be used where other bearings cannot be placed due to lack of space or when replenishment of lubricant is difficult. In the past a lot of research has been carried out on flow in porous media. Kumar and Rao [1] presented a theoretical investigation on the steady state characteristics of finite hydrodynamic porous oil journal bearings in turbulent regimes. Lubricant flow in the porous media is based on Darcy's model. Chattopadhyay and Majumdar [2] carried out the stability analysis of rigid rotor supported on porous journal bearing using linearized stiffness and damping coefficients of the bearing. High porosity with a maximum amount of lubricating oil is used for high-speed, light-load applications, such as fractional-horsepower motor bearings.

Quan et al. [3] conducted experimental analysis under high speed (around 69,000 rpm) and light load conditions and found that porous bearings could work under hydrodynamic conditions even at these high speeds. To maintain hydrodynamic lubrication for high speed application, it is necessary to supplement oil.

Nelson [4] utilized Timoshenko beam theory for establishing shape functions. Based on these shape functions the system finite element matrices of the governing equations were derived. The inclusion of shear deformation effects yielded a more precise element than presented previously and could be incorporated easily in the computer programs. Muszynska [5,6] studied the stability problems of oil-whirl and oil-whip in rotor-bearing system. Ping et al. [7] studied the oil-whip phenomena by obtaining the dynamic response of a single-disk symmetric flexible rotor supported by two oil-lubricating bearings. Castro et al. [8] also studied whirl and whip instabilities in rotor-bearing system considering a non-linear force model of short-bearing approximation. Laha et al. [9] carried out stability analysis of a Timoshenko Beam supported on hydrodynamic porous journal bearing using non-linear transient method. The effects of different rotor-bearing parameters on the stability margin of the rotor are investigated.

In the present study a flexible rotor with a centrally mounted disk, supported on two hydrodynamic porous journal bearings is considered. Timoshenko beam theory is used to model the rotor incorporating translational and rotational mass, shear deformation, bending and also gyroscopic effect. Waterfall diagrams or cascade diagrams are presented to observe the effect of unbalance as well as the hydrodynamic bearing forces on the dynamic response of the journal bearing.

2 Mathematical Model

2.1 Finite Element Equation of Motion of the Rotor-Disk System

A uniform shaft of length L mounted with a disk of mass m_d rotating at constant speed ω about the Z-axis and simply supported on two bearings is shown in Fig. 1.

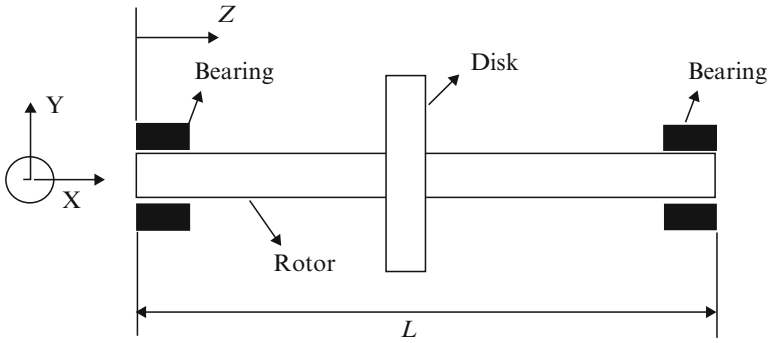

Fig. 1 Rotor supported on fluid film bearings

The shaft is discretized into a finite number of elements. The element is considered to be initially straight and is modeled as eight-degrees-of-freedom element, two translations and two rotations at each node. Axial motion is assumed to be negligible. The cross-section of the element is circular and is considered to be uniform. A typical cross-section of the shaft in a deformed state, located at a distance z from the left end can be described by translations in X and Y-directions as well as the small rotations about X and Y-directions.

The finite element equation of a rotor element of length l is given by Nelson [4]

$$\left([M_T]^e + [M_R]^e\right)\{\ddot{q}\}^e - \omega[G]^e\{\dot{q}\}^e + [K]^e\{q\}^e = \{F\}^e \tag{1}$$

Following non-dimensional scheme is introduced

$$\bar{z} = \frac{z}{C}, \bar{l} = \frac{l}{C}, \bar{v} = \frac{v}{C}, \bar{w} = \frac{w}{C}, \bar{t} = \omega t,\ \bar{F} = \frac{F}{W}$$

where, $W = \frac{1}{2}(\rho AL + m_d)$ g is the load per bearing.

Then elemental equation of motion in non-dimensional form can be written as

$$\left(\left[\bar{M}_T\right]^e + [\bar{M}_R]^e\right)\{\ddot{\bar{q}}\}^e - \left[\bar{G}\right]^e\{\dot{\bar{q}}\}^e + \left[\bar{K}\right]^e\{\bar{q}\}^e = \{\bar{F}\}^e \tag{2}$$

The non-dimensional equation of motion of the disk is written as,

$$\left[\bar{M}^d\right]\{\ddot{\bar{q}}^d\} - \left[\bar{G}^d\right]\{\dot{\bar{q}}^d\} = \{\bar{F}^d\}_{unb} \tag{3}$$

where $\{\bar{F}^d\}_{unb}$ is the vector of unbalance forces due to the disk eccentricity.

The system equation of motion of the rotor is arrived at by assembling the elemental equations and would be as follows:

$$\left(\left[\bar{M}\right]\right)\{\ddot{\bar{q}}\} - \left(\left[\bar{G}\right]\right)\{\dot{\bar{q}}\} + \left(\left[\bar{K}\right]\right)\{\bar{q}\} = \{\bar{F}\} \tag{4}$$

In the system equation of motion, Eq. (4), the right hand side is the force vector consisting of hydrodynamic forces at the bearing ends and unbalance forces at the disk location due to the disk eccentricity. The non-dimensional forces at the bearing locations can be expressed as,

$$\bar{F}_Y = -\bar{F}_\phi^B \pi S \sin\phi - \bar{F}_r^B \pi S \cos\phi - 1 \text{ (in the vertical direction)}$$
$$\bar{F}_X = \bar{F}_\phi^B \pi S \cos\phi - \bar{F}_r^B \pi S \sin\phi \text{ (in the horizontal direction)}$$

The non-dimensional unbalance forces at the disk location are given by,

$$\bar{F}_Y^d = 2\left(\frac{C\omega^2}{g}\right)\left(\frac{e_d}{C}\right)\left(\frac{\bar{m}_d}{1+\bar{m}_d}\right)\sin\bar{t} \text{ (in the vertical direction)}$$
$$\bar{F}_X^d = 2\left(\frac{C\omega^2}{g}\right)\left(\frac{e_d}{C}\right)\left(\frac{\bar{m}_d}{1+\bar{m}_d}\right)\cos\bar{t} \text{ (in the horizontal direction)}$$

2.2 Hydrodynamic Porous Bearing

Figure 2 shows the schematic diagram of the porous journal bearing. The lubricant flow through the porous bush and the clearance space is viscous and laminar. The flow through the porous bush is governed by Darcy's law and that through the clearance space is governed by modified Reynolds equation.

The differential equations for the porous hydrodynamic journal bearing are given below.

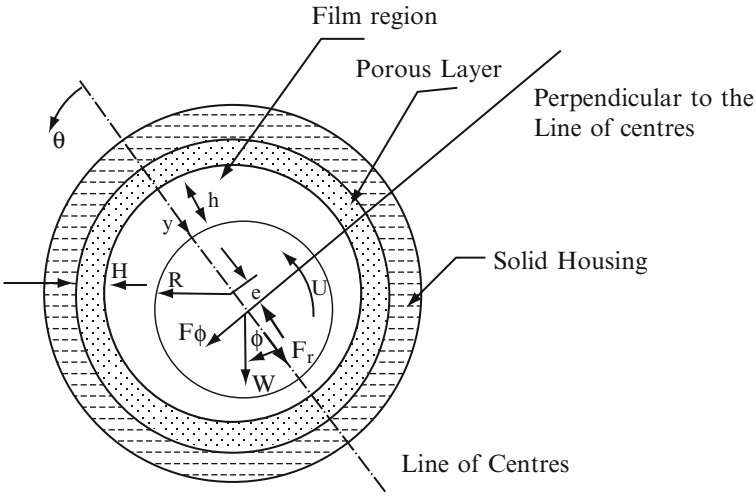

Fig. 2 Bearing geometry

For the porous media:

$$\bar{K}_x \frac{\partial^2 \bar{p}'}{\partial \theta^2} + \left(\frac{R}{H}\right)^2 \frac{\partial^2 \bar{p}'}{\partial \bar{y}^2} + \bar{K}_z \left(\frac{D}{L_B}\right)^2 \frac{\partial^2 \bar{p}'}{\partial \bar{z}^2} = 0 \tag{5}$$

For the clearance space:

$$\begin{aligned} &\frac{\partial}{\partial \theta}\left(\bar{h}^3 \frac{\partial \bar{p}}{\partial \theta}\right) + \left(\frac{D}{L_B}\right)^2 \frac{\partial}{\partial \bar{z}}\left(\bar{h}^3 \frac{\partial \bar{p}}{\partial \bar{z}}\right) \\ &\quad = 6(1 - 2\dot{\phi})(-\varepsilon \sin\theta) + 12\dot{\varepsilon}\cos\theta + \beta\left(\frac{\partial \bar{p}'}{\partial \bar{y}}\right)_{\bar{y}=0} \end{aligned} \tag{6}$$

The non-dimensional bearing forces along the radial and the circumferential directions are given by

$$\begin{aligned} \bar{F}_r^B &= -\int_0^1 \int_0^{\theta_2} \bar{p}\cos\theta d\theta d\bar{z} \\ \bar{F}_\phi^B &= \int_0^1 \int_0^{\theta_2} \bar{p}\sin\theta d\theta d\bar{z} \end{aligned} \tag{7}$$

3 Solution Procedure

Let $\bar{v}_b$ and $\bar{w}_b$ denote the non-dimensional horizontal and vertical deflection of the rotor respectively at the bearing location. From the rotor-bearing geometry, ε and ϕ are related to $\bar{v}_b$ and $\bar{w}_b$ ($\bar{v}_b = -\varepsilon\sin\phi$ and $\bar{w}_b = -\varepsilon\cos\phi$). Therefore, the eccentricity ratio and attitude angle and their derivatives are obtained as,

$$\left.\begin{aligned} \varepsilon &= \sqrt{\bar{v}_b^2 + \bar{w}_b^2} \\ \tan\phi &= \bar{v}_b \,/\, \bar{w}_b \\ \dot{\varepsilon} &= -(\dot{\bar{v}}_b \sin\phi + \dot{\bar{w}}_b \cos\phi) \\ \dot{\phi} &= -\frac{(\dot{\bar{v}}_b \cos\phi - \dot{\bar{w}}_b \sin\phi)}{\varepsilon} \end{aligned}\right\} \tag{8}$$

The non-dimensional equation of motion (4) of the rotor is solved numerically by Wilson-θ method for translational and rotational displacement, velocity and acceleration at each nodal point and thereby eccentricity ratio and attitude angle of the bearing and their derivatives are estimated at every time step by using Eq. (8). Time-step used in the Wilson-θ method is 0.0025 and it has been observed that time-step smaller than this does not improve the solution significantly. The derivatives estimated as explained above are then used in time-dependent modified Reynolds

equation for the calculation of hydrodynamic force components for the next time step. The Gauss-Seidel iteration method with successive over-relaxation scheme is used to solve the Darcy's equation and the modified Reynolds equation simultaneously along with the boundary conditions [9] for obtaining pressure distribution.

4 Results and Discussion

In the present scheme of analysis, the non-dimensional parameters obtained are $L_B/D, e/C, e_d/C, H/R, R/C, R/(2L), E/(\rho g L), m_d/(\rho AL)$ and $C\omega^2/g$. The last parameter is the mass parameter, $\bar{m}$ which is a function of the operating speed. Figures 3a–c show the variation of non-dimensional first natural frequency as a function of mass parameter of a rigidly supported rotor. The critical value of mass parameter corresponds to resonance speed at which the $\omega_p / \omega = 1$ line intersects the plot as depicted in Figs. 3a–c. Both forward and backward natural frequencies are observed.

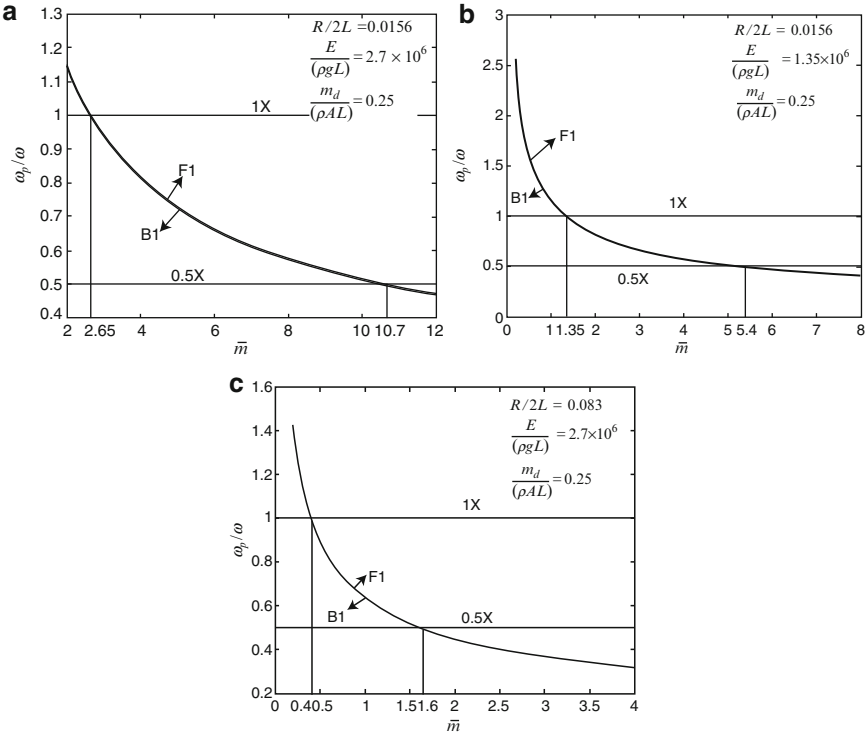

Fig. 3 (**a–c**) Variation of natural whirl frequency with mass parameter

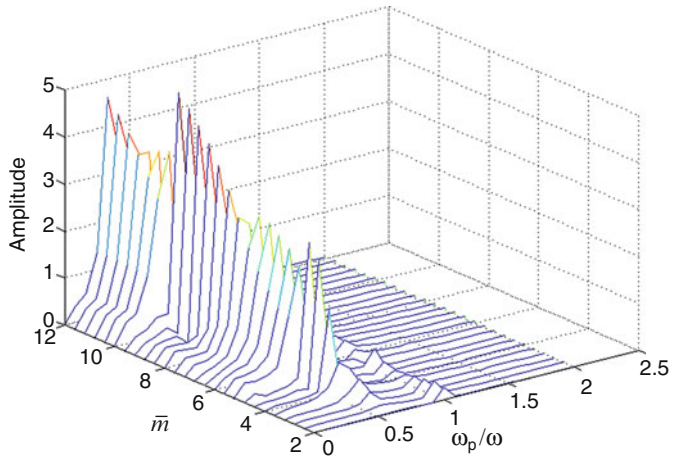

Fig. 4 Waterfall diagram of rotor with $R/2L = 0.0156$, $E/(\rho g L) = 2.7 \times 10^6$, $\beta = 0.03$

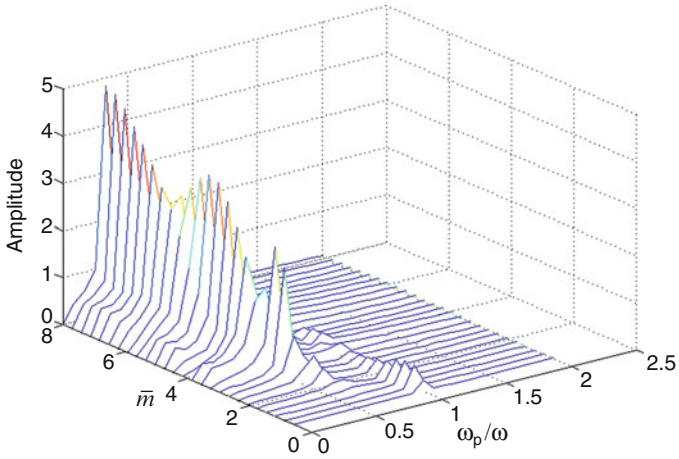

Fig. 5 Waterfall diagram of rotor with $R/2L = 0.0156$, $E/(\rho g L) = 1.35 \times 10^6$, $\beta = 0.03$

Waterfall diagrams (Figs. 4–9) of the vibration response of the rotors with different slenderness ratio and stiffness parameters are obtained at the disk location. The following parameters are kept same while obtaining the waterfall diagrams: $\frac{L_B}{D} = 1.0; \varepsilon = 0.5; \frac{m_d}{(\rho A L)} = 0.25; \frac{e_d}{C} = 0.25; \frac{H}{R} = 0.2; \bar{K}_x = \bar{K}_z = 1.0$

The waterfall diagrams of the flexible rotor exhibit the following dynamic phenomena.

1. When the mass parameter of the rotor is low, there are only the synchronous vibrations with small amplitudes as shown in Figs. 4–9, and only one peak is observed along the line $\omega_p \,/\, \omega = 1$. This is caused by the unbalance of the rotor.

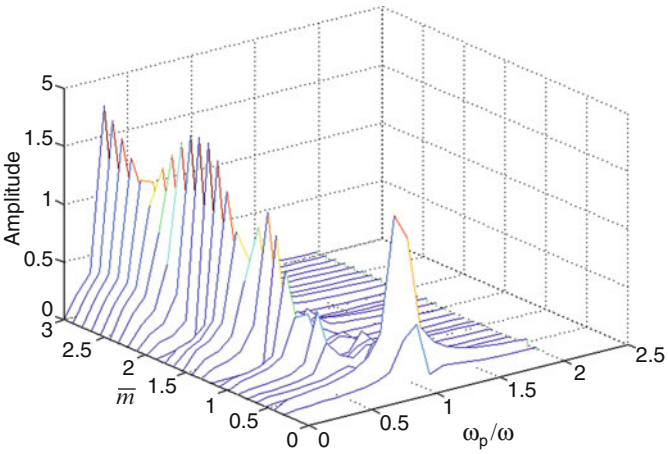

Fig. 6 Waterfall diagram of rotor with $R/2L = 0.0083$, $E/(\rho g L) = 2.7 \times 10^6$ and $\beta = 0.03$

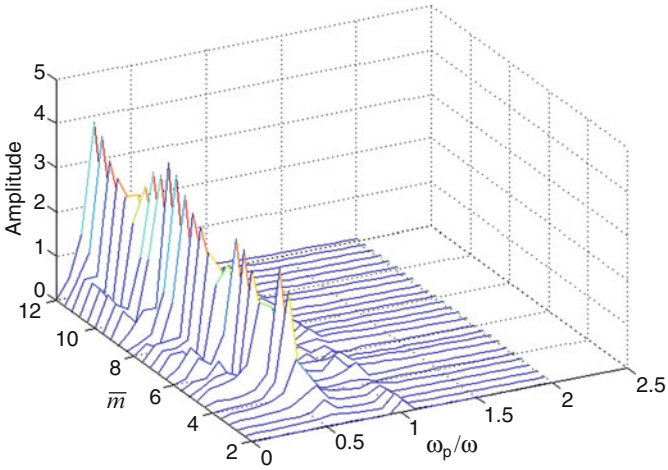

Fig. 7 Waterfall diagram of rotor with $R/2L = 0.0156$, $E/(\rho g L) = 2.7 \times 10^6$ and $\beta = 0.6$

2. Unbalance response becomes maximum at a value of mass parameter corresponding to the resonance frequency. For rotor with slenderness ratio $R/2L = 0.0156$ and stiffness parameter $E/(\rho g L) = 1.35 \times 10^6$, critical speed is at $\bar{m} = 1.35$ (Fig. 3b) and from the waterfall diagram of the same rotor, highest peak along the $\omega_p / \omega = 1$ line is observed at close to $\bar{m} = 1.4$ (Fig. 5).
3. At higher values of mass parameter apart from synchronous vibration, oil-whirl which is half-synchronous vibration also appears as observed in Figs. 4–9: one more peak is observed along $\omega_p / \omega = 0.5$ line. Amplitude of oil whirl increases with the increase of mass parameter and is much higher than that of unbalance response [5–7].

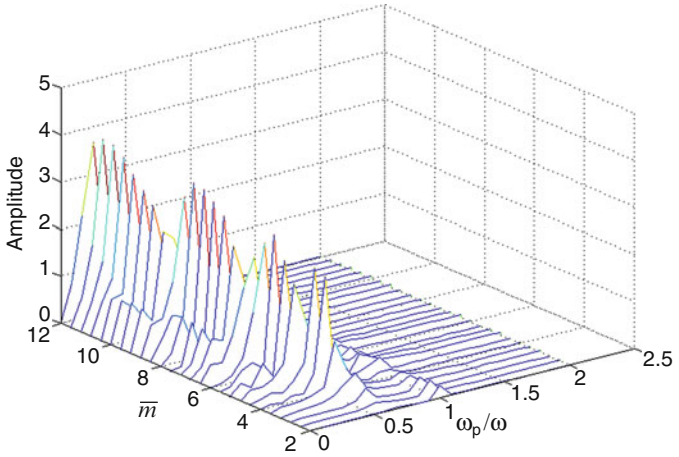

Fig. 8 Waterfall diagram of rotor with $R/2L = 0.0156$, $E/(\rho g L) = 2.7 \times 10^6$ and $\beta = 1.0$

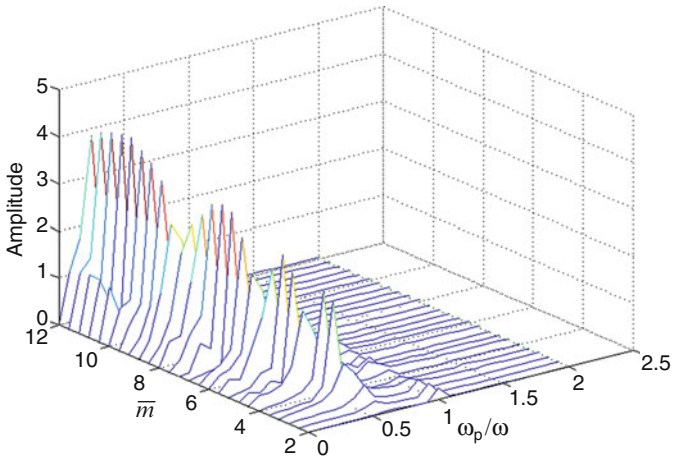

Fig. 9 Waterfall diagram of rotor with $R/2L = 0.0156$, $E/(\rho g L) = 2.7 \times 10^6$ and $\beta = 3.0$

4. When the spin speed approaches twice the value of first critical frequency, the half-synchronous oil frequency reaches the first resonance speed. Let $\bar{m}_c$ be the critical mass parameter corresponding to first critical frequency, i.e., $\bar{m}_c = C\omega_c^2/g$. Oil-whip occurs at $2\omega_c$, and the corresponding mass parameter is $\bar{m} = \frac{C(2\omega_c)^2}{g} = 4\bar{m}_c$. Therefore, when spin speed reaches twice the first critical frequency, the corresponding mass parameter is four times the critical mass parameter. For a rotor with $R/2L = 0.0156$ and $E/(\rho g L) = 1.35 \times 10^6$, the mass parameter corresponding to the first critical speed is 1.35 (Fig. 3b) and the mass parameter corresponding to twice the first critical speed is 5.4 (1.35×4). From the

waterfall diagram of the same rotor (Fig. 5) when mass parameter reaches around 5.4, oil-whirl is replaced by oil-whip, the vibration frequency of which remains close to the first critical speed. Severe vibration is observed in this regime which is known as oil-whip [5–7].

5. Figures 4 and 6 depict the waterfall diagrams for two different slenderness ratios, $R/2L = 0.0156$ and 0.0083 for $E\ /\ (\rho g L) = 2.7\times10^6$. When $R/2L = 0.0156$, maximum unbalance and oil-whirl appear at $\bar{m} = 2.67$ and 2.0 respectively. Similarly for $R/2L = 0.0083$, maximum unbalance and oil-whirl appear at $\bar{m} = 0.4$ and 0.6 respectively. It may be observed that the maximum unbalance response and oil-whirl set in at lower speeds as slenderness ratio decreases.
6. Similarly Fig. 5 shows the waterfall diagram of the rotor when $R/2L = 0.0156$ and $E/(\rho g L) = 1.35 \times 10^6$. For this case, maximum unbalance and oil whirl appear at $\bar{m} = 1.4$ and 1.8 respectively. Comparing Figs. 4 and 5 it may be concluded that maximum unbalance response and oil-whirl are observed at lower mass parameter value as the stiffness parameter $E/(\rho g L)$ decreases.
7. Figures 4, 7, 8 and 9 show the waterfall diagrams of the rotor with $R/2L = 0.0156$ and $E/(\rho g L) = 2.7 \times 10^6$ when $\beta = 0.03, 0.6, 1.0$ and 3.0 respectively. Bearing feeding parameter depends on the permeability of the porous bush and has profound effect on the dynamic characteristics of the rotor-bearing system as it may be observed from above figures. It may be observed that when $\beta = 0.03$(Fig. 4) whirl amplitude gradually increases with increase in $\bar{m}$. But for $\beta = 0.6, 1.0$ and 3.0 (Figs. 7–9) high amplitudes of oil-whirl appear even at low mass parameter and these high amplitudes are observed throughout the range of mass parameter considered in the analysis.

5 Conclusions

The present study takes up a flexible rotor Timoshenko beam supported on porous oil bearings. The simulation of the rotor/bearing has given the advantage of considering all the non-linear effects. Therefore, the results would be of utmost importance to rotor-bearing designers. The study carried out depicts the effect of different non-dimensional parameters, e.g., stiffness parameter, slenderness ratio of the rotor and bearing feeding parameter of the porous bearing. The analysis reveals that the half frequency whirling or oil-whirl dominates the unbalance forces at higher mass parameter values vis-à-vis the operating speeds for the case of disk eccentricity ratio of 0.25. The present model can be extended to investigate the effects of other non-dimensional rotor-bearing parameters.

Nomenclature

A, L, R	Cross-sectional area $\pi D^2/4$, length and radius of the rotor
C	Clearance of the bearing

e_d, ε	Eccentricity of the disk, and eccentricity ratio e_d/C
E, ρ	Young's Modulus and mass density of the rotor material
$\bar{h}$	Non-dimensional film thickness, $h/C = 1 + \varepsilon \cos\theta$
H	Thickness of the porous bush
$\bar{K}_x$, $\bar{K}_z$	Non- dimensional permeability factor of the porous bush in circumferential and axial directions respectively, K_x / K_y, K_z / K_y
L_B/D	Aspect ratio of the bearing
$\bar{m}_d$	Non-dimensional mass of the disk, $m_d/(\rho AL)$
$\bar{m}$	Mass parameter, $C\omega^2/g$
$R/2L$	Slenderness ratio of the rotor
S	Sommerfeld number
β	Bearing feeding parameter, $12K_yR^2/C^3H$
ω, ω_p	Rotor spin speed, whirling speed
ϕ	Attitude Angle

References

1. Kumar, A., Rao, N.S.: Steady state performance of finite hydrodynamic porous journal bearings in turbulent regimes. Wear **167**, 121–126 (1993)
2. Chattopadhyay, A.K., Majumdar, B.C.: On the stability of a rigid rotor in finite porous bearings in with slip. J. Tribol., Trans. ASME **108**, 190–194 (1986)
3. Quan, Y.X., et al.: Investigation of sintered bronze bearings under high speed conditions. Tribol. Int. **18**, 75–80 (1985)
4. Nelson, H.D.: A finite rotating shaft element using Timoshenko beam theory. J. Mech. Des., Trans. ASME **102**, 793–803 (1980)
5. Muszynska, A.: Whirl and whip-rotor/bearing stability problems. J. Sound Vib. **110**(3), 443–462 (1986)
6. Muszynska, A.: Stability of whirl and whip in rotor/bearing system. J. Sound Vib. **127**(1), 49–64 (1988)
7. Ping, J.J., et al.: On the non-linear dynamic behavior of a rotor–bearing system. J. Sound Vib. **274**, 1031–1044 (2004)
8. Castro, H.F., et al.: Whirl and whip instabilities in rotor-bearing system considering a non-linear force model. J. Sound Vib. **317**, 273–293 (2008)
9. Laha, S.K., et al.: Stability analysis flexible rotor supported on finite hydrodynamic porous journal bearing using non-linear transient method. Proc. IMechE, Part J., J. Eng. Tribol. 222(7), 963–973 (2008)

Analysis of Capillary Compensated Hole-Entry Hydrostatic/Hybrid Journal Bearing Operating with Micropolar Lubricant

Suresh Verma, K.D. Gupta, and Vijay Kumar

Abstract The present paper describes the performance of a capillary compensated hole-entry hydrostatic/hybrid symmetric journal bearing system operating with micropolar lubricant. The numerical solution of the modified Reynolds equation governing the flow of the micropolar lubricant is obtained using finite element method. The results presented in this paper indicate that the two parameters, non-dimensional characteristic length (l_m) and coupling number (N^2) of the micropolar lubricant affect the static and dynamic performance characteristics of bearing and herein these characteristics have been compared with that of Newtonian lubricant.

Keywords Capillary restrictor · Finite element method · Hybrid · Hydrostatic · Micropolar lubrication

1 Introduction

The design of hydrostatic journal bearing system is generally based on the assumption that the lubricant behaves as a Newtonian fluid. However, the lubricants used to lubricate the bearings are mineral in nature and additives are mixed with them to enhance their performance during lubrication. In view of the inadequacies of classical Newtonian theory, lubrication theory for micropolar fluids is applied to solve the lubrication problems of such fluids. Micropolar fluids are fluids with microstructure. They represent fluids consisting of rigid, randomly oriented particles suspended in a viscous medium, where the deformation of fluid particles is ignored. A number of studies [1–7] on micropolar lubrication have been reported. Kumar et al. [7] have presented the performance of a double row symmetric hole-entry

S. Verma and K.D. Gupta
Department of Mechanical Engineering, D. C. R. University of Science and Technology, Murthal, India
e-mail: sureshc30@yahoo.co.in

V. Kumar
Department of Mechanical Engineering, Thapar University, Patiala, India

K. Gupta (ed.), *IUTAM Symposium on Emerging Trends in Rotor Dynamics*,
IUTAM Bookseries 25, DOI 10.1007/978-94-007-0020-8_21,

hybrid journal bearing configuration containing 12 holes per row with Newtonian lubricant. A theoretical study of the performance characteristics of a constant flow valve compensated multi-recess hydrostatic journal bearings operating with micropolar lubricant have been given by Verma et al. [8]. The present work deals with the solution of the modified Reynolds equation and studies the performance of a hydrostatic/hybrid hole-entry journal bearing compensated with capillary restrictor and operating with micropolar lubricant. The results presented in the study are expected to be quite useful to the bearing designers.

2 Analysis

Figure 1 shows a geometric configuration of a capillary compensated double-row (12 holes in each row) symmetric hydrostatic/hybrid journal bearing. The journal is assumed to rotate with uniform angular velocity about its equilibrium position. The three-dimensional flow of incompressible micropolar lubricant in the convergent area of the journal bearing is governed by the modified Reynolds equation. With the usual assumptions of the lubrication film and constancy of the characteristic coefficients across the film of the micropolar lubricant, the modified Reynolds equation is given as Prakash and Sinha [3]:

$$\frac{\partial}{\partial x}\left\{\frac{h^3\Phi}{12\mu}\frac{\partial p}{\partial x}\right\}+\frac{\partial}{\partial y}\left\{\frac{h^3\Phi}{12\mu}\frac{\partial p}{\partial y}\right\}=\frac{\omega_J R_J}{2}\frac{\partial h}{\partial x}+\frac{\partial h}{\partial t} \tag{1}$$

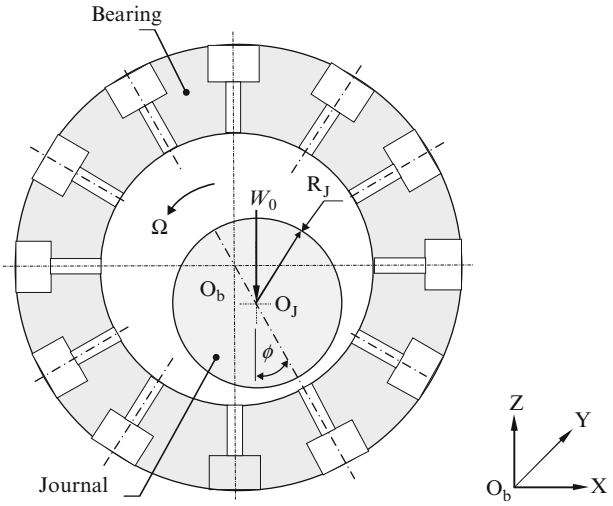

Fig. 1 Geometric details and co-ordinate system of hole-entry journal bearing

where

$$\Phi = 1 + \frac{12l^2}{h^2} - \frac{6Nl}{h}\coth\left(\frac{Nh}{2l}\right);\ N = \left(\frac{\kappa}{2\mu+\kappa}\right)^{\frac{1}{2}};\ l = \left(\frac{\gamma}{4\mu}\right)^{\frac{1}{2}};$$

Here μ is the viscosity coefficient of the Newtonian fluid, κ is the spin viscosity, γ is the material coefficient, h is the film thickness, and p is the micropolar film pressure. N and l are two parameters distinguishing a micropolar lubricant from Newtonian lubricant. N is a dimensionless parameter called the coupling number which couples the linear and angular momentum equations arising from the micro-rotational effects of the suspended particles in the lubricant. l represents the interaction between the micropolar lubricant and the film gap or clearance space of a journal bearing and is termed as the characteristic length of the micropolar lubricant. Equation (1) in its non-dimensional form can be given as

$$\frac{\partial}{\partial\alpha}\left\{\frac{\overline{h}^3\overline{\Phi}}{12\overline{\mu}}\frac{\partial\overline{p}}{\partial\alpha}\right\} + \frac{\partial}{\partial\beta}\left\{\frac{\overline{h}^3\overline{\Phi}}{12\overline{\mu}}\frac{\partial\overline{p}}{\partial\beta}\right\} = \frac{\Omega}{2}\frac{\partial\overline{h}}{\partial\alpha} + \frac{\partial\overline{h}}{\partial\overline{t}} \tag{2}$$

where

$$\overline{\Phi} = 1 + \frac{12}{\overline{h}^2 l_m^2} - \frac{6N}{\overline{h}l_m}\coth\left(\frac{N\overline{h}l_m}{2}\right)$$

Using the finite element method based on Galerkin's technique and Eq. (2), the system equation for the discretized flow field is derived and in matrix form it is given as:

$$\overline{F}\{\overline{P}\} = \{\overline{Q}\} + \Omega\{\overline{R}_H\} + \dot{\bar{X}}_J\{\overline{R}_{XH}\} + \dot{\bar{Z}}_J\{\overline{R}_{ZJ}\} \tag{3}$$

A dot over terms represents first derivative of the respective terms with respect to time. Each term of respective matrix/vector is computed using following expressions:

$$\overline{F}^e_{ij} = \int\int_{\overline{A}^e}\left\{\frac{\overline{h}^3}{12\overline{\mu}}\left(\overline{\Phi}\frac{\partial N_i}{\partial\alpha}\frac{\partial N_j}{\partial\alpha} + \overline{\Phi}\frac{\partial N_i}{\partial\beta}\frac{\partial N_j}{\partial\beta}\right)\right\} d\alpha\ d\beta \tag{3a}$$

$$\{\bar{Q}_i\}^e = \int_{\Gamma^e}\left\{\left(\frac{\overline{h}^3}{12\overline{\mu}}\left(\overline{\Phi}\frac{\partial\overline{p}}{\partial\alpha}\right) - \frac{\overline{\Omega}}{2}\overline{h}\right)l_1 + \frac{\overline{h}^3}{12\overline{\mu}}\left(\overline{\Phi}\frac{\partial\overline{p}}{\partial\beta}\right)l_2\right\} N_i\, d\overline{\Gamma}^e \tag{3b}$$

$$\overline{R}^e_{Hi} = \int\int_{\overline{A}^e}\frac{\overline{h}}{2}\frac{\partial N_i}{\partial\alpha}d\alpha\, d\beta \tag{3c}$$

(3d)

$$\overline{R}^e_{zji} = \int\int_{\overline{A}^e}\sin\alpha\ N_i\, d\alpha\, d\beta \tag{3e}$$

where l_1 and l_2 are direction cosines and $i, j = 1, 2, \ldots, n_l^e$ (number of nodes per element) are local node numbers.

2.1 Fluid-Film Thickness

For a rigid journal bearing system, operating under static conditions, the fluid film thickness expression in non-dimensional form is given as:

$$\overline{h} = 1 - \overline{X}_J \cos\alpha - \overline{Z}_J \sin\alpha \tag{4}$$

In a capillary compensated hydrostatic/hybrid journal bearing system, continuity of lubricant flow rate between the restrictor and the bearing is maintained. The lubricant flow rate $\overline{Q}_R$ through capillary restrictor neglecting gravitational force, in non-dimensional form is given as:

$$\overline{Q}_R = \overline{C}_{s2}(1 - \overline{p}_c) \tag{5}$$

The global system of governing Eqs. (3), (4) and (5) is obtained by employing Galerkin's orthogonality criterion and then solved after applying appropriate boundary conditions [7]. For two degree of freedom system, there exist four stiffness ($\overline{S}_{xx}, \overline{S}_{xz}, \overline{S}_{zx}, \overline{S}_{zz}$) and four damping coefficients ($\overline{C}_{xx}, \overline{C}_{xz}, \overline{C}_{zx}, \overline{C}_{zz}$), which can be used to study the stability of the system.

The modified Reynolds equation governing the flow of the micropolar lubricant is solved along with restrictor flow equation by finite element method so as to obtain fluid-film pressures. The iterative procedure is repeated till the converged solution for the fluid film pressure field is obtained. The detailed solution procedure is as in Verma et al. [8].

3 Results and Discussion

The mathematical model developed is used to compute the performance characteristics of a hole-entry hydrostatic/hybrid journal bearing system. The results are computed for the following non-dimensional values of bearing operating and geometric parameters:

$$\overline{\Omega} = 0.0, 1.0; \overline{W}_o = 1.0, \lambda = 1.0, \overline{a}_b = 0.25$$

Two non-dimensional parameters i.e., N^2 and l_m are used to distinguish a micropolar lubricant from a Newtonian lubricant. As N^2 approaches zero and/or l_m approaches infinity, the micropolar effect becomes insignificant and the micropolar lubricant converts into a Newtonian one. The validity of the developed program is established by computing the load W(kN) at different eccentricity ratios for hydrodynamic bearing operating with Newtonian and micropolar lubricants. The results shown in Fig. 2 have been compared with the available theoretical results of Wang and Zhu [6]. The maximum deviation of about 8% and 7% are noted at maximum

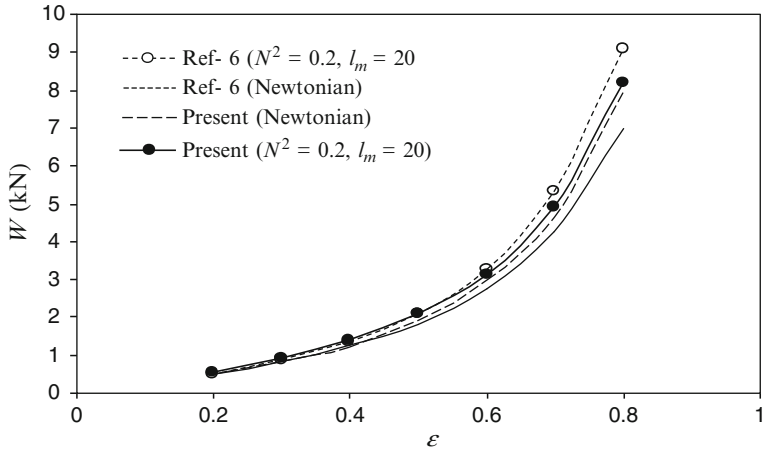

Fig. 2 Variation of W with eccentricity ratio ε

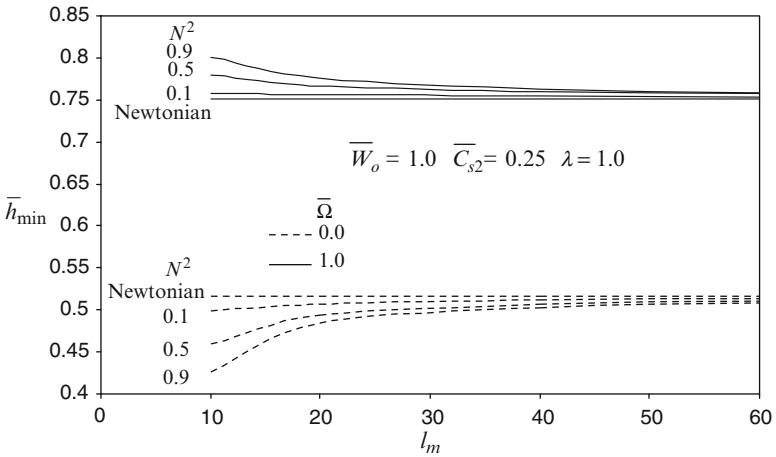

Fig. 3 Variation of minimum fluid film thickness with l_m

eccentricity ratio of 0.8 for Newtonian and micropolar lubricant respectively. The difference in the analytical solutions may be attributed to the different computational scheme used.

The variation of static and dynamic characteristics with different values of micropolar parameters and $\overline{C}_{s2}$ are shown in Figs. 3 to 11. Figure 3 depicts that for hydrostatic mode $\overline{h}_{\min}$ get reduced at high rate at lower values of l_m in comparison to the Newtonian lubricant. But for hybrid mode $\overline{h}_{\min}$ increases with increase in N^2 and this increase is marginally high at lower values of l_m. Figures 4, 5 and 6 show the variation in stiffness coefficients ($\overline{S}_{xx}, \overline{S}_{xz}, \overline{S}_{zx}, \overline{S}_{zz}$). Figure 4 indicates that the

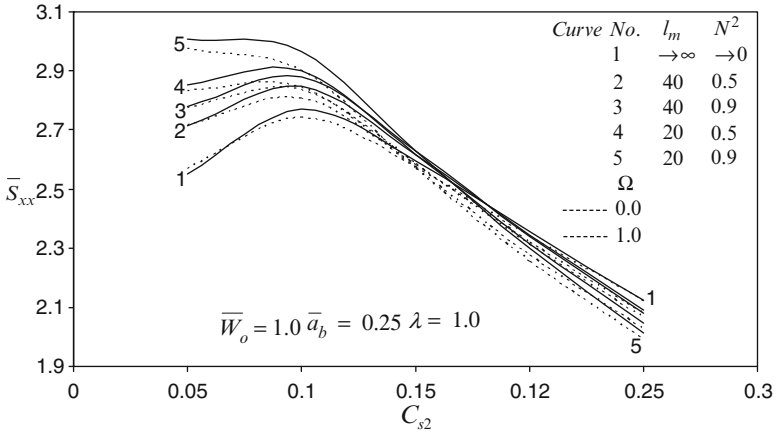

Fig. 4 Variation of direct stiffness $\overline{S}_{xx}$ with restrictor design parameter

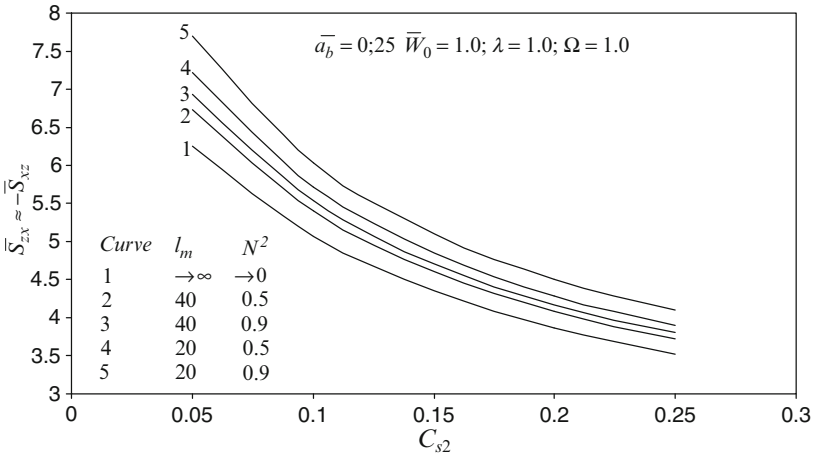

Fig. 5 Variation of cross-coupled stiffness $\overline{S}_{xz}$ and $\overline{S}_{zx}$ with restrictor design parameter

direct stiffness coefficient ($\overline{S}_{xx}$) first shows increasing trend for $\overline{C}_{s2} < 0.1$ but after $\overline{C}_{s2} > 0.15$, a decreasing trend is observed for both the modes.

The effect of l_m and N^2 on direct stiffness coefficient ($\overline{S}_{xx}$) is to enhance its value up to $\overline{C}_{s2} = 0.15$, after that there is reduction for both the modes. An important observation is that there exists an optimum value of $\overline{C}_{s2}$ which gives the maximum value of $\overline{S}_{xx}$ for different micropolar parameters. The cross-coupled coefficients ($\overline{S}_{xz}$ and $\overline{S}_{zx}$) increases with an increase in micropolar effect of the lubricant and decreases with increase in $\overline{C}_{s2}$ as shown in Fig. 5.

The direct stiffness coefficient in the direction of load i.e., $\overline{S}_{zz}$ shows a similar behavior as observed for $\overline{S}_{xx}$. For hydrostatic mode at around $C_{s2} = 0.12$

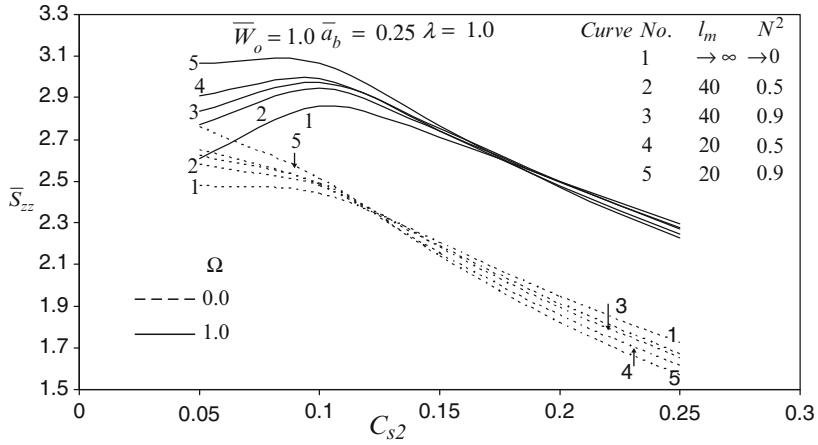

Fig. 6 Variation of $\overline{S}_{zz}$ with restrictor design parameter

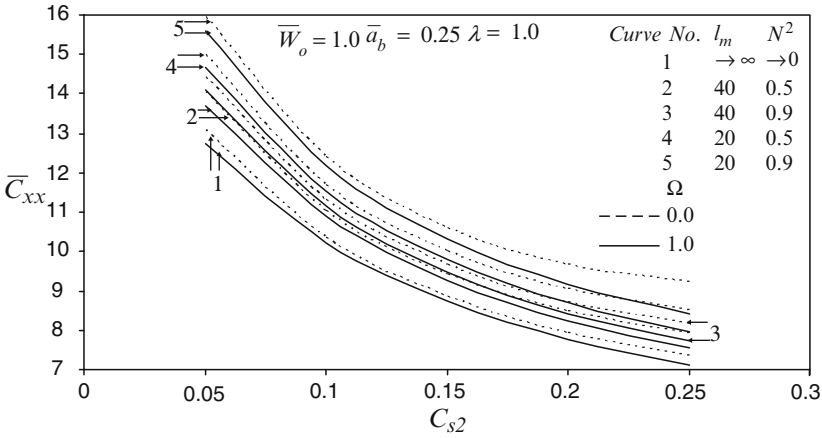

Fig. 7 Variation of $\overline{C}_{xx}$ with restrictor design parameter

the micropolar parameters have no effect on $\overline{S}_{zz}$ and beyond that $\overline{S}_{zz}$ decreases with increase in micropolar effect of lubricant as shown in Fig. 6. However, the bearing is stiff in the direction of load and is rather soft in the direction orthogonal to it.

The direct damping coefficient ($\overline{C}_{xx}$) reduces with increase in the value of $\overline{C}_{s2}$ as indicated by Fig. 7 and increases with increase in micropolar effect as compared to Newtonian lubricant for both hydrostatic and hybrid modes of operation. In Fig. 8, the cross-coupled damping coefficients ($-\overline{C}_{xz}, -\overline{C}_{zx}$) show increasing trend with increase of restrictor design parameter $\overline{C}_{s2}$ and decreases with increase in micropolar effect for $\overline{C}_{s2} < 0.125$ as compared to Newtonian lubricant. At $\overline{C}_{s2} = 0.125$ these coefficients remain unaltered towards the variation in micropolar effect. For $\overline{C}_{s2} > 0.125$ the coefficients $\overline{C}_{xz}$ and $\overline{C}_{zx}$ increasse with increase in micropolar

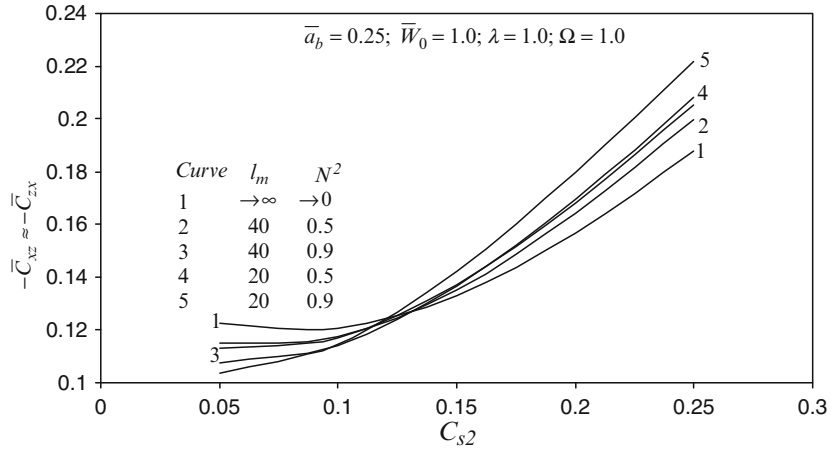

Fig. 8 Variation of $\overline{C}_{xz}$and $\overline{C}_{zx}$ with restrictor design parameter

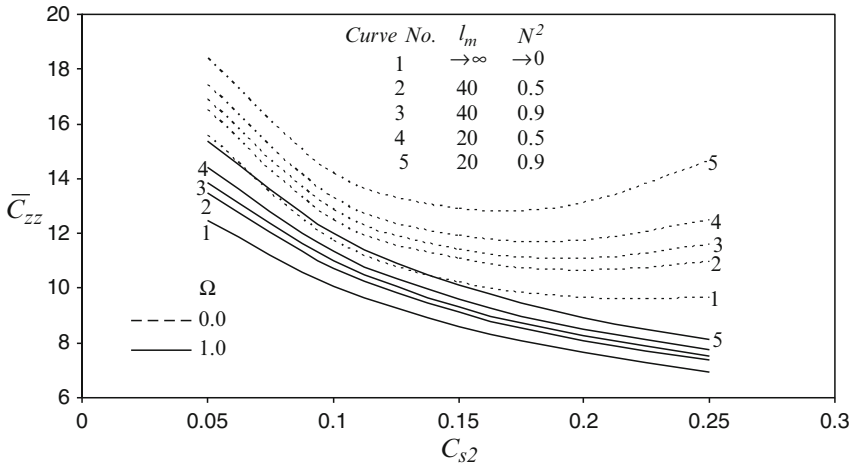

Fig. 9 Variation of $\overline{C}_{zz}$ with restrictor design parameter

effect of lubricant as compared to the Newtonian lubricant. The Fig. 9 shows that the damping coefficient in the direction of load $\overline{C}_{zz}$ increases with increase in micropolar effect of lubricant for both hydrostatic and hybrid mode of operation. The variation of threshold speed $\overline{\omega}_{th}$ with $\overline{C}_{s2}$ for different values of micropolar parameters of lubricant, are shown in Fig. 10. It may be observed from Fig. 10 that there exists an optimum value $\overline{C}_{s2} = 0.1$ at which $\overline{\omega}_{th}$ is maximum for different values of the micropolar parameters. For $\overline{C}_{s2} < 0.175$ the stable region of bearing operation increases with increase in micropolar effect of lubricant and for $\overline{C}_{s2} > 0.175$ the stable region decreases with increase in micropolar effect of lubricant as compared to the Newtonian.

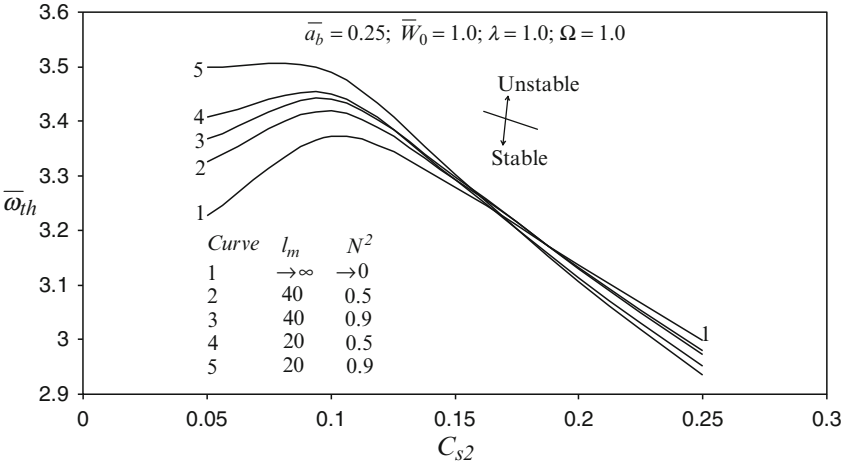

Fig. 10 Variation of $\overline{\omega}_{th}$ with restrictor design parameter

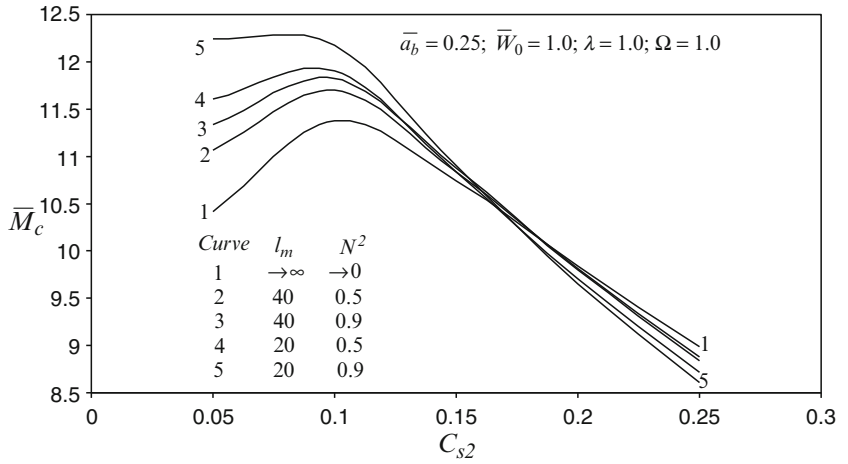

Fig. 11 Variation of $\overline{M}_c$ with restrictor design parameter

The variation of non-dimensional critical mass ($\overline{M}_c$) with $\overline{C}_{s2}$ for different values of micropolar parameters is similar to that of $\overline{\omega}_{th}$ as shown in Fig. 11. The maximum percentage increase and decrease in $\overline{M}_c$ is found to be of the order of 19.5% and 4.2% respectively, as compared to the Newtonian lubricant for $N^2 = 0.9$, $l_m = 20$ corresponding to $\overline{a}_b = 0.25$ and $\overline{C}_{s2} = 0.05$ to 0.25. A bearing designer needs to consider these effects, in order to maintain a safe stability margin of a journal bearing system.

4 Conclusions

A study of hole-entry journal bearing system capillary compensated and operating with micropolar lubricant is presented. The following conclusions are drawn from the results presented in this study:

1. For hydrostatic mode, as compared to Newtonian lubricant, $\overline{h}_{\min}$ remains unaltered at around $\overline{C}_{s2} = 0.15$, but below and above this, $\overline{h}_{\min}$ increases and decreases respectively, with increase in micropolar effect of the lubricant. For hybrid mode, $\overline{h}_{\min}$ increases with increase in micropolar effect of the lubricant.
2. There exists an optimum value of restrictor design parameter $\overline{C}_{s2}$ at which the stiffness coefficient and stability parameters are maximum and that value of $\overline{C}_{s2}$ is around 0.1 as depicted from the results for different micropolar parameters.
3. The direct damping coefficients increases with increase of micropolar effect of lubricant as compared to Newtonian lubricant for a specified operating and geometric parameters.

Nomenclature

Dimensional Parameters

a_b	Land width (m)
c	Radial clearance (m)
D	Journal diameter (m)
F	Fluid film reaction (N)
h	Fluid film thickness (m)
l	Characteristic length (m)
L	Bearing length (m)
L_{cap}	Capillary length (m)
p	Pressure (N.m^{-2})
p_c	Pressure at hole (N.m^{-2})
Q	Bearing flow (m^3.s^{-1})
r	Radial coordinate
R_{cap}	Radius of capillary (m)
R_J	Journal radius (m)
t	Time (s)
u, v, w	Velocity components in x, y, z directions (m.s^{-1})
W_0	External load (N)
x, y	Circumferential and axial coordinates (m)
X_J, Z_J	Journal coordinates
z	Coordinate across film thickness (m)
$\omega_I \sqrt{g/c}, g$	acceleration due to gravity
μ	Dynamic viscosity (Pa.s)

Non-Dimensional Parameters

$\overline{a}_b = a_b/L$; land width ratio;
$\overline{c} = c/R_J$; clearance ratio;
$\overline{C}_{s2} = \left(\pi R_{\text{cap}}^4/8\,c^3 L_{\text{cap}}\right)$;
Restrictor design parameter
$\overline{F} = F\left(1/p_s R_J^2\right)$; fluid film
reaction;
$\overline{h} = h/c, l_m = c/l$;
$\overline{p} = p/p_s$;
$\overline{Q} = (\mu_r/c^3 p_s).Q$;
$\overline{u}, \overline{v} = (u, v)\left(\mu_r R_J/c^2 p_s\right)$;
$\overline{w} = w\left(\mu_r R_J/c^2 p_s\right)(R_J/c)$;
$\overline{t} = t\left(c^2 p_s/\mu_r R_J^2\right)$;
$\overline{W}_0 = \left(W_o/p_s R_J^2\right)$;
$N = (\kappa/(2\mu + \kappa))^{1/2}$;
coupling number;
$\overline{X}_J, \overline{Z}_J = (X_J, Y_J)/R_J$;
$\overline{z} = z/h$;
$(\alpha, \beta) = (x, y)/R_J$;
$\varepsilon = e/c$; eccentricity ratio;
$\lambda = L/D$; aspect ratio;
$\overline{\mu} = \mu/\mu_r$;
$\overline{\omega}_{th} = \omega_{th}/\omega_I$; threshold
frequency;
$\overline{\Omega} = \omega_J(\mu_r R_J/c^2 p_s)$;
speed parameter;

Subscripts

cap Capillary; *J* Journal; *r* Reference value; *s* Supply condition

Matrices and Vectors

$[\overline{C}]$ Fluid-film damping coefficient
$[M]$ Journal mass matrix
$[N]$ Shape function matrix
$\{\overline{p}\}$ Pressure vector
$\{\overline{Q}\}$ Flow vector
$\{\overline{R}_x, \overline{R}_z\}$ RHS vectors for journal velocity
$\{\overline{R}_H\}$ Column vector (hydrodynamic term)
$[\overline{S}]$ Fluid-film stiffness coefficient matrix

References

1. Allen, S., Kline, K.: Lubrication theory of micropolar fluids. J. Appl. Mech., Trans ASME **38**, 646–650 (1971)
2. Khonsari, M.M., Brewe, D.E.: On the performance of finite journal bearings lubricated with micropolar fluids. STLE, Tribol. Trans. **32**(2), 155–160 (1989)
3. Prakash, J., Sinha, P.: Lubrication theory of micropolar fluids and its application to a journal bearing. Int. J. Eng. Sci. **13**, 217–232 (1975)
4. Singh, C., Sinha, P.: The three-dimensional Reynolds equation for micropolar fluid lubricated bearings. Wear **76**(2), 199–209 (1982)
5. Das, S., Guha, S.K., Chattopadhyay, A.K.: Linear stability analysis of hydrodynamic journal bearings under micropolar lubrication. Tribol. Int. **38**, 500–507 (2005)
6. Wang, X.L., Zhu, K.Q.: Numerical analysis of journal bearings lubricated with micropolar fluids including thermal and cavitating effects. Tribol. Int. **9**, 227–237 (2006)
7. Kumar, V., Sharma, S.C., Jain, S.C.: On the restrictor design parameter of hybrid journal bearing for optimum rotor-dynamic coefficients. Tribol. Int. **39**, 356–368 (2006)
8. Verma, S., Kumar, V., Gupta, K.D.: Analysis of multi-recess hydrostatic journal bearing operating with micropolar lubricant. J. Tribol., ASME 131/021103-1 (2009)

Rotordynamic Analysis of Carbon Graphite Seals of a Steam Rotary Joint

H. Hirani and S.S. Goilkar

Abstract In the present paper, a carbon graphite mechanical seal under low speed (<1 m/s), low pressure (3 to 7 bar) and high temperature (120–170°C) conditions has been analyzed. Paper manufacturing machines, where the process fluid steam transfers the heat to rotary drum for drying of paper-pulp, use a floating arrangement of such mechanical carbon graphite seals. A good design of floating ring seal permits relatively low clearance (to minimize leakage) without rubbing contacts, but in the absence of a reliable rotor dynamics tool, often floating rings are subject to excessive vibrations and subsequent brittle failure. To avoid unpredictable seal failures it is always essential to estimate reliable static and dynamic characteristics of floating seals. The present paper describes a numerical procedure for computing the static and dynamic characteristics of floating ring seals accounting for all radial and axial forces. The dynamic characteristics are predicted, based on the perturbation analysis and a finite-difference scheme. The analyzed results have been utilized to modify the geometric design of seal rings. Finally, comparative experimental studies performed on the modified and existing seals have been presented to validate the modified seal design.

Keywords Steam rotary joint · Paper industries · Carbon graphite floating seal

1 Introduction

In paper manufacturing industries, the roll of wet paper is passed over the series of steam heated drums to vaporize the water contents of paper-pulp. The steam required for heating these drums is supplied through rotary joints which work as an

H. Hirani (✉)
Department of Mechanical Engineering, Indian Institute of Technology,
Hauz Khas, New Delhi 110016, India
e-mail: hirani@mech.iitd.ac.in

S.S. Goilkar
Department of Mechanical Engineering, Indian Institute of Technology,
Powai, Mumbai 400076, India

K. Gupta (ed.), *IUTAM Symposium on Emerging Trends in Rotor Dynamics*,
IUTAM Bookseries 25, DOI 10.1007/978-94-007-0020-8_22,

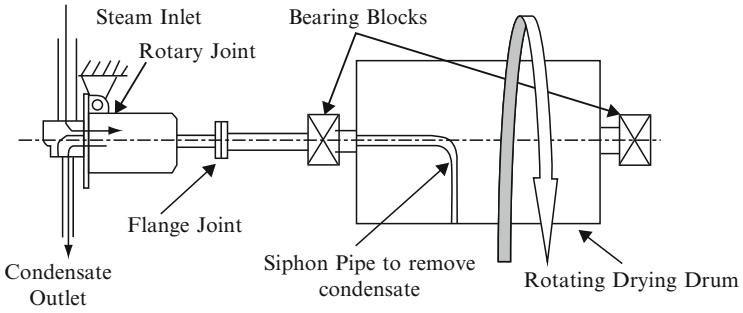

Fig. 1 Schematic of rotary joint arrangement used in paper industry

Fig. 2 Degrees of freedom in floating seal

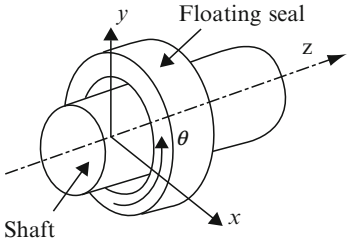

intermediate assembly in between the fixed steam/condensate pipes and the rotating drying drums. A schematic of such a rotary joint with exaggerated view of steam rotary joint is shown in Fig. 1. Avoiding leakage of steam from rotary joint to atmosphere, and allowing free relative motion of drying drum are the main design targets of steam rotary joints. These joints are equipped with floating ring carbon graphite seals. The floating arrangement of seal minimizes the frictional resistance and mechanical wear due to the formation of fluid films in between the sliding surfaces.

The floating seal ring remains in contact with the rotor surface statically at maximum eccentricity position, but during running condition due to aerodynamic (assuming high-temperature-steam behaves like air) and friction forces the seal-ring achieves a different equilibrium position. The floating ring gets locked at an eccentric location and such a non-contact position is a necessary condition to get good tribological performance [1]. In complete floating position, the seal can move freely in x and y (shown in Fig. 2) directions. Such idle floating positions may provide infinite seal life, but in practice unpredictable seal failures, with seal life equal to two days to two months, have been observed in paper manufacturing industries. To ensure the stable floating position of seal ring, it is necessary to estimate the dynamic characteristics along with static characteristics of floating seal arrangement under realistic operating conditions.

The present paper aims:

1. To estimate dynamic characteristics of floating seal based on the perturbation analysis and a finite-difference scheme.

2. To design and fabricate the test set up for testing the carbon graphite floating seal used in rotary joint.
3. To modify the geometric design of seal ring on the basis of the results obtained through the theoretical and experimental studies.

2 Working of Steam Rotary Joint

A rotary joint, studied in the present research work, is an assembly of a shaft, siphon, steam and condensate pipes, spring, Guide II, Guide III (Floating seal), primary and secondary seals, as shown in Fig. 3. The mating surfaces of shaft and floating ring are kept in continuous contact during running conditions by applying a closing force of compressive nature, created by spring and steam pressure.

The rotary joint is assembled with massive drying drum by sealed flange coupling, as shown in Fig. 1. As the shaft of drying drum is primarily supported by bearing block, only a negligible weight of drying drum is transferred to the rotary joint through the steam shaft [2]. However, the assembly of rotary joint and drying drum experiences a huge variation in the required steam pressure. Further, manufacturing of economic carbon graphite seals essentially requires relatively larger tolerance band. An engineering drawing of shaft-floating ring-housing is shown in Fig. 4. The relatively wide variation in the load-magnitude and relatively large tolerance in seal-ring dimensions (as listed in Table 1) may cause serious stability problems for floating ring and may result in brittle failure of carbon graphite seals.

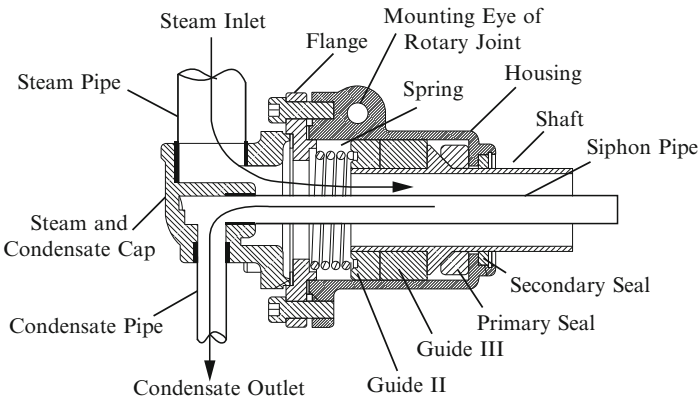

Fig. 3 Construction of steam rotary joint

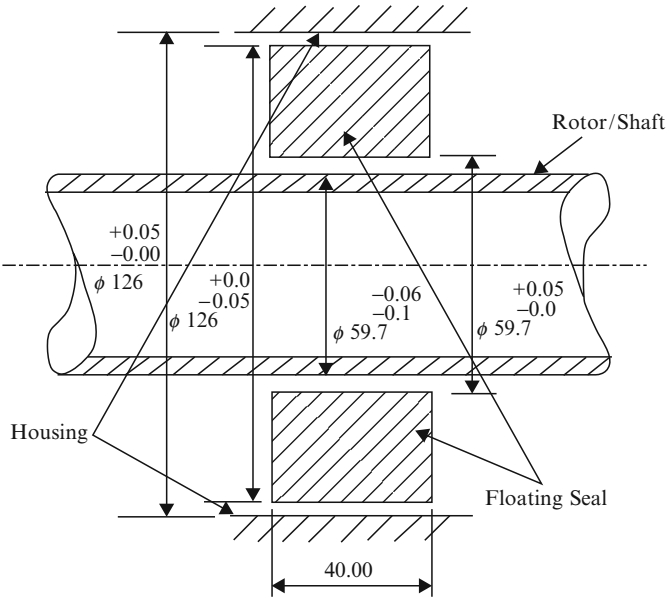

Fig. 4 Tolerances between shaft, floating seal, and housing

Table 1 Floating seal and steam shaft/rotor geometric characteristics

Outer diameter (OD) of shaft (mm)	Clearance between shaft and seal C_{ss} (mm)	Clearance between floating seal and housing C_{ch} (mm)	Seal length L (mm)	L/D ratio
59.60	0.06 to 0.15	0.0 to 0.1	40.00	0.671

3 Experimental Setup

To test the seals in actual industrial conditions a setup was fabricated in the laboratory. A steam boiler was connected to seal joint to facilitate the testing under required steam pressures. To know the lock up position of floating seal, two proximity sensors were placed at 90° phase over the circumference of floating ring, as shown in the Fig. 5a. In addition to know the running clearance (due to thermal expansion of shaft and seal materials) a thermocouple was placed near the seal surface, as shown in Fig. 5b.

Unfortunately, the measured readings of proximity sensors were unacceptably noisy. One possible reason for unreliable results from proximity sensors is high temperature (>130°C) steam environment around proximity sensors. Therefore an alternative arrangement of locating shaft position [3] was made by using torque sensor. The fabricated setup with the torque sensors and data acquisition system for online monitoring of the friction characteristics is shown in Fig. 6. A typical graph of measured torque and displacement data is shown in Fig. 7. The voltage output of

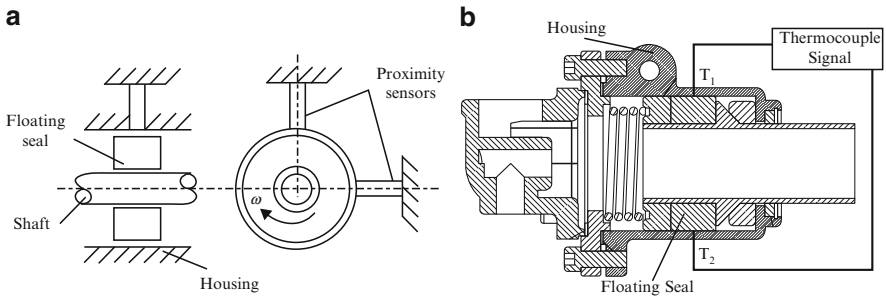

Fig. 5 **(a)** Schematic of proximity sensor arrangement **(b)** Thermocouple arrangement

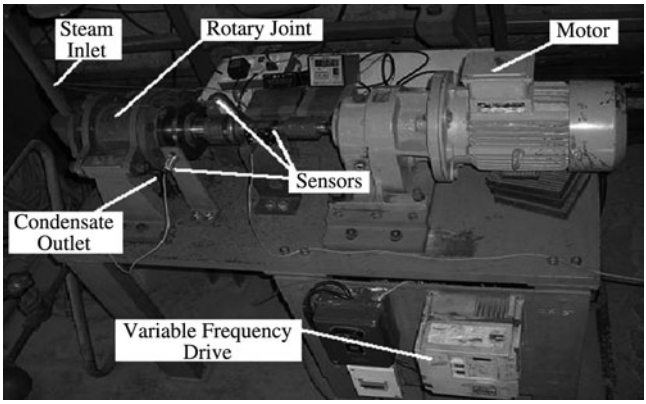

Fig. 6 Schematic of rotary joint arrangement with torque sensor and variable frequency drive

both the sensors for a total of ten cycles (256 data per cycle) are plotted on y-axis of Fig. 7. The figure clearly indicates that displacement reading do not show any definite behavior, while torque readings show sinusoidal behavior.

Figures 8 and 9 show the readings of torque sensor acquired at different steam pressure and various rotational speed. It is interesting to observe that increasing pressure (aerostatic loading) increases the frictional torque, while increasing rotational speed (aerodynamic force) reduces the frictional torque. Further, these diagrams show that rate of increase in torque with increase in steam pressure is much more than decrease in torque with increase in rotational speed. In other words, sensitivity of torque with steam pressure is very high compared to sensitivity of torque with respect to rotational speed.

The temperature results plotted in Fig. 10 show that operating temperature at housing near floating ring is substantially high and such high temperature need to be considered for reliable performance analysis of floating seal ring.

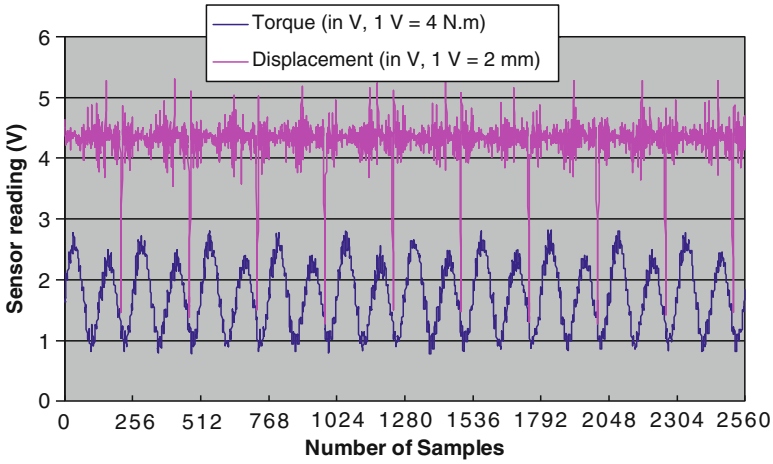

Fig. 7 Frictional torque variation in floating seal due to misalignment

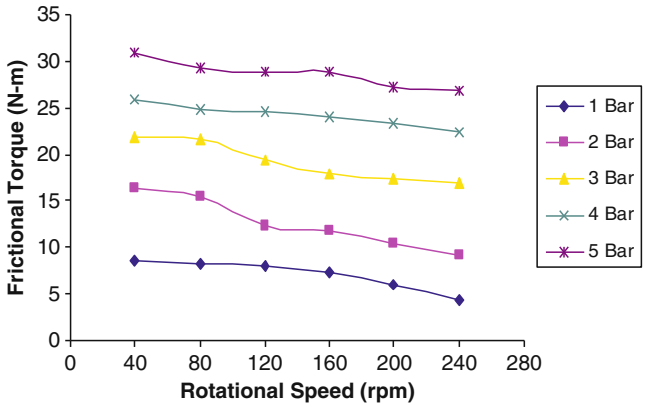

Fig. 8 Frictional torque vs. rotational speed of shaft

4 Theoretical Modeling

In stationary condition, the guide III is subject to weight of floating ring (W_g) and axial spring and radial friction forces. Under running condition, the floating seal ring is subject to two additional, aerostatic and aerodynamic forces [4]. The forces in axial direction (i.e., spring force, aerostatic force) seal the leakage path, while forces (i.e., aerostatic and aerodynamic) in radial direction support the shaft-assembly weight. A force balance on a section of floating ring is shown in Fig. 11.

The high pressure side normal load is calculated using $K\delta + \frac{\pi}{4}(OD^2 - ID^2)$ P_{steam}, where K is spring stiffness ($\sim$3.723 N/mm), δ is spring compression ($\sim$86 mm), OD is outer diameter (126 mm in the present case) and ID is inner

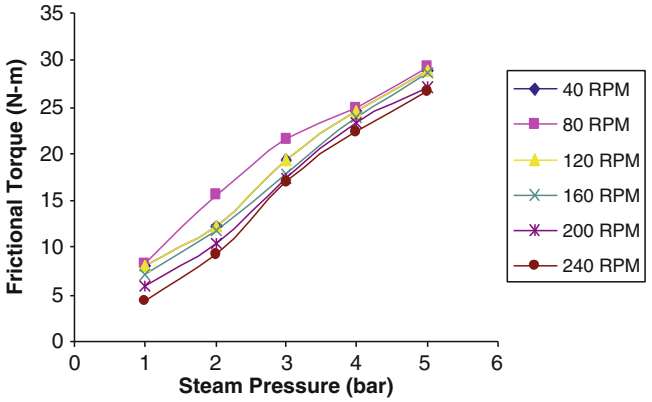

Fig. 9 Frictional torque versus steam pressure

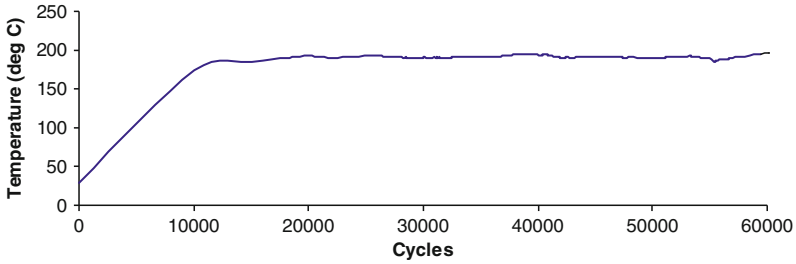

Fig. 10 Temperature history of housing at 5 bar and 120 rpm speed

Fig. 11 Forces acting on floating seal

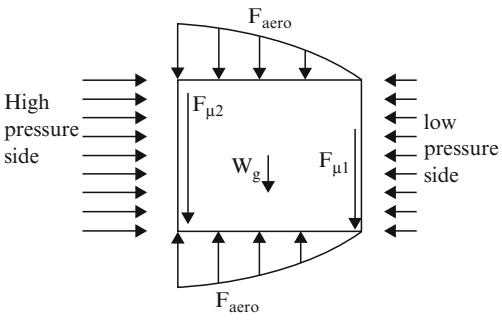

diameter (∼59.6 mm) of the seal ring. Increasing steam pressure increases the normal load on seal ring. The friction force $F_{\mu 2}$ can be evaluated using coefficient of friction (μ)*Normal load. Authors in their earlier publication [3] estimated $\mu = 0.25$.

Under rotational speed of shaft, there is a possibility of development of aerodynamic film between the floating ring and shaft, and between floating ring and

housing [5]. To determine the aerodynamic load capacity of floating seal, the compressible Reynolds equation (1) is solved.

$$\frac{\partial}{\partial x}\left[\rho h^3 \frac{\partial P}{\partial x}\right] + \frac{\partial}{\partial z}\left[\rho h^3 \frac{\partial P}{\partial z}\right] = 6\eta \left[U \frac{\partial(\rho h)}{\partial x} + 2\frac{\partial(\rho h)}{\partial t}\right] \tag{1}$$

Here ρ is the density of steam, η is steam-viscosity, and h is film thickness. The solution is complex because h, P, and ρ are functions of x/θ. On assuming that steam acts as isothermal gas ($P/\rho =$ constant), Reynolds equation can be simplified:

$$\frac{\partial}{\partial x}\left[P h^3 \frac{\partial P}{\partial x}\right] + \frac{\partial}{\partial z}\left[P h^3 \frac{\partial P}{\partial z}\right] = 6\eta \left[U \frac{\partial(Ph)}{\partial x} + 2\frac{\partial(Ph)}{\partial t}\right]$$

On rearranging,

$$\frac{\partial}{\partial x}\left[h^3 \frac{\partial P^2}{\partial x}\right] + \frac{\partial}{\partial z}\left[h^3 \frac{\partial P^2}{\partial z}\right] = 12\,\eta \left[U \frac{\partial(Ph)}{\partial x} + 2\frac{\partial(Ph)}{\partial t}\right] \tag{2}$$

This equation shows a strong dependence of pressure (P) and film thickness (h). The film thickness depends on the operating clearance between shaft and ring, and ring and housing. Due to high operating temperature, as shown in Fig. 10, the operating clearance (due to thermal expansion of shaft, seal and housing clearance) will be different than initial clearance listed in Table 1.

Material properties listed in Table 2 can be utilized to evaluate the operating clearance. A gross approximation indicates that there will be thermal expansion of shaft by 150 micron, seal ring by 50 micron, and housing by 250 micron. Such thermal expansion will increase radial clearance (25 to 100 micron) between seal ring and housing, while reduce the radial clearance (50 to 25 micron) between seal ring and shaft. This elementary analysis indicates that load carrying capacity of fluid film between seal ring and housing will be lesser than 10% compared to load capacity of fluid film between seal ring and shaft. Accounting for these facts, Eq. (2) was solved only for gas bearing between shaft and seal ring.

Table 2 Material properties of floating ring, shaft and housing

	Material grade		
Material property	CY1	FG 260 housing	SS 304 shaft
Coeff. of thermal expansion (/°C)	3.4e-6	14.5e-6	16.9e-6
Transverse bend strength (kgf/cm^2)	280	2,651	6,016
Shear strength (kgf/cm^2)	210	–	1,896
Compressive strength (kgf/cm^2)	840	7,658	6,016
Dynamic elastic modulus (kgf/cm^2)	180,000	–	–
Porosity (%)	12	–	–
Poisson ratio	0.22	0.26	0.28
Thermal conductivity (W/m.K)	12.0	15.7	16.2

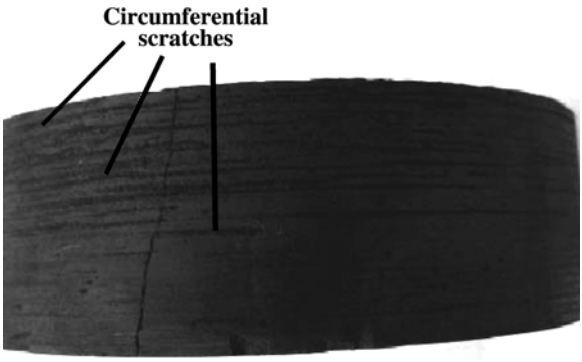

Fig. 12 Failed carbon graphite floating seal

If aerodynamic force (F_{aero}) is larger than the resultant force due to friction and the force due to weight, the floating ring begins to "float" to the geometric center of the shaft [6]. An equilibrium position is obtained by solving iteratively Eqs. (2) and (3).

$$F_{\mu} + W_g - F_{aero}\left(\varepsilon_0, \varphi_0\right) = 0 \tag{3}$$

After locating the static position (ε_0, ϕ_0), perturbation analysis [7] using Eqs. (4) and (2) can be used to evaluate the dynamic characteristics of floating seal geometry.

$$P = P\left(\varepsilon_0\,,\, \phi_0\right) + P_{\varepsilon}\,\Delta\varepsilon + P_{\phi}\,\Delta\phi + P_{\dot{\varepsilon}}\,\Delta\dot{\varepsilon} + P_{\dot{\phi}}\,\Delta\dot{\phi} \tag{4}$$

On solving Eqs. (2) and (3), and using finite difference method under 120 rpm and 5 bar steam pressure, convergence problem occurred. There was no solution even for eccentricity ratio greater than 0.99. This indicated that the friction force on the floating ring was very high and aerodynamic force was insufficient to separate the shaft from seal ring. To validate this, experiments at operating conditions of 120 rpm and 5 bar steam pressure were performed for five hours. Failure of carbon graphite seal ring, as shown in Fig. 12, was observed.

This study was directed to reduce the normal pressure on floating ring seal. Therefore the outer diameter of seal ring was reduced to 112 mm.

5 Experimental Study on Modified Seal Ring

Experiments were performed on the modified seal ring having outer diameter as 112 mm. Measured values of torque for this seal ring are shown in Fig. 13a,b. Approximately 15% reduction in torque values was observed. Further, there was no damage on the outer surface of seal ring.

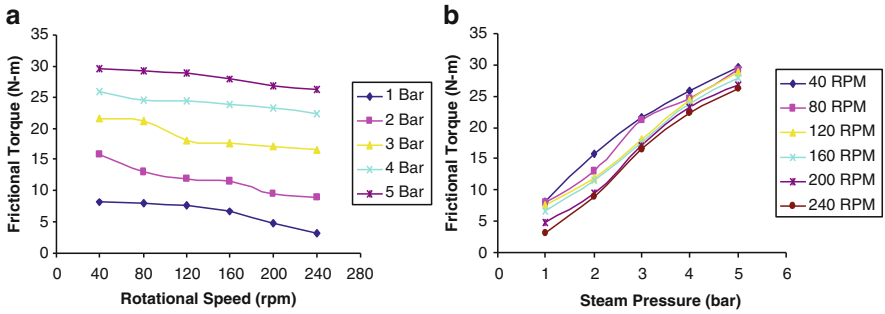

Fig. 13 **(a)** Frictional torque vs. rotational speed. **(b)** Frictional torque vs. steam pressure

6 Conclusions

In the floating seal ring, design though the fluid dynamic forces was helpful in maintaining the locked up conditions, but in actual practice the dry rubbing condition exists due to dynamic loading of the rotor during running condition.

The sinusoidal excitations generated in the rotary joint shaft can be found out easily with the help of frictional torque measured online during the testing in actual industrial conditions and environment.

The floating seal ring material is found out to be good when frictional and wear characteristics are considered. However to obtain longer seal life the loading on seals should be kept as compressive type rather than the variable transverse bending type created due to rotor dynamics effect.

References

1. Lee, Y.B., Shin, S.K., Ryu, K., Kim, C.H.: Test results for leakage and rotordynamic coefficients of floating ring seals in a high-pressure, high-speed turbopump. Tribol. Trans. **48**, 273–282 (2005)
2. Yu, J.J., Goldman, P., Bently, D.E., Muzynska, A.: Rotor/seal experimental and analytical study on full annular rub. Trans. ASME, J. Eng. Gas Turb. Power **124**, 340–350 (2002)
3. Goilkar, S.S., Hirani, H.: Design and development of a test setup for online wear monitoring of mechanical face seals using a torque sensor. Tribol. Trans. **52**, 47–58 (2009)
4. Kanemori, Y., Iwatsubo, T.: Experimental study of dynamic fluid forces and moments for a long annular seal. Trans. ASME, J. Tribol. **114**, 773–778 (1992)
5. Ismail, M., Brown, R.D.: Identification of the dynamic characteristics of long annular seals using a time domain technique. Trans. ASME, J. Vib. Acoust. **120**, 705–712 (1998)
6. Ha, T.W., Lee, Y.B., Kim, C.H.: Leakage and rotordynamic analysis of a high pressure floating ring seal in turbo pump unit of a liquid rocket engine. Tribol. Int. **35**, 153–161 (2002)
7. Rao, T.V.V.L.N., Hirani, H., Athre, K., Biswas, S.: An analytical approach to evaluate dynamic coefficients and non-linear transient analysis of a hydrodynamic journal bearing. Tribol. Trans. **23**(1), 109–115 (2000)

Applications and Research Topics for Active Magnetic Bearings

Gerhard Schweitzer

Abstract More than 30 years of research and application experience have lead to active magnetic bearings (AMB), which allow unique applications for rotating machinery with excellent performance. The paper will briefly discuss the state of art by giving historic examples and actual industrial applications. The main part is devoted to recent research topics, as a challenge to young researchers in rotor dynamics, mechatronics design and control. As an outlook, novel applications for nuclear and underwater environment, and for a superconductive bearing are addressed.

Keywords Magnetic bearings · Active magnetic bearings · Research topics · Rotor dynamics

1 Introduction

Magnetic bearings offer a novel way of solving classical problems of rotor dynamics by suspending a spinning rotor with no contact, wear and lubrication, and controlling its dynamic behavior. In a general sense such an *Active Magnetic Bearing - AMB* is a typical mechatronics product. Figure 1 presents the main components and explains the function of a simple bearing for suspending a rotor just in one direction. The suspension of a full rotor of course needs several magnets, which are connected to one another by a multivariable controller. The built-in software determines its main characteristics, which allows to control the dynamics. Thus, the control law of the feedback is responsible for the stability of the hovering state as well as the stiffness and the damping of such a suspension. Stiffness and damping can be varied widely within physical limits, and can be adjusted to technical requirements. They can also be changed during operation. Theory, design and application are detailed in [13], which is the reference to several figures of this survey and to further research

G. Schweitzer (✉)
Mechatronics Consulting, Lindenbergstrasse 18 A, CH-8700 Kuesnacht, Switzerland
e-mail: g.schweitzer@ggaweb.ch

K. Gupta (ed.), *IUTAM Symposium on Emerging Trends in Rotor Dynamics*,
IUTAM Bookseries 25, DOI 10.1007/978-94-007-0020-8_23,

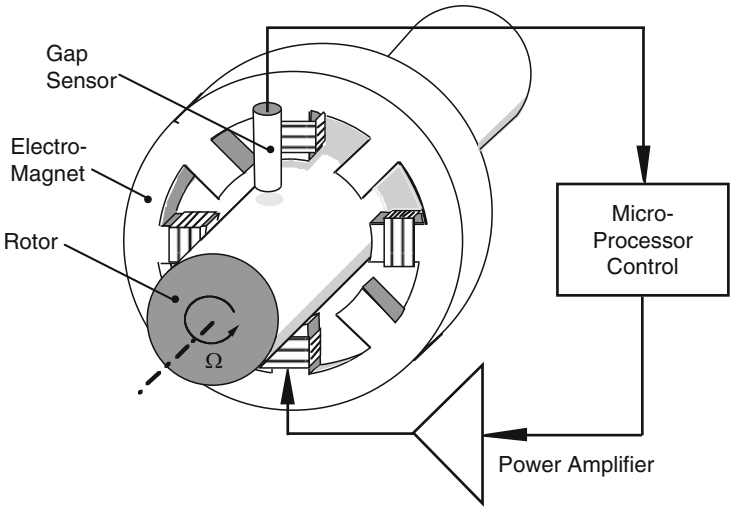

Fig. 1 Principle of the actively controlled magnetic bearing: a gap sensor measures the displacement of the rotor from its reference position, a microprocessor derives a control signal from the measurement, a power amplifier transforms this signal into a control current, and this current generates the magnetic field forces within the actuating electromagnet in such a way that the rotor remains in its hovering position

topics as well. Standards and guidelines on practical issues are given in [8]. After a brief glance on history the paper shows examples of recent industrial applications for turbomachinery and flywheels. It concentrates on actual research topics such as high speed issues, control of elastic rotors, touch-down dynamics, and the potential of using AMB as a key element for smart rotating machinery. An outlook on future applications, such as in nuclear and underwater environments, concludes the survey.

2 A Glance on History

First investigations on the physics of suspending a body freely by magnetic field forces go back to Earnshaw (1842, [3]) and Braunbek (1939, [2]). A patent of Kemper (1937, [9]) showed the potential of AMB for magnetically levitated vehicles, and the experiments of Beams demonstrated a spectacular high speed application, where mm-sized steel balls were rotated freely with up to 300 kHz until they burst [1]. First industrial-like applications of AMB were initiated by Habermann [7] for aerospace momentum wheels. The potential for the active control of rotor dynamics was shown in 1974, see Fig. 2. The interest in AMB grew with the implementation of digital control with microprocessors [15], emphasizing the role of software as a prominent element within the machine, eventually leading to the concept of smart

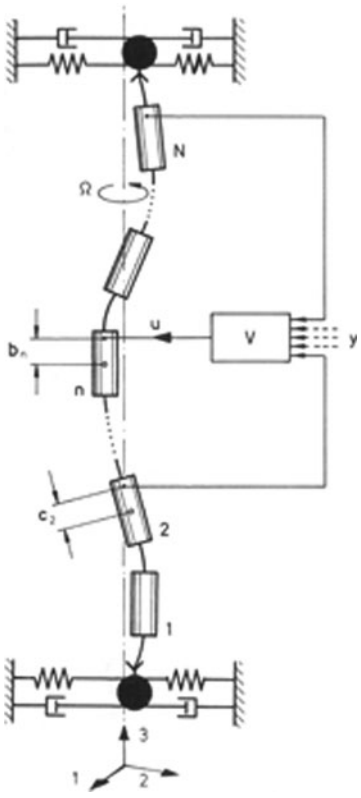

Fig. 2 Active damping: vibration control of a high-speed rotor by AMB was demonstrated in theory and experiment for a multibody centrifuge [12]. The lateral displacements of the rotor elements are measured in some selected locations, the signals are used to derive a control signal for generating suitable damping forces, which act on a specific rotor. In such a way it is possible to cross various bending resonances, and to extend the operational speed beyond the initial stability limit caused by internal damping effects

machines [4], Section 4. The industrialization, about 20 years ago, came with the availability of design tools for modeling rotor dynamics and control, and with the advances of hardware for power electronics.

3 Industrial Applications

The state of art in industrial applications will be shown by a few typical examples, Figs. 2–6. The description of the examples is given in the captions. The actual emphasis is on turbo-machinery, but of course, there are other promising areas as well, such as machine tools, high-speed motors and generators, flywheels, momentum wheels, or centrifuges. The main features are not only high speed, high power density, or the control of rotor dynamics. Other features, such as the absence of contamination by lubrication or mechanical wear, low energy consumption, and low maintenance costs are prevailing now. Furthermore, the use of AMB as a key to smart machinery allows the integration of the machine into the control of a whole production process and to manage safety and maintenance issues.

Fig. 3 Turbo-blower: cooling gas compressor (CO_2) for a power laser, cutting metal sheets up to 25 mm. The laser needs uncontaminated gas. The speed is 54,000 rpm, the rotor mass 3.6 kg, the motor power 12 kW, the radial bearing 48 mm in diameter, the bearing force 230 N (courtesy TRUMPF/MECOS)

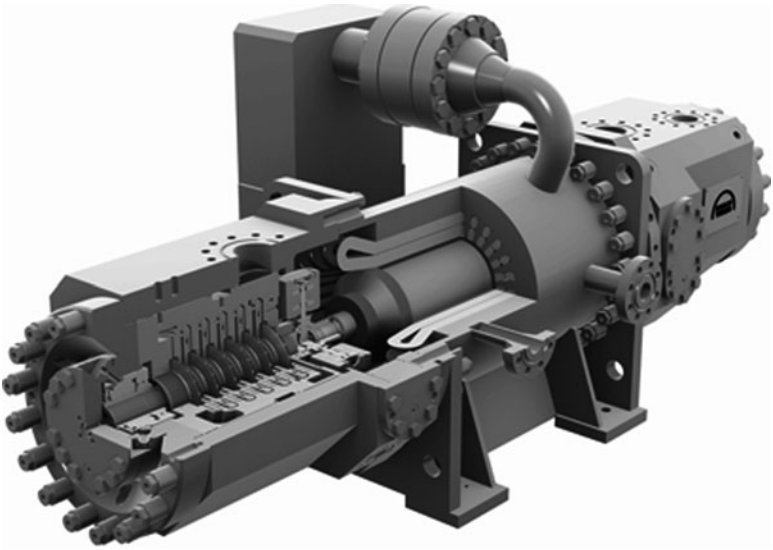

Fig. 4 Pipeline compressor HOFIM for natural gas: integration of direct drive and magnetic bearing in the turbomachine, 6 MW, 9,000 rpm (courtesy MAN Turbo/S2M)

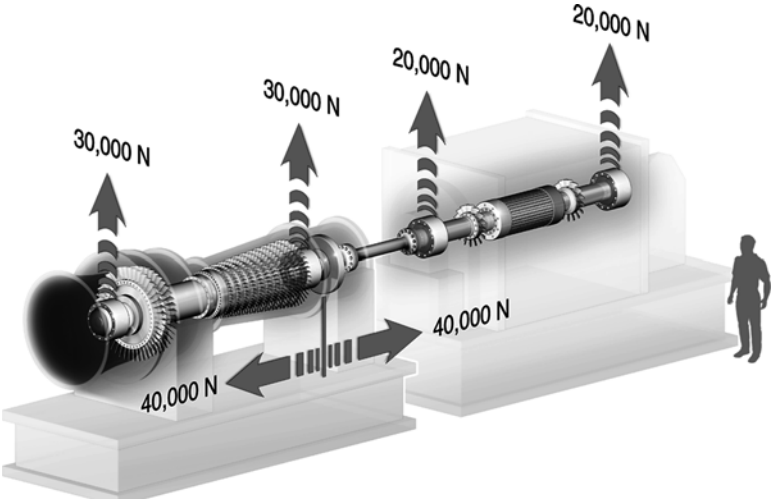

Fig. 5 Gas-turbine/Generator for power generation: four radial bearings and one thrust bearing, 6,010 rpm, 9,000 kW, bearing diameter 400 mm (courtesy S2M)

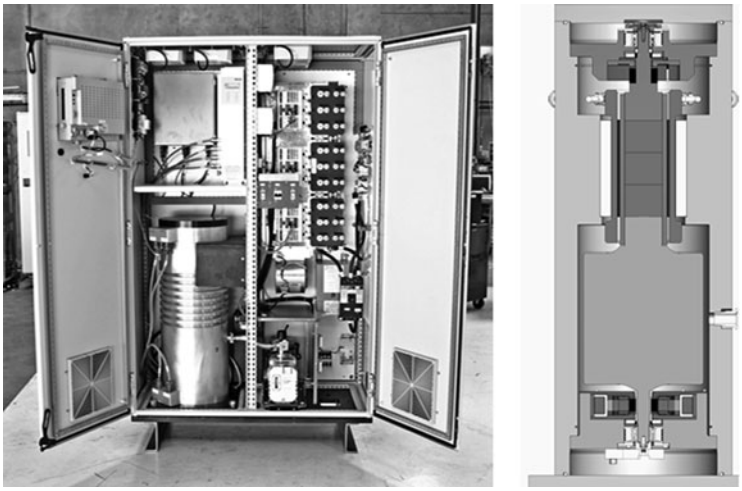

Fig. 6 Flywheel [11]: the 140 kW energy storage flywheel has been developed to provide 15 s of ride-through power and UPS service in conjunction with a diesel generator set. The flywheel operates in a vacuum. In the cabinet the flywheel is on the lower left, the magnetic bearing controller is at upper middle, motor/generator and system controller on upper left, and motor/generator power electronics on the right. The right figure shows the cross-section of the flywheel: total energy storage 1.25 kWh at 36,000 rpm for delivery of 140 kW for 15 s (0.58 kWh), flywheel rotor mass 109 kg. The flywheel has a steel hub, a 2-pole brushless DC motor/generator, and permanent magnet biased magnetic bearings (courtesy CALNETIX)

4 Research Topics

This survey will focus on five research topics, which actually appear to be most challenging, and which are illustrated in exemplary figures:

High-Speed Rotors: In industrial applications the speed usually is limited not by the bearings themselves, but by the mechanical design of the motor drive, Fig. 7. Critical elements are the usually complex structure of the motor/generator part and the laminated bushes on the rotor with their shrink fits, under the magnetic bearings. Research shows that rotor speeds of up to 340 m/s in the bearing area can be reached with iron sheets from amorphous metal (metallic glass), having good magnetic and mechanical properties. For high speeds permanent magnet synchronous drives are used, where the rotor is wound with carbon fibres, allowing speeds of about 300 m/s. As the cooling of the rotor, in particular in vacuum applications, is limited, high efficiency of the drives and optimized thermal design is essential.

Control of Elastic Rotors: "There are two reasons why flexible systems present more of a challenge to the control system designer than does a rigid rotor. The first is the simple matter that a flexible rotor has a much wider mechanical bandwidth than does a rigid rotor. This means that the mechanical response to high frequency forcing is much larger for a flexible rotor than for a rigid rotor and, as a result, the dynamic behavior of the feedback controller at high frequencies is much more important for flexible rotors than for rigid rotors. The second reason is that, when the sensors and actuators are not collocated axially along the rotor, then it is always true that at least one undamped flexible mode shape will exhibit a node between a sensor-actuator pair. If this mode has a frequency within the bandwidth of the controller, then it poses special dynamics problems for the system. Both of these issues must be attended to either explicitly or implicitly in the design of an AMB controller for a flexible rotor (cited from Maslen in [13])." Figures 8 and 9 show a simple example. For a real elastic rotor, on an elastic foundation, with several actuators and sensors,

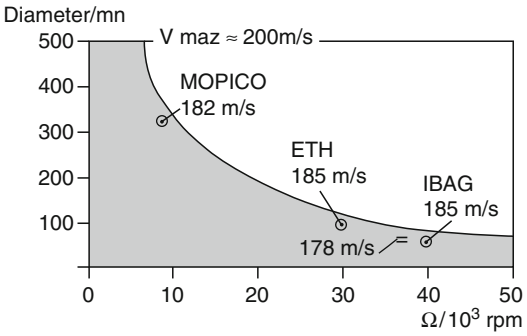

Fig. 7 Examples for the maximal diameter of the (asynchronous) motor drive in function of the rotor speed, which has been achieved in various conventional AMB applications. The (x) indicates a rotor broken at 178 m/s. The circumferential speed is a measure for the centrifugal load and leads to specific requirements on design and material

Fig. 8 A pinned, flexible beam controlled at the free end by an active magnetic bearing. Sensor and actuator are not collocated (courtesy Maslen)

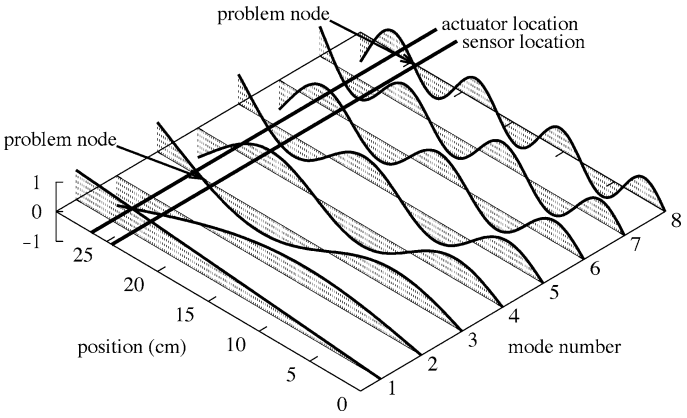

Fig. 9 Modeshapes of the flexible beam of Fig. 8. The mode numbers 3 and 8 show that the displacements measured at the sensor location are out of phase with the ones at the actuator location, causing stability problems. For this simple single input/single output control, compensation of the phase lag can be achieved classically. For real rotors more advanced concepts are necessary (courtesy Maslen)

a multiple input/multiple output control has to take into account uncertainties, and it has to be robust.

Touch-Down Dynamics: Contact between a rotor and a stator can lead to violent vibrations. As a back-up, in order to avoid potential damage, AMB supported rotors are equipped with touch-down bearings. These are an additional set of conventional bearings, and the rotor will only come into touch with them in extraordinary situations. These bearings should be able to support the rotor for a limited time period until the normal operating mode can be recovered or until the rotor can be run down safely. Dynamics of the touch-down are inherently nonlinear, with strong dependence on initial conditions, and with chaotic phases (Fig. 10). The backward whirl is the most dangerous one, generating very high contact forces. The optimal design of retainer bearings still relies mostly on experience, and a systematic, generally accepted design procedure has yet to be developed. Open research questions include the choice of material, the physical insight into high-speed contacts, i.e. for contact speeds above 200 m/s, the running down through critical speeds in retainer bearings, and control aspects in critical contact situations.

Smart Machines: Machines can be termed *smart* when their internal capability of sensing, actuating and information processing is used in an extensive way. This

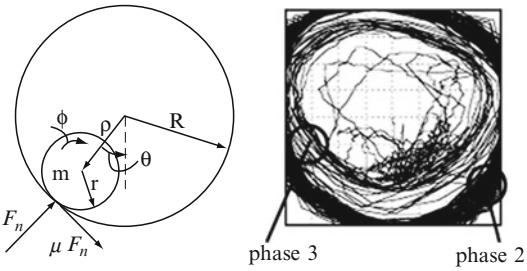

Fig. 10 *Left*: Variables for describing the touch-down dynamics of the rotor within the stator: rotor speed $\dot{\Phi}$, whirl velocity $\dot{\theta}$, air gap ρ, mass of the rotor m, normal force F_N and friction force μF_N. *Right:* motion of the rotor center within a circle with the radius of the airgap (0.3 mm). The backward whirl is initiated by a drop down of the rotor [6]

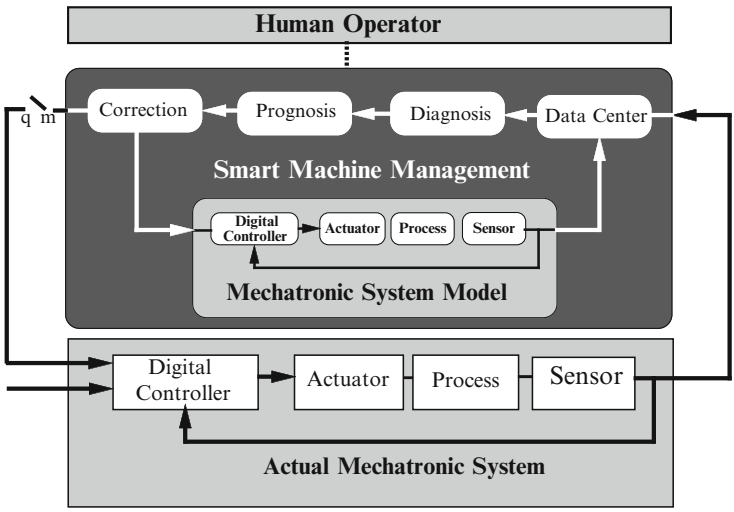

Fig. 11 Structure of a smart machine

leads to better functionality with features such as self-calibration, self-diagnostics, self-tuning, self-corrections, and eventually, it leads to less maintenance and higher safety. The smart machine in Fig. 11 consists of three main parts. One is the *Actual Mechatronic System*, the real machine with its process, sensors, actuators and the controller. The second part is the *Mechatronic System Model*, a software representation of the real machine, built up by using identification techniques. The model, or a part of it, will be used for designing, modifying or reconfiguring the control of the real machine. The third part describes the *Smart Machine Management*. It indicates the additional functions that can be incorporated into the system by making ÒsmartÓ use of the available information. Figure 12 shows the application of the smart machine concept to an AMB system, which has been built as a test rig for developing self-tuning procedures for its basic control loop.

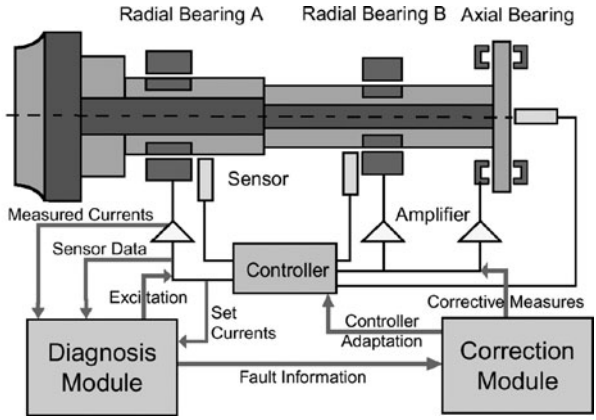

Fig. 12 Rotor in AMB with additional smart machine modules for diagnosis and correction

Fig. 13 Schematic cross-section of a turbo-generator for a nuclear power plant, the first pebble-bed high temperature gas-cooled test reactor with the gas turbine in the direct cycle (HTR-10GT, under construction, Chinese government key project): 6 MW, 15,000 rpm, vertical rotor axis, four radial bearings, two axial bearings, length of turbine 3.5 m, mass of turbine 1,000 kg. (photo courtesy Institute of Nuclear and Novel Energy Technology INET, Tsinghua University, Beijing [16])

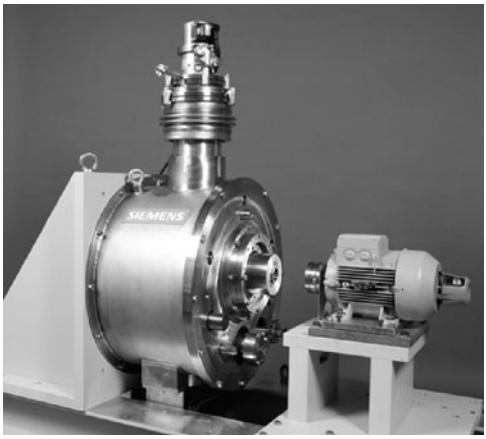

Fig. 14 Test rig for a superconductive bearing designed for a 4 MVA HTS synchronous generator, bearing capacity 500 kg, maximum speed 4,500 rpm. In the temperature range below 60 K the bearing capacity remains almost constant. The bearing, initially cooled down to 28 K, can still be operated for additional 2 h without cooling (photo courtesy SIEMENS [10])

The potential of AMB/rotor systems to become fault-tolerant is seen as a general feature of smart machinery, contributing to the already very impressive, but still growing, safety and reliability features of AMBÕs.

Advanced Applications: Advanced applications are a challenge for actual AMB research, promising novel and attractive solutions. Examples are given in Fig. 13 for a nuclear power plant, and in Fig. 14 for the use of high temperature superconductors. AMB's in aero-engines would lead to the futuristic all-electric, or rather oil-free, airplane [5]. Related research problems on high temperature materials are addressed and referenced in [13]. For the deep-sea exploration of natural gas, compressors will be needed that work autonomously and with minimal maintenance, and AMB equipped machinery is offering such performance [14].

5 Conclusions

The survey shows, after a brief glance on history and trends, the state of the art for industrial applications of active magnetic bearings in rotating machinery. Main areas are turbo-machinery, most often coupled to directly driven motor/generator units. The advantages are, next to vibration control and high power density, the absence of contamination by lubrication and mechanical wear, low costs for energy and maintenance, and high lifetime.

Five research topics are addressed and illustrated by examples: high-speed rotors, the control of elastic rotors, touch-down dynamics, the smart machine concept, and advanced applications. These include applications of AMB for nuclear power generation, superconductive bearings, aeroengines, and underwater compressors for natural gas exploration.

References

1. Beams, J.W.: High rotation speeds. J. Appl. Phys. **8**, 795–806 (1937)
2. Braunbek, W.: Frei schwebende Körper im elektrischen und magnetischen Feld. Z. Phys. **112**, 753–763 (1939)
3. Earnshaw, S.: On the nature of the molecular forces which regulate the constitution of the lumiferous ether. Trans. Camb. Phil. Soc. **7** Part I, 97–112 (1842)
4. Ewins, D., Nordmann, R., Schweitzer, G., Traxler, A. et al.: Improved machinery performance using active control technology (IMPACT). Final Report, BRITE/EURAM Research Project BRPR-CT97-0544, Europ. Commun. (2001)
5. Ewins, D., Nordmann, R. et al.: Magnetic bearings for smart aero-engines (MAGFLY). Final Report EC GROWTH Research Project G4RD-CT-2001-00625, Europ. Commun. (2006)
6. Fumagalli, M.: Modelling and measurement analysis of the contact interaction between a high speed rotor and its stator. PhD thesis, ETH Zurich No. 12509 (1997)
7. Habermann, H., Liard, G.: Le palier magnétique active: un principe révolutionaire. SKF Rev. Roulements Nr. 192 (1977)
8. ISO Standard 14839.: Mechanical vibrations – Vibrations of rotating machinery equipped with active magnetic bearings – Part 1: Vocabulary, Part 2: Evalution of vibration, Part 3: Evaluation of stability margin, Part 4: Technical guidelines, system design (Draft) (2002/2006)
9. Kemper, H.: Overhead suspension railway with wheel-less vehicles employing magnetic suspension from iron rails. Germ. Pat. Nos. 643316 and 644302 (1937)
10. Kummeth, P., Nick, W., Neumüller, HW.: Development of superconducting bearings for industrial application. In: Bleuler, H., Genta, G. (eds) Proceedings of the 10th International Symposium on Magnetic Bearings, page Keynote, Martigny, Switzerland (2006)
11. McMullen, P., Vuong, V., Hawkins, L.: Flywheel energy storage system with active magnetic bearings and hybrid backup bearings. In: Bleuler, H., Genta, G. (eds) Proceedings 10th International Symposium on Magnetic Bearings, Martigny, Switzerland (2006)
12. Schweitzer, G.: Stabilization of self-excited rotor vibrations by an active damper. In: Niordson, F.I. (ed.) Proceedings of the IUTAM Symposium on Dynamics of Rotors. Springer-Berlin, Lyngby (1974)
13. Schweitzer, G., Maslen, E.H. (eds): (contributors: Bleuler, H., Cole, M., Keogh, P., Larsonneur, R., Maslen, E.H., Nordmann, R., Okada, Y., Schweitzer, G., Traxler, A.). Magnetic Bearings – Theory, Design and Application to Rotating Machinery. Springer, Berlin Heidelberg (2009)
14. Skofteland, H., Stinessen, K.O.: Method and apparatus for protection of compressor modules against influx of contaminated gas (WO/2008/002148). Patent, Internat. Appl. No. PCT/NO2007/000222 (2007)
15. Traxler, A.: Eigenschaften und Auslegung von berührungsfreien elektromagnetischen Lagern. PhD thesis, ETH Zurich No. 7851 (1985)
16. Suyan, Y.U., Guojun, Y.A.N.G., Lei, S.H.I., Yang, X.U.: Application and research of the active magnetic bearing in the nuclear power plant of high temperature reactor. In: Bleuler, H., Genta, G. (eds.) Proceedings of the 10th International Symposium on Magnetic Bearings, page Keynote, Martigny, Switzerland (2006)

Accurate Analytical Determination of Electromagnetic Bearing Coefficients

C. Nataraj

Abstract Electromagnetic contactless bearings have unique advantages over conventional bearings including no wear, reduced pollution and maintenance, and active control prospects. Their existing mathematical models are however very simplistic, and not very accurate leading to inferior (and, sometimes, catastrophic) performance under demanding conditions. This paper seeks to derive a better model from a basic consideration of the fundamental physics of the problem. It also intends to provide a family of curves suitable for use by an engineering designer. First, the fundamental electromagnetic equations are presented for a typical radial magnetic bearing configuration. The bearing is divided into four subdomains and the resulting partial differential equations and the boundary conditions are formulated over the different subdomains. The rotor is placed into a circular orbit, which leads to a moving boundary problem. The equations are then solved in closed form using an approximate asymptotic technique. The resulting magnetic fields and forces are computed, and the results are presented in a form suitable for use by a bearing designer. The results are also in a form that is decoupled from the active control strategy which greatly enhances their applicability.

Keywords Magnetic bearings · Rotor dynamics · Electromagnetics · Analytical solutions

1 Introduction

The suspension of a rotating shaft assembly in a magnetic field thereby avoiding mechanical contact and lubrication is an idea that is very attractive and has been the subject of some research in recent years. Apart from the obvious advantage of reducing wear, the magnetic bearings are unique in that the bearing characteristics

C. Nataraj (✉)
Department of Mechanical Engineering, Villanova University, Villanova, PA 19085, USA
e-mail: nataraj@villanova.edu

K. Gupta (ed.), *IUTAM Symposium on Emerging Trends in Rotor Dynamics*,
IUTAM Bookseries 25, DOI 10.1007/978-94-007-0020-8_24,

can be changed in an active control loop just by changing the controller parameters. This makes it possible not only to reduce rotor vibration in general, but also to control the vibration of the rotor for expected and unexpected excitations including instabilities and other such potentially catastrophic situations.

There have been three kinds of models used for electromagnetic bearings.

- Linearized expressions. This is the most common model used [1, 7].
- Approximate nonlinear expressions. Nonlinear studies include [2–6, 8, 10], where the classical nonlinear phenomena including jump phenomena, bifurcations, limit cycles and chaos have been reported.
- Finite element models.

The linear models are of course very approximate and are only valid for very small excursions about the equilibrium point. In addition, they cannot predict the typical nonlinear phenomena even qualitatively. For analyses of extreme response such as due to shock, linear models are hardly suitable. The nonlinear models are better suited, but are still based on the standard magnetic circuit model. The finite element models are the most accurate and can be used to find instances when the circuit models can lead to gross errors. However, FE models are not suitable for dynamic analyses. In addition, a current distribution has to be assumed which in turn depends on the controller architecture. In other words, elaborate time-consuming investigations would have to be carried out for every possible controller and controller parameter setting, clearly an infeasible task. In fact, this kind of a problem is familiar to the rotor dynamicist faced with a finite difference solution of the hydrodynamic bearing equations, which cannot be used for nonlinear transient rotor dynamic analysis. This paper explores a completely different innovative *analytical* approach to remedy some of these problems.

This paper hence has three principal objectives:

- To validate or invalidate conventional models for electromagnetic bearings.
- To determine more accurate force expressions in a form suitable of dynamic analyses.
- To determine force expressions that are independent of the control algorithm.

2 Mathematical Development

Figure 1 illustrates a typical 8-pole electromagnetic bearing set-up with differential control. We model the geometry of the radial magnetic bearing as shown in Fig. 2. We divide the problem into four subdomains.

- Subdomain 1 (shaft): $0 < r < r_1 f(\theta)$
- Subdomain 2 (air gap): $r_1 f(\theta) < r < r_2$
- Subdomain 3 (stator with current sources): $r_2 < r < r_3$
- Subdomain 4 (stator without current sources): $r_3 < r < r_4$

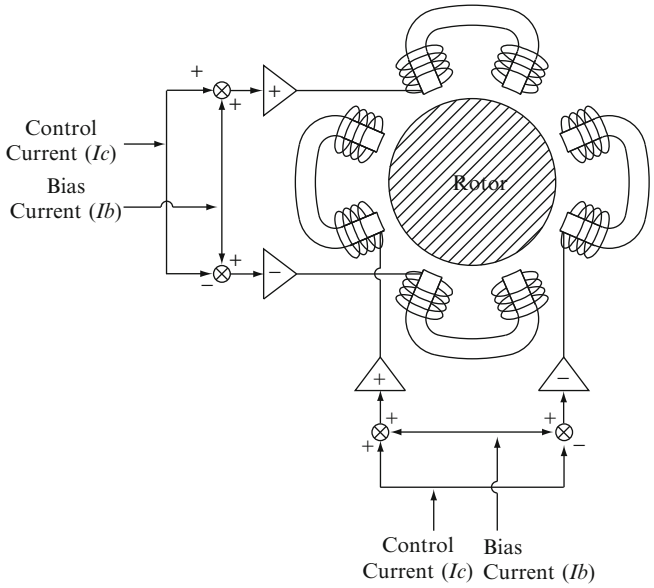

Fig. 1 A typical magnetic bearing set-up

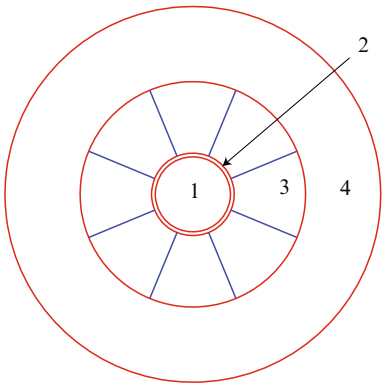

Fig. 2 Geometry of the radial bearing and subdomains

where, $f(\theta)$ is the profile of the rotor surface.

In all the four subdomains the following equation is valid [9]. This equation is essentially a restatement of Maxwell's classical electromagnetic equations with some simplifying assumptions.

$$\nabla^2 \bar{A} = -\mu \bar{J} \tag{1}$$

where, $\bar{A}$ is the magnetic vector potential. We will restrict ourselves to a two dimensional domain (essentially ignoring the axial direction). Using cylindrical coordinates we get the following equations.

$$\frac{\partial^2 A}{\partial r^2} + \frac{1}{r}\frac{\partial A}{\partial r} + \frac{1}{r^2}\frac{\partial^2 A}{\partial \theta^2} = -\mu J(r,\theta) \tag{2}$$

By definition,

$$\bar{B} = \nabla \times \bar{A} \tag{3}$$

Hence, the components of the magnetic flux density are given by

$$B_r = \frac{1}{r}\frac{\partial A}{\partial \theta}, \quad B_\theta = -\frac{\partial A}{\partial r} \tag{4}$$

In reality, the constitutive relationship between the flux density and the field is nonlinear with saturation and hysteresis. Here, we will assume a linear model which is reasonably valid. Hence, we have

$$H_r = \frac{1}{\mu}B_r, \quad H_\theta = \frac{1}{\mu}B_\theta \tag{5}$$

where, μ is the magnetic permeability.

The current density is approximately given by a line source at discrete angular locations as seen from the figure.

$$\bar{J}(\bar{r},\theta) = \begin{cases} 0, & 0 < r < r_1 \\ 0, & r_1 < r < r_2 \\ \sum_{k=1}^{N_p} J_k \delta(\theta - \phi_k), & r_2 < r < r_3 \\ 0, & r_3 < r < r_4 \end{cases} \tag{6}$$

Note that the current sources are nonzero only in subdomain 3; the equation is therefore homogeneous in subdomains 1, 2 and 4, and is nonhomogeneous in subdomain 3.

The boundary conditions are as follows.

- $A(r,\theta)$ is continuous across boundaries.
- $\hat{n} \times \mathbf{H}$ is continuous across boundaries.

The magnetic force on the rotor is determined from the following equations.

$$F_n = \frac{1}{2}\mu_0 \left(1 - \frac{\mu_1^2}{\mu_2^2}\right) H_{n1}^2 \tag{7}$$

$$F_t = \mu_0 \left(1 - \frac{\mu_1}{\mu_2}\right) H_{n1} H_{t1} \tag{8}$$

Approximation

Note that all of the surfaces are fixed except for the rotor which is subject to dynamic motion. Let the motion of the rotor be described by the polar coordinates (r_C, θ_C) where, C is the geometric center of the rotor. We assume that the rotor motion is small compared to the radius of the rotor. In practice, this would indeed be 0.001 to 0.01. The rotor surface moves with the excursions of the rotor; the maximum excursion of the rotor is the air gap which is much smaller in practice than the other dimensions. Hence it is reasonable to keep all corrections to first order.

$$\frac{r_C}{r_1} \ll 1 \tag{9}$$

Then we can approximately derive an equation for the rotor surface as follows.

$$f(\theta) \approx 1 + \left(\frac{r_c}{r_1}\cos\theta_c\right)\cos\theta + \left(\frac{r_c}{r_1}\sin\theta_c\right)\sin\theta \tag{10}$$

Solution

In subdomains 1, 2 and 4, the homogeneous PDE can be solved by standard methods.

$$A(r,\theta) = a_0 + b_0 \log r + \sum \left[(a_n r^n + b_n r^{-n})\cos n\theta + (c_n r^n + d_n r^{-n})\sin n\theta\right]$$

The constants would be determined after applying the boundary conditions.

In subdomain 3,

$$A(r,\theta) = A_{\texttt{homogeneous}} + A_{\texttt{particular}}$$

We seek a particular solution in the form,

$$A(r,\theta) = C_0(r) + \sum_{n=1}^{\infty}\left[C_n(r)\cos n\theta + D_n(r)\sin n\theta\right] \tag{11}$$

After substantial algebra, it can be shown that the solution results in the following form:

$$A(r,\theta) = A_0 + A_x i_x + A_y i_y \tag{12}$$

$$\mathbf{B}(r,\theta) = \mathbf{B}_0 + \mathbf{B}_x i_x + \mathbf{B}_y i_y \tag{13}$$

where, the individual terms are given by the following expressions.

$$A_1(r,\theta) = a_{01} + \sum_{n=1}^{\infty}\left[a_{n1} r^n \cos n\theta + c_{n1} r^n \sin n\theta\right] \tag{14}$$

$$A_2(r,\theta) = a_{02} + b_{02}\log r + \sum_{n=1}^{\infty}[(a_{n2}r^n + n_{n2}r^{-n})\cos n\theta + (c_{n2}r^n + d_{n2}r^{-n})\sin n\theta] \tag{15}$$

$$\begin{aligned} A_3(r,\theta) = {} & a_{03} + b_{03}\log r + \sum_{n=1}^{\infty}[(a_{n3}r^n + b_{n3}r^{-n})\cos n\theta \\ & + (c_{n3} + d_{n3}r^{-n})\sin n\theta] \\ & + \mu_3 J_0 r^2 \left\{ \sum_{n\neq 2}^{\infty}\left[\frac{1}{(n^2-4)}(\cos n\phi_1 - \cos n\phi_2)\cos n\theta \right.\right. \\ & \left. + \frac{1}{(n^2-4)}(\sin n\phi_1 - \sin n\phi_2)\sin n\theta \right] \\ & + \frac{(1-4\log r)}{16}[(\cos 2\phi_1 - \cos 2\phi_2)\cos 2\theta \\ & \left. + (\sin 2\phi_1 - \sin 2\phi_2)\sin 2\theta] \right\} \end{aligned} \tag{16}$$

$$A_4(r,\theta) = a_{04} + \sum_{n=1}^{\infty}[b_{n4}r^{-n}\cos n\theta + d_{n4}r^{-n}\sin n\theta] \tag{17}$$

Using the first boundary conditions (the vector field is continuous across the boundaries), we get:

$$A_1(r_1 f(\theta),\theta) = A_2(r_1 f(\theta),\theta) \tag{18}$$

$$A_2(r_2,\theta) = A_3(r_2,\theta) \tag{19}$$

$$A_3(r_3,\theta) = A_4(r_3,\theta) \tag{20}$$

The second boundary condition is that the normal component of H is continuous across the subdomains 1 and 2, which is a moving boundary. To a first approximation, this is given by

$$\begin{aligned} \hat{e}_n \times \mathbf{H} &= \left(\hat{e}_r + \frac{r_C}{r_1}\sin(\theta-\theta_c)\hat{e}_\theta\right) \times (H_r\hat{e}_r + H_\theta\hat{e}_\theta) \\ &= \left[H_\theta - \frac{r_C}{r_1}\sin(\theta-\theta_C)H_r\right]\mathbf{e}_z \end{aligned} \tag{21}$$

This leads to the following boundary condition in terms of the vector potential.

$$\begin{aligned} & \frac{1}{\mu_1}\left[\frac{\partial A_1}{\partial r} + \frac{r_c}{r_1}\sin(\theta-\theta_c)\frac{1}{r}\frac{\partial A_1}{\partial\theta}\right]|_{r=r_1 f(\theta)} \\ & = \frac{1}{\mu_1}\frac{1}{\mu_2}\left[\frac{\partial A_2}{\partial r} + \frac{r_c}{r_1}\sin(\theta-\theta_c)\frac{1}{r}\frac{\partial A_2}{\partial\theta}\right]|_{r=r_1 f(\theta)} \end{aligned} \tag{22}$$

Across the subdomains (2, 3) and (3,4),

$$\frac{1}{\mu_2}\frac{\partial A_2}{\partial r}\|_{r=r_2} = \frac{1}{\mu_3}\frac{\partial A_3}{\partial r}\|_{r=r_2} \tag{23}$$

$$\frac{1}{\mu_3}\frac{\partial A_3}{\partial r}\|_{r=r_3} = \frac{1}{\mu_4}\frac{\partial A_4}{\partial r}\|_{r=r_3} \tag{24}$$

In general, the substitution of the boundary conditions leads to a determination of the unknown coefficients. Here, however, since one of the boundaries is a function of the motion of the rotor, it is a function of θ. We deal with this problem by satisfying the boundary conditions in an average manner by integrating over the angle. This leads to a set of 18 complicated linear algebraic equations that have to be solved simultaneously; they are not listed here to conserve space, and can be obtained from the author.

After solving for the coefficients, the vector potential A can be determined, and from it, the two components of the flux density, B and the field, H. Then, the forces that are generated can be determined; they are exceedingly complicated; it is nevertheless extremely useful to note that they have the following form:

$$F_x = F_{x0} + F_{x,xx}i_x^2 + F_{x,yy}i_y^2 + F_{x,xy}i_x i_y + F_{x,x}i_x + F_{x,y}i_y \tag{25}$$

Note that the force expressions are independent of the control algorithm. They are hence suitable for dynamic analyses and also render the control system design relatively independent of the magnetic bearing design.

3 Numerical Results

The equations were solved for various rotor eccentricities and angular positions. The magnetic fields obtained were then integrated to get the forces, or more specifically, the force coefficients. These force coefficients show the dependence on powers and products of the currents; it should be recalled the currents are determined from the control architecture about which we have said nothing. Hence, knowing the behavior of the force coefficients, one can now design the controller to deliver the appropriate currents to get the dynamic response we wish from the rotor system. All the results are shown in a scaled form and hence do not show any units. Future work will include nondimensionalization and parameter groups.

Solving the flux density coefficients (Eq. 13) are very interesting functions, but cannot all be shown here for reason of space. However, a typical distribution is shown in Figs. 3 and 4 for $\epsilon = 0.5$.

The forces derived from the above fluxes show the following important and interesting features. In the expression for F_x, $F_{x,xx}$ is the only 'standard' coefficient found in the nonlinear circuit equations; all other terms are new and not reported previously. (Similarly, $F_{y,yy}$ in the expression of F_y.) Figure 5 shows the

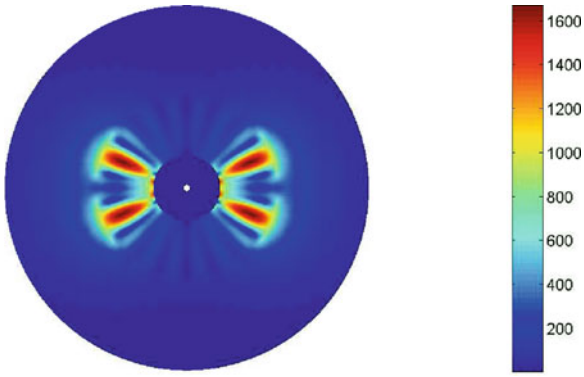

Fig. 3 B_x magnitude plot

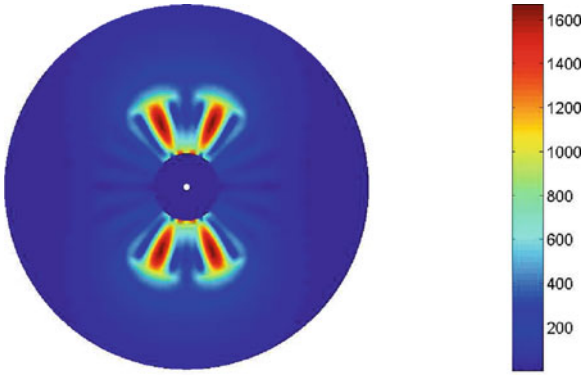

Fig. 4 B_y magnitude plot

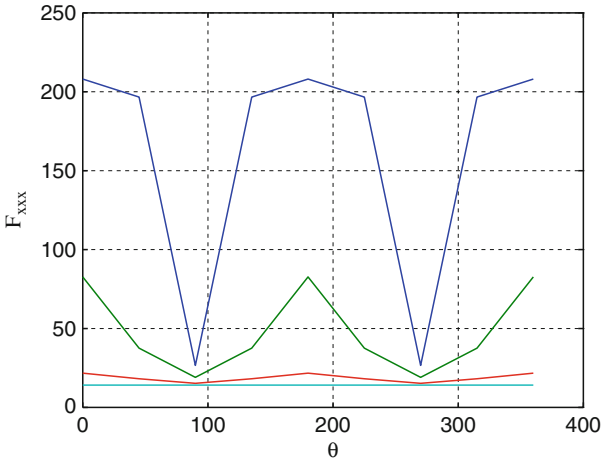

Fig. 5 $F_{x,xx}$ coefficient vs. θ for values of $\epsilon = 0.4, 0.7, 0.9$

coefficient vs. the angular position for the various values of ϵ. Clearly, the coefficient peaks opposite the energized poles as it should; however, it is not isolated, and does result in a force in the y-direction as well.

Next, we plot $F_{x,yy}$, Fig. 6, which is the coefficient associated with the force in the x direction due to the current in the y direction, a cross- coupling effect similar to that in hydrodynamic bearings. Note that the force is smaller than the principal force by a factor of 5 or so, but is not negligible. Also shown in Figs. 7–9 are the other coefficients from Eq. 25. These coefficients reveal surprising new dependencies on the currents and have not been reported anywhere. Lastly, there is a current-independent term, F_{x0}, not shown here.

Other forces reveal similar behavior and are not shown here to conserve space.

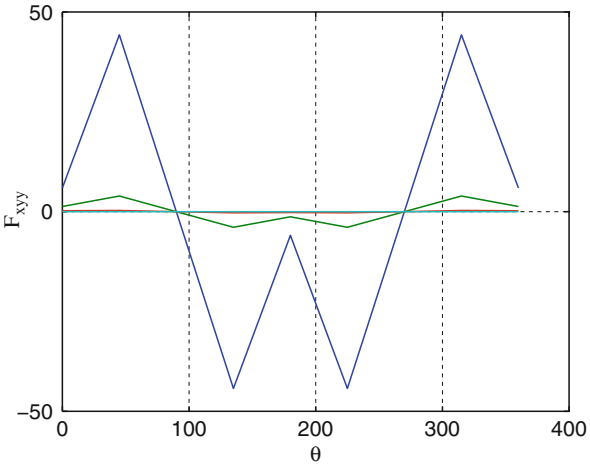

Fig. 6 $F_{x,yy}$ coefficient vs. θ for values of $\epsilon = 0.4, 0.7, 0.9$

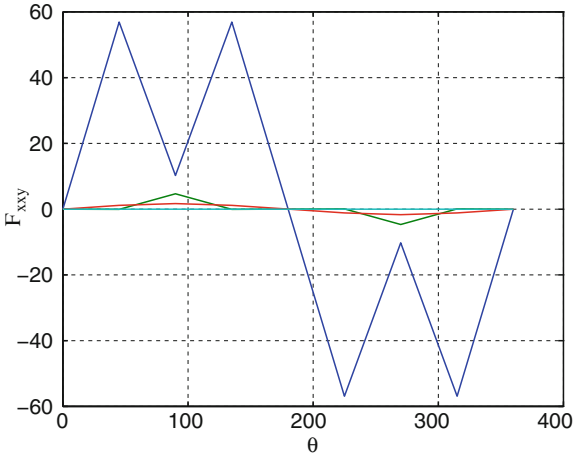

Fig. 7 $F_{x,xy}$ coefficient vs. θ for values of $\epsilon = 0.4, 0.7, 0.9$

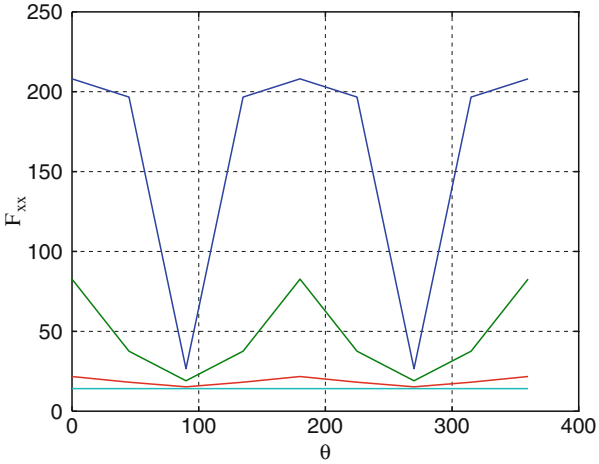

Fig. 8 $F_{x,x}$ coefficient vs. θ for values of $\epsilon = 0.4, 0.7, 0.9$

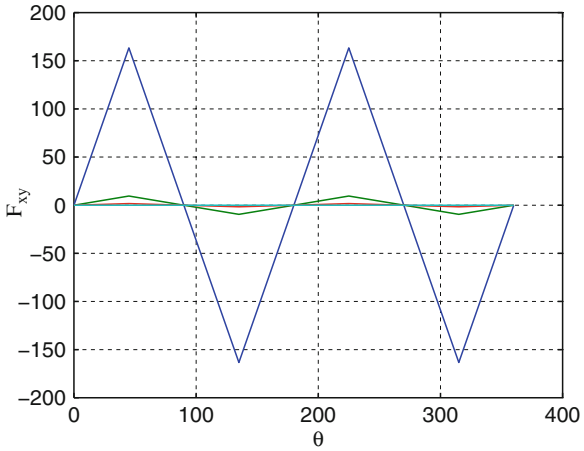

Fig. 9 $F_{x,y}$ coefficient vs. θ for values of $\epsilon = 0.4, 0.7, 0.9$

4 Conclusions

This paper modeled a standard eight pole electromagnetic bearing using Maxwell's equations and used an asymptotic technique to derive approximate expressions for the magnetic forces. The mathematical problem is one of a partial differential equation with a moving boundary and is non-trivial. The solutions obtained of the magnetic flux and the resulting forces reveal some surprising and interesting results.

The forces are not just dependent on the square of the current in the x or y direction as they are normally assumed from conventional linear and nonlinear magnetic circuit models. Instead, we note that they are much more complex. For example, F_x

depends upon i_x, i_x^2, i_y^2, $i_x i_y$, i_x and i_y. These dependencies get larger for larger excursions of the rotor as computed and plotted in this research. In essence, this means that it would be wise for the control strategy needs to consider this cross dependence, and would help control the vibration of the rotor much better especially under large excursions (such as in the case of shock, for example).

In addition, this paper provided the mathematical model and an innovative procedure for a very complex problem in a manner that is independent of the control algorithm. Unlike a solution with the Finite Element Method, this procedure hence provides a much deeper insight as well as a design tool for optimal selection of both the magnetic bearing parameters as well as the control algorithm.

Acknowledgements This work was partially supported by a grant from Office of Naval Research under Grant No. N00014-07-10866. The author would like to gratefully acknowledge Dr. Mark Spector who is the project manager; in addition, much appreciation is due to the assistance of Matthew Frank (NAVSSES – Philadelphia).

References

1. Allaire, P.E.: Magnetic bearings. In: Booser, E.R. (ed.) CRC Handbook of Lubrication and Tribology, Taylor and Francis Group, LLC, vol III. (1994)
2. Chinta, M., Palazzolo, A.B.: Stability and bifurcation of rotor motion in a magnetic bearing. J. Sound Vibr. **214**(5), 793–803 (1998)
3. Hebbale, K.V.: Theoretical model for the study of nonlinear dynamics of magnetic bearings. PhD thesis, Cornell University (1985)
4. Mohamed, A.M., Fawzi, P.E.: Nonlinear oscillations in magnetic bearing systems. IEEE Trans. Automat. Control **38**(8), 1242–1245 (1993)
5. Nataraj, C.: Nonlinear analysis of a rigid rotor on a magnetic bearing. International GasTurbine Institute Conference, Houston, TX (1995)
6. Nataraj, C., Marx, S.: Bifurcation Analysis of a One dof Rotor on Electromagnetic Bearings, vol. 1, Part C, pp. 1775–1782. New York, NY 10016-5990 (2008)
7. Schweitzer, G., Bleuler, H., Traxler, A.: Active Magnetic Bearings. vdf Hochschulverlag an der ETH Zurich (1994)
8. Virgin, L.N., Walsh, T.F., Knight, J.D.: Nonlinear behavior of a magnetic bearing system. Trans. ASME **117**, 582–588 (1995)
9. Woodson, H.H., Melcher, J.R.: Electromechanical Dynamics. Wiley, New York (1968)
10. Zhang, W., Zhan, X.P.: Periodic and chaotic motions of a rotor-active magnetic bearing with quadratic and cubic terms and time-varying stiffness. Nonlinear Dyn. **41**, 331–359 (2005)

Sensitivity Analysis of the Design Parameters in Electrodynamic Bearings

G. Genta, X. De Lépine, F. Impinna, J. Girardello, N. Amati, and A. Tonoli

Abstract Electrodynamic bearings exploit the eddy current effects that take place in a conductor rotating in a constant magnetic field to achieve passive levitation without the need of additional devices, as sensors, power electronics, etc. Nevertheless, the instability issues require a dynamic analysis that would guarantee the rotor stability. In the literature, electrodynamic bearings modeling is mainly based on quasi-static analysis, i.e., the study of the forces induced in a disk that rotates with a fixed eccentricity relative to the constant magnetic field. Although this approach is useful for a first-approximation analysis, it is intrinsically related to steady state conditions, and therefore limited. Besides, the quasi-static analysis is generally based on finite element simulations, in which geometries and material properties are tested through a trial-and-error method. In the following, a model of the bearing including a few parameters, but still able to describe both the quasi-static and the dynamic performance is presented. A sensitivity analysis based on the variation of the main design parameters of the electrodynamic bearing is performed.

Keywords Electrodynamic bearings · Quasi static analysis · Finite element modeling · Sensitivity analysis

1 Introduction

Electrodynamic supports can be used to realize contactless suspensions. The principle relies on the combination of a conductor in motion and a constant magnetic field. The relative motion causes eddy currents within the conductor that interact

G. Genta (✉)
Politecnico di Torino, Department of Mechanics and Mechatronics Laboratory,
Corso Duca degli Abruzzi 24, 10129 Torino, Italy
e-mail: giancarlo.genta@polito.it

X. De Lépine, F. Impinna, J. Girardello, N. Amati, and A. Tonoli
Politecnico di Torino, Mechatronics Laboratory,
Corso Duca degli Abruzzi 24, 10129 Torino, Italy

K. Gupta (ed.), *IUTAM Symposium on Emerging Trends in Rotor Dynamics*,
IUTAM Bookseries 25, DOI 10.1007/978-94-007-0020-8_25,

with the magnetic field to produce a levitation force. The type of mechanical effect is a function of the frequency of the motion. If the mechanical frequency is lower than the R-L dynamics of the eddy currents, the interaction generates a viscous damping force. By converse if it is higher, an elastic restoring force is produced.

In electrodynamic bearings levitation is obtained by passive means, which implies that no electronic equipment, such as power electronics or sensors, is necessary for them to be functional. As such, electrodynamic suspensions are an alternative to active magnetic suspensions, as they are less complex, less susceptible to failure, and possibly, far lower in cost. Nevertheless, electrodynamic bearings have drawbacks: the achievable stiffness and damping are relatively low compared to active magnetic devices. Besides, similar to hydrodynamic supports, electrodynamic systems provide levitation only when the relative speed is above a threshold value which opens up stability issues at low speeds.

Interest in electrodynamic bearings dates back the 1980s and 1990s for flywheel [1–5] and maglev trains [6, 7] applications. In the past few years, Lembke studied electrodynamic bearings for turbomolecular pumps [8, 9]. Different configurations of bearings were investigated through finite element modeling. Most analyses were performed for an off-centered shaft rotating at constant speed (quasi-static). In [10, 11], Filatov and Maslen presented theoretical and experimental developments about a high speed flywheel, designed for energy storage applications. A discussion on the influence of the electrical parameters of the rotating conductor was initiated, and stability issues were introduced. In [12], the same authors presented a finite element analysis performed for another flywheel. In that work, the electrodynamic bearing was characterized in quasi-static configurations, and the conditions needed to stabilize the bearing were quantified. In the developments presented by Sandtner and Bleuler in [13, 14], test rigs were built to evaluate the efficiency of various configurations of electrodynamic bearings to control the axial vibrations of the rotor.

Altogether, literature on electrodynamic bearings is relatively poor if compared to active magnetic bearings. Nowadays, the design of electrodynamic bearings is based on the force-to-angular-speed characteristic obtained for a fixed eccentricity. Although this characteristic describes the behavior of the bearing in quasi-static conditions, it is not suitable for dynamic conditions where the rotor performs a non-synchronous whirl, or even a non periodic motion about the stator axis. Therefore, a model that could take explicitly into account both the quasi-static and the dynamic conditions is still lacking. In the work presented in [15–18], mathematical tools have been developed to model eddy current dampers. The influence of the electrical dynamics on the mechanical dynamics has been demonstrated analytically and experimentally [19].

The aim of the present paper is to model the dynamic behavior of rotors supported by electrodynamic bearings to study their stability. Therefore, it becomes possible to single out the parameters that are relevant for an electrodynamic bearing to be functional, and thus optimize the design procedure. The approach is based on the electromechanical dynamics of a conductor in translation in a constant magnetic field, and is transposed to the case of a rotating conductor. The model is valid for both quasi-static and dynamic conditions. It is firstly used to study the

characteristics of the bearing at fixed eccentricity. As the stability of a rotor supported by electrodynamic bearings has already been presented in [21], the paper concludes with the sensitivity analysis (in finite element modeling) with respect to the geometrical parameters of the bearing. This approach should give insight on the design procedure of such bearings.

2 Modeling of Electrodynamic Bearings

The aim of this section is to describe the proposed model of an electrodynamic bearing. The model of a one degree of freedom eddy current damper is firstly introduced, and is then extended to the case of a conductor rotating in a stationary magnetic field (Sect. 2.1). The model is then used to characterize the electrodynamic bearing in quasi-static conditions (Sect. 2.2).

2.1 Modeling of the Forces Generated by a Conductor Rotating in a Magnetic Field

In its simplest form, the dynamics of a motional eddy current damper (short-circuited) is characterized by:

$$\begin{cases} \dfrac{di}{dt} = -\omega_{RL} i + \left(\dfrac{K_m}{L}\right) \dot{x} \\ F = K_m i \end{cases} \tag{1}$$

where $\dot{x}$ and i are the relative velocity between the actuator's coil and the constant magnetic field and the resulting current, respectively. The output equation gives the force F as function of the state i. Besides, ω_{RL} is the electrical pole of the system:

$$\omega_{RL} = \frac{R}{L} \tag{2}$$

The input velocity to the output force transfer function that can be obtained from Eq. (1) is formally the same as for a purely mechanical system made of a linear spring and a viscous damper in series, whose coefficients are $k = K_m^2/L$, and $c = K_m^2/R$ respectively [15], and the equations are

$$\begin{cases} \dot{q} = -\omega_{RL} q + \dot{x} \\ F = kq \end{cases} \tag{3}$$

where q is the elongation of the equivalent spring. The analogy between the electromechanical system and the spring-damper in series is considered in the following

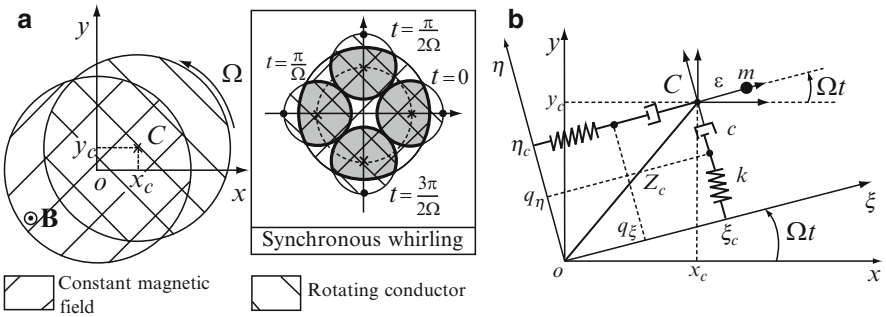

Fig. 1 Rotating conductor in a constant magnetic field. **(a)** Simplified scheme of a conductor rotating in a magnetic field. Ω is the rotation speed of the conductor. The synchronous whirling is presented as a particular configuration of rotation: The whirl speed is equal to the rotation speed, and the part of the conductor that crosses the magnetic field is always the same (darkened area). **(b)** Variables and parameters of the electrodynamic bearing model

as a shorthand representation of the electromechanical dynamics occurring in the direction of motion. This approach is chosen to establish a more intuitive basis to the reference frame issues, which is a key point when dealing with rotating machines.

A simplified scheme of a conductor rotating in a constant magnetic field is presented in Fig. 1a. The magnetic field is defined as going towards the reader. O and C are the geometrical centers of the magnetic field and the rotating conductor, respectively. Axes (O, x, y) refer to the reference frame fixed to the magnetic field. Ω is the rotation speed of the conductor.

In the following, axes (O, ξ, η) are simply referred as the rotating frame; by comparison, axes (O, x, y) are referred as the inertial frame and are fixed to the magnetic field. The pairs (x_c, y_c) and (ξ_c, η_c) are then the coordinates of C in (O, x, y) and (O, ξ, η), respectively.

The state and output equations of the conductor are obtained at this point taking the following assumptions into account:

1. The conductor is isotropic, which means that the inductive and resistive parameters are independent from the angle between the conductor frame and the magnetic frame.
2. The magnetic field of the stator is constant and its distribution is axisymmetric about point O.
3. The speed of point C in the rotating frame $(\dot{\xi}, \dot{\eta})$ is assumed as input in the model, the forces (F_ξ, F_η) being the corresponding output.
4. No thermal properties have been introduced into the model, which implies that the inductive and resistive parameters of the conductor remain unchanged whatever the temperature and the rotation speed. For some rotation speeds, the influence of temperature could become an issue, and in that case an improvement of the model would be necessary.

Consistent with the fact that the force is expressed in the rotating frame (O, ξ, η), the spring-damper behavior described in the previous paragraph is simply duplicated in both directions of (O, ξ, η). The state and output equations of the electrodynamic bearing are thus:

$$\begin{cases} \dot{q}_\xi = -\omega_{RL} q_\xi + \dot{\zeta}_C \\ F_\xi = k q_\xi \end{cases} \tag{4}$$

where $\zeta_C = \xi_C + j\eta_C$, $q_\xi = q_\xi + jq_\eta$ and $F_\xi = F_\xi + jF_\eta$ are the position of point C, the elongation of the spring and the force generated by the bearing, respectively, expressed in complex notation [20]. The coordinates of point C in (O, x, y) are also expressed in complex notation as $z_C = x_C + jy_C$, where z_C is the complex coordinate of C in the magnetic field frame, and is assumed to be small compared to the dimension of the conductor. Axes (O, ξ, η) rotate at the angular speed Ω, and is related to (O, x, y) as $\zeta_C = z_C e^{-j\Omega t}$. Likewise, the relation between the force in the inertial frame F_z and in the rotating frame F_ξ is given by $F_\xi = F_z e^{-j\Omega t}$. The relative velocity between the conductor and the magnetic field is then computed as $\dot{\zeta}_C = (\dot{z}_C - j\Omega z_C)e^{-j\Omega t}$. The various parameters of the model are presented in Fig. 1b.

2.2 Characterization of the Bearing Through a Quasi-Static Analysis

A quasi-static analysis consists in positioning the conductor at a constant eccentricity, and imposing a constant rotation speed relative to the magnetic field. The amplitude and the orientation in space of the force generated by the bearing are then used to estimate the capabilities of the bearing. A constant eccentricity of the conductor means that $z_C = z_0 =$constant. Therefore, the relative velocity of point C is obtained as $\dot{\zeta}_C = -j\Omega z_0 e^{-j\Omega t}$. This relationship shows that point C describes a circle in the rotating frame, with an angle equal to $-\Omega t$ and a constant radius equal to $|z_0|$. It also shows that the velocity has a direction perpendicular to the eccentricity z_0 (complex parameter j) and a value of $\Omega|z_0|$. The external force needed to balance the force generated by the bearing in the inertial frame is then obtained as:

$$F_z = F_\xi e^{j\Omega t} = \frac{k\Omega(\Omega - j\omega_{RL})}{\omega_{RL}^2 + \Omega^2} z_0 \tag{5}$$

Equation (5) shows that the electromagnetic force acting on C is a function of the rotation speed Ω. It can be seen that $|F_z|$ goes from zero (for $\Omega = 0$) to a limit value for high rotation speeds. It is interesting to note that also the phase shift θ covers the $[\pi/2, 0]$ range angle for increasing rotation speeds. For $\theta = \pi/2$, the force is perpendicular to the eccentricity z_0, while for $\theta = 0$, the force is opposed to z_0. This property can be formalized using the complex notation, as it takes into

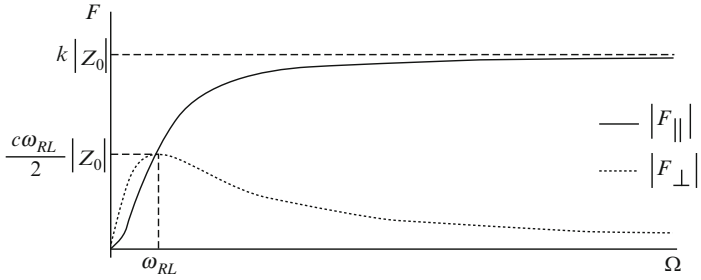

Fig. 2 Qualitative plot of the forces generated by the electrodynamic bearing. $F_\perp$ and $F_{||}$ are perpendicular and parallel to the constant eccentricity, respectively. They have the same value $k|z_0|/2 = c\omega_{RL}|z_0|/2$ for $\Omega = \omega_{RL}$. For high rotation speeds, $|F_{||}|$ and $|F_\perp|$ tend to $k|z_0|$ and 0, respectively

account both amplitude and phase of the force with respect to the eccentricity. For simplicity, Eq. (5) can be expressed more conveniently as:

$$F_z = \frac{k}{1+\left(\frac{\omega_{RL}}{\Omega}\right)^2} z_0 - j\,\frac{c\Omega}{1+\left(\frac{\omega_{RL}}{\Omega}\right)^2} z_0 = F_{||} + jF_\perp \tag{6}$$

where $F_{||}$ and $F_\perp$ are the components of the force parallel and perpendicular to the eccentricity z_0 respectively. A plot of both forces is presented in Fig. 2. $F_\perp$ can be used in two steps:

1. Identify the electric pole of the bearing.
2. Identify the value of the damping parameter of the bearing.

In fact, $F_\perp$reaches a maximum for $\Omega = \omega_{RL}$ at a value of $F_{\perp\,\max}$ as:

$$\begin{cases} \Omega = \omega_{RL} \\ |F_\perp|_{\max} = \dfrac{c\omega_{RL}}{2}|z_0| \end{cases} \tag{7}$$

3 Finite Element Model and Sensitivity Analysis

As the parameters of the electrodynamic bearing have a great influence on the stability of a rotor, it is important to perform a numerical analysis providing some insight on how the geometrical characteristics of the system affect its dynamic behavior.

3.1 FEM Model

The software chosen for the analysis is MEGA. The Maxwell equations are solved through a Minkowski transform method. The finite element model, shown in Fig. 3,

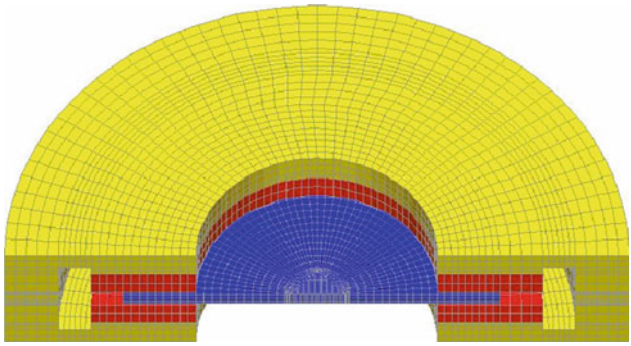

Fig. 3 Cut view of the model of the electrodynamic bearing used for the analysis

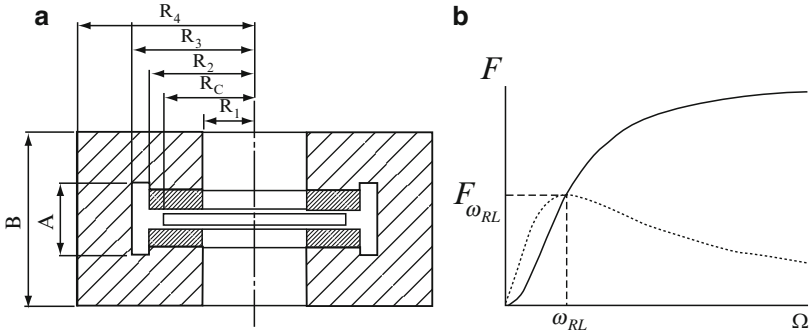

Fig. 4 FEM analysis **(a)** geometry of the model; **(b)** qualitative results, very similar to those obtained using the simplified model (Fig. 2)

is made by a conducting disk rotating in a fixed magnetic field. Unlike the configuration shown in Fig. 1a, the magnetic field has an annular configuration for constructional reasons, owing to the presence of a shaft connected to the rotating conductor. The results so obtained show that the original model is still relevant.

3.2 Sensitivity Analysis

The objective of this analysis is to obtain an insight on which geometrical parameters have more influence on the electrical parameters, and then on the dynamic behavior of the bearing. The analysis was performed by changing all the radial dimensions of the system keeping constant the scale of these with respect to the conductor radius. Also the axial dimensions and the eccentricity were kept constant. The model and some qualitative results are shown in Fig. 4.

The numerical values are reported in Table 1, and the eccentricity is 1 mm. For each configuration, the forces in both directions are computed, and the characteristic

Table 1 Initial parameters of the sensitivity analysis

Variable parameters	Value (mm)	Fixed parameters	Value (mm)
R_C	12.5	Conductor thickness	3
R_1	8	Air gap	1
R_2	15	Magnet thickness	6
R_3	19	A	19
R_4	22	B	27

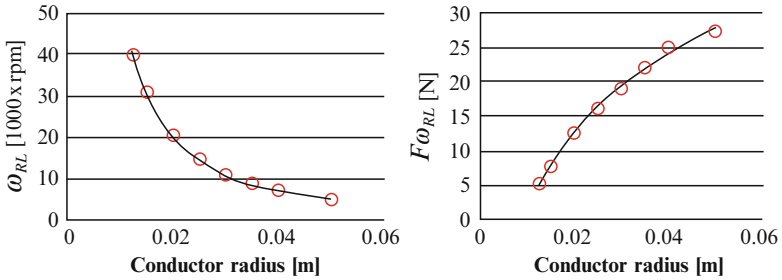

Fig. 5 Sensitivity analysis for various conductor radii

points are chosen as the intersection of both plots. This point has the advantage to give the electric pole and the damping coefficient at the same time. The results for various radii of the conductor are shown in Fig. 5.

The results of the sensitivity analysis show that the electrical pole of the system decreases with increasing conductor radius, while the relative force increases significantly. This is an interesting result since the stability analysis reported in [21] shows that the speed at which the system levitates in a stable way decreases with a decreasing electric pole. Actually, the bearing is more stable when its stiffness contribution is more important.

4 Conclusions

A new model for electrodynamic bearings is presented in this paper. This model is based on the electromechanical state equations of a motional eddy current damper and takes the RL dynamics into account. The state equations of the eddy currents that develop in the conductor are written in a rotating coordinate frame resorting to complex coordinates. This choice, common in rotordynamics, is demonstrated to be powerful as it allows to take the vector nature of the eddy current forces into account.

The model can be used to study both the quasi-static and the dynamic behavior of the bearing. In the quasi static case the conductor is spun at a fixed off-center position relative to the magnetic field and the electromagnetic forces are measured

as functions of the rotating speed. This characterization is simple and effective as it allows to determine the fundamental parameters that characterize the model. It is also shown that the quasi static characteristic alone is not adequate to model the behavior of the bearing in dynamic operating conditions.

A finite element model has been built to study the influence of the geometrical parameters of the bearing on its performance (electric pole and load capacity). It has been shown that in the case of axial flux electrodynamic bearings, for constant axial dimensions, the electric pole decreases and the load capacity increases with increasing conductor radii. These results will be used to build a test rig for experimental validation.

References

1. Basore, P.A.: Passive Stabilization on Flywheel Magnetic Bearings. MS Thesis, MIT, USA (1980)
2. Post, R.F., Ryutov, D.D.: Ambient-temperature passive magnetic bearings: theory and design equations. In: Proceedings of the Sixth International Symposium on Magnetic Bearings, MIT Cambridge, USA, 5–7 August 1998
3. Murakami, C., Satoh, I.: Experiments of a very simple radial-passive magnetic bearing based on eddy currents. In: Proceedings of the Seventh International Symposium on Magnetic Bearings, Zurich, Switzerland, 23–25 August 2000
4. Bender, D.A., Post, R.F.: Ambient-temperature passive magnetic bearings for flywheel energy storage systems. In: Proceedings of the Seventh International Symposium on Magnetic Bearings, Zurich, Switzerland, 23–25 August 2000
5. Moser, R., Regamey, Y.J., Sandtner, J., Bleuler, H.: Passive diamagnetic levitation for flywheels. In: Proceedings of the Eigth International Symposium of Magnetic Bearings, Mito, Japan 26–28 August 2002
6. Post, R.F., Ryutov, D.D.: The inductrack: a simpler approach to magnetic levitation. IEEE Trans. Appl. Superconductivity **10**(1), 901–904 (2000)
7. Thornton, R.D., Thompson, M.T.: Magnetically based ride quality control for an electrodynamic Maglev suspension. In: Proceedings of the Fourth International Symposium on Magnetic Suspension Technology, Gifu city, Japan, 30 Octorber–1 November 1997
8. Lembke, T.A.: Induction Bearings, a homopolar Concept for High Speed Machines. Ph.D. Thesis, Royal Institute of Technology, Sweden (2003)
9. Lembke, T.A.: 3D-FEM analysis of a low loss homopolar induction bearing. In: Proceedings of Ninth International Symposium on Magnetic Bearings, Lexington, Kentucky, USA, 3–6 August 2004
10. Filatov, A., Maslen, E.H.: Passive magnetic bearing for flywheel energy storage systems. IEEE Trans. Magn. **37**(6), 3913–3924 (2001)
11. Filatov, A.: Null-E Magnetic Bearings. Ph.D. Thesis, University of Virginia, USA (2002)
12. Filatov, A.: Flywheel energy storage system with homopolar electrodynamic magnetic bearing. In: Proceedings of the Tenth International Symposium on Magnetic Bearings, Martigny, Switzerland, 21–23 August 2006
13. Sandtner, J., Bleuler, H.: Electrodynamic passive magnetic bearing with planar halbach arrays. In: Proceedings of the Ninth International Symposium on Magnetic Bearings, Lexington, Kentucky, USA, 3–6 August 2004
14. Sandtner, J., Bleuler, H.: Passive electrodynamic magnetic thrust bearing especially designed for constant speed applications. In: Proceedings of the Tenth International Symposium on Magnetic Bearings, Martigny, Switzerland, 21–23 August 2006

15. Tonoli, A.: Dynamic characteristics of eddy current dampers and couplers. J. Sound Vib. **301**, 576–591 (2006)
16. Genta, G., Macchi, P., Carabelli, S., Tonoli, A., Silvagni, M., Amati, N., Visconti, M.: Semi-active electromagnetic dampers for the dynamic control of rotors. In: Proceedings of the Seventh International Conference on Rotordynamics (IFToMM), Vienna, Austria, 25–28 September 2006
17. Tonoli, A., Amati, N.: Dynamic modeling and experimental validation of eddy current dampers and couplers. J. Vib. Acoust. **130**(2), 021011-1-021011-9 (2008)
18. Crandall, S.H., Karnopp, D.C., Kurtz, E.F., Pridmore-Brown, E.C.: Dynamics of Mechanical and Electromechanical Systems. McGraw-Hill, New York (1968)
19. Karnopp, D.: Permanent magnets linear motors used as variable mechanical dampers for vehicle suspensions. Vehicle Syst. Dyn. **18**, 187–200 (1989)
20. Genta, G.: Dynamics of Rotating Systems. Springer, New York (2005)
21. Amati, N., De Lépine, X., Tonoli, A.: Modeling of electrodynamic bearings. J. Vib. Acoust. **130**(6) (2008)

Advanced Analysis and Optimization of Nonlinear Resonance Vibrations in Gas-Turbine Structures with Friction and Gaps

E.P. Petrov

Abstract A methodology is developed for analysis and the global optimization of resonance peak forced response levels and frequencies. Essentially nonlinear vibrations of gas-turbine structures with friction and gap contact interfaces are considered. The methods developed allow effective analysis for large-scale finite element models containing millions of degrees of freedom and detailed description of friction contact interfaces in jointed structures. The resonance peak characteristics can be calculated directly as functions of design parameters and excitation. The efficiency of the methodology is demonstrated on a representative set of practical test cases.

Keywords Friction · Vibration · Optimization · Resonance peak · Gas turbines · Bladed discs

1 Introduction

Gas-turbine engines are complex assembled structures consisting of many components which interact at contact interfaces. Forces occurring at these interfaces are essentially nonlinear due to the friction, presence of clearances and interferences, variation of contact area during vibrations, use of devices specially designed to have nonlinear properties, etc.

Currently, there are methods and computer codes, mostly based on finite element modeling, which allow detailed modeling of linear components of gas-turbine structures. Such detailed models, which in industrial applications customarily comprise $10^5 \ldots 10^6$ degrees of freedom (DOFs), allow accurate and reliable determination of the dynamic properties of the components in the absence of the contact interactions.

E.P. Petrov (✉)
Mechanical Engineering Department, Imperial College London,
South Kensington Campus London, SW7 2AZ, UK
e-mail: y.petrov@imperial.ac.uk

K. Gupta (ed.), *IUTAM Symposium on Emerging Trends in Rotor Dynamics*,
IUTAM Bookseries 25, DOI 10.1007/978-94-007-0020-8_26,

However, when these components are joined, the contact interaction forces can significantly affect the resonance frequencies, response levels and other dynamic characteristics.

To date, the resonance peak responses could be only determined for nonlinear structures as a result of forced response analysis performed over a prescribed frequency range. Such analysis requires calculation of forced response for a multitude of excitation frequencies, although the forced response is actually sought for only one frequency: the resonance peak frequency. For nonlinear structures, the resonance peak frequency is dependent on the level of forced response, it is generally unknown and has to be determined as a result of the frequency response analysis. Because of this, the conventional analysis of the resonance response is inefficient and highly computationally expensive.

Methods and models for forced response analysis of industrial-size finite element models allowing for detailed description for friction and gap contact interfaces are developed [1–7]. In the paper proposed here, the methodology is developed further and focused on the effective analysis and optimization of resonance peak forced response.

The methods developed allow calculation of the resonance peak frequency and response levels directly as functions of design parameters. Steady-state resonance peak regimes are calculated in frequency domain using multiharmonic balance formulations of the equations of motions. All expressions required for the calculation of resonance peaks, tracing of the solutions with parameter variation and determination of resonance peak sensitivities are derived analytically which ensures exceptionally fast and accurate calculations.

The problem of the search for the optimum parameter values is formulated and solved as the global optimization problem. An effective approach for search for the parameter values providing the global optimum is proposed. The methodology developed is demonstrated for large-scale finite element models of practical bladed discs with friction contact interfaces.

2 Method for Analysis of Resonance Peak Forced Response

2.1 Frequency-Domain Equation for Resonance Peak Forced Response

The equation for motion for a jointed structure can be written in the following form:

$$\boldsymbol{K}\boldsymbol{q}(t) + \boldsymbol{C}\dot{\boldsymbol{q}}(t) + \boldsymbol{M}\ddot{\boldsymbol{q}}(t) + \boldsymbol{f}(\boldsymbol{q}(t), \boldsymbol{b}(\lambda)) - \boldsymbol{p}(t, \lambda) = 0 \tag{1}$$

where $\boldsymbol{q}(t)$ is a vector of displacements; $\boldsymbol{K}$, $\boldsymbol{C}$ and $\boldsymbol{M}$ are stiffness, viscous damping and mass matrices of the structure obtained in absence of the contact interface forces, $\boldsymbol{f}(\boldsymbol{q}(t), \boldsymbol{b}(\lambda))$ is a vector of nonlinear interface forces, which is dependent

on the displacements $\boldsymbol{q}(t)$, and on the parameters of the contact interfaces combined in vector $\boldsymbol{b}(\lambda)$, and $\boldsymbol{p}(t,\lambda)$ is a vector of periodic external excitation forces, i.e., $\boldsymbol{p}(t,\lambda) = \boldsymbol{p}(t + 2\pi/\omega, \lambda)$, where ω is the principal frequency of vibrations. The parameter λ, is introduced here for the description of interdependencies of the contact interface parameters and, moreover, any contact interface parameter can be selected as the tracing parameter.

The steady-state periodic vibration response is sought; therefore, the variation of displacements in the time can be represented by a Fourier series:

$$\boldsymbol{q}(t) = \boldsymbol{Q}_0 + \sum_{j=1}^{n} \left(\boldsymbol{Q}_j^{(c)} \cos m_j \omega t + \boldsymbol{Q}_j^{(s)} \sin m_j \omega t \right) \tag{2}$$

where $\boldsymbol{Q}_j^{(c)}$ and $\boldsymbol{Q}_j^{(s)}$ $(j = 1, \ldots, n)$ are vectors of cosine and sine harmonic coefficients for system DOFs, marked by superscripts $^{(c)}$ and $^{(s)}$ accordingly; $\boldsymbol{Q}_0$ is a vector of constant components of the displacements; m_j $(j = 1, \ldots, n)$ are individual numbers of harmonics that are kept in the displacement expansion. Application of the multiharmonic balance method provides a frequency domain equation of motion. Finite element models used customarily in industrial applications can contain millions DOFs and methods for condensation and accounting for symmetry properties of the nonlinear dynamic structures allow the exclusion of all DOFs where there are no nonlinear interaction (see Ref. [3]):

$$\boldsymbol{R}(\boldsymbol{Q}, \lambda) = \boldsymbol{Q} + \boldsymbol{A}(\omega) \left(\boldsymbol{F}(\boldsymbol{Q}, \boldsymbol{b}(\lambda)) - \boldsymbol{P}(\lambda) \right) = 0 \tag{3}$$

where $\boldsymbol{Q}$, $\boldsymbol{P}$ and $\boldsymbol{F}(\boldsymbol{Q}, \boldsymbol{b}(\lambda))$ are vectors combining harmonic coefficients of the displacements; the excitation forces and the non-linear forces respectively. $\boldsymbol{A}(\omega)$ is a multiharmonic matrix of dynamic compliances including FRF matrices for all harmonics kept in the multiharmonic expansion Eq. (2):

$$\boldsymbol{A} = diag[\boldsymbol{A}_0, \boldsymbol{A}_1, \ldots, \boldsymbol{A}_n] \tag{4}$$

In order to calculate the resonance peak forced response levels and resonance frequency a criterion defining the resonance peak regime are formulated. One of the most effective and simple criteria is the condition that some characteristic amplitude of displacement takes its extreme value at a resonance frequency, i.e.,

$$r = \frac{\partial a}{\partial \omega} \tag{5}$$

As the characteristic amplitude a value of squared amplitude for a selected kth DOF and jth harmonic number can be frequently chosen, i.e.,

$$a = \frac{1}{2} \left[\left(q_{jk}^c \right)^2 + \left(q_{jk}^s \right)^2 \right] = \frac{1}{2} \boldsymbol{Q}^T \boldsymbol{I}_1 \boldsymbol{Q} \tag{6}$$

where $\boldsymbol{I}_1$ is a diagonal matrix which has the only two units at the main diagonal corresponding to sine and cosine harmonic coefficients involved here. Combining the multiharmonic equation of motion, Eq. (3) and the resonance peak criterion a nonlinear equation for direct calculation of the resonance peak forced responses is obtained:

$$\boldsymbol{R}^{res}(\boldsymbol{Q},\omega,\lambda) = \left\{ \begin{array}{c} \boldsymbol{R}(\boldsymbol{Q},\omega,\boldsymbol{b}(\lambda)) \\ r(\boldsymbol{Q},\omega,\boldsymbol{b}(\lambda)) \end{array} \right\} = 0 \tag{7}$$

The solution of this nonlinear equation gives a resonance frequency, $\omega^{res}(\boldsymbol{b}(\lambda))$ and a vector of harmonic coefficients, $\boldsymbol{Q}^{res}(\boldsymbol{b}(\lambda))$.

2.2 Calculation and Tracing of the Resonance Peaks Under Parameter Variation

The solution of Eq. (7) is performed iteratively by the Newton-Raphson method and a set of special methods are used to trace solutions corresponding to the resonance peaks (e.g., see Ref. [4]). These methods allow efficient calculation of the resonance frequencies and resonance forced response levels directly as a function of any chosen design parameter, b_j, i.e., $\omega^{res}\left(b_j\right)$ and $\boldsymbol{Q}^{res}\left(b_j\right)$, or when all or a selected group of design parameters are varied and their variation is prescribed, i.e., $\omega^{res}(\boldsymbol{b}(\lambda))$ and $\boldsymbol{Q}^{res}(\boldsymbol{b}(\lambda))$. To perform such calculation an extended Jacobian has to be evaluated, which has for the case of resonance peak analysis the following form:

$$\boldsymbol{J} = \left[\frac{\partial \boldsymbol{R}^{res}}{\partial \boldsymbol{X}} \middle| \frac{\partial \boldsymbol{R}^{res}}{\partial \lambda} \right] = \left[\begin{array}{cc|c} \frac{\partial \boldsymbol{R}}{\partial \boldsymbol{Q}} & \frac{\partial \boldsymbol{R}}{\partial \omega} & \frac{\partial \boldsymbol{R}}{\partial \lambda} \\ \frac{\partial r}{\partial \boldsymbol{Q}} & \frac{\partial r}{\partial \omega} & \frac{\partial r}{\partial \lambda} \end{array} \right] \tag{8}$$

The Jacobian is derived analytically and the expressions for all matrices involved in Eq. (8) are obtained by differentiating Eq. (7) with respect to $\boldsymbol{Q}$, ω, and λ. From Eq. (3) one can obtain the following expressions:

$$\frac{\partial \boldsymbol{R}}{\partial \boldsymbol{Q}} = \boldsymbol{I} + \boldsymbol{A}\frac{\partial \boldsymbol{F}}{\partial \boldsymbol{Q}};\ \frac{\partial \boldsymbol{R}}{\partial \omega} = \frac{\partial \boldsymbol{A}}{\partial \omega}(\boldsymbol{F}-\boldsymbol{P});\ \frac{\partial \boldsymbol{R}}{\partial \lambda} = \boldsymbol{A}\frac{\partial (\boldsymbol{F}-\boldsymbol{P})}{\partial \lambda} \tag{9}$$

where $\boldsymbol{I}$ is an identity matrix, and differentiating Eq. (5) the expressions for the other blocks of the Jacobian can be obtained:

$$\frac{\partial r}{\partial \boldsymbol{Q}} = \boldsymbol{I}_1\frac{\partial \boldsymbol{Q}}{\partial \omega} + \boldsymbol{Q}^T\boldsymbol{I}_1\frac{\partial^2 \boldsymbol{Q}}{\partial \boldsymbol{Q}\partial \omega};\ \frac{\partial r}{\partial \omega} = \boldsymbol{Q}^T\boldsymbol{I}_1\frac{\partial^2 \boldsymbol{Q}}{\partial \omega^2};\ \frac{\partial r}{\partial \lambda} = \boldsymbol{Q}^T\boldsymbol{I}_1\frac{\partial^2 \boldsymbol{Q}}{\partial \lambda \partial \omega} \tag{10}$$

Derivatives of the harmonic coefficients: $\partial \boldsymbol{Q} / \partial \omega, \partial^2 \boldsymbol{Q} / \partial \omega^2$, $\partial^2 \boldsymbol{Q} / \partial \lambda \partial \omega$, $\partial^2 \boldsymbol{Q} / \partial \boldsymbol{Q} \partial \omega$ are calculated from the equation obtained by differentiation of Eq. (3) with respect to ω and λ. All derivatives of the nonlinear contact interface forces involved in the Jacobian evaluation: $\partial \boldsymbol{F} / \partial \boldsymbol{Q}$, $\partial \boldsymbol{F} / \partial \lambda$, $\partial^2 \boldsymbol{F} / \partial \boldsymbol{Q} \partial \lambda$, etc.

are also derived analytically (see Refs. [1] and [6]), which allows very accurate and fast calculations including cases of non-smooth contact forces (e.g., when clearances/interferences are closed/opened).

3 Optimization of Resonance Peak Responses

Contact interface parameter values, level of excitation and other design parameters affect resonance peak forced response and the resonance frequency. In many practical applications it is necessary to select a set of parameters which provide optimal values for the resonance peaks while satisfying constraints on a range of variation of the design parameters. These constraints are often simple bound constraints:

$$\boldsymbol{b}^- \leq \boldsymbol{b} \leq \boldsymbol{b}^+ \tag{11}$$

Sometimes these constraints can have more complex representation, e.g.,

$$\boldsymbol{f}(\boldsymbol{b}) \leq 0 \tag{12}$$

where $\boldsymbol{f}(\boldsymbol{b})$ is a vector of functions which can be prescribed analytically or numerically, by a table of values. If domain described by Eq. (12) can be mapped to the simple bound domain described by Eq. (11), then both types of these constraints are topologically identical and can be analysed similarly. The constraints on the excitation force level variation within a given range can be also considered:

$$\boldsymbol{P}^- \leq |\boldsymbol{P}| \leq \boldsymbol{P}^+ \tag{13}$$

Choice of the merit function depends on needs of the design, and it can be selected, e.g., as minimization of the characteristic amplitude:

$$a^{res} \rightarrow \min \tag{14}$$

or maximization of the distance of the resonance frequency from an operating frequency range $\left[\omega^-, \omega^+\right]$, so-called "de-tuning":

$$\min\left(\omega^{res} - \omega^-, \omega^+ - \omega^{res}\right) \rightarrow \max \tag{15}$$

Search for an optimal set of parameters which provides the best merit function value is a rather complex problem, when conventional optimization techniques are applied, especially if the global optimum is sought for. It becomes much more complex when strongly nonlinear vibrations are optimized, which customarily can have many different forced response regimes even for the same set of design parameters and excitation and, moreover, a multitude of local extrema of the merit function.

An approach proposed here allows the determination of parameter value providing the global minimum for the resonance peak forced response value and removing the resonance frequency from a given frequency range. It can also determine domains of parameter values which satisfy: (i) the restriction on the resonance peak forced response level: $a^{res} < a^{+}$, (ii) the restriction that the resonance frequency is within a given range: $\omega^{res} \in \left[\omega^{-}, \omega^{+}\right]$, or (iii) both such conditions.

The approach is based on extremely high efficiency of the method developed for analysis of the resonance regimes. In order to find the global maximum and solution for other problems, it calculates dependency $\omega^{res}(\boldsymbol{b}(\lambda))$ and $\boldsymbol{Q}^{res}(\boldsymbol{b}(\lambda))$ for specially selected "sweep" functions – functions of variation of the vector of parameters, $\boldsymbol{b}(\lambda)$ which have to cover the space defined by the constraints on the design parameter variation in Eq. (11). These functions have to satisfy several requirements including the following: (i) all these functions have to be continuous with respect to λ, together with its 1st derivatives; (ii) the trajectories of the parameter variation have to cover the whole domain of possible values given by Eq. (11) or Eq. (12) more or less uniformly; (iii) the facility allowing choice of density of this coverage should be available; (iv) absence of the repetitive trajectories is desirable. The first from the above requirements has to be satisfied in order to allow effective application of the method for tracing of the resonance peaks. Meeting the three other requirements increases the efficiency of the search by avoiding spending time on gaining unusable data. One of possible choices for the sweeping functions is the Lissajous curves which are generalized for n-dimensional case and used as the sweep functions, e.g.,

$$b_j = \frac{1}{2}\left(b_j^{-} + b_j^{+}\right) + \frac{1}{2}\left(b_j^{+} - b_j^{-}\right)\sin(l_j\lambda + \phi_j)\; j = 1..n \tag{16}$$

It is convenient to have closed trajectories for the parameter variation and accordingly the closed Lissajous curves are used with l_j chosen to be integer numbers. An example of the trajectories of the parameter variation is given in Fig. 1 for a case of three varied parameters (with $l_1 = 20$; $l_2 = 18$; $l_3 = 19$ and $\varphi_1 = \pi/2$, $\varphi_2 = \varphi_3 = 0$) where the ranges of parameter variation are normalized to $[-1, 1]$.

It should be noted that the method developed for the resonance peak analysis, when it follows a chosen trajectory varies the step size accordingly to the rate of

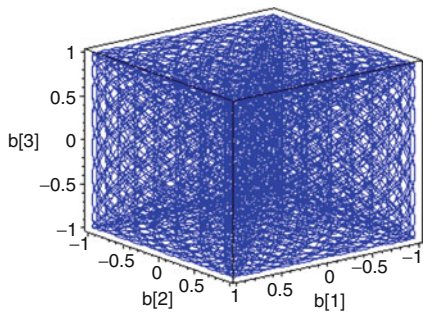

Fig. 1 An example of the parameter variation trajectory used in the global optimization

variation of the resonance peak response level and frequency. Hence the step size is chosen small when the resonance peak response is sensitive to parameter variation and it is chosen large when it is not sensitive. The algorithm developed for the selection of the step size allows the capture of all variations of the resonance peaks, even where, as frequently happens in nonlinear analysis, these variations are abrupt, and provide high computationally efficiency.

4 Numerical Examples

As an example of application of the developed method a bladed turbine disc was considered with damping generated at blade root friction contact interfaces. A sector finite element model used in the analysis is shown in Fig. 2b and the total number of blades in the bladed disc analysed is 64. The number of DOFs in the sector model is 73,245. Damping loss factor,η, due to material and aerodynamic damping was assumed to be 0.001. Aerodynamic forces exciting the vibration analysed were determined from aerodynamic calculations and are distributed over the blade airfoils. Travelling wave excitation by 43rd engine-order (EO) is considered in the frequency range containing the first blade flap-wise (1F) mode and the forced response was determined at a node located at the blade tip. The contact interaction is modelled by the area friction contact elements distributed over the contact interfaces.

The blade root fir-tree has two lobes (see Fig. 2c) and in the analysis performed, the area friction contact elements were distributed over contact surfaces of first lobe and the lower lobes are assumed to be fully stuck. Parameters of the area friction contact elements considered in the analysis are: (i) a value of the friction coefficient, μ, varied in a range [0.1, 0.5], and (ii) values of the gap/interferences applied at the friction interfaces, δ, varied in range [-100%, +100%] of a reference value.

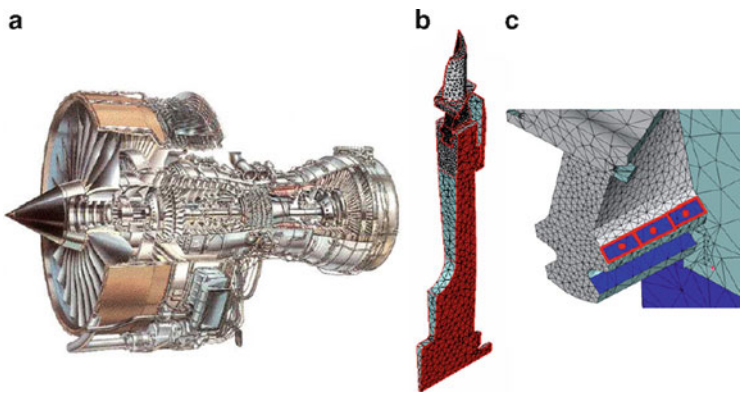

Fig. 2 A gas-turbine engine (© Rolls-Royce plc.), **(a)** model of the bladed turbine disc with friction interfaces at blade-disc root joints, **(b)** a sector bladed disc FE model, and **(c)** area friction contact elements applied at contact interfaces

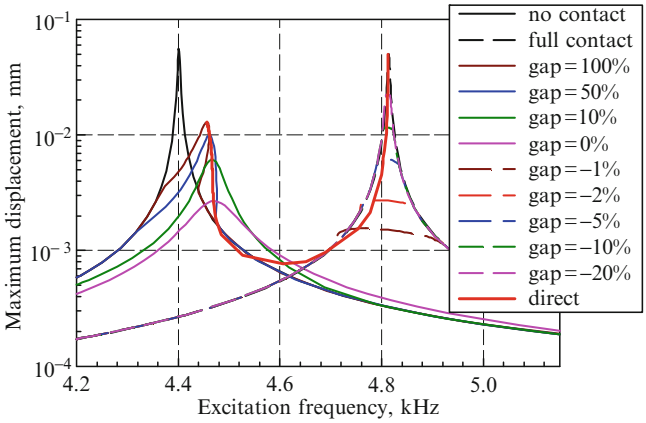

Fig. 3 Forced response calculated for different gap values and results of the direct parametric analysis

In Fig. 3, the results of the direct parametric analysis for the resonance peaks are compared with the forced response dependencies on the excitation frequency calculated for selected values of the gap.

Positive gap values correspond to initial clearances and negative values correspond to interferences which appear when centrifugal forces due to rotor rotation are applied to blades. The range of the gap values examined is from −100% to +100% of the reference value. For comparison, the forced responses of two limiting cases are also displayed: (i) the forced response of the bladed disc without any contact at the first blade root lobe, and (ii) the forced response calculated when there is full contact over the first lobe and slip does not occur. Similar to previous case, one can see that the direct parametric analysis allows calculation of the resonance peaks accurately and reliably. For cases of positive gap values the forced response exhibit stiffening behaviour, since for higher amplitude levels the gaps are closed and stiffness of the contact interfaces increases. For cases of negative gaps, there is a weak softening effect due to opening interferences, and accordingly stiffness reduction, with higher amplitudes. Moreover, a decrease of the interference values facilitates the friction damping and, hence, a decrease of the resonance amplitudes.

The optimization search proposed in this paper has been applied to find dependencies for the resonance peak level and frequency and the optimum values of the contact interface parameters. The dependency of the resonance peak response level and frequency on friction coefficient and interference values are shown in Fig. 4. The maximum and minimum values of the response levels and frequencies and contact interface parameters corresponding to these values were determined as a result of the optimization search, and found values are given in Table 1. One can see that the resonance frequency is almost independent on the friction coefficient and changes sharply when the gap value changes its sign, i.e., when interferences turn into clearances. The resonance response level is affected by values of the interference and the friction coefficient. For high interference values the resonance

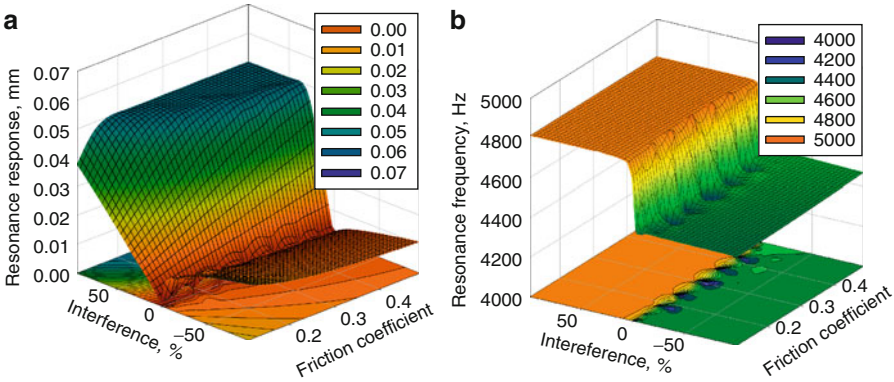

Fig. 4 Dependency oresonance response level (**a**) and resonance frequency (**b**) on friction coefficient value and on the interference value at the shroud contact interface

Table 1 Results of the search for maximum and minimum resonance peak characteristics

	Maximization		Minimization	
Factor	Frequency	Amplitude	Frequency	Amplitude
μ	0.45	0.48	0.10	0.10
δ (%)	74.49	78.19	−99.99	0.94
Freq. (Hz)	4, 812.5	4, 812.5	4, 447.3	4, 610.1
Ampl (mm)	0.050	0.050	0.020	7.644e-4

response level becomes independent of the friction coefficient, which is due to the fact that the large normal stresses eliminate any slip at the contact interface and all contact nodes stay stuck over the whole vibration period. The minimum response level is achieved for $\mu = 0.1$, $\delta = 0.94\%$ and the minimum response level is 65 times smaller than the maximum one achieved for $\mu = 0.48$ and $\delta = 78\%$.

The first lobe of the blade fir-tree root has two contact interfaces: (i) on the left side and (ii) on the right side of the lobe (see Fig. 2b). The initial gaps/interferences are produced by centrifugal forces and their values at the left and right contact interfaces usually differ. In the examples shown above it is assumed that, although the reference gap values at both sides are different, they are varied proportionally with δ and the ratio $\delta_{left}/\delta_{right}$ stays constant.

In order to explore the effects of different contact conditions, the analysis of resonance response has also been performed for cases when the gap value is varied for each of the two contact interfaces independently. This case can occur due to scatter in the manufacture and assembling of blades in discs and under certain variation of operating conditions. The dependency of the resonance response levels on interference values for each of two contact surfaces is plotted in Fig. 5 for a case of friction coefficient value 0.3. The results show a sharp change of the resonance frequency with a change of the sign of the interference value at each contact interface (see Fig. 5b). When there are clearances at both interfaces the resonance frequency

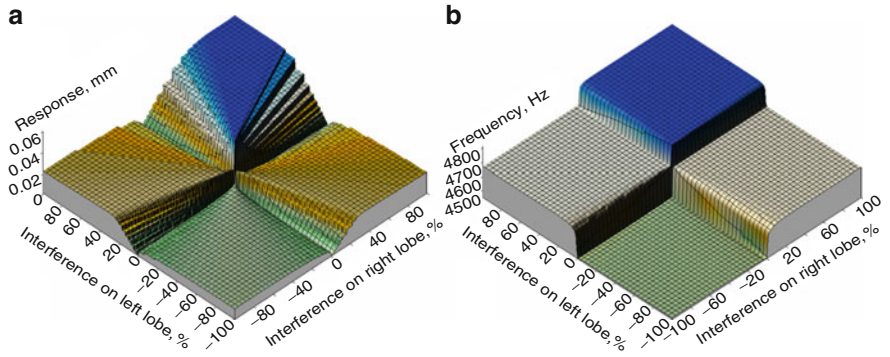

Fig. 5 Dependency of resonance response level (**a**) and resonance frequency (**b**) on the interference values

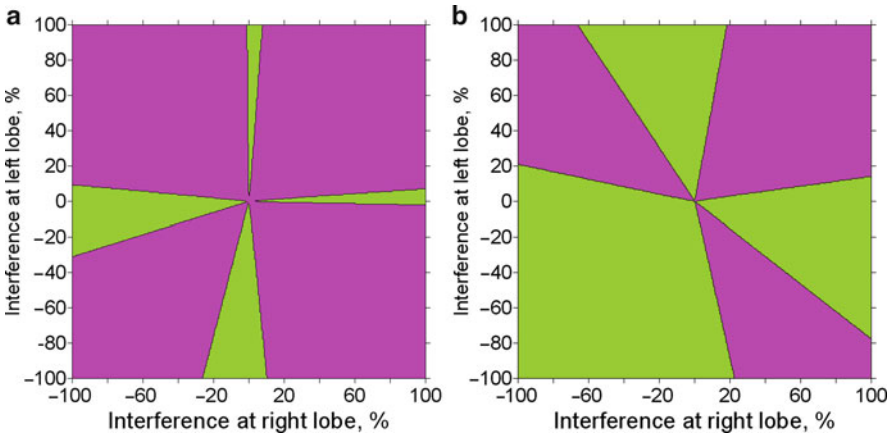

Fig. 6 Domains of interference values providing resonance response level less than: **(a)** 0.1 mm and **(b)** 0.2 mm

is 4,447 Hz, when there are interferences it is 4,812 Hz, and when one of contact surfaces has interferences and another clearances then the resonance frequency is 4,601 Hz. The resonance response levels are minimum when gaps at one or at both contact surfaces are close to zero.

The method proposed allows also solution of the problem of determination of domains of acceptable values of design parameters. There is no difficulty, e.g., to determine interference values which provide levels of the resonance forced response lower than a prescribed threshold. Domains of the interference values calculated for two levels of acceptable resonance response level ($a^{res} < 0.1$ mm and $a^{res} < 0.2$ mm) are shown in Fig. refch26:fig26.6 in green. Selection of interference value from these domains ensures that the restriction on the resonance peak response level is satisfied.

5 Conclusions

A generic methodology has been developed to calculate and to perform the global optimization of resonance forced response levels and resonance frequencies for essentially nonlinear vibrations of gas-turbine structures with friction and gap contact interfaces. The methods developed allow effective analysis for large-scale finite element models containing millions of degrees of freedom and detailed description of friction contact interfaces in jointed structures.

The resonance peak characteristics can be calculated directly as functions of design parameters and excitation. The resonance peak forced response and frequency are calculated in frequency domain using multiharmonic representation of the periodic forced response.

Acknowledgments The author is grateful to Rolls-Royce plc. for providing the financial support for this project and for giving permission to publish this work.

References

1. Petrov, E.P., Ewins, D.J.: Analytical formulation of friction interface elements for analysis of nonlinear multi-harmonic vibrations of bladed discs. ASME J. Turbomach. **125**, 364–371 (2003)
2. Petrov, E.P., Ewins, D.J.: State-of-the-art dynamic analysis for nonlinear gas turbine structures. J. Aerosp. Eng., Proc. o IMechE, Part G **218**(G3), 199–211 (2004)
3. Petrov, E.P.: A method for use of cyclic symmetry properties in analysis of nonlinear multiharmonic vibrations of bladed discs. Trans. ASME, J. Turbomach. **126**, 175–183 (2004)
4. Petrov, E.P.: Method for direct parametric analysis of nonlinear forced response of bladed discs with friction contact interfaces. Trans. ASME, J. Turbomach. **126**, 654–662 (2004)
5. Petrov, E.P., Ewins, D.J.: Method for analysis of nonlinear multiharmonic vibrations of mistuned bladed discs with scatter of contact interface characteristics. Trans. ASME, J. Turbomach. **127**, 128–136 (2005)
6. Petrov, E.P.: Sensitivity analysis of nonlinear forced response for bladed discs with friction contact interfaces. In: Proceedings of ASME Turbo Expo 2005, GT2005-68935, p. 12. Reno-Tahoe, USA, 6–9 June 2005
7. Petrov, E.P.: A sensitivity-based method for direct stochastic analysis of nonlinear forced response for bladed discs with friction interfaces. Trans. ASME, J. Eng. Gas Turb. Power **130**, 022503-1–022503-9 (2008)

Non-Parametric Identification of Rotor-Bearing System through Volterra-Wiener Theories

Nalinaksh S. Vyas and Animesh Chatterjee

Abstract The structure of the Volterra and Wiener series, which model the relationship between system response and input in terms of series of first and higher order convolution integrals, provide analytical platforms which can be utilized for parameter estimation. These are non-parametric forms of response representation. Non-parametric identification concerns modeling in a function space by input-output mapping, for systems where sufficient information on the mathematical structure or class is not available. Parametric identification, on the other hand, refers to systems where sufficient *a-priori* information about the mathematical structure of the class to which the system belongs, is available. In the present study, structured Volterra and Wiener response representations are employed to develop identification and parameter estimation procedures for nonlinear rotor systems. Experimental investigations and validation of algorithms have been carried out on a laboratory test rig. Linear and nonlinear stiffness parameters are estimated and compared with approximate theoretical formulations and some previous experimental results.

Keywords Volterra series · Wiener series · Nonlinear system identification · Rotor-bearing system

1 Introduction

While extensive research has been carried out in identification and parameter estimation of linear systems, research on nonlinear system identification has been relatively less. Rotor-bearing systems are often modeled through linear stiffness

N.S. Vyas (✉)
Department of Mechanical Engineering, Indian Institute of Technology, Kanpur, Uttar Pradesh 208 016, India
e-mail: vyas@iitk.ac.in

A. Chatterjee
Department of Mechanical Engineering, Visvesvaraya National Institute of Technology, Nagpur 440 011, Maharashtra, India

K. Gupta (ed.), *IUTAM Symposium on Emerging Trends in Rotor Dynamics*,
IUTAM Bookseries 25, DOI 10.1007/978-94-007-0020-8_27,

parameters, mainly for the convenience of mathematical analysis. Recently, researchers [1–3] have studied the nonlinear model to investigate various response characteristics like stability, oil whip etc. These studies show that dynamic behavior of rotor bearing systems can be better understood through nonlinear stiffness modeling. Earlier, Tiwari and Vyas [4] carried out nonlinear parameter estimation of rotor bearing system through Markov process and F-P-K equations. The procedure was based on the analysis of random response signals measured from the bearing housing. The procedure did not require *a-priori* knowledge of the random excitation force induced by bearing defects. The response was modeled as Markov process and F-P-K equations. This paper describes non parametric identification of rotor bearing systems using Volterra and Wiener theories. Non-parametric identification seeks input-output mapping in a functional series form. Frechet [5] was first to explore the possibility of a continuous functional on a set of functions to be represented in a power series form. Volterra [6] studied these functionals as early as 1913 and represented the input-output relationship of a general system in a functional series form, which later came to be known as Volterra series.

2 Volterra Series

Volterra series represents the input-output mapping of a physical system, with $f(t)$ as input excitation and $x(t)$ as output response, in a form of functional series given by

$$\begin{aligned} x(t) = & \int_{-\infty}^{\infty} h_1(\tau_1) f(t-\tau_1) d\tau_1 + \int_{-\infty}^{\infty}\int_{-\infty}^{\infty} h_2(\tau_1,\tau_2) f(t-\tau_1) f(t-\tau_2) d\tau_1 d\tau_2 \\ & + \int_{-\infty}^{\infty}\int_{-\infty}^{\infty}\int_{-\infty}^{\infty} h_3(\tau_1,\tau_2,\tau_3) f(t-\tau_1) f(t-\tau_2) f(t-\tau_3) d\tau_1 d\tau_2 d\tau_3 + \cdots . \\ = & \; x_1(t) + x_2(t) + \cdots + x_n(t) + \cdots \end{aligned} \tag{1}$$

where, $h_1(\tau_1)$, is the familiar impulse response function of a linear system and $h_n(\tau_1, \ldots, \tau_n)$ are the nth order Volterra kernel. Higher order frequency response functions or Volterra kernel transforms can be defined as the multi-dimensional Fourier transforms of the higher order Volterra kernels as

$$H_n(\omega_1, \omega_2, \ldots, \omega_n) = \int_{-\infty}^{\infty}\int_{-\infty}^{\infty} \cdots \int_{-\infty}^{\infty} h_n(\tau_1, \tau_2, \ldots, \tau_n) \prod_{i=1}^{n} e^{-j\omega_i \tau_i} d\tau_1 d\tau_2 \ldots d\tau_n \tag{2}$$

For a nonlinear system, with general stiffness nonlinearity, $g[x(t)]$, and single-tone harmonic excitation,

$$\ddot{x}(t) + 2\xi\dot{x}(t) + g[x(t)] = A\cos\omega t \tag{3}$$

the response can be written in terms of Volterra series as

$$x(t) = x_1(t) + x_2(t) + x_3(t) + \ldots\ldots\ldots \tag{4}$$

with

$$x_1(t) = \frac{A}{2}H_1(\omega)e^{j\omega t} + \frac{A}{2}H_1(-\omega)e^{-j\omega t} \tag{5a}$$

$$x_2(t) = \frac{A^2}{2}H_2(\omega,-\omega) + \frac{A^2}{4}H_2(\omega,\omega)e^{j2\omega t} + \frac{A^2}{4}H_2(-\omega,-\omega)e^{-j2\omega t} \tag{5b}$$

$$x_3(t) = \frac{A^3}{8}H_3(\omega,\omega,\omega)e^{j3\omega t} + \frac{3A^3}{8}H_3(\omega,\omega,-\omega)e^{j\omega t} + \frac{3A^3}{8}H_3(\omega,-\omega,-\omega)e^{-j\omega t} + \frac{A^3}{8}H_3(-\omega,-\omega,-\omega)e^{-j3\omega t} \tag{5c}$$

Response amplitude for the first three harmonics, $\omega, 2\omega$ and 3ω, from Eq. (5), can be expressed as

$$X(\omega) = AH_1(\omega) + \frac{3A^3}{4}H_3(\omega,\omega,-\omega) + \text{higher order terms} \tag{6a}$$

$$X(2\omega) = \frac{A^2}{2}H_2(\omega,\omega) + \frac{A^4}{2}H_4(\omega,\omega,\omega,-\omega) + \text{higher order terms} \tag{6b}$$

$$X(3\omega) = \frac{A^3}{4}H_3(\omega,\omega,\omega) + \text{higher order terms} \tag{6c}$$

For a system with polynomial form of stiffness nonlinearity, given by $m\ddot{x}(t) + c\dot{x}(t) + k_1x(t) + k_2x^2(t) + k_3x^3(t) + \cdots = f(t)$, the higher order FRFs can be synthesized [4] from the first order FRFs as

$$H_2(\omega,\omega) = -k_2H_1^2(\omega) * H_1(2\omega) \tag{7a}$$

$$H_3(\omega,\omega,\omega) = H_1^3(\omega) * H_1(3\omega) * \left[2k_2^2H_1(2\omega) - k_3\right] \tag{7b}$$

3 Wiener Series

Two basic difficulties associated with practical application of Volterra series are convergence of the series and measurement of individual Volterra kernels. Measurement of individual kernels is possible only if the contribution of each of the Volterra operators can be separated from the total response. Wiener circumvented these difficulties by constructing a new functional series with a set of orthogonal functionals known as Wiener G-functionals. These functionals are orthogonal with respect to Gaussian white noise excitation. Due to orthogonality, Wiener kernels can be conveniently separated through cross-correlation techniques. Wiener kernels are related

to Volterra kernels and once Wiener kernels are separated, Volterra kernels can be subsequently determined. For a white noise function $\bar{f}(\tau)$, Wiener series is

$$F[f(\tau)] = \sum_{n=0}^{\infty} [G_n(w_n, f(\tau)] \tag{8}$$

$$\begin{aligned}
G_0 &= w_0 \\
G_1 &= \int_{\infty}^{\infty} w_1(\tau_1)\bar{f}(\tau-\tau_1)d\tau_1 \\
G_2 &= \int_{-\infty}^{\infty}\int_{-\infty}^{\infty} w_2(\tau_1,\tau_2)\bar{f}(\tau-\tau_1)\bar{f}(\tau-\tau_2)d\tau_1 d\tau_2 - A\int_{-\infty}^{\infty} w_2(\tau_1,\tau_1)d\tau_1 \text{ etc.,} \\
G_3 &= \int_{-\infty}^{\infty}\int_{-\infty}^{\infty}\int_{-\infty}^{\infty} w_3(\tau_1,\tau_2,\tau_3)\bar{f}(\tau-\tau_1)\bar{f}(\tau-\tau_2)\bar{f}(\tau-\tau_3)d\tau_1 d\tau_2 d\tau_3 \\
&\quad -3A\int_{-\infty}^{\infty}\int_{-\infty}^{\infty} w_3(\tau_1,\tau_1,\tau_2)\bar{f}(\tau-\tau_2)d\tau_1 d\tau_2
\end{aligned} \tag{9}$$

A is the power spectral density of the input white noise. The nth order Wiener kernel, is generally written as

$$G_n[w_n, w_{n-1(n)}, \ldots\ldots, w_{0(n)}; \bar{f}(\tau)] \tag{10}$$

G_n is orthogonal to Volterra functionals $H_m[\bar{f}(t)]$, of degree less than n, i.e.,

$$\overline{\{H_m[\bar{f}(\tau)]\}\{G_n[w_n, w_{n-1(n)}, \ldots\ldots, w_{0(n)}; \bar{f}(\tau)\}} = 0 \tag{11}$$

The bar in the above equation indicates the time average over the interval $(-\infty, \infty)$.

Wiener and Volterra kernels [7] can be shown to bear the following mutual relations (for a third order system response representation)

$$\begin{gathered}
h_3(\tau_1,\tau_2,\tau_3) = w_3(\tau_1,\tau_2,\tau_3); h_2(\tau_1,\tau_2) = w_2(\tau_1,\tau_2); \\
h_1(\tau_1) = w_1(\tau_1) + w_{1(3)}(\tau_1); h_0 = w_0 + w_{0(2)}(\tau_1) \\
w_{1(3)}(\tau_1) = -3A\int_{-\infty}^{\infty} w_3(\tau_1,\tau_2,\tau_2)d\tau_2; \quad w_{0(2)} = -A\int_{-\infty}^{\infty} w_2(\tau_1,\tau_1)d\tau_1
\end{gathered} \tag{12}$$

For identification, the kernels are expanded in a series of Laguerre functions l_m, as

$$w_n(\tau_1,\tau_2,\ldots.\tau_n) = \sum_{m_0=0}^{\infty} \ldots.. \sum_{m_n=0}^{\infty} C_{m_0\ldots..m_n} l_{m_0}(\tau_1)\ldots\ldots.l_{m_n}(\tau_n) \tag{13}$$

where $C_{m_0\ldots..m_n} = \int_{-\infty}^{\infty}\ldots..\int_{-\infty}^{\infty} w_n(\tau_1,\tau_2,\ldots.\tau_n) l_{m_0}(\tau_1)\ldots.l_{m_n}(\tau_n) d\tau_1 \ldots. d\tau_n$.

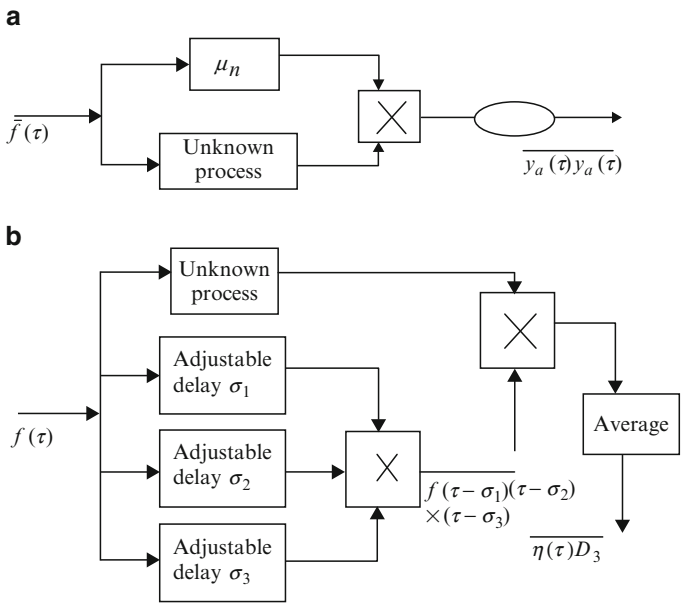

Fig. 1 (**a**) Wiener kernel determination. (**b**) Third order kernel determination

The coefficient $C_{m_0 \ldots . m_n}$, determined through the scheme shown in the Fig. 1a, is where $\mu_n = l_{m_0}(\tau_1) \ldots \ldots . l_{m_n}(\tau_n)$. The output of the scheme, gives the coefficients as

$$C_{m_0 \ldots . m_n} = (1/n!A^n)\ \overline{y_a(\tau)y_a(\tau)} \tag{14}$$

An alternative method of determination of Wiener kernels was provided by Lee and Schetzen [8], through multi-dimensional correlation functions. The scheme (for determination of the third order kernel) is illustrated in Fig. 1b.

4 Nonlinear Stiffness Modeling in a Rotor-Bearing System

A Jeffcot rotor, supported on bearings with nonlinear stiffness, is shown in Fig. 2. Rotor is considered rigid and cross-coupling stiffness coefficients of the bearings are neglected. Theoretical stiffness values based on Hertz's theory of elastic contact, can be obtained from analytical formulations of Harris [9] and Ragulski et al. [10]. Figure 3 shows a typical isolated ball bearing where external forces act along x-axis. η_i is the angle between load axis (i.e., x-axis) and the radial direction of the ith ball element.

For a displacement (x, y) of the moving ring along the respective axes, total elastic force acting in radial direction and its projections along x and y axes respectively are

Fig. 2 Jeffcott rotor

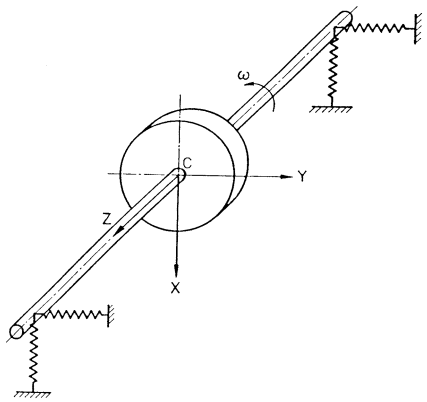

Fig. 3 Bearing model

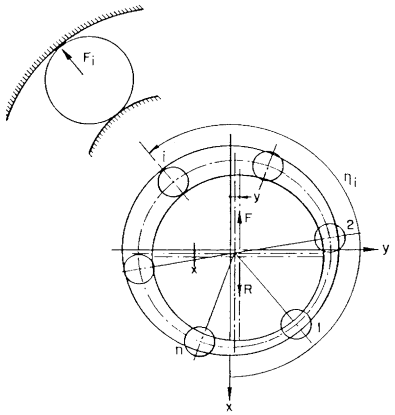

$$F_i = k_n(g + x\cos\eta_i + y\sin\eta_i)^{3/2} \tag{15}$$

$$F_{xi} = k_n(g + x\cos\eta_i + y\sin\eta_i)^{3/2}\cos\eta_i \tag{16}$$

$$F_{yi} = k_n(g + x\cos\eta_i + y\sin\eta_i)^{3/2}\sin\eta_i \tag{17}$$

where g is the radial pre-load; k_n is a proportionality coefficient. The total force of the bearing is

$$F = \sum_{i=1}^{n} F_{xi} \tag{18}$$

where n is the number of rolling elements in the bearing. Using the condition of zero elastic force along y-axis (16, 17), deformation y is

$$y = \sum_{i=1}^{n} [g + x\cos\eta_i]^{3/2}\sin\eta_i \Big/ \sum_{i=1}^{n} [g + x\cos\eta_i]^{1/2}\sin^2\eta_i \tag{19}$$

Equations (16) and (19) are used in Eq. (18) and the bearing stiffness is determined as a function of deformation x as

$$k(x) = \partial F/\partial x \tag{20}$$

It can be shown that for small range of elastic deformation of the rolling elements, stiffness function is of the form $k(x) = A - Bx^2$, which indicates that the nonlinear restoring force can be represented by the cubic polynomial nonlinearity similar to a typical Duffing's oscillator, given by $g[x(t)] = k_1 x(t) + k_3 x^3(t)$.

5 Parameter Estimation Using Volterra Theory and Harmonic Probing

For vibration along vertical direction only, the rotor-bearing system can be idealised by a single-degree-of-freedom model as

$$m\ddot{x}(t) + c\dot{x}(t) + k_1 x(t) + k_3 x^3(t) = A cos\omega t \tag{21}$$

For system with cubic nonlinearity in the restoring force, response spectra will have first and then third harmonics, whose amplitudes can be approximated by (neglecting higher order terms)

$$X(\omega) = AH_1(\omega) + \frac{3A^3}{4} H_3(\omega, \omega, -\omega) = AH_1(\omega) - \frac{3k_3 A^3 H_1^3(\omega) H_1(-\omega)}{4} \tag{22}$$

$$X(3\omega) = \frac{A^3}{4} H_3(\omega, \omega, \omega) = -\frac{k_3 A^3 H_1^3(\omega) H_1(3\omega)}{4} \tag{23}$$

This indicates that first and third order harmonic amplitudes are functions of first order FRFs and the nonlinear parameter only. Using recursive iteration discussed in Chatterjee and Vyas [11], linear as well as the nonlinear parameters can be estimated from the measured values of first and third harmonic amplitudes.

5.1 Experimentation and Parameter Estimation

The laboratory rotor-bearing set up consists of a disc centrally mounted on a 10 mm diameter shaft supported in two ball bearings, SKF 6200 (Fig. 4). The excitation is given in vertical direction and response of bearing housing vibration is also measured in vertical direction. The rap test response spectrum (Fig. 5) shows that the natural frequency is in the vicinity of 1,010 Hz. For estimation of first order kernel transforms, $H_1(\omega)$, an excitation frequency range 925–1,035 Hz is selected. Excitation level is varied over the frequency range to obtain response amplitude at constant level. Preliminary estimate of the first order kernel transform, $H_1(\omega)$, is obtained through Eq. (22) and subsequent curve fitting gives estimates of linear parameters $\omega_n = 1012.2$ Hz, $\varsigma = 0.01156$.

Estimation of nonlinear stiffness parameter k_3 is done through measurement of third response harmonic amplitude $X(3\omega)$. The ratio between the amplitudes at third

Fig. 4 Experimental set-up

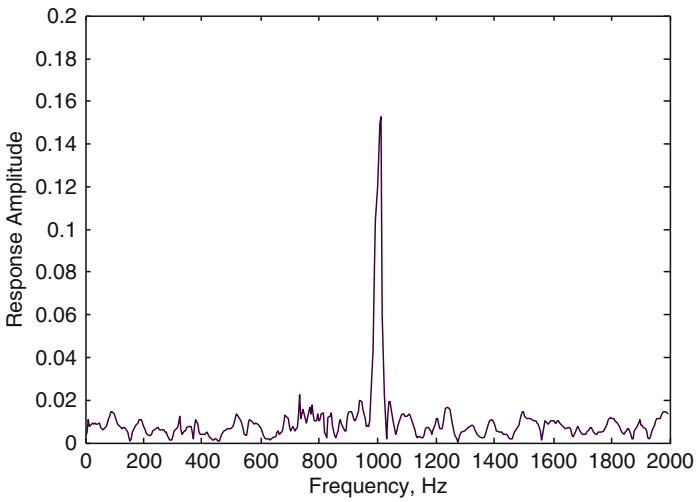

Fig. 5 Natural frequency from rap test

harmonic and first harmonic is defined as measurability index, which provides the basis of selecting the excitation level and frequency range for measurement of third response harmonic amplitude $X(3\omega)$. Excitation frequencies are selected at 330 Hz, 335 Hz, 340 Hz and 345 Hz, as measurability is relatively higher in this range. Third response harmonic amplitude $X(3\omega)$ is then measured at these selected frequencies for three different excitation levels as Case I: Excitation level = 4 N for 10% measurability; Case II: Excitation level = 3 N for 5% measurability; Case III: Excitation level = 2 N for 2% measurability. Measured response acceleration spectra at the four selected frequencies for the typical Case I, is shown in Fig. 6a–d.

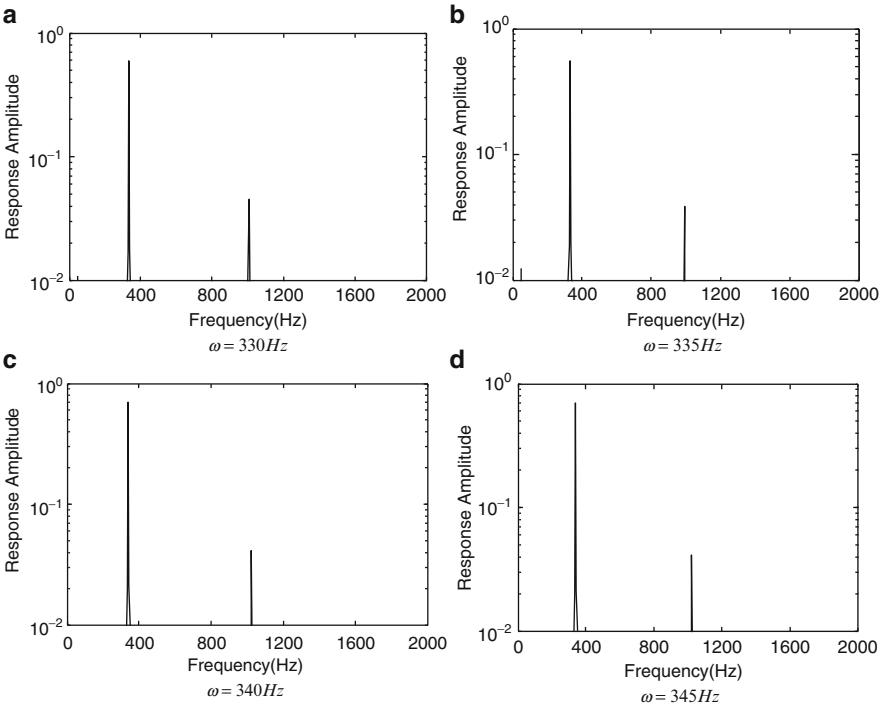

Fig. 6 Response spectra for Case I: Excitation amplitude = 4N

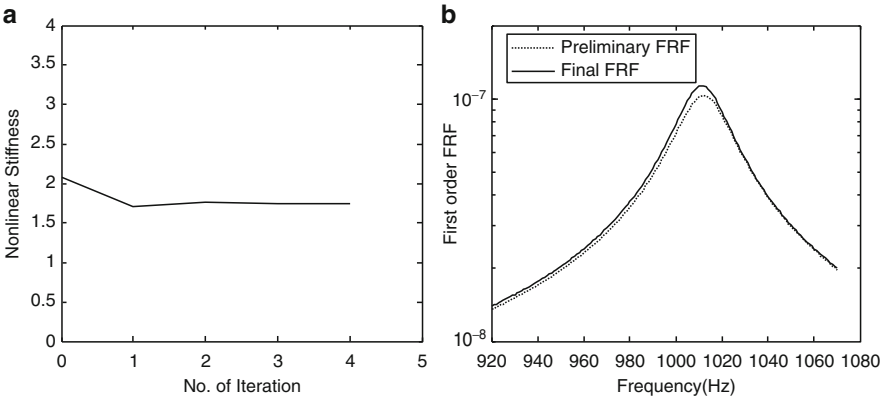

Fig. 7 (**a**) Iterative estimate of k_3. (**b**) Final estimate of $H_1(\omega)$

A preliminary estimate of nonlinear parameter k_3 is made and the iteration procedure is repeated till estimated value of the nonlinear parameter converges within a limit of 0.1%. Figure 7a shows the estimated values of nonlinear parameter k_3 over the stages of successive iteration. Final estimate of k_3 is found to be $1.75 \times 10^{19}\ N/m^3$. Assuming that both the bearings are identical and act in parallel,

Table 1 Estimated and theoretical bearing stiffness parameters [9, 10]

Theoretical stiffness (N/m)		Estimated stiffness (N/m)
Pre-load (μm)	$k(x)$ from Eq. (22)	$(k_1 - 3k_3x^2)$
0.2	$1.20 \times 10^7 - 4.01 \times 10^{19}x^2$	Case (i): $1.585 \times 10^7 - 2.625 \times 10^{19}x^2$
0.3	$1.47 \times 10^7 - 2.18 \times 10^{19}x^2$	Case (ii): $1.535 \times 10^7 - 4.285 \times 10^{19}x^2$
0.4	$1.69 \times 10^7 - 1.42 \times 10^{19}x^2$	Case (iii): $1.586 \times 10^7 - 5.240 \times 10^{19}x^2$
0.5	$1.89 \times 10^7 - 1.02 \times 10^{19}x^2$	
0.6	$2.08 \times 10^7 - 0.61 \times 10^{19}x^2$	

the nonlinear stiffness parameter of each bearing then becomes $0.875 \times 10^{19}\ N/m^3$. Figure 7b shows the final estimate of the first order kernel transform along with its preliminary estimate. It is seen that the successive iterations have improved the FRF values significantly near and around the natural frequency. Final estimates of natural frequency and damping become $\omega_n = 1011.47$ Hz,$\varsigma = 0.01078$.

The linear stiffness parameter, k_1, of the bearing system is computed from the natural frequency and the equivalent rotor mass per bearing and is found to be 1.585×10^7 N/m. Similar exercises are carried out with excitation level of 3 N (Case II) and 2 N (Case III) and the estimates of nonlinear stiffness parameter of each bearing is found to be $1.4285 \times 10^{19}\ N/m^3$ (Case II) and $1.740 \times 10^{19}\ N/m^3$ (Case III) respectively. Damping and linear stiffness parameter are found as

Case II: $\varsigma = 0.01015,\ \ k_1 = 1.535 \times 10^7$ N/m.
Case III: $\varsigma = 0.01002,\ k_1 = 1.586 \times 10^7$ N/m.

Table 1 summarizes the theoretical bearing stiffness parameters for different pre-load along with experimentally obtained stiffness parameters.

6 Wiener Series Application

Khan and Vyas [12, 13], considered the problem of kernel and parameter estimation in rotor-bearing systems through white noise excitation at the bearing caps. The resultant response is modeled, through Volterra and Wiener kernels, up to the third order, with cubic nonlinearity in stiffness. Considering the non-dimensional equation

$$\eta''(\tau) + 2\xi\eta'(\tau) + \eta(\tau) + \lambda\eta^3(\tau) = \bar{f}(\tau) \tag{24}$$

and replacing the applied force $\bar{f}(\tau)$ by $c\,\bar{f}(\tau)$, Eq. (24), gives the following power series representation of the governing equation

$$\left\{\sum_{n=1}^{\infty} c^n \eta_n(\tau)\right\}'' + 2\xi\left\{\sum_{n=1}^{\infty} c^n \eta_n(\tau)\right\}' + \left\{\sum_{n=1}^{\infty} c^n \eta_n(\tau)\right\} + \lambda\left\{\sum_{n=1}^{\infty} c^n \eta_n(\tau)\right\}^3 = c\,\bar{f}(\tau) \tag{25}$$

which is solved by equating the coefficients of like powers of c, to obtain

$$H_1(\omega) = 1/(\omega^2 + 2\zeta\omega + 1); \quad H_2(\omega_1, \omega_2) = 0;$$
$$H_3(\omega_1, \omega_2, \omega_3) = \lambda\,[\Psi(\omega_1, \omega_2, \omega_3)] \tag{26}$$

where, $\Psi(\omega_1, \omega_2, \omega_3)$ has been called Third-Order-Kernel-Factor which can be synthesized from the first order kernel transforms $H_1(\omega)$, as

$$\Psi(\omega_1, \omega_2, \omega_3) = -H_1(\omega_1)H_1(\omega_2)H_1(\omega_3)H_1(\omega_1 + \omega_2 + \omega_3) \tag{27}$$

The estimation procedure involves, experimental measurement of the first and third order kernel transforms, $H_1(\omega)$ and $H_3(\omega_1, \omega_2, \omega_3)$, respectively. The third-order-kernel factor, $[\Psi(\omega_1, \omega_2, \omega_3)]$ is synthesised from the measurements $H_1(\omega)$, using Eq. (27) and is employed along with the measured $H_3(\omega_1, \omega_2, \omega_3)$, in Eq. (26) for determination of the nonlinear parameter λ. The problems of measurement of individual Volterra kernels and convergence of the Volterra series, are circumvented through usage of Wiener functionals for a stationary Gaussian white noise excitation $\bar{f}(\tau)$, with variance A. The measurement scheme employs a complex exponential filter [14]. The ensemble average of the circuit output, can be shown to be

$$\langle \eta(\tau)z(\tau)\rangle = AW_1(\omega) \tag{28}$$

The ensemble average $\langle \eta(\tau)z(\tau)\rangle$ can also be written as

$$\langle \eta(\tau)z(\tau)\rangle = \lim_{T\to\infty} \frac{1}{T} \int_{-T/2}^{T/2} \eta(\tau)z(\tau)d\tau = \bar{F}^*(\omega)\eta(\omega) \tag{29}$$

Equations (28) and (29) give the expression for the first order kernel transform

$$W_1(\omega) = \bar{F}(\omega)\eta(\omega)/A \tag{30}$$

The measurement of the third order kernel transform, through a three exponential delay filter circuit, is obtained as

$$W_3(\omega, \omega, \omega) = (1/6A^3)\left[\{\bar{F}^*(\omega)\}^3\eta(3\omega)\right] - (1/2A)\,[W_1(\omega)\delta(\omega)] \tag{31}$$

Subsequently, noting the equivalence between the Volterra and Wiener kernels (Eq. 12), the first and third order Volterra kernel transforms can be computed as $H_1(\omega) = W_1(\omega) + W_{1(3)}(\omega)$; $H_3(\omega, \omega, \omega) = W_3(\omega, \omega, \omega)$ where,

$$W_{1(3)}(\omega) = -3A \int_{-\infty}^{\infty} W_3(\omega, \omega_2, -\omega_2)d\omega_2 \tag{32}$$

The linear parameters, ω_n and ξ can be readily obtained from the measured first order Volterra transform through standard curve fitting techniques. The estimate for λ is obtained by equating the synthesized expression, Eqs. (26) and (27) and the measured value (Eq. (32)) of the third order Volterra kernels of the system. Thus

$$\lambda = \left\{(1/6A^3)\left[\{\bar{F}^*(\omega)\}^3\eta(3\omega)\right] - (1/2A)\left[W_1(\omega)\delta(\omega)\right]\right\} / \left[\Psi(\omega,\omega,\omega)\right]. \quad (33)$$

7 Conclusion

A non-parametric identification procedure is described for rotor-bearing systems using Volterra–Wiener series. Restoring force from rolling element bearing has been modeled as a cubic nonlinear force. Experimental studies have been carried out on a simple rotor-bearing test rig in the laboratory for investigating the applicability and validation of the parameter estimation procedures. Both Harmonic and Gaussian white excitations have been used. Analysis shows that linear parameters can be very well estimated and the cubic nonlinear parameter is estimated within reasonable accuracy.

References

1. Zhabanch, N., Jean, W.Z.: Nonlinear dynamic analysis of a rotor shaft system with viscoelastically supported bearings. ASME J. Vib. Acoust. **125**, 290–298 (2004)
2. Harsha, S.P.: Nonlinear dynamic analysis of an unbalanced rotor supported by roller bearings. Chaos, Solitons and Fractals **26**(1), 47–66 (2005)
3. Bonnelo, P., Brennan, M.J., Homes, R.: Nonlinear modelling of rotor dynamic systems with squeeze film dampers-an efficient integrated approach. J. Sound Vib. **249**(4), 743–773 (2002)
4. Tiwari, R., Vyas, N.S.: Nonlinear bearing stiffness parameter extraction from random response in flexible rotor-bearing systems. J. Sound Vib. **203**(3), 389–408 (1997)
5. Fretchet, M.: Sur les fonctionnels continues. Annls. Scient. Ec. Norm. Sup. **27**, 193–219 (1910)
6. Volterra, V.: Theory of Functionals. Blackie & Sons, Glasgow (1930)
7. Schetzen, M.: The Volterra and Wiener Theories of Nonlinear Systems. Wiley, New York (1980)
8. Lee, Y.W., Schetzen, M.: Measurement of Wiener kernels of nonlinear systems by cross correlation. Int. J. Control **2**(3), 237–254 (1965)
9. Harris, T.A.: Rolling Bearing Analysis. Wiley, New York (1984)
10. Ragulskis, K.M., Jurkauskas, A.Y., Atstupenas, V.V., Vitkute, A.Y., Kulvec, A.P.: Vibration in Bearings. Mintis Publishers, Vilnyus (1974)
11. Chatterjee, A., Vyas, N.S.: Nonlinear parameter estimation through Volterra series using method of recursive iteration through harmonic probing. J. Sound Vib. **268**(4), 657–678 (2003)
12. Khan, A.A., Vyas, N.S.: Nonlinear bearing stiffness parameter estimation in flexible rotor-bearing systems using Volterra and Wiener approach. Probab. Eng. Mech. **6**(2), 137–157 (2001)
13. Khan, A.A., Vyas, N.S.: Application of Volterra and Wiener theories for nonlinear parameter estimation in a rotor-bearing system. Nonlinear Dyn. **24**(3), 285–304 (2001)
14. French, A.S., Butz, E.G.: Measuring the Wiener kernels of a nonlinear system using the Fast Fourier Transform algorithm. Int. J. Control **17**(3), 529–539 (1973)

Nonlinear Dynamics and Chaos of an Unbalanced Flexible Rotor Supported by Deep Groove Ball Bearings with Radial Internal Clearance

T.C. Gupta, K. Gupta, and D.K. Sehgal

Abstract The flexible rotor modeling has an advantage over rigid rotor modeling, by its suitability to model rotors of complex shapes with multiple discs and bearings. In this paper, the non-linear dynamic behavior of a horizontal unbalanced flexible rotor supported on deep groove ball bearings is theoretically studied in detail for instability and chaos. A generalized Timoshenko beam FE formulation, which can be used for both flexible and rigid rotor systems with equal effectiveness, is developed. The shape functions are derived from the exact solutions of governing differential equations. The formulation is validated for mass, stiffness and, gyroscopic matrices and for nonlinear dynamic response. The steady state quasi-periodic solution is obtained by the non-autonomous shooting method, which also gives the monodromy matrix. The eigenvalues of monodromy matrix give information about stability and nature of bifurcation. The maximum value of Lyapunov exponent is used to decide upon the chaotic nature of the dynamic response. Different sets of clearance values, unbalance excitation force, and shaft flexibility are investigated for the presence of instability and chaos. Finally the range of parameters is established for the same.

Keywords Flexible rotor · Ball bearing · Shooting method · Lyapunov exponents · Quasi-periodic response · Instability · Chaos

T.C. Gupta (✉)
Department of Mechanical Engineering, National Institute of Technology, Jaipur, India
e-mail: tcgmnit@gmail.com

K. Gupta
Department of Mechanical Engineering, Indian Institute of Technology, Delhi, India
e-mail: kgupta.mech.iitd.ac.in

D.K. Sehgal
Department of Applied Mechanics, Indian Institute of Technology, Delhi, India
e-mail: dks@am.iitd.ac.in

K. Gupta (ed.), *IUTAM Symposium on Emerging Trends in Rotor Dynamics*,
IUTAM Bookseries 25, DOI 10.1007/978-94-007-0020-8_28,

1 Introduction

During the past decades, a number of authors have addressed the problem of predicting the non-linear dynamic behavior of rotor ball bearing system. To develop an in-depth understanding of the effect of ball bearing nonlinearities upon dynamic behavior, the rotor was considered rigid and modeled as two-degrees-of-freedom system. The aim of these studies was to investigate the influence of bearing nonlinearities i.e., Hertzian contact force, varying compliance and, clearance, on nonlinear dynamic response of balanced and unbalance rigid rotors supported by deep groove ball bearing [1–9]. The regimes of super-harmonic, sub-harmonic and chaotic behavior were investigated by Fukata et al. [3] and Tiwari et al. [5, 6]. Also, Tiwari et al. [7] showed experimentally that bearing clearance changes the response of a rotor significantly because of the change in dynamic stiffness of the bearing. The instability due to clearance [8] and effect of geometric nonlinearity [9] were also studied. Dong-Soo and Dong-Hoo [10] used transfer matrix method to obtain non-linear dynamic behavior of flexible rotor ball bearing system. El-Saeidy [11] developed rotating shaft finite element model using c° four nodded isoparametric element to predict the dynamic behavior of rotor shaft rolling bearing system with bearing nonlinearities.

From literature it is observed that the effect of the ball bearing nonlinearities on the dynamic response have been investigated with rigid rotor modeling quite exhaustively. There is not much work on the nonlinear dynamic response of unbalanced flexible rotor mounted on ball bearings with radial internal clearance, which has been attempted in present work. To incorporate the flexibility of the shaft, a locking free Timoshenko beam finite element model is used [12]. The exact solution of differential equations of motion is used to derive the shape functions. The gyroscopic moments, rotary inertia, shear deformation and proportional damping are included. Stiffness and damping of radial ball bearing are also accounted for. The disc is considered to be rigid and mounted at the mid-span.

The shooting method [13] is used to derive the steady state response of the nonlinear system. The finite element formulation is validated by comparing the computed natural frequencies, whirl frequencies [14] and, nonlinear dynamic response [3] with the results available in the literature. The maximum values of Floquet multipliers and Lyapunov exponents are taken as signatures to determine the instability and chaotic nature of the dynamical system.

2 Problem Formulation

A locking free Timoshenko beam finite element formulation [12] is carried out, in which the exact solution of differential equations of motion is used to derive the shape functions.

2.1 Rotor Model

The rotor is treated as a free-free body in space upon which combination of static and dynamic forces (e.g., gravity, bearing, imbalances and gyroscopic moments) can act.

The rotor is modeled by circular Timoshenko beam finite elements to account for shear deformation and rotary inertia [15]. The equations of motion of a rotating Timoshenko beam element, in two perpendicular planes of motion XZ and YZ (Fig. 1) can be written as follows:

$$\begin{aligned}
&\frac{\partial}{\partial Z}\left[\rho A G_S\left(\frac{\partial x}{\partial Z}-\alpha\right)\right]+p_x(Z,t)=m_z\frac{\partial^2 x}{\partial t^2}\\
&\frac{\partial}{\partial Z}\left[\rho A G_S\left(\frac{\partial y}{\partial Z}-\beta\right)\right]+p_y(Z,t)=m_z\frac{\partial^2 y}{\partial t^2}\\
&\frac{\partial}{\partial Z}\left(E I\frac{\partial \alpha}{\partial Z}\right)+\rho A G_S\left(\frac{\partial x}{\partial Z}-\alpha\right)=J_T\frac{\partial^2\alpha}{\partial t^2}+\omega_r J_z\frac{\partial\beta}{\partial t}\\
&\frac{\partial}{\partial Z}\left(E I\frac{\partial \beta}{\partial Z}\right)+\rho A G_S\left(\frac{\partial y}{\partial Z}-\beta\right)=J_T\frac{\partial^2\beta}{\partial t^2}-\omega_r J_z\frac{\partial\alpha}{\partial t}
\end{aligned}\tag{1}$$

Here the following relations hold in the XZ plane.

$$\alpha=\frac{\partial x}{\partial Z}+\phi_{sx};\quad \phi_{sx}=\frac{V_x}{\rho G_s A};\quad M_Y=E I\frac{\partial\alpha}{\partial Z}\tag{2}$$

The corresponding relations in the YZ plane are employed. Further p_x and p_y are the distributed external forces with respect to XZ and YZ planes respectively, G_s and ρ are the shear modulus and the shear form factor ($= 0.75$). For circular beam sections, m_z, J_T, and J_z are the mass and lateral and polar mass moments of inertia, all specified per unit length of the beam; V_z and M_y are the shear and moment in the XZ plane; α and β represent angular displacements in the XZ and YZ plane; and ω_r is rotor speed.

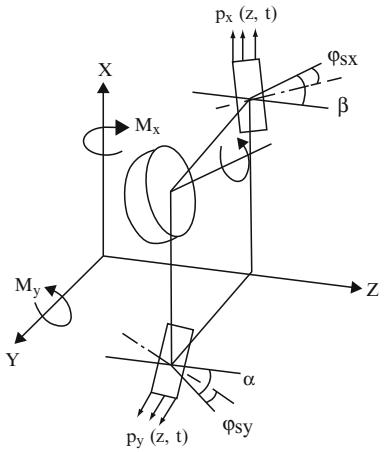

Fig. 1 A beam segment and the analogous motion planes

Applying Lagrange's equations, we get [15]

$$\begin{bmatrix} [M_{t1}] & 0 \\ 0 & [M_{t1}] \end{bmatrix} \{\ddot{q}_e\} + \begin{bmatrix} [M_{r1}] & 0 \\ 0 & [M_{r1}] \end{bmatrix} \{\ddot{q}_e\} + \begin{bmatrix} 0 & [G_y] \\ [-G_y] & 0 \end{bmatrix} \{\dot{q}_e\} + \begin{bmatrix} [k_1] & 0 \\ 0 & [k_1] \end{bmatrix} \{q_e\} = \{Q^e\} \tag{3}$$

Here subscripts t and r refer to translation and rotation. The forces $\{Q^e\}$ are given for the XZ plane as

$$Q_i^e = \int_0^l p_x(Z,t)\, N_i(Z) dZ, \quad i = 1, 2, \ldots, 4 \tag{4}$$

where $N_i(Z)$ are shape functions. The foregoing procedure using analogous plane treatment simplifies the procedure when it is needed to add further details of the system such as internal damping and bearing stiffness, damping and support flexibility. More details of the formulation are given in Hashish and Sankar [15].

2.2 Ball Bearing

Assuming perfect rolling of balls on the races, the varying compliance frequency of a ball bearing is given by: $\omega_{vc} = \omega_{\text{rotor}} {}^* BN$, where $BN = \{(R_i/(R_i + R_o)\}^* N_b$ the BN number depends on the specifications and dimensions of the bearing. In Fig. 2, (x, y) denote the displaced position (O′) of the centre of the inner race. From simple geometrical analysis, the expression for elastic deformation ($\delta(\theta_i)$) is,

$$\delta(\theta_i) = (x cos\theta_i + y sin\theta_i - \gamma_0) \tag{5}$$

In case of $\delta(\theta_i) > 0$, ball at angular position θ_i is loaded giving rise to restoring force with nonlinear characteristics because of Hertzian contact [16]. If $\delta(\theta_i) < 0$,

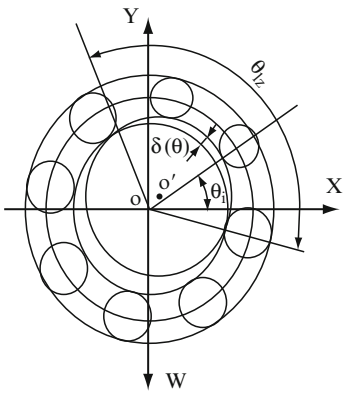

Fig. 2 Deformation in balls and races

the ball is not in the load zone (θ_{LZ}), and restoring force from the ball is set to zero. The total restoring force is sum of restoring forces from each of the balls. Thus the total restoring forces in x and y directions are,

$$F_X = \sum_{i=1}^{N_b} C_b(xcos\theta_i + ysin\theta_i - \gamma_0)^{3/2} cos\theta_i \tag{6}$$

$$F_Y = \sum_{i=1}^{N_b} C_b(xcos\theta_i + ysin\theta_i - \gamma_0)^{3/2} sin\theta_i \tag{7}$$

$$\text{Here } \theta_i = \frac{2\pi}{N_b}(i-1) + \omega_{cage} \times t \tag{8}$$

It must be noted that θ_i is a function of time and this imparts parametric effect to the system. Clearance in a bearing makes the contact arc less than 180°. C_b is the load-deflection factor from Hertzian theory.

Bearing stiffness and damping: The damping of ball bearing is usually small. Kramer [17] has provided an estimation of the bearing damping,

$$c = (0.25\ to\ 2.5) \times 10^{-11} K \text{ (Ns/m)} \tag{9}$$

where K is the linearized stiffness of the ball bearing. In the present analysis, the value of bearing damping used is 100 Ns/m, which is well within the range of 33.75 Ns/m to 337.5 Ns/m, given by the above relation.

2.3 Methods of Solution and Analysis

The steady state solution is obtained by non-autonomous shooting method [13]. The implicit type numerical time integration scheme Newmark-β and Newton-Raphson methods [18] are used to solve the nonlinear equations of motion for the assumed time period. This method gives the monodromy matrix as a by-product, the eigenvalues of which define the stability of the solution and indicates the onset of bifurcation.

One of the features of chaos is the sensitive dependence on initial conditions; for a dynamical system at least one Lyapunov exponent must be positive [19]. To determine the Lyapunov exponents, the simplest method is perhaps the Wolf's algorithm [20], which has been used in the present analysis.

3 Validation

In order to ensure the accuracy of present finite element formulation, mass, stiffness, gyroscopic matrices, and force vector are validated in succession. The mass, stiffness and gyroscopic matrices are validated by comparing natural frequencies and whirl frequencies which are reported in Gupta et al. [21]. To establish the

Table 1 Specifications and parameters of rotor system

Shaft & disc		Ball bearing	
Notation	value	Notation	value
d_s, l_s	15 (mm), 0.4 (m)	N	8
E, G	208, 80 GPa	R_i, R_0	20.0468, 31.953 (mm)
ρ, m_d	7,800 (kg/m^3), 15.96 (kg)	γ_0, C_b	20 (micron), 3.527×10^9 (N/m$^{3/2}$)
J_P^d, J_T^d	1.28×10^{-2}, 0.64×10^{-2} (kg m^2)	C, W	100 (Ns/m), 58.8 (N)

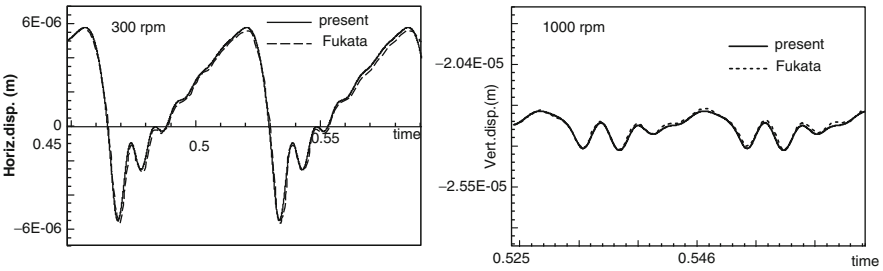

Fig. 3 Vibration wave forms at low rotor speeds

accuracy of non-linear dynamic response using the present formulation, the steady state vibration wave forms at low rotor speeds are generated for a rotor-ball bearing system and compared with the results available for the same system [3]. The specifications and parameters of the system are given in Table 1. The horizontal and vertical rotor displacements are compared at four rotor speeds 300, 450, 900 and 1,000 rpm, with the results reported by Fukata et al. [3]. An excellent matching of results is observed at all the four speeds. Two typical results, horizontal response at 300 rpm and the vertical response at 1,000 rpm are shown in Fig. 3.

4 Results and Discussion

In the present work, a parametric study has been carried out for the flexile rotor ball bearing system to determine the sets of parameters corresponding to instability and chaos. The parameters considered are disc mass eccentricity, clearance in the ball bearing and, the ratio of shaft stiffness ($K_{\text{shaft}} = 48\,EI/l^3$) to Hertzian load deflection factor (K_{shaft}/C_b; referred as stiffness ratio λ in present paper). The specifications of ball bearing 6,306/JIS [3] used in the present analysis are given in Table 1. The different combinations of parameters used in the present study are given in Table 2.

The rotor ball bearing system is bi-periodically excited. The two sources of excitation are due to rotating imbalance and stiffness variation of the ball bearing (the varying compliance effect). The two excitations are at different locations of the rotor. For the rotor bearing system considered here, the *BN* number comes out to be an irrational number (3.084 . . .). The frequencies of excitations are incommensurate.

Table 2 Different combination of parameters

Eccentricity = 10 microns, Clearance = 20, 10, 5 microns, Shaft dia. = 15 mm							
Shaft length (cm)	30	25	20	15	10	5	3
Stiffness ratio ($\lambda = K_{shaft}/C_b$)	2.49E-04	4.31E-04	8.43E-04	2.0E-03	6.77E-03	5.43E-02	2.52E-01

The period of the dynamic response is large. In case of input excitations of incommensurate frequencies, Sang-Kyu and Noah [22] proposed a scheme to analyze quasiperiodic response. In this method, state of the system is defined intermittently in phase space, at an interval of time kT_R satisfying the condition given by Eqs. (10) and (11).

$$\theta_k = \frac{kT_R}{T_{VC}} \,(\text{mod } 1)$$

$$\tau_k = 1 + \theta_k \quad for\, 0 \le \theta_k < 0.5; \quad \tau_k = \theta_k \quad for\, 0.5 \le \theta_k < 1 \tag{10}$$

$$(1 - \varepsilon) \le \tau_k \le (1 + \varepsilon) \tag{11}$$

Here kT_R is considered as time period to study quasi-periodic response, $k = (0, 1, 2, 3, \ldots)$; ε is a very small number and T_R is the time period of rotating unbalance. The value of k computed for the present rotor bearing system is 12. Therefore, the time period equal to $12T_R$ is used in the present analysis. To investigate the chaotic nature of the non-linear dynamic response of the system, Lyapunov characteristic exponents are computed using Wolf's algorithm.

For each set of parameters, the amplitudes of disc centre are computed at different rotational speeds, with a sufficiently small step length of rotational speed. Here, the amplitude is defined as the maximum displacement during steady state response. Then the frequency response curves are generated for each set of parameters. The frequency response curves for clearance value equal to 20 μm only are reported here which are shown in Fig. 4. It can be observed that as the stiffness ratio increases, the location of the peak shifts to higher rotational frequencies. It is due to increase in the natural frequencies of the system. Compared to maximum vertical displacement, the maximum horizontal displacement occurs at lower rotational frequency for the same set of parameters, as also observed by Tiwari et al. [6] by using rigid rotor formulation as well as experiments. This is due to difference in linearized bearing stiffness in two directions, caused by gravitational force acting on the rotor in the vertical direction. From Fig. 4a–f, it is found that when the stiffness ratio is less than 6.77E-03, the nature of the dynamic response at disc location, is not affected by varying compliance of the bearing. The location of peak in the frequency response curve is found close to the average fundamental natural frequency. To compute the average natural frequencies of the nonlinear system, the variation in the linearized bearing stiffness due to orientation of the balls (the varying compliance effect) is taken into account [21]. The natural frequencies were found invariant of rotational speed. For the stiffness ratio equal to 6.77E-03 and above (Fig. 4g–l), the peaks observed in the response curves are more than one. At $\lambda = 6.77\text{E-}03$, as shown in Fig. 4g, h, there are two peaks in the response plot. The rotational speed

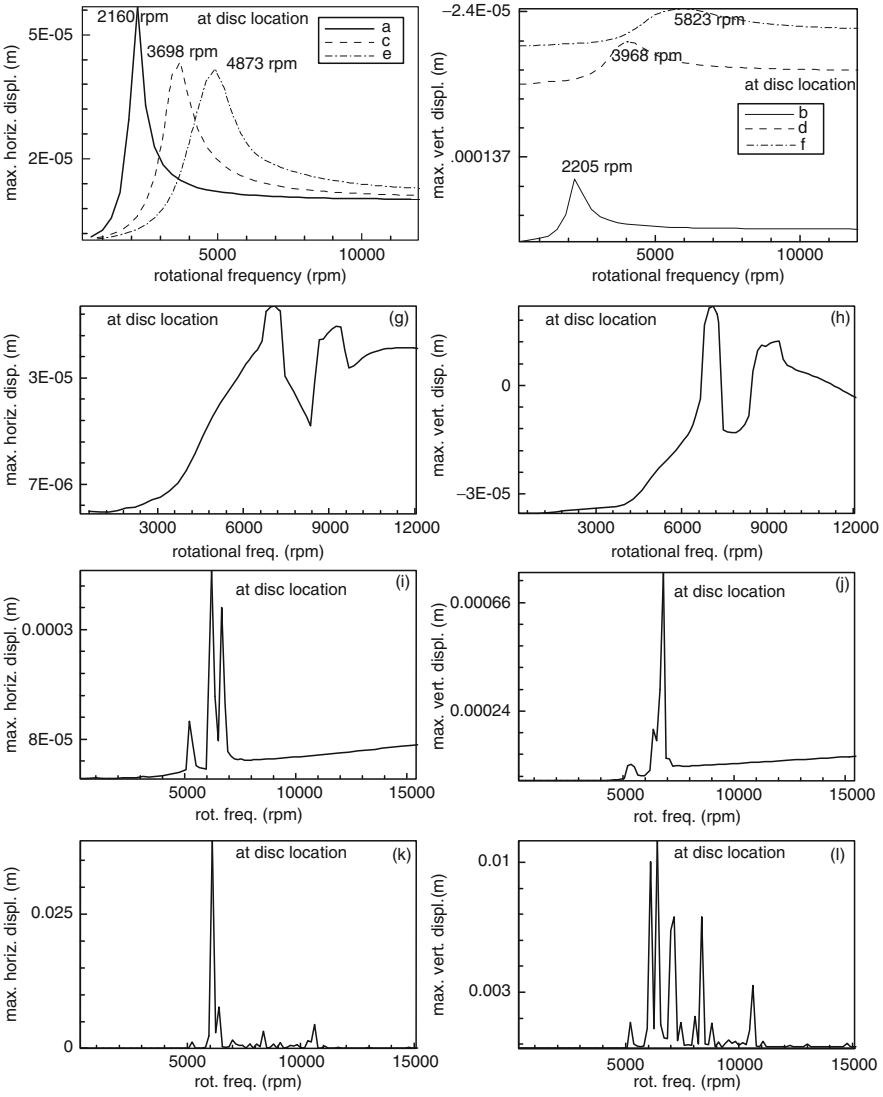

Fig. 4 Frequency response curves for e = 10 μm, γ_0 = 20 μm, & (**a, b**) λ = 2.49E-04, (**c, d**) λ = 8.43E-04, (**e, f**) λ = 2.00E-03, (**g, h**) λ = 6.77E-03, (**i, j**) λ = 5.43E-02, (**k, l**) λ = 2.52E-01

corresponding to second peak is 1.5 times rotational speed for first peak. This indicates that the bearing nonlinearities are now contributing to the dynamic response, at a threshold stiffness ratio equal to λ = 6.77E-03.

On further increase in the stiffness ratio, as shown in Fig. 4i–l, the frequency response curve consists of many peaks. Thus as the flexibility of the shaft decreases (stiffness increases), the dynamic response of rotor ball bearing system is influenced more and more by the bearing nonlinearities. The response curves shown in

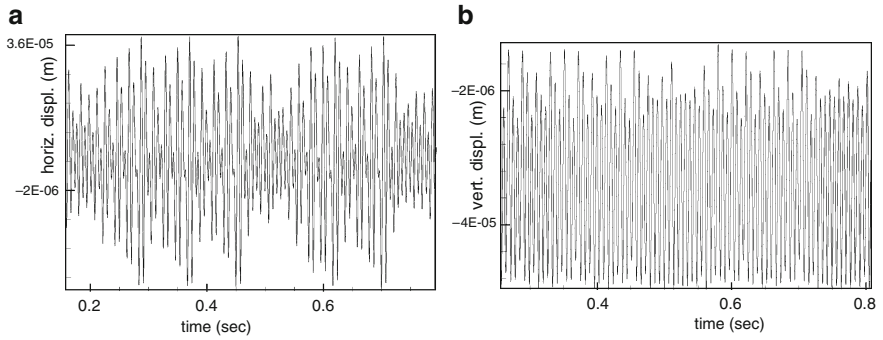

Fig. 5 Response at disc location for $\omega = 8650$ rpm, $\lambda = 6.77\text{E-}03$, ecc. $= 10\,\mu$m, clea. $= 20\,\mu$m, **(a)** horizontal **(b)** vertical

Fig. 4g–l are more complex. Therefore to fully characterize the dynamic response, exact numerical values of Floquet multipliers and Lyapunov exponents which are indicators of onset of instability and chaos respectively are computed at each rotational frequency for sets of parametric values given in Table 2. For the system under consideration, typical time response curves depicting chaotic motion, are shown in Fig. 5a, b. The horizontal and vertical displacement-time response curves neither represent periodic nor quasiperiodic motion. The dynamic response is repeatedly and gradually attaining a certain maximum value of displacement but not at same interval of time. The maximum eigenvalue of monodromy matrix is also found to be more than one and maximum Lyapunov exponent is positive. Based upon these qualitative analysis and quantitative measures, it can be concluded that such time response plots, as shown in Fig. 5a, b represent chaotic motion.

The presence of instability and chaos for different values of clearance, stiffness ratio and, range of speeds is depicted using maps as shown in Fig. 6a–f. The dark filled triangles and circles represent presence of instability and chaos and unfilled triangles and circles signify the absence of the same respectively. It is observed that there is no indication of instability and chaos in the dynamic solution when stiffness ratio is less than 6.77E-03 at clearance values equal to 20 and 5 μm. But at clearance value equal to 10 μm, the system starts showing presence of instability and/or chaos at lesser value of stiffness ratio i.e., 2.0E-03. There can be defined a limiting value of stiffness ratio corresponding to any clearance value, below which the dynamic response is stable and non-chaotic at all the rotational speeds considered in the present study. This limiting value is called "threshold value of stiffness ratio" in the following discussion. At stiffness ratio equal to 6.77E-03 and above, the flexible rotor ball bearing system is found to be prone to instability and/or chaos at various rotational speeds and at all the clearance values considered in the present study i.e., 5 to 20 μm. Thus, the threshold value of stiffness ratio is same (i.e., 6.77E-03) at clearance values equal to 20 and 5 μm but it is lesser (i.e., 2.0E-03), when clearance value is equal to 10 μm. This observation for a flexible rotor is at variance with those reported by Tiwari et al. [6] for a rigid rotor. Tiwari et al. [6] observed that increase in clearance will monotonically increase nonlinear effects in the dynamic response.

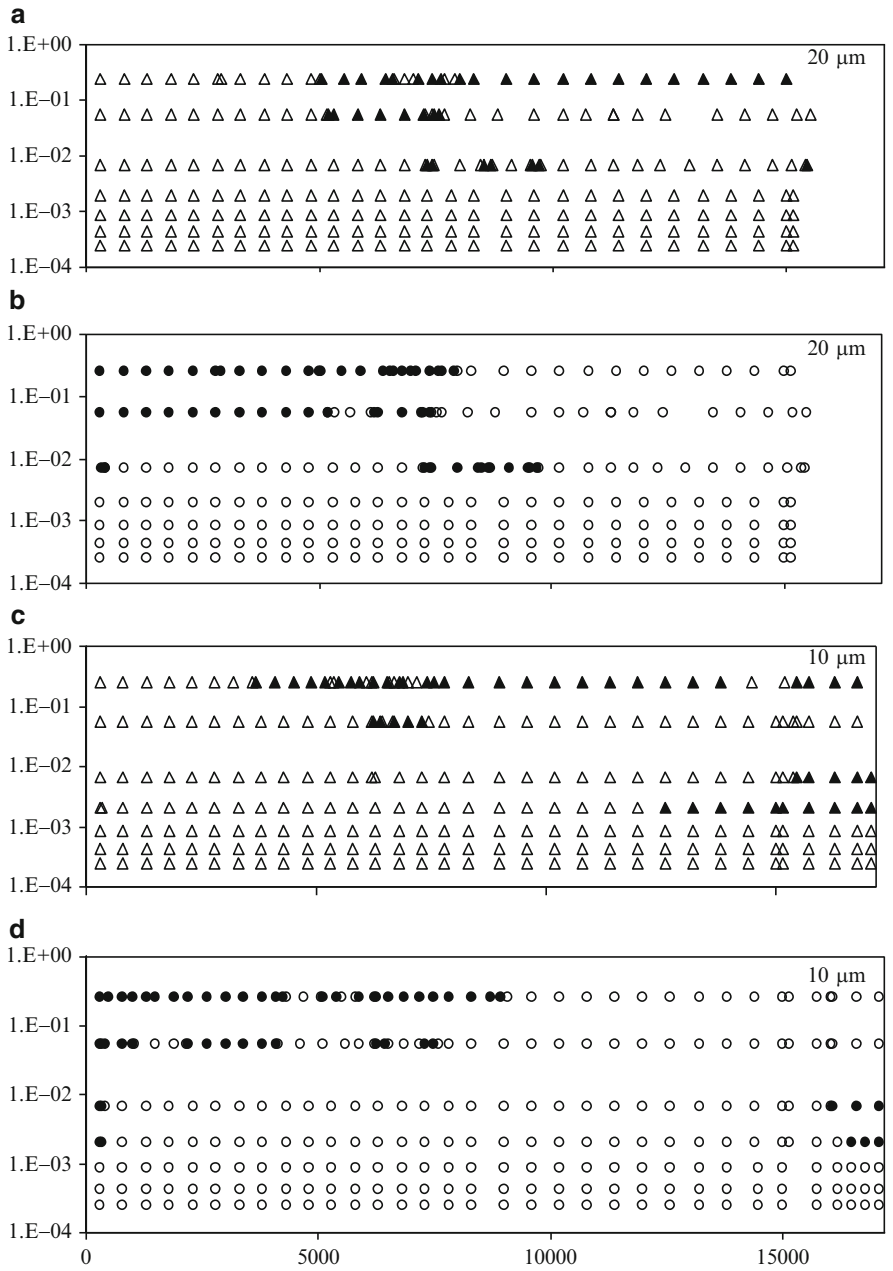

Fig. 6 Maps for instability and chaos at e = 10 μm, (**a, b**) $\gamma_0 = 20$, (**c, d**) $\gamma_0 = 10\,\mu$m, (**e, f**) $\gamma_0 = 5\,\mu$m (▲ unstable, △ stable, ● chaotic, ◯ non-chaotic)

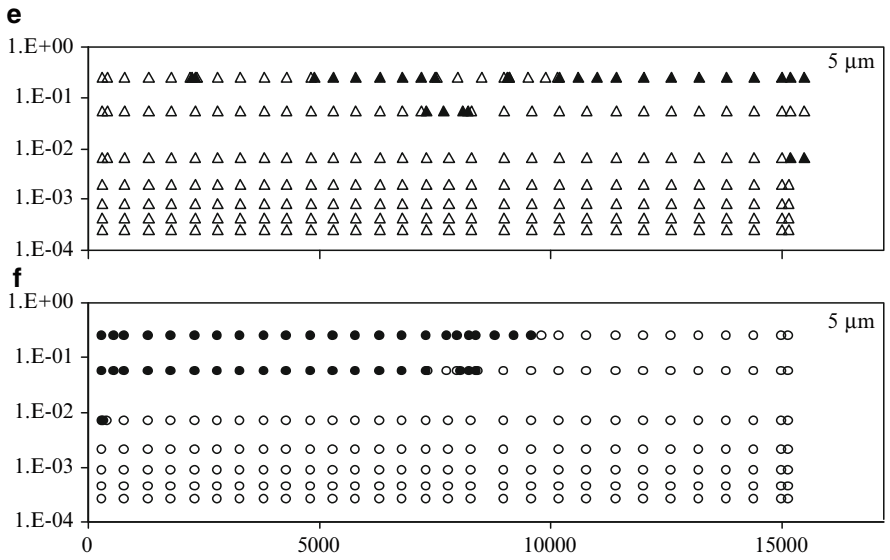

Fig. 6 (continued)

It may be noted that the limiting value of stiffness ratio, above which the varying compliance and clearance nonlinearities become prominent in the dynamic response, can be identified only by flexible rotor formulation and analysis.

The maps for instability shown in Fig. 6a, c, e reveal that the dynamic response starts showing instability at stiffness ratio equal to 6.77E-03 with bearing clearance values equal to 20 μm and 5 μm, but the response becomes unstable in the higher rotational speed range at reduced value of stiffness ratio equal to 2.0E-03 when bearing clearance is 10 μm. At stiffness ratio 6.77E-03 and clearance values equal to 5 μm and 10 μm, as shown Fig. 6c, e, the system response starts showing instability at nearly 15,000 rpm and continues up to maximum rotational speed considered in this study i.e., 17,100 rpm. When the clearance is increased to 20 μm, as shown in Fig. 6a, the system becomes unstable at comparatively lower speeds and the instability in the dynamic response is observed only for a finite range of rotational speeds. When the stiffness ratio is more than 6.77E-03, the system response shows onset of instability at comparatively lower speeds for a small range of rotational speed, at all the clearance values used in present study. Hence, upon increasing the clearance and/or the stiffness ratio beyond threshold value, the rotational speed corresponding to onset of instability decreases. At stiffness ratio equal to 2.52E-01, at which the rotor is effectively rigid, the range of rotational speeds corresponding to instability increases with decrease of bearing clearance. Moreover, the system response is found stable at a few discrete values of the rotational speeds. Comparing the instability maps shown in Fig. 6a, c, e, the dynamic solution of rotor ball bearing system is quite stable at small bearing clearance (i.e., 5 μm).

Analyzing the maps for chaos shown in Fig. 6b, d, f, it is observed that at $\lambda <$ 6.77E-03 and $\gamma_0 = 20\,\mu$m and $5\,\mu$m, there is no presence of chaos in the dynamic response of the system. But at $\gamma_0 = 10\,\mu$m and $\lambda =$ 2.0E-03, the system becomes chaotic at higher rotational speed (i.e., 16,400 rpm). Thus threshold value of stiffness ratio for chaos is also dependent upon clearance and it does not vary monotonically with clearance. At threshold value of stiffness ratio and above, the system has always been found to be chaotic at low speeds; nearly 300 rpm. At $\lambda =$ 6.77E-03 and $\gamma_0 =$ $20\,\mu$m, shown in Fig. 6b, the dynamic response starts becoming chaotic again at nearly 7,300 rpm and continues up to 9,700 rpm and then system response becomes stable at higher speeds. With $\gamma_0 = 10\,\mu$m and $\lambda =$ 6.77E-03 and 2.0E-03, shown in Fig. 6d, the dynamic solution is chaotic at nearly 300 rpm and becomes chaotic again at high speed, i.e., 16,100 and 16,500 rpm, respectively. At $\gamma_0 = 5\,\mu$m and $\lambda =$ 6.77E-03, shown in Fig. 6f, the system response is chaotic only at 300 rpm. Thus, at threshold value of stiffness, as the bearing clearance is reduced, the system is less prone to chaos and the onset of chaotic motion is found to start at comparatively lower rotational speeds. At $\lambda =$ 5.43E-02 and $\gamma_0 = 20\,\mu$m, which is greater than threshold value, the dynamic response is chaotic up to nearly 7,400 rpm, as shown in Fig. 6b. Keeping the stiffness ratio same, when the clearance is reduced, as shown in Fig. 6d, f, the dynamic response continues to be chaotic up to comparatively higher rotational speeds. When the stiffness ratio is further increased to, $\lambda =$ 2.52E-01, the upper limit of the rotational speed, corresponding to chaotic motion increases. Hence, the tendency of the system response towards chaos increases with increase in stiffness ratio but on the contrary, the system is less prone to chaos with decrease in clearance, when the stiffness ratio is greater than the threshold value. Moreover, the dynamic solution is non-chaotic at few discrete rotational speeds, in the speed range corresponding to chaotic motion.

In the present analysis, this limiting value of stiffness ratio is found to be the same, from all three modes of analyses viz., frequency response curves and numerical values of eigenvalues of monodromy matrix and Lyapunov exponents.

5 Conclusion

The non-linear dynamic behaviors of rotor ball bearing systems depend explicitly upon stiffness ratio (shaft stiffness/Hertzian load deflection factor) of rotor shaft and ball bearing clearance. With the increase in bearing clearance and stiffness ratio, the dynamic response is more prone to instability and/or chaos at various speeds. The threshold value of stiffness ratio, below which the dynamic response is stable and non-chaotic at all the rotational speeds, does not vary monotonically with clearance. The system response is found chaotic but not unstable at very low speeds i.e., nearly 300 rpm in the present case with stiffness ratio greater or equal to threshold value.

A range of parameters can always be identified for which the flexible rotor system is susceptible to instability and/or chaos. This can not be predicted from a rigid rotor formulation and a flexible rotor analysis as carried out in present paper is

essential. For the specific case, BN number 3.084 . . .. for ball bearing 6,306/JIS and disc eccentricity of ten micron, the threshold value of stiffness ratio (K_{shaft}/C_b below which there is no instability or chaos) identified are; ≥6.77E-03 for bearing clearance values of 5 and 20 micron, and ≥2.00E-03 for clearance of 10 micron.

References

1. Perret, H.: Elastiche spielschwingungen konstant belaster walzlger. Werkstatt und Betrieb **3**, 354–358 (1950)
2. Sunnersjo, C.S.: Varying compliance vibrations of rolling bearings. J. Sound Vib. **58**(3), 363–373 (1978)
3. Fukata, S., Gad, E.H., Kondou, T.A., Tamura, H.: On the radial vibrations of ball bearings (computer simulation). Bull. JSME **28**, 899–904 (1985)
4. Mevel, B., Guyader, J.L.: Routes to chaos in ball bearings. J. Sound Vib. **162**, 471–487 (1993)
5. Tiwari, M., Gupta, K., Prakash, O.: Effect of radial internal clearance of a ball bearing on the dynamics of a balanced horizontal rotor. J. Sound Vib. **238**(5), 723–756 (2000)
6. Tiwari, M., Gupta, K., Prakash, O.: Dynamic response of an unbalanced rotor supported on ball bearings. J. Sound Vib. **238**(5), 757–779 (2000)
7. Tiwari, M., Gupta, K., Prakash, O.: Experimental study of a rotor supported by deep groove ball bearing. Int. J. Rotat. Mach. **8**(4), 243–258 (2002)
8. Chang-qing, B., Qingyu, X.: Dynamic model of ball bearings with internal clearance and waviness. J. Sound Vib. **294**(1–2), 23–48 (2006)
9. Harsha, S.P.: Nonlinear dynamic analysis of a high-speed rotor supported by rolling element bearings. Nonlinear Dyn. **1**, 65–100 (2006)
10. Dong-Soo, L., Dong-Hoo, L.: A dynamic analysis of a flexible rotor in ball bearing with nonlinear stiffness characteristics. Int. J. Rotat. Mach. **3**(2), 73–80 (1997)
11. El-Saeidy, F.M.A.: Finite element modeling of rotor-shaft-rolling bearing systems with consideration of bearing nonlinearities. J. Vib. Control **4**, 541–602 (1998)
12. Reddy, J.N.: On locking-free shear deformable beam beam finite elements. Comput. Methods in Appl. Mech. Eng. **149**, 113–132 (1997)
13. Nayfeh, A.H., Balachandram, B.: Applied Non Linear Dynamics: Analytical, Computational and Experimental Methods. John Willey & Sons, New York (1995)
14. Ku, D.M.: Finite element analysis of natural whirl speeds for rotor-bearing systems with internal damping. Mech.l Syst. Signal Process. **12**(5), 599–610 (1998)
15. Hashish, E., Sankar, T.S.: Finite element and modal analysis of rotor-bearing system under stochastic loading conditions. Trans. ASME, J. Vib. Acoust. Stress Reliab. Design **106**, 80–89 (1984)
16. Harris, T.A.: Roller Bearing Analysis. John Wiley and Sons, New York (1984)
17. Kramer, E.: Dynamics of Rotors and Foundations. Springer-Verlag, New York (1993)
18. Bathe, K.J.: Finite Element Procedures. Prentice Hall of India, New-Delhi (1996)
19. Parker, T., Chua, L.: Practical Numerical Algorithms for Chaotic Systems. Springer, Berlin (1989)
20. Wolf, A., Swift, J., Swinney, H., Vastano, J.: Determining lyapunov exponents from a time series. Phys. D **16**, 285–317 (1985)
21. Gupta, T.C., Gupta, K., Sehgal, D.K.: Nonlinear vibration analysis of an unbalanced flexible rotor supported by ball bearings with radial internal clearance. ASME Turbo-Expo-2008, Paper No. GT-2008-51204 (2008)
22. Sang-Kyu, C., Noah, S.T.: Response and stability analysis of piecewise linear oscillations under multi-forcing frequencies. Nonlinear Dyn. **3**, 105–121 (1992)

Bifurcation Analysis of a Turbocharger Rotor Supported by Floating Ring Bearings

Aydin Boyaci, Wolfgang Seemann, and Carsten Proppe

Abstract Today, rotors of high-speed turbochargers are commonly supported by floating ring bearings due to their low costs and reduced power losses. A well known effect of such rotor bearing-systems is the occurrence of self-excited vibrations. In order to study the different nonlinear vibration effects with the methods of numerical continuation, a perfectly balanced flexible turbocharger rotor is considered which is supported by two identical floating ring bearings. Here, the bearing forces are modeled by applying the short bearing theory for both fluid films. After deriving the equations of motion of the turbocharger rotor, bifurcation analyses are carried out with both rigid and flexible model. Thereby, the main focus of the investigation is on the limit-cycle oscillation of higher amplitudes, which may cause rotor damage. In the lower speed range of operation the equilibrium position of the turbocharger rotor becomes unstable by a Hopf bifurcation emerging limit-cycle oscillations. By increasing the rotor speed the limit-cycle may lose its stability by a torus bifurcations leading into an area of quasi-periodic vibrations of the system. Further torus bifurcations, which emanate stable limit-cycles again, and various jump phenomena are also observed. For higher speed ranges a saddle-node bifurcation may occur from which stable limit-cycle oscillations of high amplitudes arise. The rotor speed, where this saddle-node bifurcation takes place, may be defined as a nonlinear critical speed of the turbocharger system supported by floating ring bearings. In the range of the nonlinear critical speed the bifurcation behavior of the turbocharger in floating ring bearings is quite complicated, since a further stable solution coexists beside the critical limit-cycle oscillation.

Keywords Turbocharger · Floating ring bearing · Stability · Bifurcation · Nonlinear vibrations · Numerical continuation

A. Boyaci (✉), W. Seemann, and C. Proppe
Institut für Technische Mechanik, Universität Karlsruhe (TH),
76128 Karlsruhe, Germany
e-mail: boyaci@itm.uni-karlsruhe.de

K. Gupta (ed.), *IUTAM Symposium on Emerging Trends in Rotor Dynamics*,
IUTAM Bookseries 25, DOI 10.1007/978-94-007-0020-8_29,

1 Introduction

The accurate prediction of critical speeds as well as the safe operation throughout the rotating speed range are the major technical interests in rotordynamics and very important for the design of the rotating equipment. With regard to linear phenomena, the critical speed often describes an angular velocity, at which the frequency of an external force coincides with a natural frequency of the system [4]. By considering highly nonlinear vibrations, it is still possible to define a critical speed. In the case of nonlinearities, which are caused by hydrodynamic journal bearings, the critical speed is usually defined as the onset of nonlinear vibrations. Since high-speed rotors normally operate in an unstable mode in the linear stability sense, this linear critical speed is not essential for secure operation of the rotor (cf. [5]).

One typical example for such a high-speed rotor is the turbocharger rotor supported by floating ring bearings. As illustrated in Fig. 1, at the first critical speed the equilibrium position of the rotor loses its stability by a Hopf bifurcation, which is widely investigated by many authors [1, 14]. After undergoing the Hopf bifurcation noncritical oscillations occur, whereas the amplitudes of the rotor vibrations are very well tolerable. While trespassing the second critical speed, the noncritical oscillations become unstable and the system jumps to a limit-cycle of higher amplitudes, which may cause the damage of the rotor. Until now, this kind of bifurcation occurring in rotors supported by floating ring bearings is only analyzed by Schweizer [9–11]. He carried out numerical simulations including a detailed hydrodynamic model of the floating ring bearings and called the onset of the dangerous limit-cycle oscillations "total instability". In the following, the second critical speed is denoted by the nonlinear critical speed. The limit-cycle emanating from the bifurcation at the nonlinear critical speed is called critical limit-cycle or critical solution.

Although many works investigate the bifurcation behavior of rotors in single-oil film bearings (e.g. [6, 7, 12, 15]), none of the existing literature provides information about the bifurcation behavior of a rotor in floating ring bearings in detail after undergoing the Hopf bifurcation. Since engineers are interested in a further increase of the revolution speed and performance, it is necessary to understand which type of bifurcation may lead to the destruction of the rotor as well as which nonlinear phenomena may be observed in the range of this nonlinear critical speed. While only self-excited vibrations are of interest and resonance phenomena shall not be addressed, it is sufficient to consider a perfectly balanced turbocharger rotor.

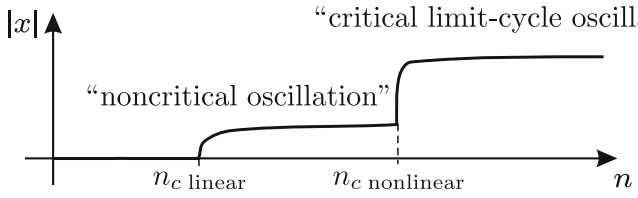

Fig. 1 Schematic of the typical behavior of vibration amplitudes $|x|$ of a turbocharger rotor supported by floating ring bearings as a function of the revolution speed n

2 Mechanical Model of the Turbocharger Rotor

A perfectly balanced turbocharger rotor model supported by two identical floating ring bearings is to be considered as mechanical model to study and analyze the bifurcation behavior. As shown in Fig. 2, the mechanical model of the turbocharger rotor consists of five parts. The two rigid disks representing the turbine and compressor wheel are attached rigidly to the rotor shaft which is modeled as a rotating Rayleigh beam with uniform cross section properties. To simplify matters, the shaft is of constant diameter and rotates with constant angular speed Ω. While the gyroscopic effects of both flexible shaft and rigid disks are taken into account, torsional vibrations, axial vibrations and deformations due to shearing are neglected. The hydrodynamic forces F_{y1i}, F_{z1i}, F_{y2i}, F_{z2i} generated by the inner film act both on the flexible shaft at the bearing locations and on each center of mass of the two rigid rings. In addition to the forces F_{y1o}, F_{z1o}, F_{y2o}, F_{z2o} exerted by the outer film on both floating rings the difference of the friction torques from the inner film and the outer film causes each ring to rotate with variable angular velocity Ω_{R1} and Ω_{R2}, respectively. In the following, quantities referring to the inner film are denoted by the index $()_i$, while those referring to the outer film have the index $()_o$. Furthermore, the subscripts $()_1$, $()_2$ indicate the bearing 1 ($x = \ell_1$) on the compressor side and bearing 2 ($x = \ell_2$) on the turbine side, respectively.

An analytical solution for the hydrodynamic forces is obtained by applying the short bearing approximation to solve the Reynolds equation, using Gümbel boundary conditions (cf. [6,13]). Hence, the forces F_{y1i}, F_{z1i}, F_{y2i}, F_{z2i} and torques T_{1i}, T_{2i} generated on the shaft and the ring by the inner film are nonlinear functions of the relative position and relative velocity of the shaft center to the center of the floating ring as well as of the angular velocity of both ring and shaft. The forces F_{y1o}, F_{z1o}, F_{y2o}, F_{z2o} and torques T_{1o}, T_{2o} generated by the outer film on the ring depend solely on the position, velocity and the angular velocity of the ring.

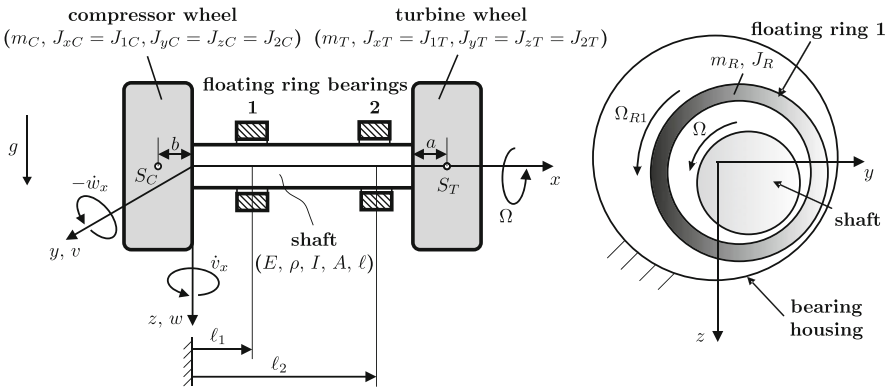

Fig. 2 Mechanical model of a turbocharger rotor supported by floating ring bearings

The equations of motion are derived using Hamilton's principle, which may be stated as

$$\delta \int_{t_0}^{t_1} (T - V)\,\mathrm{d}t + \int_{t_0}^{t_1} \delta W\,\mathrm{d}t = 0. \tag{1}$$

Thereby, the total kinetic energy and the total potential energy of the rotating turbocharger supported by floating ring bearings are given by the sums of the energies of its particular parts, e.g., shaft, compressor, turbine and floating rings, so they may be rewritten as $T = T_S + T_C + T_T + T_R$ and $V = V_S + V_C + V_T + V_R$, respectively.

By assuming small deformations, the deflections of the points on the neutral axis of the shaft are described by two transverse displacements $v = v(x,\, t)$, $w = w(x,\, t)$ in a fixed reference coordinate system $(x,\, y,\, z)$. The kinetic energy T_S of the rotating beam can be expressed as

$$T_S = \frac{1}{2}\int_0^{\ell} \left(\rho A(\dot{v}^2+\dot{w}^2)+\rho I(\dot{v}_x^2+\dot{w}_x^2)+2\rho I\,\Omega(v_x\dot{w}_x-w_x\dot{v}_x)+2\rho I\,\Omega^2\right)\mathrm{d}x, \tag{2}$$

where ρ is the density per unit length, A is the cross section area, I is the second area moment of inertia of the cross section, and ℓ is the length of the beam. The dot $\dot{()} = \frac{\partial}{\partial t}$ and the index $()_x = \frac{\partial}{\partial x}$ denote partial differentiation with respect to time t and location x, respectively. The potential energy V_S of the shaft is

$$V_S = \frac{1}{2}\int_0^{\ell} EI(v_{xx}^2 + w_{xx}^2)\,\mathrm{d}x - g\int_0^{\ell} \rho A w\,\mathrm{d}x, \tag{3}$$

in which E is the Young's modulus and g is the gravitational acceleration. The kinetic energies T_T of the turbine and T_C of the compressor are given by

$$\begin{aligned} T_T = {} & \frac{m_T}{2}\left(\dot{v}(\ell) + a\,\dot{v}_x(\ell)\right)^2 + \frac{m_T}{2}\left(\dot{w}(\ell) + a\,\dot{w}_x(\ell)\right)^2 + \frac{1}{2}J_{1T}\Omega^2 \\ & + \frac{1}{2}\Omega J_{1T}\left(v_x(\ell)\dot{w}_x(\ell) - w_x(\ell)\dot{v}_x(\ell)\right) + \frac{1}{2}J_{2T}\left(\dot{v}_x^2(\ell) + \dot{w}_x^2(\ell)\right) \end{aligned} \tag{4}$$

and

$$\begin{aligned} T_C = {} & \frac{m_C}{2}\left(\dot{v}(0) - b\,\dot{v}_x(0)\right)^2 + \frac{m_C}{2}\left(\dot{w}(0) - b\,\dot{w}_x(0)\right)^2 + \frac{1}{2}J_{1C}\Omega^2 \\ & + \frac{1}{2}\Omega J_{1C}\left(v_x(0)\dot{w}_x(0) - w_x(0)\dot{v}_x(0)\right) + \frac{1}{2}J_{2C}\left(\dot{v}_x^2(0) + \dot{w}_x^2(0)\right), \end{aligned} \tag{5}$$

where m_T, m_C are the masses of the compressor as well as of the turbine, J_{1T}, J_{1C} are the polar mass moments of inertia and J_{2T}, J_{2C} are the mass moments of inertia of the cross section each with respect to its centers of mass S_T, S_C. While the length a describes the distance from the end of the shaft $x = \ell$ to the turbine center S_T, b

is the distance between the beginning of the shaft $x = 0$ and compressor center S_C. From this follows the potential energies V_T, V_C of both bodies

$$V_T = -m_T g\Big(w(\ell) + b\, w_x(\ell)\Big) \tag{6}$$

and

$$V_C = -m_C g\Big(w(0) - b \cdot w_x(0)\Big), \tag{7}$$

respectively. By introducing the coordinates y_{R1}, z_{R1}, y_{R2}, z_{R2} for the horizontal and vertical displacements of the floating rings at the two bearing locations 1 and 2, the kinetic energies of both identical rings can be summed up to

$$T_R = \frac{m_R}{2}\left(\dot{y}_{R1}^2 + \dot{y}_{R2}^2 + \dot{z}_{R1}^2 + \dot{z}_{R2}^2\right) + \frac{J_R}{2}\left(\Omega_{R1}^2 + \Omega_{R2}^2\right), \tag{8}$$

in which m_R is the mass of one ring and J_R its polar mass moment of inertia with respect to its center of mass. The potential energy V_R of both rings can be written as

$$V_R = -m_R g(z_{R1} + z_{R2}). \tag{9}$$

The virtual work, which is not only done by the nonlinear bearing forces acting on the flexible shaft as well as on both rings, but also produced by the friction torques on the rings, has the form

$$\begin{aligned}\delta W = {} & F_{y1i}\,\delta v(\ell_1) + F_{z1i}\,\delta w(\ell_1) + F_{y2i}\,\delta v(\ell_2) + F_{z2i}\,\delta w(\ell_2) \\ & + (F_{y1o} - F_{y1i})\delta y_{R1} + (F_{z1o} - F_{z1i})\delta z_{R1} + (F_{y2o} - F_{y2i})\delta y_{R2} \\ & + (F_{z2o} - F_{z2i})\delta z_{R2} + 2\pi(T_{1o} - T_{1i})\delta\varphi_{R1} + 2\pi(T_{2i} - T_{2o})\delta\varphi_{R2},\end{aligned} \tag{10}$$

where φ_{R1}, φ_{R2} are the absolute rotational angles of the rings. Inserting the kinetic energies (2), (4), (5), (8), the potential energies (3), (6), (7), (9) as well as the virtual work (10) in Hamilton's principle (1), the variational problem can be approximated by using the Ritz method with appropriate approximation functions $\mathbf{\Phi}(x)$

$$\tilde{v}(x,t) = \mathbf{\Phi}^T(x)\,\mathbf{q_1}(t), \qquad \tilde{w}(x,t) = \mathbf{\Phi}^T(x)\,\mathbf{q_2}(t). \tag{11}$$

To determine the approximate solutions for the horizontal and vertical displacements $\tilde{v}(x,t)$, $\tilde{w}(x,t)$ of the turbocharger rotor, standard variational techniques [8] are applied, which yield to the nonlinear equations of motion of the discretized model

$$\mathbf{M}\,\ddot{\mathbf{q}} + \mathbf{G}\,\dot{\mathbf{q}} + \mathbf{K}\,\mathbf{q} = \mathbf{F_1}(\mathbf{q},\,\dot{\mathbf{q}},\,\Omega_{R1}) + \mathbf{F_2}(\mathbf{q},\,\dot{\mathbf{q}},\,\Omega_{R2}) + \mathbf{F_g}, \tag{12}$$

$$J_R\dot{\Omega}_{R1} = T_{1i}(\mathbf{q},\,\dot{\mathbf{q}},\,\Omega_{R1}) - T_{1o}(\mathbf{q},\,\dot{\mathbf{q}},\,\Omega_{R1}), \tag{13}$$

$$J_R\dot{\Omega}_{R2} = T_{2i}(\mathbf{q},\,\dot{\mathbf{q}},\,\Omega_{R2}) - T_{2o}(\mathbf{q},\,\dot{\mathbf{q}},\,\Omega_{R2}). \tag{14}$$

Hence, the vector $\mathbf{q}$ is described by the generalized coordinates $\mathbf{q} = [\mathbf{q_1}, \mathbf{q_2}, y_{R1}, z_{R1}, y_{R2}, z_{R2}]^T$. Moreover, the coefficients of the symmetric mass matrix $\mathbf{M}$, of the stiffness matrix $\mathbf{K}$ and of the skew-symmetric gyroscopic matrix $\mathbf{G}$ are constant in time. Whereas the vectors $\mathbf{F_1}$ and $\mathbf{F_2}$ represent the nonlinear bearing forces at both bearing locations, $\mathbf{F_g}$ is the gravitational force. Two conical rigid body modes and N flexible modes are used as approximation functions

$$\mathbf{\Phi}(x) = \begin{pmatrix} \frac{x}{\ell} \\ 1 - \frac{x}{\ell} \\ a_1 \sin\left(\frac{\lambda_1 x}{\ell}\right) + b_1 \cos\left(\frac{\lambda_1 x}{\ell}\right) + c_1 \sinh\left(\frac{\lambda_1 x}{\ell}\right) + d_1 \cosh\left(\frac{\lambda_1 x}{\ell}\right) \\ \vdots \\ a_N \sin\left(\frac{\lambda_N x}{\ell}\right) + b_N \cos\left(\frac{\lambda_N x}{\ell}\right) + c_N \sinh\left(\frac{\lambda_N x}{\ell}\right) + d_N \cosh\left(\frac{\lambda_N x}{\ell}\right) \end{pmatrix}, \tag{15}$$

which are the solution of the unsupported Euler-Bernoulli beam with free ends. The equations of motion for the rigid rotor are given, if only the rigid body modes in (2) are chosen as approximation functions ($N = 0$).

3 Bifurcation Analysis

The dynamical behavior of turbochargers supported by floating ring bearings is dominated by various nonlinear phenomena, which can be observed in experiments. For this reason a bifurcation analysis is proceeded to identify the type of bifurcations, occurring in such rotor-bearing systems. The main focus of this contribution is especially to analyze the bifurcation behavior of the turbocharger in the range of the nonlinear critical speed, which often leads to the destruction of the rotor. Furthermore, the influence of the shaft elasticity on the stability is discussed.

The parameters of the considered rotor model are listed in Table 1. The computation of equilibrium and periodic solutions are carried out by the numerical continuation software package MATCONT [3], which also provides methods for detecting bifurcations of these stationary solutions.

The results of such a numerical bifurcation analysis for the lower speed range and stable orbits at chosen rotational speeds are outlined in Fig. 3. In the following, the local maxima and minima of the nondimensionalized displacements $\bar{w}_T = \frac{w_T}{C_i}$ of the turbine center in the vertical direction are always plotted against the rotor speed n chosen as bifurcation parameter. At very low speeds the equilibrium position of the rotor-bearing system is stable, until it loses its stability by a subcritical Hopf bifurcation leading to an unstable limit-cycle. Below the linear threshold the unstable limit-cycle (dashed lines) changes its stability by a saddle-point bifurcation. By increasing the rotor speed, the stable limit-cycle undergoes a torus bifurcation (Neimark–Sacker) which leads into an area of quasi-periodic vibrations (grey-colored) computed by time integration. A further increase in rotor speed leads

Table 1 Physical and geometrical parameters of turbocharger rotor

Parameters	Values
Mass	$m_T = 1.257$ kg, $m_C = 0.619$ kg, $m_R = 0.0255$ kg
Moment of inertia	$J_{1T} = 914.7 \cdot 10^{-6}$ kg m^2, $J_{2T} = 660.0 \cdot 10^{-6}$ kg m^2 , $J_{1C} = 441.7 \cdot 10^{-6}$ kg m^2, $J_{2C} = 526.5 \cdot 10^{-6}$ kg m^2, $J_R = 2.745 \cdot 10^{-6}$ kg m^2
Shaft parameters	$\ell = 0.116$ m, $A = 251.6 \cdot 10^{-6}$ m^2, $I = 5,039.4 \cdot 10^{-12}$ m^4, $\rho = 7,900$ kg/m^3, $E = 210,000 \cdot 10^6$ N/m^2
Bearing and wheel location	$\ell_1 = 0.00766$ m, $\ell_2 = 0.08416$ m, $a = 0.0244$ m, $b = 0.0405$ m
Bearing parameters	$D_i = 0.017$ m, $L_i = 0.0058$ m, $D_o = 0.024$ m, $L_o = 0.0055$ m, $C_i = 2.97 \cdot 10^{-5}$ m, $C_o = 4.3 \cdot 10^{-5}$ m, $\eta_i = 0.92 \cdot 10^{-2}$ Ns/m^2, $\eta_o = 1.0 \cdot 10^{-2}$ Ns/m^2
Gravitational acceleration	$g = 9.81$ m/s^2

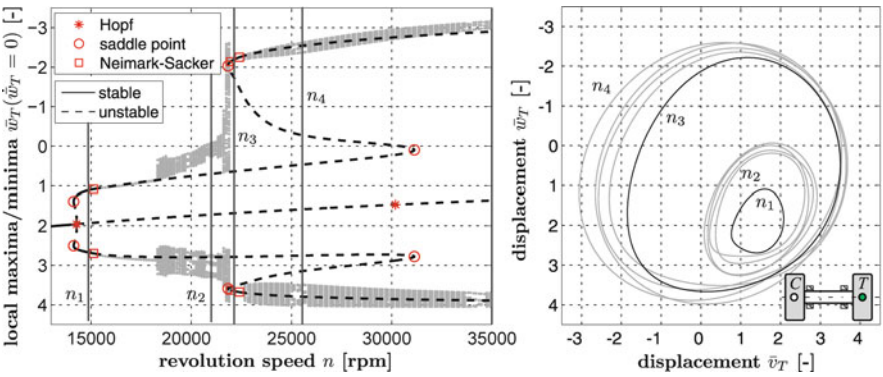

Fig. 3 Exemplary bifurcation diagram (flexible rotor) of the vertical turbine displacements (nondimensionalized by the radial bearing clearance C_i of the inner film) and stable orbits at different rotational speeds (— equilibrium and periodic solutions, — torus solutions)

the quasi-periodic solution to jump and to perform oscillations with much higher amplitudes, before it becomes unstable at a Neimark–Sacker bifurcation and a stable limit-cycle occurs again. This branch of periodic solutions ends very soon in a torus bifurcation exhibiting quasi-periodic oscillations.

By looking at the eccentricities of inner and outer film of both bearings one can observe that after undergoing the Hopf bifurcation only the outer film of the bearing on the turbine side indicates higher eccentricities, while the jump of the quasi-periodic oscillations is caused by the outer film of the bearing on the compressor side.

3.1 Rigid Rotor

Although the turbocharger rotor in floating ring bearings loses its stability of the equilibrium position and shows various jump phenomena for the lower speed range,

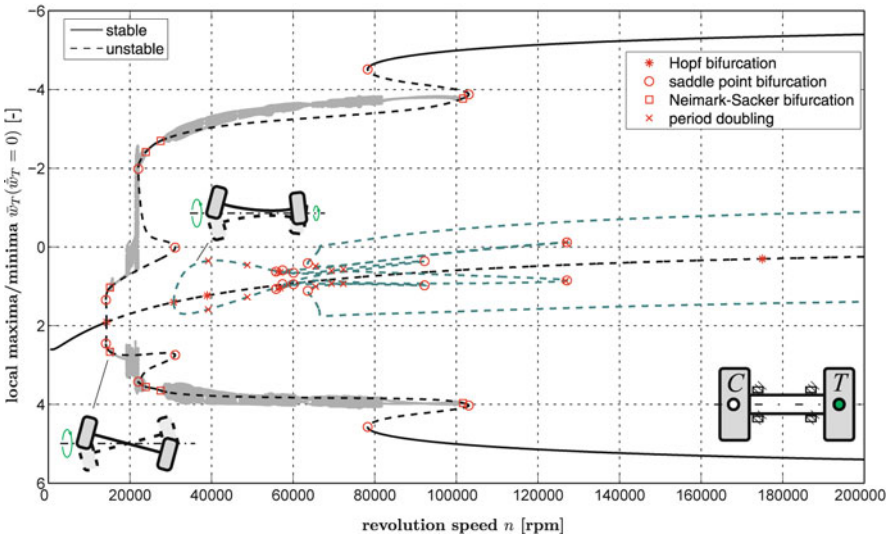

Fig. 4 Bifurcation diagram (rigid rotor) of the vertical turbine displacements (— equilibrium and periodic solutions, — torus solutions)

it may be operated very well up to a nonlinear critical speed with regard to practical applications. First, a rigid rotor model is considered, in order to investigate the bifurcation behavior near to the nonlinear critical speed. The bifurcation diagram of the rigid turbocharger rotor in floating ring bearings is given in Fig. 4 showing that different vibration modes of the rotor exhibit from different Hopf bifurcations. Thus, the periodic solution emanating from the first Hopf bifurcation as well as all further quasi-periodic solutions emerging from the torus bifurcations on the corresponding limit-cycle are mainly dominated by the conical forward mode of the rotor. Here, in the case of the second Hopf bifurcation the vibration mode of the rotor is primarily a cylindrical forward mode, at which the eccentricities of the outer film get higher. The third and fourth Hopf bifurcation correspond again to conical and cylindrical forward modes caused by high eccentricities of the inner films. For the sake of clarity the corresponding unstable branches are not plotted in the bifurcation diagram. When analyzing the rotor-bearing system for different parameters, the stability loss of the equilibrium position may be first reached by one of these four Hopf bifurcation types (cf. [2]). Hence, for higher rotor speeds the (quasi-)periodic solutions may jump to other stable branches arising from other Hopf bifurcations. These described bifurcation sequences are already known from experiments and numerical simulations (see also [10, 11]).

As mentioned before, the limit of operation is determined by a nonlinear critical speed, at which the bearing eccentricities of both films are very high (nearly 1) and as a consequence the amplitudes of the rotor vibrations become too large. Figure 5 shows again the bifurcation behavior of the rigid turbocharger rotor in the speed range, where a stable limit-cycle oscillation occurs accompanied by high bearing

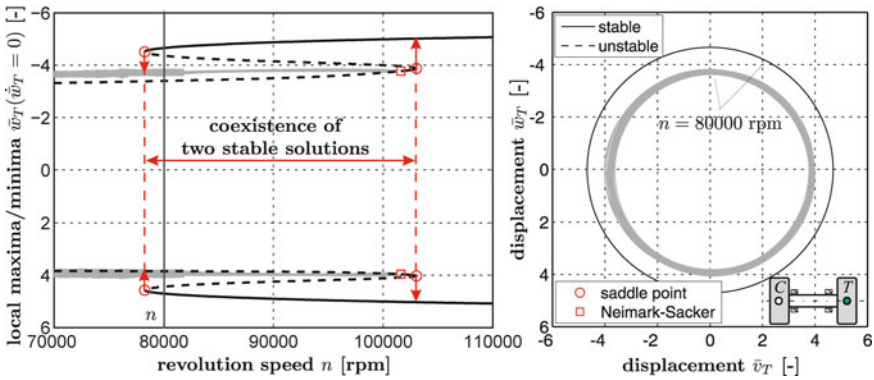

Fig. 5 Bifurcation diagram (rigid rotor) of the vertical turbine displacements in the range of the critical solution and stable orbits at a rotor speed of 80,000 rpm (— equilibrium and periodic solutions, — torus solutions)

eccentricities of both films. The quasi-periodic oscillations lose its stability by a torus bifurcation leading to a stable branch of periodic solutions. After undergoing a saddle-node bifurcation the limit-cycle jumps to a second limit-cycle with higher amplitudes which can be identified as a critical solution due to high bearing eccentricities of both films. By decreasing the rotor speed the critical solution jumps back to the quasi-periodic solution by means of a further saddle-node bifurcation. Thus it appears that for a turbocharger supported by floating ring bearings a nonlinear critical speed cannot be clearly determined, since for a wide speed range a further nonhazardous quasi-periodic solution may coexist beside a critical solution. Nevertheless, finite perturbations of the quasi-periodic solution may even cause the system's state to leave this basin and to jump to the critical limit-cycle which may be the reason for destructive vibrations. Therefore, with regard to practical applications the saddle-node bifurcation emanating the critical limit-cycle should be defined as nonlinear critical speed. Hereby, the second saddle-node bifurcation marks the absolute limit speed in safely operating the rotor.

Additionally, the orbits of the two stable solutions at a rotational speed of 80,000 rpm are outlined in Fig. 5. As can be seen from Fig. 6, high bearing eccentricities are existent when reaching the critical limit-cycle. In the case of the quasi-periodic solutions the eccentricities of the inner film are still moderate.

3.2 Flexible Rotor

While the nonlinear critical speed may also be determined by means of a rigid body model, only moderate amplitudes of the rotor vibrations are even observed on the critical limit-cycle. For this reason, the flexible shaft of the turbocharger rotor is considered in this section. Regarding the results of a bifurcation analysis of the flexible

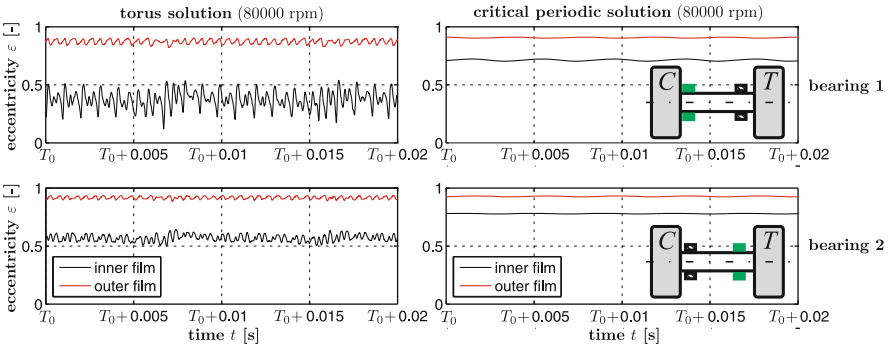

Fig. 6 Eccentricities of inner and outer film of both bearings versus time of the two stable solutions at a rotor speed of 80,000 rpm (steady state solutions exist after a time T_0)

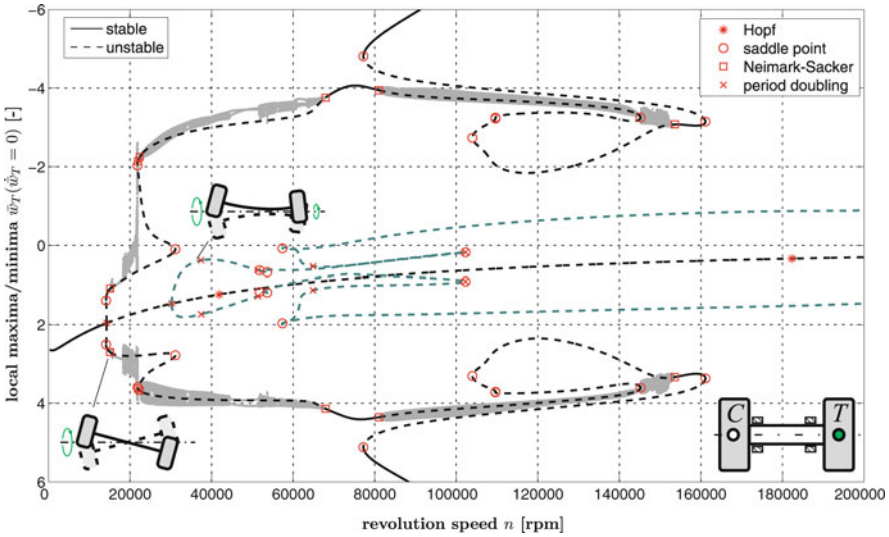

Fig. 7 Bifurcation diagram (flexible rotor) of the vertical turbine displacements (— equilibrium and periodic solutions, — torus solutions)

rotor model in Fig. 7 it is obvious that after reaching the corresponding saddle-node bifurcation the amplitudes of the rotor vibrations grow rapidly with increased rotor speed. However, it is remarkable, that the value for the nonlinear critical speed is nearly not influenced by the elasticity of the shaft which defines the saddle-node bifurcation emanating the critical limit-cycle. Further bifurcation analyses show that for different bearing parameters the computed value for the nonlinear critical speed remains nearly the same for both rigid and flexible rotor. Moreover, the global solution behavior is quite similar to each other for the lower speed range. However, the range of speeds, where two stable solutions coexist, is much wider than in the

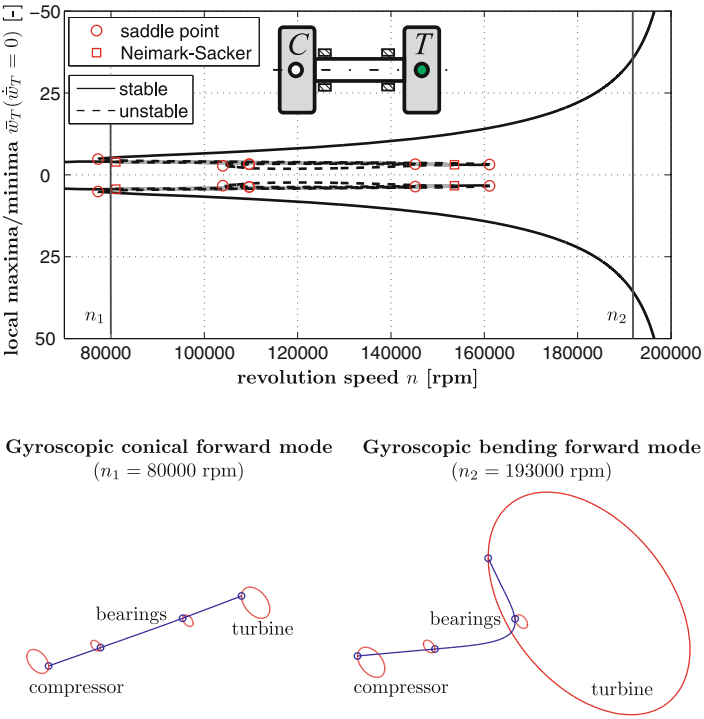

Fig. 8 Bifurcation diagram (flexible rotor) of the vertical turbine displacements in the range of the critical solution and the rotor vibration mode of the critical limit-cycle oscillations at different rotational speeds

case of a rigid rotor model. Hence, the saddle-node bifurcation, which represents the absolute limit speed for a secure operation of the turbocharger rotor, takes place at higher rotational speeds. Furthermore, in the higher speed range more bifurcations are detected resulting in a quite different global solution behavior.

A further phenomenon, which is not comprised by the bifurcation analysis of the rigid turbocharger model, is shown in Fig. 8, where the growth of the critical limit-cycle oscillations and the corresponding rotor vibration modes are illustrated. By considering the elasticity of the shaft, a gradual transition from a conical forward to a bending forward mode is observed on the critical limit-cycle. While after reaching the nonlinear critical speed the rotor vibration mode is mainly dominated by the conical rigid body mode (cf. Fig. 8), it changes into a bending forward mode with increased rotational speeds. A possible explanation of this phenomenon may be given with the statements of Schweizer [9, 10]. The synchronization of both oil films on the critical limit cycle leads to an excitation of the natural mode of the rotor, which changes here from a conical into a bending mode due to the increased stiffening of the oil films.

It is supposed, that the high amplitudes of the critical limit-cycle oscillations may cause the destruction of the rotor. In experiments, these amplitudes may be not achieved, since there is always sufficient damping in the system (e.g. from the bearing housing or the circulating fluid) which guarantees a limitation of the amplitudes.

4 Conclusion

By applying the methods of numerical continuation analysis it is possible to analyze the detailed bifurcation behavior of turbocharger rotors especially with regard to the determination of the critical speeds observed in experiments. The bifurcation type, which may lead to the destructive vibration of the rotor, is identified as a saddle-node bifurcation from which a critical limit-cycle occurs with growing amplitudes in the case of a flexible shaft. Since a further stable noncritical solution may coexist beside the critical solution, it is difficult to define a certain critical speed. The nonlinear critical speed marks the beginning of the critical limit-cycle oscillation, while the absolute limit speed indicates the end of the noncritical oscillations. In practical applications, perturbations of the stable noncritical solution may even cause the system to jump to the critical limit-cycle before reaching the absolute limit speed. Therefore, the design of floating ring bearings demands that the operation speed of the rotor is below the nonlinear critical speed, which is nearly not influenced by the elasticity of the shaft for the considered rotor. With regard to computation time, at first it may be sufficient to evaluate the nonlinear critical speed with a rigid body model. However, by considering the elasticity of the shaft the global solution behavior changes especially for the higher speed range and the range of speeds is much wider, where the critical and noncritical solutions coexist. In conclusion, the reason for the higher amplitudes of the rotor vibration after reaching the critical limit cycle is the gradual transition from the conical forward mode to a bending forward mode of the rotor with increased rotational speed.

References

1. Boyaci, A., Hetzler, H., Seemann, W., Proppe, C., Wauer, J.: Analytical bifurcation analysis of a rotor supported by floating ring bearings. Nonlinear Dyn. DOI: 10.1007/s11071-008-9403-x (2008)
2. Boyaci, A., Steinhilber, G., Seemann, W., Proppe, C.: Zur Stabilität eines in Gleitlagern laufenden elastischen Rotors. SIRM 2009–8. Internationale Tagung Schwingungen in rotierenden Maschinen, ISBN 978-3-200-01412-1, Wien (2009)
3. Dhooge, A., Govaerts, W., Kuznetsov, Yu.A., Mestrom, W., Riet, A.M., Sautois, B.: MATCONT and CL MATCONT: Continuation toolboxes in MATLAB, Ghent University and Utrecht University, Ghent and Utrecht (2006)
4. Genta, G.: Dynamics of rotating systems. Springer, New York (2005)

5. Li, C.H. Dynamics of rotor bearing systems supported by floating ring bearings. ASME J. Lubric. Technol. **104**, 469–477 (1982)
6. Moser, F.: Stabilität und Verzweigungsverhalten eines nichtlinearen Rotor-Lager-Systems, Dissertation, Technische Universität Wien, Wien (1993)
7. Myers, C.J. Bifurcation theory applied to oil whirl in plain cylindrical journal bearings. ASME J. Appl. Mech. **51**, 244–250 (1984)
8. Riemer, M., Wauer, J., Wedig, W.: Mathematische Methoden der Technischen Mechanik. Springer, Berlin/Heidelberg (1993)
9. Schweizer, B.: Oil whirl, oil whip and whirl/whip synchronization occurring in rotor systems with full-floating ring bearings. Nonlinear Dyn. DOI: 10.1007/s11071-009-9466-3 (2009)
10. Schweizer, B.: Vibrations and bifurcations of turbocharger rotors. SIRM 2009 – 8th International Conference on Vibrations in Rotating Machines, ISBN 978-3-200-01412-1, Wien (2009)
11. Schweizer, B., Sievert, M.: Nonlinear oscillations of automotive turbocharger turbines. J. Sound Vibr. DOI:10.1016/j.jsv.2008.10.013 (2009)
12. Sundararajan, P., Noah, S.T.: Dynamics of forced nonlinear systems using shooting/arc-length continuation method : Application to rotor systems. ASME J. Vibr. Acoust. **119**(1), 9–20 (1997)
13. Szeri, A.Z.: Fluid Film Lubrication. Cambridge University Press, Cambridge (1998)
14. Tanaka, M., Hori, Y.: Stability characteristics of floating bush bearings. ASME J. Lubric. Technol. **93**(3), 248–259 (1972)
15. Wang, J.K., Khonsari, M.M.: Bifurcation analysis of a flexible rotor supported by two fluid-film bearings, ASME J. Tribol. **128**(3), 594–603 (2006)

Vibration Analysis of High Speed Rolling Element Bearings due to Race Defects

S.H. Upadhyay, S.C. Jain, and S.P. Harsha

Abstract This paper presents a mathematical model to investigate the nonlinear dynamic behavior of a high speed rotor-bearing system due to surface waviness with varying number of waves. In the formulation, the contact between rolling elements and inner/outer races are considered as nonlinear springs with nonlinear damping incorporated, which is developed by correlating the contact damping force with the equivalent contact stiffness and contact deformation rate. The equations of motion are formulated using Lagrange's equation, considering the vibration characteristics of the individual components such as inner race, outer race, rolling elements and rotor. For high speed rolling element bearing supported by a rigid balanced rotor with defective bearings, nonlinear dynamic responses are found to be associated with wave passage frequency and also with the interactive effect of wave passage and inner race frequencies (ω_{inner}). Results presented in the form of fast Fourier transformation are in agreement with authors' various experimental results.

Keywords Nonlinear dynamics · Rolling bearing · Wave passage frequency · Poincaré maps

1 Introduction

In recent years, as high-speed rotary machines with roller bearings found wide applications, their dynamics properties were extensively studied. An analysis of rolling element bearing dynamic behavior is important to predict the system vibration responses. When rolling element bearings are operated at high speed, they generate vibrations and noise. The principal forces, which drive these vibrations, are the time varying nonlinear contact forces, which exist between the various components of the bearings, i.e., the rolling elements, and races with the rotor.

S.H. Upadhyay (✉), S.C. Jain, and S.P. Harsha
Mechanical & Industrial Engineering Department,
Indian Institute of Technology, Roorkee, India
e-mail: upadhyaysanjayh@yahoo.com; surajfme@iitr.ernet.in

K. Gupta (ed.), *IUTAM Symposium on Emerging Trends in Rotor Dynamics*,
IUTAM Bookseries 25, DOI 10.1007/978-94-007-0020-8_30,

In the rotor bearing assembly supported by perfect rolling element bearings, the vibration spectrum is dominated by the vibrations at the natural frequency and the ball passage frequency (BPF). By vibration monitoring, down time and risk of accident in highly productive industrial plants (power generation, steel production), traffic systems (automotive, railway, aircraft), industrial manufacturing (textile, machine tool industry) and domestic appliances (washing machine) can be minimized.

Ball passage vibrations were first documented, by Perret [1] and Meldau [2] as a static running accuracy problem. Tamura and Tsuda [3] performed a theoretical study of radial spring characteristics of a ball bearing based on the work of Perret [1] and Meldau [2]. They suggested that an increase in the number of the balls in a bearing reduces its untoward effects. However, its nature and importance was not properly understood until a research by Gustafsson et al. [4], who called this vibration as variable compliance. BPF is an inherent frequency of the system. They studied the effects of waviness and pointed out that lower order ring waviness affects the amplitude of the vibrations at the ball passage frequency. They showed that clearance is an important parameter for ball passage vibrations (BPV). They observed that vibrations at higher harmonics of the ball passage frequency are also present in the vibration spectrum and their amplitudes depend on the radial load, radial clearance, rotational speed and the order of harmonics. Wardle [5] has studied theoretically the relation between the frequency harmonics of waviness and bearing dynamic performance. Aktürk [6] has studied some characteristic parameters affecting the natural frequency of a rotating shaft supported by defect-free ball bearings. The conclusion of this work shows that large values of axial preload cause stiffer spring characteristics and result in higher natural frequency values. As the number of balls is increased, the system becomes stiffer, since a larger number of balls support the shaft. The change in natural frequency is cyclic for the change in ball set position. The number of changes is equal to the number of rolling elements in the bearing. This is also the reason for ball passage vibrations.

Recently, Tiwari et al. [7] investigated the stability of a rigid rotor supported by deep-grooved ball bearings and described the unstable ranges for different radial clearances but the stability of a rolling bearing rotor system containing local surface defects has not been studied before. Harsha and Kankar [8] developed an analytical model to predict nonlinear dynamic response in a rotor bearing system due to surface waviness. The conclusion of this work shows that for the outer race waviness, the severe vibrations occur when the number of balls and waves are equal. Harsha et al. [9] have studied the stability analysis of a rotor bearing system due to surface waviness and number of balls. They suggested that the system express dynamic behaviors that are extremely sensitive to small variations of the system parameters, such as number of balls and number of waves.

In this paper, a theoretical investigation has been conducted to observe the effect of race waviness with varying the number of waves on the vibration characteristics of a balanced rotor bearing system. A nonlinear damping formula, correlating the contact damping force with the equivalent contact stiffness and contact deformation rate (determined by the surface profiles and radial speed of inner/outer races and rollers), is developed to improve model fidelity.

2 Problem Formulation

For investigating the structural vibration characteristics of rolling element bearing, a model of bearing assembly can be considered as a spring mass damper system. Elastic deformation between races and rolling elements gives a non-linear force deformation relation, which is obtained by Hertzian theory. In the mathematical modeling, the rolling element bearing is considered as spring mass system and rolling elements act as non-linear contact spring as shown in Fig. 1 Since, the Hertzian forces arise only when there is contact deformation, the springs are required to act only in compression. In other words, the respective spring force comes into play when the instantaneous spring length is shorter than its unstressed length, otherwise the separation between balls and the races takes place and the resultant force is set to zero. The excitation is because of the varying compliance vibrations of the bearing which arise because of the geometric and elastic characteristics of the bearing assembly varying according to the cage position.

2.1 Mathematical Modeling

The rolling element bearing model considered here has equi-spaced balls rolling on the surfaces of the inner and outer races. For developing the theoretical model it is assumed that the outer race is fixed rigidly to the support and the inner race is fixed rigidly to the rotor and there is no bending of races.

$$\omega_{cage} = \omega_{rotor} \left(\frac{r}{r + R} \right) \tag{1}$$

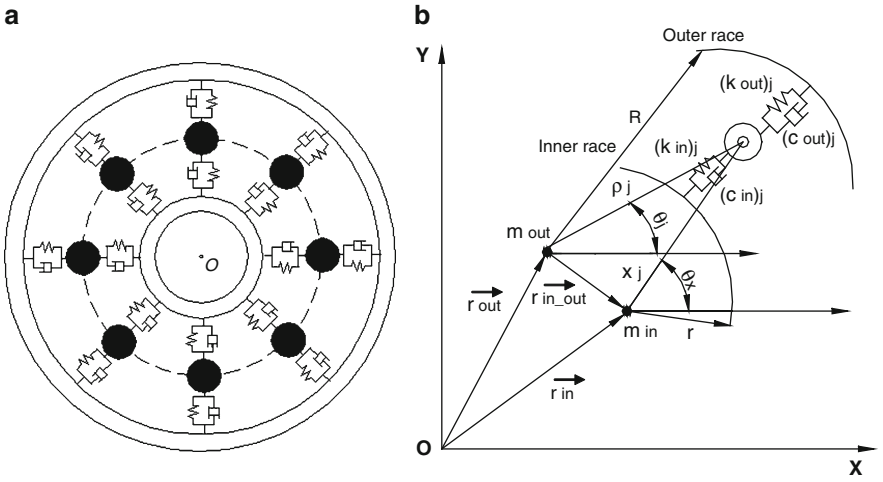

Fig. 1 Mass – spring-damper model of rolling element bearings

The ball passage frequency is given by

$$\omega_{bp} = \omega_{cage} \times N_b \tag{2}$$

where N_b is the number of balls.

2.2 Race Waviness

When the rolling element is moving round the inner race, it follows the rolling surface contours continuously. It is assumed that there exists no slip condition i.e., rolling element always in contact with inner race and also it is assumed that the inner race surface has a circumferential sinusoidal wavy feature. The amplitude of wavy surface is often measured with respect to central point at a certain angle from the reference axis. Hence the sinusoidal wave is:

$$\Pi = \Pi_p \sin\left(2\pi \frac{L}{\lambda}\right) \tag{3}$$

The inner race has circumferential sinusoidal wavy surface (Fig. 2a), therefore the radial clearance consists of a constant part and a variable part. Hence the amplitude of the wave of inner race is:

$$(\Pi)_{in} = (\Pi_O) + \left(\Pi_p\right) \sin\left(2\pi \frac{L}{\lambda}\right) \tag{4}$$

Here Π_p is the maximum amplitude of wave and Π_o is initial wave amplitude (or constant clearance) as shown in Fig. 2b. The arc length (L) of the wave of inner race at the contact angle is:

$$L = r\theta_j \tag{5}$$

For an imperfect surface with N waves, the wavelength (λ) inversely proportional to the number of waves N_w is:

$$\lambda \propto \frac{1}{N_w} \tag{6}$$

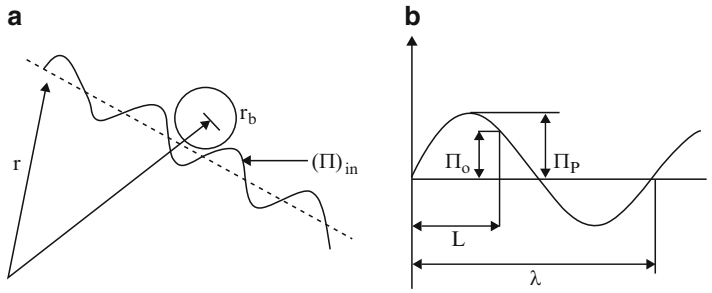

Fig. 2 **(a)** Contact between inner race and rolling element. **(b)** Wave of the race

For the inner race the wavelength is ratio of length of the inner race circumference to the number of waves on circumference, which is:

$$\lambda = \frac{2r\pi}{N_w} \tag{7}$$

The amplitude of the waves of inner race at the contact angle is:

$$(\Pi)_{in} = (\Pi_O) + \left(\Pi_p\right) \sin\left(N_w \theta_j\right) \tag{8}$$

2.3 Formulation of Equations of Motion

A real rotor-bearing system is generally very complicated and difficult to model. First the expression for energies of the individual components of the bearing is formulated. Using these energies, the equations of motion are derived with the help of Lagrange's equation.

2.3.1 Energy Expression of the Rolling Element Bearings

The total energy of system is considered to be the sum of kinetic energy, potential energy, strain energy of the springs representing contact and dissipation energy due to contact damping. The detail description of the energy expressions due to different parts of rolling bearings, which have been already derived in the papers published by Harsha [8, 9], are used in this paper. The contacts between rolling elements and races are treated as nonlinear springs, whose stiffness is obtained by Hertzian theory of elasticity. In those previous papers a constant damping value was chosen, but here a nonlinear viscous damping model is adopted.

Energy Dissipation

The lubrication is assumed to behave in a Newtonian way. Hence, a viscous damping model is adopted in which the dissipative forces are proportional to the time derivate of the mutual approach. The resulting equation yields:

$$F_d \;=\; c\;(\delta)\;\dot{\delta}^q \tag{9}$$

where $c\;(\delta)$ is also a function of the contact geometry, the material properties of the elastic bodies, the properties of lubricant and the contact surface velocities.

Contact Damping

For the jth rolling element the equivalent contact stiffness between the rolling element and race is

$$k_{Eq} = \frac{3}{2} k_{contact}\, \delta^{1/2} \tag{10}$$

The deforming forces for the jth rolling element and inner race is

$$F_{d\_in} = c_{in}\, k_{Eq} \left(\dot{\delta}_{in}\right)_+^q \tag{11}$$

$$F_{d\_in} = \frac{3}{2} c_{in}\, (k_{in\_contact})\, \delta_{in+}^{1/2}\, \dot{\delta}_{in+}^q \tag{12}$$

Similarly, the damping force for the jth rolling element with the outer race is:

$$F_{d\_out} = c_{out}\delta_{out+}k_{eq} \tag{13}$$

$$F_{d\_out} = \frac{3}{2} c_{out}\, (k_{out\_contact})\, \delta_{out+}^{1/2}\, \dot{\delta}_{out+}^q \tag{14}$$

Hence total energy dissipation at both contact points of rolling element with inner and outer race is

$$E_{dissipation} = \frac{3}{2\,(q\,+\,1)} \sum_{j=1}^{N_{r.e.}} \left[\left\{ c_{in}\, (k_{in\_contact})\, \delta_{in+}^{3/2}\, \dot{\delta}_{in+}^{q+1} \right\} + \left\{ c_{out}\, (k_{out\_contact})\, \delta_{out+}^{3/2}\, \dot{\delta}_{out+}^{q+1} \right\} \right] \tag{15}$$

2.4 Equations of Motion

The kinetic energy and potential energy contributed by the inner race, outer race, balls, rotor and springs, can be differentiated with respect to the generalized coordinates $\rho_j (j = 1, 2, \ldots, N_b)$, x_{in}, and y_{in} to obtain the equations of motion. For the generalized coordinates ρ_j, where $j = 1, 2, \ldots, N_b$, the equations are:

$$\ddot{\rho}_j + g \sin\theta_j + \rho_j \dot{\theta}^2 - \frac{1}{m_j} (k_{in\_contact})\, [\delta_{in}]_+^{3/2} \frac{\partial \chi_j}{\partial \rho_j} + \frac{1}{m_j} (k_{out\_contact})\, [\delta_{out}]_+^{3/2} + \frac{1}{2\,m_j} \frac{\partial \left[(k_{in\_contact}) \left([\delta_{in}]_+^{1/2} \right) \right]}{\partial \rho_j} [\delta_{in}]_+^2 + \frac{1}{2\,m_j} \frac{\partial \left[(k_{out\_contact}) \left([\delta_{out}]_+^{1/2} \right) \right]}{\partial \rho_j} [\delta_{out}]_+^2$$

$$+\frac{3}{2m_j}\sum_{j=1}^{N_{r.e.}}\left\{c_{in}\left(k_{in\_contact}\right)\delta_{in+}^{3/2}\left(-\chi_j\right)^q\ \frac{\partial\chi_j}{\partial\dot{\rho}_j}\right\}$$

$$+\frac{3}{2m_j}\sum_{j=1}^{N_{r.e.}}c_{out}\left(k_{out\_contact}\right)\delta_{out+}^{3/2}\left(-\dot{\rho}_j\right)^q\ =0\ \ j=1,2,\ldots,N_{r.e.} \tag{16}$$

For the generalized coordinate x_{in} the equation is:

$$\begin{aligned}&\ddot{x}-\frac{1}{m_{rotation}}\sum_{j=1}^{N_{r.e.}}\left(k_{in\_contact}\right)\left[\delta_{in}\right]_+^{3/2}\frac{\partial\chi_j}{\partial x_{in}}\\&+\frac{3}{2m_{rotation}}\sum_{j=1}^{N_{r.e.}}\left\{c_{in}\left(k_{in\_contact}\right)\delta_{in+}^{3/2}\left(-\dot{\chi}_j\right)^q\ \frac{\partial\dot{\chi}_j}{\partial\dot{x}_{in}}\right\}=\frac{F_u\ \sin\left(\omega_s\,t\right)}{m_{rotation}}\end{aligned} \tag{17}$$

For the generalized coordinate $\boldsymbol{y_{in}}$ the equation is:

$$\begin{aligned}&\ddot{y}_{in}+g-\frac{1}{m_{rotation}}\sum_{j=1}^{N_{r.e.}}\left(k_{in\_contact}\right)\left[\delta_{in}\right]_+^{3/2}\frac{\partial\chi_j}{\partial y_{in}}\\&+\frac{3}{2m_{rotation}}\sum_{j=1}^{N_{r.e.}}\left\{c_{in}\left(k_{in\_contact}\right)\delta_{in+}^{3/2}\left(-\dot{\chi}_j\right)^q\ \frac{\partial\dot{\chi}_j}{\partial\dot{y}_{in}}\right\}=\frac{\left(W+F_u\ \sin\left(\omega_s\,t\right)\right)}{m_{rotation}}\end{aligned} \tag{18}$$

where $m_{rotation}=(m_{inner}+m_{rotor})$.

This is a system of (N_b+2) coupled non-linear differential equations. There is no external radial force allowed to act on the bearing system and no external mass is attached to the outer race. The "+" sign as subscript in these equations signifies that if the expression inside the bracket is greater than zero, then the rolling element at angular location θ_j is loaded giving rise to restoring force and if the expression inside bracket is negative or zero, then the rolling element is not in the load zone, and restoring force is set to zero. The deformation of spring at inner race χ_j, is derived in [9, 10], and is used in the present paper.

3 Methods of Solution

The two coupled non-linear second order differential equations are solved by numerical integration which is a time domain approach. The non-analytic nature of the stiffness term renders the system equations difficult for analytical solution.

Table 1 Geometric and physical properties used for the ball bearings

Ball radius	4.762 mm
Inner race diameter	18.738 mm
Outer race diameter	28.262 mm
Radial load	6 N
Mass of rotor	0.6 kg
Pitch radius of the ball set	27 mm
Speed of the rotor	5,000 rpm

3.1 Numerical Integration

The equations of motion (10–12) are solved using the modified Newmark-β method to obtain the radial displacement, velocity and acceleration of the rolling elements. With inclusion of damping, transient vibrations are eliminated and peak steady state amplitudes of vibration can be estimated. To observe the nonlinear behavior of the system, parameters of the ball bearing are selected and are shown in Table 1. The time step for the numerical integration is taken as $\Delta t = 10^{-5}$ sec.

4 Results and Discussion

The equations of motion are solved by modified Newmark-β method to obtain the radial displacement and velocity of the rolling elements. The predicted vibrations are clearly observed in case of two waves, as shown in Fig. 3a. A dominant peak appears at $2\omega_{inner} = 166.67$ Hz with the other peaks at super harmonics of the rotor speed $3\omega_{inner} = 250$ Hz, $4\omega_{inner} = 333.5$ Hz, and at the wave passage frequency (WPF) $\omega_{wp} = N_b\left(\omega_{inner} - \omega_{cage}\right) = 400$ Hz. Other peaks also appear which are more complicated at $(2/3)\omega_{wp} - 2\omega_{inner} = 100$ Hz. However, a more complicated response is observed for three waves. A dominant peak of relatively smaller amplitude is observed at $3\omega_{inner} = 250$ Hz, implying a change of shape in the vibration spectrum. The other peaks are observed at $\omega_{wp} - {}^3/_2\omega_{inner} = 275$ Hz, and at $\omega_{wp} + {}^3/_2\omega_{inner} = 525$ Hz as shown in Fig. 3b. However, when damping is not considered in the model, the peak excitation occurs in vertical displacement, and is at 1 micron [9].

For five waves a dominant peak of relatively smaller amplitude (0.14) is observed at $5\omega_{inner} = 416.65$ Hz, implying a change of shape in the vibration spectrum. The other peaks are observed at ${}^3/_2\omega_{wp} - 5\omega_{inner} = 183.35$ Hz for horizontal and vertical displacement response as shown in Fig. 3c. For eight waves, the vibrations are predicted at wave passage frequency $(\omega_{wp}) = 400$ Hz, where $q = 1$ and $k = 0$ in Eq. (13), as shown in Fig. 3d. The amplitude of peak is 0.25 μm. But when damping is not considered in the model, the peak excitation occurs in vertical displacement, and is at 10 μm [9], which is quite high. Hence, the peak excitation is drastically

reduced mainly due to damping effect. For waviness of order 12, the predicted peak is either at $\omega_{wp} - 4\omega_{cage}$ or at $2\omega_{wp} - 4\omega_{inner}$ depending on the parameter q and k chosen in Eq. (13). The peak for 12 waves are at $2\omega_{wp} - 4\omega_{inner} = 467$ Hz where $q = 2$ and $k = 4$ in Eq. (13) as shown in Fig. 3e.

Vibration amplitudes in the spectrum for 12 waves become negligible (<1.5 μm). However, there is another peak at $\omega_{wp} + 4\omega_{inner} = 733.5$ Hz, where $q = 1$ and $k = 4$ in Eq. (13). A clear transformation from $q = 1$ to 2 can be observed in the vibration spectrum obtained for the waviness of order 12. Results of Fig. 3a–e are summarized in Table 2.

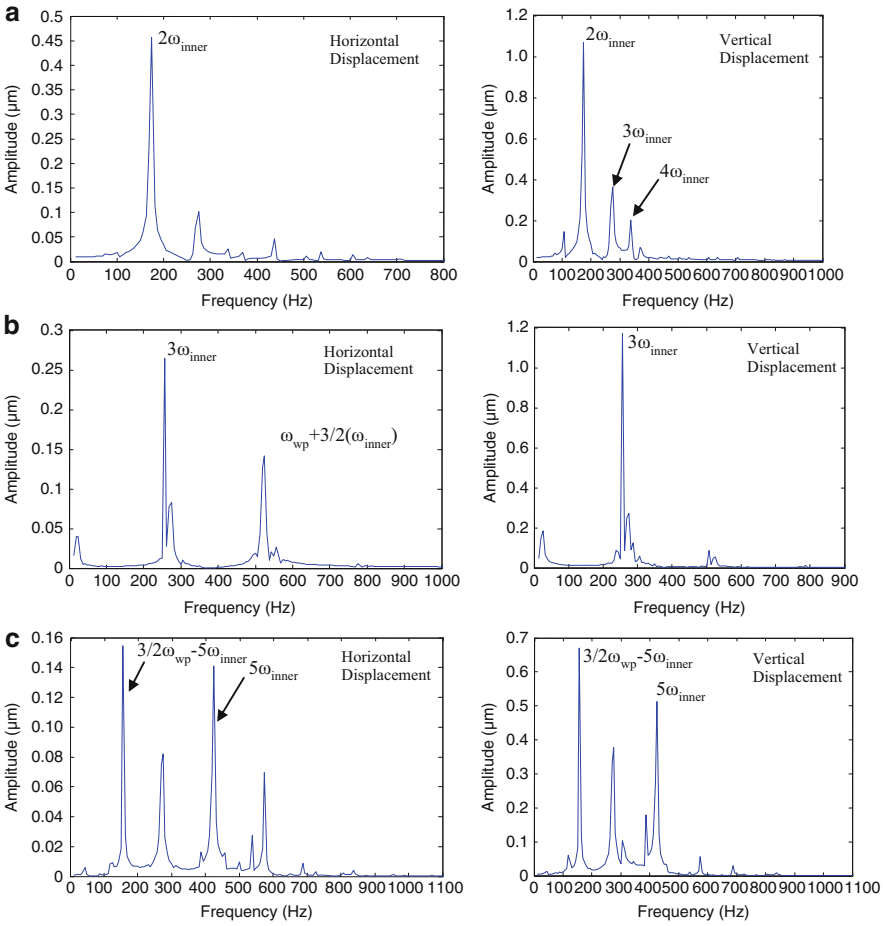

Fig. 3 FFT for defective bearings, **(a)** $N_w = 2$, **(b)** $N_w = 3$, **(c)** $N_w = 5$, **(d)** $N_w = 8$, **(e)** $N_w = 12$

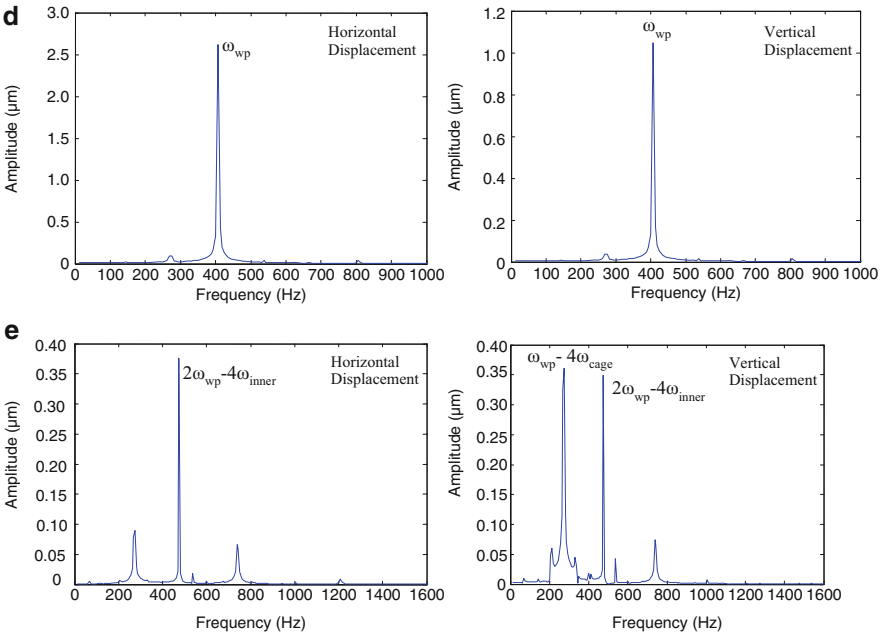

Fig. 3 (continued)

Table 2 Summary of inner race waviness

Waviness order	Peak amplitude at	Vibration spectrum at
2	$2\omega_{inner}$	$3\omega_{inner}$, $4\omega_{inner}$
3	$3\omega_{inner}$	$\omega_{wp} + {}^{3}/_{2}\omega_{inner}$
5	$5\omega_{inner}$	${}^{3}/_{2}\omega_{wp} - 5\omega_{inner}$
8	ω_{wp}	–
12	$\omega_{wp} - 4\omega_{cage}$ or $2\omega_{wp} - 4\omega_{inner}$	$\omega_{wp} + 4\omega_{inner}$

5 Conclusions

A lumped parameter model has been introduced in this paper to investigate structural vibrations in rolling element bearings. Using this model, effect of race waviness with varying the number of waves, nonlinear stiffness and nonlinear damping on the vibration response of the bearing have been studied. With the addition of the damping, the peak amplitude of vibration reduced drastically. The foregoing results provide the following conclusion:

a. The frequency of the vibrations due to inner race waviness depends on the waviness order given as $n = qN_b \pm k$ and frequency of vibration caused by waviness is $\omega = qN_b\left(\omega_{inner} - \omega_{cage}\right) \pm k\omega_{inner}$. However, this equation is applicable to major peaks only.
b. For the inner race waviness order (n), the peaks or its super-harmonics are observed at wave passage frequency (WPF) $\omega_{wp} = N_b\left(\omega_{inner} - \omega_{cage}\right)$.

References

1. Perret, H.: Elastic spielschwingungen konstant walzlger. Werkstalt und Betrieb **3**, 354–358 (1950)
2. Meldau, E.M.: Die bewegung der achse von walzlagern beigeringen drehzahlen. Werkstalt und Betrieb 7–19 (1955)
3. Tamura, H., Tsuda, Y.: On the spring characteristics of ball bearing (extreme characteristics with many balls). Bull. JSME **23**, 961–990 (1980)
4. Gustafsson, O.G., et al.: Research Report on Study of the Vibration Characteristics of Bearings. Report: AL 631 023, Reg: 585 14: 4223, December, SKF Ind. Inc (1963)
5. Wardle, F.P.: Vibration forces produced by waviness of the rolling surfaces of thrust loaded ball bearings, Part I: theory. Proc. IMechE **202**(C5), 305–312 (1988)
6. Aktürk, N.: Some characteristic parameters affecting the natural frequency of a rotating shaft supported by defect-free ball bearings. Proc. Inst. Mech. Engrs. Part K: J. Multi-body Dyn. **217**, 145–151 (2003)
7. Tiwari, M., Gupta, K., Prakash, O.: Effect of radial internal clearance of ball bearing on the dynamics of a balanced horizontal rotor. J. Sound Vib. **238**(5), 723–756 (2000)
8. Harsha, S.P., Kankar, P.K.: Stability analysis of a rotor bearing system due to surface waviness and number of balls. Int. J. Mech. Sci. **46**, 1057–1081 (2004)
9. Harsha, S.P., Sandeep, K., Prakash, R.: Nonlinear dynamic behaviors of rolling element bearings due to surface waviness. J. Sound Vib. **272**, 557–580 (2004)
10. Harris, T.A.: Rolling **B**earing Analysis. Wiley, New York (2001)

Beneficial Effects of Parametric Excitation in Rotor Systems

Horst Ecker

Abstract For a long time parametric excitation in rotor systems was associated only with the gravity effect on the bending vibration of rotors with anisotropic shafts. Parametric excitation seemed to have only negative effects on the dynamics of rotating systems and therefore the focus of research studies was on how to avoid or at least minimize the adverse consequences of parametric excitation.

However, recent research results have shown that parametric excitation may not only cause harmful instabilities in a dynamical system but can also improve the capability of a system to suppress vibrations. In particular it is possible to avoid the onset of an instability by introducing parametric excitation to the system. These findings are quite new and the numerous possibilities of making use of it still need to be explored and discussed.

This article presents the basics of parametric excitation as a means to suppress vibrations in rotating machines. Several theoretical and experimental studies are reviewed. The potential of this novel design concept is discussed and directions for further research and future practical applications are outlined.

Keywords Rotor instability · Vibration damping · Time-periodic stiffness variation

1 Introduction

The expression *parametric excitation*, which will be abbreviated in the latter by the symbol *PE*, is commonly used for time-periodic coefficients in second order differential equations [1]. The most simple but nevertheless very useful equation of this type is the well-known Mathieu equation. Already this equation has interesting solutions, exhibiting unexpected unstable but also stable behavior (e.g. the inverted pendulum) depending on the amplitude and frequency parameters of the time-periodic (harmonic) term.

H. Ecker (✉)
Vienna University of Technology, Institute of Mechanics and Mechatronics,
Wiedner Hauptstrasse 8-10/E325, A-1040, Vienna, Austria
e-mail: horst.ecker@tuwien.ac.at

K. Gupta (ed.), *IUTAM Symposium on Emerging Trends in Rotor Dynamics*,
IUTAM Bookseries 25, DOI 10.1007/978-94-007-0020-8_31,

In general, a mathematical model of a rotor system will not lead to equations with time-periodic coefficients, since in most cases the shaft will have isotropic stiffness properties. There are, however, certain electrical machines with significantly different bending stiffness characteristics of the rotor with regard to the two main geometric axes. Such a design is found e.g. in two-pole electrical generators, see [12]. A horizontally mounted rotor shaft with different bending stiffness properties in two perpendicular directions will exhibit different bending deflection due to gravity forces, depending on the angular position of the anisotropic (orthotropic) shaft. Since the period of the time-varying stiffness parameter is two times the rotational speed of the shaft, so-called *parametric resonances* with possibly large vibration amplitudes will occur at and near half of the first critical speed, see e.g. [2] and [12]. Parametric excitation in rotor systems is almost exclusively known for this adverse effect. In this contribution, however, we will not consider an orthotropic shaft, but we will investigate positive consequences of an additional external time-periodic stiffness on the rotor system behavior.

A major issue in rotor dynamics is the dynamic stability of the system [2, 16, 21]. Practically every rotor has a speed limit beyond which the rotor system becomes unstable and may run under critical conditions. The level of this threshold depends mainly on the balance between external damping available and destabilizing forces present in the rotor system and determines the useful speed range of the rotor system. If the speed threshold has to be increased, an effective measure is to increase external damping. But at some point the design options are exhausted and a certain amount of damping provided to the rotor system cannot be exceeded. This is the point where additional parametric excitation can be useful and beneficial, since it provides a mechanism to virtually enhance the damping properties of the system. The conditions under which this effect can be achieved will be explained in the next section.

2 Stability of Parametrically Excited Rotor Systems

The linearized equations of motion of a rotor system with the position vector $\mathbf{r}$ and harmonic parametric stiffness excitation $\cos(\eta\tau)\mathbf{P}^C$ can be written in matrix notation as

$$\mathbf{M}\,\mathbf{r}'' + [\mathbf{C} + \mathbf{G}(\nu)]\,\mathbf{r}' + [\mathbf{K} + \mathbf{N}(\nu) + \cos(\eta\tau)\mathbf{P}^C]\,\mathbf{r} = \mathbf{F}(\tau). \tag{1}$$

The size of the position vector $\mathbf{r}$ and the well-known system matrices $\mathbf{M}$, $\mathbf{C}$, $\mathbf{G}$, $\mathbf{K}$, and $\mathbf{N}$ is determined by the number of degrees of freedom assumed for the system.

A rotor system as described by Eq. 1 will become unstable beyond a speed limit constituted by a threshold of instability ν_{lim} due to the destabilizing effect of non-conservative forces generated by $\mathbf{N}(\nu)$. For the system without parametric excitation ($\mathbf{P}^C = \mathbf{0}$) this is well known and the stability threshold can be calculated by a standard numerical eigenvalue analysis where the rotor speed ν is iterated until the largest real part of the complex eigenvalues changes sign from minus to plus, i.e. becomes zero.

In the presence of time-varying parameters ($\mathbf{P}^C \neq \mathbf{0}$) this standard procedure cannot be used anymore and, moreover, additional regions of instability may occur due to parametric excitation. So-called *parametric resonances* may occur for certain values of the parametric excitation (PE) frequency η which are essentially determined by the natural frequencies ω_j^e of the homogeneous, conservative system.

$$\eta_{j/N} = \frac{2\omega_j^e}{N}, \qquad \eta_{jk/N}^{\pm} = \frac{|\omega_j^e \pm \omega_k^e|}{N}, \qquad (j,k = 1,2,...n^e; N = 1,2,...). \tag{2}$$

Whereas the PE-resonances of the first kind $\eta_{j/N}$ and those of the second kind $\eta_{jk/N}^{+}$ usually generate small regions of instability in the vicinity of the respective η_{fk}, the opposite may occur for $\eta_{jk/N}^{-}$, the difference type of the possible PE combination resonance frequencies.

Tondl [17] was the first to report on the interesting properties of $\eta_{jk/N}^{-}$ combination resonance frequencies and to point out that near these frequencies not only stability of the system is observed but also self-excited vibrations can be suppressed. This effect was investigated in further studies ([3,18] and others) and turned out to be quite effective in stabilizing an otherwise unstable system. Therefore it was obvious to apply the idea also to rotor systems [19].

With the increasing number of dofs needed to establish a valid model of a rotor system and no symmetries present in the system to take advantage of, analytical methods can hardly be used anymore. Numerical methods have to be applied and among them a method based on Floquet's theorem has turned out to be computationally quite efficient. For a system of first order differential equations

$$\mathbf{y}' = \mathbf{A}(\tau)\,\mathbf{y}, \qquad \mathbf{A}(\tau) = \mathbf{A}(\tau + T), \tag{3}$$

with a T-periodic matrix $\mathbf{A}(\tau)$ each fundamental matrix $\mathbf{M}(\tau)$ of the system can be represented as a product of two factors

$$\mathbf{M}(\tau) = \mathbf{P}(\tau)e^{\mathbf{C}\tau}, \tag{4}$$

where $\mathbf{P}(\tau)$ is a T-periodic matrix function and $\mathbf{C}$ is a constant matrix. See e.g. [20] for a discussion of various aspects of Floquet's theorem and the short proof. The stability of the system can be determined either from the eigenvalues of the *Floquet exponent matrix* $\mathbf{C}$ or from the *monodromy matrix* $\mathbf{M}(T)$, which essentially is the state transition matrix evaluated after a period T. The monodromy matrix can be calculated numerically by repeated integration of the system equations over one period. By starting from independent sets of initial conditions the system response is calculated after one period T. It is convenient to generate such sets by using the columns of the identity matrix $\mathbf{I}$ as initial vectors to start from. For a rotor system with n degrees of freedom, $2n$ initial value problems over one period T need to be solved

$$\mathbf{y}' = \mathbf{A}(\tau)\mathbf{y}, \quad [\mathbf{y}(0)_1, \mathbf{y}(0)_2, ..., \mathbf{y}(0)_{2n}] = \mathbf{I}, \quad \tau = [0, T], \tag{5}$$

and then the results are ordered as follows

$$\mathbf{M}(T) = [\mathbf{y}(T)_1, \mathbf{y}(T)_2, ..., \mathbf{y}(T)_{2n}]. \tag{6}$$

The last step in the procedure is to calculate the eigenvalues of the monodromy matrix

$$[\Lambda_1, \Lambda_2, ..., \Lambda_{2n}] = \text{eig}(\mathbf{M}(T)). \tag{7}$$

The system is unstable if any of the eigenvalues is larger than unity in magnitude

$$\max(|\Lambda_1|, |\Lambda_2|, ..., |\Lambda_{2n}|) \quad \begin{cases} < 1 \text{ stable} \\ > 1 \text{ unstable.} \end{cases} \tag{8}$$

By applying this method, the computational effort to determine the stability of the rotor system with 8 dofs and time-varying stiffness parameters consists of 16 numerical integration runs with the equivalent first order system over one period T^{PE} of the parametric excitation $\cos(\eta\tau)$, plus the calculation of all eigenvalues of the (16×16) monodromy matrix.

This computational method was used almost exclusively for the numerical studies presented in the next section. Only when vibration amplitudes had to be calculated, and also when non-linearities had to be considered, the numerical solution was sought by integration of the system equations (1) in the time domain.

3 Vibration Suppression by PE in Rotor Systems

In this section three numerical studies and also one experimental study will be reviewed and discussed. These studies demonstrate how parametric excitation could be employed in a rotor system to enhance its performance. At present these design concepts may seem to be futuristic and not readily applicable in a real world machine. Since this is a well known scenario for an emerging new technology, it is likely worth the time and effort to investigate and explore the positive aspects of parametric excitation.

All the following studies have two facts in common which we can put ahead of this discussion. (1) Parametric excitation is introduced by *open-loop control* of a system parameter. (2) The *frequency* of the harmonic parameter variation where the *best performance* is achieved will be near the difference type of the *combination resonance frequency* $\eta^{-}_{21/1} = \omega^e_2 - \omega^e_1$.

Note that the available space does not allow to fully document the models and parameters used in the examples below. The reader is referred to the references where the models are explained comprehensively and details are listed.

3.1 Rigid Rotor and Time-Periodic Bearing Mounts

There is a multitude of rotor systems where the rotor can be considered as a rigid body and the flexibility of the system is located within the rotor bearings and the bearing mounts. Especially air-bearings, but also fluid-film bearings can create destabilizing forces at high rotor speeds and the rotor may become unstable beyond a speed threshold. By introducing a time-varying stiffness of the bearing support, the system becomes parametrically excited and can benefit from an increased stability limit. In first studies [7] and [10] this concept was investigated.

Figure 1 shows a sketch of a simple rotor model with parametric stiffness excitation of the bearing mounts and the associated critical speed map for the rotor without PSE. Due to bearing instabilities the rotor becomes unstable beyond a scaled speed of about $\nu \cong 0.8$. With harmonic stiffness variation of the bearing mounts at $\eta_{21/1}^{-} = \omega_2^e - \omega_1^e$ this speed limit can be increased significantly. Figure 2 (left) is a stability map for various PSE-amplitudes and shows the beneficial effect of PSE at $\eta \cong 2.0$. The diagram to the right demonstrates how the optimal PSE-frequency η depends on the bearing masses $m_{B1,2}$ as they also determine the dynamic properties (natural frequencies) of the system.

3.2 Rotor with Flexible Shaft and Time-Periodic Bearing Stiffness

The onset of instability can be improved for flexible rotors, as well. This has been confirmed by the detailed studies [6] and [8] of a Jeffcott/Laval-rotor with parametric stiffness excitation inside the bearings. See the sketch of a vertical rotor with elastic shaft and open-loop controlled bearings in Fig. 3. The technology needed to

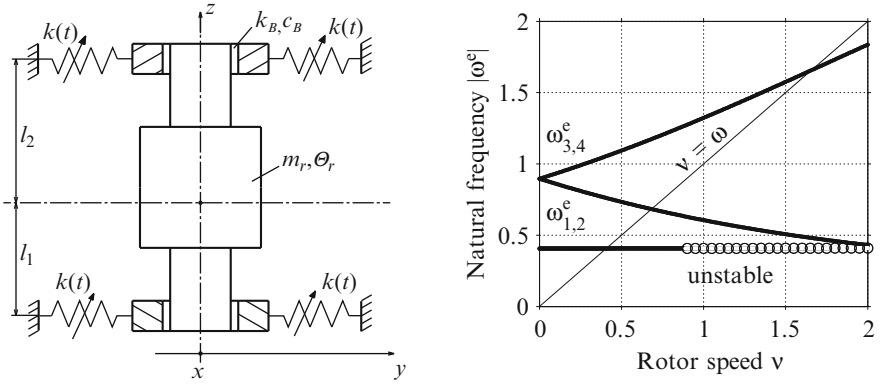

Fig. 1 Rigid rotor m_R, θ_R supported by flexible bearing mounts with time-periodic stiffness component $k(t)$. Bearing parameters k_B, c_B lead to instability of first vibrational mode beyond stability threshold $\nu \cong 0.8$, see speed map to the right

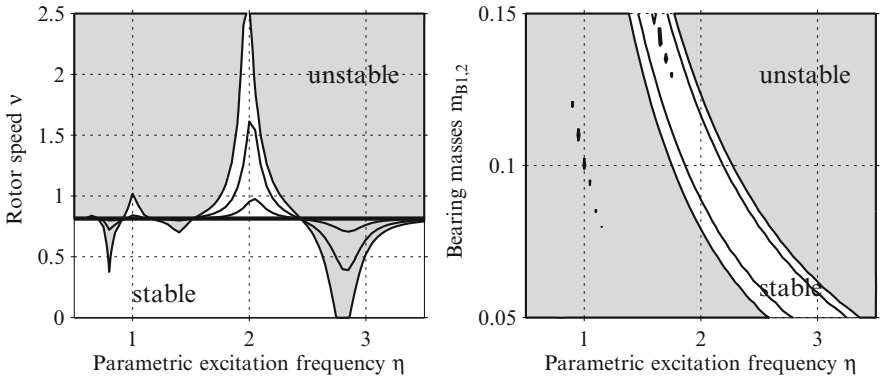

Fig. 2 Stability charts for rotor system with PSE of bearing mounts. *Left*: Increase of stability threshold at $\eta = 2.0$ for different levels of PSE amplitude (0%, 20%, 40%, 60% of k_{avg}). *Right:* Change of optimal PSE-frequency and stability interval as a function of bearing masses due to change of natural frequencies. See [7] for details and system data

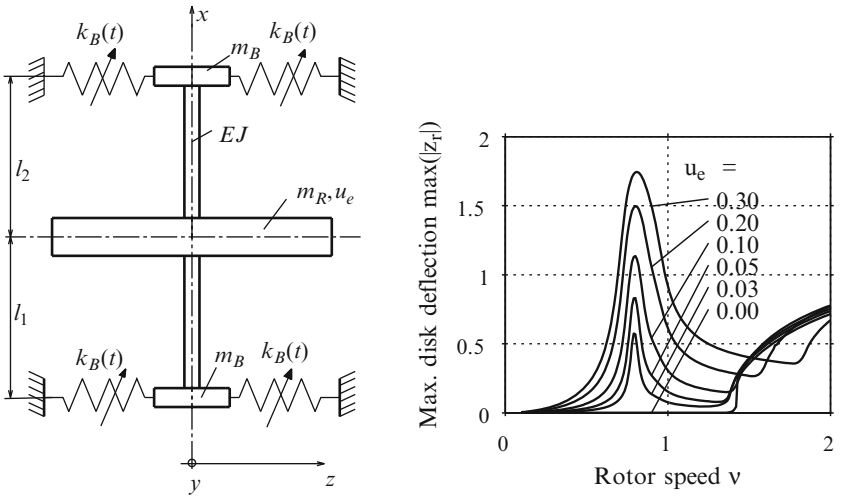

Fig. 3 Symmetric flexible rotor m_R with mass unbalance u_e and external non-linear damping. Bearings with time-periodic stiffness component $k(t)$. Internal damping of shaft EJ leads to instability of first vibrational mode. *Right:* Vibration amplitudes at resonance speed and onset of instability for unbalance parameter u_e. See [8] for system data

realize stiffness control is already available. PSE can be achieved by either active magnetic bearings or by pressure-controlled fluid bearings. Similar to the previous and also to the next example, one can easily increase the stability threshold by a factor of two, if the necessary amplitude of the PSE can be provided. The bearing arrangement of Fig. 3 is only suitable for vertical rotors, since the static weight of the rotor must not be supported or transmitted by the time-periodic stiffness element.

Another important issue is rotor unbalance and how it possibly interacts with parametric excitation. This question has been addressed and answered in a numerical study in [8]. In Fig. 3 (right) the vibration amplitudes at the disk station are plotted. As one can easily see, the first resonance speed appears at a scaled rotor speed of $\nu \cong 0.8$. The onset of instability is at $\nu \cong 1.4$ due to parametric stiffness excitation. Without PSE the instability region starts at about $\nu \cong 1.0$. As the unbalance excitation, which is represented by symbol u_e, is increased, no adverse interaction between forced excitation and parametric excitation is observed. Quite the contrary, the onset of instability moves to higher rotor speeds as the unbalance eccentricity is increased. This figure and result was not obtained by a stability investigation but by numerical integration of the non-linear and inhomogeneous set of differential equations of the rotor system.

Let us briefly raise the question of a time-periodic damping variation, since it might be impossible to completely separate stiffness and damping properties with certain PSE-devices. In general, only energy-conserving system parameters may create enhanced damping, if they are changed periodically. According to a recent study [4], however, it seems to be possible to further increase the damping by additional time-periodic damping parameters.

3.3 Flexible Multi-station Rotor with Local Time-Periodic Stiffness

In the previous examples it was assumed that PSE is introduced at the bearing station of a rotor, either by a special type of bearing or an open-loop controlled bearing mount. The incorporation of an additional device in a rotor design is quite difficult, no matter whether the system is open-loop or closed-loop controlled. Consequently, the bearing stations might not be the best positions for a device to create PSE. Moreover, in other positions there would be the advantage that one does not have to deal with static loads being transmitted by the PSE device.

Therefore, it is also important to study various positions along the rotor axis as possible and feasible stations for PSE. Such an investigation is under way, with a simple model in use as depicted in Fig. 4. Note that for reasons of simplicity this model assumes rigid bearings at both shaft ends and a rather flexible rotor shaft. At station (1) a small lumped mass is assumed and parametric stiffness excitation $k(t)$ is introduced. Instability of the rotor is caused by internal damping of the shaft, which leads to a speed threshold at $\nu = 1.25$. The stability map on the right hand side demonstrates that also such a system can be stabilized at $\eta = \omega_2^e - \omega_1^e$ up to twice the original speed threshold and even higher, if large PSE-amplitudes are permitted.

There are of course PE-frequencies at which the system is destabilized. In this numerical example, the scaled frequencies in the range between $1.5 < \eta < 2.0$ would result in a completely unstable system at any speed. This instability is caused by the primary parametric resonance for $2\omega_1^e$. Note that there is no need to select this

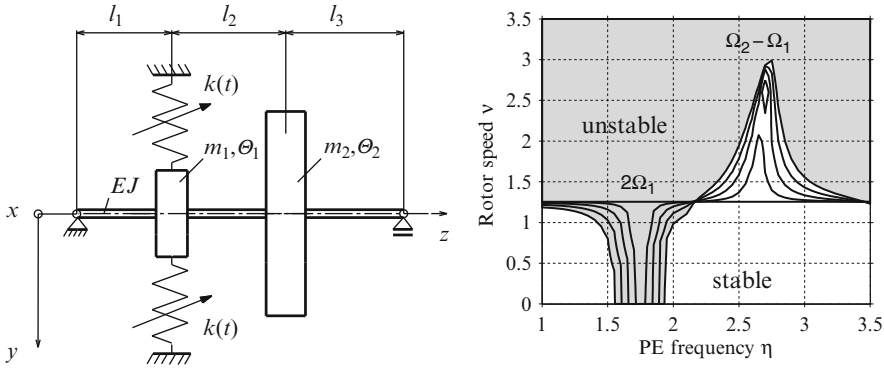

Fig. 4 Flexible rotor with PSE-device attached to the rotor shaft at a station along the shaft. *Right:* Exemplary stability map with increased rotor stability for PSE-frequency $\eta \cong 2.6$ and parametric resonance at $\eta = 1.8$. Contour lines hold for increased PSE-amplitudes

dangerous frequency. Also, there is no passing or running through this frequency. Therefore, such PE-resonance frequencies can be avoided easily and are not a limiting factor to the basic idea.

3.4 Flexible Rotor Blade with Axial Time-Periodic Forcing

The last example to demonstrate beneficial aspects of parametric excitation deals with a cantilever beam that is loaded axially by a time-periodic force [9]. It is known that the analysis of such a system leads to equations where the time-periodic force appears in the stiffness matrix of the system. Therefore, the system is in fact parametrically excited, although this might not be obvious at first glance.

The sketch in Fig. 5 gives a brief idea how a string running from the root to the tip of the beam can be used to create a force that mimics an axial load. By pulling at the lower end of the string, the force at the tip can be controlled. This system has been investigated theoretically [14], but also a test rig was built and measurements were taken. Another experimental study of a cantilever beam, employing a different type of PSE, is found in [5]. For more general experiments to prove the basic idea of vibration suppression by PSE, see [13] and [15].

In [11] one will find a detailed description of the test rig as sketched in Fig. 5 and selected results from the experiments. Two measured and typical time series of first mode vibrations are shown in Fig. 5. The plot on top is a time series for the beam tip deflection $y_1(x = L, t)$ when no parametric is active. One can see a rather slow decay of the vibration amplitudes that will serve as a reference result. The diagram below shows the same signal, but with PE activated and operating near the optimal PE-frequency. Although strong beats do appear in the signal, it is easy to recognize that the PE-generated signal exhibits a much faster vibration decay.

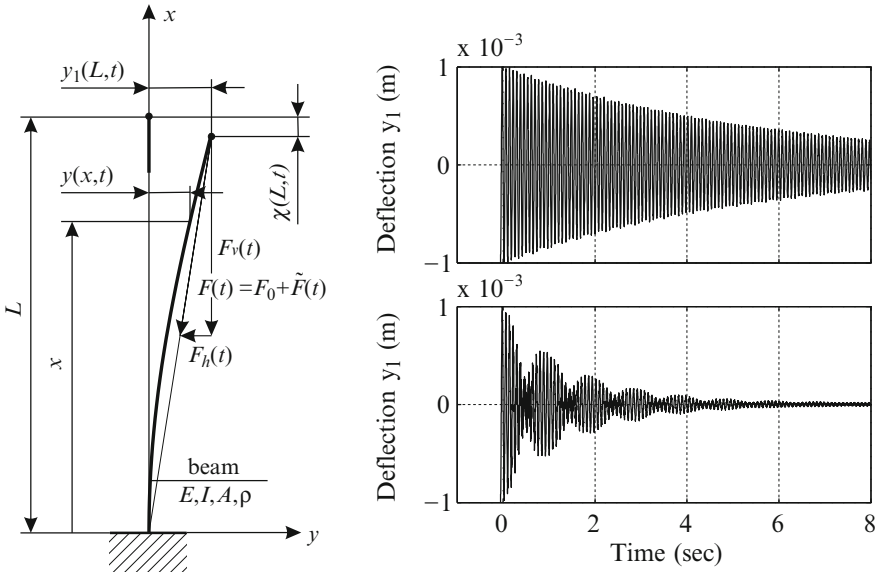

Fig. 5 Cantilever beam with time-periodic tip force oriented to the root of the beam. *Top right:* Measured signal of free lateral vibration $y_1(t)$ at the tip of the beam, $\tilde{F}(t) = 0$. *Bottom right*: Signal $y_1(t)$ with time-periodic forcing $F(t) = F_0 + \tilde{F}(t)$ at $\eta = \omega_2^e - \omega_1^e$, see [11] for details

It might indeed be too optimistic to think that, in the near future, this idea could be realized in turbo-rotors and may help to provide more damping to turbine blades. But at least this example demonstrates that it is possible to experimentally verify the theoretical results and prove the vibration suppression effect. Moreover, it shows that the basic effect can be used in many different ways and configurations. This example might also serve as a thought-provoking impulse and trigger further ideas.

4 Conclusions

Time-periodic parameters in rotor systems, in particular stiffness parameters, can be used to faster suppress vibrations in a lower mode by energy transfer to a higher and better damped mode. This effect can be achieved if the frequency of the periodic function, which varies the parameter, is chosen as the difference between the respective higher and lower natural frequency of the system. The virtually increased damping parameter of the lower vibration mode is especially of avail if this mode becomes unstable. Depending on the amplitude of the parameter variation, the stability threshold is raised and the rotor may run stable at higher speeds than before.

There is a number of ways to take advantage of this basic principle in a rotor system. Several of them are outlined in this paper and the possible benefit is confirmed by either numerical or experimental studies. Further application ideas will emerge from future work on this topic which may evolve into a key solution for rotor instability in certain cases.

References

1. Cartmell, M.: Introduction to Linear, Parametric and Nonlinear Vibrations. Chapman and Hall, London (1990)
2. Childs, D.: Turbomachinery Rotordynamics: Phenomena, Modelling, and Analysis. Wiley, New York (1993)
3. Dohnal, F.: Damping of mechanical vibrations by parametric excitation. PhD Thesis, Vienna University of Technology, Vienna, Austria (2005)
4. Dohnal, F.: Damping of a flexible rotor by time-periodic stiffness and damping variation. In: Proceedings of the IMECHE 9th International Conference on Vibrations in Rotating Machinery, Exeter, UK (2008)
5. Dohnal, F.: Amplification of damping of a cantilever beam by parametric excitation. In: Ulbrich, H., Ginzinger, L. (eds.). Proceedings of MOVIC 2008. Munich, Germany (2008)
6. Ecker, H., Pumhössel, T., Tondl, A.: A study on parametric excitation for suppressing self-excited rotor vibrations. In: Proceedings of the Sixth International Conference on Rotor Dynamics, IFToMM, ISBN: 0-7334-1963-1, Sydney, Australia (2002)
7. Ecker, H., Tondl, A.: Stabilization of a rigid rotor by a time-varying stiffness of the bearing mounts. In: IMechE (eds.) Vibrations in Rotating Machinery, ISBN: 1-86058-447-0, Professional Engineering Publishing Limited, Suffolk, UK (2004)
8. Ecker, H.: Suppression of Self-excited Vibrations in Mechanical Systems by Parametric Stiffness Excitation. Argesim/ASIM, Vienna, Austria (2005)
9. Ecker, H., Dohnal, F., Springer, H.: Enhanced Damping of a Beam Structure by Parametric Excitation. In: van Campen, D.H., Lazurko, M.D., van den Oever W.P.J.M. (eds.) Proceedings ENOC-2005, ISBN 90-386-2667-3, Eindhoven, Netherlands (2005)
10. Ecker, H., Tondl, A.: Increasing the stability threshold of a rotor by open-loop control of the bearing mount stiffness. In: Sawicki, J.T., Muszynska, A. (eds.) Proceedings Third International Symposium on Stability Control of Rotating Machinery, Cleveland, USA (2005)
11. Ecker, H., Pumhössel, T.: Experimental results on parametric excitation damping of an axially loaded cantilever beam. In: Proceedings of the 2009 ASME International Design Engineering Technical Conference (IDETC), San Diego, USA (2009)
12. Gasch, R., Nordmann, R., Pfützner, H.: Rotordynamik. Springer, Berlin (2002)
13. Paradeiser, W.: Experimental Verification of a parameter-antiresonance (in German). MS Thesis, Vienna University of Technology, Vienna, Austria (2006)
14. Pumhössel, T., Ecker, H.: Active damping of vibrations of a cantilever beam by axial force control. In: Proceedings of the 2007 ASME International Design Engineering Technical Conference (IDETC), Las Vegas, USA (2007)
15. Schmidt, E., Paradeiser, W., Dohnal, F., Ecker, H.: Design of an electromagnetic actuator for parametric stiffness excitation. COMPEL **26**(3), 800–813 (2007)
16. Tondl, A.: Some problems of rotor dynamics. Academia, Prague, Czech Republic (1965)
17. Tondl, A.: To the problem of quenching self-excited vibrations. Acta Technica ČSAV **43**, 109–116 (1998)
18. Tondl, A., Ecker, H.: Cancelling of self-excited vibrations by means of parametric excitation. In: Proceedings of the 1999 ASME Design Engineering Technical Conferences (DETC), Las Vegas, USA (1999)

19. Tondl, A.: Self-excited vibration quenching in a rotor system by means of parametric excitation. Acta Technica ČSAV **45**, 199–211 (2000)
20. Verhulst, F.: Nonlinear Differential Equations and Dynamical Systems. Springer, Berlin (2000)
21. Yamamoto, T., Ishida, Y.: Linear and Nonlinear Rotordynamics. Wiley, New York (2001)

Simulation and Experiment of a Rotor with Unilateral Contacts and Active Elements

Lucas Ginzinger and Heinz Ulbrich

Abstract A simulation environment for rotordynamical problems has been developed at our institute. The environment is based on a framework for the efficient simulation of multibody systems with unilateral contacts and elastic elements. The simulation comprises the modelling of a 3D flexible rotor, unilateral contacts with and without friction between the rotor and stationary parts and an interface to Matlab/Simulink to co-simulate the feedback control of active elements. The fundamentals of unilateral constraints allow a detailed simulation of processes like contact /detachment, stick/slip or impacts with and without friction. The simulation environment has been tested and verified using experimental results from a rotor test rig with an active auxiliary bearing. In this project the possibilities of controlling a rubbing rotor with an active auxiliary bearing have been investigated in experiments and theory.

Keywords Simulation environment · Unilateral contacts · Active elements · Rotor rubbing · Active auxiliary bearing

1 Introduction

During the last years much effort has been devoted to develop sophisticated models for the simulation of rotor systems. No modern rotating machine can be designed without performing rotordynamic analysis, particularly when it's operating on high speed. The increasing computational power of computers allows the simulation of very complex rotating machines, including nonlinear and non-stationary effects, performing numerical investigations when the machine is still in its design stage. There are several applications of accurate rotor simulations: at the design

L. Ginzinger and H. Ulbrich (✉)
Institute of Applied Mechanics, Technische Universitaet Muenchen,
Boltzmannstr. 15, 85748 Garching, Germany
e-mail: ginzinger@amm.mw.tum.de; ulbrich@amm.mw.tum.de

K. Gupta (ed.), *IUTAM Symposium on Emerging Trends in Rotor Dynamics*,
IUTAM Bookseries 25, DOI 10.1007/978-94-007-0020-8_32,

stage, to predict possible dynamical problems; in diagnostics, to investigate various problems; in the active control of vibrations to design optimized control systems; to help planning experiments and saving time and costs.

2 Simulation Environment

The simulation environment MBSim (http://mbsim.berlios.de), which was developed at the Institute of Applied Mechanics, is based on a framework for the efficient simulation of multi-body-systems with unilateral contacts and elastic elements. The framework comprises the description of the system dynamics as well as numerical methods as provided in [3, 6]. A brief overview will be given in the following. For a more comprehensive introduction to the formulation and numerics of non-smooth dynamics see [1, 6]. The non-smooth dynamics of the system is described in terms of a measure differential equation. The dynamics of a bi- and unilateral constrained system can be expressed by

$$\mathbf{M}d\,\mathbf{u} = \mathbf{h}dt + \mathbf{W}d\,\boldsymbol{\Lambda} \tag{1}$$

The matrix $\mathbf{M} = \mathbf{M}(\mathbf{q})$ denotes the symmetric, positive definite mass matrix and depends on the f-dimensional vector of generalized coordinates $\mathbf{q} \in \mathbb{R}^f$. The vector $\mathbf{u} = \dot{\mathbf{q}}$ denotes the velocity vector of the generalized coordinates. The acceleration measure

$$d\,\mathbf{u} = \dot{\mathbf{u}}dt + (\mathbf{u}^+ - \mathbf{u}^-)d\eta \tag{2}$$

is the sum of the continuous part $\dot{\mathbf{u}}dt$ and the discrete parts $(\mathbf{u}^+ - \mathbf{u}^-)d\eta$. The second term is the difference of the left and the right limit of the velocities weighted by the sum of the DIRAC delta functions $d\,\delta_i$ at the discontinuities t_i:

$$d\eta = \sum_i d\,\delta_i, \qquad d\,\delta_i = d\,\delta(t - t_i) = \begin{cases} \infty & \text{if } t = t_i \\ 0 & \text{if } t \neq t_i \end{cases} \tag{3}$$

On the right hand side of Eq. 1 the vector $\mathbf{h} = \mathbf{h}(\mathbf{u}, \mathbf{q}, t)$ contains all smooth external, internal and gyroscopic forces. The reaction measure in the contacts $\mathbf{W}d\,\boldsymbol{\Lambda}$ is decomposed by the generalized force directions $\mathbf{W} = \mathbf{W}(\mathbf{q})$ and the magnitudes $\boldsymbol{\Lambda}$. In analogy to the acceleration measure, the reaction measure $d\,\boldsymbol{\Lambda}$ contains forces $\boldsymbol{\lambda}$ due to persisting contacts as well as impulses $\boldsymbol{\Lambda}$ due to conditions of bodies at the impact time t_i:

$$d\boldsymbol{\Lambda} = \boldsymbol{\lambda}dt + \boldsymbol{\lambda}d\eta \tag{4}$$

Integrating (1) under consideration of the DIRAC delta (3) yields the classical equations of motion for a constrained system and the impact equations.

The computation of the accelerations $\dot{\mathbf{u}}$ as well as the post-impact velocities $\mathbf{u}_i^+$ in Eq. 1 requires the knowledge of the unknown contact reactions $\boldsymbol{\lambda}$ and $\boldsymbol{\lambda}_i$, respectively. Thus, additional contact laws must be constituted. Contacts between bodies

in the system are modeled as discrete point contacts whereby the contact zone is assumed to be totally rigid. Deformations of elastic components are only regarded in form of the overall discretization, no local deformation e.g. of a beam cross-section is modeled. Consequently, a contact corresponds to a constraint. In this context two different types of contacts are considered, for which different contact laws hold: persisting contacts which are always closed and contacts that may be open or closed. In the following, the force laws of the two contact types are explained for smooth and non-smooth motion. For this the contact reactions

$$\mathbf{W}d\boldsymbol{\lambda} = (\mathbf{W}_N \quad \mathbf{W}_T)\begin{pmatrix} d\boldsymbol{\lambda}_N \\ d\boldsymbol{\lambda}_T \end{pmatrix} = (\mathbf{W}_B \quad \mathbf{W}_U \quad \mathbf{W}_T)\begin{pmatrix} d\boldsymbol{\lambda}_B \\ d\boldsymbol{\lambda}_U \\ d\boldsymbol{\lambda}_T \end{pmatrix} \tag{5}$$

are decomposed into components normal (index N) – split up in bilateral (B) and unilateral(U) – and tangential (T) to the contact plane.

3 Dynamics Between Impacts

First of all, only smooth motion is considered, i.e. no impacts occur. Then a bilateral contact implies a bilateral constraint of the form

$$g_B = 0, \quad \lambda_B \in \mathbb{R}. \tag{6}$$

where g_B denotes the normal distance of the interacting bodies in the contact point. The second type of contact also allows for detachment. The associated unilateral constraint is given by the SIGNORI-FICHERA-condition:

$$g_U \geq 0, \quad \lambda_U \geq 0, \quad g_U \lambda_U = 0 \tag{7}$$

The respective force laws are shown in Figs. 1a,b. For both bi- and unilateral constraints dry friction is considered. In order to establish Coulomb's law the force of a

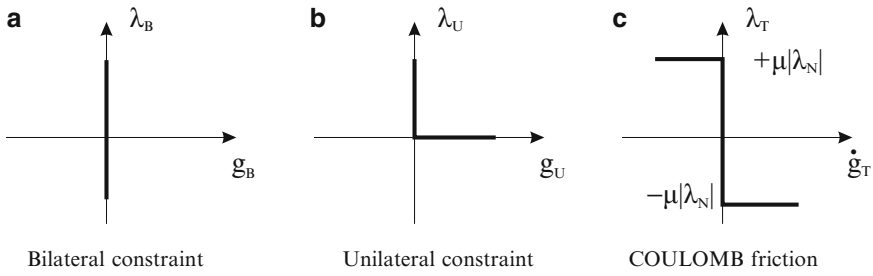

Fig. 1 Force laws for **(a)** bilateral **(b)** unilateral contacts and **(c)** Coulomb friction

single contact is decomposed in a component $\lambda_N \in \{\lambda_B, \lambda_U\}$ normal to the contact plane – in case of planar dynamics – a tangential component λ_T in friction direction. Using the relative tangential velocity $\dot{g}_T$, Coulomb's friction law is given by

$$\dot{g}_T = 0 \quad \Rightarrow \quad |\lambda_T| \leq \mu_0 |\lambda_N| \tag{8}$$

$$\dot{g}_T \neq 0 \quad \Rightarrow \quad \lambda_T = -\frac{\dot{g}_T}{|\dot{g}_T|} \mu |\lambda_N| \tag{9}$$

The force law of a tangential frictional contact is plotted in Fig. 1c.

4 Impact Dynamics

In contrast to persisting and detaching contact, a closing contact implies a discontinuity in the relative and therewith possibly all generalized velocities. Therefore impacts must be treated separately. The effect of an impact of a specific contact may concern all other constraints, the bilateral as well as the unilateral ones. The impact law for a bilateral contact is given by

$$\dot{g}_T^+ = 0, \quad \Lambda_B \in \mathbb{R} \tag{10}$$

and ensures that relation (6) is not violated after collisions. Given on impulsive level, NEWTON's impact law in the formulation of MOREAU

$$\dot{g}_U^+ \geq 0, \quad \Lambda_U \geq 0, \quad \dot{g}_U^+ \Lambda_U = 0. \tag{11}$$

and Coulomb's friction law with the normal reaction $\Lambda_N \in \{\Lambda_B, \Lambda_U\}$

$$\dot{g}_T^+ = 0 \quad \Rightarrow \quad |\Lambda_T| \leq \mu_0 |\Lambda_N| \tag{12}$$

$$\dot{g}_T^+ \neq 0 \quad \Rightarrow \quad \Lambda_T = -\frac{\dot{g}_T^+}{|\dot{g}_T^+|} \mu |\Lambda_N| \tag{13}$$

hold for active contacts with ($g_N = 0$) only.

5 Elastic Components

The rotor shaft is modeled by a spatial bending-torsional beam using a polynomial finite element formulation for slender structures, see [6]. Based on the Euler-Newton theory with superposed torsion and small deflections, all deformations are described in rotating reference systems individually attached to each node. This formulation

allows for arbitrary dynamic contact situations as introduced in the previous section, especially non-smooth dynamics including unilateral contacts and dry friction. For the present case, rigid discs are bilaterally bound to the shaft. The two unilateral contacts to the top and bottom circles of the journal bearing are modeled rigid including Coulomb friction.

6 Numerical Framework

Two different groups of numerical schemes can be used to integrate unilateral constrained equations of motion: event-driven and time-stepping schemes. The first one detects events like detachments or impacts and resolve the exact transition times. Between these events the motion of the system is smooth and all contact laws are reduced to bilateral constraints. Thus the equation of motion can be integrated by a standard ODE/DAE-integrator with root-finding. In contrast, time-stepping methods are based on a time-discretization of the system dynamics including the constraints. A detection of events is not needed and the discretization can be chosen such that the constraints are fulfilled either on position or on velocity level. Moreover, a time-stepping algorithm turns out to be very robust in terms of numerical errors.
The presented multibody simulation uses a time-stepping method on position level. A detailed description of the numerical framework can be found in [3]. A comprehensive review on time integration of non-smooth systems is provided in [5].

7 Co-simulation with Simulink

A co-simulation between MBSim and MATLAB/SIMULINK is used to integrate active elements. The feedback controller is calculated in MATLAB/SIMULINK with a fixed time step size using an EULER discretization as it is done by realtime hardware, for example dSpace. The simulation is calculated with the much lower time step size of the time stepping integrator. At each synchronization point the positions and velocities, which are used by the feedback controller, are transferred to MATLAB and one calculation step of the controller is started in MATLAB. In the meanwhile the multibody simulation MBSim calculates until the next synchronization point is reached. Then, the calculated control force for the actuators is transferred to MBSim and the actuator force in the multibody simulation is updated.

The advantages of the co-simulation are the following. Since many real-time hardware boards use SIMULINK for the code generation of the controller, a single SIMULINK model of the controller can be used for both – simulation and experiment. So a very rapid controller development and optimization can be achieved. There is also no error source caused by the modeling of the test rig controller in another simulation software. On the other hand, the Co-simulation takes advantage of recent multi-core-processors, because between the synchronization steps MBSim and MATLAB are two independent processes.

8 Example: Rotor Test Rig with an Active Auxiliary Bearing

To validate the simulation environment results from a test rig with rotor-stator-contact and feedback control are used. The presented example deals with the developement of an active auxiliary bearing, see Fig. 2. In this new approach, the control force is applied indirectly by an auxiliary bearing only in case of rubbing. The auxiliary bearing which is attached to the foundation via two unidirectional actuators. The electromagnetic actuators are mounted in a 90 degree alignment.

The advantages of this control concept are the following: If the rotor system runs in the usual operation state, the active auxiliary bearing does not take effect, so the original design of the rotor system can be kept to largest extent unchanged. In case of a rotor to stator contact, the auxiliary bearing does not only limit a too large response amplitude of the rotor and prevents the rotor/blades and the casing/seals from direct contact, but also effectively reduces the rubbing severity and especially avoids the occurrence of destructive rubbing states such as backward whirling [2]. The effectiveness and success of the control strategy has been discussed in [4].

8.1 Feedback Control

A three-phase control strategy is used, which guarantees a smooth trapping of the rotor followed by a state of “synchronous rubbing". To keep the principal purpose of an auxiliary bearing in mind, the control scheme also has to limit the rotor amplitude as a passive auxiliary bearing does. After the impact load has ceased, the auxiliary bearing is separated again. As input the controller only needs the position of the auxiliary bearing, the position of the rotor shaft inside the auxiliary bearing and the information of the shaft encoder.

The operation phases of the control concept are shown in Fig. 3. During normal operation condition, which means that the rotor deflection $\mathbf{r}_N$ is smaller than a defined limit $\mathbf{r}_{limit}$, the controller is deactivated. When the rotor deflection becomes too large, e.g. due to a sudden arising unbalance, and $\mathbf{r}_N$ exceeds $\mathbf{r}_{limit}$, the controller is activated. In the first control phase, the movement of the auxiliary bearing is

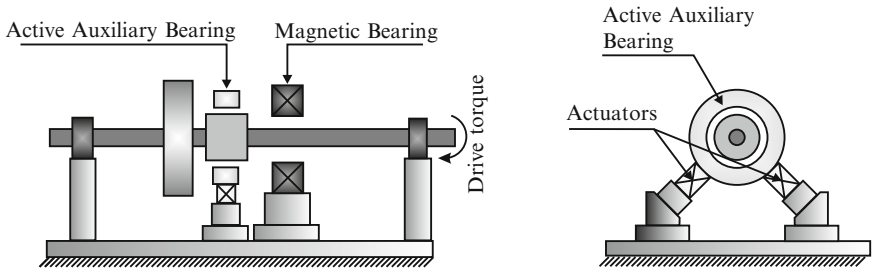

Fig. 2 Active auxiliary bearing

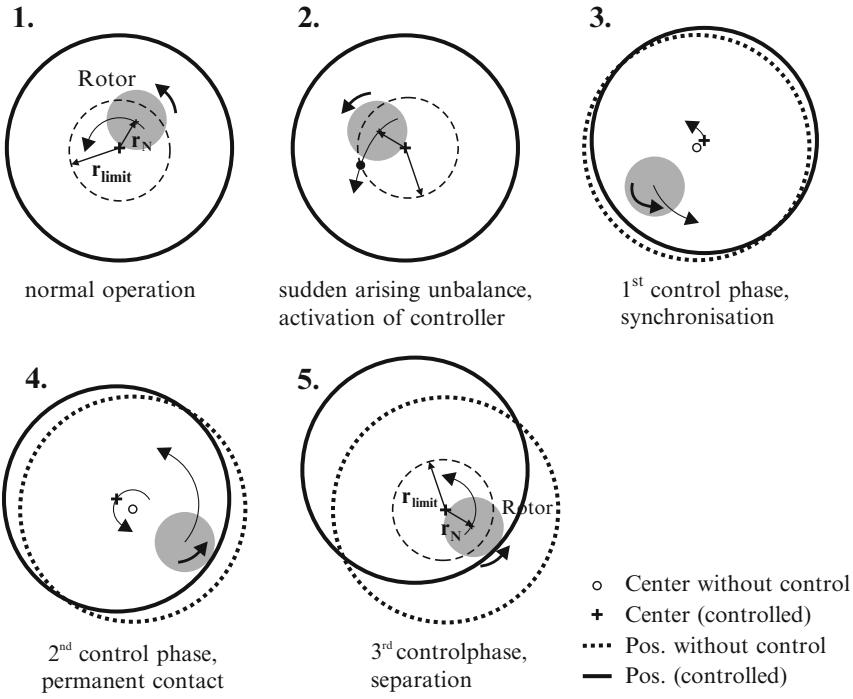

Fig. 3 Principle of the control concept

synchronized with the rotor orbit followed by a smooth transition to a contact. In the second phase, the feedback control assures a permanent contact in the rubbing state of “synchronous full annular rub" and low contact forces. The second phase is active as long as the additional load is present. In the third phase the rotor is separated from the auxiliary bearing after the additional load has disappeared.

In order to define the essential geometrical variables a cross section of the auxiliary bearing and the rotor is shown schematically in Fig. 4. The origin of the coordinate system coincides with the center of the undeformed rotor, $\mathbf{r}_r$ is the position vector to the center of the deformed rotor (in the cross section) and $\mathbf{r}_a$ to the center of the auxiliary bearing. The air gap in the auxiliary bearing is δ_0 and $\mathbf{r}_N$ represents the vector from the center of the auxiliary bearing to the center of the rotor. Additionally the polar angles φ_a and φ_r of the vectors $\mathbf{r}_a$ and $\mathbf{r}_r$ are introduced.

The overall control target of the first and second phase can be specified as

$$\mathbf{q}_{ad} = \begin{matrix} arg\ min \\ (\ddot{\mathbf{q}},\dot{\mathbf{q}},\mathbf{q}) \end{matrix} \left\{ \begin{matrix} g_N \\ \dot{g}_N \end{matrix} \right., \tag{14}$$

with *arg min* = values of $\ddot{\mathbf{q}}, \dot{\mathbf{q}}, \mathbf{q}$ that minimizes g_N and $\dot{g}_N$. The vector $\mathbf{q}$ are the generalized coordinates of the rotor and the auxiliary bearing, g_N is the distance between the contact points and $\mathbf{q}_{ad}$ the target trajectory for the auxiliary bearing.

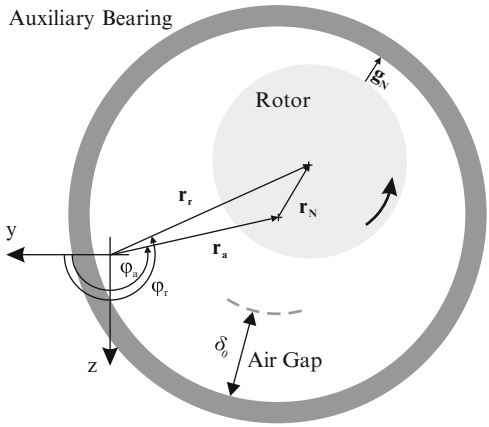

Fig. 4 Contact kinematics

Equation 14 includes that the relative distance becomes zero to get a permanent contact and the relative velocity in normal direction should be as small as possible to get a smooth transition from free rotor motion to the state of full annular rub. The relative velocity of the contact point in tangential direction $\dot{g}_T$ will not be taken in consideration in Eq. 14 because a non-sliding contact would cause a backward whirl, which is not wanted.

In the first two phases of the control scheme, the desired position of the auxiliary bearing is chosen in a way that the movement of the auxiliary bearing is synchronized with the orbit of the rotor and the contact point coincides with the point of the surface of the rotor which is farthest from the origin of coordinate system (Fig. 4). This means that

$$\varphi_{a\ desired} = \varphi_r \ . \tag{15}$$

In case of contact this results in a movement pattern of “synchronous full annular rub". The destructive “backward whirl" is avoided.

Furthermore the desired polar radius $|\mathbf{r}_{N\ desired}|$ is needed to determine the desired position of the auxiliary bearing according to the equation

$$\mathbf{r}_{a\ desired} = \begin{pmatrix} \varphi_a \\ |\mathbf{r}_a| \end{pmatrix} = \begin{pmatrix} \varphi_r \\ |\mathbf{r}_r| - |\mathbf{r}_{N\ desired}| \end{pmatrix}. \tag{16}$$

So the 2D problem to control the orbit has turned into a 1D control problem of $|\mathbf{r}_{N\ desired}|$. In the first control phase (free rotor motion), which means $|\mathbf{r}_N| \leq \delta_0$, the target position of the auxiliary bearing follows

$$|\mathbf{r}_{N\ desired}| = |\mathbf{r}_N| - \int (|\dot{\mathbf{r}}_N| - \mathrm{v}_{pmax}) dt \tag{17}$$

$$= |\mathbf{r}_N| - \int \left(|\dot{\mathbf{r}}_N| - A\, e^{\alpha |\mathbf{r}_r|} \right) dt, \tag{18}$$

where v_{pmax} is the maximum relative velocity of the contact points. The constant factors A and α are chosen in such a way that first impact is kept small but also that the amplitude of the rotor does not exceed δ_0, to meet the principal purpose of an auxiliary bearing.

In case of contact (second control phase), which means $|\mathbf{r}_N| = \delta_0$, the desired distance $|\mathbf{r}_{N\ desired}|$ follows:

$$|\mathbf{r}_{N\ desired}| = \delta_0 + \frac{1}{K_P} f_{perm}, \tag{19}$$

with f_{perm} the desired contact force during the permanent contact and $\frac{1}{K_P}$ a conversion coefficient. Note that it is necessary to choose a desired contact force, which is large enough to ensure a permanent contact despite of elements of uncertainty of the measurement and control system. As soon as the additional load is over, the rotor deflection decreases. The permanent contact is separated when the deflection falls below the limit $\mathbf{r}_{limit}$. The auxiliary bearing is moved to a position concentric to the undeformed rotor shaft.

8.2 Modeling

The simulation model of the rotor system represents the test rig and comprises the flexible rotor, a unilateral contact with friction between the rotor and the auxiliary bearing and a co-simulation between MBSim and MATLAB/SIMULINK to integrate the feedback controller. Using the presented theory of unilateral contact the simulation model covers totally free motion, impacts as well as a permanent contact. There are three rigid discs – two big discs and one small disc which is running inside the auxiliary bearing. The discs are rigidly coupled on the elastic rotor. The rotor is attached to the environment via two spring-damper elements, which represents the ball bearings and bearing housings. The modeling of the auxiliary bearing is shown on Fig. 5 and includes the actuators, the three joints and the joint friction. The contact between the rotor and the auxiliary bearing is modeled as a rigid contact as described above. The overall model is a full 3D model of the presented rotor system.

8.3 Test rig

The rotor test rig can be assembled in various modifications. The presented results have been gained using a very flexible rotor shaft (diameter 12mm). The air gap between the rotor and the auxiliary bearing is 0.3 mm. The length of the rotor shaft is 590 mm. Several sensors are used to gather information. There are two eddy

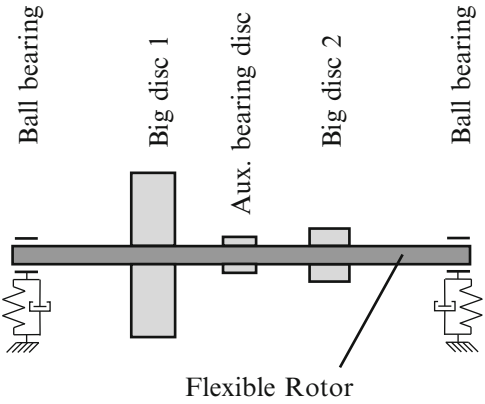

Fig. 5 Model of the rotor

current displacement sensors to measure the position of the rotor besides the auxiliary bearing. The same sensors are installed inside the actuators. Load washers in each actuator are measuring the actuator forces, from which the contact forces are determined indirectly. With the help of accelerometers the load of the bearings are recorded. The measured forces and accelerations are only used to show the performance of the control system.

8.4 Comparison: experiments-simulation

For the analysis of the dynamics of the system, the contact forces between rotor and the auxiliary bearing during rubbing are highly important. For this reason the contact forces have been taken for the comparison between experiment and simulation. It is hardly possible to measure these forces directly without manipulating the whole system. Therefore the contact forces have been determined indirectly via measurements of the forces of the actuators using the mechanical model.

The presented results deal with the state “Without Control" and “With Control". For the case “Without Control" the auxiliary bearing has been fixed mechanically and was working as a conventional passive auxiliary bearing. In Fig. 6 a comparison between experiment and simulation in case of a deactivated as well as an activated control system are shown. The contact force versus the time is plotted. The experimental results are plotted on the left, the simulation results on the right. For this experiment the rotor is running at a constant speed without rotor to stator contact. At a time of $t = 1.0$ s the magnetic bearing applies a sudden arising unbalance. At first the experiment has been performed without using the control system. Then the experiment has been repeated with an activated controller. In case of “Without Control" (Fig. 6, top) rubbing in a state of backward whirling occurs with very high contact forces up to 5,500 N. The simulation shows an excellent agreement with the experiment. On a typical “dual core" personal computer one simulation

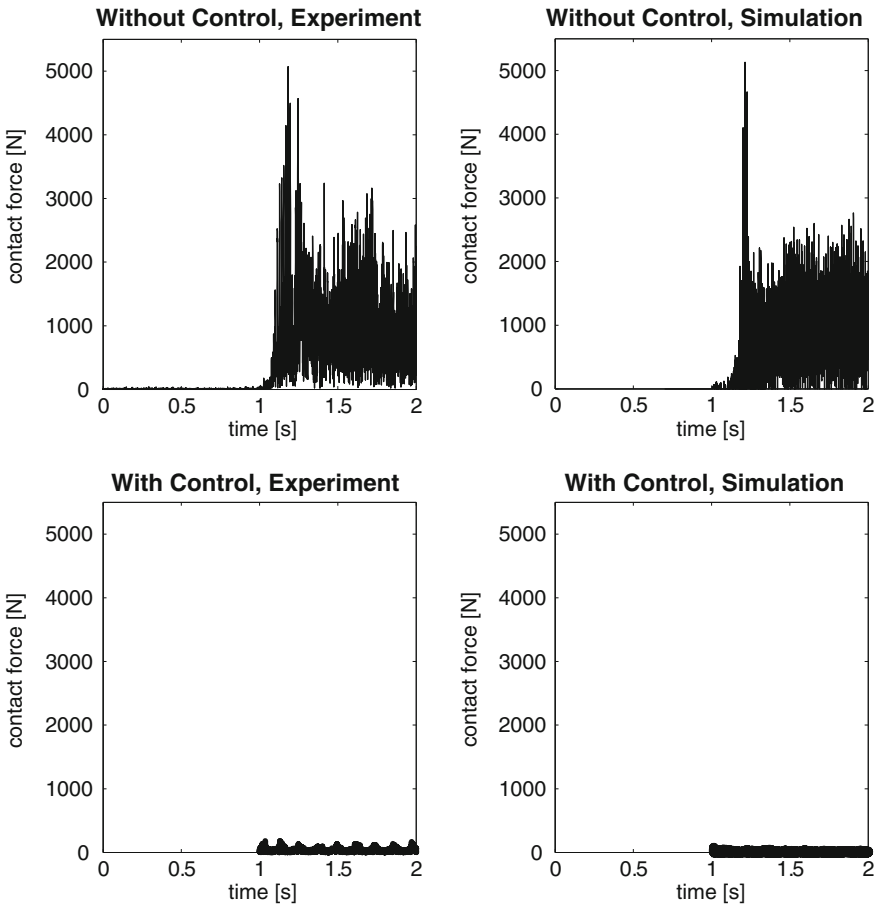

Fig. 6 Contact force: The rotor runs at a constant speed of 500 rpm, at $t = 1.0$ s there is a sudden arising unbalance

needs about 10 min for computation. By using the control system a rubbing state of synchronous full annular rub with very low contact forces (below 200 N) are assured. Also in this case the simulation shows a very good agreement. The oscillation of the contact force of the experiment is caused by measurement errors, which are not covered by the simulation. As a result the plot of the simulation is smoother than the experimental measurement. In Fig. 7 the rotor orbit of each discussed experiment is plotted. Also regarding the orbit plots, there is a very good agreement between experiment and simulation in case of “without control" as well as in case of “with control".

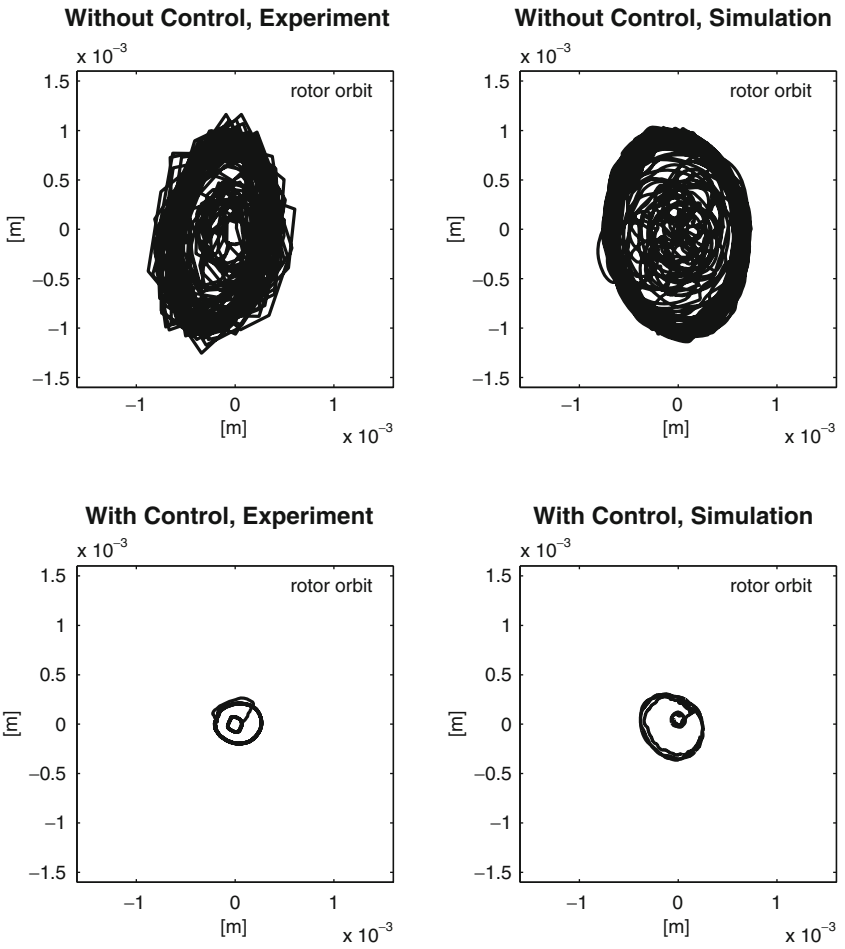

Fig. 7 Rotor orbit: The rotor runs at a constant speed of 500 rpm, at $t = 1.0$ s there is a sudden arising unbalance

9 Conclusions

The developed simulation environment has been successfully verified using experimental results. The environment is based on a framework for the efficient simulation of multibody systems with unilateral contacts and elastic elements. The simulation may comprise the modeling of a 3D flexible rotor, unilateral contacts with and without friction between the rotor and stationary parts and an interface to Matlab/Simulink to co-simulate the feedback control of active elements. The fundamentals of unilateral constraints allow a detailed simulation of processes like contact /detachment, stick/slip or impacts with and without friction. The presented experimental results and simulations deal with rotor rubbing controlled by

an active auxiliary bearing. The simulation shows an excellent agreement with the experimental results and works very efficient. One simulation run needs about 10 min on a typical “dual core" personal computer.

References

1. Brogliato, B., Ten Dam, A.A., Paoli, L., Génot, F., Abadie, M.: Numerical simulation of finite dimensional multibody nonsmooth mechanical systems. ASME Appl. Mech. Rev. **55**, 107 (2002)
2. Ehehalt, U.: Bewegungsformen elastischer rotoren bei statorkontakt. Dissertation, Technische Universität Darmstadt (2007). Fortschr.-Ber. VDI Reihe 11 Nr. 335. Düsseldorf: VDI Verlag 2008
3. Förg, M., Zander, R., Ulbrich, H.: A framework for the efficient simulation of spatial contact problems. In: Proceedings of the ECCOMAS Conference on Multi-Body Systems. Milano, Italy (2007)
4. Ginzinger, L., Ulbrich, H.: Parameter study of rotor rubbing control with an active auxiliary bearing. In: The 12th International Symposium on Transport Phenomena and Dynamics of Rotating Machinery, February 17–22. Honolulu HI, USA (2008)
5. Studer, C.: Augmented time-stepping integration of non-smooth dynamical systems. In: ETH E-Collection (2008)
6. Zander, R., Schindler, T., Friedrich, M., Huber, R., Förg, M., Ulbrich, H.: Non-smooth dynamics in academia and industry: recent work at tu münchen. Acta Mech **195**(1–4), 167–183 (2008)

New Passive Control Methods for Reducing Vibrations of Rotors: Discontinuous Spring Characteristics and Ball Balancers

Yukio Ishida

Abstract This paper introduces a new passive vibration suppression method called the discontinuous spring characteristics and provides a methods to improve the efficiency of automatic ball balancers. The former method can be used to suppress the amplitude at a resonance and also be applied to suppress unstable oscillations of an asymmetrical shaft and a rotor partially filled with liquid. An automatic ball balancer can suppress vibrations above the major critical speed theoretically. However, the friction reduces the effect of this balancer. This paper introduces a very simple method to eliminate the influence of the friction. Finally, the simultaneous use of these two methods is recommended.

Keywords Vibration suppression · Resonance · Unstable oscillation · Nonlinear vibration · Discontinuous spring characteristics · Rotor with liquid · Ball balancer

1 Introduction

So far, various kinds of passive and active vibration suppression methods have been proposed in rotor systems. For example, Tallian and Gustafsson [1] supported bearings by leaf springs which has large damping. Kirk and Gunter [2] and Ota and Kanbe [3] applied the dynamic vibration absorber theory. In practice, tilting pad bearings, squeeze-film damper bearings, and seals are widely used to suppress rotor vibrations [4].

This section introduces a very simple and effective method which utilizes the discontinuous spring characteristics and the ball balancer simultaneously.

Y. Ishida (✉)
Department of Mechanical Science and Engineering, Nagoya University, Furo-cho, Chikusa-ku, Nagoya 464-8603, Japan
e-mail: ishida@nuem.nagoya-u.ac.jp

K. Gupta (ed.), *IUTAM Symposium on Emerging Trends in Rotor Dynamics*,
IUTAM Bookseries 25, DOI 10.1007/978-94-007-0020-8_33,

2 Discontinuous Spring Characteristics [5]

2.1 Theoretical Model

Figure 1a shows the theoretical model. The rectangular coordinate system $O - xyz$ is considered. Let the geometrical center of the disk be M(x, y), the angular velocity be ω, the unbalance be e, the damping coefficient be c_1, the spring constant of the shaft be k_1, and t be time. The disk is covered by a casing which does not rotate. The total mass of the disk and the casing is m. The casing is surrounded by a ring with clearance δ and this ring is supported by springs with spring constant k_2 and dampers with damping coefficient c_2 in the x- and y-directions. The casing, the ring, the stoppers, the springs k_2 and the damper c_2 make up a vibration suppression devise. The corresponding experimental set-up is shown in Fig. 1b where the outer ring of the bearing corresponds to the casing and the leaf spring corresponds to the spring k_2 and the damper c_2. The dry friction between the leaves gives comparatively large damping. Pins set on the plates work as stoppers.

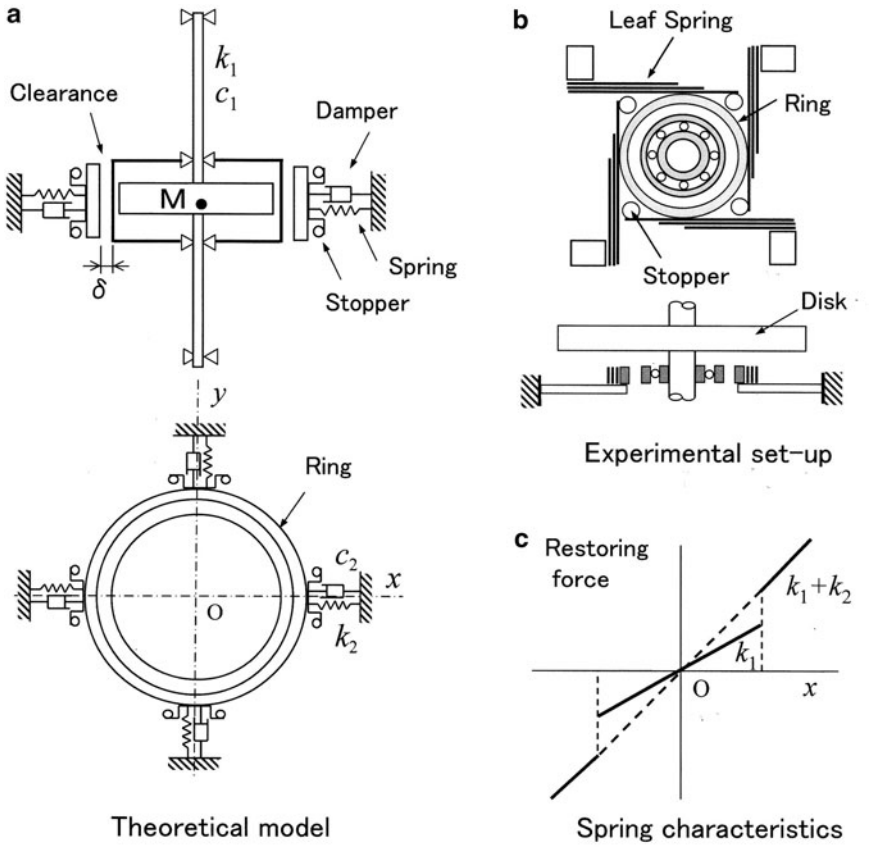

Fig. 1 System with the discontinuous spring characteristics

2.2 Discontinuous Spring Characteristics

In Fig. 1a, the springs are installed with preload by making initial shrinkage δ. These springs can shrink further but cannot elongate due to the stoppers. As a result, we get the discontinuous spring characteristics shown in Fig. 1c. The spring constant depends on the radial deflection $r\left(=\sqrt{x^2+y^2}\right)$ of the rotor. The spring forces $(F_{2x},\ F_{2y})$ due to springs and the damping forces $(D_{2x},\ D_{2y})$ due to dampers in the suppression device are represented by

$$\left.\begin{array}{ll} F_{2x}=-k_2x, \quad F_{2y}=-k_2y, \quad D_{2x}=-c_2\dot{x}, \quad D_{2y}=-c_2\dot{y} & (r>\delta) \\ F_{2x}=F_{2y}=D_{2x}=D_{2y}=0 & (r\le\delta) \end{array}\right\} \tag{1}$$

3 Suppression of the Steady State Resonance of a Symmetrical Rotor by the Discontinuous Spring Characteristics [5]

3.1 Equations of Motion

When $r<\delta$, the equations of motion are written as follows.

$$\left.\begin{array}{l} \ddot{x}+c_1\dot{x}+x=e\omega^2\cos\omega t \\ \ddot{y}+c_1\dot{y}+y=e\omega^2\sin\omega t \end{array}\right\} \tag{2}$$

When $r\ge\delta$, the equations of motions are given as follows.

$$\left.\begin{array}{l} \ddot{x}+c_1\dot{x}+x=e\omega^2\cos\omega t+F_{2x}+D_{2x} \\ \ddot{y}+c_1\dot{y}+y=e\omega^2\sin\psi+F_{2y}+D_{2\dot{y}} \end{array}\right\} \tag{3}$$

The harmonic solution is given as follows:

$$x=R\cos(\omega t+\beta), \qquad y=R\sin(\omega t+\beta) \tag{4}$$

3.2 Principle of Vibration Suppression and Numerical Simulation

The resonance curves are shown in Fig. 2. This system can be divided into two subsystems: System 1 for $r\le\delta$ and System 2 for $r\ge\delta$. System 1 resonates at $\sqrt{k_1/m}=1$ and System 2 resonates at $\sqrt{(k_1+k_2)/m}$. The system with the characteristics of Fig. 1c has resonance curves designated by solid lines. A corresponding result of numerical simulations for clearance $\delta=0.07$ and a comparatively large damping c_2 is shown in Fig. 3. In the range BE, the amplitude increases in System 1 and decreases in System 2, as a result, rotor whirls with the amplitude of about δ.

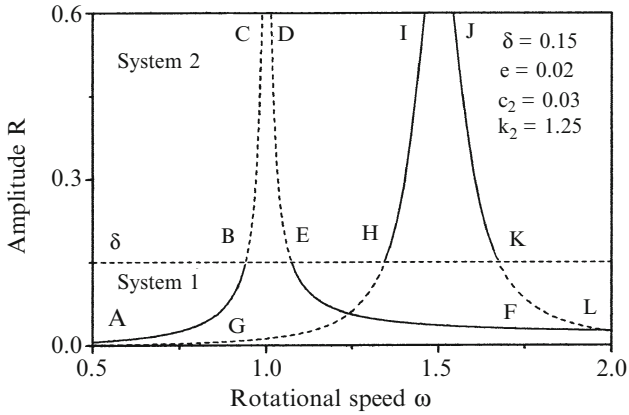

Fig. 2 Principle of suppression

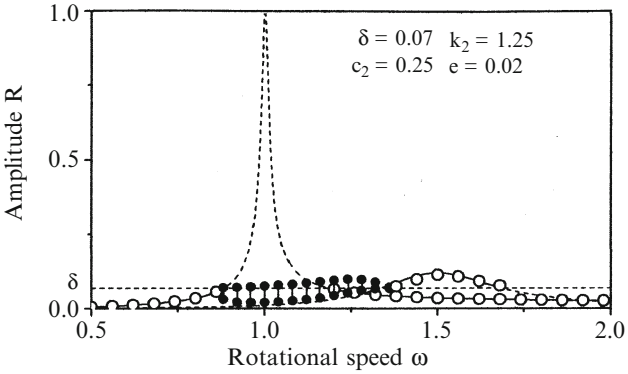

Fig. 3 Numerical simulation

We call this whirling motion an almost periodic motion, here. When the rotational speed increases, this almost periodic motion still appears in the range EH without following the curve EF. But this motion can be eliminated by making the spring constants in the suppression device unequal. By increasing the damping coefficient c_2 further, the peak of the higher side in System 2 can be made smaller than the clearance δ.

3.3 Experimental Set-up and Results

In the experimental setup, a disk is mounted on an overhung elastic shaft which is supported by two bearings at the upper end. The length and the diameter of shaft are 700 mm and 12 mm, respectively. The diameter and the thickness of the disk are

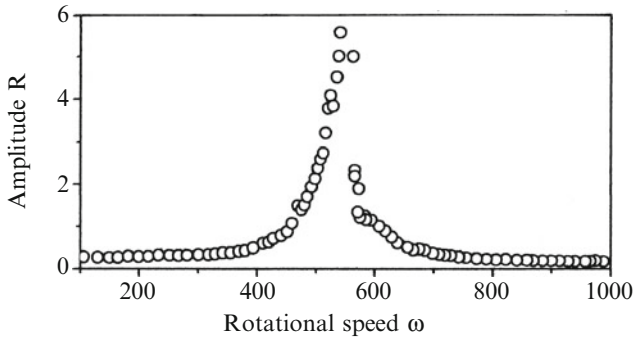

Fig. 4 Original system (experiment)

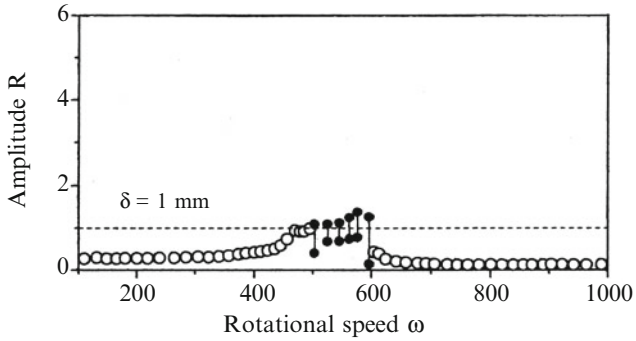

Fig. 5 System with a suppression device (experiment)

260 mm and 10 mm, respectively. The disk is mounted at about 60 mm upward from the shaft end and a suppression device is mounted under the disk. The clearance in the suppression device is $\delta = 1$ mm.

Figure 4 shows resonance curves of the original system. Figure 5 shows those of the system with a suppression device with unequal stiffness $k_{2x} \neq k_{2y}$. The peak amplitude was suppressed to about 1mm corresponding to the clearance.

4 Elimination of an Unstable Range of an Asymmetrical Shaft Utilizing Discontinuous Spring Characteristics [6]

4.1 Theoretical Model and Equations of Motion

The model is shown in Fig. 6. This system is obtained by replacing the shaft in Fig. 1 to an asymmetrical shaft which has directional difference in stiffness Δk. The equations of motion are given as below using $\Delta = \Delta k / k$.

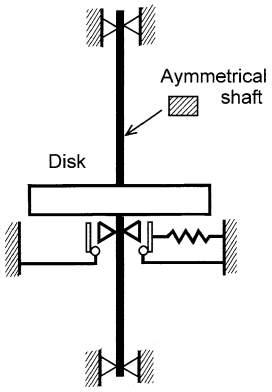

Fig. 6 Model of an asymmetrical rotor

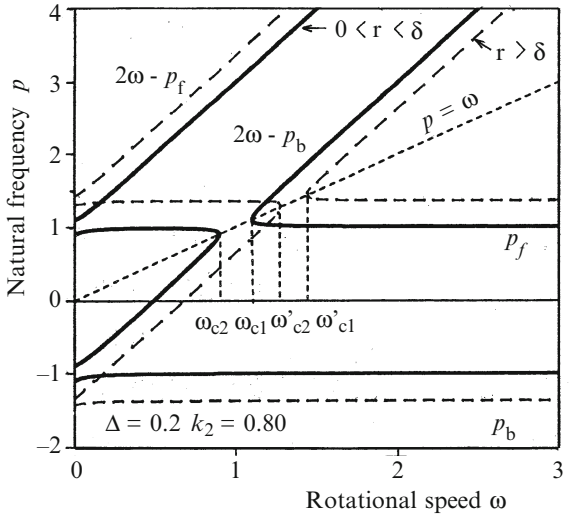

Fig. 7 Natural frequency diagram

$$\left.\begin{aligned} \ddot{x} + c\dot{x} + x - \Delta(x\cos 2\omega t + y\sin 2\omega t) &= e\omega^2\cos\omega t + F_{2x} + D_{2x} \\ \ddot{y} + c\dot{y} + y - \Delta(x\sin 2\omega t - y\cos 2\omega t) &= e\omega^2\sin\omega t + F_{2y} + D_{2y} \end{aligned}\right\} \tag{5}$$

4.2 Natural Frequency

The frequency equation of this asymmetrical shaft system is given by

$$(1 + k_2 - p^2)\{1 + k_2 - (2\omega - p)^2\} - \Delta^2 = 0 \tag{6}$$

Natural frequency diagram is shown in Fig. 7. The solid line curves represent natural frequencies of System 1 and the broken lines represent those of System 2. In the case of System 1, unstable vibrations occur in the range between ω_{c2} and ω_{c1}. In the case

of System 2, unstable range occurs between ω'_{c2} and ω'_{c1} which is higher enough not to overlap to the unstable range of System 1.

4.3 Numerical Simulation

Figure 8 shows a case that the suppression device has a comparatively small damping coefficient c_2. The theoretical resonance curves and the unstable ranges of System 1 and System 2 are also illustrated. In this case, the amplitude increases exponentially when the almost periodic motion enters into the unstable range of System 2. This unstable range can be eliminated by giving comparatively large damping c_2 as shown in Fig. 9. The unstable range in System 2 disappeared. The almost periodic motion changes to a steady-state oscillation at about $\omega = 1.7$ when the rotational speed increase.

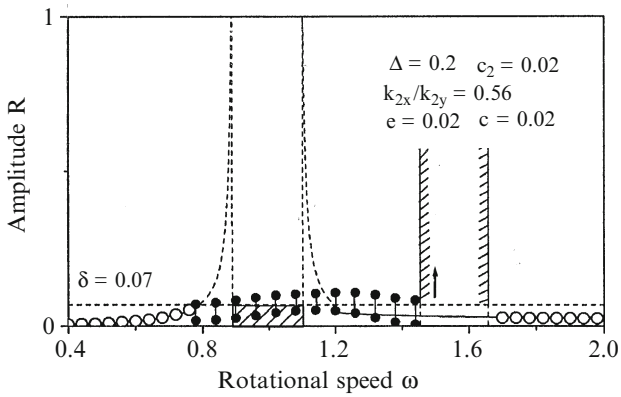

Fig. 8 Response curve (c_2: small)

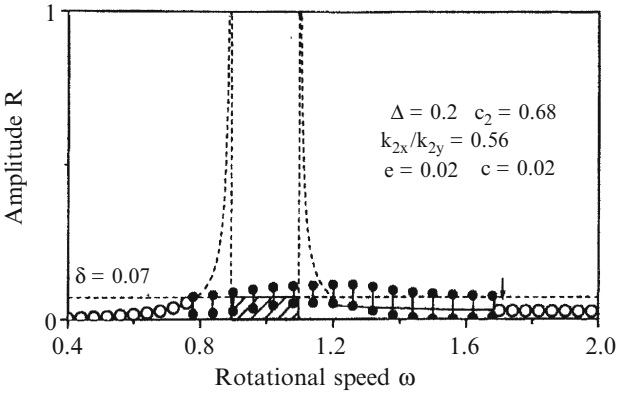

Fig. 9 Response curve (c_2: large)

4.4 Experimental Set-up and Results

In the experimental setup, the disk is mounted at the middle of the vertical shaft. The diameter and the thickness of the disk are 260 mm and 10 mm, respectively. The suppression device was installed a little lower than the disk. The shaft is 700 mm in length and 12 mm in diameter. This asymmetry was made by cutting parallely both sides of the shaft, and the thickness of this part is 9 mm. The clearance δ in the suppression device is 1 mm.

Figure 10 shows resonance curves of the original system without the vibration suppression devise. The unstable range appeared between $\omega = 671 \sim 750$ rpm. Figure 11 shows the case with a vibration suppression device. The unstable range disappeared and the amplitude was limited at about 1 mm.

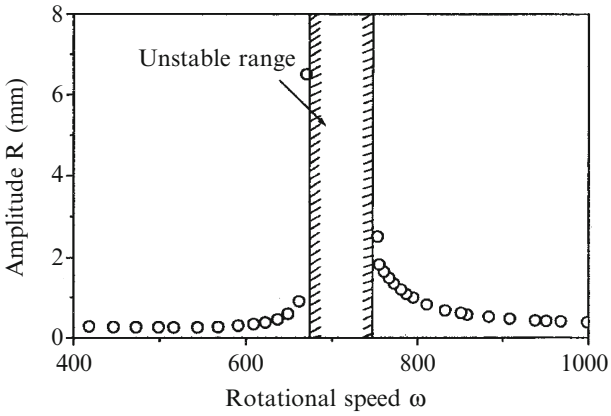

Fig. 10 Original asymmetrical shaft

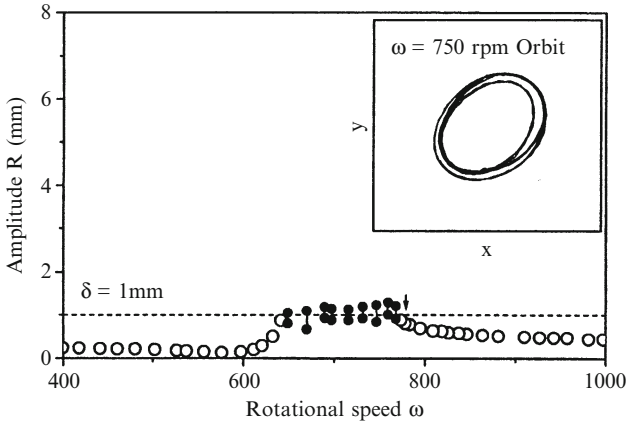

Fig. 11 System with a device

5 Elimination of an Unstable Range of a Hollow Rotor Partially Filled with Liquid Utilizing Discontinuous Spring Characteristics [6]

5.1 Theoretical Model and Natural Frequency

The theoretical model is shown in Fig. 12. The disc has a cavity partially filled with liquid. The vibration suppression device is installed just under the disk. It is assumed that the rotor rotating with the angular velocity ω is whirling with the angular velocity p. Let the inner radius of the hollow rotor be a, the inner radius of the liquid free surface when the liquid is distributed uniformly be b, the inner height of the rotor be h, and the density of liquid be ρ. The liquid applies pressure on the inside wall due to the centrifugal force. Wolf [7] derived the following expression of the resultant liquid force F_L.

$$F_L = \varepsilon \Omega^2 m_{Lf} \frac{(\sigma^2 - 2\sigma\omega - \omega^2)}{(\alpha\sigma^2 - 2\sigma\omega - \omega^2)} \tag{7}$$

where $\alpha = \{(a/b)^2 + 1\}/\{(a/b)^2 - 1\}$, $m_{Lf} = \rho\pi a^2 h$.

When the rotor whirls with a constant radius r, the restoring force $(k + k_2)r$, the centrifugal force mrp^2 and the fluid force F_L balance. Then, we have

$$k_2 + 1 = p^2 + p^2 \mu \frac{(\sigma^2 - 2\sigma\omega - \omega^2)}{(\alpha\sigma^2 - 2\sigma\omega - \omega^2)} \tag{8}$$

where $\mu = m_{Lf}/m$. When the casing does not contact with the ring of the suppression device ($k_2 = 0$), the natural frequency diagram is shown in Fig. 13. Point A represents the major critical speed. Two roots of Eq. (7) become imaginary in the range BB ($\omega \approx 1.33$–1.7) and unstable vibrations occur. When the shaft deflection becomes larger than the clearance and the suppression device works, the unstable range shifts to the higher side ($\omega \approx 1.92$–2.7).

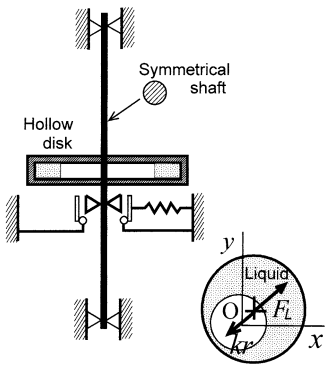

Fig. 12 Model of a rotor with liquid

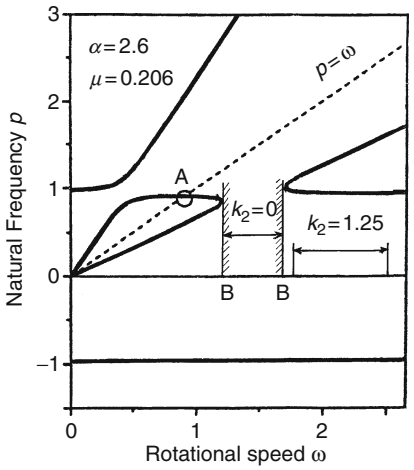

Fig. 13 Natural frequency diagram

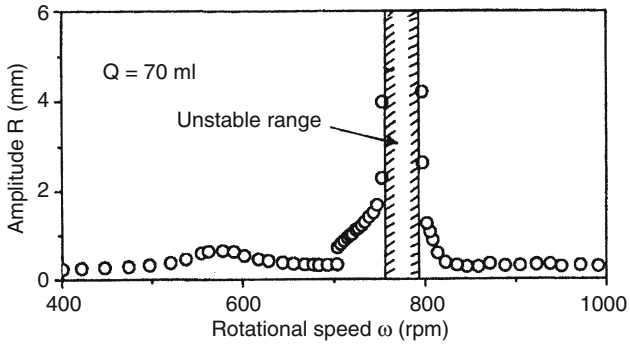

Fig. 14 Response with no device (experiment)

5.2 Experimental Set-up and Experimental Results

In the experimental setup, a hollow disk is mounted at the middle of the vertical shaft. The shaft with a circular cross section is 700 mm in length and 12 mm in diameter. The outer and inner diameters and the outer and inner thickness of the disk are 300 mm, 230 mm, 20 mm, and 10 mm, respectively. The clearance in the suppression device is 1 mm.

In the original system where the disk contained 70 ml liquid, the resonance curve shown in Fig. 14 was obtained. The major critical speed was 570 rpm and unstable vibrations appeared in the range $\omega = 750$–797 rpm. When the suppression device is installed, the resonance curve shown in Fig. 15 was obtained. The unstable vibrations changed to almost periodic motions with the amplitude of about 1 mm.

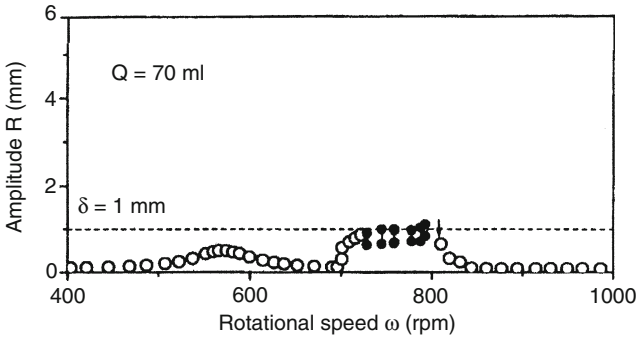

Fig. 15 Response with a device (experiment)

6 Elimination of the Effect of Friction and the Self-Excited Oscillation in a Ball Balancer [8]

In 1932, Thearle [9] invented an automatic ball balancer which balance the rotor automatically in the post-critical speed range. Inoue et al. [10, 11] studied the dynamic behavior of ball balancers extensively. However, due to the inevitable friction between the balls and the inside wall, the balls can not locate at the optimal positions and the perfect balancing is not attained [12]. In addition, a self-excited oscillation where balls rotate in the rotor occurs near the critical speed. This section introduces a simple counter measure to eliminate the effect of friction and that to suppress self-excited oscillations.

6.1 Theoretical Analysis with No Friction

Figure 16 shows the theoretical model of a ball balancer. A disk has a cavity (channel) and two balls are contained. The friction is ignored. Theoretical resonance curves and the results of numerical simulations are shown in Fig. 17. The solid lines represent stable solutions and broken lines represent unstable solutions. Open circles represent steady-state solutions obtained by numerical simulations. In the pre-critical speed range, the two balls gather in the same direction as the unbalance and the amplitude increases. In the post-critical speed range, the balls locate with the optimal angle in the opposite side to the unbalance and the unbalance is canceled completely. In the neighborhood of the resonance, balls whirl in the cavity and, as a result, the amplitude varies as shown by the time history. The maximum and minimum amplitudes are shown by dots at both ends of the straight lines.

Fig. 16 Model

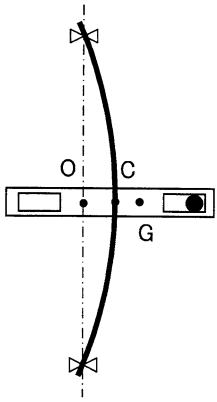

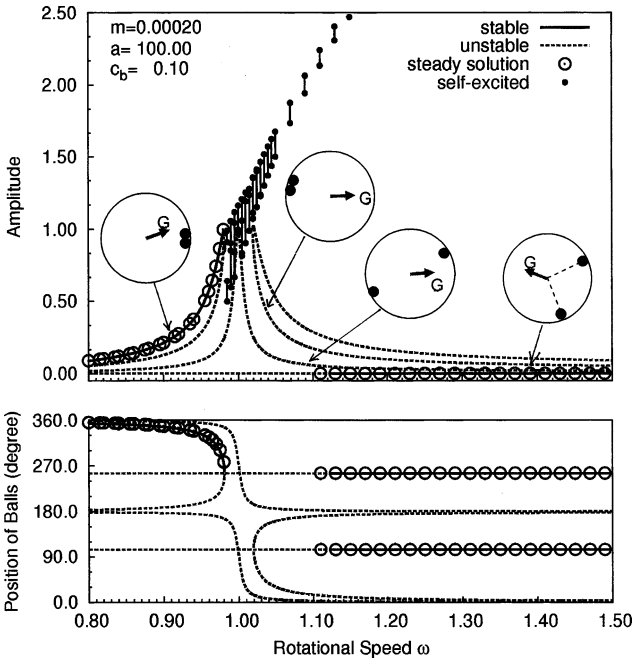

Fig. 17 Response curve (no friction)

6.2 Experimental Set-up and Experimental Results

Experimental setup is the same type as the Jeffcott rotor. The shaft is 700 mm in length and 12 mm in diameter. The disk is 260 mm in diameter and 30 mm in thick ness. This disk is made of stainless steel. Two balls are installed in a circular channel grooved in the disk.

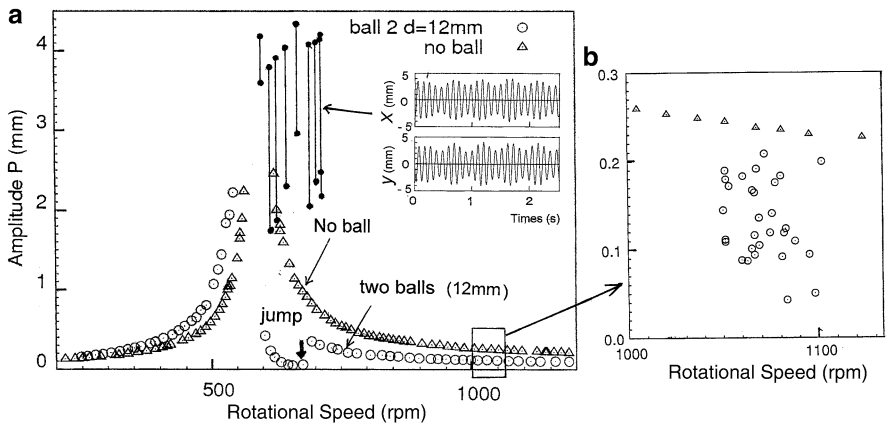

Fig. 18 Response curve (experiments). **(a)** Overall response. **(b)** Thirty times trial

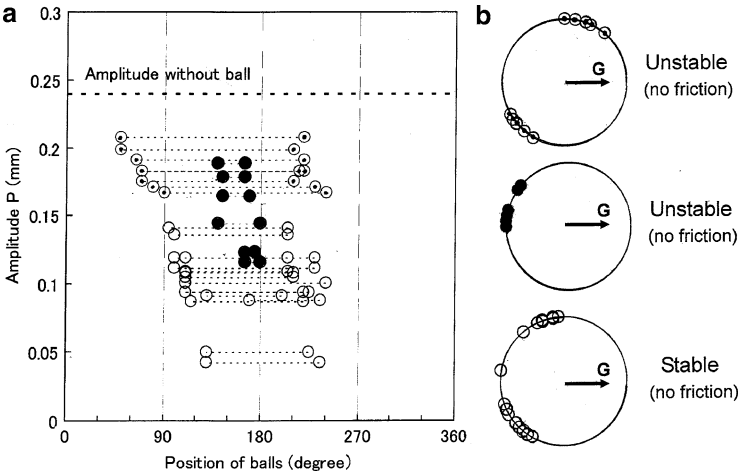

Fig. 19 Summary of 30 times experiments at about 1,100 rpm. **(a)** Angular positions and amplitudes. **(b)** Angular positions

Experimental results with two balls of 12 mm in diameter are shown in Figs. 18 and 19. The triangles show the response of the original system and open circles show that of a system with balls. We see that the amplitude does not become zero even if a ball balancer is used. When the rotational speed is decreased, the amplitude jumped to a small one at about $\omega \approx 680$ rpm. Since the force working to the balls to move to the optimal positions is proportional to the rotor deflection, the balls rolled from the stick condition. This jump phenomenon proves that the friction is caused by the initial rolling friction. Furthermore, self-excited oscillations are observed in the neighborhood of the resonance.

Figure 18b shows a result of 30 trials. Since balls stick around the optimal positions due to friction, various amplitudes are obtained. Figure 19a shows the relationship between ball positions and amplitudes. Figure 19b shows angular positions of the two balls. According to the observations, these positions can be classified into three types. One corresponds to the sable solution and the others correspond unstable solutions in Fig. 17 in the case of no friction.

6.3 Elimination of the Effect of Friction and Self-excited Oscillation

Horvath et al. [13] show that the effect of friction is small in an automatic pendulum balancer. In this section, a more simple method is introduced. The probability of occurrence of Fig. 18b can be expressed by a bar graph in Fig. 20. This is a result for balls of 15 mm in diameter. If several couples of balls are used, each couple

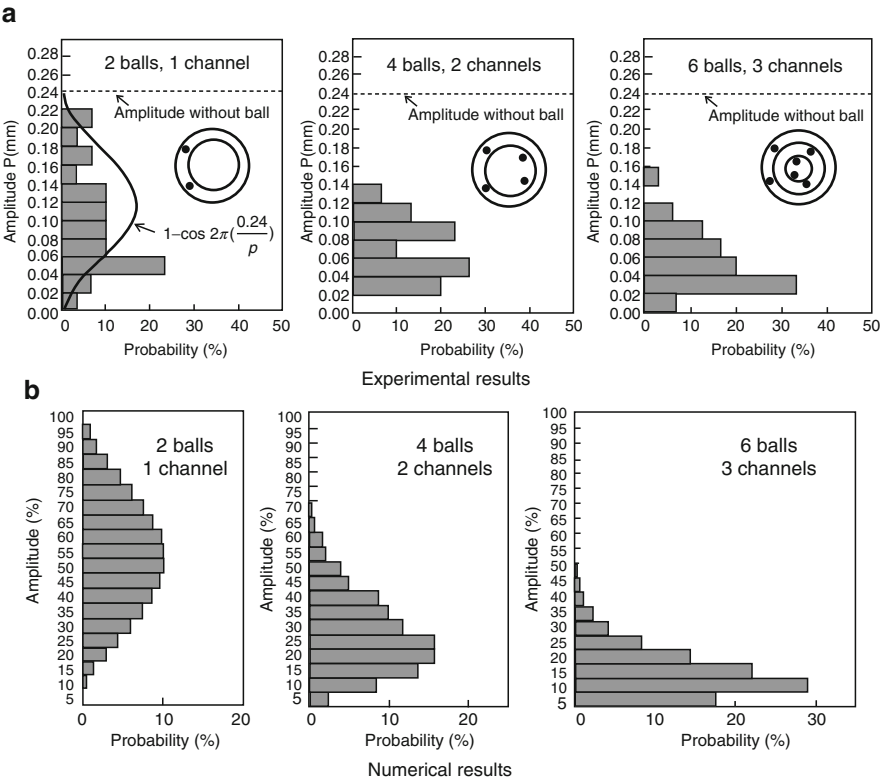

Fig. 20 Comparison of probability among one, two and three channels. **(a)** Experimental results. **(b)** Numerical results

will stop one by one. Figure 20a shows experimental results for one (2 balls), two (4 balls), and three (6 balls) channels, respectively. Let us approximate the distribution of the left one by a cosine function Then, the probability distribution will be given by Fig. 20b. This figure shows that the efficiency of balancing improves by increasing the channel number. Figure 21 is the typical resonance curve which was mostly observed when three channels were used Self-excited oscillations can be easily eliminated by making partitions in the channels. Figure 22 shows the probability distribution in case with partitions and with three channels.

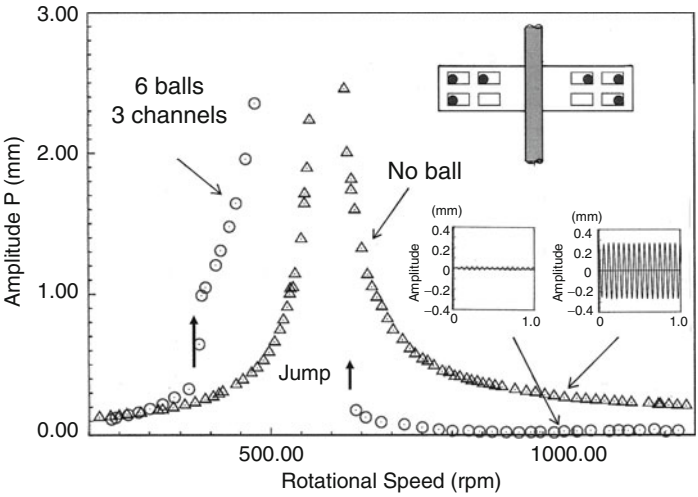

Fig. 21 Results with three channels balancer

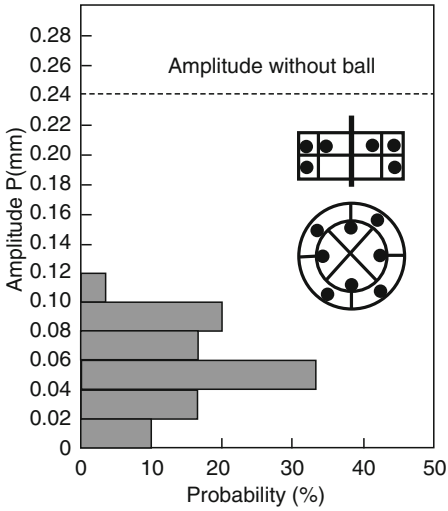

Fig. 22 Ball balancer with partitions

7 Conclusion: Combination of Discontinuous Spring Characteristics and a Ball Balancer

The most recommended vibration suppression method is the usage of the discontinuous spring characteristics and a ball balancer simultaneously. Figure 23 shows an experimental result for such a case [14]. Resonance peak was suppressed to about 1 mm. The response in post-critical range was suppressed enough. (Figure 23 shows a result for one channel. At the time when this result was obtained, the effect of friction and its countermeasure were not known.)

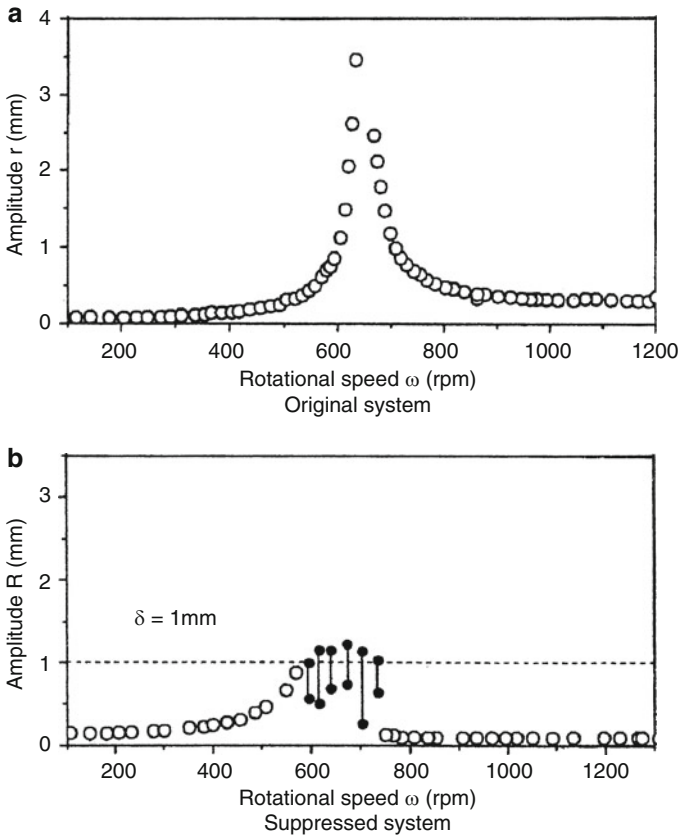

Fig. 23 Case with a discontinuous spring characteristics and a ball balancer. **(a)** Original system. **(b)** Suppressed system

References

1. Tallian, T.E., Gustafsson, O.G.: Progress in rolling bearing vibration research and control. ASLE Trans. **8**(3), 195–207 (1965)
2. Kirk, R.G., Gunter, E.J.: The effect of support flexibility and damping on the synchronous response of a single-mass flexible rotor. Trans. ASME, J. Eng. Ind., Ser. B **94**(3), 221–232 (1972)
3. Ota, H., Kanbe, Y.: Effects of flexible mounting and damping on the synchronous response of a rotor-shaft system. Trans. ASME, J. Appl. Mech., Ser. E **98**(1), 144–149 (1976)
4. Ehrich, F.: Handbook of Rotordynamics, Chapter 1. McGraw-Hill, Inc. (1992)
5. Ishida, Y., Liu, J.: Vibration suppression of rotating machinery utilizing discontinuous spring characteristics (stationary and nonstationary vibrations). Trans. ASME, J. Vib. Acoust. **130**(3), 031001-1–131001-7 (2008)
6. Ishida, Y., Liu, J.: Elimination of unstable ranges in rotating machinery utilizing discontinuous spring characteristics: An Asymmetrical Shaft System, an Asymmetrical Rotor System, and a Rotor System With Liquid. Trans. ASME, J. Vib. Acoust. **132**(1), 011011 (2010)
7. Wolf, J.A., Jr.: Whirl dynamics of a rotor partially filled with liquid. Trans. ASME, J. Appl. Mech., Ser. E **35**(4), 676–682 (1968)
8. Ishida, Y., et al.: Efficiency improvement of a ball balancer for friction and self-excited oscillations. Trans. ASME, J. Vib. Acoust., Submitted
9. Thearle, E.L.: A new type of dynamic-balancing machine. Trans. ASME, J. Appl. Mech. **54**(12), 131–141 (1932)
10. Inoue, J., et al.: Dynamic behavior of automatic ball balancer. In: Proceedings of the 8th International Conference on Nonlinear Oscillations, pp. 361–366 (1978)
11. Inoue, J., et al.: Dynamic behavior of a new type of automatic balancer. In: Proceedings of the 9th International Conference on Nonlinear Oscillations, vol. 3, pp. 116–120 (1984)
12. Yang, Q., et al.: Study on the Influence of friction in an automatic ball balancing system. J. Sound Vib. **285**, 3–99 (2005)
13. Horvath, R., Flowers, G.T., Fausz, J.: Passive balancing of rotor systems using pendulum balancers. Trans. ASME, J. Vib. Acoust. **130**(4), 041011-1–041011-11 (2009)
14. Liu, J., Ishida, Y.: Vibration suppression of rotating machinery utilizing an automatic ball balancer and discontinuous spring characteristics. Trans. ASME, J. Vib. Acoust. **131**(4), 041004-1–041004-7 (2009)

Modeling and Diagnostics of Heavy Impeller Gyroscopic Rotor with Tilting Pad Journal Bearings

V. Barzdaitis, M. Bogdevičius, R. Didžiokas, and M. Vasylius

Abstract The work presents the study of dynamics of heavy impeller rotor and failure diagnostics of tilting-pad journal bearings. The started rubbing process in the bearings at resonance and increased rubbing phenomenon in both bearings by measurement of radial gaps, were identified experimentally in situ. The rotational speed was established when gravitational force became dominant compared to rotor gyroscopic force. Rotating system model was designed, simulated and verified.

Keywords Gyroscopic rotor · Tilting-pad journal bearings · Vibration · Diagnostic

1 Introduction

The stationary condition monitoring, safety and diagnostic systems are mainly applied to critical, expensive machines, and are based on vibration and technological parameters of measurements [1–3]. The high efficiency air blower machine is operating in continuous long running mode term. The vibration source of the machine's induction electric motor housings of journal bearings were identified and eliminated by increasing the stiffness of inductor and journal bearings [1]. The technical condition and failures of the radial hydrodynamic tilting-pad journal bearings of the blower rotor are monitored, experimentally tested, modeled and analysis results are implemented in industry [4]. In this article the details of this study are presented.

V. Barzdaitis (✉)
Kaunas University of Technology, Department of Engineering Mechanics,
Donelaičio St. 73, Kaunas LT-44244, Lithuania
e-mail: vytautas.barzdaitis@ktu.lt

M. Bogdevičius
Vilnius Gediminas Technical University, Department of Transport Technological Equipment,
Plytines St. 27 LT-10105, Vilnius, Lithuania

R. Didžiokas and M. Vasylius
Klaipėda University, Mechatronic Science Institute,
Bijūnų St. 17, Klaipėda LT-91225, Lithuania

K. Gupta (ed.), *IUTAM Symposium on Emerging Trends in Rotor Dynamics*,
IUTAM Bookseries 25, DOI 10.1007/978-94-007-0020-8_34,

Nomenclature

Names	Description	Names	Description
$\{q\}$	The nodal element displacement vector	pol	Number of EM pole
$[N]$, $[N_\theta]$	The matrices of shape functions	M_e	Torque of EM
$\left\{\dot{\theta}\right\}$, $\{\omega\}$	Angular velocity	$[M\,(q)]$	Mass matrix
$\{\psi\}$, $\{\dot{\psi}\}$	Flux space vector and time derivative	$[C]$, $[G]$, $[K]$	Damping, gyroscopic, stiffness matrices
I_e	Inertia mass moment of rotor	$\varphi_{i\,\min}$, $\varphi_{i\,\max}$	Position of ith segment
$\left[A_\psi\right]$	Matrix of resistors and inductive reactance of stator and rotor	$\{F\,(q, \dot{q}, \Psi)\}$	The load vector of the finite element
$\left\{B_\psi\,(t, \psi, \dot{\varphi}_e)\right\}$	Vector of nonlinear functions	ψ	Angle of rotor centre
φ_e	Angle of rotor	ε	Eccentricity ratio
$M_e\,(\psi)$	Electrical torque	e	Radius of rotor geometrical displacement
$M_r\,(\varphi_i, \dot{\varphi}_i, p_{Gi})$	Resistance torque	Δ	Radial clearance
r_s, r_r	Resistor of stator and rotor	F_{Ni}, F_{Ti}	The normal and tangential forces
L_r, L_s, L_μ	Inductive reactance of stator and rotor	h	Parameter of tilting-pad bearing
L_0	Inductive resistor of magnetization contour	φ_{ci}	Angle of centre of ith segment
w_s	Angular velocity of voltage	F_{br}	Hydrodynamic force

2 Air Blower Rotor BR Condition Monitoring and Diagnostics

The air blower machine comprises of an electric motor EM, and a double-helical gear multiplier GB which increases rotational speed of the blower rotor BR (Fig. 1). The 5.6 MW power EM has rotational speed of 1,500 rpm and BR nominal rotational speed is ~3,119 rpm.

The technical condition of BR was evaluated by monitoring rotor position in the bearings (gaps) and vibration displacement peak-to-peak values $s_{p\text{-}p7,8}$ were measured permanently with four proximity probes fixed at the 7th and 8th bearings and rotational speed with keyphasor transducer SP.

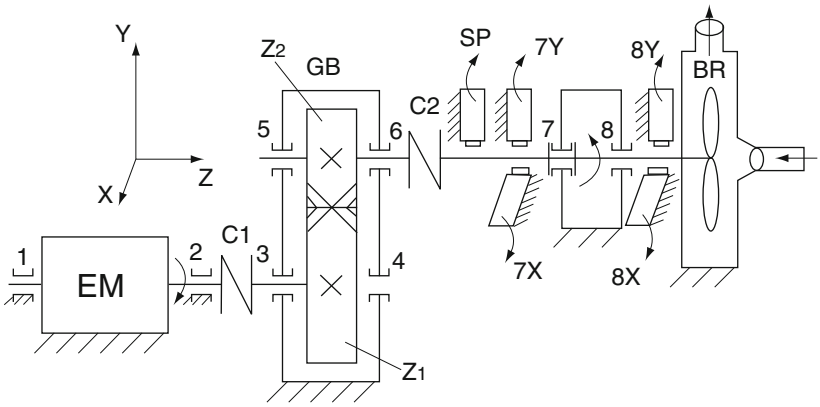

Fig. 1 The air blower machine scheme with proximity probes location: 1, 2 – journal bearings of EM; 3–6 – journal bearings of GB ($u = 0.477$, $z_2 = 43$, $z_1 = 90$); 7, 8 – tilting-pad journal bearings of BR; $C1$, $C2$ – flexible couplings; 7X, 7Y and 8X, 8Y – proximity probes fixed at the 7th and 8th bearings, SP – keyphasor transducer

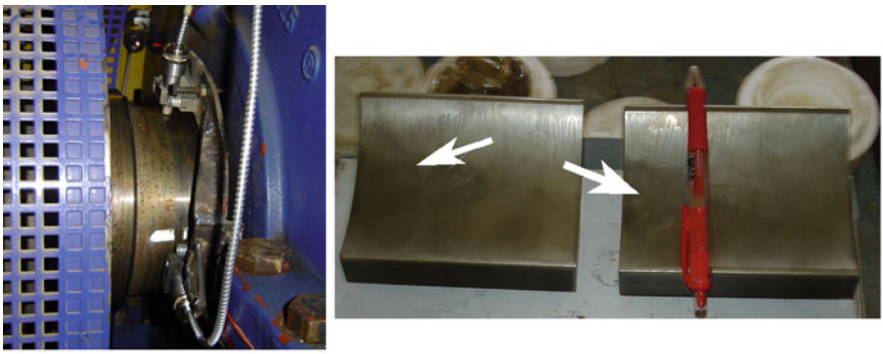

Fig. 2 The BR at 7th bearing vibration displacements peak-to-peak values $s_{p\text{-}p7X}$, $s_{p\text{-}p7Y}$ and gaps-radial clearances Δ7X, Δ7Y measurement set with two sensors 7X and 7Y and damaged pads

In this article the failures of the radial hydrodynamic tilting-pad journal bearings 7th and 8th of the blower rotor BR are monitored, experimentally tested in situ and modeled. The task is to determine the main reasons of the tilting-pad journal bearings 7th and 8th failure and to set up recommendations for increasing operation time of the bearings avoiding damages (Fig. 2).

Each tilting-pad bearing consists of four pads. The failure in 7th and 8th bearings pads led to additional testing during two years continuous operation after replacement of BR new bearings. The experimental testing of the blower rotor was based on rotor vibration measurement of displacements at 100%, 50% loading and at free run, coast down and run up including resonance rotational speed.

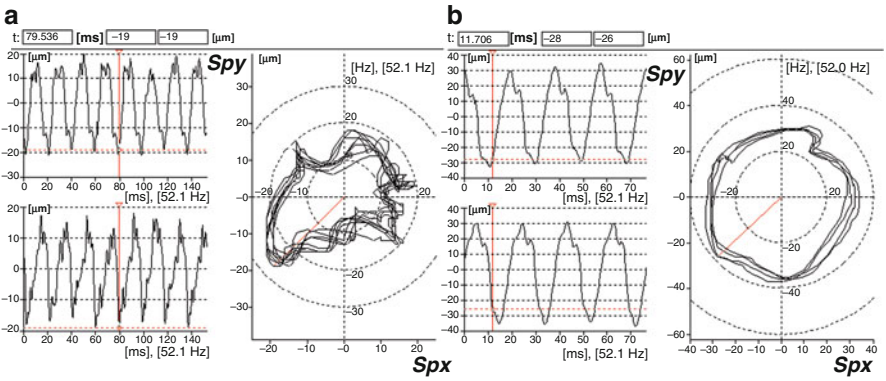

Fig. 3 BR bearings shaft displacement vibrations $s_{p\text{-}p\mathrm{X}}$, $s_{p\text{-}p\mathrm{Y}}$ plots versus time and shafts kinetic orbits: **(a)** 7th bearing at 100% load, $s_{\max 7} = 27\,\mu\mathrm{m}$; **(b)** 8th bearing at 100% load, $s_{\max 8} = 38\,\mu\mathrm{m}$

3 Vibration at Varying Loading

For the bearings of BR shaft, typical vibration displacement $s_{p\text{-}p\mathrm{X}}$, $s_{p\text{-}p\mathrm{Y}}$ plots versus time and shafts kinetic orbits are presented in Fig. 3. The intensity of vibration of 7th and 8th bearings is independent at different loading. The vibration displacement values of both bearings in X and Y directions were low and described by calculated maximum vibration displacements value $s_{\max}$ [ISO 7919-1:1996(E)]. The amplitudes of synchronous frequency vibration displacement are dominant in the spectra. The vibration of 8th bearing is ~30% higher compared with 7th bearing – the stiffness of BR at 7th bearing is higher than at 8th bearing.

4 Vibration Severity at Resonance

The coast down running after EM switch off till stand still takes long interval of time, 841 s in comparison with run up mode from stand still till nominal rotational speed, 30–31 s (Fig. 4).

After two years of continuous operation the BR dynamic stiffness decreases. The resonance frequencies decrease in comparison with new bearings case [4]. After one year of continuous operation resonance speed was 1,455 rpm, whereas after two years – it decreased up to 1,350 rpm. The maximum vibration displacements s_{max7} values of the 7th bearing became six times higher at the resonance (from 25 to 165 μm) and $\boldsymbol{s_{max8}}$ values of the 8th bearing became more than eight times higher at the resonance (from 37 to 307 μm) (Fig. 5). The maximum of vibration displacement peak-to-peak value $s_{p\text{-}pmax}$ during coast down at resonance rotational speed reached 350–420 μm. At run up mode the maximum vibration displacement peak-to-peak value $s_{p\text{-}pmax}$ at resonance, reached 100–120 μm. Vibration

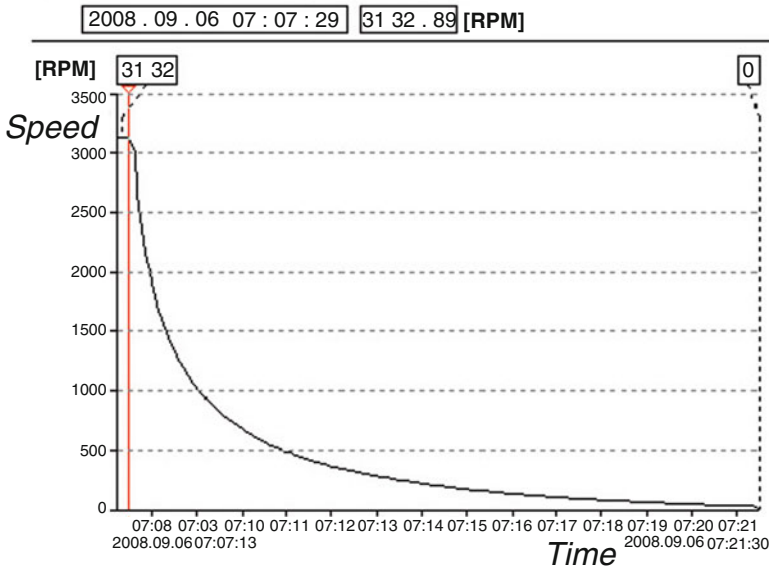

Fig. 4 The rotational speed timebase plot at coast down, time 841 s

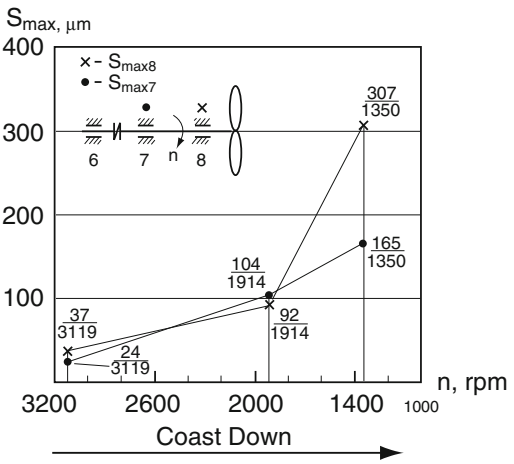

Fig. 5 Maximum vibration displacements $s_{max7,8}$ values of the 7th and 8th bearings shaft versus rotational speed at coast down

displacement was measured near resonance rotation speed at coast down and run up mode at 1,914 rpm rotation speed (31.9 Hz). It was found that 7th bearing's vibration displacement $s_{max\,7} = 104\,\mu m$ and 8th bearing's $s_{max\,8} = 92\,\mu m$.

The kinetic orbits are far from elliptical form (Fig. 6).The vibration severity at resonance rotation speed ~1,350 rpm (22.5 Hz) reduces the clearances between the rotors and bearings. The BR provides stationary part rubbing of the tilting pad bearing elements. The BR vibration is poliharmonic with high peak amplitudes that

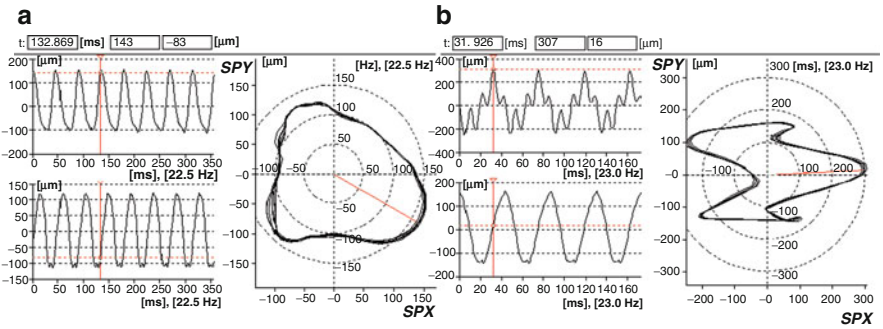

Fig. 6 The vibration displacement plots and kinetic orbits acquired at resonance rotational speed: **(a)** 7th bearing's $s_{max\,7rez} = 165\,\mu m$, $s_{p\text{-}p\,max\,7Xrez} = 240\,\mu m$, $s_{p\text{-}p\,max\,7Yrez} = 250\,\mu m$; **(b)** 8th bearing's $s_{max\,8rez} = 307\,\mu m$, $s_{p\text{-}p\,max\,8Xrez} = 300\,\mu m$, $s_{p\text{-}p\,max\,8Yrez} = 550\,\mu m$

caused rubbing at first at 8th bearing. The damages were checked at the upper pad of the 7th bearing and the lower pad of the 8th bearing (Fig. 2). These damaged pads are located in vertical plane in BR.

The first reason of damaged tilting-pad journal bearings is inadmissible vibration displacement values at 8th bearing $s_{p\text{-}p\,max\,8Yrez} = 550\,\mu m$. The vibration displacement signal at 7th bearing is lower $s_{p\text{-}p\,max\,7Yrez} = 250\,\mu m$, because the rotor part at 7th bearing is designed with higher stiffness in comparison with free end of the rotor at 8th bearing (Fig. 1). At run up the resonance phenomenon provide less vibration displacement amplitudes of the shafts in both bearings in comparison with coast down because run up time interval is comparatively short and dynamic forces have not enough time to rise up and generate high vibration amplitudes.

5 Shaft Displacements (Gaps) in the Bearings

The dynamic forces that damage bearings at rubbing – contact between the rotor and stationary tilting pads – depend not only on resonance phenomenon of rotating system but on the decreasing horizontal rotor gyroscopic effect when rotational speed is going down. The rotor shaft position in the 7th and 8th bearings is described by the gaps in horizontal X direction $\Delta 7X$, $\Delta 8X$ and gaps in vertical Y direction $\Delta 7Y$ (Fig. 7), $\Delta 8Y$. The gap value measured between tip of proximity probe and shaft cylindrical surface is described by DC signal from proximity probe output. This gap parameter evaluates gyroscopic effect of the rotor, when machine rotational speed decreases from nominal value till stand still.

At coast down from nominal rotational speed, the gaps $\Delta 7X$ and $\Delta 8X$ are of the same order ($+48\,\mu m, \ldots, +73\,\mu m$) and practically independent of rotational speed up to resonance (Table 1).

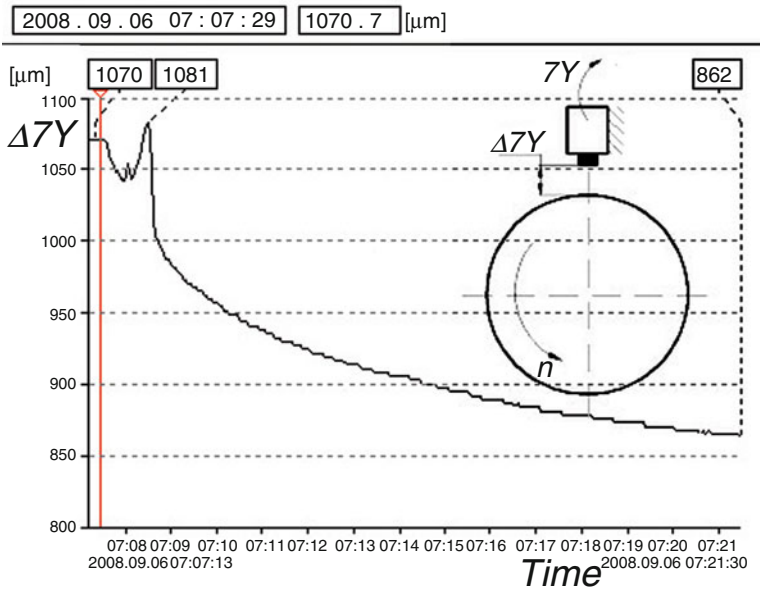

Fig. 7 The 7th bearing vertical direction gap Δ7Y plot versus time at coast down: nominal gap decreased −208 μm at 3,119 rpm; resonance gap −219 μm at 1,350 rpm and reference position 862 μm at stand still, at 0 rpm

Table 1 The radial gaps (μm) between tips of proximity probes and shaft cylindrical surface relative to reference point at stand still (0 rpm)

	Counterclockwise direction at coast down; rotational speed of BR (rpm)			
Gap, direction	3,132	1,914	1,350	Reference point
Δ7X, horizontal	948–889 = +59 +from 7X probe	948–900 = +48	948–883 = +65	948
Δ7Y, vertical (Fig. 7)	862–1,070 = −208 −towards 7Y probe	862–1,050 = −188	862–1,081 = −219	862
Δ8X, horizontal	845–775 = +70 +from 8X probe	845–785 = +60	845–772 = +73	845
Δ8Y, vertical	779–602 = +177 +from 8Y probe	779–645 = +134	779–607 = +172	779

The rotor displacements in vertical plane are different: the 7th bearing shaft displaced towards the 7Y probe decreasing gap by −208 μm and the 8th bearing shaft displaced downward increasing gap by +177 μm from the 8th probe. This is because the gravitation force becomes dominant versus gyroscopic force when rotational speed decreases below 1,250 rpm value. The gap values Δ7Y and Δ8Y

are displaced in opposite directions with reference to horizontal rotation axes at nominal rotational speed, but the values are slightly dependent on rotation speed up to resonance. Resonance rotational speed was reached after ∼1 min interval of time at coast down.

The measured gap Δ7X in horizontal direction at the 7th bearing changes only by 6–17 μm when rotational speed slows down from 3,119 to 1,350 rpm. The gap Δ7X provides valuable changes (up to 325 μm) in horizontal direction at 1,200 rpm indicating increased rubbing in both bearings. The rubbing phenomenon of the rotor shaft with bearing pads occurred not only at 7th bearing with heavy damages of upper pad and at 8th bearing lower pad (Fig. 2), but in all pads. The rubbing process starts at resonance speed following severe vibration and substantially increases from 1,250 rpm up to stand still when gravitation force of the blower rotor exceeds gyroscopic effect force.

The schematic view of rotational axes displacements are presented in Fig. 8. The bold lines indicate rotor position at nominal speed of 3,119 rpm and dashed lines – rotor position at 0 rpm. The upper figure presents shaft axes positions in vertical *YZ* plane and lower figure – in horizontal *XZ* plane, when rotation direction is counterclockwise as viewed from 7th to 8th bearing.

The modeling and simulation of the blower rotor is provided including gyroscopic effect of the rotor. The main task of theoretical modeling is to evaluate forces acting on journal tilting-pad bearings and to simulate shaft kinetic orbit in the bearing.

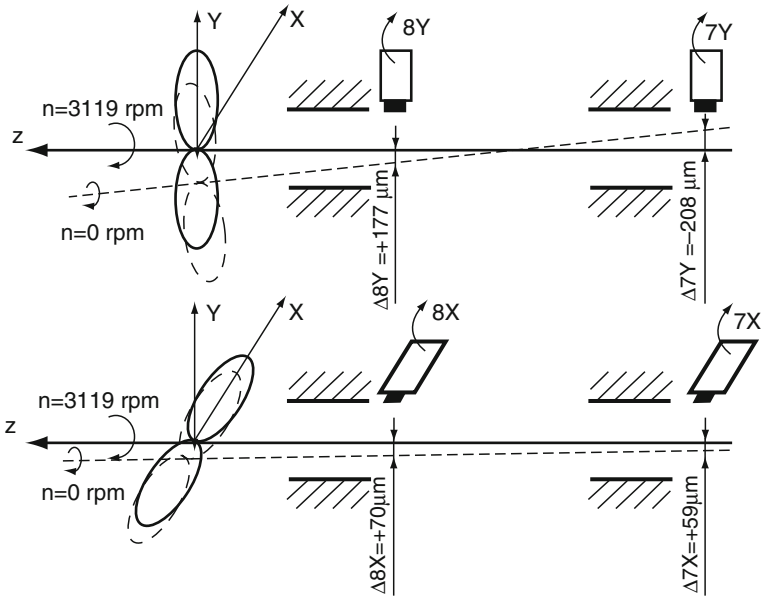

Fig. 8 The rotation axes positions of BR at nominal rotational speed and stand still

6 Mathematical Modeling and Simulation of Air Blower Machine

The rotating system general physical model is shown in Fig. 9 (see Fig. 1). All rotors are supported by tilting-pad journal bearings. The following general assumptions have been made during modeling: the materials of rotors and coupling are elastic; shear forces are taken into account; the deflection of the rotor is described by the displacement of points of the centre line; the axial motion of the rotors is neglected.

The dynamics of rotor is simulated by the finite element method when the finite element consists of two nodes and five degrees of freedom (DOF) at each node. The two DOF are displacements along X and Y axes (u, v) and the three DOF are angles around X, Y and Z axes (α, β, γ). The vector of translation displacements and rotation angles of rotor finite element can be described as follows [5]:

$$\begin{Bmatrix} u \\ v \end{Bmatrix} = \begin{bmatrix} N_u(\xi) \\ N_v(\xi) \end{bmatrix} \{q(t)\} = [N]\{q\}, \{\theta\} = \begin{Bmatrix} \alpha \\ \beta \\ \gamma \end{Bmatrix} = \begin{bmatrix} N_{1\theta}(\xi) \\ N_{2\theta}(\xi) \\ N_{3\theta}(\xi) \end{bmatrix} \{q(t)\} = [N_\theta]\{q\} \quad (1)$$

Cardin's angles are used to determine the relation between angular velocity $\left\{\dot{\theta}\right\}$ and angular velocity $\{\omega\}$ in the body coordinate system:$\{\omega\} = [G_2(\theta)]\left\{\dot{\theta}\right\}$.

Where

$$[G_2(\theta)] = \begin{bmatrix} \cos(\beta)\cos(\gamma) & \sin(\gamma) & 0 \\ -\cos(\beta)\sin(\gamma) & \cos(\gamma) & 0 \\ \sin(\beta) & 0 & 1 \end{bmatrix}; \left\{\dot{\theta}\right\} = \begin{Bmatrix} \dot{\alpha} \\ \dot{\beta} \\ \dot{\gamma} \end{Bmatrix} \quad (2)$$

Total kinetic energy of rotating system consists of all rotor elements. The kinetic, potential energies and gyroscopic matrix and load vectors of the finite element are presented in Barzdaitis and Bogdevicius [5].

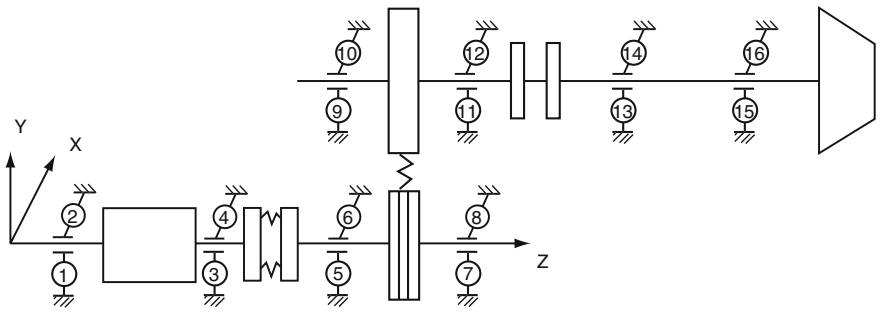

Fig. 9 The dynamic model of rotating system (see Fig. 1)

To estimate dynamic regimes of EM, two-phase mathematical models are used. In the general case, EM two-phase model consists of the system of differential and algebraic equations [6]:

$$\{\dot{\psi}\} = [A_\psi]\{\psi\} + \{B_\psi(t, \psi, \dot{\varphi}_e)\} \tag{3}$$

$$I_e \frac{d^2\varphi_e}{dt^2} = M_e(\psi) - M_r(\varphi_i, \dot{\varphi}_i, p_{Gi}) \tag{4}$$

$\{\Psi\}$ is flux space vector; matrix $[A_\Psi]$ and vector $\{B(t, \Psi, \dot{\varphi}_e)\}$ are

$$[A_\psi] = a_\psi \begin{bmatrix} -r_s L_r & 0 & r_s L_\mu & 0 \\ 0 & -r_s L_r & 0 & r_s L_\mu \\ r_r L_\mu & 0 & -r_r L_s & 0 \\ 0 & r_r L_\mu & 0 & -r_r L_s \end{bmatrix} \tag{5}$$

$$\{B_\psi(t, \psi, \dot{\varphi}_e)\} = \begin{Bmatrix} \sqrt{2}U_{nom}\cos(w_s t) \\ -\sqrt{2}U_{nom}\sin(w_s t) \\ \dot{\varphi}_e \psi_4 \\ -\dot{\varphi}_e \psi_3 \end{Bmatrix} \tag{6}$$

Here r_s, r_r are resistors of stator and rotor, respectively; L_s, L_r are inductive resistors of stator and rotor, respectively; I_e – moment of inertia of the EM rotor; torque of EM is equal to,

$$M_e = \frac{3}{2} \cdot pol \cdot L_\mu a_\psi (\psi_1 \psi_4 - \psi_2 \psi_3) \tag{7}$$

$$a_\psi = 1/L_s L_r - L_\mu^2;\ L_\mu = 1.5\, L_0; \tag{8}$$

L_0 is inductive resistor of magnetization contour.

The equations of motion of the rotor finite element are derived by applying Lagrange equation of the second order and can be written as follows:

$$[M(q)]\{\ddot{q}\} + ([C] + [G])\{\dot{q}\} + [K]\{q\} = \{F(q, \dot{q}, \psi)\} \tag{9}$$

7 Tilting-Pad Journal Bearing Model

The tilting-pad journal bearing has four segments. The position of the four segments with respect to the system of coordinates XY Fig. 10 is described by angles $\varphi_{i\,\min}$ and $\varphi_{i\,\max}$ ($i = 1, 2, 3, 4$).

The maximum normal and tangential hydrodynamic forces of ith segment depend on position of segment (angles $\varphi_{i\,\min}$ and $\varphi_{i\,\max}$), angle ψ of rotor centre and eccentricity ratio $\varepsilon = e/\Delta$ (e – radius of rotor geometrical displacement, Δ – maximum radial clearance), parameter h of tilting-pad bearing (range of parameter is 2–3):

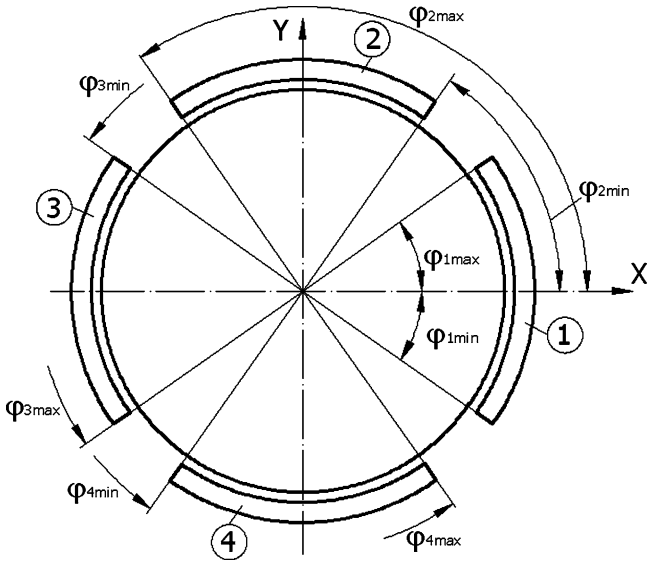

Fig. 10 The scheme of tilting-pad journal bearing

$$F_{Ni} = F_{N\max}(\varepsilon)\exp\left(-h\Delta\alpha_i^2\right) \tag{10}$$

$$F_{Ti} = F_{T\max}(\varepsilon)\exp\left(-h\Delta\alpha_i^2\right) \tag{11}$$

Here $\Delta\alpha_i = \psi - \varphi_{ci}$; where φ_{ci} is angle of centre of ith segment given by $\varphi_{ci} = 0.5\,(\varphi_{i\,\min} + \varphi_{i\,\max})$; $\psi = \arctan(v/u)$; u, v are displacements of rotor centre along the X and Y axes respectively; $F_{N\max}(\varepsilon)$, $F_{T\max}(\varepsilon)$ are maximum normal and tangential forces Fig. 11.

The normal and tangential forces are determined as presented in Khonsari and Chang [7].

The hodograph of the relative hydrodynamic force ($F_{br}/F_{br\max}$) in the radial direction of tilting-pad journal bearing is presented (Fig. 12).

8 Simulation Results

The air blower rotor mass is 1,660 kg and mass inertia moments are $I_{xx} = I_{yy} = 287\,kgm^2$, and $I_{zz} = 436\,kgm^2$. The density and elastic modulus of the rotors and coupling material are $\rho = 7850\,kg/m^3$, $E = 210 \times 10^9\,N/m^2$ respectively. The journal diameters of the 7th and 8th bearing are $0.200\,m$ and $0.250\,m$ respectively. The radial clearances of 7th and 8th tilting-pad journal bearings are $200\,\mu m$ and $300\,\mu m$ respectively. The run-up angular velocity of BR and torque of asynchronous electric motor are presented in Fig. 13. The simulation results are

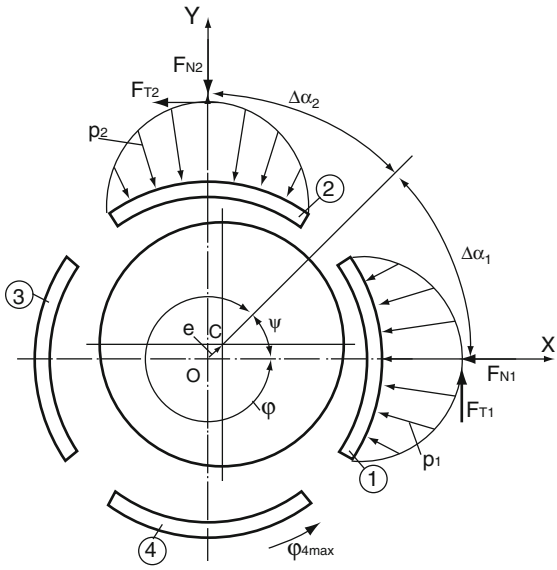

Fig. 11 The scheme of forces acting in the tilting-pad journal bearing

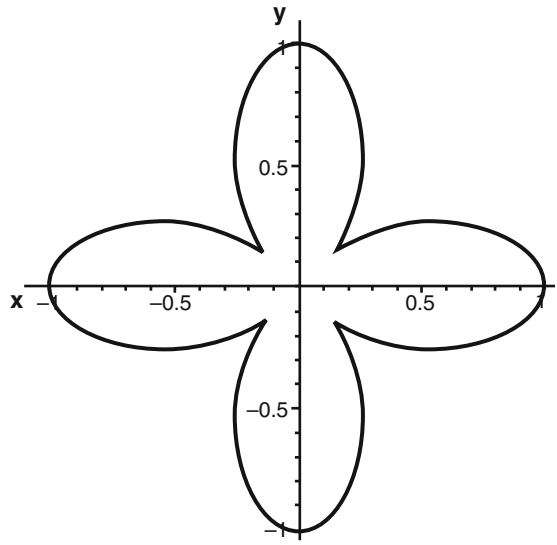

Fig. 12 The hodograph of relative tilting-pad journal bearing forces

shown in shaft kinetic orbit format, Fig. 14, at nominal rotational speed and verified by experimental measurements (Fig. 3). Horizontal and vertical displacements of rotor points are shown in Figs. 8 and 11.

The simulated results indicate that rotor vibrations depend on unbalance, variable dynamic stiffness and impeller gyroscopic effect. In case of rotor center of mass, shift for geometrical axis is 0.02 mm, when mass of the rotor is 2,900 kg, rotational speed 3,120 rpm, inertia force is 6,190 N. Gyroscopic moment of the rotor has the

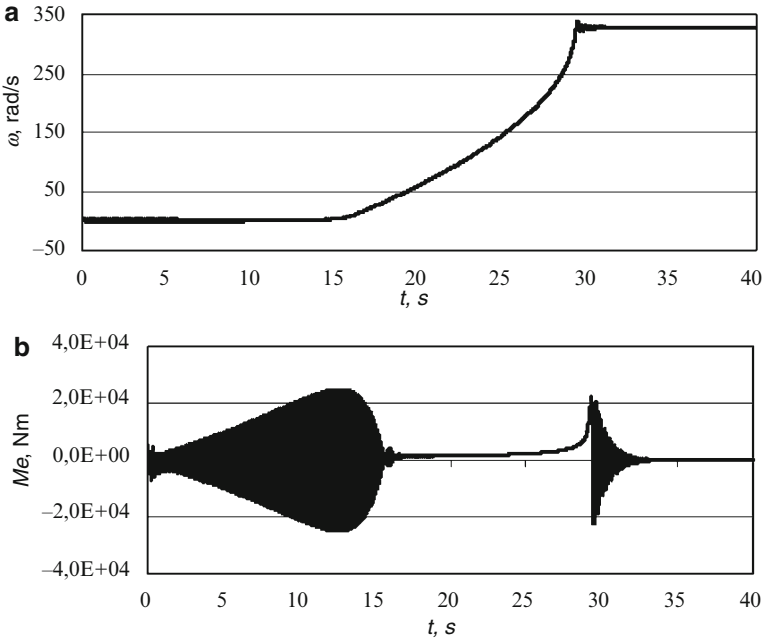

Fig. 13 Angular velocity of blower rotor and torque versus time of electric motor: **(a)** – angular velocity; **(b)** – torque

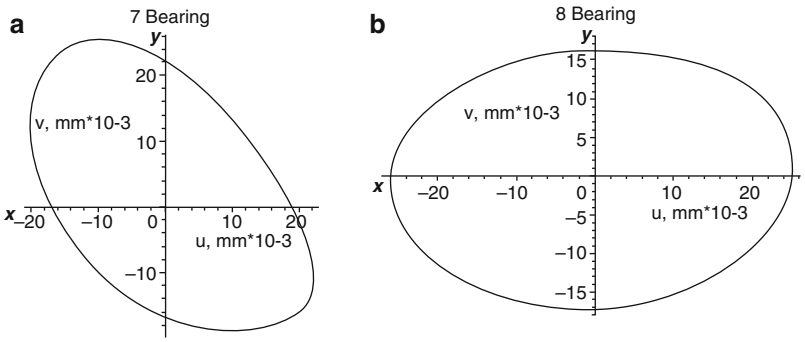

Fig. 14 Simulated kinetic orbits of 7th (**a**) and 8th (**b**) bearings shaft at nominal rotational speed 3,132 rpm: $u - X$ axes, $v - Y$ axes; parameter h approx. equal to 2.75

same influence. Nominal rotational speed of the rotor is more than twice higher than its resonance frequency as experimentally measured $\sim$ 22.5 Hz. The transient rotation running processes of BR acceleration and deceleration should be performed as fast as possible to pass resonance frequency and as slow as possible after resonance rotational speed in coast down mode.

9 Conclusions

The coast down mode is most dangerous running mode for the blower rotor tilting-pad journals bearings because it provides rub phenomenon of the rotating rotor shafts with bearings pads.

The rubbing process starts first at 8th bearing at resonance rotational speed 1,350 rpm because of inadmissible vibration displacement amplitude of maximum value $s_{max8} = 307\,\mu m$.

The gyroscopic effect of the BR wheel changes shaft's position described by gaps in the 7th and 8th bearings increasing rubbing process at 1,250 rpm till stoppage of the rotor, and it takes long interval of time, 13 min; the experimental measurements indicated that 7th bearing's shaft goes up (in vertical direction) 208 μm and 8th bearing shaft displaced down by 177 μm during the coast down mode.

Experimental testing results are in reasonable agreement with theoretical model and simulation results, which will serve to simulate dynamics of whole machine.

References

1. Barzdaitis, V., Bogdevičius, M., Gečys, St.: Vibration problems of high power air blower machine. In: Proceedings of 2nd International Symposium on Stability Control of Rotating Machinery, ISCORMA-2, pp. 606–616. Gdansk, Poland; Minden, Nevada, USA (2003)
2. Bently, D.E.: Fundamentals of Rotating Machinery Diagnostics. Library of Congress Control Number 2002094136, Bently Pressurized Bearing Company, printed in Canada, p. 726 (2002)
3. Goldin, A.S.: Vibration of Rotating Machines. ISBN 5-217-02927-7, UDK 621.752, BBK 22.23 G63. Mashinostroenie, Moscow, p. 344 (2000) (in Russian)
4. Vasylius, M., Didžiokas, R., Mažeika, P., Barzdaitis, V.: The rotating system vibration and diagnostics. Mechanika. – Kaunas, Lithuania: Technologija, Nr. **4**(72), 54–58 (2008)
5. Barzdaitis, V., Bogdevicius, M.: The dynamic behavior of a turbine rotating system. J. Mech. Eng. **52**(10), 653–661 (2006)
6. Aladjev, V., Bogdevičius, M.: Maple 6: Solution of the Mathematical, Statistical and Engineering – Physical Problems. Laboratory of Basic Knowledge, Moscow, p. 824 (2001) (in Russian)
7. Khonsari, M.M., Chang, Y.J.: Stability boundary of non-linear orbits within clearance circle of journal bearings. ASME J. Vib. Acoust. **115**, 303–307 (1993)

A Mechanical Engine Simulator for Development of Aero Engine Failure Analysis Methods

Robert Liebich

Abstract A mechanical engine simulator for method development is under construction at Berlin Institute of Technology. The new experimental rig reflects nearly all mechanical characteristics of an aero engine. The mechanical engine simulator will enable the analysis of diverse failure cases that need to be considered for an aero engine certification. Based on the experimental results using the mechanical simulator, analytical and numerical methods will be developed in order to demonstrate the capability of future engine projects. Those experimentally validated methods will predict the behavior of aero engines due to failures and provide a better understanding of their behavior during past failure events such as compressor and turbine blade loss, continued rotation after a fan blade loss or bird strike. The paper gives an overview of the principle certification specifications regarding engine failure cases, explains the background of failure analysis and provides design drawings and sketches of the future simulator test rig at the institute.

Keywords Whole engine analysis · Engine simulator · Rotor dynamics · Blade loss · Vibration · Imbalance · Rotor-to-stator contacts · Active and passive bearings

1 Introduction

Modern aero engines are developed in an economically aggressive environment. Today, technical challenges like low noise and weight, high efficiency and performance go along with strict cost targets and tight development times. In addition, the aviation authorities develop a better understanding for the technical challenges of aero engines with each new engine project. That leads to new or more detailed

R. Liebich (✉)
Engineering Design and Product Reliability, Berlin Institute of Technology – School V,
Sekr. H66, Strasse des 17. Juni 135,
10623 Berlin, Germany
e-mail: robert.liebich@tu-berlin.de

K. Gupta (ed.), *IUTAM Symposium on Emerging Trends in Rotor Dynamics*,
IUTAM Bookseries 25, DOI 10.1007/978-94-007-0020-8_35,

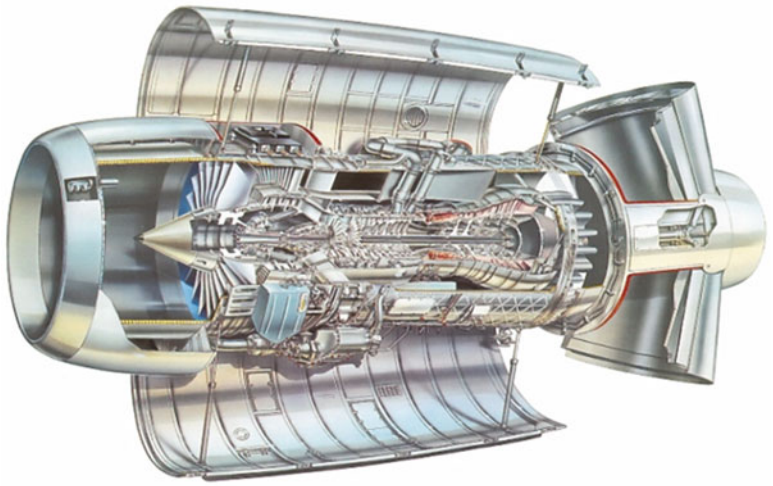

Fig. 1 Picture of a Rolls-Royce BR715 two-shaft engine [1]

guidelines or directives. As a result, each engine manufacturer focuses on better and faster performance regarding its engineering analyses. Figure 1 shows a Rolls-Royce BR 715, one of the most advanced two-shaft engines today.

The certification of an aero engine needs many different analyses and testing. Several studies and investigations need to be done up front a certification. Some of the major failures have to be analyzed or even tested in order to ensure a safe-failure condition during flight. Those major failures are the loss of a fan blade (Fan Blade Off – FBO) [2, 3], the loss of one or more compressor or turbine blade (Core Blade Off – CBO) [2, 3], the impact of a bird (Bird Strike) [4], hail and water ingestion during heavy rain [5]. Each aero engine has to withstand such a failure without leading to a major hazard to the aircraft.

The most severe failure case is an FBO. For new aero engine projects, the authorities request a full engine test for certification. A read across from previous FBO test without new testing is allowed only for minor changes from a previous engine design to the new one. In order to prepare such an FBO test a so called whole engine mechanical finite element model (WEMM) is prepared and provides estimated forces, vibrations and deflections for the test situation. The aim of an FBO test is to ensure a contained blade loss and an immediate and controlled rundown of the engine. A major engine damage due to an FBO is allowed, whereas a detachment of engine parts or even the full engine from the aircraft is not. The same procedure is requested for a bird strike. A WEMM is developed in advance and provides the necessary impact forces, vibrations and deflections in order to ensure a later successful bird strike test for certification. Here, the authorities focus on minor damages of the engine and a minor loss of performance during a bird strike. The engine has to run nearly perfectly after a bird strike, a shutdown is usually not allowed. Hail and heavy

rain ingestions are tested without a pre-analysis using a WEMM. The certification of those engine failure cases is more a question of performance, pressure loss and combustion and not driven by mechanics.

A further failure case to be demonstrated for certification is the loss of one or multiple compressor or turbine blades (CBO). While the loss of a fan blade dominates all other engine failure cases regarding impact forces, imbalance level, structural stress and vibrations, such a CBO causes lower impact, imbalance and vibration levels due to the much smaller blades. But nevertheless, a CBO has to be demonstrated via engineering analysis at least. A testing, necessary for FBO and bird strike certification, was not requested by the authorities in the past for a CBO due to the lower stress and vibration level. In most cases the engine will run further on after a CBO event.

Today, the world faces a global reduction of fuel resources. As a result, several scientists are looking for alternative fuels and engine propulsion concepts. Those alternatives need time to demonstrate their ability to replace the conventional engine concepts. For the time being, alternative engine concepts which reduce the fuel consumption have to be developed. As a result, the old fashioned turboprop engine is coming back. Several EU-projects are looking for an improvement in performance and concurrent low fuel consumption for those turboprop engines. Concept studies for two counter rotating propellers or swept propeller blades are under investigation for instance. As the design of the core engine – meaning compressor, combustor and turbine – is nearly the same for today's jet and turboprop engines, the engine front differs. A jet engine owns a fan as the first compressor stage surrounded by the bypass duct, whereas a turboprop engine owns an open propeller. As a result, the certification for turboprop engines must differ regarding FBO failure case and bird strike. Changing the name "Fan Blade Off" into "Propeller Blade Off" would provide a first hint of what to do for certification. Modern propellers are obviously much larger than fans even when considering the rising bypass ratios for new jet engines we have seen in the past decades. One example is the turboprop engine TP400 for the Airbus military transporter A400M. The propeller has a diameter of more than 5 m. Assuming that such a propeller loses a blade during flight, the imbalance generated forces would destroy the engine. The engine detaches itself from the aircraft subsequently. This scenario results in a special design for propeller blades and the disks. The design must provide a low stress level and a high resistance against foreign object damage that could lead to a not allowed propeller blade loss. Therefore, a propeller blade off test for turboprop engine certification is not requested. Such a test is meaningless as the result would always be a full damaged and detached engine.

The major failure case for jet engine is the FBO. The correspondent major failure case for turboprops is not the propeller blade off as shown above. For turboprop engines, the compressor and turbine blade off (CBO) takes the place as the major failure case to be demonstrated for engine certification. Naturally, the authorities could request a testing of a compressor or blade loss event. But it is obvious that this request will end in several tests for different stages as multiple compressor and turbine stages exist in the core engine. Each blade loss may lead to different results

during the tests due to different geometries of blades, disks and casing at the stages. Considering ten compressor and five turbine stages for instance, the certification will end in 15 full engine tests that cost several million dollars each. This amount of tests would stop every new engine program. It may be possible to limit the number of CBO tests by identification of the major event of all possible stages using WEMM analyses. A complete omission of CBO testing would be even more desirable for engine manufacturers. Previous CBO analyses for jet engines base on whole engine mechanical models (WEMM) which are not sufficiently validated regarding CBO events. As there exist only a few CBO tests worldwide, the amount of data for a finite element model validation is quite low. As a consequence, engine manufacturers may look for whole engine mechanical models that are validated for core blade off events. As full engine tests are too expensive for validation purposes, the solution may be a full sized mechanical engine simulator that provides enough data in order to allow a validated method for a better computational analysis of CBO events. This validated method could be adopted in classic WEMM analyses regardless of the engine type and provide sufficient evidence to convince the authorities with respect to an omission of CBO testing.

2 An Engine Mechanical Vehicle for CBO Event Simulation

The development of an engine mechanical vehicle for CBO event simulation should consider all rotordynamic effects, the basic geometries of rotors and casings as well as bearing support structures and pylons for engine to aircraft attachment. Typical jet-engines have a two-spool concept, i.e., there exist a high and a low pressure shaft. Some manufacturers offer a three shaft concept providing an intermediate pressure shaft for additional thrust demands. However, as the main challenges for a CBO event simulation are the same for two- or three-shaft engine concepts, the engine mechanical vehicle for CBO simulation at Berlin Institute of Technology bases on the simpler and cheaper two shaft concept. One of the major challenges for the development is the mechanical simulation of a sudden imbalance due to a blade loss. Those blade off simulations need to be repeated without damaging the engine simulator. Additionally, the mechanical vehicle must ensure a longtime period of imbalance running at maximum speed, since the loss of a small compressor blade is not detected from the vibration monitoring of the aircraft sometimes due to the relative small unbalance level. In practice such a blade loss will be detected during the next C-check with a partial demounting of the engine.

The mechanical simulator will provide typical rotor dynamic conditions of a small or midsize two shaft engine, i.e., a maximum running speed at 7,000 rpm for the low pressure shaft and up to 14,500 rpm for the high pressure shaft. The low pressure shaft has an operational speed above its first critical speed whereas the high pressure shaft runs below its critical speed. Although called “low” and “high pressure” shaft, the two shafts of the mechanical simulator at Berlin Institute of Technology will not provide any aerodynamic feature. The mechanical simulator

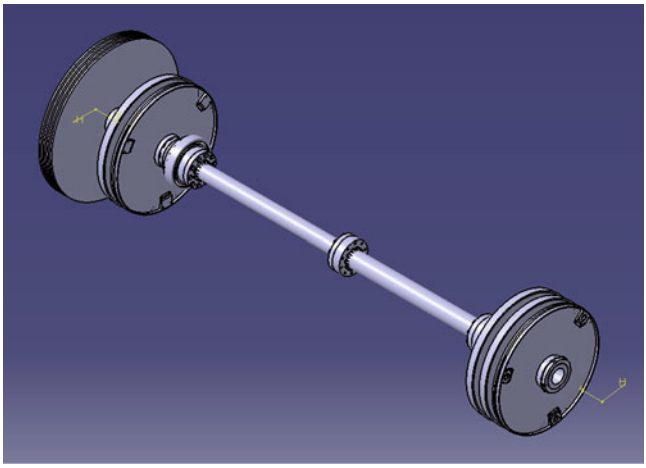

Fig. 2 3D-view of the low pressure shaft of the mechanical simulator

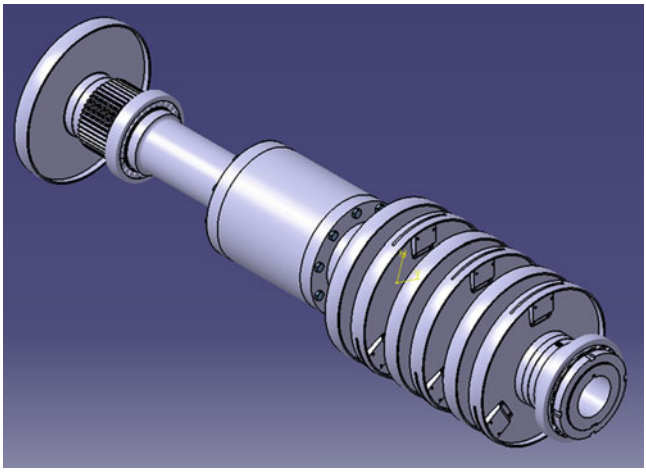

Fig. 3 3D-view of the high pressure shaft of the mechanical simulator

has no combustion chamber also as there exist no combustion process for the rotor drive. Both shafts will have disks that provide the equivalent mass and inertia properties of compressor and turbine stages of a typical small respectively midsize engine (see Figs. 2 and 3). The idea was to rebuild an engine condensed to its mechanical properties and characteristics.

There existed several ideas how to build a mechanical vehicle for the CBO event simulation. Typical test rigs for experimental investigations in rotordynamics are small in comparison to the later applications of the tested features. After a successful investigation on a smaller test rig, the transfer or read-across of results to the

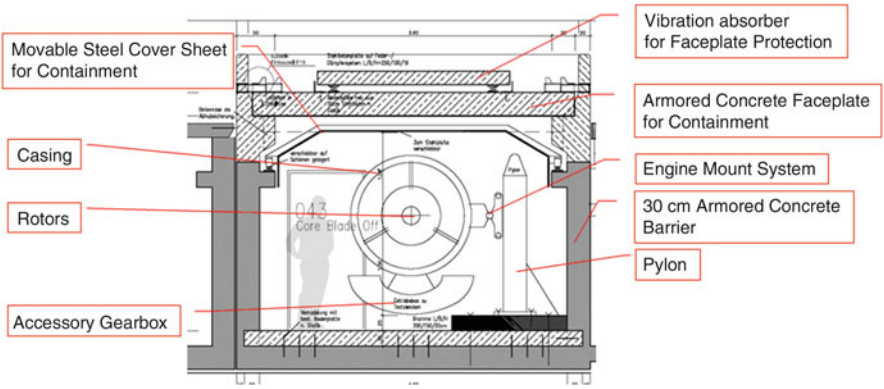

Fig. 4 Sketch of the experimental rig for the mechanical simulator at Berlin Institute of Technology, view in axial direction

larger applications is often an additional challenge. Here, the decision was made to concentrate on the later computational simulation and method development since it is ambitious enough. Therefore, a full size engine vehicle is planned in order to provide equivalent masses, stiffness, damping and operational speed. Figure 4 shows the experimental rig at Berlin Institute of Technology.

From an engineering design point of view, the drive train of the mechanical engine vehicle is a real challenge. The new drive train must power the low and the high pressure shafts instead of the airflow. The drive train should not influence the rotordynamics of the two shafts regarding undesired additional forces, moments or vibrations. Gear trains or belt drives are possible. While gear trains tend to additional vibrations of higher order, belt drives are speed limited (max. 120 m/s). Nevertheless, a belt drive concept was chosen using a special belt that allows higher speeds in order to provide the necessary operational speed for the faster high pressure shaft. Two belts are driving the shaft in order to avoid a shaft bending induced by one belt only, see Fig. 5.

A special mass release device was designed in order to simulate the incidence of a sudden imbalance at full operational speed. The imbalance device allows a release of different well defined masses and could be used without limitation for multiple blade release investigations. The device is installed at nearly all vehicle disks representing the compressor or turbine stages. The following rotordynamic subjects shall be investigated using the engine mechanical simulator: Rotor-to-Stator contacts, intershaft contacts, vibration monitoring and blade loss detection. Later on, alternative damping devices and actuator concepts shall be investigated regarding CBO events and common rotor vibrations.

Academic institutes tend to develop own analysis software for computational simulation of rotordynamic subjects. Here, the idea is to go both ways. On the one hand, special methods and algorithms shall be developed in order to support the simulation and analysis of CBO events. On the other hand, commercial

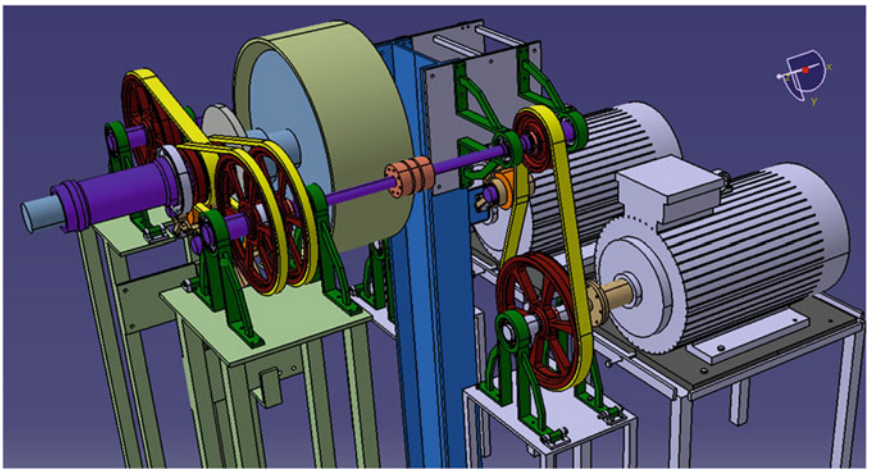

Fig. 5 3D-view of the belt drive concept for the low pressure shaft of the experimental rig

FE-software shall be used as well in order to provide a modeling and simulation method to be used in whole engine models embedded in the IT environment of engine manufacturers. Individual academic software solutions are often unaccepted by manufacturers even if they provide better solutions. The integration in existing whole engine simulation models or tools and the IT environment inside the companies are limitations for the acceptance of academic software solutions. The new method for a better modeling and simulation of CBO events should match into the manufacturer's whole engine simulation. The most common FE-software used by aircraft and engine manufacturers is NASTRAN. So, the decision was clear to provide a NASTRAN based CBO event simulation beside more detailed in-house academic software solutions for detailed analyses.

3 Further Use of the Mechanical Engine Simulator

Only a few years ago a new engine certification specification has been released by the European aviation agency EASA and the American aviation agency FAA. The new specification CS-E 525 [6] requests the demonstration of a safe continued rotation of the affected engine after a blade off event. Especially after fan blade off events this requirement is a quite challenging one. In all cases a loss of a fan blade will end in an immediate shutdown of the engine. That is done by the engine control automatically or via mechanical devices triggered by centrifugal forces. Civil aircrafts own two engines at least. While the blade off affected engine is shut down, the unaffected one is still providing sufficient thrust for a safe flight home. But the affected engine is still running due to the incoming flow during flight. The amount of rotation is quite high depending on the fan airfoil design and the rub forces

inside the damaged engine. The rotation due to the incoming flow only is called "Windmilling". Hence, the amount of the imbalance induced vibration and the dynamic stress may affect the engine life and even the aircraft life during the flight home phase. A lower flight speed or the approach of the next airport will reduce the risk of further damaging the engine and aircraft. But, in some cases those fan blade off events occur above the middle of the Atlantic or Pacific Ocean, far away from any airport.

Aircraft manufacturers tend to develop two engine instead of four engine aircrafts for cost reasons. Those engines need to be larger than the ones for a four engine application. Hence, the diameter of the fan is significantly larger and the blade foil is therefore bigger and heavier. That results in even higher imbalance and vibration levels. The "Extended-range Twin-engine Operation Performance Standards" ETOPS request an aircraft and engine design which allow a single engine flight up to 207 minutes. Considering such a long time for a damaged engine rotation, it is quite obvious that engine and aircraft structures are challenged dynamically. The new mechanical engine simulator to be built at Berlin Institute of Technology shall be used for lifing of aircraft engines as well, especially under high imbalance operation during windmilling. The vehicle is designed to allow general lifing investigations or special investigations on original aircraft parts that are assembled in the vehicle. Those investigations are definitely not possible for all engine parts but for a couple of parts, as engine mount systems, bearing support structures or intermediate casings for instances.

Further investigations using the new experimental rig are planned. While common aero engines have squeeze film dampers (SFD) for rotor damping purposes, alternatives as piezoelectric actuators or simple rubber rings could be used. The application of piezoelectric actuators is under investigation already, see Ehmann [7] and EU-financed project DREAM by Prof. Nordmann of TU Darmstadt as well. Figure 6 shows a principle sketch of such an application in the bearing's direct load path and the promising results from a computational analysis [7]. Ordinary rubber rings are much simpler and foremost cheaper devices for rotor damping. Those elastomer rings for aero engine application are investigated already, see Liebich and Bormann [8]. A more detailed investigation is performed within the EU-Project DREAM by Berlin Institute of Technology currently. A possible integration of rubber rings in an aero engine design is presented in Fig. 7.

There exist many more tasks in the mechanical design of aero engines that could be investigated using the mechanical engine simulator. New bearing solutions as magnetic bearings are under consideration by aero engine manufacturers. The MEE – More Electric Engine – Concepts of engine manufacturers focus on several non mechanical but electric devices and applications for use in aero engines. The old fear of magnetic bearings to be used in aero engines is gone now. The application of those new bearings in other machines has shown sufficient reliability to convince the engine manufacturers to give it a try. One challenge when using magnetic bearings is a sudden failure of the power supply and the subsequent rundown of the rotor inside the retainer bearings. Here, the mechanical engine simulator is a perfect vehicle for a detailed experimental investigation of such events in an aero

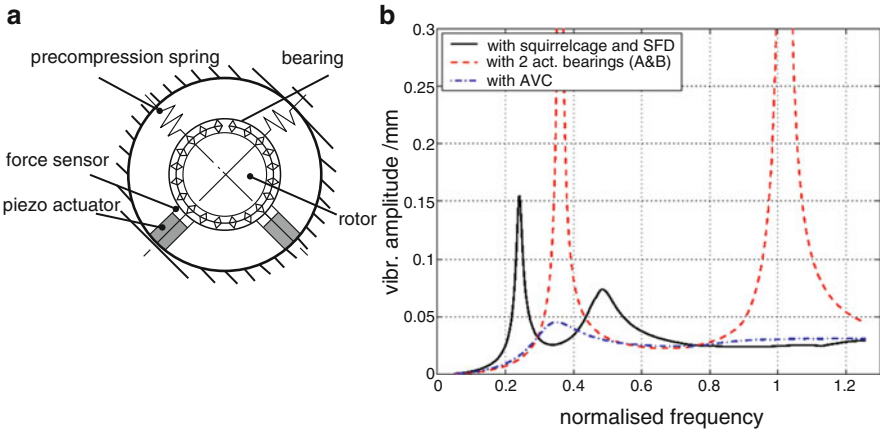

Fig. 6 **(a)** Principle sketch of piezoelectric actuator in the bearing's direct load path [7]. **(b)** Results from a computational simulation: solid line – solution with common SFD, dash line – solution with not activated piezoactuators (stiffening effect), dot and dash line – solution with activated piezoactuators [7]

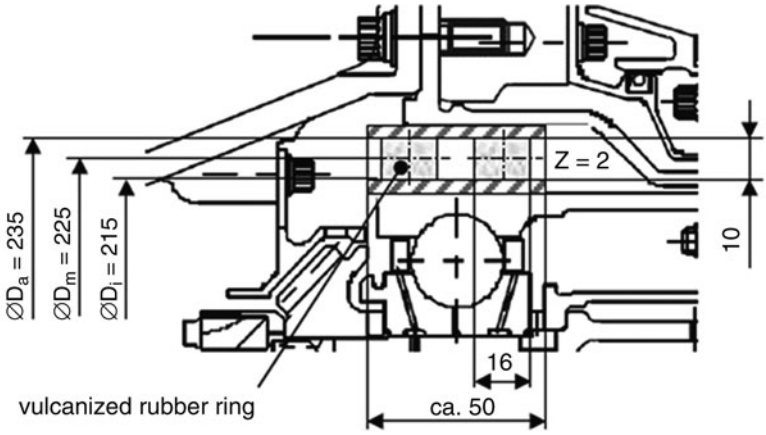

Fig. 7 A possible integration of rubber rings in an aero engine HP front bearing design [8]

engine environment. Another task for further investigation is given by the inverse unbalance identification. As the number of vibration pick-ups in aero engines is often very low, the final balancing procedure before dispatch or a balancing later in the field is sometimes challenging. It is worth to use the mechanical engine simulator for investigations on better balancing procedures considering inverse methods when being limited to one or maximum two vibration pick-ups for instance. This idea of future use of the mechanical engine simulator leads to a further task – the machine diagnosis of aero engines. The new experimental rig reflecting nearly all

mechanical characteristics of aero engines is a perfect vehicle for investigations on machine diagnosis. Questions regarding how many, which type and where to put sensors could be answered using the new rig.

4 Conclusion

A mechanical engine simulator for method development is under construction at Berlin Institute of Technology. The mechanical engine simulator will enable the analysis of diverse failure cases that need to be considered for an aero engine certification. Based on the experimental results using the mechanical simulator, analytical and numerical methods will be developed in order to demonstrate the capability of future engine projects. The experimental results help to provide a better understanding of failure cases and better methods for predictions of engine behavior during and after blade off events. In addition to that, the test rig provides a realistic vehicle for research into different vibration reduction devices. The new experimental rig reflecting nearly all mechanical characteristics of aero engines is a perfect vehicle for investigations on machine diagnosis as well.

References

1. Liebich, E.: Alternative schwingungsreduktion von triebwerksrotoren – piezoaktor versus quetschöldämpfer. DGLR Jahrestagung (2005)
2. EASA Certification Specifications for Engines, CS-E 520 Strength
3. EASA Certification Specifications for Engines, CS-E 810 Compressor and Turbine Blade Failure
4. EASA Certification Specifications for Engines, CS-E 800 Bird Strike and Ingestion
5. EASA Certification Specifications for Engines, CS-E 790 Rain and Hail Ingestion
6. EASA Certification Specifications for Engines, CS-E 525 Continued Rotation
7. Ehmann, L.: Piezo actuators for vibration reduction of aero engine rotors – a case study. In: Proceedings of the ISCORMA-3, Cleveland, OH (2005)
8. Liebich, E., Bormann, A. Vibration damping of aero engine rotors by elastomer ring bearings. In: Proceedings of the 7th IFToMM Conference on Rotor Dynamics, Vienna (2006)

Signal Processing Tools for Tracking the Size of a Spall in a Rolling Element Bearing

R.B. Randall and N. Sawalhi

Abstract There is considerable interest in diagnostics and prognostics of operating machines based on vibration analysis and signal processing, because the major economic benefit from condition-based monitoring comes from being able to predict with reasonable certainty the likely lead time before breakdown. In the case of rolling element bearings, a number of powerful techniques have been developed in recent years to separate the rather weak signals coming from faulty bearings from strong background vibrations, and to diagnose the type of fault. The MED (minimum entropy deconvolution) technique was initially applied to bearings to reduce the overlap of adjacent impulse responses in high speed bearings and thus allow their diagnosis by envelope analysis. It was then suspected that the technique also might have the potential to separate the impulses from entry into, and exit from an individual fault, and thus give information on the fault size. This paper gives the results of an initial study into the application of MED, and other techniques, to obtain the best measure of the length of a developing spall, to use in prognostic algorithms to estimate safe remaining life, based on current size and rate of evolution with time. It was found that the response to the entry and exit events was markedly different, so considerable pre-processing was required before the MED could be applied. The paper also discusses a number of methods to reduce noise and obtain an averaged estimate of the spall length.

Keywords Bearing diagnostics · Bearing prognostics · Fault size determination · Vibration analysis · Machine condition monitoring

1 Introduction

It is now generally acknowledged that vibration analysis and signal processing provides a very powerful tool for use in condition-based monitoring of operating machines. In the last several years a number of powerful techniques have been

R.B. Randall (✉) and N. Sawalhi
School of Mechanical and Manufacturing Engineering, The University of New South Wales, Sydney 2052, Australia
e-mail: b.randall@unsw.edu.au

K. Gupta (ed.), *IUTAM Symposium on Emerging Trends in Rotor Dynamics*,
IUTAM Bookseries 25, DOI 10.1007/978-94-007-0020-8_36,

developed for the three main phases of this work, namely detection, diagnosis, and prognosis (prediction of remaining safe life). For bearings, the authors recently published a semi-automated method for diagnosing bearing faults, which included separation of the rather weak bearing signals from strong background vibrations, often dominated by deterministic signals such as from gears [1]. This often requires the signals to be first "order-tracked" by resampling at equal shaft angles so that the phase-locked deterministic components can be removed. It is based on the fact that the bearing signals, while having "characteristic frequencies", are in fact stochastic, because of a small amount of random slip between the components. For this reason, the "periodicity" of the fault bursts is not revealed by direct frequency analysis of the raw signals, because the low harmonics of the repetition rate (which would in principle be separated) are too low to be measurable, while the high order "harmonics", amplified by high frequency resonances, are smeared because of the randomly varying period. For more than 30 years the solution to this problem has been provided by "envelope analysis", where the envelope of the high frequency bursts is determined by amplitude demodulation, and then frequency analyzed [2]. This technique is often referred to as the "high frequency resonance technique (HFRT)". The random period variation of about 1% has little effect on the low harmonics of the envelope spectrum. The technique has undergone many improvements over the years, many brought about by the introduction of digital techniques to achieve things not possible or difficult with the original analogue techniques. Ho and Randall [3] demonstrated the benefits of Hilbert transform techniques to simultaneously demodulate a signal with a one-sided spectrum (thus eliminating masking from irrelevant negative frequency components) and at the same time achieve bandpass filtering with a near ideal filter. It was also shown that the squared envelope was normally preferable to the envelope previously used. At the same time SANC (self adaptive noise cancellation) was shown to be a powerful method for removing gear signals.

There was always some speculation as to the choice of the best frequency band to demodulate, but in recent years it has been shown that spectral kurtosis (SK) often finds the optimum band where the signal/noise ratio of bearing signal to background is maximized [4, 5]. In fact, the "kurtogram" [4, 5] gives the optimum combination of centre frequency and bandwidth to maximize the kurtosis (impulsiveness) of the filtered signal, this often being dominated by the faulty bearing signal. Antoni proposed a "fast kurtogram" in Antoni [5] while the current authors proposed a "wavelet kurtogram" in Sawalhi and Randall [1].

In the case of high speed bearings, the impulse responses from successive impacts of rolling elements on a fault in a bearing race can be overlapping, meaning that the envelope no longer reveals the pulse repetition rate, and the method in Sawalhi and Randall [1] also includes the use of MED (minimum entropy deconvolution) to separate them. This method finds the optimum inverse filter to deconvolve the transfer function (from the source to the measurement point) from the original impulses, assuming that these are very localized in time. MED was first proposed by Wiggins [6] and applied to bearing diagnostics in Sawalhi et al. [7]. It uses a maximum kurtosis criterion to find the most impulsive source signal which could have caused the resulting measurement. The SK technique is applied after sharpening of the pulses through MED.

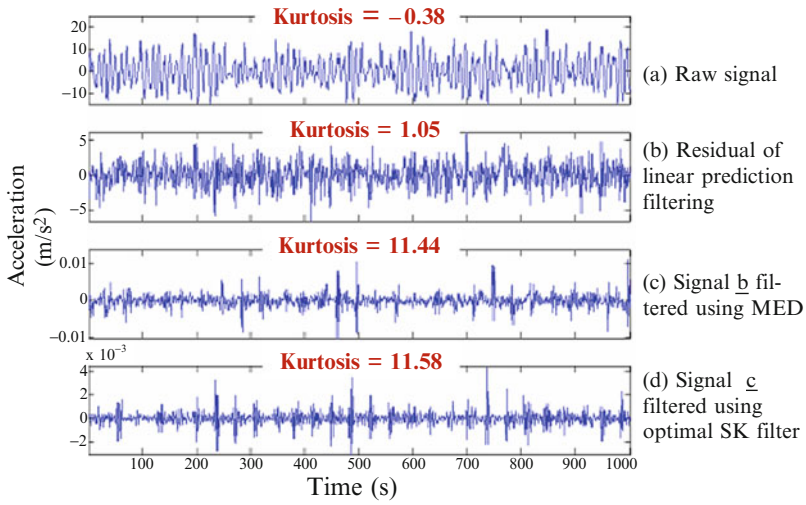

Fig. 1 Bearing time signals after various stages of the processing [1]

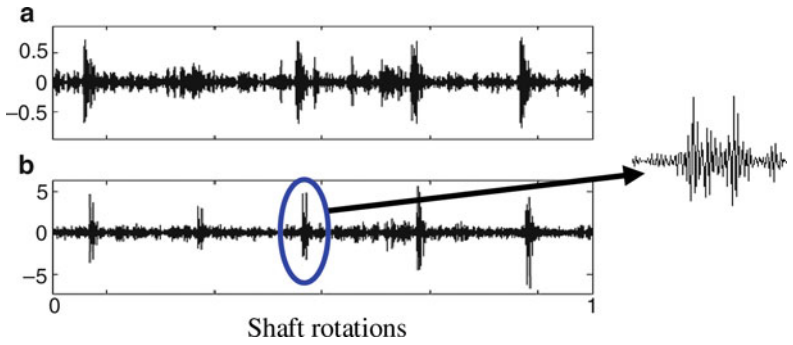

Fig. 2 **(a)** Filtered signal using SK enhanced with AR. **(b)** Filtered signal using SK enhanced with both AR and MED

Figure 1 shows an example from Sawalhi and Randall [1] of the application of this approach. It is from a high speed bearing typical of a gas turbine engine running at 12,000 rpm. Even after removal of discrete frequency components in Fig. 1b the signal is not very impulsive because the length of individual impulse responses is greater than the spacing between them. The application of MED in Fig. 1c increases the kurtosis from 1.05 to 11.44 and separates the individual impulses.

The MED technique was then applied to signals from lower speed bearings, and this revealed double impulses for the passage of every rolling element over a spall-type fault. This is illustrated in Fig. 2.

1.1 Signals from Entry into and Exit from a Spall

It was initially thought that the double impulses came from entry into, and exit from the spall, so that their separation could be used as a measure of the size of the spall. This was made more plausible by the fact that the separation in this case actually corresponded approximately to the size of the fault. Even so, it was somewhat disconcerting that the size of the two impulses was approximately the same, when analysis of the reason for their generation was different. The first should occur because of de-stressing of the rolling element when rolling over the leading edge of the fault, which would not be instantaneous, while the second would occur when it struck the trailing edge of the fault, and would have to change direction almost instantaneously. It would be expected that this re-stressing would give a considerably larger and sharper shock. The only prior examples found in the literature of the double impulses caused by a bearing fault were by Dowling [8] and Epps and McCallion [9].

The result from Dowling [8] is shown in Fig. 3, and could be considered compatible with the original interpretation. It shows the change in phase of the signal at the commencement of the second impulse. Dowling [8] describes a number of different cases rather briefly, however, he does not give many details.

A typical result from Epps and McCallion [9] is shown in Fig. 4. It is an extract of Epps's Ph.D. thesis work from the University of Canterbury, Christchurch, New Zealand, and contains somewhat more details. In this case there is a greater difference between the effects of entry to the fault and exit from it, in better accordance with the analysis given above. The entry into the fault could be classified as a step response, with mainly low frequency content, while the impact on exit excites a much broader band impulse response.

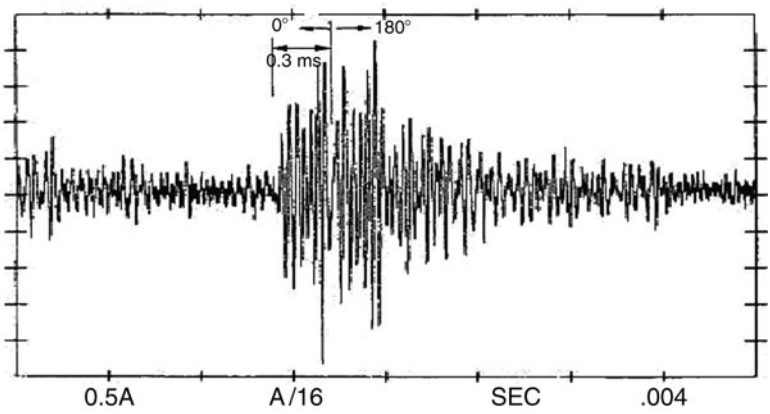

Fig. 3 Bandpass filtered trace from a helicopter gearbox bearing with a spall in the outer race, from Dowling [8]

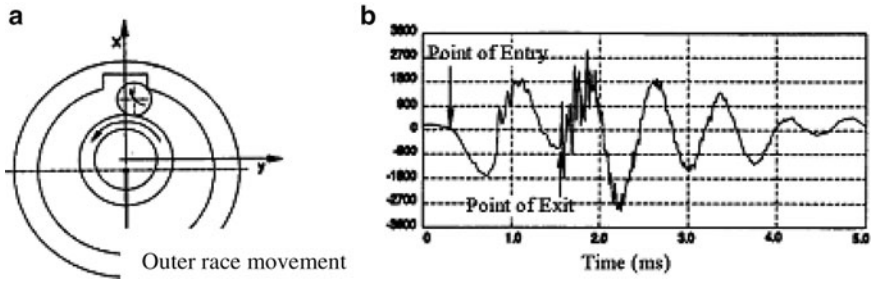

Fig. 4 Left: model of rolling element travelling into a fault, right: typical measured response [9]

When the experiment shown in Fig. 2 was repeated at different shaft speeds, it was found that the spacing of the two impulses did not change, meaning that they were not directly linked to the size of the fault. A series of tests was then planned on a different rig, with the possibility of being run over a wider speed range, to show the effects of both speed and fault size. The results of this paper are based primarily on those tests.

2 Test Equipment and Measurements

A set of measurements was carried out on a bladed disk test rig at the Vibration and Acoustics Lab at UNSW. The test rig is designed to develop models and techniques for monitoring the health of turbomachine blades. It has 19 flat blades attached to a disk, which is mounted on a shaft. The shaft is supported by two self-aligning, double row ball bearings (NACHI 2206 GK), which are mounted on sleeves and are contained within plummer blocks. The test rig is driven by a motor, which is coupled to the test rig via a 1:1 ratio multi-rib V belt. The motor speed can be controlled via a VVVF (variable voltage and frequency) drive.

Notch faults were introduced into the inner race of one row of the double-row ball bearing to simulate spalls. This was performed using electric spark erosion and generated a gap in the inner race with a rectangular cross-section as shown in Fig. 5. Vibration signals were collected using an accelerometer positioned on the top of the non drive end plummer block above the defective bearing. The 10s (655,360 sample) signals were sampled at 65.536 kHz. A once-per-rev tachometer is placed next to the coupling to facilitate order tracking.

Different sizes of the fault were to be tested at different speeds to develop algorithms enabling the detection of the size of the fault regardless of the speed. Currently, only two sizes have been tested. Later tests will comprise larger faults and also outer race faults.

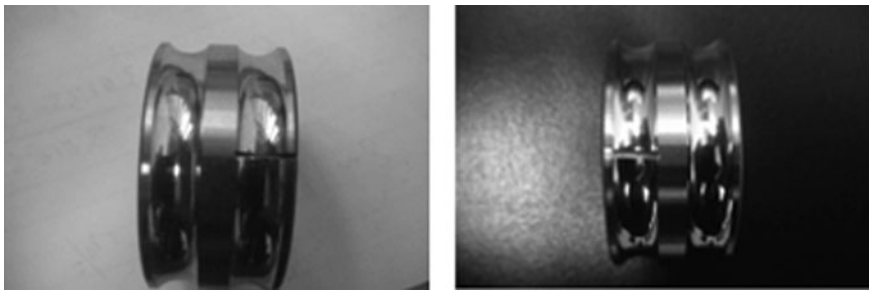

Fig. 5 The two fault sizes tested in this study (left) 0.6 mm, (right) 1.1 mm

3 Measurement Results and Analysis

In some of the first measurements made comparing the results with the two sizes of notch, it was discovered that the difference in fault size was not manifested in the separation of two impulses as in Fig. 2. Figure 6 shows a typical comparison of the raw signals.

The signal processing problem therefore consists in enhancing and isolating these two different events, so that their separation can be measured. It is evident that the impact event is more energetic than the entry event, and comprises a wider frequency range, so the first step was to prewhiten the signals using AR methods, with the result (residual signal) shown in Fig. 7. Prewhitening applied to bearing signals is described in Sawalhi and Randall [10]. It consists in using linear prediction to generate the predictable part of a signal via an autoregressive (AR) model, the difference from the measured signal (the residual) containing noise and unpredictable nonstationarities (of interest here) both with a white spectrum. It is clear that this increases the relative energy of the entry event, but the two events are still different in frequency content.

As illustrated in Fig. 8, a number of steps were then enacted to make the two events more similar, then convert each to a positive pulse so as to measure the spacing between them.

The multi-resolution analysis under (c) consists of a wavelet analysis using complex Morlet wavelets with 1/1 octave bandwidth. Morlet wavelet analysis (specifically for the wavelet kurtogram) is described in Sawalhi and Randall [1], with references.

The wavelet analysis was performed over five octaves (scales) and the one was chosen which made the entry and exit impulses most similar in strength. In Fig. 9, this is seen to be the octave band centered on 3.3 kHz in Fig. 9c, for the same case as the large fault in Figs. 6 and 7.

Hilbert transform methods were then used to obtain the squared envelope of the selected signal, giving a pair of pulses, whose separation represented the fault size. The procedure used is the same as that proposed for envelope analysis in Ho and

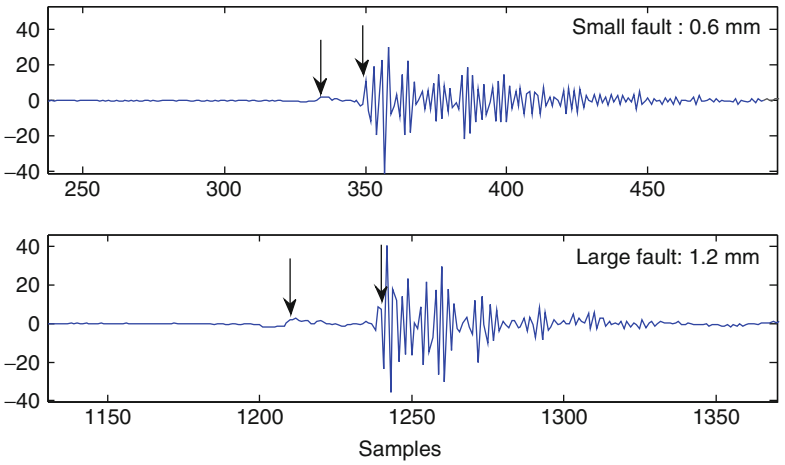

Fig. 6 Comparison of the raw accelerometer signals for the short (0.6 mm) and extended (1.1 mm) faults: (left arrow) step at entry, (right arrow) impact at exit

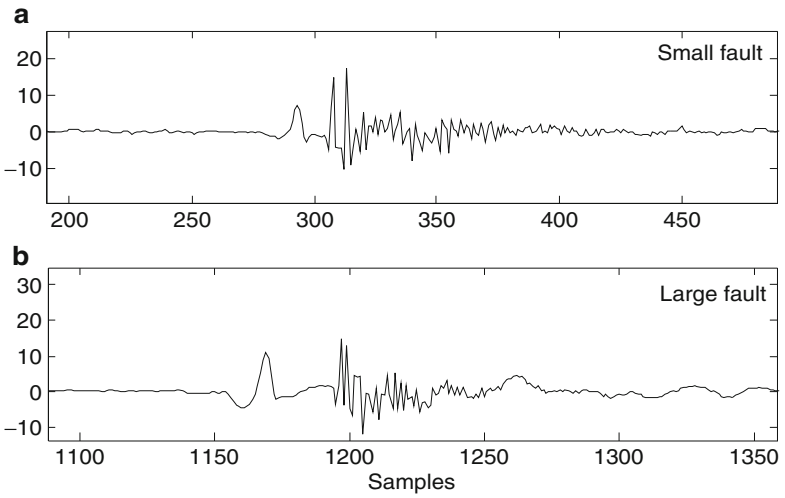

Fig. 7 Application of prewhitening to the raw signals

Randall [3]. The result of the whole procedure of Fig. 8 on a typical signal (large fault at 1,200 rpm) is given in Fig. 10.

The separation could of course have been measured manually for a number of occurrences, and then averaged, but an automated method was sought that would include averaging as part of the procedure. The procedure decided on is illustrated in Fig. 11 with two alternatives.

It was found that MED applied at this stage gave sharper pulses with a better defined separation. The cepstrum was applied to measure the pulse separation, as

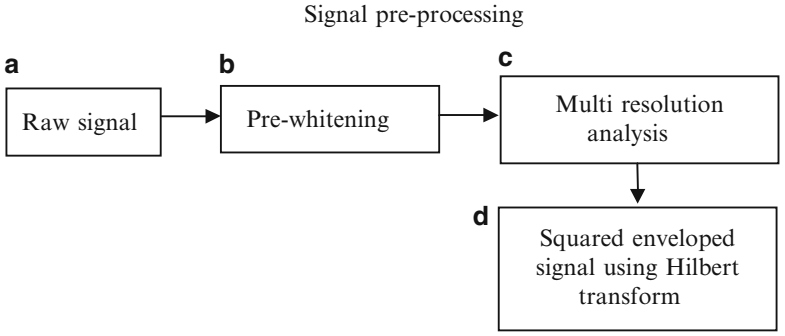

Fig. 8 Signal pre-processing to obtain positive pulses for the entry and exit events

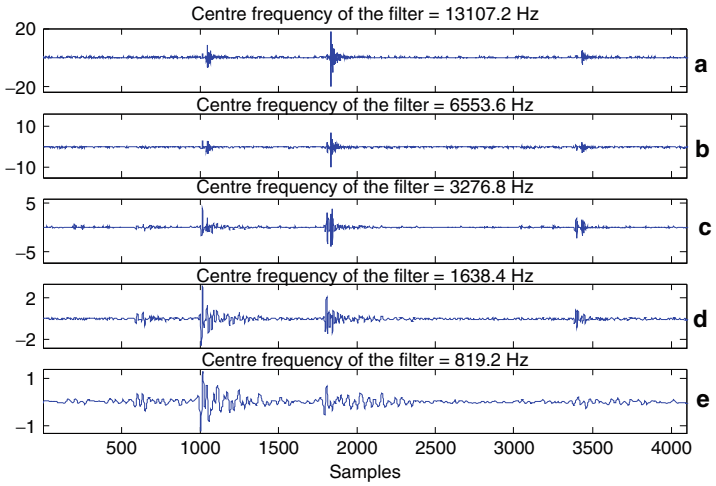

Fig. 9 Effect of multi-resolution analysis using 1/1 octave Morlet wavelets with centre frequency (**a**) 13,107 Hz (**b**) 6,554 Hz (**c**) 3,277 Hz (**d**) 1,638 Hz (**e**) 819 Hz

this gives a result not so dependent on the frequency content (than for example the autocorrelation function). The cepstrum is the inverse Fourier transform of the log spectrum [11], where the latter can include the phase as imaginary part (giving the "complex cepstrum") or just the log amplitude (giving the "real cepstrum" or "power cepstrum"). The power cepstrum is best in this case as the second pulse (the "echo") is sometimes larger than the first, giving problems with the phase.

Echoes add a periodic structure to the log amplitude spectrum, whose frequency spacing is the reciprocal of the echo delay time [8]. One advantage of using the power cepstrum is that it can be based on the averaged power spectrum, giving an average over several realizations. On the other hand the averaging can also be done over the individual power cepstra of each realization, and both methods were tried and compared here, as shown in Figs. 11 and 12.

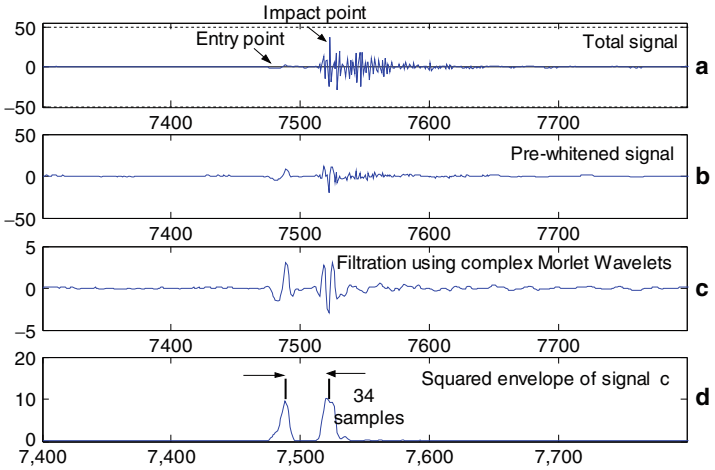

Fig. 10 Result of complete pre-processing procedure of Fig. 9

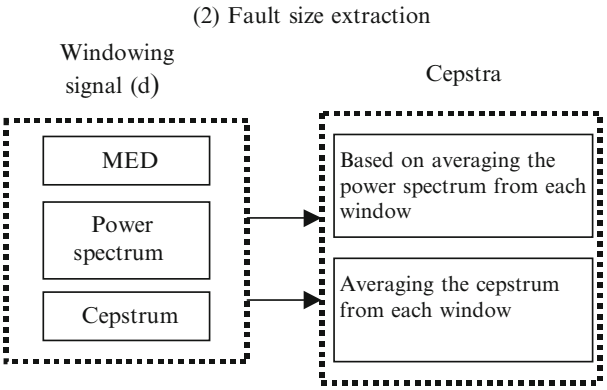

Fig. 11 Post-processing procedure to determine averaged fault size estimate

Because these results are for an inner race fault, the signals are amplitude modulated once per rev as the fault passes through the load zone (see, e.g., Fig. 9), and when the load is light or zero, the pulses are not generated clearly. For this reason, a threshold was set at the stage after application of MED to select only those impacts with reasonable excitation. This was done by eye, but corresponded in general to about 20% of the maximum peak size. Each pulse pair was selected by a window of total length about 80% of the spacing between the pairs (corresponding to the ball pass frequency). This window had a uniform section about 1/3 of the total and centered on the pulse pair, and a half Hanning taper at each end. The number then averaged was typically of the order of 100. Figure 12 shows a comparison of the two methods illustrated in Fig. 11, for a particular example. In this case the power spectrum average gave a slightly better result.

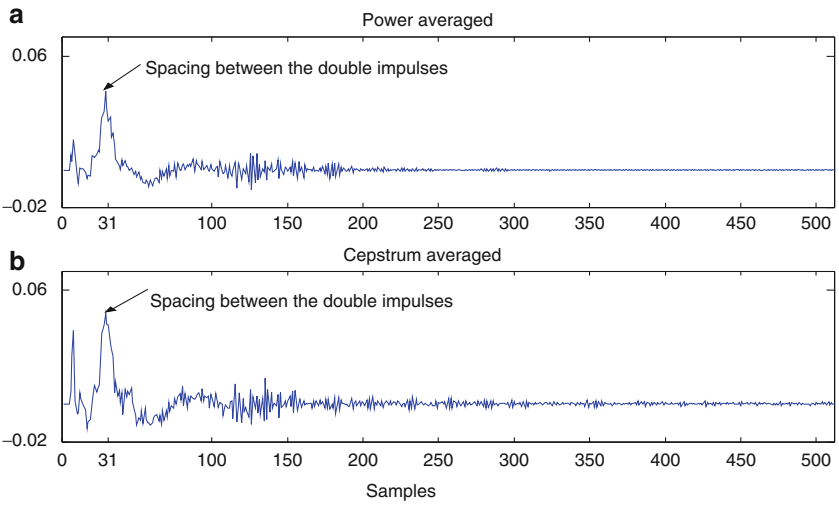

Fig. 12 Comparison of the two methods of obtaining an averaged estimate of fault size, (upper) averaged in the power spectrum, (lower) averaged in the cepstrum

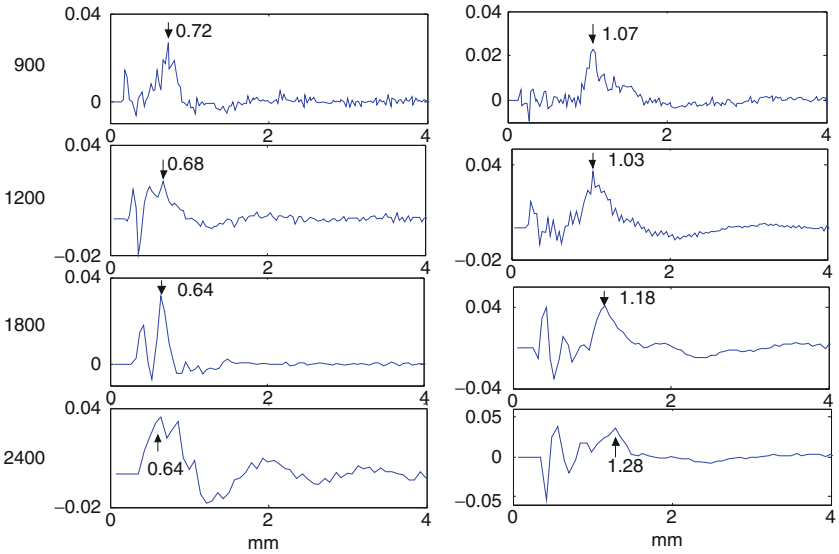

Fig. 13 Results of fault size estimation for the two fault sizes over a range of speeds

This procedure was repeated for the two fault sizes, and the four speeds, 900, 1,200, 1,800 and 2,400 rpm, and the results are shown in Fig. 13. Note that the x-axis is scaled directly in mm, rather than the time (or sample number) scale used hitherto. For the larger fault, and slower speed, the results are quite clear, but it can be seen

that the smallest fault size studied (0.6 mm) is about at the limit of measurability, in particular at high speed, but even the 1,200 rpm result has problems. For the 1.1 mm fault all results are reasonably clear, though that at the highest speed of 2,400 rpm is on the borderline. It is presumed that results for even larger faults will be clearer, but this will be investigated in future studies.

4 Discussion and Conclusion

This study has shown that the acceleration response from entry into a spall-like fault in a bearing race, and exit from it, are very different, with the first being a low frequency step response, and the second a broadband impulse response. To measure the spacing between these events, so as to get an estimate of the fault size, it is necessary to apply signal processing so as to make them more similar. This has been achieved by first pre-whitening, using AR methods, so as to balance the low and high frequency energy, followed by octave band wavelet analysis to allow selection of the best band (or scale) to balance the two pulses with similar frequency content. The squared envelope was next generated using Hilbert transform methods, and sharpened using MED. Finally, the power cepstrum could be used to find the average separation of the two pulses over a number of realizations, and this was found to agree well with the actual fault size. The demonstration has so far been for inner race faults, but will be applied to the simpler case of outer race faults in the future. Future work will also apply the methods to real, naturally generated spalls in bearings.

Acknowledgements This research was supported by the Australian Defence Science and Technology Organisation (DSTO) through the Centre of Expertise in Helicopter Structures and Diagnostics at UNSW.

References

1. Sawalhi, N., Randall, R.B.: Semi-Automated Bearing Diagnostics – Three Case Studies. Comadem Conference, Faro, Portugal, June (2007)
2. Darlow, M.S., Badgley, R.H., Hogg, G.W.: Application of high frequency resonance techniques for bearing diagnostics in helicopter gearboxes, US Army Air Mobility Research and Development Laboratory, Technical Report: 74–77 (1974)
3. Ho, D., Randall, R.B.: Optimisation of bearing diagnostic techniques using simulated and actual bearing fault signals. Mech. Syst. Signal Process. **14**(5), 763–788 (2000)
4. Antoni, J., Randall, R.B.: The spectral kurtosis: application to the vibratory surveillance and diagnostics of rotating machines. Mech. Syst. Signal Process. **20**(2), 308–331 (2006)
5. Antoni, J.: Fast computation of the kurtogram for the detection of transient faults. Mech. Syst.Signal Process. **21**, 108–124 (2007)
6. Wiggins, R.A.: Minimum entropy deconvolution. Geoexploration, Elsevier Sci. Publ. **16**, 21–35 (1978)
7. Sawalhi, N., Randall, R.B., Endo, H.: The enhancement of fault detection and diagnosis in rolling element bearings using minimum entropy deconvolution combined with spectral kurtosis. Mech. Syst. Signal Process. **21**, 2616–2633 (2007)

8. Dowling, M.: Application of non-stationary analysis to machinery monitoring. IEEE paper, 0-7803-0946-4/93, 159–162 (1993)
9. Epps, I.K., McCallion, H.: An Investigation into the Characteristics of Vibration Excited by Discrete Faults in Rolling Element Bearings. Annual Conference of the Vibration Association of New Zealand, Christchurch (1994)
10. Sawalhi, N., Randall, R.B.: Spectral Kurtosis Enhancement using Autoregressive Models. ACAM Conference, Engineers Australia, Melbourne (2005)
11. Randall, R.B.: Frequency Analysis, 3rd edn. Bruel & Kjaer, Naerum, Denmark (1987)

Cracked Rotating Shafts: Typical Behaviors, Modeling and Diagnosis

N. Bachschmid, P. Pennacchi, and E. Tanzi

Abstract Cracks can develop in rotating shafts and can propagate to relevant depths without affecting consistently the normal operating conditions of the shaft. In order to avoid catastrophic failures, accurate vibration analyses have to be performed for crack detection. Identification of crack location and depth is possible by means of model based diagnostic approach, provided that the model of the crack and the model of the cracked shaft dynamical behavior are accurate and reliable. Typical dynamical behavior of cracked shafts is shown and tests for detecting cracks are presented. The modeling of cracks is described in the paper, the simulation of the dynamical behavior of cracked shaft is shown and numerical results are compared to experimental results. All effects of cracks on the vibrations of rotating shafts are analyzed and some results of a numerical sensitivity analysis of the vibrations to the presence and severity of the crack are shown. Finally the model based identification procedure is described and some results in crack identification in position and depth are shown.

Keywords Cracks · Cracked shafts · Rotor-dynamics · Experimental behavior · Cracked shaft modeling · Crack identification

1 Introduction

One of the most common incipient losses of structural integrity is the development and propagation of cracks in mechanical structures. Cracks may propagate from some small imperfections on the surface of the body or inside the material, are most likely to appear in correspondence of high stress concentration, may be generated by fretting corrosion (in case of shrink fitted connections) and are apparently favored by wet and corrosive environments. Thermal stresses and thermal shocks are also

N. Bachschmid (✉), P. Pennacchi, and E. Tanzi
Department of Mechanical Engineering, Politecnico di Milano,
Via La Masa 1, 20156 Milano, Italy
e-mail: nicolo.bachschmid@polimi.it

K. Gupta (ed.), *IUTAM Symposium on Emerging Trends in Rotor Dynamics*,
IUTAM Bookseries 25, DOI 10.1007/978-94-007-0020-8_37,

responsible for generating high local stress intensity factors, which can cause the initiation of a crack and its propagation. Once a crack, although small, has appeared, high stress and strain intensity factors will develop at the crack tip and allow the crack to propagate deeper, even if the external loads are not changing.

The development and propagation of transverse cracks in rotating shafts is not as uncommon in industrial machinery as one could imagine, but generally the cracked shafts have been removed from service before the occurrence of a catastrophic failure. The obvious difficulty in inspecting a rotating shaft during the operation of the machines makes the detection of cracks in these structures much more difficult than in static (non-rotating) structures. Therefore symptoms are needed that can be easily measured (typically vibrations in correspondence of the bearings of the machine) and that are able to indicate clearly the presence of a crack in a rotating shaft.

A very rich literature has been produced in the last decades, mainly focused on crack modeling using the fracture mechanics approach applied to simple Jeffcott rotors, with the purpose to show, with analytical or semi-analytical approach, linear and non linear behavior, instability and several "side-effects". A rather complete state of art review has been published by Dimarogonas [1], and some topics that were not completely covered or analyzed have been presented in Bachschmid and Pennacchi [2]. Not always these results can be transferred to industrial machinery. Very few experimental results of industrial machinery have been presented in literature and these have never been compared to simulated results, with only one or two exceptions.

The aim of this paper is to present typical dynamical behavior of cracked rotating shafts, to describe the modeling applied to real power plant machinery, to analyze all the effects due to the presence of a crack on the vibrations and finally to present some results in model based crack detection. A complete analysis of all these aspects and something more is going to be presented in a book to be published by Springer [3].

2 Typical Cracked Shaft Dynamical and Static Behavior

When a horizontal cracked shaft is rotated slowly and its static deflections are measured in several locations along its axis, it will be found that the different harmonic components of the periodically changing deflection, mainly the once (1X) and the twice per revolution (2X) components, have linear distribution along the axis with a maximum in correspondence of the crack. This is the effect of the local flexibility change introduced by the crack, which "breaths" or changes gradually 1X from closed to the open situation and back again to the closed situation. Depending on the angular position of the crack during the rotation, the static bending moment due to the weight forces the crack to open or to close. When the shaft is rotating, e.g., at rated speed, then 1X and 2X vibrations are excited by the crack, which are superposed to the 1X vibrations due to residual unbalances and bow, and to the 2X vibrations caused by residual stiffness axial asymmetries (that occur mainly in 2-poles generators). Therefore a propagating crack produces increasing changes in 1X and 2X vibration behavior: components may increase or decrease, depending on

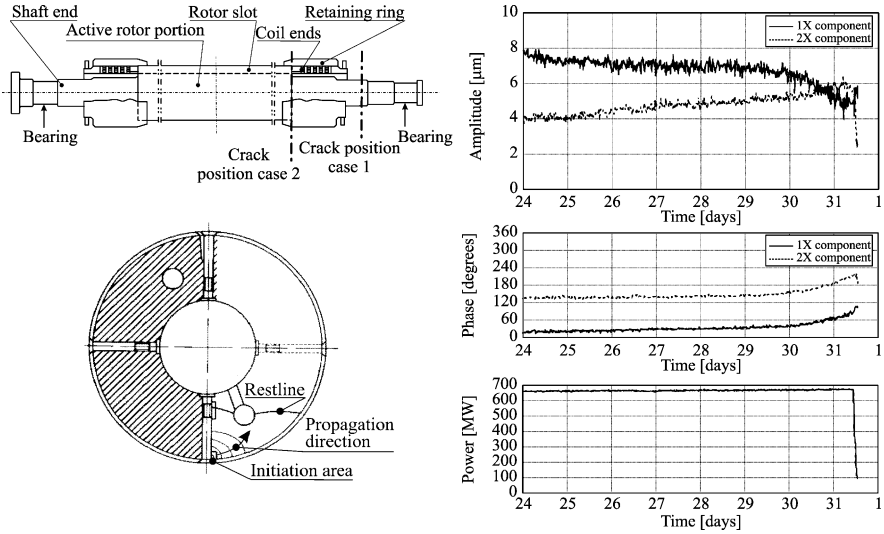

Fig. 1 The occurrence of a deep crack in a generator: trend of 1X and 2 X vibrations measured in one bearing and of output power during the last days of operation, before shut down and inspection

the relative position of crack and unbalance (for 1X component) and on that one of crack and residual axial un-symmetry. An interesting result is shown in Fig. 1 (from Nilsson [4]), where 1X and 2X trends in the last days of operation of a 2-poles generator are shown: vibration levels are very low, 1X is decreasing, 2X is slowly increasing and phases of both components are changing.

These symptoms have been sufficient to convince the plant manager to stop and inspect the machine; the position and severity of the crack affecting the shaft, discovered after removal of the shaft, are also shown in Fig. 1.

When the vibrations in the bearings are measured during a run-down transient of the unit then 1X resonances at critical speeds as well as 2X resonances at secondary critical speeds (at rotating speeds that are half the value of critical speeds) are excited. These are symptoms that strengthen the suspicion of a crack. Figure 2 shows the Bode plots during the run-down before the inspection of a cracked generator, measured in one bearing: also in this case the crack had already propagated to roughly 50% of the section. Vibration amplitudes at critical speeds are in this case very high indicating a critical situation. Also here the shaft was removed just in time.

Another interesting effect of a crack is that it introduces thermal sensitivity into the rotor: during heating transients (shaft "skin" heating), crack lips close reducing crack induced vibrations; during cooling transients, crack lips open and vibrations increase. By means of this thermal sensitivity of cracked shafts in almost two shafts (one of a HP steam turbine, as reported in Passleva and Pira [6] and one of a generator, as reported in Lapini et al. [7]) cracks have been found.

Once the shaft has been removed from service, it can be inspected and/or subject to tests in order to confirm the presence of a crack and to define its location and

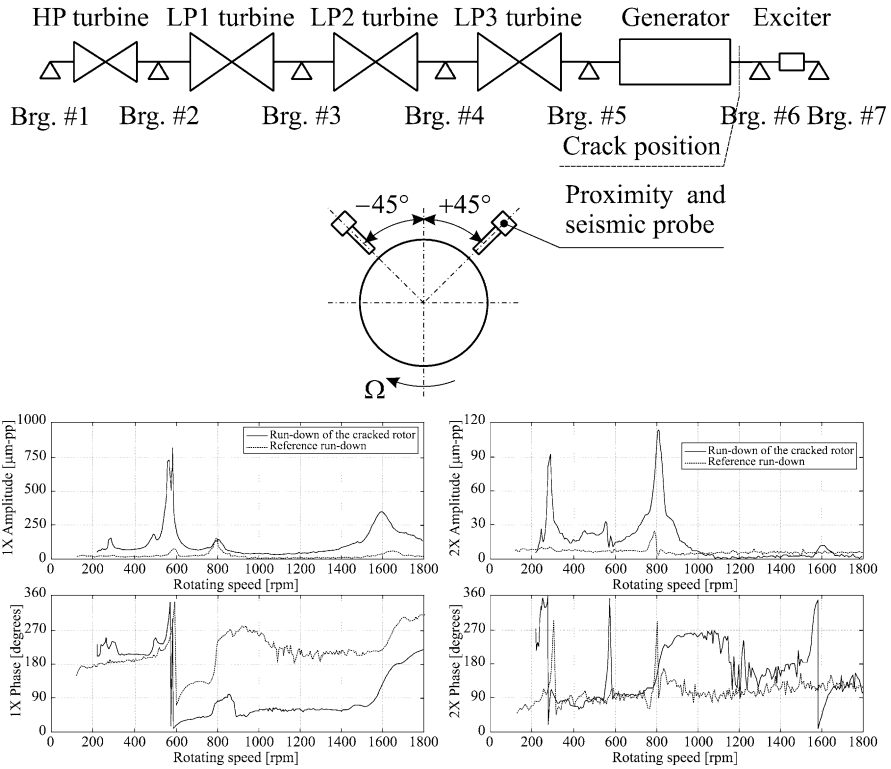

Fig. 2 Bode plots of 1X (left) and 2X (right) vibration components in the generator bearing during a run-down of the deeply cracked rotor compared to a previously recorded run down of the uncracked shaft (from Sanderson [5])

extension. Non-destructive tests like *dye-penetrant* can be used first for detecting surface cracks (as shown in Fig. 3), but when nothing can be found on the surface, the presence of the crack can be confirmed by a *static test*, with accurate deflection measurements during one revolution of the shaft, or by *dynamic tests* with natural frequency measurements in different angular positions of the horizontal shaft.

Due to crack breathing (opening and closing) the shaft stiffness changes between a maximum (closed crack) and a minimum (open crack), consequently also static deflection and natural frequencies change. However deep cracks often generate only a few percent change in stiffness and still less in frequency; moreover this value depends strongly on the position of the crack and can be much smaller.

Finally accurate *ultrasonic (US) inspection*, preferably from inside of hollow shafts, can detect position and size of cracks that are not recognizable from rotor surface. These tests and the final US inspection allowed to confirm the presence and to define position and depth of a crack in a generator that had already propagated to more than 50% of the section, without appearing on the surface. Figure 4 shows the crack surface after generator rotor dismantling and cutting.

Fig. 3 Surface crack revealed by dye penetrant inspection

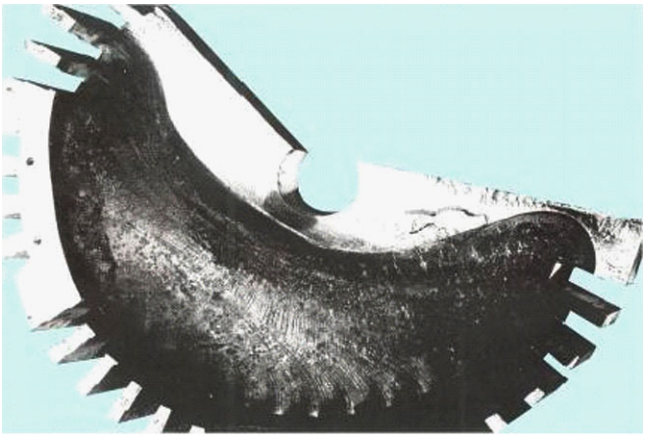

Fig. 4 This crack could be revealed only by means of US inspection from internal hole: photo shows cracked rotor slice (after cutting)

3 Modeling

The simulation of static and dynamic behavior of rotating cracked shaft requires the modeling of several phenomena: (i) first *breathing behavior* modeling, (ii) then crack induced local variable, breathing dependent *stiffness reduction modeling*, and (iii) finally rotating shaft-line with variable stiffness static and *dynamic behavior modeling*. Almost all authors used Strain Energy Release Rate (SERR) approach, which models accurately the additional flexibility due to open cracks, but is unable

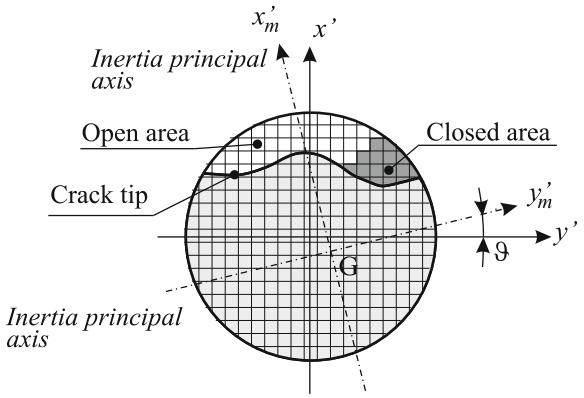

Fig. 5 Numerical breathing simulation

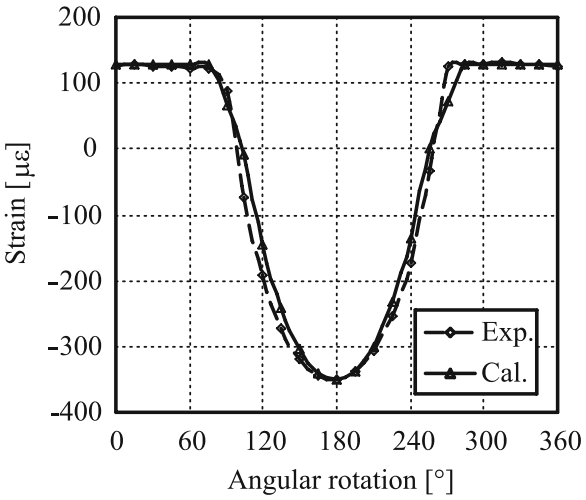

Fig. 6 Closure effect

to model accurately the flexibility changing related to breathing. The authors have developed a method to evaluate breathing and, using breathing results, to calculate the changing stiffness of a cracked element. Both breathing and stiffness changing have been validated with non-linear (due to contact between crack lips) 3D calculation for many different crack shapes and depths.

Cracked surface is discretized (as shown in Fig. 5) and open and closed crack surfaces are evaluated by considering actual loads on the shaft (weight and dynamic loads). Experimental tests have also validated the breathing model and have shown that the *crack closure* effect, which holds the crack closed unless the bending moment overcomes a threshold load and which affects obviously the breathing, can be accounted for with the model, as shown in Fig. 6, where measured axial strains on crack lips due to bending load are compared to calculated ones.

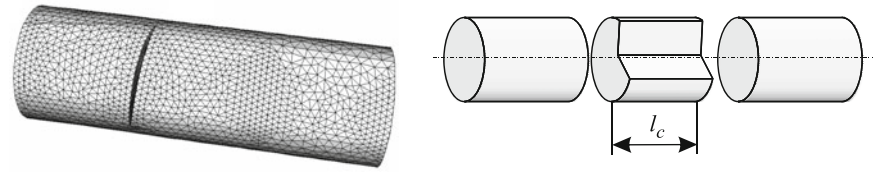

Fig. 7 3D model for breathing and deflection evaluation (left) and equivalent beam model (FLEX approach) for static and dynamic behavior evaluation (right)

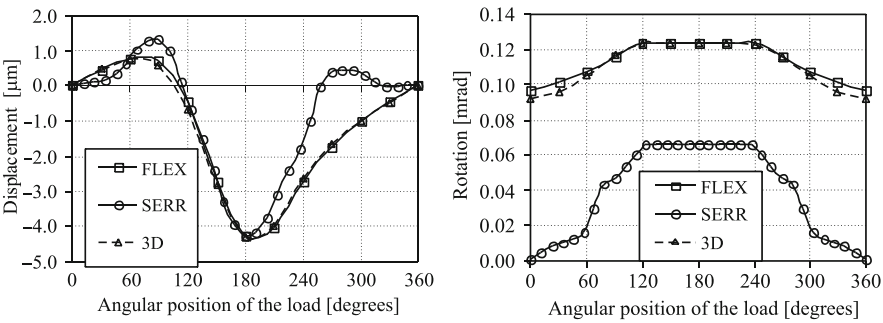

Fig. 8 Deflections of a test beam with 50% crack loaded with bending and torsion: comparison among different models: FLEX is more accurate than SERR, compared to 3D model

Breathing and flexibility have been evaluated using 3D models as shown in Fig. 7 (left) and the flexibility has been simulated by means of the equivalent beam with a changing reduced section (according to breathing results during one revolution) and with suitable length (to fit the 3D results), as represented in Fig. 7 (right).

This method, which has been called FLEX, is described in detail in Bachschmid et al. [8] and has shown excellent accuracy if compared to other methods. This is shown e.g., in Fig. 8, where the SERR approach had been modified for taking account of true breathing: the boundary between open and closed crack surface has been considered as crack tip in order to apply SERR approach. This is a rough estimation, because the strain-stress behavior of the open/closed boundary is certainly different from the crack tip behavior. Moreover the SERR approach cannot account for the friction stresses caused by bending induced normal stresses on the crack surface: this might produce some errors in torsion behavior. Figure 8 shows static bending and torsion deflections of a test specimen loaded with bending and torsion, due only to the crack. FLEX results are rather close to 3D results.

The stiffness of the cracked element, calculated by means of FLEX, taking account of actual breathing defined by static and dynamic loads, will depend on the angular position of the crack with respect to the weight induced bending moment and to the actual dynamic bending moment due to the dynamic loads induced vibration. The stiffness of the shaft is then composed by a mean stiffness $[\mathbf{K}_m]$ and

a variable part $[\Delta\mathbf{K}(\Omega t, \mathbf{x})]$, where Ω is the rotating speed and $\mathbf{x}$ is the vibration vector:

$$[\mathbf{K}] = [\mathbf{K}_m] + [\Delta\mathbf{K}(\Omega t, \mathbf{x})] \tag{1}$$

The dependence of stiffness on the vibration $\mathbf{x}$ makes the problem of crack induced vibration calculation non-linear.

The stiffness matrix $[\mathbf{K}]$, along with mass matrix $[\mathbf{M}]$, damping matrix $[\mathbf{C}]$ and gyroscopic matrix $[\mathbf{Gyr}]$ of the finite element model of the shaft-line, are on the left hand side of the dynamic equation of the system:

$$[\mathbf{M}]\ddot{\mathbf{x}} + ([\mathbf{C}] + [\mathbf{Gyr}]\Omega)\dot{\mathbf{x}} + ([\mathbf{K}_m] + [\Delta\mathbf{K}(\Omega t, \mathbf{x})])\mathbf{x} = \mathbf{F}\,\mathrm{e}^{\mathrm{i}n\Omega t} + \mathbf{W} \tag{2}$$

where $\mathbf{F}$ is the vector of rotating excitations (with $n = 1$) or of nth harmonic excitations and $\mathbf{W}$ is the vector of stationary weight forces. Equation (2) must be integrated in the time domain. If the shaft is horizontal and heavy, as it occurs in most industrial machinery, then the static bending moment normally prevails over the dynamic loads: in this case the stiffness depends only on the angular position, becomes periodical and can be expanded in a Fourier series. Equation (2) becomes:

$$[\mathbf{M}]\ddot{\mathbf{x}} + ([\mathbf{C}] + [\mathbf{Gyr}]\Omega)\dot{\mathbf{x}} + \left([\mathbf{K}_m] + \sum_j [\Delta\mathbf{K}_j]\,\mathrm{e}^{\mathrm{i}j\Omega t}\right)\mathbf{x} = \sum_n \mathbf{F}\,\mathrm{e}^{\mathrm{i}n\Omega t} + \mathbf{W} \tag{3}$$

By splitting $\mathbf{x}$ in static and dynamic components $\mathbf{x} = \mathbf{x}_s + \mathbf{x}_d$ and substituting the value of the static component $\mathbf{x}_s = [\mathbf{K}_m]^{-1}(\mathbf{W} + \mathbf{F}_0)$, where $\mathbf{F}_0$ is the vector of static forces that are calculated by means of the iterative procedure shown below, we get:

$$[\mathbf{M}]\ddot{\mathbf{x}}_d + ([\mathbf{C}] + [\mathbf{Gyr}]\Omega)\dot{\mathbf{x}}_d + [\mathbf{K}_m]\mathbf{x}_d = \sum_n \mathbf{F}_{e_n}\,\mathrm{e}^{\mathrm{i}n\Omega t} - \sum_j [\Delta\mathbf{K}_j]\,\mathrm{e}^{\mathrm{i}j\Omega t}\,(\mathbf{x}_s + \mathbf{x}_d) \tag{4}$$

The last term of Eq. (4) is the equivalent crack force vector. Assuming $\mathbf{x}_d = \sum \mathbf{x}_n \mathrm{e}^{\mathrm{i}n\Omega t}$ (with $n = 1, 2, 3\ldots$), Eq. (4) can be solved in the frequency domain using the harmonic balance approach and an iterative procedure for calculating the different harmonic components of the vibration $\mathbf{x}_n$.

From the iterative procedure applied to the equivalent crack force vector in Eq. (4), it can be shown that the equivalent crack force amplitudes are given by a sum of terms:

$$\mathbf{F}_n = [\Delta\mathbf{K}_n]\mathbf{x}_s + \sum \frac{1}{2}[\Delta\mathbf{K}_j]\mathbf{x}_i \text{ with } i \neq j \text{ and } |i \pm j| = n \tag{5}$$

Also a static force will be obtained in the form $\mathbf{F}_0 = \sum \frac{1}{4}[\Delta\mathbf{K}_i]\mathbf{x}_i$. These forces, called *crack forces*, excite the vibrations of the cracked shaft.

The procedure, which must be repeated for each different rotating speed, is very fast compared to the cumbersome non-linear approach with time domain integration: the vibrations during a speed transient can be evaluated in a few minutes compared to many hours of computing time for the non-linear approach.

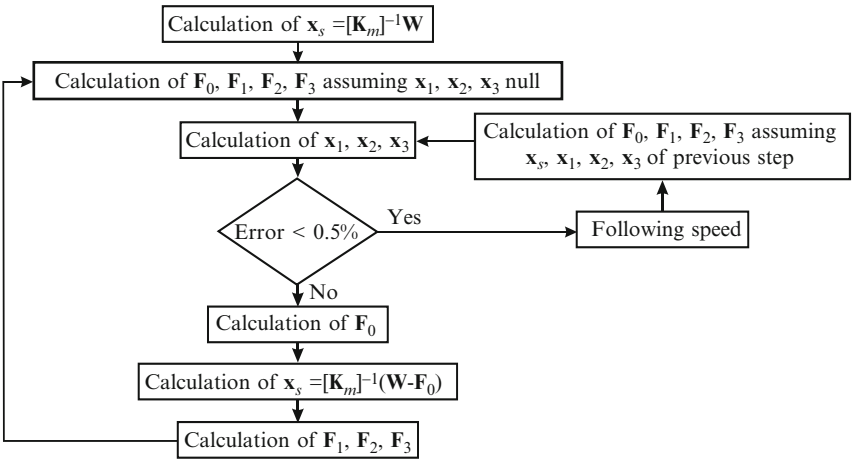

Fig. 9 Flow chart of the iterative procedure used to evaluate the cracked rotor response

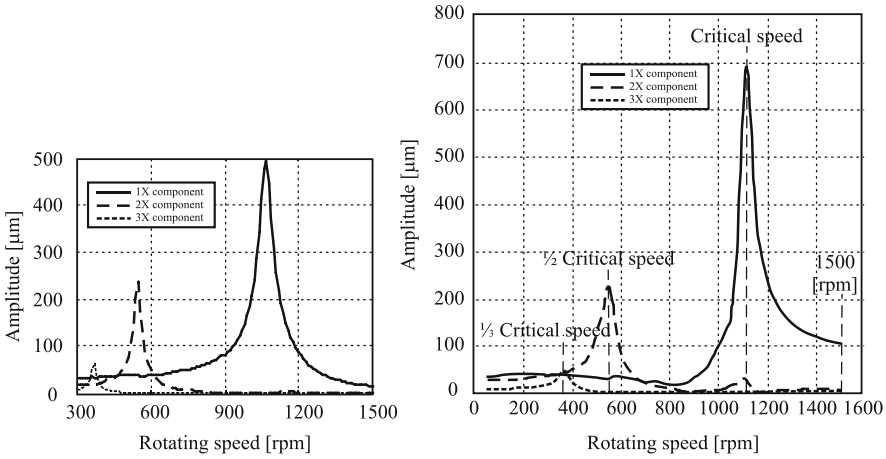

Fig. 10 Vibration components due to a crack (depth 41%), measured at the cracked shaft section

Figure 9 shows the iterative procedure, used for several simulations. Figure 10 shows experimental results obtained on a test-rig, represented in Fig. 11, compared to simulated results obtained with the above models and methods.

Experimental and simulated 2X and 3X components, which are due to crack only, show very good agreement. Experimental 1X component, due to original shaft unbalance (and/or bow) combined with crack, cannot be fitted by simulation due to crack only. From the diagnostic point of view it is essential to know the crack excited vibration levels that can be measured in the bearings of a machine. Therefore above procedure has been used for a sensitivity analysis of crack excited vibrations in an industrial turbo-group to crack depth and position.

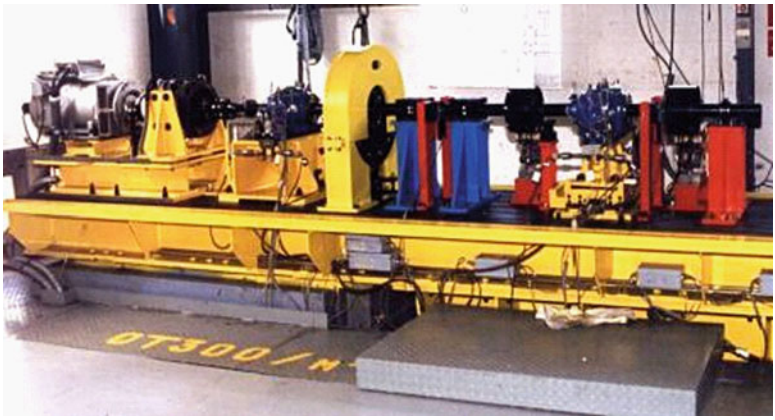

Fig. 11 EURoPE test-rig of Électricité de France (EDF-AMA) equipped with two oil-film bearings and one composed shaft, allowing the insertion of different cracked specimen. Shaft diameter $d = 70\,\text{mm}$

4 Sensitivity Analysis

The dependence of 1X, 2X and 3X horizontal and vertical components on the crack depth, which shows crack propagation effects, is presented in Fig. 12.

The diagrams are related to cracks with rectilinear tip. The components, calculated at low rotating speed in order to neglect all dynamic effects, are referred to the same reference deflection and show the intensity of crack force excitation at increasing depth. Crack force excitation depends not only on the depth by means of $[\Delta\mathbf{K}]$ as shown in Eq. (5), but also on $\mathbf{x}_s$ and on $\mathbf{x}_i$. Here $[\Delta\mathbf{K}]$ is primarily the variation of bending stiffness (as it can be shown that the variation of shear stiffness is negligible), also $\mathbf{x}_s$ and $\mathbf{x}_i$ are mainly static and dynamic angular deflections. Now $\mathbf{x}_s$ is proportional to the value of the static bending moment, and $\mathbf{x}_i$ is calculated iteratively by applying the force Eq. (5) to the shaft. Also $\mathbf{x}_i$ is proportional to the static bending moment, if we neglect dynamic magnification factors (at low rotational speed) and the presence of other exciting forces.

Therefore at low speed, *crack forces* are proportional to the static *bending moment* value in correspondence of the crack position.

Vibration excitation due to cracks depends not only on its depth, but also on its position: crack forces in positions where the bending moment is high (typically at midspan between bearings) will be much higher than crack forces that develop in positions close to bearings or to couplings.

The presence of other exciting forces shown in Eq. (4) may change the intensity of the crack forces. At higher speed, crack forces will be different due to dynamic amplification factors of $\mathbf{x}_i$ that depend on the rotational speed and on the position of the crack. Finally the total response of the shaft that will be measured (generally in correspondence of the bearings), will obviously be different from the statical one,

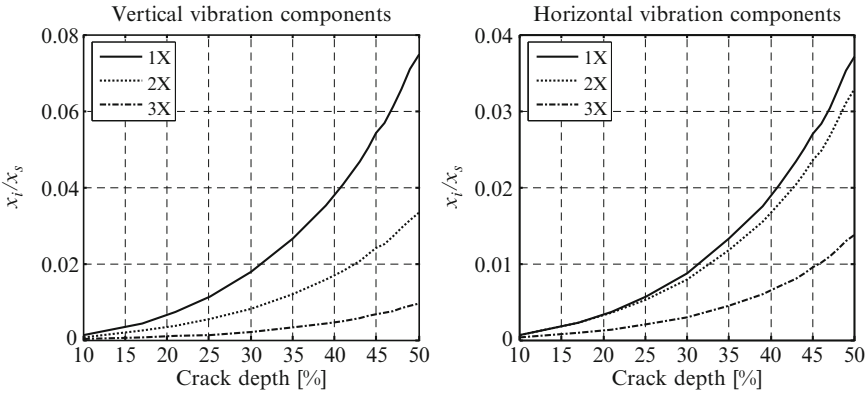

Fig. 12 Sensitivity analysis of crack induced vibration components to crack depth

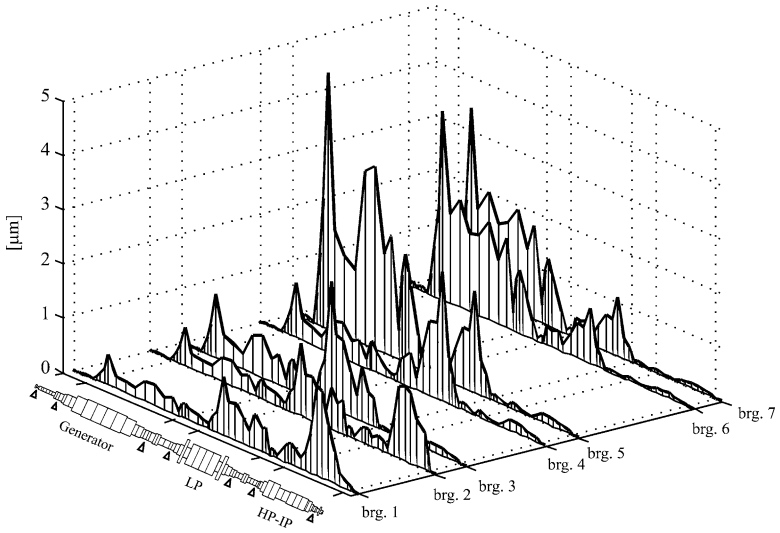

Fig. 13 Sensitivity analysis of crack induced 2X vibrations to the position of the crack along the shaft-line of a turbo-generator unit: crack depth is 25%

due to the dynamic behaviour of the shaft, which again depends on speed and on position of the measuring station.

Figure 13 shows the sensitivity of the 2X component, which is the *most significant symptom* of the presence of a crack, measured in the bearings of a turbo-generator unit, to the positions of crack along the shaft-line, at rated speed (3,000 rpm).

The diagram represents the effect of the position of the crack (with respect to the bending moment distribution on the shaft) and the effect of the dynamic behaviour at the rotational speed both in correspondence of the crack position and in

correspondence of the bearing position. Due to the small amplitudes, significant vibrations can be measured in some bearings only for cracks that have developed in particular few positions. This demonstrates the difficulty in early detection of cracks at rated speeds. During run down transients, resonances can be crossed where dynamic magnification factors amplify the vibration amplitudes as shown e.g., in Fig. 2, allowing better detection of cracks in early propagation stage.

Other symptoms of cracks in rotating shafts are torsion and axial vibrations.

The *axial vibration* excited by means of a bending-axial 1X coupling mechanisms is very weak and can hardly be used as a symptom, also because axial natural frequencies are generally far from the rotational frequency. *Torsion vibrations* are also weakly excited by bending-torsion coupling mechanism, but due to large static torque at rated speed (combined to the variable torsion stiffness) parametric excitation occurs that produces high torsion vibrations when 1X or 2X frequency is close to a natural torsion frequency (because torsion natural frequencies are lightly damped and allow high dynamic amplification factors).

Some authors claim that *non-linear effects* might be significant, allowing instability and even chaos to arise. An analysis [8] made on a very lightly damped shaft, with a low bending load and a rather high unbalance, running close to its first critical speed (so that breathing and stiffness depends mainly on the vibration itself), has shown that the main effect is that linear analysis underestimates vibration amplitudes in general. Only for certain combinations of crack and unbalance, when unbalance forces the crack to open during almost the complete revolution, the instability typical of axially unsymmetrical shafts occurs, when the rotating speed is in between the two main natural frequencies. This is shown in Fig. 14.

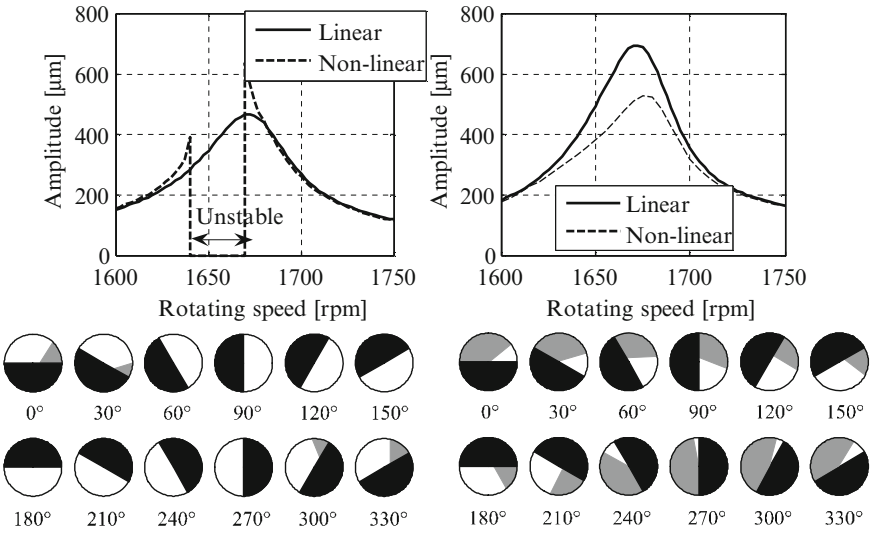

Fig. 14 Unstable (left) and stabilized – by means of suitable unbalance – (right) behavior, compared to linear behavior and related breathing mechanism

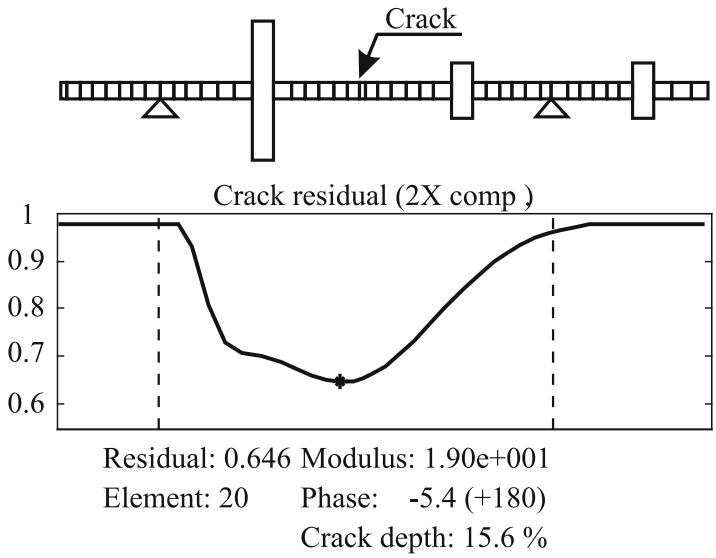

Fig. 15 EURoPE test-rig with 14% deep slot and crack: relative residual of the fault identified from 2X component by means of model based identification method in the frequency domain

Many efforts have been dedicated to the *diagnosis* of cracks in rotating machinery. A wide review on the state of the art is presented in Sawicki et al. [9].

The described model can be used for *model based* crack position and depth identification. The authors have developed a method based on a least square approach in the frequency domain, described in Pennacchi et al. [10], which uses the measured vibrations in the bearings of the machine (during a run-down transient), compared to the simulated ones, which proved to be robust, reliable and accurate. Position and depth are identified with high accuracy, as shown e.g. in Fig. 15. In each element of the finite element model of the shaft the value of a *residual* is calculated that is proportional to the squared difference between measured vibrations at the different rotating speeds and calculated results. The calculated results are obtained with the crack force value applied to the considered element that minimizes the squared difference between measured and simulated vibrations. In the position where the residual has the *minimum value*, there is the most probable location of the crack. The corresponding crack force allows to determine the crack depth from value of $[\Delta \mathbf{K}]$ using only the first term of Eq. (5), assuming a crack with rectilinear depth.

5 Conclusions

In the paper, the dynamic behavior of cracked shafts, including the accurate modeling of the breathing mechanism, is described with the aid of a simplified original model. The excellent agreement with the results obtained using refined 3D models

and with experimental tests validates the proposed model. Numerical simulations allow establishing how sensitive are the vibrations of industrial machinery to the presence of a transverse crack of different depths that could develop in different positions along the shaft-line. Also additional symptoms are analyzed using the proposed model. It is finally shown that measured vibrations could be used successfully for identifying with excellent accuracy, crack position and depth by means of a model based diagnostic approach.

This paper aims to contribute substantially to understand cracked rotor behavior, which is an extremely important step for avoiding catastrophic failures.

References

1. Dimarogonas, A.D.: Vibration of cracked structures: a state of the art review. Eng. Fract. Mech. **55**, 831–857 (1996)
2. Bachschmid, N., Pennacchi, P.: Special issue: crack effects in rotordynamics. Mech. Syst. Signal Process. **22**, 761–762 (2008)
3. Bachschmid, N., Pennacchi, P., Tanzi, E.: Cracked rotors: a survey on static and dynamic behaviour including modelling and diagnosis. Springer (2010)
4. Nilsson, L.R.K.: On the vibration behaviour of a cracked rotor. IFToMM International Conference on Rotordynamic Problems in Power Plants, pp. 515–524. Rome, Italy, (1982)
5. Sanderson, A.F.P.: The vibration behaviour of a large steam turbine generator during crack propagation through the generator rotor. IMechE International Conference on Vibrations in Rotating Machinery, pp. 263–273. Bath, UK, paper C432/102 (1992)
6. Passleva, G., Pira, G.: Cracked shaft vibration sensitivity to steam temperature variations. IFToMM International Conference on Rotordynamic Problems in Power Plants, Rome, Italy (1982)
7. Lapini, G.L., Zippo, M., Bachschmid, N., Collina, A., Vallini, A.: Experimental tests and model based calculations for the diagnosis of a crack in a 320 MW generator. CISM/IFToMM Symposium Proc., pp. 87–97. Udine, Italy (1993)
8. Bachschmid, N., Pennacchi, P., Tanzi, E.: Rotating shafts affected by transverse cracks: experimental behaviour and modelling techniques. Int. J. Mater. Struct. Integrity **1**, 71–116 (2007)
9. Sawicki, J.T., Gyekenyesi, A.L., Baaklini, G.Y.: Modal-based diagnostics of cracked rotors. Proceedings of SPIE, Int. Soc. Opt. Eng. **4704**, 133–138 (2002)
10. Pennacchi, P., Bachschmid, N., Vania, A.: A model based identification method of transverse cracks in rotating shafts suitable for industrial machines. Mech. Syst. Signal Process. **20**, 2112–2147 (2006)

Fault Identification in Industrial Rotating Machinery: Theory and Applications

P. Pennacchi, A. Vania, and N. Bachschmid

Abstract Fault identification plays a fundamental role in reducing maintenance costs and off-line time of industrial rotating machinery. In the past years the authors developed methods for fault identification of rotating machines. This paper summarizes this experience and introduces the necessary theory in the first part. A model based method in the frequency domain is briefly described and identification algorithms are presented, including also robust estimate. The last section of the paper is devoted to the presentation of some case histories of industrial machines, affected by common faults like unbalances, misalignment, rotor-to-stator rub and bow.

Keywords Fault identification · Model based methods · Rotor dynamics · Unbalance · Misalignment · Rotor-to-stator rub · Bow

1 Introduction

Even if the fine distinction between *fault diagnosis* and *fault identification* could seem significant only under a semantic point of view, it is actually important also from practical standpoint.

Once the condition monitoring system of an industrial rotating machine has signalled alarms and the stored time histories – especially those related to machine vibrations – these are analyzed to assess the presence of impending faults, there are two possibilities:

- the first is to simply classify the fault type and this task is here defined with the term *diagnostics*;
- the second possibility is a more complete solution: the fault is not only classified but is also localized in a specific position of the machine and its quantitative evaluation is given, if it is pertinent. In this case, the process is more precisely termed as *identification*.

P. Pennacchi (✉), A. Vania, and N. Bachschmid
Department of Mechanical Engineering, Politecnico di Milano,
Via La Masa, 1, 20156 Milano, Italy
e-mail: paolo.pennacchi@polimi.it

K. Gupta (ed.), *IUTAM Symposium on Emerging Trends in Rotor Dynamics*,
IUTAM Bookseries 25, DOI 10.1007/978-94-007-0020-8_38,

Diagnostics of fault does not exclude identification of fault, but may be propaedeutic to the last one. The possibility to localize the fault along the shaft train is a fundamental characteristic of identification, because it allows focused operations during the maintenance. Thus fixing costs and off-line time are reduced. Moreover, also a quantitative estimation of fault severity is possible: this can be relevant when the unbalance of a machine should be evaluated or the depth of a transverse crack should be estimated. In other cases this is less important, for instance when a rub is identified: the corresponding position along the axis is the main goal.

2 Model Based Identification in Rotor Dynamics

Model based identification of faults in rotor systems is essentially a MIMO inverse problem. Some examples have been presented in the time domain [1], but since many types of faults of rotating machinery have effect on a few harmonic components (as well known in literature starting from Sohre's chart), the harmonic balance approach is preferable. The method is fully described in Pennacchi et al. [2] and requires the assembling of the complete model of the machine composed of the rotor, the bearings and the supporting structure.

The rotor is modelled by means of finite beam elements with four degrees of freedom (d.o.f.s) per node including gyroscopic effect, whilst the bearing by means of linearized dynamic stiffness coefficients, see respectively Lalanne and Ferraris [3] and Someya [4] for details. The supporting structure can be considered rigid or, more accurately, modelled by means of pedestals or modal representation [2, 5–7]. Also *common faults* of rotating machinery can be modelled by means of *equivalent excitation* systems [1, 28], therefore these terms are considered as synonymous.

With regard to the experimental data, *additional vibrations* are used. These are obtained by means of the vector difference of the vibrations in the faulty condition and in a reference condition. Under the hypothesis of linearity of the system, which is satisfied in many cases of common faults in rotating machinery, the additional vibrations are caused by the developing faults only. Further discussion about this topic can be found in Pennacchi et al. [8].

2.1 Definition of the Equivalent Excitations

In industrial rotating machines, the measuring points of the vibration along the shaft are few and the transducers are normally placed in correspondence of the bearings. The consideration of further measuring planes is practically impossible, therefore methods that reconstruct modal shapes of the rotor cannot be used. Measured vibrations are the multiple outputs (MO) of the system. So, if the system of dynamic equations of a rotating machine, with several d.o.f.s, is considered:

$$[\mathbf{M}]\,\ddot{\mathbf{x}}_t + [\mathbf{C}]\,\dot{\mathbf{x}}_t + [\mathbf{K}]\,\mathbf{x}_t = \mathbf{F}(t) \tag{1}$$

it seems difficult to identify the changes due to the developing fault in the matrices [**M**], [**C**] and [**K**], which are of high order, from measurement of vibration $\mathbf{x}_t$ in only few measuring planes along the shaft. The right hand side (r.h.s.) external forces $\mathbf{F}(t)$ are composed of the weight (which is known) and of the original unbalance and bow (which are unknown). The system parameter changes caused by the fault are indicated as $[d\,\mathbf{M}]$, $[d\,\mathbf{C}]$ and $[d\,\mathbf{K}]$, and Eq. (1) becomes:

$$([\mathbf{M}] + [d\,\mathbf{M}])\,\ddot{\mathbf{x}}_t + ([\mathbf{C}] + [d\,\mathbf{C}])\,\dot{\mathbf{x}}_t + ([\mathbf{K}] + [d\,\mathbf{K}])\,\mathbf{x}_t = \mathbf{W} + (U + M_u)\,e^{i\,\Omega t} \tag{2}$$

If the system is considered as linear, then the total vibration $\mathbf{x}_t$ is due to two superposed effects:

$$\mathbf{x}_t = \mathbf{x}_1 + \mathbf{x} \tag{3}$$

The first vibration vector $\mathbf{x}_1$ is the pre-fault vibration, which is due to the weight **W** and the unknown unbalance force $U\,\mathrm{e}^{\mathrm{i}\Omega t}$ and unbalance moment $M_u\,\mathrm{e}^{\mathrm{i}\Omega t}$. The second vibration **x** is due to the developing fault and is also called additional vibration. The vibration component **x** may be obtained by calculating the vector differences of the actual vibrations (due to weight, original unbalance, bow and fault) and the original vibrations measured, in the same operating conditions as in a reference case (rotation speed, flow rate, power, temperature, etc.) before the fault was developing. Recalling the definition of the pre-fault vibration $\mathbf{x}_1$, the following equation holds:

$$[\mathbf{M}]\,\ddot{\mathbf{x}}_1 + [\mathbf{C}]\,\dot{\mathbf{x}}_1 + [\mathbf{K}]\,\mathbf{x}_1 = \mathbf{W} + (U + M_u)\,e^{i\,\Omega t} \tag{4}$$

which substituted in Eq. (2) with Eq. (3) gives:

$$[\mathbf{M}]\,\ddot{\mathbf{x}} + [\mathbf{C}]\,\dot{\mathbf{x}} + [\mathbf{K}]\,\mathbf{x} = -[d\,\mathbf{M}]\,\ddot{\mathbf{x}}_t - [d\,\mathbf{C}]\,\dot{\mathbf{x}}_t - [d\,\mathbf{K}]\,\mathbf{x}_t \tag{5}$$

The r.h.s. of Eq. (5) can be considered as a system of equivalent external excitations $\mathbf{F}_f(t)$ that force the fault-free system to have the change of the additional vibration **x** that is due to the developing fault only:

$$[\mathbf{M}]\,\ddot{\mathbf{x}} + [\mathbf{C}]\,\dot{\mathbf{x}} + [\mathbf{K}]\,\mathbf{x} = \mathbf{F}_f(t) \tag{6}$$

A rather complete overview of the equivalent forcing systems to the most common faults in rotating machinery is presented in Platz et al. [1] and Bachschmid et al. [9]. Note that in Eq. (6) system parameters are time invariant and known, but depending on the operating speed. Moreover, using this last approach, the problem of fault identification is reduced to external force identification by means of parity equations. This fact reduces sensibly the number of unknowns to be identified.

Harmonic balance is applied to Eq. (6):

$$\left[-(n\Omega)^2[\mathbf{M}] + i\,n\Omega[\mathbf{C}] + [\mathbf{K}]\right]\,\mathbf{X}_n = \mathbf{F}_{f_n} \tag{7}$$

Since the system is considered linear, the effect of m faults developing simultaneously can be considered by means of the superposition of the effects for each harmonic component:

$$\mathbf{F}_{fn} = \sum_{i=1}^{m} \mathbf{F}_{fn}^{(i)} \tag{8}$$

These excitations are the multiple inputs (MI) of the system. Moreover, the mth fault acts on a few d.o.f.s of the system, therefore the vector $\mathbf{F}_{fn}^{(k)}$ is not a full-element vector, which is convenient to be represented by means of:

$$\mathbf{F}_{fn}^{(k)} = \left\{\mathbf{L}^{(k)}\right\} \theta^{(k)}(\Omega), \quad \theta^{(k)}(\Omega) \in \mathbb{C} \tag{9}$$

where $\left\{\mathbf{L}^{(k)}\right\}$ is the localisation vector which has all null-elements, except for the d.o.f.s to which the exciting system is applied, and $\theta^{(k)}(\Omega)$ is a complex number representing the amplitude and the phase of the fault. Obviously, as many nodes are used for the model, as much the location of the fault is accurate. For instance, the unbalance can be expressed as:

$$\begin{aligned}\mathbf{F}_{f_1}^{(k)} &= \left\{ 0 \vdots \underbrace{1\ 0\ i\ 0}_{j\text{-th rotor node}} \vdots 0 \quad \underbrace{0 \cdots 0}_{\text{foundation d.o.f.s}} \right\}^{\mathrm{T}} \cdot (mr)^{(k)}\, \Omega^2 e^{i\phi^{(k)}} \\ &= \Omega^2 \left\{\mathbf{F}_L^{(k)}\right\} \theta^{(k)}\end{aligned} \tag{10}$$

2.2 Algorithms: From Least Squares to Robust Estimation

Since the faults have to be identified not only in their severity but also in their position, the identification procedure starts by assuming the positions as known, then identifies the corresponding amplitudes and phases. All the subsequent permutations of fault number and position have to be evaluated, until the search of the faults is limited to within a specified interval of the nodes. These iterations are implemented in one loop. In the first step of the loop, all the equivalent excitations are supposed to be in the first node.

The effect on the measured d.o.f.s, due to all the exciting systems applied to the first node on the model and assumed to have unitary value ($\theta^{(k)} = 1,\ \forall k$), is the vector $\left[\mathbf{Y}_{(1,\cdots,1)}\right]$. The kth column of the vector corresponds to the effect of the kth equivalent excitation. The calculation of $\left[\mathbf{Y}_{(1,\cdots,1)}\right]$ is done first by substituting the matrix composed by all the localization vectors in the r.h.s. of Eq. (7), inverting the admittance matrix of the system $[\mathbf{Z}(\boldsymbol{\Omega})]$ and obtaining the matrix $[\mathbf{H}(\boldsymbol{\Omega})]$.

$$\mathbf{X} = [\mathbf{Z}(\boldsymbol{\Omega})]^{-1}\,\mathbf{F}_L(\boldsymbol{\Omega}) = [\mathbf{H}(\boldsymbol{\Omega})]\,\mathbf{F}_L(\boldsymbol{\Omega}) \tag{11}$$

Then, the vibrations of the d.o.f.s that are measured, are separated from all the d.o.f.s of the system, by considering only the rows of $[\mathbf{H}(\boldsymbol{\Omega})]$ corresponding to the measured d.o.f.s. The partitioned matrix $\left[\underset{\sim}{\mathbf{H}}(\boldsymbol{\Omega})\right]$ is rectangular and results:

$$\left[\mathbf{Y}_{(1,\ldots,1)}\right] = \left[\underset{\sim}{\mathbf{H}}(\boldsymbol{\Omega})\right]\left[\,\mathbf{F}_L^{(1)} \vdots \mathbf{F}_L^{(m)}\,\right] \tag{12}$$

Now the array $\boldsymbol{\theta}$ of the complex values $\theta^{(i)}$ (i.e., the amplitudes and phases) of the equivalent excitation systems applied to the first node that best fits the experimental data $\boldsymbol{\Xi}$, has to be estimated. Under a statistical point of view, a linear regression model is used, where $\boldsymbol{\theta}$ is the parameter vector to be estimated and $\mathbf{e}$ the error vector:

$$\boldsymbol{\Xi} = [\mathbf{Y}_{(1,\ldots,1)}]\,\boldsymbol{\theta} + \mathbf{e} = [\mathbf{Y}_{(1,\ldots,1)}]\left\{\theta^{(1)} \;\cdots\; \theta^{(m)}\right\}^T + \mathbf{e} \tag{13}$$

Note that Eq. (13) indicates a linear system also under a mechanical point of view, since the measured vibrations are caused by the superposition of the effects of all the excitation systems applied. The fitting of the regression model i.e., the minimization of the error, can be done with different approaches.

The traditional approach is the least squares estimate (LS), since the number of the unknown (the modules and the phases of the equivalent excitations) is less than the equations. In fact data are corresponding to several rotating speeds and each of the sets is composed by several measuring planes, while the number of the faults in practical rotor dynamic applications is one or two; the occurrence of more than two simultaneous faults is an improbable event. The objective function to be minimized is:

$$\min \sum (e_i)^2 \leftrightarrow \min \sum \left(\Xi_i - [\mathbf{Y}_{(1,\ldots,1)i}]\,\boldsymbol{\theta}\right)^2 \tag{14}$$

where $[\mathbf{Y}_{(1,\ldots,1)_i}]$ indicates the ith row of $[\mathbf{Y}_{(1,\ldots,1)}]$. By skipping well-known mathematical derivations, the general solution of Eq. (14) is obtained by means of the Moore-Penrose's inverse calculation:

$$\hat{\boldsymbol{\theta}}_{(1,\ldots,1)} = \left(\left[\mathbf{Y}_{(1,\ldots,1)}\right]^{\mathrm{T}}\left[\mathbf{Y}_{(1,\ldots,1)}\right]\right)^{-1}\left[\mathbf{Y}_{(1,\ldots,1)}\right]^{\mathrm{T}}\boldsymbol{\Xi} \tag{15}$$

The amplitudes and the phases of the complex values in the m rows of $\hat{\boldsymbol{\theta}}_{(1,\ldots,1)}$ are the identified faults in the first rotor node. Finally the *relative residual* between the experimental data and the system response due to the identified faults in the first rotor node is determined, first by obtaining the calculated response due to the identified faults in the first node:

$$\hat{\boldsymbol{\Xi}}_{(1,\ldots,1)} = \left[\mathbf{Y}_{(1,\ldots,1)}\right]\hat{\boldsymbol{\theta}}_{(1,\ldots,1)} \tag{16}$$

then calculating the difference with the experimental data and normalizing it:

$$\hat{\delta}_{r_{(1,\ldots,1)}} = \left(\frac{\left[\boldsymbol{\Xi} - \hat{\boldsymbol{\Xi}}_{(1,\ldots,1)} \right]^{*\,\mathrm{T}} \left[\boldsymbol{\Xi} - \hat{\boldsymbol{\Xi}}_{(1,\ldots,1)} \right]}{\boldsymbol{\Xi}^{*\mathrm{T}}\, \boldsymbol{\Xi}} \right)^{1/2} \tag{17}$$

The procedure is subsequently iterated for all the permutations ${}_{n_r}P_m$ of the fault number and rotor nodes. If m faults are taken into account, all the permutations of the faults and the nodes have to be considered and the set of the relative residuals is in $\mathbb{R}^m$ space. The minimum of the set indicates in each one of the m dimensions, the location of the corresponding fault and their estimation is given by the corresponding value of the m rows, Eq. (15). The closer to zero is the minimum value of Eq. (17), the better is the estimation of the faults.

Anyhow, it is well known that LS is not a robust estimate (see Huber [10] for a detailed discussion about the concept of robustness in estimate). The presence of gross or systematic errors in experimental measurements can greatly reduce the accuracy of the identification. Some different methods are available to increase the robustness of LS, the simplest of which is the use of weighted least squares (WLS). WLS has given satisfactory results when applied to real rotating machines [11, 12], but the selection of the weight should be made carefully, normally by a skilled operator.

Robust estimate can be made by means of *M-estimate* and allows selecting automatically the weights. It requires two nested loops, so it requires longer calculation time, but greatly increases the robustness and therefore the accuracy of the obtained results. The external loop is relative to the localization of the fault and it is equal to that of the LS method.

The idea is to obtain a robust estimate by replacing the objective function of Eq. (14) with another function ρ of the errors, the analytic expression of which will be introduced afterwards. The new function to be minimized is:

$$\min \sum \rho\left(e_i\right) \leftrightarrow \min \sum \rho\left(\Xi_i - \left[\mathbf{Y}_{(1,\ldots,1)_i}\right] \boldsymbol{\theta}\right) \tag{18}$$

To obtain the minimum, Eq. (18) is derived with respect to e_i and put equal to zero. The *M-estimator* of $\boldsymbol{\theta}$ based on function $\rho(\mathbf{e})$ is the vector $\widehat{\theta}$ solution of the m equations:

$$\sum \psi(e_i) \frac{\partial e_i}{\partial \theta^{(j)}} = 0 \quad \text{for} \quad j = 1, \ldots, m \tag{19}$$

Now, a *weight function* is defined as:

$$w(e_i) = \frac{\psi(e_i)}{e_i} \tag{20}$$

so that Eq. (19) is rewritten as:

$$\sum w(e_i)\, e_i \frac{\partial e_i}{\partial \theta^{(j)}} = 0 \quad \text{for} \quad j = 1, \ldots, m \tag{21}$$

If the weights $w(e_i)$ are constant, the system Eq. (21) corresponds to that obtained to solve the problem:

$$\min \sum w\left(e_i\right) e_i^2 \tag{22}$$

which is actually a weighted least squares WLS with weights $w(e_i)$. However, the weights depend on the errors, the errors depend on the estimated excitations and the estimated excitations depend on the weights. To solve this vicious circle and justify the assumption of constant weights in the passage from Eq. (21) to Eq. (22), the second and inner loop is introduced by means of the use of an iterative solution, called *iterated re-weighted least squares* (IRLS) [13]. This way the weights are considered as constant during iteration:

1. The initial estimate of the amplitudes and phases of the excitation systems is selected using the results of least squares estimate, obtained by using Eq. (15).
2. At iteration t, the errors $e_i^{(t-1)}$ and the associated weights $w_i^{(t-1)}$ are calculated from the previous iteration.
3. The new weighted least squares estimate at iteration t is:

$$\widehat{\theta}_{(1,\ldots,1)}^{(t)} = \left(\left[\mathbf{Y}_{(1,\ldots,1)}\right]^{\mathrm{T}} \left[\mathbf{W}^{(t-1)}\right] \left[\mathbf{Y}_{(1,\ldots,1)}\right]\right)^{-1} \left[\mathbf{Y}_{(1,\ldots,1)}\right]^{\mathrm{T}} \left[\mathbf{W}^{(t-1)}\right] \boldsymbol{\Xi} \tag{23}$$

where:

$$\left[\mathbf{W}^{(t-1)}\right] = \operatorname{diag}\left[w_i^{(t-1)}\right] \tag{24}$$

Steps 2 and 3 are iterated until convergence of the values of $\widehat{\theta}_{(1,\ldots,1)}$ is achieved upon a stated criterion. The inner loop is then ended and the relative residual for the first rotor node, obtained with M-estimate, is calculated similar to that in case of least squares.

Several ρ functions have been proposed in statistical literature and a complete survey is reported in Zhang [14]. Some tests on different ρ functions have been performed by the author Pennacchi [15] to select the most suitable one for mechanical application and Huber's function presented satisfactory performance. The resulting ρ, ψ and w functions are:

$$\rho(e_i) = \begin{cases} e_i^2/2 & |e_i| \le c \\ c\left(|e_i| - c/2\right) & |e_i| > c \end{cases}; \psi(e_i) = \begin{cases} e_i & |e_i| \le c \\ c \ \operatorname{sgn}(e_i) & |e_i| > c \end{cases};$$

$$w(e_i) = \begin{cases} 1 & |e_i| \le c \\ c/|e_i| & |e_i| > c \end{cases} \tag{25}$$

The tuning parameter c is set so that $c = 1.3450\,\hat{\sigma}$, where $\hat{\sigma}$ is the scale parameter of the error distribution, see Pennacchi [15] for further details.

3 Case Histories

Some case histories related to common faults affecting rotating machinery are presented hereafter. All the cases are very shortly described and full details can be found in the references. Case histories of cracked shaft are not reported because these are discussed in another specific paper [16].

3.1 Unbalance

The case presented is actually the identification of a known balancing mass and was one of those employed in order to have a comparative evaluation of the performance of the methods. In particular, results obtained using simply LS and M-estimate are compared. The machine is a 125 MW gas turbo generator, employed in combined cycle plants, operating at rated speed of 3,000 rpm. Model of the machine has not been tuned. The balancing mass of 0.270 kg with phase 52° was placed on the balancing plane immediately close to turbine intake, which corresponds to node 39 of the model. Additional vibrations are available in the speed range 3–3,000 rpm and no pre-emptive data selection is made. Robust method has in this case greater accuracy than LS, as shown in Fig. 1. Further details can be found in Pennacchi et al. [17].

3.2 Misalignment

The following case study is related to the heavy misalignment between a gas turbine of 100 MW combined cycle power unit and its load gear shaft. Complete description is presented in Pennacchi and Vania [18]. The misalignment eventually caused the

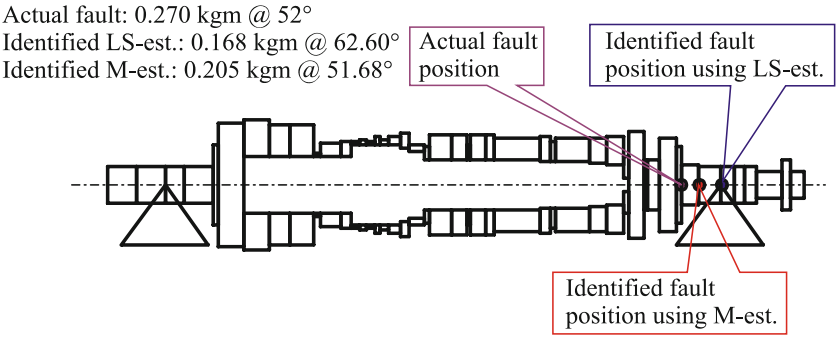

Fig. 1 Results of balancing mass identification on a gas turbine (generator and connecting shaft omitted for clarity)

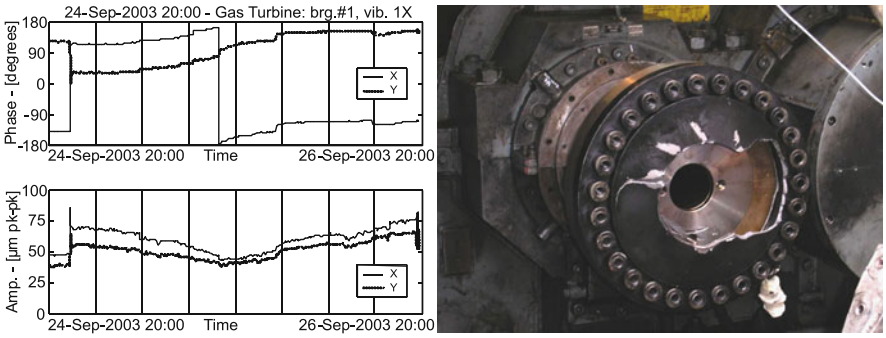

Fig. 2 1X vibration time history measured in the bearing on the compressor side of the gas turbine and diaphragm coupling after failure caused by heavy misalignment

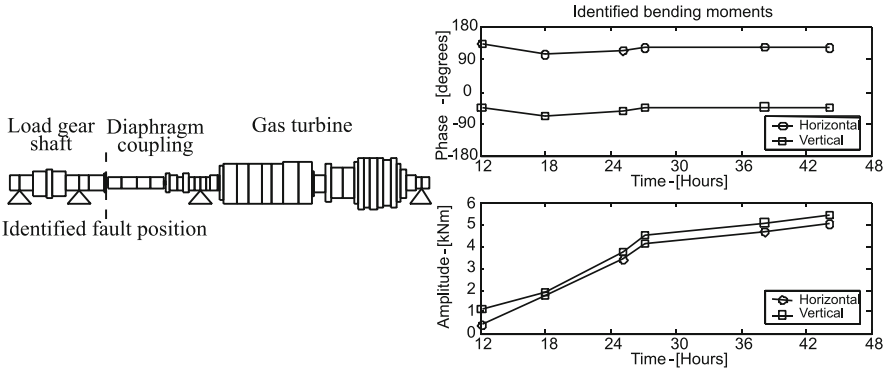

Fig. 3 Position of the identified fault and equivalent bending moment trend during the observation interval

cracking and the failure of the diaphragm coupling. Figure 2 shows the time history of the 1X vibration with some sudden increase that indicates the gradual coupling cracking and the close up of the broken diaphragm on the gearbox side.

Machine model and additional vibrations were used to evaluate if the impending fault could be promptly detected and the failure avoided. The equivalent bending moments were identified in the correct diaphragm and showed increasing trend that would have warned about the forthcoming failure (see Fig. 3).

3.3 Rotor to Stator Rub

Rotor to stator rub is a very common topic in rotor dynamics but case histories related to real machines are seldom presented and analyzed. Two cases are briefly introduced in this paper and in detail in Pennacchi and Vania [19] and

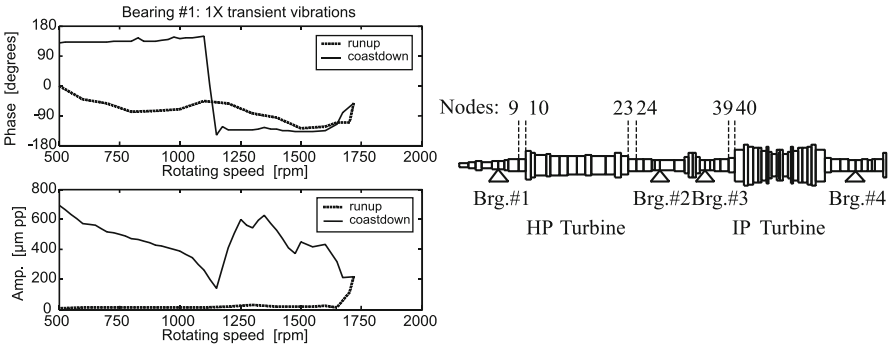

Fig. 4 1X vibration during the aborted run-up and the following coast-down. Position of the identified bending moments on HP and IP turbine

Bachschmid et al. [20] respectively. The first occurred in a 320 MW steam unit whose machine-train was composed of a high pressure steam turbine (HP), an intermediate pressure turbine (IP), two low pressure turbines (LP1, LP2) and a generator. Figure 4 shows 1X vibrations measured at bearing #1 during the first start up of the unit that occurred at the end of a large planned maintenance during which the machine-train was subjected to important overhauls. At 1,720 rpm the amplitude of the HP turbine vibrations increased owing to the effects caused by the first balance resonance. However, in a very short time the vibration levels reached abnormal values. At the same time, the amplitude of the 2X and 3X vibrations showed a quick and noticeable increase.

Since the shaft vibrations showed clear symptoms of a machine fault, the run up was immediately aborted. The levels of the vibrations measured at bearing #1 significantly increased and they exceeded 700 µm-pp in the final part of this coast down. Using the method described in the paper, the position of the rubs were identified on both sides of the HP turbine and on one side of IP turbine, by means of equivalent bending moments (see Fig. 4). The visual inspection of the machine train carried out after this aborted start-up confirmed the occurrence of heavy rubs: the major damages were found in the HP turbine while the IP turbine was affected by minor but not negligible damages.

The second case is again related to a 320 MW steam unit but with rotor train composed of a high-intermediate pressure turbine (HP–IP), a low pressure turbine (LP) and a generator. At the end of a long scheduled outage the machine was started-up, but the first run-up was aborted just before reaching the operating speed. During the coast-down operators decided to avoid the machine passing through the resonance and increased the rotating speed up to 1,848 rpm in order to straighten the rotors. During this partial run-up the 1X vibrations were quite different from those occurred during the first phase of the coast-down and during the final coast-down 1X vibrations increased progressively and reached 307 µm-pp in bearing #2 (see Fig. 5). The two cross-sections where the bending moments have been identified are near the mid-span of the rotor: in this zone some labyrinth seals separate the HP turbine from the IP turbine.

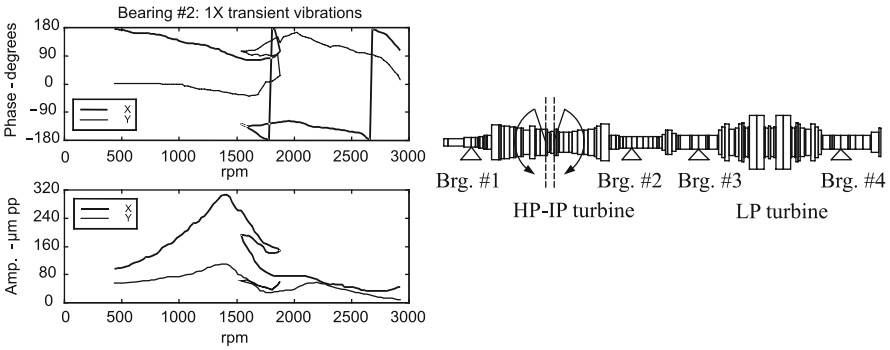

Fig. 5 1X vibration during the speed transient. Position of the identified bending moments on HP-IP turbine

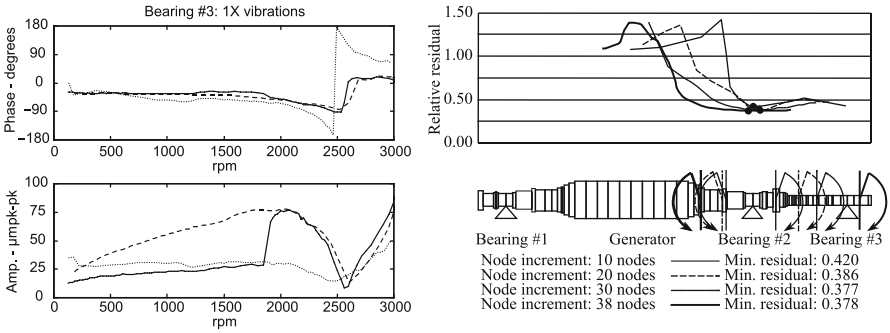

Fig. 6 1X vibration during three different speed transients. Position of the identified bending moments on HP-IP turbine

3.4 Rotor Bow

An example of extended rotor bow is reported in Pennacchi and Vania [21] using the vibrations of the generator of a 50 MW power unit. During usual planned coast-downs, in which the rotating speed dwell is performed, the change in the temperature of the copper bars and shaft induces a change in the thermal bow of the hollow part of shaft. This introduces a sort of hill in the bode plot of the 1X vibrations (solid line in Fig. 6) which is not present during the run-up (dashed line) or emergency coast-down (dotted line).

Extended bows have been modelled by applying the two opposite bending moments to couples of nodes of the FE model whose identification numbers differed significantly: increments in the node numbers of 10, 20, 30 and 38 have been considered. Shaft bows whose extension was rather large have caused very low values of the relative residual. The best results obtained with the maximum extension of the shaft bow are associated with two opposite bending moments applied to nodes of

the rotor model that are very close to the ends of the hollow part of the shaft. That is, the locations of these moments are very close to the sections at which the copper bars are constrained to the rotor. Therefore, when shaft and copper bars were subjected to a significant thermal transient, e.g., during planned coast-downs, the hollow part of the generator rotor could be subjected to a thermal bow. Then, the identification of two equivalent bending moments applied in the shaft locations above described the likely location of fault.

4 Conclusions

In this paper the state of the art of fault identification, using model based methods, in rotating machinery has been presented. The necessary theory is briefly introduced along with the necessary algorithms. Case histories of common faults of industrial rotating machines are presented in the last part.

References

1. Platz, R., Markert, R., Seidler, M.: Validation of online diagnostics of malfunctions in rotor systems. In: Proceedings of IMechE-7th Int. Conf. on Vibrations in Rotating Machinery, pp. 581–590. University of Nottingham, UK, 12–14 Sept.2000
2. Pennacchi, P., Bachschmid, N., Vania, A., et al.: Use of modal representation for the supporting structure in model based fault identification of large rotating machinery: part 1 – theoretical remarks. Mech. Syst. Signal Process. **20**, 662–681 (2006)
3. Lalanne, M., Ferraris, G.: Rotordynamics Prediction in Engineering. John Wiley & Sons Inc, Chichester, England (1998)
4. Someya, T.: Journal-Bearing Databook. Springer-Verlag, Berlin, Germany (1989)
5. Konishi, T., Allaire, P., Untaroiu, C.: Modal analysis of a large turbine-generator system with foundation effects. In: IFToMM-6th International Conference on Rotor Dynamics, pp. 846–853. Sydney, Australia, September–October 2002
6. Smart, M., Friswell, M.I., Lees, A.W., et al.: Estimating turbogenerator foundation parameters. Proc. Instn. Mech. Engrs. **C212**, 635–665 (1998)
7. Kang, Y., Chang, Y.-P., Tsai, J.-W., et al.: An investigation in stiffness effects on dynamics of rotor – bearing-foundation systems. J. Sound Vib. **231**, 343–374 (2001)
8. Pennacchi, P., Bachschmid, N., Vania, A., et al.: Use of modal representation for the supporting structure in model based fault identification of large rotating machinery: part 2 – application to a real machine. Mech. Syst. Signal Process. **20**, 682–701 (2006)
9. Bachschmid, N., Pennacchi, P., Vania, A.: Identification of multiple faults in rotor systems. J. Sound Vib. **254**, 327–366 (2002)
10. Huber, P.J.: Robust Statistics. John Wiley, New York (1981)
11. Bachschmid, N., Pennacchi, P.: Accuracy of fault detection in real rotating machinery using model based diagnostic techniques. JSME Int. J. **C46**, 1026–1034 (2003)
12. Bachschmid, N., Pennacchi, P., Vania, A., et al.: Identification of rub and unbalance in a 320MW turbogenerator. Int. J. Rot. Mach. 9:97–112 (2003)
13. Coleman, D., Holland, P., Kaden, N., et al.: A system of subroutines for iteratively reweighted least squares computations. ACM Trans. Math. Softw. **6**, 327–336 (1980)
14. Zhang, Z.: Parameter estimation techniques: a tutorial with application to conic fitting. Image Vision Comput. **15**, 59–76 (1997)

15. Pennacchi, P.: Robust estimate of excitations in mechanical systems using M-estimators – Theoretical background. J. Sound Vib. **310**, 923–946 (2008)
16. Bachschmid, N., Pennacchi, P., Tanzi, E.: Cracked rotating shafts: typical behaviors, modeling and diagnosis. IUROTOR 2009 – IUTAM Symposium on Emerging trends in Rotor Dynamics, pp. 1–12. New Delhi, India, 23–26 March 2009
17. Pennacchi, P., Vania, A., Bachschmid, N.: Increasing the robustness of fault identification in rotor dynamics by means of M-estimators. Mech. Syst. Signal Process. **21**, 3003–3029 (2007)
18. Pennacchi, P., Vania, A.: Diagnostics of a crack in a load coupling of a gas turbine using the machine model and the analysis of the shaft vibrations. Mech. Syst. Signal Process. **22**, 1157–1178 (2008)
19. Pennacchi, P., Vania, A.: Analysis of rotor-to-stator rub in a large steam turbogenerator. Int. J. Rot. Mach., 2007, 1–8 Article ID 90631 (2007)
20. Bachschmid, N., Pennacchi, P., Vania, A.: Diagnostic significance of orbit shape analysis and its application to improve machine faults detection. J. Brazilian Soc. Mech. Sci. Eng. **XXVI**, 200–208 (2004)
21. Pennacchi, P., Vania, A.: Accuracy in the Identification of a generator thermal bow. J. Sound Vib. **274**, 273–295 (2004)

Cracked Continuous Rotors Vibrating on Nonlinear Bearings

C.A. Papadopoulos, A.C. Chasalevris, and P.G. Nikolakopoulos

Abstract The dynamic behavior of cracked rotors continues to attract the interest of both designers and maintenance engineers. In this work, a continuum mechanics approach is used to simulate rotor vibration. The case of the cracked continuous rotor is examined by introducing suitable complex boundary conditions. The shaft rotates on two journal bearings that are simulated as forces acting on it and the boundary conditions are expressed accordingly. When the angular velocity passes through critical speeds, these forces become highly nonlinear. Identifications of cracking and wear of the bearing are separately investigated.

The current challenge for design engineers is to provide lighter, quieter, more efficient, compact, and stable, as well as less expensive and ecologically friendly, rotating machines, operating even in severe conditions. In other words, new targets must be seen from the following three points of view: (a) analysis and design, (b) new material technology, and (c) new production techniques.

Keywords Rotor · Shaft · Crack · Bearing · Wear · Nonlinear

1 Introduction

Rotor vibrations are expressed by the Timoshenko differential equation which includes the effects of the transmitting torque, the rotary inertia, the transverse shear and the gyroscopic moments, as described by Eshleman and Eubanks [1]. The rotating crack is modeled using the Strain Energy Release Rate (SERR) method as a function of both the crack depth and the angle of rotation. A state-of-the-art review is presented by Papadopoulos [2]. The complex boundary conditions for the rotating crack and for the bearings are also introduced by Chasalevris and Papadopoulos [3]. The rotor is supported by two journal bearings that operate in nonlinear conditions.

C.A. Papadopoulos (✉), A.C. Chasalevris, and P.G. Nikolakopoulos
Department of Mechanical Engineering & Aeronautics, University of Patras,
Patras 26504, Greece
e-mail: chris.papadopoulos@mech.upatras.gr

K. Gupta (ed.), *IUTAM Symposium on Emerging Trends in Rotor Dynamics*,
IUTAM Bookseries 25, DOI 10.1007/978-94-007-0020-8_39,

The journal bearings are modeled by two forces calculated under the validity of Reynolds equation for laminar, isothermal and isoviscous flow using the finite difference method. Highly nonlinear bearing forces are present when the rotor-bearing system operates near or at resonance. These forces affect the dynamic behavior of the rotor-bearing system, and conversely the bearing hydrodynamic functionality takes into account the dynamic properties of the entire shaft instead of the journal mobility, thus resulting in more precise journal mobility.

The main aim of the present paper is to construct an accurate continuous rotor model that is mount-bounded from the finite bearing boundary conditions, which enable importing of the entire model and provide accurate properties of nonlinear forces regardless of where or how the journal trajectories are developed. The results include time frequency analysis of the resulting time series (rotor response), rotor orbits and frequency response computation. Methods are presented for crack identification and wear assessment (using the model of Dufrane et al. [4]) by exploitation of the vibration at the bearings.

2 Continuous Model of a Cracked Rotor

In this approach, the equations of a continuous rotating shaft are used, and the boundary conditions of the rotating crack are introduced, thus enabling the continuous modeling of a cracked rotor [5]. Let us assume a uniform, homogenous and cracked rotating Timoshenko shaft (Fig. 1), with Young's modulus E, shear modulus G, density ρ, moment of inertia of the cross-section about X axis I, shear factor $k = 10/9$, length L, radius R, surface of cross section A, radius of gyration $r_0 = \sqrt{I/A}$, and Poisson ratio ν. The shaft is rotating with an angular velocity Ω, whirling with ω, and transmitting an axial torque T.

Consider also a transversely located disk in the mid-span ($x = L/2$) of the shaft of the same material, with radius R_d, mass m_d, and thickness L_d. A breath-

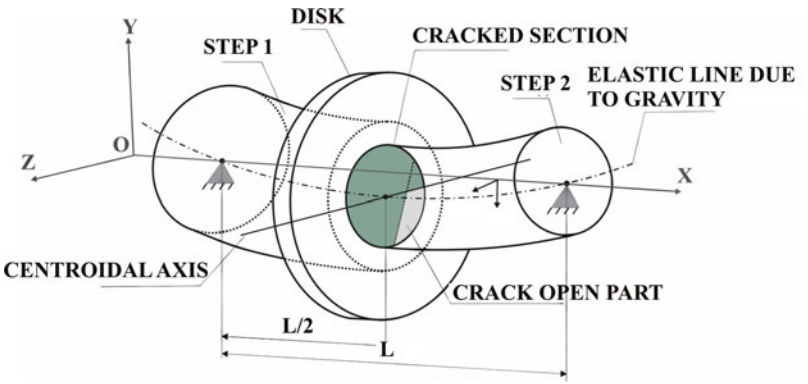

Fig. 1 Two step cracked rotor-bearing system carrying a disk

ing crack, of depth $\bar{a} = a/R$, is located at the mid-span, adjacent to the disk. If $Y(x,t)$ and $Z(x,t)$ are the vertical and horizontal responses at an axial coordinate x and time t, respectively, then by supposing the complex notation $U(x,t) = Y(x,t) + i\ Z(x,t)$, the coupled governing equation of motion is given by Eq. (1), [1, 6]:

$$\begin{aligned} E\,I\,\frac{\partial^4 U_j}{\partial x^4} - i\,T\,\frac{\partial^3 U_j}{\partial x^3} - \left(\frac{E\,I\,\rho}{k\,G} + \rho\,A\,r_0^2\right)\frac{\partial^4 U_j}{\partial x^2 \partial t^2} + 2i\,\rho\,A\,r_0^2\,\Omega\,\frac{\partial^3 U_j}{\partial x^2 \partial t} \\ + i\,\frac{T\rho}{k\,G}\,\frac{\partial^3 U_j}{\partial x \partial t^2} + \frac{\rho^2 A\,r_0^2}{k\,G}\,\frac{\partial^4 U_j}{\partial t^4} - 2i\,\frac{\rho^2 A\,r_0^2 \Omega}{k\,G}\,\frac{\partial^3 U_j}{\partial t^3} + \rho A\,\frac{\partial^2 U_j}{\partial t^2} = 0 \end{aligned} \tag{1}$$

where $j = 1$ for the first part of the shaft from the left end up to the crack and $j = 2$ for the part from the crack up to the right end (Fig. 1). Equation (1) is a complete fourth order complex partial differential equation of motion for the U_j. The solution procedure of the above equation and the usual boundary conditions are presented in [5].

For the boundary condition due to the crack the Strain Energy Release Rate (SERR) method, introduced by Dimarogonas and Paipetis [7], was applied to the calculation of compliance due to a rotating crack by Chasalevris and Papadopoulos [8]. Crack breathing could be linear with periodically varying coefficients when the weight deformation dominates the response amplitude, or nonlinear when the inverse occurs. Numerical analysis must follow the resulting bending moment in the two main directions relative to the crack in the rotating coordinate system at each time step of the integration. Afterwards, the decision of whether the crack is open, closed or partially open could be made, and the respective compliances, in the fixed coordinate system, should be used.

At the crack position if $\Theta_1(L_1,t)$ and $\Theta_2(L_1,t)$ are the complex slopes before and after the crack and $\mathbf{C}_{2x2} = [\{c_{44},\ c_{45}\},\{c_{54},\ c_{55}\}]$ is the well-known compliance matrix, then the boundary condition due to the rotating crack is described by Eq. (2):

$$\begin{aligned} &\Theta_2(L_1,t) - \Theta_1(L_1,t) = (\beta + i\,\gamma)\,M(L_1,t) + (\delta + i\,\varepsilon)\,\widehat{M}(L_1,t) && \text{open crack} \\ &\Theta_2(L_1,t) - \Theta_1(L_1,t) = 0 && \text{closed crack} \end{aligned} \tag{2}$$

where $\beta = (c_{55} + c_{44})/2, \gamma = (c_{45} - c_{54})/2, \quad \delta = (c_{55} - c_{44})/2, \quad \varepsilon = (c_{45} + c_{54})/2$, and $\widehat{M}(x,t)$ is the conjugate of $M(x,t)$.

3 Journal Bearing Support – Worn Bearing

The nonlinear fluid film forces generated by the journal bearing are derived from the solution of the Reynolds equation, which, for laminar, isothermal, and isoviscous flow, is written as Eq. (3), [9, 10]:

$$\frac{\partial}{\partial l}\left(\frac{h(\theta)^3}{6\mu}\,\frac{\partial P_{t_k}(\theta,l)}{\partial x}\right) + \frac{1}{R^2}\,\frac{\partial}{\partial \theta}\left(\frac{h(\theta)^3}{6\mu}\,\frac{\partial P_{t_k}(\theta,l)}{\partial \theta}\right) = \Omega\,\frac{\partial h(\theta)}{\partial \theta} + 2\,\frac{\partial h(\theta)}{\partial t} \tag{3}$$

In Eq. (3), the term $P_{t_k}(\theta, \ell)$ is the developed oil pressure at time t_k, μ is the lubricant viscosity, R is the journal radius, and θ is the angular coordinate relative to the attitude angle axis. The fluid film thickness $h(\theta)$ is given by Dufrane et al. [4] as in Eq. (4):

$$h(\theta) = \begin{cases} 1 + \varepsilon \cos(\theta - (\varphi - \pi)), & \text{for } 0 \le \theta \le \theta_a \,,\ \theta_b \le \theta \le \pi \\ 1 + \varepsilon \cos(\theta - (\varphi - \pi)) + \delta_h(\theta), & \text{for } \theta_a < \theta < \theta_b \end{cases} \tag{4}$$

where,

$$\delta_h(\theta) = \delta_0 - \left(1 + \cos\left(\theta - \frac{\pi}{2}\right)\right) \qquad \text{and} \begin{cases} \theta_\alpha = \dfrac{3\pi}{2} - \cos^{-1}(1 - \delta_0) \\ \theta_b = \dfrac{3\pi}{2} + \cos^{-1}(1 - \delta_0) \end{cases}$$

In previous equations, ε is the eccentricity ratio $\varepsilon = e/c_r$, φ is the attitude angle of the journal, $\dot{\varepsilon}$ and $\dot{\varphi}$ are their respective time derivatives, c_r is the radial clearance, and d_0 and $\delta_0 = d_0/c_r$ are the absolute and relative wear depths (see Fig. 2). Note that all angles are defined with respect to the coordinate system in Fig. 2. Three loads exist in each journal: a percentage of the weight W_g of the rotor, a percentage of external force E_F (here, the gravity force of the disk, $E_F = W_d$), and a percentage of the unbalance force F_u that acts in the plane of the disk. The fluid film hydrodynamic reaction in this dynamic load consists of a tangential force F_t and a radial force F_r, which consequently are functions of time. The finite difference method is used here to solve the Reynolds equation.

$$F_t = \sum_{\eta=0}^{\eta_v} \sum_{\lambda=0}^{\lambda_v} \left(P_{t_k\ \eta,\lambda} \sin(\theta_\lambda) R\, \Delta\theta\, \Delta l\right) \quad \text{and}$$

$$F_r = \sum_{\eta=0}^{\eta_v} \sum_{\lambda=0}^{\lambda_v} \left(P_{t_k\ \eta,\lambda} \cos(\theta_\lambda) R\, \Delta\theta\, \Delta l\right) \tag{5}$$

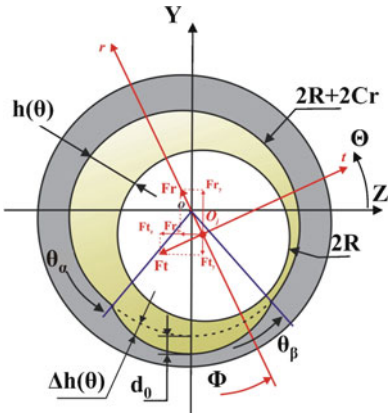

Fig. 2 Worn journal bearing. Loads and wear zone for a specific equilibrium position

Besides the previous solutions, FLUENT package was also used in order to obtain the journal bearing characteristics and to test the results of this code. The continuity and momentum conservation equations have been solved and the method, as well as the results, are presented by Gertzos et al. [11, 12].

4 Rotor – Bearing System

In this Section the fluid film impedance forces are applied in the rotor at the points of the two journals in order to construct a system of equations using boundary conditions. In Eq. (3), there are four variables as inputs for the calculation of the bearing impedance force, which must be expressed as functions of the rotor (journal) response. These variables, i.e., the eccentricity e_{i,t_k} and the attitude angle φ_{i,t_k} of each journal ($i = 1, 2$) together with their respective velocities $\dot{e}_{i,t_k}$, $\dot{\varphi}_{i,t_k}$, are expressed as functions of $Y_i(x, t_k)$ and $Z_i(x, t_k)$ for the time t_k, in Eq. (6):

$$\left.\begin{aligned} e_{i,t_k} &= \sqrt{\left(Y_i(0,t_k)\right)^2 + \left(Z_i(0,t_k)\right)^2}, \\ \varphi_{i,t_k} &= \tan^{-1}\left(Y_i(0,t_k)/Z_i(0,t_k)\right) \\ \dot{e}_{i,t_k} &= \left(e_{i,t_k} - e_{i,t_k-\Delta t}\right)/\Delta t, \\ \dot{\varphi}_{i,t_k} &= \left(Z_i(0,t_k)\,\dot{Y}_i(0,t_k) - Y_i(0,t_k)\,\dot{Z}_i(0,t_k)\right)/e^2_{i,t_k} \end{aligned}\right\} \quad i = 1, 2 \qquad (6)$$

From the above equations, it is clear that the pressure deviation in each bearing is a function of Y and Z that depends on the solution constants $q_i(t)$. Thus, a system of 32 equations (16 of real and 16 of imaginary parts) is obtained using the 16 complex boundary conditions for displacements, slopes, bending moments, and shearing forces [5].

The boundary conditions at both ends of the system (bearings) are expressed as the equality of fluid film impedance forces to the journal shearing force. The impedance moment developed of fluid film as a reaction to journal misalignment is not taken into account yielding boundary conditions of bending moment equal to zero. Under this consideration the shearing force boundary conditions become a function of rotor response and consequently the unique variable incorporated in the system is the time (Fig. 3). The resulting dynamic system yields nonlinear oscillations presenting sometimes quasi-periodic or even chaotic motions, especially near resonance operation. The solution of the system is achieved numerically in discrete time with the time interval to be the significant parameter. In brief, the 32×32 system of equations (boundary conditions) is solved using a modified Newton-Raphson method, providing the ability of random initial guess. The evaluation result in the definition of parameters p_i and q_i (Fig. 3) at every time step and thus the response is calculated. The main benefit of this consideration is that no bearing coefficients are used since no journal equilibrium position has to be defined. Additionally, the bearing properties are incorporated at any operational condition no matter what the trajectory of the journal is inside the bearing.

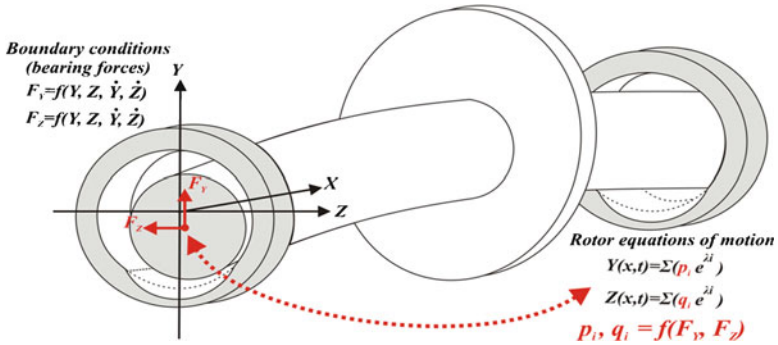

Fig. 3 Nonlinear system due to the interdependency of the bearing forces and the rotor response

5 Experimental Crack Identification using External Exciter

An external electromagnetic excitation device was designed, constructed, and used (Fig. 4), as suggested by Lees et al. [13], to externally excite the rotor in the horizontal direction during its operation for identification purposes. The applicability of this method depends on the possibility to install on the system an external exciter. Instead of this exciter, the method can be applied in cases where magnetic bearings are used, as it is easy in such cases to impose an excitation to the rotating system using the controller of the magnets.

The shaft is rotating at $n = 500$ rpm, the excitation is of a steady frequency, in the horizontal direction, and the steady-state vertical response should be measured in order to develop a method of crack detection using the dynamic coupling between horizontal and vertical response due to crack breathing. When the horizontal external excitation is introduced in the system at $n_{EX} = 4,000$ cycles/min, the vertical response is altered (it is suggested to use $n_{\mathrm{EX}} = 8n$). The magnitude of the electromagnetic force used is estimated to be approximately 10% of total system weight (here is about 40 N). The horizontal excitation intrudes on the vertical response signal through the mechanism of coupling of the system due to both the bearing asymmetry and the crack. Subsequently, the responses of the intact and cracked rotor ($\alpha/R = 20\%$) are subtracted, the resulting difference is transformed using the Continuous Wavelet Transform (Morlet Wavelet), and the corresponding component (Scale 61, resulting from Eq. (7)) of the frequency of external excitation is extracted.

$$a = \frac{F_c}{F_a \Delta} = \frac{0.8125\,Hz}{(4000\,rpm/60)Hz \times (1/5000)} = 60.93 \approx 61 \tag{7}$$

Here a is the monitored scale of the wavelet, F_c is the centre frequency of Morlet wavelet, $F_a = n_{\mathrm{EX}}/60$ Hz is the excitation frequency and Δ is the sampling period (here the sampling frequency is 5,000 samples/sec).

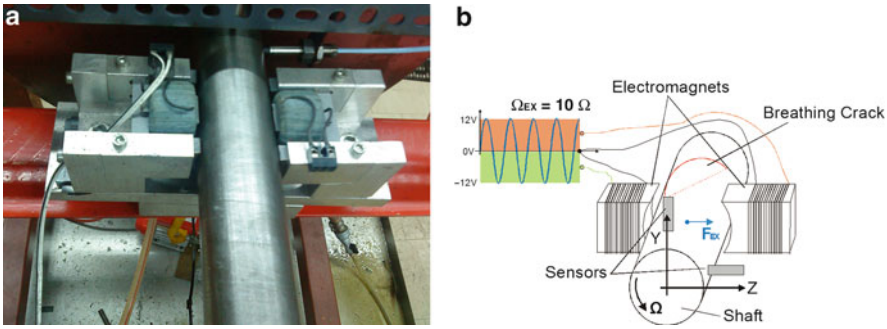

Fig. 4 **(a)** The electromagnets arrangement in the horizontal direction provides the external excitation sinusoidal force, with variable excitation frequency. **(b)** The electromagnet operation scheme

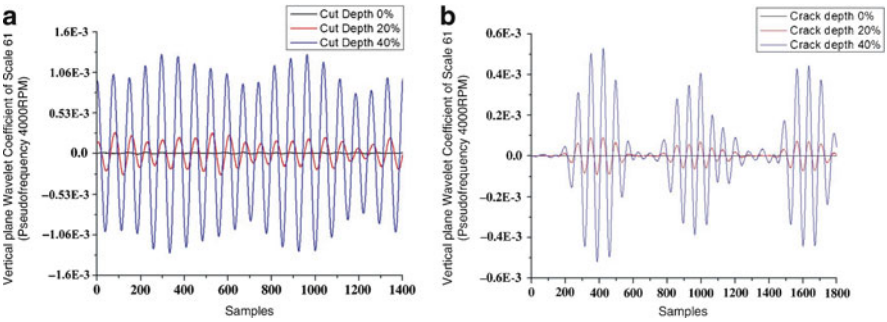

Fig. 5 Extraction of wavelet coefficient of Scale 61 (pseudo frequency 4,000 rpm), (**a**) Experiment and (**b**) simulation

Figure 5 shows the plot of the extracted component for both the experiment and the simulation. The wavelet coefficient of scale corresponding to the external excitation frequency properly demonstrates the coupling due to the crack, during the rotation of the shaft. It contains only one frequency (4,000 RPM), the amplitude of which is well localized in the time necessary to determine whether or not the coupling exists. The coupling presence during rotation is a function of the crack rotational angle, and Fig. 5b clearly shows that the coupling intensifies at the time steps when the crack is totally open, near samples at 400, 1,000, and 1,600 s (Fig. 5). This fact enables the detection of a crack, since only the defect of a crack can yield this dynamic coupling.

In the experimental case, the variation of the amplitude of the wavelet coefficient is also noticed during the rotation but not as clearly as in simulation. The differences between Fig. 5a, b are due to two reasons: (a) the experimental crack (a cut was used) remains open during the rotation and does not breathe as the crack does in the simulation and (b) the force in the simulation is of constant magnitude (−40 N to 40 N)

while in the experiment this force is also depending on the fluctuations of the gap between the rotor and the magnets. Thus it was expected for the experiment to give higher values to the coefficient.

Thus, the coupling due to a cut exists for most of the time needed for an entire rotation. However, the current wavelet coefficient is judged to be very sensitive to crack depth variation and can be used for detection of cracks as small as 20% of the radius as shown in Fig. 5. It is highly beneficial that bearing measurements can also yield crack detection as this facilitates the applicability of the method in real machines, since bearing measurements are widely used in large machine monitoring.

6 Wear Assessment

The wear assessment can be done by weighing the bearing before and after its use. The difference indicates the material lost due to wear. This method cannot be carried out during operation. Saridakis et al. [14] used artificial neural networks in order to detect the wear percentage and the misalignment angles for a journal bearing during its operation. Gertzos et al. [12] investigated the operational and easily measurable characteristics, such as eccentricity ratio, bearing attitude angle, lubricant side flow, and friction coefficient that could be used for bearing wear assessment without stopping the machine. They used Computational Fluid Dynamics (CFD) analysis in order to solve the Navier-Stokes equations. A graphical detection method was used to identify the wear depth associated with the measured characteristics. The Archard's model was also used in order to predict the wear progress when the journal is in full contact with the bearing pad or wears out the bearing under the abrasive mechanism, and finally to predict the volume loss of the bearing material. Nikolakopoulos et al. [15, 16] also proposed a mathematical model and an experimental setup in order to investigate the wear influence on the dynamic response of the system and on other dynamic characteristics of the frequency and time domain.

A numerical application with the physical and geometric properties listed in Table 1 is used here in order to investigate the effects of a worn bearing on the dynamic properties of the system.

The system start-up is performed from the initial rotational speed of $\Omega = 30\,\mathrm{rad/s}$ to the maximum of $\Omega = 100\,\mathrm{rad/s}$, with an acceleration of $\dot{\Omega} = 4\,\mathrm{rad/s^2}$, while the

Table 1 Geometric and physical properties of the current rotor bearing system

Item	Symbol and value	Item	Symbol and value
Shaft radius	$R = 0.025\,\mathrm{m}$	Material loss factor	$\eta = 0.001$
First step length	$L_1 = 1\,\mathrm{m}$	Bearing length	$L_b = 0.05\,\mathrm{m}$
Second step length	$L_2 = 1\,\mathrm{m}$	Bearing radial clearance	$c_\mathrm{r} = 100\,\mu\mathrm{m}$
Disk radius	$R_d = 0.19\,\mathrm{m}$	External load	$E_F = W_d\mathrm{N}$
Shaft/disk density	$\rho = 7832\,\mathrm{kg/m^3}$	Oil viscosity	$\mu = 0.005\,\mathrm{Pa.s}$
Disk width	$L_d = 0.022\,\mathrm{m}$	Young's modulus	$E = 206\,\mathrm{GPa}$

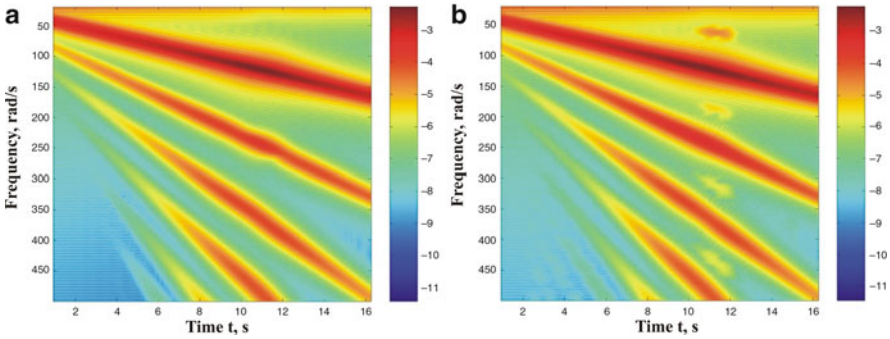

Fig. 6 Log modulus of STFT of time history through first critical in Journal 1 for relative wear depths of (**a**) 0% and (**b**) 40%

sampling frequency is $1/\Delta t = 800$ Samples/s. Note that the sampling frequency is a significant parameter and is a result of various tests performed to render the algorithm computable. A time step of $\Delta t = 0.00125$ s is used in all evaluations. The material loss factor is set arbitrarily to this low value to "cut" the infinite response just enough to make the start-up computable.

In this work, the variable loss factor is not included because the internal damping is treated as a tool in order to avoid the infinite response that cannot be damped by the bearing damping coefficients. The left journal (Journal 1) vertical response is calculated for wear depths of 0% and 40%. A time frequency analysis using Short Time Fourier Transform (STFT) is applied to these signals, and the result is shown in Fig. 6. The development of 1/2X, 3/2X, 5/2X etc. harmonics can be easily observed. These harmonics are due to the wear defect.

7 Conclusions

A continuous approach is used here to simulate the dynamic behavior of a rotor-bearing system. The finite difference method is used to solve the Reynolds equation. A crack of the rotor and the wear of the bearing are considered as defects and dynamic methods are presented for their identification, both analytically and experimentally. In the future, rotordynamics is expected to be influenced by the use of new and better materials, whether composites or conventional. In the era of nanotechnology, micro- and nano-rotors are expected to open new horizons in this field. New smart materials and fluids are also expected to be used in journal bearings to confront the problem of friction and wear minimization.

References

1. Eshleman, R.L., Eubanks, R.A.: On critical speeds of continuous rotor. ASME-Paper 69-Vibr-52 (1969)
2. Papadopoulos, C.A.: The strain energy release approach for modeling cracks in rotors: A state of the art review. Mech. Syst. Signal Process. **22**(4), 763–789 (2008)
3. Chasalevris, A.C., Papadopoulos, C.A.: Crack identification using external excitation and coupled response of a continuously modeled rotor with internal damping. In: The Ninth International Conference on Computational Structures Technology, Civil Comp Press, Athens, Greece, 2–5 September 2008
4. Dufrane, K.F., Kannel, J.W., McCloskey, T.H.: Wear of steam turbine journal bearings at low operating speeds. J. Lubr. Technol. **105**(3), 313–317 (1983)
5. Chasalevris, A.C., Papadopoulos, C.A.: A continuous model approach for cross-coupled bending vibrations of a rotor-bearing system with a transverse breathing crack. Mech.Mach. Theor. **44**(6), 1176–1191 (2009)
6. Lee, C.: Vibration Analysis of Rotors. Springer, The Netherlands (1993)
7. Dimarogonas, A.D., Paipetis, S.A.: Analytical Methods in Rotor Dynamics. Applied Science Publishers, London (1983)
8. Chasalevris, A.C., Papadopoulos, C.A.: Identification of multiple cracks in beams under bending. Mech. Syst. Signal Process. **20**(7), 1631–1673 (2006/10)
9. Childs, D.: Turbomachinery Rotordynamics: Phenomena, Modeling, & Analysis. Wiley-Interscience (1993)
10. Vance, J.M.: Rotordynamics of Turbomachinery. Wiley-Interscience (1988)
11. Gertzos, K.P., Nikolakopoulos, P.G., Papadopoulos, C.A.: CFD analysis of journal bearing hydrodynamic lubrication by Bingham lubricant. Tribol. Int. **41**(12), 1190–1204 (2008)
12. Gertzos, K.P., Nikolakopoulos, P.G., Chasalevris, A.C., Papadopoulos, C.A.: Wear identification in rotor-bearing systems by volumetric and bearing performance characteristics measurements. In: The Nineth International Conference on Computational Structures Technology, Civil Comp Press, Athens, Greece, 2–5 September 2008
13. Lees, A.W., Sinha, J.K., Friswell, M.I.: Model-based identification of rotating machines. Mech. Syst. Signal Process. **23**(6), 1884–1893 (2009)
14. Saridakis, K.M., Nikolakopoulos, P.G., Papadopoulos, C.A., Dentsoras, A.J.: Fault diagnosis of journal bearings based on artificial neural networks and measurements of bearing performance characteristics. In: Proceedings of the Ninth International Conference on Computational Structures Technology, Civil-Comp Press, Athens, Greece, 2–5 September 2008
15. Nikolakopoulos, P.G., Chasalevris, A.C., Papadopoulos, C.A.: Applying external excitation to a rotor for wear identification of the non-linear fluid-film bearings. Civil Comp Press, Athens, Greece, 2–5 September 2008
16. Nikolakopoulos, P.G., Papadopoulos, C.A.: A study of friction in worn misaligned journal bearings under severe hydrodynamic lubrication. Tribol. Int. **41**(6), 461–472 (2008)

Identification of the Bearing and Unbalance Parameters from Rundown Data of Rotors

R. Tiwari and V. Chakravarthy

Abstract An identification algorithm for the simultaneous identification of the bearing and unbalance parameters for flexible rotor-bearing systems has been developed by using run-down measurements. Speed-dependent bearing dynamic coefficients for each bearing and residual unbalances at predefined balancing planes are estimated simultaneously by the algorithm. The proposed identification algorithm is demonstrated through a numerical model. The identification procedure is found to be highly ill-conditioned and the Tikhonov regularization is applied to deal with this problem.

Keywords Bearing · Unbalance · Identification · Regularization

1 Introduction

Residual unbalance is one of the principal causes of excessive vibrations in high-speed rotating machineries; it results in a considerable reduction of the machine fatigue life. Hence, the identification of residual unbalances is imperative to accurately balance the rotor system during the installation and subsequently during every overhaul [1–6].

Bearing dynamic coefficients play a significant role in determining the dynamic behavior of rotor-bearing systems. Reliable estimates of bearing coefficients are difficult to obtain with theoretical models due to the difficulty in accurately modelling the multitude of factors controlling their dynamic behavior. Conversely, identification methods based on experimental data from actual test conditions provide accurate bearing coefficients. Conventionally, the identification of bearing dynamic coefficients is achieved by using the impulse, step change in force, random, synchronous and non-synchronous unbalance excitation techniques. Methods using

R. Tiwari (✉) and V. Chakravarthy
Department of Mechanical Engineering, Indian Institute of Technology,
Guwahati 781 039, India
e-mail: rtiwari@iitg.ernet.in

K. Gupta (ed.), *IUTAM Symposium on Emerging Trends in Rotor Dynamics*,
IUTAM Bookseries 25, DOI 10.1007/978-94-007-0020-8_40,

unbalance forces find wide application because no sophisticated equipment is required for the excitation. Moreover, the run-down/coast-up synchronous response data of the turbo-machines are relatively easy to obtain for such excitation [7, 8].

The recent trend in the identification of system parameters is the development of methods that can simultaneously estimate bearing/support dynamic coefficients and residual unbalances [9–14] with the support of advanced sensor technology and augmented computing power. However, in practice, it is quite difficult and unsafe to excite large turbo-machines by external means, hence the response data of the rundown/coast-up of rotating machines would be of more practical use for identification procedures. Hardly any attempt has been made [12] to estimate parameters of the residual unbalance, bearing and foundation, simultaneously. This shows the gravity of the problem and this is due to the vast difference in values of these parameters leading to ill-conditioning during estimation [13]. The present work is a step forward toward a more comprehensive simultaneous estimation of residual unbalance, bearing and foundation parameters.

This paper presents an algorithm for simultaneous identification of the residual unbalance and bearing dynamic coefficients of flexible rotor-bearing systems by using unbalance response measurements. For numerical illustrations, responses at bearings of a rotor-bearing system are generated by using assumed residual unbalances; and known bearing coefficients, which in turn are derived from closed form solutions of the short bearing approximation. The present identification problem is found to be ill-conditioned; however, quite accurate identification of the parameters is achieved by applying the Tikhonov regularization.

2 Modeling of Rotor-Bearing Systems

A general rotor-bearing system model can be divided into the rotor, bearings and the foundation substructures. Each substructure is separately modelled and then combined to give the overall system model. The flexibility of the foundation and shaft damping are not considered in the present case. Subsequent sections describe the mathematical modelling of the rotor, bearings, and unbalance forces. The present analysis is based on the assumption that the system is linear.

Rotor model: The shaft is divided into finite number of elements, and an element is uniform in terms of the shape of the cross section, and material constants. The appropriate number of elements is determined depending on the order of vibration modes, the geometry of the shaft and the mounting of discs. The equation of motion (EOM) of the rotor element is given as

$$[M]^{(e)}\{\ddot{u}\}^{(ne)} - \Omega_s [G]^{(e)}\{\dot{u}\}^{(ne)} + [K]^{(e)}\{u\}^{(ne)} = \{f\}^{(ne)} \tag{1}$$

where $\{u\}^{(ne)}$ and $\{f\}^{(ne)}$ are the elemental nodal displacement and force vectors respectively, and Ω_s is the rotor angular speed. Matrices $[M]^{(e)}$, $[G]^{(e)}$, and $[K]^{(e)}$ are the elemental mass, gyroscopic and stiffness matrices, respectively [14, 15].

***Bearing model*:** The eight linearised dynamic coefficient model, including the direct and cross-effects of stiffness and damping is used to model bearings. Generalized forces acting on bearings can be written as

$$\{f_B\} = \begin{bmatrix} c_{xx} & c_{xy} \\ c_{yx} & c_{yy} \end{bmatrix} \{\dot{u}_B\} + \begin{bmatrix} k_{xx} & k_{xy} \\ k_{yx} & k_{yy} \end{bmatrix} \{u_B\} \tag{2}$$

where vectors $\{u_B\}$ and $\{f_B\}$ denote the bearing displacement and force vectors, respectively. For numerical illustration, bearing coefficients (k's and c's) are derived from the closed form solution of the short bearing approximation [14].

***Unbalance force model*:** The unbalance force vector is defined as

$$\{f_{unb}(t)\} = \{F_{unb}\} e^{j\Omega_s t} \tag{3}$$

where $\{F_{unb}\}$ is the complex unbalance force vector.

***System EOMs*:** The response can be expressed as $\{u(t)\} = \{U\} e^{j\Omega_s t}$, where $\{U\}$ is a complex displacement vector. Hence, governing equations of the rotor and bearing substructures in frequency domain have the following form

$$[Z_R]\{U_R\} = \{F_R\} \text{ and } [Z_B]\{U_B\} = \{F_B\} \tag{4}$$

where subscripts R and B relate to the rotor and the bearing, respectively. DOFs of the rotor-bearing system is composed of the internal and connection DOFs. DOFs of the rotor at bearing locations are called the connection DOFs, $U_{R,B}$; and DOFs of the rotor other than at bearing locations are called as the internal DOFs, $U_{R,I}$. Equations of motion of two sub-structures i.e., Eq. (4) are partitioned to the internal and connection DOFs as

$$\begin{bmatrix} Z_{R,II} & Z_{R,IB} \\ Z_{R,BI} & Z_{R,BB} \end{bmatrix} \begin{Bmatrix} U_{R,I} \\ U_{R,B} \end{Bmatrix} = \begin{Bmatrix} F_{R,I} \\ -F_{B,B} \end{Bmatrix} \text{ and } \begin{bmatrix} Z_{B,BB} & Z_{B,BI} \\ Z_{B,IB} & Z_{B,II} \end{bmatrix} \begin{Bmatrix} U_{R,B} \\ U_{B,I} \end{Bmatrix} = \begin{Bmatrix} F_{B,B} \\ 0 \end{Bmatrix} \tag{5}$$

where $\{U_{B,I}\}$ is the bearing internal DOFs vector. Combining expressions in Eq. (5) leads to EOMs for the global rotor-bearing system, and it could be written as

$$\begin{bmatrix} Z_{R,II} & Z_{R,IB} \\ Z_{R,BI} & (Z_{R,BB} + Z_{B,BB}) \end{bmatrix} \begin{Bmatrix} U_{R,I} \\ U_{R,B} \end{Bmatrix} = \begin{Bmatrix} F_{R,I} \\ 0 \end{Bmatrix} \tag{6}$$

Bearings can be modeled by using DOFs on the rotor only, hence, the bearing model does not contain any internal DOFs. In Eq. (6), it is assumed that no external forces act at bearing locations and for a given unbalance force the unbalance response can be obtained. Equation (6) will be used for development of the proposed identification algorithm as described in the following section.

3 Identification Algorithms

The top and bottom sets of terms in Eq. (6) can be expressed as

$$\begin{aligned}&[Z_{R,II}]\{U_{R,I}\} + [Z_{R,IB}]\{U_{R,B}\} = \{F_{R,I}\};\\ &[Z_{R,BI}]\{U_{R,I}\} + ([Z_{R,BB}] + [Z_{B,BB}])\{U_{R,B}\} = \{0\}\end{aligned} \tag{7}$$

From above, the second equation can be written as

$$\{U_{R,I}\} = [Z_{R,II}]^{-1}(\{F_{R,I}\} - [Z_{R,IB}]\{U_{R,B}\}) \tag{8}$$

The vector $\{F_{R,I}\}$ contains superposition of unbalance forces applied at the rotor substructure due to the residual and trial unbalances. It can be expressed as $\{F_{R,I}\} = \{F_{Runb}\} + \{F_{Tunb}\}$ where $\{F_{Runb}\}$ and $\{F_{Tunb}\}$ are the residual and trial unbalance force vectors, respectively. On substituting this into Eq. (8), we get

$$\{U_{R,I}\} = [Z_{R,II}]^{-1}(\{F_{Runb}\} + \{F_{Tunb}\} - [Z_{R,IB}]\{U_{R,B}\}) \tag{9}$$

In Eq. (9), the vector $\{U_{R,B}\}$ is the connection DOFs at bearing locations, and can be measured in most of the practical cases. Substituting Eq. (9) into the first expression of Eq. (7), it eliminates $\{U_{R,I}\}$, which is immeasurable or inaccessible in most of practical cases. Remaining terms are arranged so that unknown terms (i.e., the residual unbalance and bearing parameters) are on the left hand side and known terms (i.e., trial unbalances) on the right hand side of the expression, and are given as

$$[Z_{B,BB}]\{U_{R,B}\} + [Z_{R,BI}][Z_{R,II}]^{-1}\{F_{Runb}\} = \{P\} \tag{10}$$

with

$$\begin{aligned}\{P(\Omega_s)\} = &\left([Z_{R,BI}][Z_{R,II}]^{-1}[Z_{R,IB}] - [Z_{R,BB}]\right)\{U_{R,B}\}\\ &- [Z_{R,BI}][Z_{R,II}]^{-1}\{F_{Tunb}\}\end{aligned}$$

where the vector, $\{P(\Omega_s)\}$, contains terms collected at a given shaft angular speed Ω_s. The size of $\{P(\Omega_s)\}$ is $n_c \times 1$ where n_c is the number of connection DOFs. $\{F_{Runb}\}$ could be expressed as $\{F_{Runb}\} = \Omega_s^2\{e\}$ where $\{e\}$ is the residual unbalance vector and can be expanded as

$$\{e\}_{2p\times 1} = \left\{e_{x_1}\ e_{y_1}\ e_{x_2}\ e_{y_2}\ \ldots\ e_{x_p}\ e_{y_p}\right\}^T \tag{11}$$

where subscript in the vector represent its size. Residual unbalance vector components, e's, are assumed to be present at p number of balance planes and in two orthogonal directions. The term $[Z_{B,BB}]\{U_{R,B}\}$ in Eq. (10) is then regrouped into a vector $\{\beta\}$, containing unknown bearing coefficients and a corresponding matrix

$[W(\Omega_s)]_{n_c \times 8n_b}$ containing the related response terms at a given shaft angular speed, Ω_s. Substituting Eq. (11) into Eq. (10) gives

$$[W\,(\Omega_s)]\,\{\beta\,(\Omega_s)\} + [R\,(\Omega_s)]\,\{e\} = \{P\,(\Omega_s)\} \tag{12}$$

with $[R\,(\Omega_s)]_{n_c \times 2p} = \Omega_s^2\,[Z_{R,BI}]\,[Z_{R,II}]^{-1}$;

$$\{\beta\,(\Omega_s)\}_{8n_b \times 1} = \left\{ k_{xx}^1\ k_{xy}^1\ k_{yx}^1\ k_{yy}^1\ \ k_{xx}^2 \cdots k_{yy}^{n_b}\ c_{xx}^1\ c_{xy}^1\ c_{yx}^1\ c_{yy}^1\ \ c_{xx}^2 \cdots c_{yy}^{n_b} \right\}^T$$

Parameters contained in vector $\{\beta\}$, depend on the form of the dynamic stiffness matrix specified for bearings and/or seals, Eqs. (2), and ordering of these parameters may be arranged as desired. The size of the matrix $[W(\Omega_s)]$ and vector $\beta(\Omega_s)$, in Eq. (12) are $n_c \times (8n_b)$ and $8n_b \times 1$, respectively; where n_b is the number of bearings. The size of the matrix $[R(\Omega_s)]$ is $2p \times 2p$, where p is the number of balancing planes p. Parameters intended to be identified are real numbers, however, matrices W and R and the vector P in Eq. (12) are in general complex, hence these matrices are separated into their real and complex parts, which leads to a doubling of the size of these matrices. Equation (12) takes the following form

$$[W_1\,(\Omega_s)]\,\{\beta\,(\Omega_s)\} + [R_1\,(\Omega_s)]\,\{e\} = \{P_1\,(\Omega_s)\} \tag{13}$$

with

$$[W_1(\Omega_s)] = \begin{bmatrix} \mathrm{Re}\,[W(\Omega_s)] \\ \mathrm{Im}\,[W(\Omega_s)] \end{bmatrix}; \quad [R_1(\Omega_s)] = \begin{bmatrix} \mathrm{Re}\,[R(\Omega_s)] \\ \mathrm{Im}\,[R(\Omega_s)] \end{bmatrix};$$
$$[P_1(\Omega_s)] = \begin{bmatrix} \mathrm{Re}\,[P(\Omega_s)] \\ \mathrm{Im}\,[P(\Omega_s)] \end{bmatrix}$$

Equation (13) can be used to develop the final form of estimation equations for simultaneous identification of the residual unbalance and bearing coefficients, and it can be written for three different unbalance configurations (one with residual unbalances and two with assumed trial unbalances along with residual unbalances) at a particular rotor angular speed Ω_s. All such equations are grouped together and written as

$$[W_2\,(\Omega_s)]\,\{\beta\,(\Omega_s)\} + [R_2\,(\Omega_s)]\,\{e\} = \{P_2\,(\Omega_s)\} \tag{14}$$

with

$$[W_2(\Omega_s)]_{6n_c \times 8n_b} = \left[W_1(\Omega_s)_{unb1} \quad W_1(\Omega_s)_{unb2}\ W_1(\Omega_s)_{unb3} \right]^T$$
$$[R_2(\Omega_s)]_{6n_c \times 2p} = \left[R_1(\Omega_s)_{unb1} \quad R_1(\Omega_s)_{unb2}\ R_1(\Omega_s)_{unb3} \right]^T$$
$$[P_2(\Omega_s)]_{6n_c \times 1} = \left[P_1(\Omega_s)_{unb1} \quad P_1(\Omega_s)_{unb2}\ P_1(\Omega_s)_{unb3} \right]^T$$

Equation (14) is for a single rotor angular speed. Several angular speeds, Ω_s (where $s = 1, 2, \ldots, N$) can be selected depending upon the operating speed, which in

turn is chosen based upon critical speeds of rotating machine. Writing Eq. (14) for each of these rotor angular speeds and on combining, it gives

$$[A_1]\{\gamma_1\} = \{d_1\} \tag{15}$$

with

$$[A_1]_{(6n_cN)\times 2(4n_bN+p)} = \begin{bmatrix} W_2(\Omega_1) & 0 & \cdots & 0 & R_2(\Omega_1) \\ 0 & W_2(\Omega_2) & \cdots & 0 & R_2(\Omega_2) \\ \vdots & \vdots & \ddots & \vdots & \vdots \\ 0 & 0 & \cdots & W_2(\Omega_N) & R_2(\Omega_N) \end{bmatrix}$$

$$\{\gamma_1\}_{2(4n_bN+p)\times 1} = \left\{ \{\beta(\Omega_1)\}\ \{\beta(\Omega_2)\} \cdots \{\beta(\Omega_N)\}\ \{e\} \right\}^T$$

$$\{d_1\}_{(6n_cN)\times 1} = \left\{ P_2(\Omega_1)\ P_2(\Omega_2)\ P_2(\Omega_3) \ldots P_2(\Omega_N) \right\}^T$$

The desired unknown parameters consisting of bearing coefficients at speeds $\Omega_1,\ \Omega_2, \ldots, \Omega_N$ and residual unbalances at p planes are then estimated by applying the ordinary least squares estimation technique in Eq. (15). The regression matrix $[A_1]$ may have the high condition number that leads to a non-unique identification of bearing coefficients. Column scaling with different scaling factors for the stiffness and damping coefficients improves the condition of $[A_1]$. However, the estimation of bearing coefficients still suffers from ill-conditioning [13, 14]. It is also observed that the increase in the number of trial runs to four or even more does not offer any improvement in the condition of $[A_1]$.

The Tikhonov regularization method [16] can be used to solve the ill-posed Eq. (15). Ill-conditioning of the matrix $[A_1]$ implies that the solution is sensitive to perturbations and the regularization is imperative for a stabilized solution. Hence, the regularized solution $[\gamma_1]$ is a solution to the following weighted combination of the residual norm and side constraints

$$\gamma_1 = \min \left\{ \|A_1\gamma_1 - d_1\|_2^2 + \lambda^2 \|L(\gamma_1 - \bar{\gamma})\|_2^2 \right\} \tag{16}$$

where for the present case L is the identity matrix I_n, $\bar{\gamma}$ is an initial estimate of the solution, and λ is the regularization parameter that controls the relative minimization of the side constraint with respect to the residual norm. λ is obtained from the *L-curve* which is a log-log plot of the side norm $\|L(\gamma)\|_2$ versus the corresponding residual norm $\|A_1\gamma - d_1\|_2$. The *L-curve* aids in seeking a compromise between the minimization of the two norms.

4 Results and Discussions

The rotor-bearing model shown in Fig. 1 is considered for numerical illustration of the present identification algorithm. The rotor model is discretized into six two-noded elements. Details of the rotor-bearing model are: the shaft diameter is 10 mm;

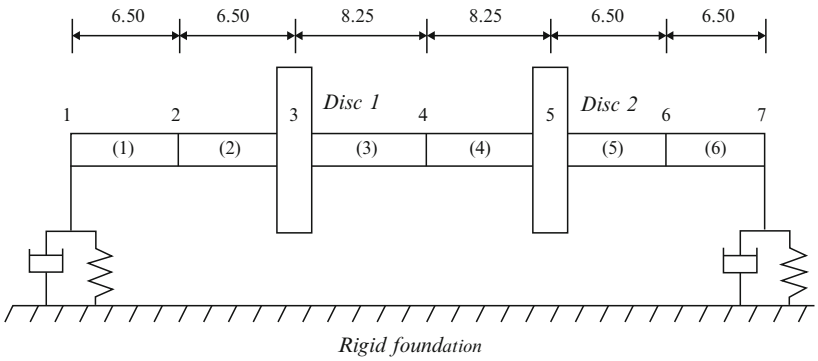

Fig. 1 A typical rotor-bearing model (all dimensions are in cm)

rigid discs have the inner and outer diameters, and thickness of 10 mm, 74 mm, and 25 mm, respectively; both bearings have diameter of 25 mm and $L/D = 1$; the radial clearance of bearing 1 is 0.075 mm, the radial clearance of bearing 2 is 0.080 mm, the kinetic viscosity is 28 centi-Stokes, the temperature of lubricant is 40 °C, and the specific gravity of lubricant is 0.87.

Residual unbalances are created in the numerical model by placing known unbalance masses of 3 g at 30° and 1 g at 60° (angular locations are measured from a common shaft reference point) at discs 1 and 2, respectively. Both the residual and trial unbalance masses are assumed to be present at 30 mm radius from the centre of discs 1 and 2. For the present case, disc locations are chosen as balancing planes. The rotor spin speed is varied from 10 to 139 Hz with a speed step of 1 Hz. The upper rotor speed is well above the second critical speed of the present rotor-bearings system since the first and second critical are 36 Hz and 125 Hz, respectively. Unbalance responses are simulated by solving Eq. (6) for the following three unbalance configurations (i) with residual unbalances only, (ii) with trial unbalance masses of 4.38 g at 60° in disc 1 and 2.19 g at 30° in disc 2, in addition to residual unbalances, (iii) with trial masses of 5.0 g at 35° in disc 1 and 3.0 g at 55° in disc 2, along with residual unbalances. Measured unbalance responses simulated at bearings are corrupted with 5% noise to incorporate the inherent measurement noise. These contaminated responses are utilized in the identification algorithm.

The condition number of the regression matrix $[A_1]$ in Eq. (15) is high for the present algorithm due to its large size (for example, the size of the regression matrix $[A_1]$ is 480×324 (since $p = 2,\ n_c = 4,\ N = 20,\ n_b = 2$ and the matrix size is $(6n_cN) \times 2(4n_bN + p)$). Column scaling imparts a substantial reduction in the condition number of the regression matrix $[A_1]$. Scaling factor of 10^5 is applied to the columns 1 to 8 and scaling factor of 10^3 is applied to the columns 9 to 16 of $[A_1]$.

Tikhonov regularization is used to tackle the ill-posed problem of the regression matrix. The regularization parameter λ is found to be 0.0021. The residual unbalance and bearing coefficients of the entire frequency band are obtained in

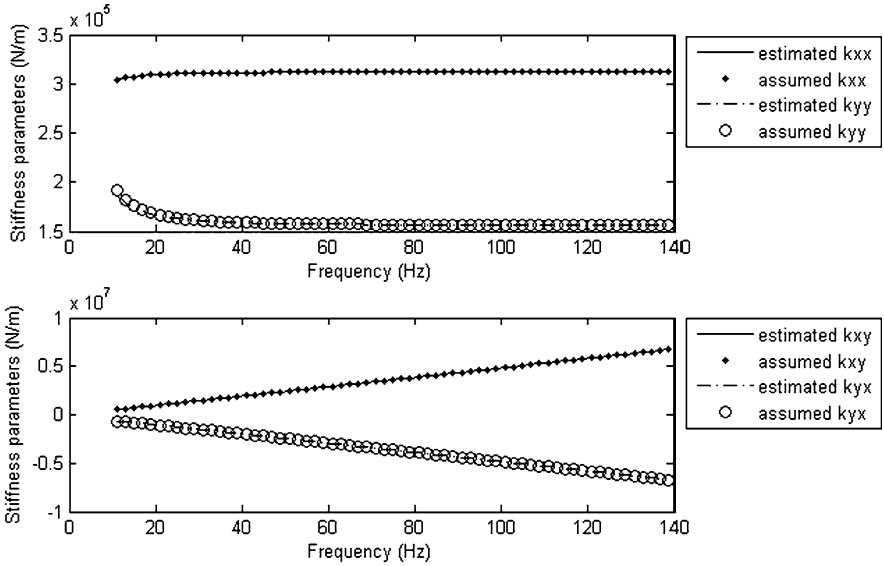

Fig. 2 The estimated and assumed stiffness coefficients of bearing 2 (5% measurement noise)

a single run of the computer code. Figure 2 shows the estimated and assumed stiffness coefficients for bearing 2 with 5% noise in simulated responses. The identified and assumed damping coefficients of bearing 2 with the same level of noise are illustrated in Fig. 3. The regularized solution provides estimated bearing coefficients close to the assumed values, which are otherwise quite deviating due to ill-conditioning.

The identified residual unbalance and bearing coefficients are substituted back in Eq. (6) to obtain the estimated responses. The comparison of the estimated and measured (responses which are used for identification of parameters) responses is done to ensure the validity of the identified parameters. Figure 4 shows the variation of the estimated (solid line) and measured (dotted line) vertical displacement amplitude and phase with respect to rotor speeds of bearing 2 for unbalance configuration 3. The two peaks in the amplitude plot show critical speeds clearly and the phase plot also exhibits a sharp phase change at critical speeds. Due to relatively flexible shaft as compared to the direct stiffness of bearings, which is asymmetrical in two orthogonal directions, the effect of splitting of natural frequencies is not distinct in the responses. Estimated responses generated with the identified parameters demonstrate an excellent fit with measured responses used for the identification of parameters.

Table 1 shows identified unbalances for various levels of assumed residual unbalances (other than mentioned in the configuration 1) in the rotor model. The identification is done for a constant speed band, 10Hz to 49Hz, with 5% measurement noise in measured responses. The estimated residual unbalances match closely

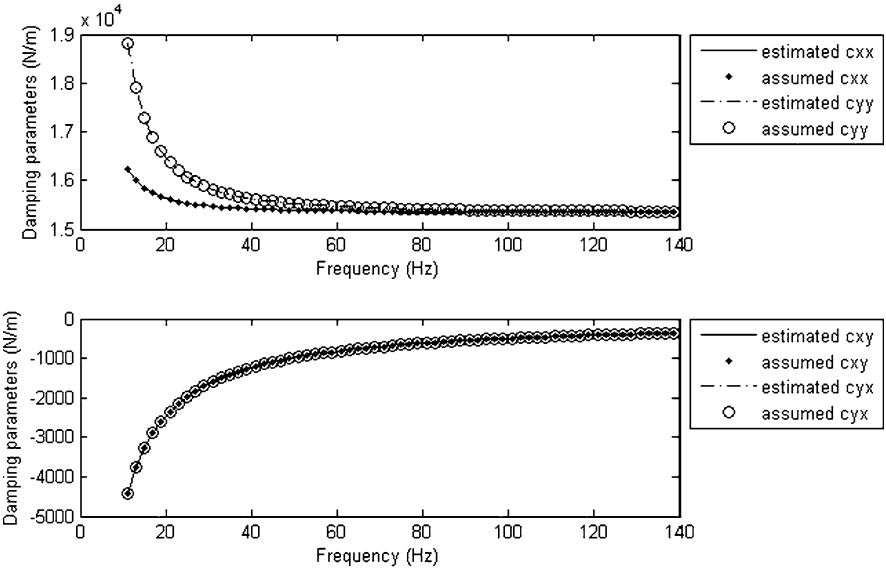

Fig. 3 The estimated and assumed damping coefficients of bearing 2 (5% measurement noise)

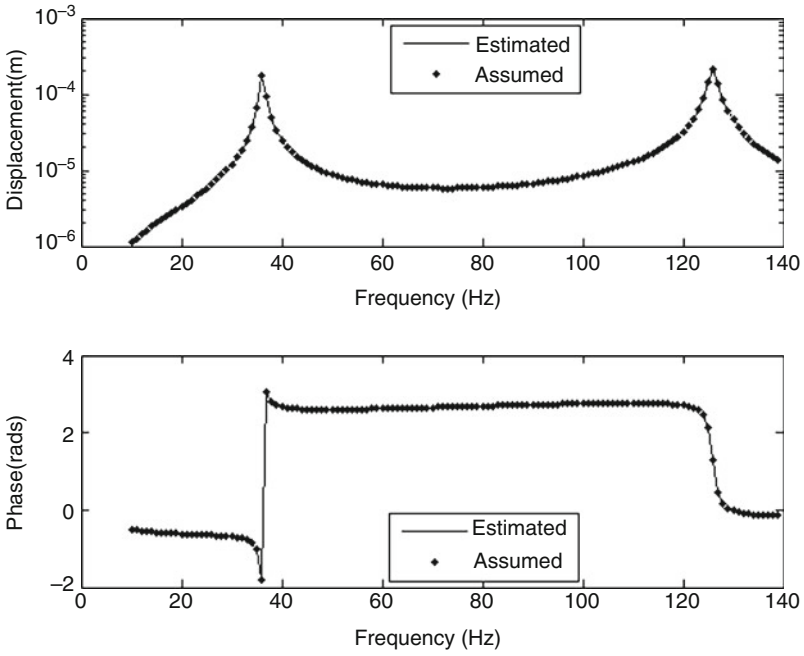

Fig. 4 The estimated and measured response of bearing 2 in the vertical direction

Table 1 The identified residual unbalances for different assumed residual unbalances

	Residual unbalance in plane 1 (g-mm@degrees)		Residual unbalance in plane 2 (g-mm@degrees)	
S.No.	Assumed	Estimated	Assumed	Estimated
1	15.0@45	15.00@44.93	22.5@115	22.51@115.03
2	36.0@70	36.08@70.04	52.5@225	52.57@225.07
3	93.0@120	94.54@120.09	75.0@10	75.16@10.09
4	129.0@220	130.62@229.92	105.0@85	105.22@85.02
5	180.0@310	180.14@310.08	156.0@180	156.32@180.02

Table 2 The identified residual unbalances for different disc masses

S.No.	Mass of discs (kg)	Residual unbalance in plane 1 (g-mm@degrees)	Residual unbalance in plane 2 (g-mm@degrees)
		Assumed – 120 g-mm@20°	Assumed – 60 g-mm@170°
1	0.5	120.13@20.00	60.11@170.09
2	1.5	120.15@20.05	60.09@170.19
3	2.5	120.18@20.10	60.06@170.28
4	3.5	120.21@20.14	60.04@170.38
5	4.5	120.23@20.18	60.01@170.49

with the assumed ones in both balancing planes, thus proving the capability of the algorithm to identify diverse residual unbalance configurations in the rotor-bearing system. The influence of various levels of the mass of disc on the estimation of residual unbalances is also studied and estimates are given in Table 2. Residual unbalances of 120 g-mm at 20° and 60 g-mm at 170° are assumed in planes 1 and 2, respectively. Both disc masses are varied from 0.5 to 4.5 kg with an increment step of 1 kg. Identified residual unbalances are very close to assumed residual unbalances for different level of disc masses considered.

5 Conclusions

A method for the identification of residual unbalances and bearing dynamic coefficients of flexible rotor systems is presented. Residual unbalances at predefined planes and speed-dependent bearing coefficients for each bearing are estimated by using frequency domain synchronous unbalance measurements at bearings. The present method solves the ill-posed problem by using the Tikhonov regularization. This algorithm is found to be robust against the noise and the obtained residual unbalances and bearing coefficients are in good agreement with the assumed parameters. The proposed algorithm is applicable for different rotor-bearing systems, given that, it offers the flexibility to include any number of bearings/seals and balancing planes. However, it would be interesting and challenging to implement the proposed method in a real turbomachinery.

References

1. Wowk, V.: Machinery Vibration: Balancing. McGraw-Hill Inc, NY (1995)
2. Darlow, M.S.: Balancing of high speed-rotating machinery: theory, methods and experimental results. Mech. Syst. Signal Process. **1**, 105–134 (1987)
3. Gnielka, P.: Modal balancing of flexible rotors without test runs: an experimental investigation. J. Vib. **90**, 157–172 (1983)
4. Parkinson, A.G.: Balancing of rotating machinery. Proc. Inst. Mech. Eng., Part C: J. Mech. Eng. Sci. **205**, 53–66 (1991)
5. Edwards, S., Lees, A.W., Friswell, M.I.: Experimental identification of excitation and support parameters of a flexible rotor-bearings-foundation system from a single run-down. J. Sound Vib. **232**, 963–992 (2000)
6. Mendez-Adriani, J.A.: Considerations of field balancing of rigid rotors. Shock Vib. Dig. ***37***, 179–187 (2005)
7. Tiwari, R., Lees, A.W., Friswell, M.I.: Identification of dynamic bearing parameters: a review. Shock Vib. Dig. **36**, 99–124 (2004)
8. Tiwari, R., Manikandan, S., Dwivedy, S.K.: A review on the experimental estimation of the rotor dynamic parameters of seals. Shock Vib. Dig. **37**, 261–284 (2005)
9. Lee, A.C., Shih, Y.P.: Identification of the unbalance distribution and dynamic characteristics of bearings in flexible rotors. Proc. IMechE, Part C: J. Mech. Eng. Sci. **210**, 409–432 (1996)
10. Tiwari, R., Vyas, N.S.: Parameter estimation in unbalanced non-linear rotor-bearing systems from random response, J. Sound Vib. **208**, 1–14 (1997)
11. Sinha, J.K., Friswell, M.I., Lees, A.W.: The identification of the unbalance and the foundation model of a rotating machine from a single run-down. Mech. Syst. Signal Process. **16**, 255–271 (2002)
12. Lees, A.W., Sinha, J.K., Friswell, M.I.: Model-based identification of rotating machines. Mech. Syst. Signal Process. **23**, 1884–1893 (2009)
13. Tiwari, R.: Conditioning of regression matrices for simultaneous estimation of the residual unbalance and bearing dynamic parameters. Mech. Syst. Signal Process. **19**, 1082–1095 (2005)
14. Tiwari, R., Chakravarthy, V.: Simultaneous identification of residual unbalances and bearing dynamic parameters from impulse responses of rotor-bearing systems. Mech. Syst. Signal Process. **20**, 1590–1614 (2007)
15. Nelson, H.D.: A finite rotating shaft element using timoshenko beam theory. Trans. ASME, J. Mech. Design **102**, 793–803 (1980)
16. Tikhonov A.N., Arsenin, V.Y.: Solutions of Ill-Posed Problems. Winston & Sons, Washington D.C (1977)

Some Recent Studies on Cracked Rotors

A.S. Sekhar

Abstract An important rotor fault, which can lead to catastrophic failure if undetected, is fatigue crack in the shaft. Cracked rotating shafts have been the subject of studies and investigations for more than four decades, with some review papers published over this period. The aim of this paper is to discuss very recent developments of the research on cracked rotors, including the inverse problem of the identification of cracks in rotating machinery.

Keywords Cracks · Shaft · Identification

1 Introduction

Fatigue cracks because of their potential to cause catastrophic failures are a grave threat to an uninterrupted operation and performance of the modern day machines. The research in the past few decades on cracked structures and rotors is well documented in a review paper by Wauer [1]; a survey on simple rotors by Gasch [2]; reviews by Dimarogonas [3] and more recently by Sabnavis et al. [4]. Important achievements have been made during these years; the knowledge of the dynamical behavior of cracked shafts has allowed to recognize the presence of a crack and to stop the cracked shafts in time before catastrophic failures.

Very recently, the journal of Mechanical Systems and Signal Processing has brought out a special issue on cracked rotors [5]. This issue consists of papers on fracture mechanics approaches [6]; simple model of cracked shaft [7]; industrial machine case histories and non-linear effects [8]; crack detection in power plant rotating machinery [9]; multiple cracks [10]; and accurate modeling, helical/slant cracks and the non-linear effects [11]. Subsequent to the special issue, some more papers have contributed to this important field. This paper brings out recent

A.S. Sekhar (✉)
Department of Mechanical Engineering, Indian Institute of Technology,
Chennai – 600 036, India
e-mail: as_sekher@iitm.ac.in

K. Gupta (ed.), *IUTAM Symposium on Emerging Trends in Rotor Dynamics*,
IUTAM Bookseries 25, DOI 10.1007/978-94-007-0020-8_41,

developments for the last five years, mostly after ref. [4] on the dynamical behavior of cracked rotors and identification of cracks. The discussion ends with a note on scope for further research works in this area.

2 Modeling Aspects

2.1 Breathing Mechanism

The crack gradually opens and closes periodically, in other words breaths during the revolution of the shaft, however, it is not yet entirely clear how partial closure interacts with key variables of the problem. Hence there is a need for a model that accounts for the crack breathing mechanism and for the interaction between external loading and dynamic crack behavior [11]. The crack breathing in rotors is often simulated using two well-known models [12]. One is the switching/hinge crack model, in which the stiffness of the rotor switches from one corresponding to the closed crack to the stiffness corresponding to the fully open crack state. The other model is the response dependent breathing crack model [13].

2.1.1 SERR Approach

The local flexibilities can be calculated analytically or numerically for various loading cases, according to the strain energy release rate (SERR) approach, under the linear elastic fracture mechanics regime. The SERR approach for calculating the additional flexibility due to the crack is valid only for the fully open crack, but cannot be extended to other intermediate situations. Darpe et al. [14, 15] calculated the breathing by evaluating on the rectilinear crack tip the point where the crack is starting to close, assuming that the closed part of the crack surface is delimited by a boundary, the "crack closure line" (CCL) represented by a segment, orthogonal to the crack tip, that can be drawn from that point on the crack tip. The same approach has been used also by Wu et al. [16] in time step calculations where breathing was determined by vibrations also.

Unlike the previous studies, in Chasalevris and Papadopoulos [17] each crack is characterized by its depth, position and relative angle. The compliance calculation method is applied for the first time in cracked shafts with rotated cracks. The compliance matrix of the crack in bending is calculated using the well-known method of integration of the strain energy density function over the opened crack surface.

2.1.2 3D-FEM Approach

The inherent nonlinearity implied by crack breathing mechanism demands for the development of more sophisticated models. Three dimensional (3D) FEA appears to hold special promise as an investigative tool for the study of crack breathing

mechanism. Researchers of EDF [18] have developed a model in the time domain and directly the compliance of the cracked element is evaluated by means of a 3D model as a function of the applied forces in each time step. As compared to Darpe et al. [14] it was observed that the results are slightly deviating.

The stress singularity at the crack tip is a major consideration always and has to be evaluated. One approach is to utilize singular elements. Among those, the quarter-point element has found considerable popularity because of its accuracy and simplicity [19, 20]. Most scientific effort has been focused on the prediction of fractured rotor dynamics rather than on the accurate simulation of the fracture itself. The exact time dependency of the crack breathing mechanism and its relationship with the aperture angle is yet partially unresolved. Bachschmid and Tanzi [21] have looked at the straight front crack.

Recently, Georgantzinos and Anifantis [22] studied the effect of the crack breathing mechanism on the time-variant flexibility due to the crack in a rotating shaft considering quasi-static approximation and using advanced nonlinear contact-FEM procedure. This method predicts the partial contact of crack surfaces, and it is appropriate to evaluate the instantaneous crack flexibilities. The effect of friction is also considered in the cracked area, using Coulomb's law. In the vicinity of the crack region, a mesh refinement is adopted, while the crack surfaces are constrained with appropriate contact conditions.

2.1.3 Modified 3D FEM

A simplified model, which assumes linear stress and strain distributions, to calculate the breathing mechanism, has been developed by Bachschmid et al. [11] and proved to be very accurate. Unlike the previous studies, transient thermal stresses that can arise in rotating shafts and pre-stresses develop during the crack propagation have been considered. These pre-stresses can further open the crack or can tend to hold the crack more closed, influencing the breathing mechanism. The different steps for calculation of the breathing mechanism are discussed.

2.1.4 Motion Coupled with Crack Opening

In Jun and Gadala [23] additional slope is used to consider the crack breathing and is expressed explicitly in the equation of motion as one of the inputs to produce the bending moment at the crack position. By considering the coupling between the response and the additional slope due to crack breathing, an iterative method is proposed to simulate the dynamic behavior of cracked rotor.

2.2 Wavelet Finite Element Method

For many complex problems with high gradient (e.g., crack tip) or strong nonlinearity in engineering, traditional FEM has some disadvantages, such as low

efficiency, insufficient accuracy, slow convergence to correct solutions etc. In order to overcome these difficulties, wavelet spaces have been employed as approximate spaces and then wavelet finite element methods (WFEM) have been derived [24,25].

The advantages of WFEM are multi-resolution properties and various basis functions for structural analysis [26]. Xiang et al. [27–29] construct some classes of 1D and 2D B-spline wavelet on the interval (BSWI) elements for structural analysis. Li et al. [30] proposed a methodology to detect crack location and size, which takes advantage of WFEM in the modal analysis for singularity problems like a cracked beam. By using WFEM model, Chen et al. [31] gave the experimental identification results in cantilever beams with small identification errors. Xiang et al. [32] proposed a BSWI Euler beam model for detecting crack in a beam, the simulation and experimental results show the high performance of the BSWI Euler beam element. Further, they have extended the same for effective identification in a rotor system [33].

2.2.1 Other Methods

Jun and Gadala [23] used the transfer matrix method [34], while Mohammad and Hosein [35] used Bond graph approach for cracked rotor studies. A modular dynamic network is constructed, consisting of a mass, springs and dampers, resembling shaft segments between cracks.

3 Dynamic Analysis

3.1 Coupled Vibrations

The coupling of lateral and longitudinal vibrations is utilized for crack detection earlier [14,36,37]. Recently, Chasalevris and Papadopoulos [38] discussed the coupled horizontal and vertical bending vibrations in case of a stationary shaft with two cracks. In another paper by them [39], main focus is made in the introduction of coupling due to crack compliance variance while in rotation, with the cross-coupling terms of the local compliance matrix due to the crack taken into account. This new model approximates the phenomenon of coupling between bending vibrations existing only in a specific rotational range. The equation of motion is solved for every rotational step of the shaft making the model dependent on time.

3.2 Multiple Faults

3.2.1 Multiple Cracks

The problem of a structure with multiple cracks has received less attention due to the robust damage assessment techniques needed, and only relatively few papers paid

attention [40]. In a recent review, Sekhar [10] summarizes the different studies on double/multi-cracks and brings out the state of the research on multiple cracks effects and their identification. Faverjon and Sinou [41] proposed the use of frequency response function (FRF) and the "Constitutive Relation Error" updating method for the study of multiple cracks in a simply supported beam. Behavior of the damages could be observed by the special element or connection models [42]. Recently, Chasalevris and Papadopoulos [38] investigated on the coupled vibrations of stationary shaft with two cracks.

Mazanoglu et al. [43] extending the energy-based method [44] presents the vibration identification of non-uniform Euler–Bernoulli beams having multiple open cracks. The distribution of the energy consumed is determined by taking into account not only the strain change at the cracked beam surface, but also the considerable effect of the stress field caused by the angular displacement of the beam due to bending. This method is found useful in reducing the processing time.

3.2.2 Cracks Together with Other Faults

Sekhar [45] used model based identification process to simulate when both unbalance and crack are acting simultaneously on the rotor. Recently, Sinou [46] analysed the non-linear behavior of the rotor system with a breathing crack with unbalance interactions, while Patel and Darpe [47] studied the vibration response of cracked rotor in the presence of rotor-stator rub.

3.2.3 Slant and Helicoidal Cracks

Normally, bending induced fatigue causes cracks to propagate in surfaces that are transverse to the rotation axis of the shaft. But if large torque combines with high bending loads, the crack may also propagate along a helicoidal path, therefore these cracks are called helicoidal or slant cracks [11]. Although failure due to these has never been reported in published literature, some recent studies were done on comparisons with transverse crack [48, 49]. Bachshmid et al. [11] studied crack developed along a helicoidal path with an angle of 6° on the outer surface of the shaft, due to the combined action of bending and torsion. They have summarized the results that at full load the differences between helicoidal and flat crack are so small that they could be neglected. When torsional load is removed then higher differences arise but mainly for the torsional degree of freedom, which is excited by the bending load by means of a coupling effect.

3.3 Nonlinear, Chaos and Bifurcation

A cracked rotor has nonlinear spring characteristics of a piecewise linear type. These piecewise linear characteristics make a directional difference in stiffness and this

difference rotates with the rotor [8]. Recently, simple Jeffcott rotors were used to emphasize non-linear behaviors like resonances at speeds which are twice or 2/3 of the critical speed or even chaotic behavior and bifurcation [12].

Bachschmid et al. [11] evaluated all the non-linear effects due to a rather deep transverse crack that has developed in a full size shaft. Time integration has been used for the non-linear analysis of a heavy, horizontal axis and well-damped steam turbine rotor. The results confirmed that neither instabilities nor subharmonic components did appear, and that the overall deviations from linear behavior were rather small. Zhou et al. [50] investigated nonlinear dynamic behavior of the cracked rotor experimentally. Recently, a few of the studies on oscillations induced by crack have indicated that besides well-known super-harmonic response, chaotic [51–54] and quasi-periodic [52, 55] motions are also possible.

In all the previous studies [51–55] only switching crack model is used. However, Patel and Darpe [12] address the influence of the crack time dependent breathing model also on the nonlinear vibration characteristics of the cracked rotors. Distinct differences have been found in bifurcation, amplitude, orbit and Poincare' map when carrying out the comparison between two models for the assumed rotor parameters.

Bovsunovsky and Surace [56] have claimed that the nonlinear effects are more sensitive to the presence of a crack than the changes of natural frequencies, mode shapes, and they studied the effect of the damping on the nonlinear effects. Based on a simple bilinear oscillator, very recently, Peng et al. [57] analyzed the nonlinear effects due to cracks using a new concept known as nonlinear output frequency response functions (NOFRFs). The results show that higher order NOFRFs are extremely sensitive to the appearance of cracks in the beam, and can therefore be used as crack damage indicators.

4 Identification and Condition Monitoring

4.1 Use of High Precision Modal Parameters and Wavelet FEM

Dong et al. [58] introduced a novel crack detection method based on high-precision modal parameter identification in the BSWI finite element framework, where empirical mode decomposition and Laplace wavelet is proposed. From the selected ten largest correlation coefficients and the corresponding parameters, natural frequency and damping are identified. The errors in the WFE model are minimized by finite element model updating technique, such as output error method. The effectiveness of the proposed method is verified by an experiment and crack parameters are identified.

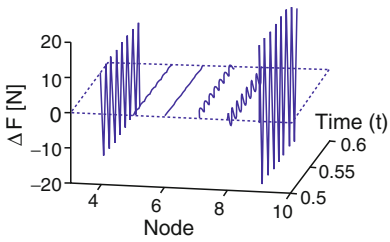

Fig. 1 Forces identified for crack and unbalance [45]

4.2 Model Based Methods

It has been observed that model-based identification has played a significant role in the rapid resolution and quantification of faults [59]. In Sekhar [45] the fault-induced change is taken into account by equivalent loads, which are virtual forces and moments acting on the linear undamaged system to generate a dynamic behavior identical to the measured one of the damaged system.

The rotor has been modeled using FEM with unbalance (nodes 4,9) and crack (seventh element). Using model-based methods, these faults are identified (Fig. 1) for severity and location, while the nature and symptoms of the faults are ascertained using the FFT. Pennacchi et al. [60] have further used the method to identify the cracks not only in slotted rotor; but also breathing type and in a relatively large experimental rig.

4.3 Advanced Signal Processing Techniques

4.3.1 Wavelet

Wavelet methods combine the structural dynamic parameters such as modal frequencies, modal shape and modal damping, etc. with the determined Lipschitz exponent to detect the damage location and depth. Loutridis et al. [61] applied wavelet transform to identification of cracks in cantilever beams by using the sudden changes in the spatial variation of the vibration response to determine the crack location. Further, wavelet packet energy rate index (WPERI) method [62] and wavelet analysis [63] have been used for damaged beam structures, while for rotor systems WFEM is used in [33].

4.3.2 HHT

Wavelet methods may also prove inadequate because, although wavelet is well-suited for analyzing data with gradual frequency changes, its non-locally adaptive approach causes leakage [64]. This leakage can spread frequency energy over a

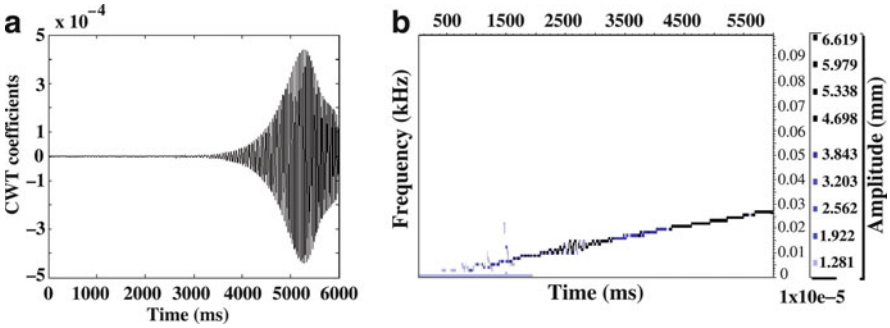

Fig. 2 Comparison of (**a**) CWT (**b**) HHT of cracked

wider range, removing definition from data and giving it an overly smooth appearance. Recently, Hilbert-Huang Transform which is potentially viable for nonlinear and non-stationary data analysis, especially for time-frequency-energy representations has been tried for crack detection in [65, 66]. Some typical result for transient rotor [65] is shown in Fig. 2, where HHT appears to be a better tool compared to wavelet for crack detection.

4.4 Operational Deflection Shapes

Traditionally, an operational deflection shape (ODS) has been defined as the deflection of a structure at a particular frequency or speed. However, an ODS can be defined more generally as any forced motion of two or more points on a structure. The ODS's can be defined for nonlinear and non stationary structural motion, while mode shapes are only defined for linear, stationary motion. The identification of small cracks using the concept of ODS is quite difficult, so a new curve called amplitude deviation curve (ADC) has been developed by Ramesh Babu and Sekhar [67]. The information of the crack parameters like depth of cracks, number of cracks, position of cracks and the angle between the cracks are also available from the ADC. A typical result is presented in Fig. 3.

4.5 Constitutive Relation Error Updating Method

Faverjon and Sinou [68] presented a robust damage assessment technique for the nondestructive detection and estimation of size of open cracks in beams. The damage detection, based on the constitutive relation error updating method, is used for the identification of the crack's location and size in a simply-supported beam. This identification algorithm is illustrated through numerical examples involving different positions and sizes of a transverse open crack and even in the presence of 20% noise. They have used FRF for multiple cracks in [41].

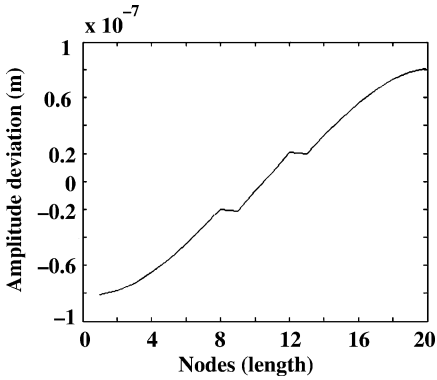

Fig. 3 SDC of cracked rotor with cracks rotor with $a = 30$ rad/s2 [65] in 8th and 12th element [67]

4.6 Soft Computing Methods

In Saridakis et al. [69] a model for the coupling effect of bending vibrations on the cracked shaft is first introduced and then used to identify the rotational angle of the crack. Towards this goal, five different objective functions are proposed and validated; two of these are based on fuzzy logic. More computational intelligence is added through a genetic algorithm, which is used to find the characteristics of the cracks through artificial neural networks that approximate the analytical model. Both the genetic algorithm and the neural networks contribute to a remarkable reduction of the computational time without any significant loss of accuracy.

Recently, Xiang et al. [70] constructed BSWI rotating Rayleigh-Euler and Rayleigh-Timoshenko beam elements to obtain a precision crack detection database, whereas the inverse problem of normalized crack location and depth are detected using genetic algorithm.

5 Real Rotor Systems – Case Studies

In a recent review paper Ishida [8] introduces case histories of cracks found in industrial machines, while Stoisser and Audebert [9] presented the crack detection in power plant turboset or turbo pump units. Bachschmid et al. [71] set up a rotordynamics modeling approach to predict the typical vibration behavior of a vertical axis cooling pump that would exhibit hypothetical deep crack. In this article, the fact is emphasized that the crack behavior is likely to be influenced by the thermal field and by the water pressure in the cracked area.

Pennachi and Vania [72] have analysed the shaft vibrations of a 100MW power unit. The results obtained with a model-based analysis of the shaft vibrations caused by the propagation of a crack occurred in the load coupling connected to the gas turbine of a power unit are discussed.

6 Future Trends

A question arises, what is the scope for further investigations on this topic of cracked rotors started over four decades back. In spite of so much developments in this field, a great need exists for higher accuracy in crack modeling and detection. More research on modeling aspects of crack propagation and residual life estimation is expected in future. Several numerical simulations have to be validated experimentally, which will be increasing in future. With lot of advancement in the signal processing techniques, new and reliable fault diagnostics have to be developed. Studies on crack sensitivity factors for condition monitoring are required.

References

1. Wauer, J.: Dynamics of cracked rotors: Literature survey. Appl. Mech. Rev. **43**, 13–17 (1990)
2. Gasch, R.: A survey of the dynamic behaviour of a simple rotating shaft with a transverse crack. J. Sound Vib. **160**, 313–332 (1993)
3. Dimarogonas, A.D.: Vibration of cracked structures: A state of the art review. Eng. Fract. Mech. **55**, 831–857 (1996)
4. Sabnavis, G., Kirk, R.G., Kasarda, M., Quinn, D.: Cracked shaft detection and diagnostics: a literature review. Shock Vib. Dig. **36**, 287–296 (2004)
5. Bachschmid, N., Pennacchi, P.: Crack effects in rotordynamics. Editorial, Mech. Syst. Signal Process. **22**, 761–762 (2008)
6. Papadopoulos, C.A.: The strain energy release approach for modelling cracks in rotors: A state of the art review. Mech. Syst. Signal Process. **22**, 763–789 (2008)
7. Gasch, R.: Dynamic behaviour of the Laval rotor with a transverse crack. Mech. Syst. Signal Process. **22**, 790–804 (2008)
8. Ishida, Y.: Cracked rotors: industrial machine case histories and nonlinear effects shown by simple Jeffcott rotor. Mech. Syst. Signal Process **22**, 805–817 (2008)
9. Stoisser, C.M., Audebert, S.: A comprehensive theoretical, numerical and experimental approach for crack detection in power plant rotating machinery. Mech. Syst. Signal Process. **22**, 818–844 (2008)
10. Sekhar, A.S.: Multiple cracks effects and identification. Mech. Syst. Signal Process. **22**, 845–878 (2008)
11. Bachschmid, N., Pennacchi, P., Tanzi, E.: Some remarks on breathing mechanism, on nonlinear effects on slant and helicoidal cracks. Mech. Syst. Signal Process. **22**, 879–904 (2008)
12. Patel, T.H., Darpe, A.K.: Influence of crack breathing model on nonlinear dynamics of a cracked rotor. J. Sound Vib. **311**, 953–972 (2008)
13. Jun, O.S., Eun, H.J., Earmme, Y.Y., Lee, C.W.: Modelling and vibration analysis of a simple rotor with breathing crack. J. Sound Vib. **155**, 273–290 (1992)
14. Darpe, A.K., Gupta, K., Chawla, A.: Coupled bending, longitudinal and torsional vibrations of a cracked rotor. J. Sound Vib. **269**(1–2), 33–60 (2004)
15. Darpe, A.K., Gupta, K., Chawla, A.: Dynamics of bowed rotor with a transverse surface crack. J. Sound Vib. **296**, 888–907 (2006)
16. Wu, X., Friswell, M.I., Sawicki, J.T., Baaklini, G.Y.: Finite element analysis of coupled lateral and torsional vibrations of a rotor with multiple cracks. In: Proceedings of ASME Turbo Expo 2005 Gas Turbine Technology: Focus for the Future, vol. 4, pp. 841–850. Reno (NV), 6–9 June 2005
17. Chasalevris, A.C., Papadopoulos, C.A.: Identification of multiple cracks in beams under bending. Mech. Syst. Signal Process. **20**(7), 1631–1673 (2006)

18. Vare, C., Andrieux, S.: Modeling of a cracked beam section under bending. In: 18th International Conference on Structural Mechanics in Reactor-Technology (SMIRT 18), pp. 281–290. Beijing, China, 7–12 August— 2005
19. Andrier, B., Garbay, E., Hasnaoui, F., Massin, P., Verrier, P.: Investigation of helix-shaped and transverse crack propagation in rotor shafts based on disk shrunk technology. Nucl. Eng. Des. **236**, 333–349 (2006)
20. Shin, C.S., Cai, C.Q.: Experimental and finite element analyses on stress intensity factors of an elliptical surface crack in a circular shaft under tension and bending. Int. J. Fract. **129**, 239–264 (2004)
21. Bachschmid, N., Tanzi, E.: Deflections and strains in cracked shafts due to rotating loads: a numerical and experimental analysis. Int. J. Rotat. Mach. **10**, 283–291 (2004)
22. Georgantzinos, S.K., Anifantis, N.K.: An insight into the breathing mechanism of a crack in a rotating shaft. J. Sound Vib. **318**, 279–295 (2008)
23. Jun, O.S., Gadala, M.S.: Dynamic behavior analysis of a cracked rotor. J. Sound Vib. **309**, 210–245 (2008)
24. Ma, J.X., Xue, J.J., Yang, S.J., He, Z.J.: A study of the construction and application of a Daubechies wavelet-based beam element. Finite Ele. Anal. Des. **39**(10), 965–975 (2003)
25. Chen, X.F., Yang, S.J., Ma, J.X., He, Z.J.: The construction of wavelet finite element and its applications. Finite Ele. Anal.Des. **40**(5–6), 541–554 (2004)
26. Chen, X.F., He, Z.J., Xiang, J.W., et al.: A dynamic multiscale lifting computation method using Daubechies wavelet. J. Comput. Appl. Math. **188**(2), 228–245 (2006)
27. Xiang, J.W., Chen, X.F., He, Z.J., Dong, H.B.: The construction of 1D wavelet finite elements for structural analysis. Comput. Mech. **40**(2), 325–339 (2007)
28. Xiang, J.W., Chen, X.F., He, Y.M., He, Z.J.: The construction of plane elastomechanics and Mindlin plate elements of B-spline wavelet on the interval. Finite Ele. Anal. Des. **42**, 1269–1280 (2006)
29. Xiang, J.W., He, Z.J., Chen, X.F.: The construction of wavelet-based truncated conical shell element using B-spline wavelet on the interval. Acta Mec. Solida Sin. **19**(4), 316–326 (2006)
30. Li, B., Chen, X.F., Ma, J.X., He, Z.J.: Detection of crack location and size in structures using wavelet finite element methods. J. Sound Vib. **285**, 767–782 (2005)
31. Chen, X.F., He, Z.J., Xiang, J.W.: Experiments on crack identification in cantilever beams. Exp. Mech. **45**(3), 295–300 (2005)
32. Xiang, J.W., Chen, X.F., Li, B., He, Y.M., He, Z.J.: Identification of crack in a beam based on the finite element method of a B-spline wavelet on the interval. J. Sound Vib. **296**, 1046–1052 (2006)
33. Xiang, J., Chen, X., Mo, Q., He, Z.: Identification of crack in a rotor system based on wavelet finite element method. Finite Ele. Anal. Des. **43**, 1068–1081 (2007)
34. Jun, O.S.: Influence coefficients on rotor having thick shaft elements and resilient bearings. J. Sound Vib. **272**, 657–673 (2004)
35. Mohammad, D., Hosein, B.: Discrete dynamic modelling of shafts with transverse cracks using bond graph. In: Proceedings of DETC.03 ASME 2003 Design Engineering Technical Conferences and Computers and Information in Engineering Conference Chicago, Sharif University of Technology, Illinois, USA, 2–6 September 2003
36. Papadopoulos, C.A., Dimarogonas, A.D.: Coupled longitudinal and bending vibrations of a cracked shaft. J. Vib., Acoust., Stress Reliab. Des. **110**(1), 1–8 (1988)
37. Gounaris, G.D., Papadopoulos, C.A.: Crack identification in rotating shafts by coupled response measurements. Eng. Fract. Mech. **69**(3), 339–352 (2002)
38. Chasalevris, A.C., Papadopoulos, C.A.: Coupled horizontal and vertical vibrations of a stationary shaft with two cracks. J. Sound Vib. **309**, 507–528 (2008)
39. Chasalevris, A.C., Papadopoulos, C.A.: A continuous model approach for cross-coupled bending vibrations of a rotor-bearing system with a transverse breathing crack. Mech. Mach. Theor. (2008). doi: 10.1016/j.mechmachtheory.2008.09.001
40. Alvandia, A., Cremona, C.: Assessment of vibration-based damage identification techniques. J. Sound Vib. **292**, 179–202 (2006)

41. Faverjon, B., Sinou, J.J.: Robust damage assessment of multiple cracks based on the frequency response function and the constitutive relation error updating method. J. Sound Vib. **312**, 821–837 (2008)
42. Kisa, M., Gurel, M.A.: Free vibration analysis of uniform and stepped cracked beams with circular cross sections. Int. J. Eng. Sci. **45**, 364–380 (2007)
43. Mazanoglu, K., Yesilyurt, I., Sabuncu, M.: Vibration analysis of multiple-cracked non-uniform beams. J. Sound Vib. **320**(4–5), 977–989 (2009)
44. Yang, X.F., Swamidas, A.S.J., Seshadri, R.: Crack identification in vibrating beams using the energy method. J. Sound Vib. **244**(2), 339–357 (2001)
45. Sekhar, A.S.: Identification of unbalance and crack acting simultaneously in a rotor system: modal expansion versus reduced basis dynamic expansion. J. Vib. Control **11**(9), 1125–1145 (2005)
46. Sinou, J.J.: Detection of cracks in rotor based on the 2x and 3x super-harmonic frequency components and the crack-unbalance interactions. Commun. Nonlinear Sci. Numer. Simul. **13**, 2024–2040 (2008)
47. Patel, T.H., Darpe, A.K.: Vibration response of a cracked rotor in presence of rotor-stator rub. J. Sound Vib. **317**, 841–865 (2008)
48. Sekhar, A.S., Prabhakar, S., Mohanty, A.R.: Vibrations of cracked rotor systems: transverse crack vs. slant crack. J. Sound Vib. **279**, 1203–1217 (2005)
49. Darpe, A.K.: Dynamics of a Jeffcott rotor with slant crack. J. Sound Vib. **303**(1–2), 1–28 (2007)
50. Zhou, T., Sun, Z., Xu, J., Han, W.: Experimental analysis of cracked rotor. J. Dyn. Syst., Meas. Control **127**, 313–320 (2005)
51. Pu, J., Chen, J., Zou, J., Zhong, P.: The research on nonlinear characteristics of cracked rotor and reconstruction of crack forces. Proc. Inst. Mech. Eng., J. Mech. Eng. Sci. **216**, 1099–1108 (2002)
52. Qin, W., Meng, G., Zhang, T.: The swing vibration, transverse oscillation of cracked rotor and the intermittence chaos. J. Sound Vib. **259**, 571–583 (2003)
53. Qin, W., Meng, G., Xingmin, R.: Grazing bifurcations in the response of cracked Jeffcott rotor. Nonlinear Dyn. **35**, 147–157 (2004)
54. Yiming, F., Yufang, Y., Shijian, Z.: Analysis of the chaotic motion for the rotor system with transverse crack. Acta Mec. Solida Sin. **16**, 74–80 (2003)
55. Pu, J., Chen, J., Zou, J., Zhong, P.: Quasi-periodic vibration of cracked rotor on flexible bearings. J. Sound Vib. **251**, 875–890 (2003)
56. Bovsunovsky, A.P., Surace, C.: Considerations regarding super harmonic vibrations of a cracked beam and the variation in damping caused by the presence of the crack. J. Sound Vib. **288**, 865–886 (2005)
57. Peng, Z.L., Lang, Z.Q., Chu, F.L.: Numerical analysis of cracked beams using nonlinear output frequency response functions. Comput. Struct. **86**, 1809–1818 (2008)
58. Dong, H.B., Chen, X.F., Li, B., Qi, K.Y., He, Z.J.: Rotor crack detection based on high-precision modal parameter identification method and wavelet finite element model. Mech. Syst. Signal Process. **23**, 869–883 (2009)
59. Lees, A.W., Sinha, J.K., Friswell, M.I.: Model-based identification of rotating machines. Mech. Syst. Signal Process. (2008). doi: 10.1016/j.ymssp.2008.08.008
60. Pennacchi, P., Bachschmid, N., Vania, A.: A model-based identification method of transverse cracks in rotating shafts suitable for industrial machines. Mech. Syst. Signal Process. **20**(8), 2112–2147 (2006)
61. Loutridis, S., Douka, E., Trochidis, A.: Crack identification in double cracked beams using wavelet analysis. J. Sound Vib. **277**, 1025–1039 (2004)
62. Loutridis, S., Douka, E., Hadjileontiadis, L.J., et al.: A two-dimensional wavelet transform for detection of cracks in plates. Eng. Struct. **27**, 1327–1338 (2005)
63. Zhu, X.Q., Law, S.S.: Wavelet-based crack identification of bridge beam from operational deflection time history. Int. J.Solids Struct. **43**, 2299–2317 (2006)
64. http://techtransfer.gsfc.nasa.gov/downloads/HHT-DPS-WhitePaper.pdf
65. Ramesh Babu, T., Srikanth, S., Sekhar, A.S.: Hilbert–Huang transform for detection and monitoring of crack in a transient rotor. Mech. Syst. Signal Process. **22**(4), 905–914 (2008)

66. Guo, D., Peng, Z.K.: Vibration analysis of a cracked rotor using Hilbert-Huang transform. Mech. Syst. Signal Process. **21**(8), 3030–3041 (2007)
67. Ramesh Babu, T., Sekhar, A.S.: Detection of two cracks in a rotor-bearing system using amplitude deviation curve. J. Sound Vib. **314**, 457–464 (2008)
68. Faverjon, B., Sinou, J.J.: Identification of an open crack in a beam using an a posteriori error estimator of the frequency response function with noisy measurements. Eur. J. Mech. A/Solids **28**, 75–85 (2009)
69. Saridakis, K.M., Chasalevris, A.C., Papadopoulos, C.A., Dentsoras, A.J.: Applying neural networks, genetic algorithms and fuzzy logic for the identification of cracks in shafts by using coupled response measurements. Comp. Struct. **86**, 1318–1338 (2008)
70. Xiang, J., Zhong, Y., Chen, X., He, Z.: Crack detection in a shaft by combination of wavelet-based elements and genetic algorithm. International Journal of Solids and Structures 45: 4782–4795 (2008)
71. Bachschmid N, Pennacchi P, Tanzi E, Verrier P, Hasnaoui F, Aabadi K (2004) Crack detectability in vertical axis cooling pumps during operation. Int. J. Rotat. Mach. **10**, 121–133
72. Pennacchi, P., Vania, A.: Diagnostics of a crack in a load coupling of a gas turbine using the machine model and analysis of the shaft vibrations. Mech. Syst. Signal Process. **22**, 1157–1178 (2008)

A Multi-Crack Identification Algorithm Based on Forced Vibrations from a Shaft System

S.K. Singh, R. Tiwari, and S. Talukdar

Abstract A multi-crack identification algorithm has been developed based on the forced response from a shaft. Transverse vibrations of a cracked shaft in the two orthogonal planes are analyzed. The presence of cracks in a shaft introduces a local slope discontinuity in the elastic line of the shaft. This slope discontinuity is estimated by approximating the forced response of shaft at consecutive measurement axial locations by a polynomial. The algorithm is tested for numerically simulated responses from the FE modeling of a simply supported shaft having two cracks.

Keywords Crack identification · Multi-cracked shaft · Forced response

1 Introduction

Cracks in machine elements can arise because of several reasons. These cracks can be fatigue cracks, which develop because of limited fatigue life of machine elements. Cracks can also arise because of faulty manufacturing process or because of some mechanical defects. There can be simultaneously more than one sub-critical crack present in the machine element. Identification of all the cracks and their extent of damage is important to predict the life of machine element, and hence to schedule for the corrective measures.

There are plenty of literatures that deal with the identification of cracks in structures. A review on vibration based techniques for identification of cracks in structures is presented in Ref. [1]. Presence of cracks causes a local change in the stiffness of structures. Dimarogonas and Paipetis [2] showed that a beam with a transverse crack, in general, can be modelled in the vicinity of the crack by way of

S.K. Singh and R. Tiwari (✉)
Department of Mechanical Engineering, Indian Institute of Technology, Guwahati 781039, India
e-mail: rtiwari@iitg.ernet.in

S. Talukdar
Department of Civil Engineering, Indian Institute of Technology, Guwahati 781039, India

K. Gupta (ed.), *IUTAM Symposium on Emerging Trends in Rotor Dynamics*, IUTAM Bookseries 25, DOI 10.1007/978-94-007-0020-8_42,

a local flexibility (compliance) matrix. Karthikeyan et al. [3] developed an iterative method for the crack identification which utilized forced responses and the change in the natural frequency. Darpe [4] proposed a crack identification procedure in rotating shaft by analyzing the transient features of the resonant bending vibrations by wavelet transforms. He utilized both the nonlinear breathing phenomenon of the crack and the coupling of bending–torsional vibrations due to the presence of crack.

With multiple cracks in structures, the identification process becomes more complicated as the number of unknown crack parameters (i.e., number of cracks, their locations and sizes) is far more. Sekhar [5] presented a review of work on multi-crack identification techniques in structures such as beams, rotors, pipes etc. Chasalevris and Papadopoulos [6] analyzed the coupled bending vibrations due to presence of two cracks in a stationary shaft. The coupling was found to be dependent upon the relative orientation of the two cracks. Method, like the wavelet transform works locally and it gives number of cracks and their locations. Quek et al. [7] studied the effectiveness of different wavelet techniques in the identification of cracks with respect to crack parameters like, the size, orientation and width of the crack. The wavelet technique needs more measurement locations over the cracked structures and a high signal-to-noise ratio. These are possible only when measurements are taken near or at the resonance frequency or by photographic methods [8].

In the present work, a multi-crack identification algorithm has been developed based on the forced response from a shaft. The discontinuity in the elastic line of the shaft is found out by fitting the forced response of the shaft at consecutive points in a polynomial. *Crack probability functions* are defined with help of the estimated polynomial coefficients obtained from forced responses at different frequencies, which provide the number of cracks present and their locations over the shaft. The proposed algorithm uses shaft responses at several locations along the shaft; this may limit applicability of the method in practise, where some locations for measurements may be inaccessible.

2 System Modeling

The Timoshenko beam theory is used in the shaft modeling for transverse vibrations. The FEM is used to develop the discretized model of the shaft. The effect of the proportionate damping has been included. An open transverse surface crack is considered for the crack model. Cracks are assumed to be open and have the same orientation.

2.1 Model of a Shaft Element with a Crack

Figure 1 shows a shaft element with a crack subjected to a general loading. Here P_1 is the axial force, P_2 and P_3 are shearing forces, P_4 and P_5 are bending moments,

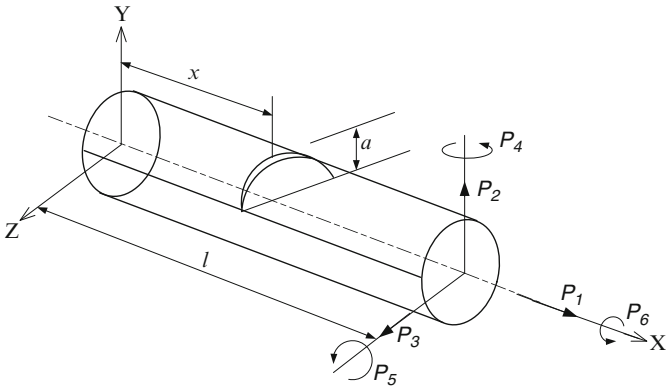

Fig. 1 A shaft element with a crack subjected to a general loading

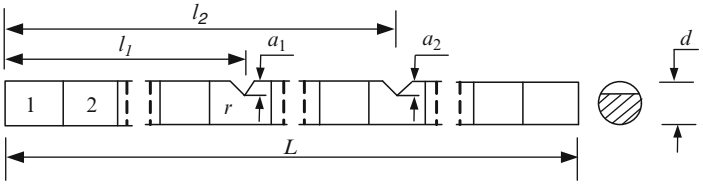

Fig. 2 Finite element discrete model of the shaft with crack

and P_6 is the torque; l is the shaft element length, a is the crack depth, and X-Y-Z is a rectilinear coordinate system. Figure 2 shows FE model of the shaft with crack.

For the transverse loading of the shaft, neglecting the axial and torsional loadings, the flexibility matrix of the crack could be expressed as [9],

$$[C_c]^{(e)} = \begin{bmatrix} c_{22} & 0 & 0 & 0 \\ 0 & c_{33} & 0 & 0 \\ 0 & 0 & c_{44} & c_{45} \\ 0 & 0 & c_{54} & c_{55} \end{bmatrix} \tag{1}$$

where $c_{22}, c_{33}, \ldots, c_{55}$ are the six non-zero flexibility coefficients of the crack, in which four are direct coefficients and remaining two are cross-coupled coefficients.

2.2 System Equations of Motion

The equation of motion for the shaft element with and without crack, respectively, can be written as in Eqs. (2) and (3)

$$[\mathbf{M}]^{(e)}\{\ddot{\mathbf{q}}_c(t)\}^{(e)} + [\mathbf{D}_c]^{(e)}\{\dot{\mathbf{q}}_c(t)\}^{(e)} + [\mathbf{K}_c]^{(e)}\{\mathbf{q}_c(t)\}^{(e)} = \{\mathbf{F}(t)\}^{(e)}, \quad (2)$$

$$[\mathbf{M}]^{(e)}\{\ddot{\mathbf{q}}(t)\}^{(e)} + [\mathbf{D}_{wc}]^{(e)}\{\dot{\mathbf{q}}(t)\}^{(e)} + [\mathbf{K}_{wc}]^{(e)}\{\mathbf{q}(t)\}^{(e)} = \{\mathbf{F}(t)\}^{(e)} \quad (3)$$

where subscripts c and wc are used to represent the cracked and intact elements respectively. Matrices $[\mathbf{M}]^{(e)}$, $[\mathbf{D}]^{(e)}$, $[\mathbf{K}]^{(e)}$, are the elemental mass, damping and stiffness matrices, and vectors $\{\mathbf{F}(t)\}^{(e)}$ and $\{\mathbf{q}(t)\}^{(e)}$ are the elemental force and response vectors, respectively. For a harmonic transverse excitation $\{\mathbf{f}(t)\} = \{\mathbf{F}\}e^{j\omega t}$, the shaft response vector is given as $\{\mathbf{q}(t)\} = \{\mathbf{Q}\}e^{j\omega t}$; and system equations after the application of boundary conditions reduce to

$$\left(-\omega^2[\mathbf{M}] + j\omega[\mathbf{D}] + [\mathbf{K}]\right)\{\mathbf{Q}\} = \{\mathbf{F}\} \quad (4)$$

3 Crack Identification Algorithms

The presence of cracks in the shaft causes a slope discontinuity in the elastic line of the shaft. This slope discontinuity is not easy to identify especially in presence of measurement noise. However, once the slope discontinuity can be identified, it could be used to identify both the number and the locations of cracks. In the present algorithm, effect of noise in the signal has been reduced by utilizing the response of the shaft at several frequencies. To find out the discontinuity in the slope of the vibrating shaft, measured forced responses are fitted with a polynomial. Estimated coefficients of polynomials are normalized in such a way that it amplifies the slope discontinuity and reduces the effect of noise in the signal.

Let the number of equidistant locations at which linear DOFs are measured is $(n-2)$, and that the number of frequencies at which the system is excited is (k). Including the boundary conditions at the two ends, we have information of linear DOFs at (n) locations. Let us denote the measured deflection of the cracked shaft at frequency ω_i and location x_j by $q_{cv_{i,j}}$ in vertical plane, and similarly $q_{ch_{i,j}}$ in the horizontal plane. Also let the deflection predicted by the model of the intact shaft be $q_{wcv_{i,j}}$ in the vertical plane, and similarly $q_{wch_{i,j}}$ in the horizontal plane. Deflections at three consecutive points are selected to find out the coefficients of the quadratic polynomial between them. Coefficients for the quadratic polynomial of the form,

$$q = ax^2 + bx + c, \quad (5)$$

could be found for the cracked shaft at frequency ω_i, as,

$$q_{cv_{i,j-1}} = a_{cv_{i,j}}x_{j-1}^2 + b_{cv_{i,j}}x_{j-1} + c_{cv_{i,j}}, \quad (6)$$

$$q_{cv_{i,j}} = a_{cv_{i,j}}x_j^2 + b_{cv_{i,j}}x_j + c_{cv_{i,j}}, \quad (7)$$

$$q_{cv_{i,j+1}} = a_{cv_{i,j}}x_{j+1}^2 + b_{cv_{i,j}}x_{j+1} + c_{cv_{i,j}}. \quad (8)$$

The fitted polynomial contains information of deflections, slopes, and curvatures in the form of its three coefficients, *a, b* and *c* respectively. Here $q_{cv_{i,j-1}}$, $q_{cv_{i,j}}$, and $q_{cv_{i,j+1}}$ are the displacements in the vertical direction at measurement locations x_{j-1}, x_j, and x_{j+1}, respectively. In matrix notation, Eqs. (6)–(8) can be written as

$$\begin{Bmatrix} a_{cv_{i,j}} \\ b_{cv_{i,j}} \\ c_{cv_{i,j}} \end{Bmatrix} = \begin{bmatrix} x_{j-1}^2 & x_{j-1} & 1 \\ x_j^2 & x_j & 1 \\ x_{j+1}^2 & x_{j+1} & 1 \end{bmatrix}^{-1} \begin{Bmatrix} q_{cv_{i,j-1}} \\ q_{cv_{i,j}} \\ q_{cv_{i,j+1}} \end{Bmatrix}, \; i = 1, \ldots, k; \; j = 2, \ldots, n-1 \tag{9}$$

Similarly, coefficients $a_{wcv_{i,j}}$, $b_{wcv_{i,j}}$, $c_{wc_{i,j}}$, $a_{wch_{i,j}}$, $b_{wch_{i,j}}$, $c_{wch_{i,j}}$ for the intact shaft can be written in terms of the corresponding deflections by,

$$\begin{Bmatrix} a_{wcv_{i,j}} \\ b_{wcv_{i,j}} \\ c_{wcv_{i,j}} \end{Bmatrix} = \begin{bmatrix} x_{j-1}^2 & x_{j-1} & 1 \\ x_j^2 & x_j & 1 \\ x_{j+1}^2 & x_{j+1} & 1 \end{bmatrix}^{-1} \begin{Bmatrix} q_{wcv_{i,j-1}} \\ q_{wcv_{i,j}} \\ q_{wcv_{i,j+1}} \end{Bmatrix}, \; i = 1, \ldots, k; \; j = 2, \ldots, n-1 \tag{10}$$

Now for each frequency ω_i, we obtain the difference of the maximum and minimum values of the real part of the $a_{wcv_{i,j}}$, coefficients obtained from the deflection of the intact shaft in vertical direction, over all the measurement locations from $j = 2$ to $j = n - 1$. Hence define $a^{\mathrm{I}}_{wcv_i}$ by

$$a^{\mathrm{I}}_{wcv_i} = \frac{\max\left\{\text{real}(a_{wcv_{i,2}}, \ldots, a_{wcv_{i,n-1}})\right\} - \min\left\{\text{real}(a_{wcv_{i,2}}, \ldots, a_{wcv_{i,n-1}})\right\}}{k_a}, \quad i = 1, \ldots, k \tag{11}$$

where k_a is a constant and its value could be chosen depending upon the noise in the signal and the number of excitation frequencies. At later stage we have to normalize the coefficients obtained from measured cracked shaft responses by dividing it with the coefficients obtained from FE modeling of intact shaft responses. To avoid singularity type of situations, let us shift the coefficients $a^{\mathrm{I}}_{wcv_{i,j}}$ at all the measurement locations and at all the frequencies such that minimum value of its real part is $a^{\mathrm{I}}_{wcv_i}$. Hence define $a^{\mathrm{II}}_{wcv_{i,j}}$ by

$$a^{\mathrm{II}}_{wcv_{i,j}} = a_{wcv_{i,j}} - \min\left\{\text{real}(a_{wcv_{i,2}}, \ldots, a_{wcv_{i,n-1}})\right\} + a^{\mathrm{I}}_{wcv_j}, \quad i = 1, \ldots, k; \; j = 2, \ldots, n-1 \tag{12}$$

Now shift the coefficients $a^{\mathrm{I}}_{cv_{i,j}}$ also by the same amount, hence define $a^{\mathrm{II}}_{cv_{i,j}}$ by

$$a^{\mathrm{II}}_{cv_{i,j}} = a_{cv_{i,j}} - \min\left\{\text{real}(a_{cv_{i,2}}, \ldots, a_{cv_{i,n-1}})\right\} + a^{\mathrm{I}}_{wcv_i}, \quad i = 1, \ldots, k; \; j = 2, \ldots, n-1 \tag{13}$$

We need to normalize the cracked shaft coefficients so that the coefficients at different frequencies can be added. For this purpose, divide the cracked shaft

coefficients $a^{\mathrm{II}}_{cv_{i,j}}$ by the corresponding coefficients $a^{\mathrm{II}}_{wcv_{i,j}}$ of the intact shaft obtained from the deflections in the vertical direction. Hence, define $a^{\mathrm{III}}_{v_{i,j}}$ by

$$a^{\mathrm{III}}_{v_{i,j}} = \frac{a^{\mathrm{II}}_{cv_{i,j}}}{a^{\mathrm{II}}_{wcv_{i,j}}},\ i = 1,\ldots,k;\ j = 2,\ldots,n-1 \tag{14}$$

It can be seen above that ratios of coefficients are obtained for the intact and cracked shaft. Hence, the procedure is actually capturing the variation of the deflection and its higher derivatives (up to second) between the intact and cracked shafts. Now for each measurement location, add the modified coefficients $a^{\mathrm{III}}_{v_{i,j}}$ obtained at different excitation frequencies ω_i, to get new coefficients $a^{\mathrm{IV}}_{v_j}$ as

$$a^{\mathrm{IV}}_{v_j} = a^{\mathrm{III}}_{v_{1,j}} + a^{\mathrm{III}}_{v_{2,j}} + \ldots. + a^{\mathrm{III}}_{v_{k,j}},\ j = 2,\ldots,n-1 \tag{15}$$

The coefficients obtained above can be scaled down to vary between 0 and 1. For this purpose, define, $a^{\mathrm{V}}_{v_j}$ by

$$a^{\mathrm{V}}_{v_j} = \mathrm{abs}\left\{\frac{a^{\mathrm{IV}}_{v_j} - \min\left(a^{\mathrm{IV}}_{v_2}, a^{\mathrm{IV}}_{v_3}, \ldots., a^{\mathrm{IV}}_{v_{n-1}}\right)}{\max\left(a^{\mathrm{IV}}_{v_2}, a^{\mathrm{IV}}_{v_3}, \ldots., a^{\mathrm{IV}}_{v_{n-1}}\right) - \min\left(a^{\mathrm{IV}}_{v_2}, a^{\mathrm{IV}}_{v_3}, \ldots., a^{\mathrm{IV}}_{v_{n-1}}\right)}\right\},\quad j = 2,\ldots,n-1 \tag{16}$$

The *crack probability functions* CPF_{av_j}, can be defined as the absolute distance of the coefficients $a^{\mathrm{V}}_{v_j}$ from their mean as,

$$CPF_{av_j} = \mathrm{abs}\left\{a^{\mathrm{V}}_{v_j} - \mathrm{mean}\left(a^{\mathrm{V}}_{v_2}, a^{\mathrm{V}}_{v_3}, \ldots., a^{\mathrm{V}}_{v_{n-1}}\right)\right\},\quad j = 2,\ldots,n-1\ j = 2,\ldots,n-1 \tag{17}$$

Here crack probability functions CPF_{av_j}, give the probability of presence of crack between locations x_{j-1} and x_{j+1}. Greater the value of these probability functions, more the chances that crack is present. Similarly crack probability functions CPF_{bv_j}, corresponding to coefficient b can be obtained. In a similar way crack probability functions from the horizontal direction response CPF_{ah_j} and CPF_{bh_j} can be defined. Since there is no response in the horizontal direction due to vertical force of the intact shaft, the quadratic coefficients obtained from the cracked shaft response in the horizontal direction are normalized by dividing the individual coefficients by their mean at each frequency, before adding them at all the frequencies.

4 Numerical Experiments

Algorithm is tested for a simply supported shaft and its parameters are given in Table 1.

Table 1 Shaft parameters for the numerical experiments

Parameters	Values
Diameter and length of the shaft	0.01 m, 0.1 m
Young's modulus and density of shaft material	$2.06 \times 11\,\mathrm{N/m^2}$, $7{,}800\,\mathrm{kg/m^3}$
Number of finite elements	80
Number of measurement locations	19
Location of the first cracked element	32
Location of the second cracked element	60
Depth of first crack	0.0030 m
Depth of second crack	0.0035 m
Damping ratio	0.01
Measurement noise	1%
Excitation frequencies (in rad/s)	5, 10, . . . , 110, 140, 145, . . . , 190

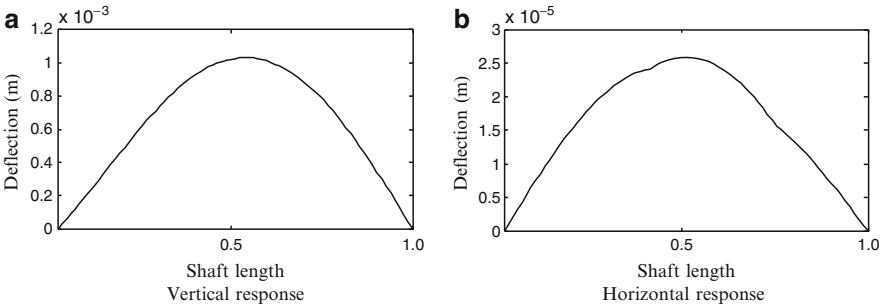

Fig. 3 Cracked shaft response amplitudes at 150 rad/s, (**a**) vertical (**b**) horizontal

Two cracks are introduced in the shaft. Responses for the intact shaft for a vertical harmonic forcing at 150 rad/s are obtained from Eq. (4). Responses for the cracked shaft are also generated for the same forcing and are plotted in Fig. 3.

The forced response of the cracked shaft is treated as the measured response after adding 1% noise in the response.

Figure 4a shows variation of coefficients $a^{\mathrm{II}}_{wcv_{i,j}}$ and $a^{\mathrm{II}}_{cv_{i,j}}$ with measurement locations and are defined in Eqs. (12) and (13) respectively. After normalizing cracked shaft coefficients $a^{\mathrm{II}}_{cv_{i,j}}$ with help of intact shaft coefficients $a^{\mathrm{II}}_{wcv_{i,j}}$, as defined in Eq. (14), coefficients $a^{\mathrm{III}}_{v_{i,j}}$ are obtained and are plotted in Fig. 4b. Now coefficients $a^{\mathrm{III}}_{v_{i,j}}$, at different frequencies are added, as given in Eq. (15).

Algorithm is found to be better when value of k_a defined in Eq. (11), is taken to be 0.1, and its value is found out by the trial and error method. *CPF* is obtained by Eq. (17). Crack probability functions obtained from vertical direction responses are plotted in Figs. 5a, b, while those obtained from horizontal direction responses are given in Figs. 5c, d. Crack probability functions have high values at those measurement locations which are near to the cracked element, e.g., at measurement locations

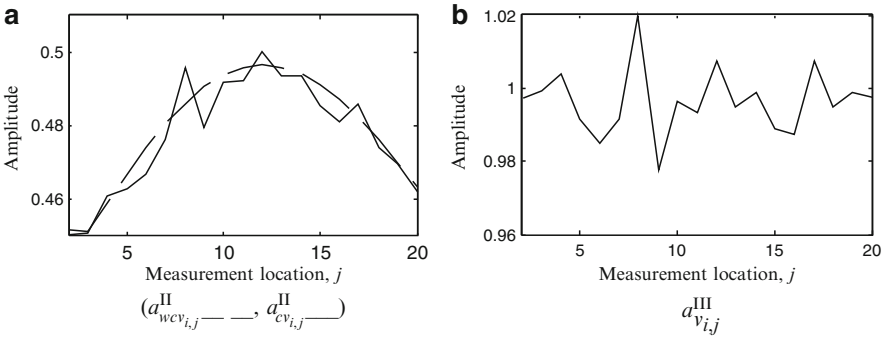

Fig. 4 Variation of coefficients (**a**) $a^{II}_{wcv_{i,j}}$, $a^{II}_{cv_{i,j}}$, (**b**) and $a^{III}_{v_{i,j}}$ with measurement location

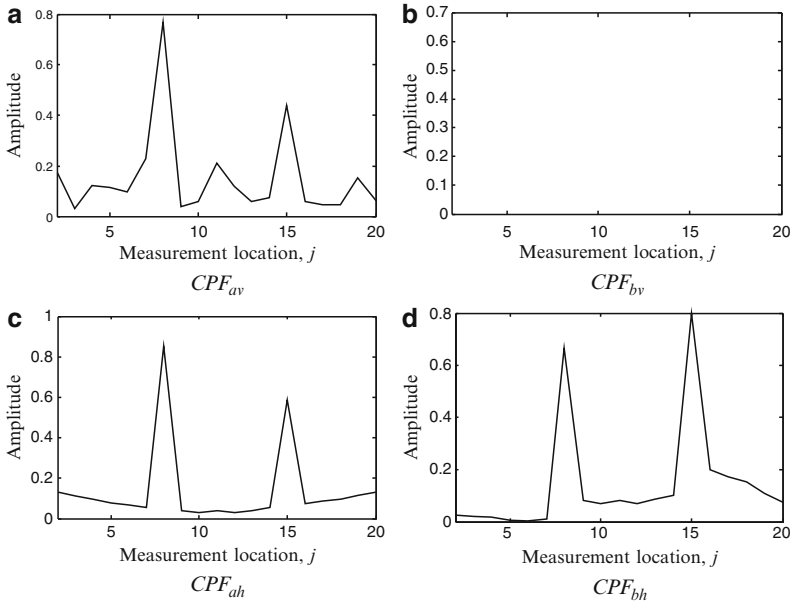

Fig. 5 Crack probability functions (**a**) CPF_{av} (**b**) CPF_{bv} (**c**) CPF_{ah} and (**d**) CPF_{bh}

x_8 and x_{15}. Hence it indicates presence of two cracks in the shaft, one between locations x_7 and x_9 while the other between locations x_{14} and x_{16}.

The present method is equally valid for different orientations of cracks, whereas for breathing cracks (non-rotating shaft), a total of four CPF values (the vertical upward and downward directions, and similarly in the horizontal upward and downward directions) need to be estimated. For this case we need to take measurements in all four transverse directions of the shaft with respect to the static equilibrium position.

5 Conclusions

An identification algorithm has been developed to find out the number of cracks and their locations over the shaft length. The algorithm relies on forced responses of the cracked shaft, and the response predicted by the FEM modeling of the uncracked shaft. Compared to wavelet techniques, resonance frequencies can be avoided very well as the proposed algorithm utilizes the shaft response at several frequencies to reduce the effect of noise in the signal. It would be interesting to obtain the severity of the cracks and its orientations in conjunction with the present algorithm as a base.

References

1. Dimarogonas, A.D.: Vibration of cracked structures: a state of the art review. Eng. Fract. Mech. **55**, 831–857 (1996)
2. Dimarogonas, A.D., Paipetis, S.A.: Analytical Methods in Rotor Dynamics. Elsevier Applied Science, London (1983)
3. Karthikeyan, M., Tiwari, R., Talukdar, S.: Development of a novel algorithm for a crack detection, localization, and sizing in a beam based on forced response measurements. Trans. ASME, J. Vib. Acoust. **130**, 021002-(1–14) (2008)
4. Darpe, A.K.: A novel way to detect transverse surface crack in a rotating shaft. J. Sound Vib. **305**, 151–171 (2007)
5. Sekhar, A.S.: Multiple cracks effects and identification. Mech. Syst. Signal Process. **22**, 845–878 (2008)
6. Chasalevris, A.C., Papadopoulos, C.A.: Coupled horizontal and vertical bending vibrations of a stationary shaft with two cracks. J. Sound Vib. **309**, 507–528 (2008)
7. Quek, S., Wang, Q., Zhang, L., Ang, K.: Sensitivity analysis of crack detection in beams by wavelet techniques. Int. J. Mech. Sci. **43**, 2899–2910 (2001)
8. Chasalevris, A.C., Papadopoulos, C.A.: Identification of multiple cracks in beams under bending. Mech. Syst. Signal Process. **20**, 1631–1673 (2006)
9. Papadopoulos, C.A., Dimarogonas, A.D.: Coupled longitudinal and bending vibration of rotating shaft with an open crack. J. Sound Vib. **117**, 81–93 (1987)

Vibration Based Condition Monitoring of Rotating Machines: A Future Possibility?

Jyoti K. Sinha

Abstract Adopted conventional practice is to use number of vibration sensors at a bearing pedestal of a rotating machine for the vibration based condition monitoring. Number of bearings in a machine, say, a Turbo-Generator (TG) set is likely to be very high, hence increasing the number of sensors to large number. Therefore data acquisition results in huge data sets to analyze to track any fault/faults which often depend on the experience and the engineering judgment. The effort of the present study is to reduce the number of sensors per bearing pedestal based on the higher order spectra (HOS) and data fusion so that the vibration data is managed efficiently and is able to detect fault uniquely. The preliminary results of the suggested approach have been discussed here.

Keywords Rotating machine · Fault detection · Higher order spectra · Bispectrum · Trispectrum · Data fusion

1 Introduction

Rotating machines in general consist of three major parts – a rotor, journal bearings (fluid or anti-friction bearings) and a foundation. Turbogenerator (TG) set is one such major rotating machine. It consists of a High Pressure (HP) turbine, a Low Pressure (LP) turbine and an Electric Generator. A simplified block diagram of a TG set is shown in Fig. 1. In some high capacity power plants the TG sets also have a few Intermediate Pressure (IP) turbines between the HP and LP turbines. The shafts of the individual systems are joined together by means of couplings, and the complete shaft is known as the rotor of the TG set. The shafts of each turbine are designed to have a number of rows of turbine blades along the shaft length.

J.K. Sinha (✉)
School of Mechanical, Aerospace and Civil Engineering (MACE),
The University of Manchester, Manchester M60 1QD, UK
e-mail: Jyoti.Sinha@manchester.ac.uk

K. Gupta (ed.), *IUTAM Symposium on Emerging Trends in Rotor Dynamics*,
IUTAM Bookseries 25, DOI 10.1007/978-94-007-0020-8_43,

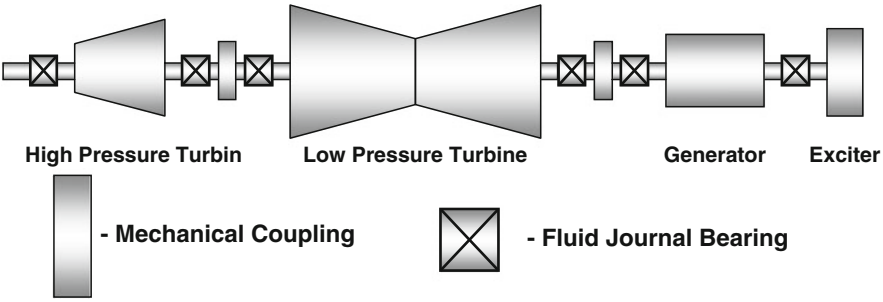

Fig. 1 Schematic of a simple layout of a TG set

Each rotor of an individual system is normally supported by its own journal bearings, which are supported on foundation structures which are often flexible.

Experience shows that faults develop in rotating machines during normal operation. Vibration based condition monitoring is popular and well accepted in plants to meet this requirement, perhaps because the machine vibration response is sensitive to any small structural or process parameter change. However the accepted practice requires four sensors at each bearing – two accelerometers on the bearing pedestals and two proximitors to measure shaft relative vibration. So if a TG set has eight bearings; a total of 32 sensors are needed. In addition, a tacho sensor is also required for the phase reference of the rotor with respect to the stationary part (bearing pedestal) and for the rotor speed measurement [1]. To aid understanding, Fig. 2 gives the different kinds of instrumentation used at a bearing. Then number of data processing methods are commonly used for tracking down a number of well recognized faults (mass unbalance, shaft bent or bow, misalignment and preloads, crack, shaft rub, fluid induced instability, mechanical looseness/bearing assembly looseness) during normal and/or transient machine operation. Often these analyses include (a) overall vibration (bearing pedestal and/or shaft relative vibration), (b) spectrum analysis, (c) orbit plot, (d) 3-D waterfall spectra plot, (e) Bode plot, (f) shaft centre line plot, and (g) polar plot or amplitude-phase versus time plot.

Experience shows that even with these advances, tracking a fault requires significant experience and engineering judgment. Hence the present objectives are concerned with:

1. Reducing the number of sensors per bearing pedestal which is definitely welcomed by any industry.
2. Utilization of computational power in signal processing to compensate the effect of reduction in number of sensors.
3. Data fusion of all signals from number of bearing pedestals to get a composite signal for a machine to reduce the experience and engineering judgment in identification of a fault.

Presently the proposed method has been applied for the crack detection only in a simulated example of a rotating rig with three bearings supported on the flexible

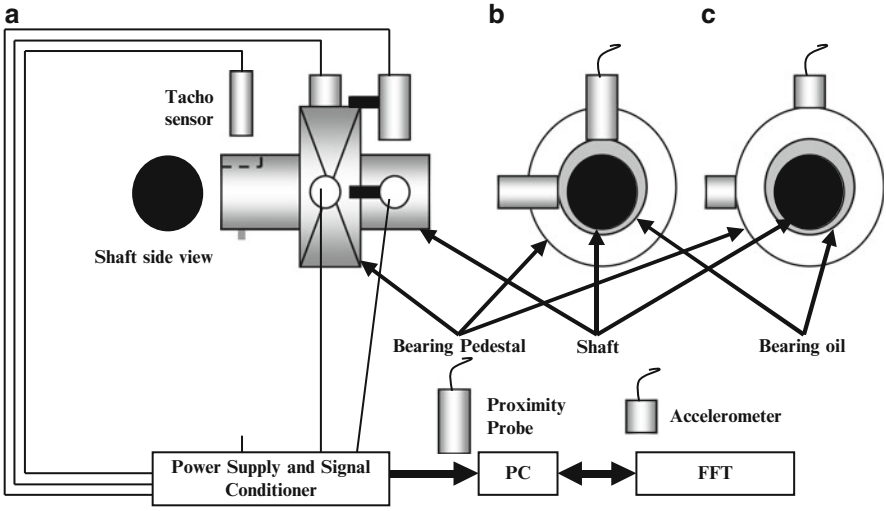

Fig. 2 Mounting of different types of vibration transducers, (**a**) front view of bearings and shaft, (**b**) side view –accelerometers not shown for clarity and (**c**) side view – proximity probes (not shown for clarity)

foundation. Results seem to be encouraging and indicate a potential possibility of the future direction in the condition monitoring of rotating machines with significantly reduced number of sensors.

2 The Proposed Method

Although the adopted practice of conventional vibration-based condition monitoring of rotating machines uses a number of sensors to identify any fault, in general practical diagnosis is related to the machine speed and its sub and higher harmonics. Hence it was natural that the proposed research has again looked into the features of the higher and sub-harmonics, but in a different ways. Presently the relations of the harmonics behaviour of one sensor with the other sensor placed in orthogonal direction are used, however in the proposed method the relations of different harmonics of the same signal measured at a bearing pedestal using the higher order spectra (HOS), namely bispectrum and trispectrum have been explored [2], thus reducing the number of sensors at a bearing to one. It is because the bispectrum is the double Fourier transformation of the third order moment of a time signal that involves two frequency components (both amplitudes and phases) of the signal with a third frequency component summation of first two frequencies. Similarly, the tricoherence is the Fourier transformation of the fourth order moment of a signal that relates four frequency components (three frequency components with a frequency component summation of the three frequencies).

The steps involved are the data fusion between the measured signals from all the bearings which enables the computation of a composite signal [3] to reduce the dependency of the vibration responses from individual bearings. The composite signal is defined as the geometric mean of the coherent cross-power spectra of the vibration responses from all the bearing pedestals. Sinha Jyoti [3] gave the details of this composite spectrum. The composite spectrum of the machine is then used for the computation of a single composite bispectrum for a machine.

3 Example 1

The Example 1 study based on HOS has been at an exploratory level for the crack and misalignment detection in a simple small experimental rig [4]. The rig [4] consists of a 10 mm OD steel shaft of 550 mm length through two bush bearings, which are directly mounted on a rigid massive base plate. The one end of the shaft is coupled with motor through a flexible coupler. One bearing is placed near the motor and the second bearing at the other end of the shaft. The shaft also carries one balance disk made of steel and placed at mid-span of the two bearings. Balance disk dimensions are 75 mm OD, 10 mm ID and 25 mm thickness. Two kind of experiments were conducted, one with the cracked shaft and other with the shaft misalignment at the coupling between the motor and the rotor shafts. The crack in the shaft was developed such that the breathing of the crack can be possible during the shaft rotation.

Here the vertical response data only (one sensor per bearing only) has been used to compute the bispectrum and trispectrum [4]. The amplitude plots for bispectra and trispectra are shown in Fig. 3 when rotating speed was half of the critical speed. The bispectrum component, B_{mn}, means the response at mth and nth orders related to the $(m + n)$th order response. The component, B_{22}, means that the second order response (two times) is related to a fourth order response. Similarly, the trispectrum component, T_{mnp}, means the response at mth, nth and pth orders related to the $(m + n + p)$th order response. The diameter of the ball in Fig. 3 represents the amplitude of the component.

The amplitude spectra for both faults contain number of higher harmonics in the shaft responses [6] as expected, however a total four peaks are only seen in the bispectrum shown in Fig. 3 for the cracked shaft. Since the crack in structures produced multiple harmonics of the exciting frequency, the viewing of the bispectrum results in terms of their components like $\mathbf{B}_{11}$, $\mathbf{B}_{12}$, $\mathbf{B}_{22}$, etc. would be useful. A total of five peaks have always appeared in the bispectrum for the misaligned shaft. An additional off-diagonal peak $\mathbf{B}_{13}$ $(= \mathbf{B}_{31})$ observed in the misaligned shaft and the non-existence of $\mathbf{B}_{22}$ indicate that the dynamics of the misaligned shaft in terms of the phase relation between 2X, 3X and 4X components is certainly much different from the cracked shaft. Similarly, the trispectrum for the cracked shaft response contains several trispectral components ($\mathbf{T}_{111}$, $\mathbf{T}_{112} = \mathbf{T}_{121} = \mathbf{T}_{211}$, $\mathbf{T}_{122} = \mathbf{T}_{212} = \mathbf{T}_{221}$, and $\mathbf{T}_{222}$), however the only component of $\mathbf{T}_{111}$ has been observed for the misaligned shaft.

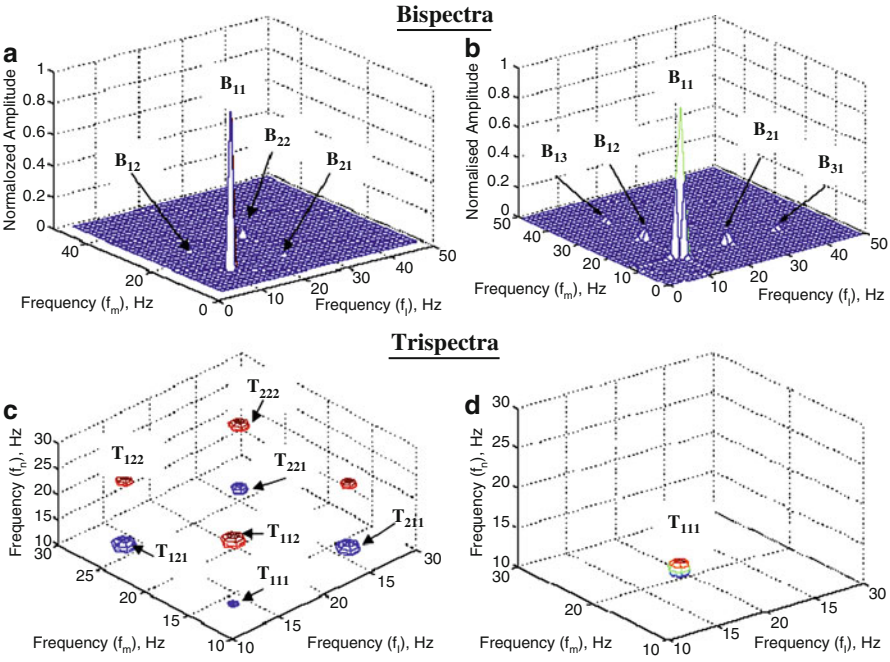

Fig. 3 Comparison of bispectra and trispectra plots for the cracked (left – **a, b**) and misaligned shaft (right – **c, d**) at a constant Machine RPM for Example 1

The observations on the bispectra and tri-spectra behaviour clearly indicate that the shaft responses may have several higher harmonics related to the machine speed in their amplitude spectra but the phase relations among them are significantly different, which can be brought out through the HOS analysis. The phase information may be useful for distinguishing the different faults as two of them are demonstrated here.

It is clearly seen that the two kinds of faults can be identified uniquely for this preliminary experimental case and shows the potential for general use. However if the number of bearings are more than two then the identification based on number of bispectra and trispectra plots may become subjective. Hence the data fusion in the frequency domain suggested in [3] has been utilized to compute a composite spectrum for a machine which has then been used to compute bispectrum. The advantage of this concept has been tested on a numerically simulated rig in Example 2.

4 Example 2

The schematic of the numerically simulated experimental example is shown in Fig. 4 [3]. It consists of a shaft made of steel supported on three anti-friction bearings on flexible bearing pedestals. The length and diameter of the shaft are 1.2 m and

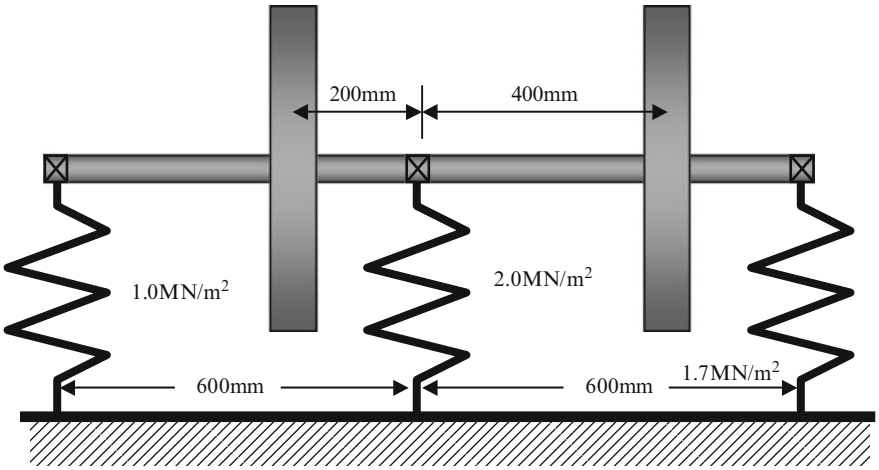

Fig. 4 The simulated rig of Example 2

20 mm, and the Young's modulus and the density of the rotor material are assumed as 210 GPa and $7,800\,\mathrm{kg/m^3}$ respectively. The shaft carries two balance disks of thickness 25 mm and the outer diameter 250 mm, one between the bearings 1 and 2, and other between 2 and 3 as shown in Fig. 4.

An FE model has been constructed for the rig [3]. The first three critical speeds of the numerical rig have been estimated at 42.28 Hz, 61.55 Hz and 201.14 Hz when there was no crack in the shaft, however these were estimated to be 41.66 Hz, 60.55 Hz and 198.20 Hz when a small crack of 10% of the diameter (for fully open condition) was assumed at 250 mm from bearing 1. The measured responses at all the bearing pedestals polluted with 30dB SN ratio were estimated for the machine run-up 900 rpm to 2,700 rpm with the linear chirp rate of 0.5 Hz/s. The measured responses were estimated for the shaft with a crack and without crack [3]. The crack was modeled using the method proposed by Sinha Jyoti et al. [5]. The breathing of the crack during the machine run-up was also considered [6].

4.1 Results and Discussion

A typical acceleration response of the cracked shaft in the vertical direction at bearing # 2 during machine startup from 900 to 2,700 rpm is shown in Fig. 5 which shows presence of the critical speed and its half at around 54 s and 32 s respectively.

The bispectrum was computed first for both the cracked and no crack responses for all the three bearings during machine startup. A few typical components of the bispectrum (B_{12} and B_{22}) are shown in Fig. 6 as these two components show prominent features for the crack detection as observed from the experimental Example 1. Definitely most of the individual components of the bispectrum show difference

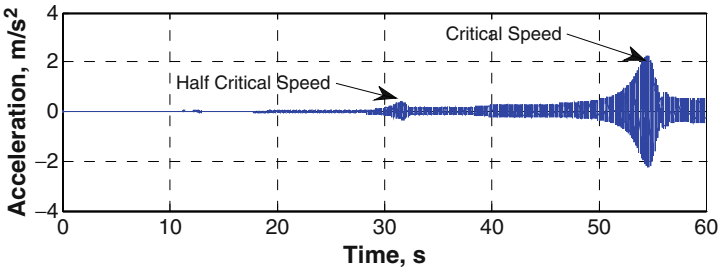

Fig. 5 A typical acceleration response of the cracked shaft in the vertical direction at bearing # 2 for Example 2

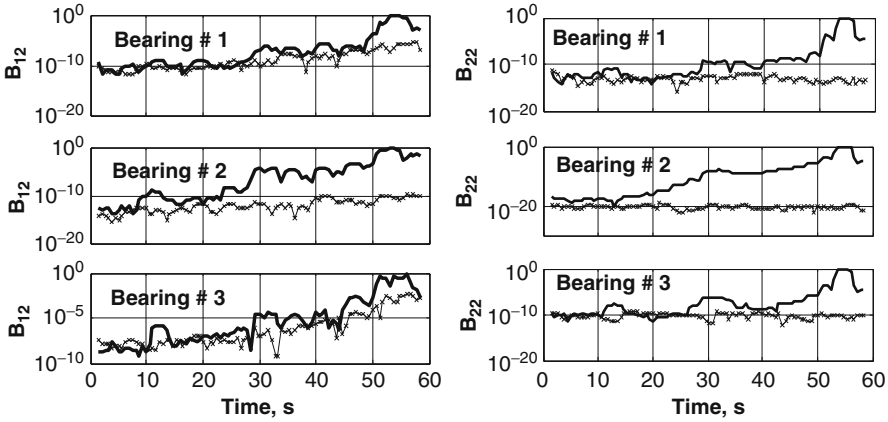

Fig. 6 Typical variation of bispectrum components – B_{12} and B_{22} at bearings 1 to 3 during machine startup for Example 2 (line with x for no crack, solid line for crack)

between the crack and no crack cases near 32 s and 54 s of the machine startup which corresponds to half the critical speed and the critical speed. However the discrimination was not that significant at bearings 1 and 3 for the bispectrum component B_{12}, even for the simple case considered here.

Now the composite bispectrum components were computed for both the crack and no crack cases. A few typical composite bispectrum components (B_{12} and B_{22}) are shown in Fig. 7. The components B_{12} and B_{22} – show significant improvement in the composite bispectrum compared to the individual bispectrum at bearings 1 to 3 at the half critical speed and at the critical speed, during the machine start-up. This study definitely shows much better discrimination feature between the crack and no crack cases. Sinha Jyoti [3] gave the details of this study.

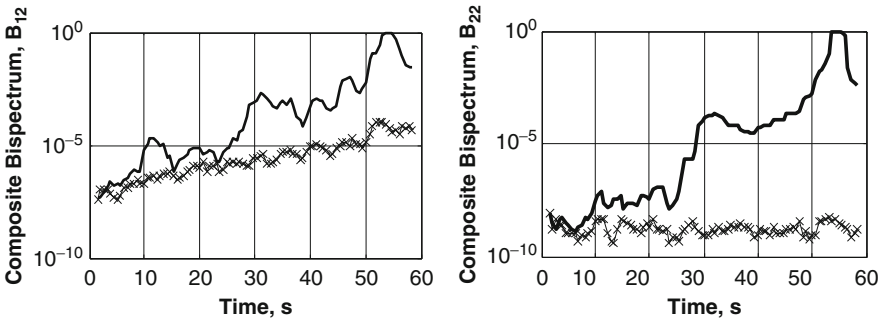

Fig. 7 Typical variation of composite bispectrum components – B_{12} and B_{22} during machine startup for Example 2 (line with x for no crack case, solid line for crack case)

5 Conclusion

The proposed method on the vibration based condition monitoring for rotating machines is an attempt to reduce the number of vibration sensors by increasing the computational effort (advanced signal processing and data fusion) and to get better discriminating feature for any fault to reduce the dependency on the experience and the engineering judgments in fault detection process. Example 1 establishes the effective use of the HOS – bispectrum and trispectrum in identifying and distinguishing two faults – crack and misalignment in a simple experimental rig. Then the usefulness of the proposed method – the bispectrum of the composite spectrum has been demonstrated through a simple numerical example of a rotating rig with a small rotor crack in Example 2. The significant advantage of the proposed method is that it reduces the number of measurements at all bearings to one and may ease the fault detection process in the rotating machine. Hence the proposed method seems to be a future possibility in the vibration based condition monitoring of rotating machines, however number of experiments on a laboratory rig with different faults need to be carried out to further enhance the confidence level in the proposed methodology.

References

1. Sinha Jyoti, K.: Health Monitoring Techniques for Rotating Machinery. Ph.D. Thesis, University of Wales Swansea, Swansea, UK (2002)
2. Collis, W.B., White, P.R., Hammond, J.K.: Higher-order spectra: the bispectrum and trispectrum. Mech. Syst. Signal Process. **12**(3), 375–394 (1998)
3. Sinha Jyoti, K.: Bi-spectrum of a Composite Coherent Cross-Spectrum for Faults Detection in rotating Mmachines. In: Proceedings of IMechE 9th International Conference on Vibration in Rotating Machinery, Paper C663/076:565-572, Exeter, UK, 8–10 September 2008
4. Sinha Jyoti, K.: Bispectrum of a rotating shaft with a breathing crack. Adv. Vib. Eng. **7**(4), 301–310 (2008)
5. Sinha Jyoti, K., Friswell, M.I., Edwards, S.: Simplified models for the location of cracks in beam structures using measured vibration data. J. Sound Vib. **251**(1), 13–38 (2002)
6. Sinha Jyoti, K.: Higher order spectra for crack and misalignment identification in shaft of machine a rotating. Struct. Health Monitoring: An Int. J. **6**(4), 325–334 (2007)

Feature Selection for Bearing Fault Detection Based on Mutual Information

Karthik Kappaganthu, C. Nataraj, and Biswanath Samanta

Abstract This paper deals with the important task of feature selection for the detection of faulty bearings in a rotor-bearing system. Various time, frequency and time-frequency based features are obtained from signals measured from bearings with and without outer race defect. The features are divided into a training set, a validation set and a test set. The task is to develop an optimal subset of features for a pattern classification algorithm which can efficiently and accurately classify the state of the machine as healthy or faulty. The features are ranked based on the mutual information content between the feature subset and the state of the machine. A validation set from the measured data is then used to obtain the optimal subset for classification. The performance of the method is evaluated using the test set.

Keywords Bearing defect · Feature selection · Mutual information · Optimal feature set

1 Introduction

Rotating machinery are probably among the most important components in industry. It is important to constantly maintain these machines in proper working conditions. The ability to confidently determine the state of the system and predict failures would greatly increase the productivity of the plant. Rotating machines are composed of different sub-systems interacting with each other in a nonlinear fashion; changes in any of these components can significantly affect the overall performance. Among all the components of a rotating machine, bearings which are load bearing members are key to effective functioning of the machine and often the cause of failure. Hence it is critical to be able to detect and classify a bearing as healthy or faulty.

K. Kappaganthu, C. Nataraj (✉), and B. Samanta
Department of Mechanical Engineering, Villanova University,
Villanova, PA 19085, USA
e-mail: c.nataraj@villanova.edu

K. Gupta (ed.), *IUTAM Symposium on Emerging Trends in Rotor Dynamics*,
IUTAM Bookseries 25, DOI 10.1007/978-94-007-0020-8_44,

Classification involves extracting features from the measured signal (usually vibration from an accelerometer or displacements from proximity probes) and training a classifier like ANN (Artificial Neural Network), ANFIS (Adaptive Neuro-Fuzzy Interference System), etc. These trained classifiers can then be used to classify the new data. The performance of a classifier depends on the training data and the quality of the features.

Over the past decade or so, extensive research has been carried out in the field of bearing signal analysis and numerous techniques have been developed. The techniques involve measuring vibration signals and processing them using signal processing techniques to obtain the features. Based on the techniques used the features can be classified into time [16], frequency [2, 14, 18] and time-frequency [4, 9, 18] domains.

In this research the quality of the features is studied as the mutual-information content between features and the state of the bearing (faulty or healthy). Various features are considered and a subset of the features that have maximum mutual-information is obtained.

Each of the extracted features is considered as a continuous random variable and ParzenŠs estimate is used to obtain the probability densities and joint probability densities of the features [7]. However, the task of estimating joint probability densities for more than two random variables is time consuming and often erroneous [5]. This task can be simplified if mutual information between the feature set and the state of the machine is estimated as difference between relevance and redundancy [13]. Greedy search algorithm [3] is then used to rank the features based on the mutual information estimate.

The methodology and the algorithm are explained in the next section and each of the steps are explained in detail in the following sections. The final sections provide the results and conclusions.

2 Methodology

The data collection is the first step in the proposed method. Vibration data is collected from a system with a faulty bearing and a defect free bearing over a span of rotating speeds (Ω) and used for training, validation and testing of the algorithm. The faulty bearing has a localized outer race defect. Moment, Fast Fourier Transform, Envelope Transform and Discrete Wavelet Transforms are used to obtain the relevant features. Skewness, Fast Fourier Transform (FFT), Envelope magnitudes at Ball Pass Frequency (ω_{bpfo}), Cage Frequency (ω_{cage}), 1/2X, 1X, 2X, and Discrete Wavelet Transform (DWT) energies and skewness up to level six are used as features. The data is divided into a training set, a validation set and a test set. Care is taken that data in each set is distributed evenly over the entire operating range.

Next, a greedy search algorithm is used to rank the features based on the mutual information. Greedy search algorithm is a sequential search technique that appends a feature to the solution space which maximizes the function at each iteration. It is

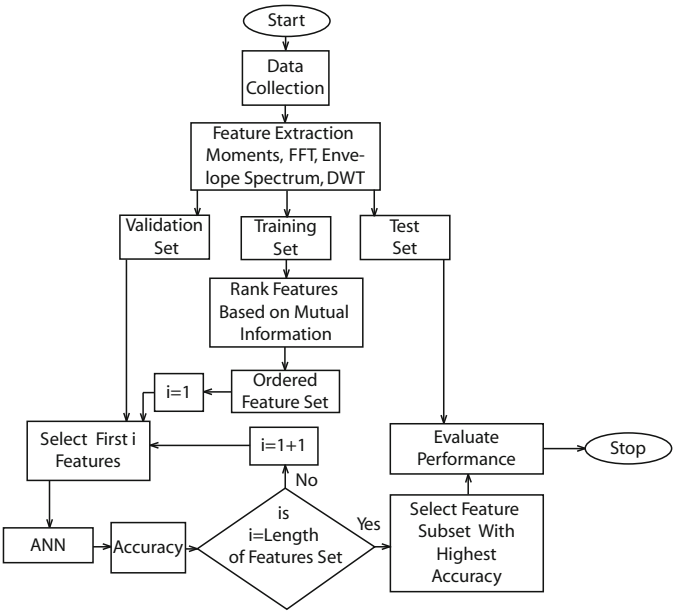

Fig. 1 Algorithm for feature selection

a popular technique used in statistical research [7]. Now the validation set is used to extract an optimal feature subset for classification using ANN as the classifier. The feature subset selection is performed incrementally using the ordered feature set obtained in the previous stage. The subset with the best ANN classification performance is the optimal solution. This optimal feature subset is then used to test the performance using the test set data. The flowchart of the complete process is provided in Fig. 1.

3 Feature extraction

One of the first feature extraction techniques for rolling element bearing fault detection were the time domain techniques. Rolling element bearings with faults showed higher peak to peak vibration compared to a healthy bearing [16]. Some of the common time domain features considered are skewness and kurtosis. Another important feature extraction technique is in the frequency domain. Fast Fourier Transform and Envelope Spectrum are used to obtain frequency information [14]. A rolling element bearing with an outer race defect usually has peaks at ball pass frequency and harmonics of ball pass frequency. Ball pass frequency can be calculated from the geometry of the bearing and the rotating speed [10]. Typical spectrum of the signal also contains peaks at rotating speed, harmonics of rotating speeds and cage

frequency. A system with a defect would tend to excite more nonlinearities than a defect free system which would appear as peaks in the FFT at sub-harmonics and super-harmonics of the rotating frequency, hence the FFT magnitudes at these frequencies are important characteristics of the system and are used as features. Typical spectrum of a defect free and a faulty bearing are shown in Figs. 2 and 3 respectively.

Wavelet transform is a time-frequency technique useful for detecting transients in signals. Wavelet transform is a method for obtaining the time-scale information of the signal. The wavelet transform provides coefficients which are dependent on the time and scale of the signal. Discrete Wavelet Transform (DWT), in particular, is a useful tool to extract and visualize the signal content at various scales and frequencies. In the DWT, the signal is decomposed into signals based on the frequency

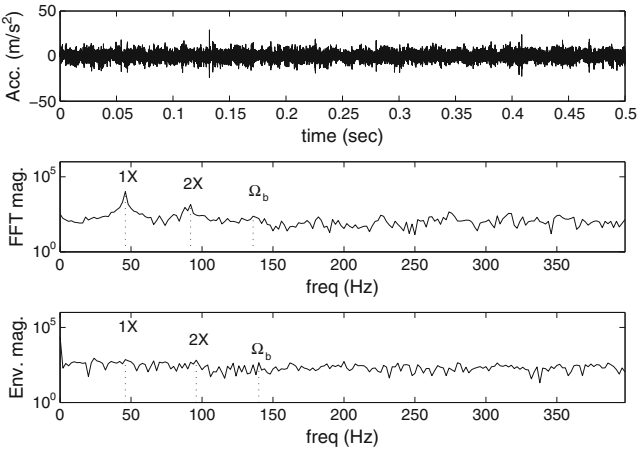

Fig. 2 Feature extraction for a defect free bearing

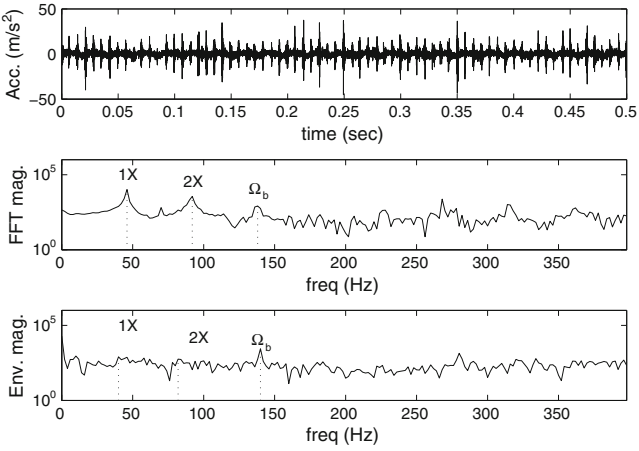

Fig. 3 Feature extraction for a bearing with an outer race defect

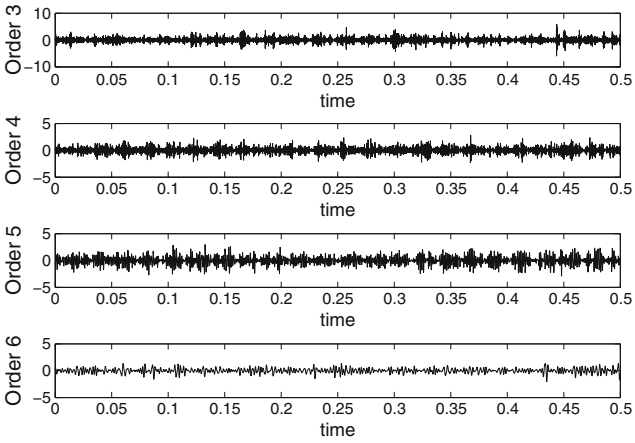

Fig. 4 DWT of a bearing signal with an outer race defect

content. At each stage the signal is split into high frequency and low frequency content, and the length of the signal gets halved. First, the signal is passed through a low pass filter which gives the approximation coefficients, then it is passed through high pass filters which gives the detail coefficients. The original signal can be re-calculated using inverse DWT. The reconstructed signal from a DWT of the bearing vibration with a faulty bearing is shown in Fig. 4.

If orthogonal wavelets like Daubechies are used Parseval's theorem can be used to extract the energy information at each stage [1, 17]. DWT-based energy features have been used as features for diagnostics of bearings [8, 17]. Some of the recent works on bearing diagnostics using DWT are [4, 6, 11, 12].

4 Feature ranking

As explained earlier the feature ranking is based on mutual information. Let x and c be random variables with the probability density functions (pdf), $p(x)$ and $p(c)$ respectively. The entropy and mutual information are defined as in Eqs. (1) and (2).

$$H(x) = -\int p(x) \log p(x) dx \tag{1}$$

$$I(x;c) = -\int p(x,c) \log \frac{p(x,c)}{p(x)p(c)} dxdy \tag{2}$$

Further, the entropy and mutual information are related by Eq. (3).

$$I(x;c) = H(c) - H(c|x) \tag{3}$$

The feature selection process using these measures can be defined as in Eq. (4).

$$max\ I(x;c),\ x = \{x : x\varepsilon S \subset X\} \tag{4}$$

where, X is the set containing the features and S is some subset of it. If the size of S is equal to size of X then the solution to Eq. (4) will be an ordered set of features.

Equation (4) can be solved using the greedy search technique. In the first step of this technique, set S is initialized to an empty set and a feature pool set defined as F to X. Next, S is populated iteratively with a feature from the feature pool such that it maximizes $I(x;c)$ at each stage. The selected feature is then removed from the feature pool. This process is continued till the feature pool is empty. To implement this search algorithm the mutual information should be calculated. This is explained in the following subsection.

4.1 Mutual information

Let x_i be the random variable with pdf $p(x_i)$ corresponding to the ith feature. Let C be any classifier that maps the features into N_C classes c_k with pdf $p(c_k)$, $k = 1, , 2, ..., N_C$. Note that c_k is a discrete random variable. The entropy and mutual information corresponding to the ith feature and kth class are defined by substituting x with x_i and c with c_k in Eqs. (1) and (2). Thus, in order to calculate the mutual information we need to find $p(c_k)$ and $p(c_k|x_i)$ from the data. It is easy to find $p(c_k)$ as it is a discrete random variable. By Bayesian rule we have

$$p(c_k|x_i) = \frac{p(x_i|c_k)p(c_k)}{p(x_i)} \tag{5}$$

The pdf of a continuous random variable x can be calculated from a given data using Parzen's Window as given in Eq. (6).

$$p(x) = \frac{1}{N}\sum_{i=1}^{N}\phi(x - x_i, h) \tag{6}$$

Where, N is the number of samples, h is a parameter that defines the size of the window, x_i are the data points and ϕ is a finite valued non-negative density function called the window function. In this work a Gaussian function is used for ϕ (as is done typically).

Using Eqs. (6) and (7), $p(x_i|c_k)$ can be calculated.

$$p(x_i|c_k) = \frac{1}{N_k}\sum_{i=1}^{N_k}\phi(x - xk_i, h) \tag{7}$$

where, N_k are the number of data points in the kth class and xk_i are the data points belonging to kth class. Using Eqs. (5–7) mutual information between a feature and a class can be calculated using Eq. (8).

$$I(x_i, c) = \sum_{k=1}^{N_C} p(c_k) \log p(c_k) - \int \sum_{k=1}^{N_C} p(x_i|c_k) p(c_k) \log p(x_i|c_k) \quad (8)$$

However, in order to calculate the mutual information between a set of features, $x = [x_1\ x_2\ ,\ ...\ ,\ x_n]$ and a class, we would need to calculate joint pdf $p(x)$ of the feature set and the conditional joint pdf $p(x|c)$. Although it is possible to do this, it is cumbersome and often inaccurate. To get around this problem in the maximization problem mutual information is estimated as the difference between the relevance and redundancy using Eq.(9). This method, when used in a sequential search, has similar performance to the actual value [13].

$$I(x; c) = \frac{1}{|S|} \sum_{x_i \varepsilon S} I(x_i; c) - \frac{1}{|S-1|^2} \sum_{x_i, x_j \varepsilon S} I(x_i; x_j),\ x = \{x : x \varepsilon S \subset X\} \quad (9)$$

The first part of the left hand side of Eq. (9) is the mean of the mutual information of each of the features and class; it is a measure of relevance of the set S. The second part consists of the information between the features themselves; it is a measure of redundancy of the set S. Using this method it is necessary to only calculate the joint pdf of two features at a time. The algorithm for ranking using this estimate and greedy search algorithm is as follows.

1. From the data find $p(c_k)$ and $H(c_k)$, $k = 1,\ 2,\ 3,\ ...,\ N_C$.
2. Set $S = \{\}$, $F = X$.
3. While F is not an empty set, DO

   - Set $i = 1$, Start Loop 1.
   - Append the ith element of F to S, i.e. $S_i = \{S,\ F_i\}$.
   - Set $j = 1$, Start Loop 2.
   - Using Eq. (8) find $I(x_j, c)$.
   - Using Eqs. (2,6) find $I(x_i, x_j)$.
   - If reached the end of S_i End Loop 2, else increment $j \rightarrow j + 1$ and go to Step 7.
   - Estimate mutual information of set S_i, $I(S_i, c)$ using Eq.(9).
   - If reached the end of F End Loop 1, else increment $i \rightarrow i + 1$ and go to Step 5.
   - Find the element x_i^* corresponding to Maximum $I(S_i, c)$.
   - Append x_i^* to S and remove it from F.

4. END WHILE
5. The final set S is the ordered feature set.

5 Feature selection

The aim of this stage is to extract an optimal subset S_{opt} from the ordered feature S set obtained in the previous stage. The criterion for optimization is least classification error using as few features as possible. The validation data is used to train an ANN and the classification accuracy is the measure of the classification. The algorithm for this is as follows.

1. Initialize $i = 1$ and $S_i = S(1)$.
2. Start loop.
3. Train an ANN using S_i and evaluate classification accuracy a_i.
4. If $S_i = S$ Stop Loop and proceed to step 6, else continue.
5. Increment $i \rightarrow i + 1$ and $S_i \rightarrow \{S_i,\ S(i + 1)\}$ and proceed to step 3.
6. From a_i find i^* corresponding to acceptable accuracy and optimal set size.
7. Obtain S_{opt} as S_{i^*}.

6 Results

Data was collected on a 'Machine Fault Simulator' [15], Fig. 5; once with a defect free bearing and once with a bearing with an outer race defect. The rotating speed was varied between 120 and 3,360 rpm with increments of 120 rpm. At each speed, 10 sets of data were collected. Five of these were used in training set, two in validation set, and three in test set. There were 280 samples in all; 140 of these were used for training, 56 for validation and 84 for testing. Twenty eight features were input to the mutual information ranking algorithm.

It is important to note that the features are strong nonlinear functions of rotating speeds. The rotating speed contains useful information and therefore needs to be a part of the feature set. The ordered feature set which is the output of the feature ranking algorithm explained in Section 4 is shown in Table 1.

Frequency based features ended up higher in the table. The DWT based features contained lesser information. Another important observation is that envelope and FFT magnitude at 1/2X, 2X are important features. These are the measures of nonlinearity in the system. Many earlier studies indicated that these frequency components are dominant in bearings with defects. This has been verified in our experiments and their importance has been validated by this procedure. DWT approximation features have very little relevant information and degrade the performance.

Using the ordered feature set and the algorithm explained earlier for feature selection, an ANN was used for classification of the validation data. The mean accuracy of ten ANN runs was the criterion for feature selection. The mean performance of the ANN per feature is shown in Fig.6. In this figure the ordinate at an abscissa 'n' is the percentage classification accuracy using the first 'n' features from Table 1. The optimum feature set consists of the first 16 features. When this feature set was

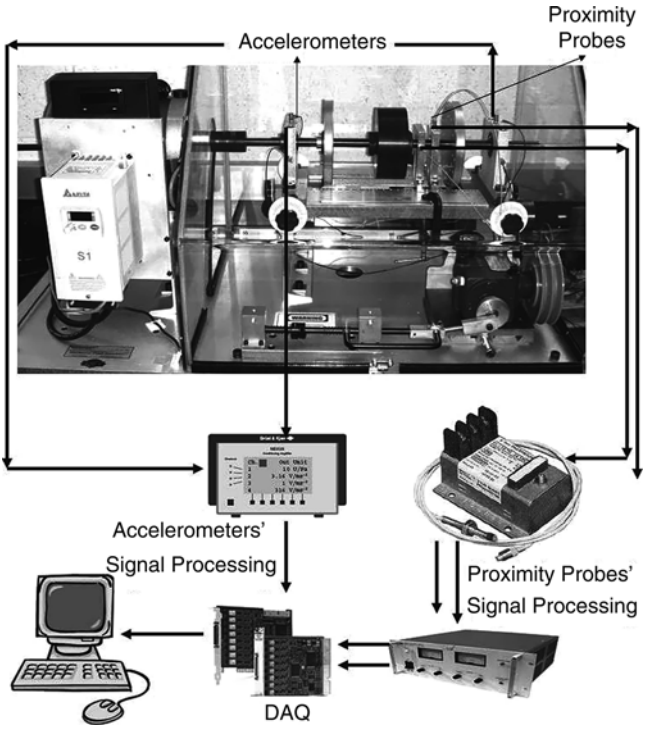

Fig. 5 Experimental setup

Fig. 6 Classification performance on validation data

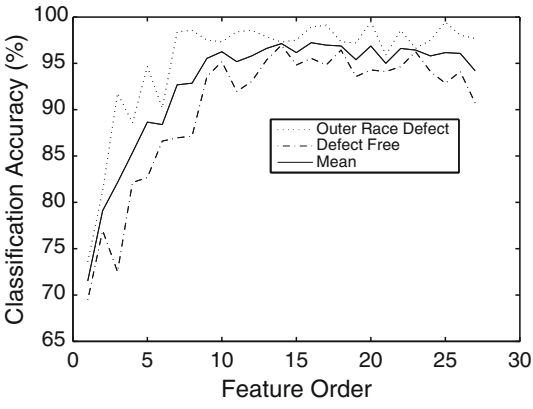

used with the validation data, the algorithm correctly classified a defect free system 95.5% of the time, a system with a faulty bearing 98.9% of the time and overall the algorithm correctly classified the system 97.2% of the time. The corresponding performance on the test set was 98.7%, 95.8% and 97.3% respectively.

Table 1 Feature order for outer race defect classification

	Ordered features
1	FFT mag at ω_{bpfo}
2	Envelope mag at $\Omega/2$
3	Rotating speed (Ω)
4	FFT mag at $\Omega/2$
5	Envelope mag at 2Ω
6	FFT mag at Ω_{cage}
7	Envelope mag at Ω_{cage}
8	DWT detail energy at level 3
9	DWT detail energy at level 4
10	DWT detail energy at level 6
11	DWT detail energy at level 2
12	Env mag at ω_{bpfo}
13	DWT approx energy at level 1
14	FFT mag at 2Ω
15	DWT approx energy at level 2
16	DWT detail energy at level 5
17	DWT approx energy at level 3
18	DWT approx energy at level 4
19	DWT approx energy at level 5
20	DWT detail energy at level 1
21	DWT skewness at level 4
22	DWT skewness at level 3
23	DWT skewness at level 5
24	DWT skewness at level 6
25	DWT approx. energy at level 6
26	DWT skewness at level 2
27	DWT skewness at level 1
28	Skewness

7 Conclusion

The mutual information based feature selection for bearing fault detection has been developed and implemented. Mutual information was estimated as a difference between the relevance and redundancy. Spectral features and DWT based features were ranked superior for the classification of a bearing with outer race defect. Using a validation data set an optimal feature subset was extracted. The optimality condition was minimum classification error using an ANN. The optimal feature set in this case had sixteen features. The method showed excellent performance on a test data set. Further work is in progress to incorporate model based features and evaluate their advantages and disadvantages for the purpose of diagnostics and prognostics.

References

1. Avci, E., Avci, D.: An expert discrete wavelet adaptive network based fuzzy inference system for digital signal processing. Expert Syst. Appl. **33**, 582–589 (2006)
2. Barkova, A., Barkov, N.: Condition assesment and life prediction of rolling element bearings. Sound Vibr. **28**, 10–17 (1995)
3. Battiti, R.: Using mutual information for selecting features in supervised neural network learning. IEEE Trans. Neur. Networks **5**, 537–550 (1994)
4. Cade, I.S., Keogh, P.S., Sahinkaya, M.N.: Fault identification in rotor/ magnetic bearing systems using discrete time wavelet coefficients. IEEE/ASME Trans. Mechatron. **10**(6), 648–657 (2005)
5. Cover, T.M., Thomas, J.A.: Elements of Information Theory. Wiley, New York (1991)
6. Djebala, A., Ouelaa, D., Hamzaoui, N.: Detection of rolling bearing defects using discrete wavelet analysis. Mechanica **43**, 339–348 (2008)
7. Duda, R.O., Hart, P.E., Stork, D.G.: Pattern Classification. Wiley-Interscience, New York (2001)
8. Feng, Y., Schlindwein, F.S.: Normalized wavelet packets quantifiers for condition monitoring. Mech. Syst. Signal Proces. **23**, 712–723 (2009)
9. Mori, K., Kasashmi, N., Yoshioka, T., Ueno, Y.: Prediction of spalling on ball bearings by applying discrete wavelet transform to vibration signals. Wear **8**, 195–162 (1996)
10. Nataraj, C., Pietrusko, R.G.: Dynamic response of rigid rotors supported on rolling element bearings with an outer raceway defect. In: ASME (ed.) Proceedings of IDETC/CIE 2005. Long Beach, CA, USA (2005)
11. Ocak, H., Loparo, K.A., Discenzo, F.M.: Online tracking of bearing wear using wavelet packet decomposition and probabilistic modeling. J. Sound Vibr. **302**, 951–961 (2007)
12. Pan, Y., Chen, J., Guo, L.: Robust bearing performance degradation assessment method based on improved wavelet packet -support vector data descriptions. Mech. Syst. Signal Proces. **23**, 669–681 (2009)
13. Peng, H., Long, F., Ding, C.: Feature selection based on mutual information: Criteria of max-dependency, max-relevance and min-redundancy. IEEE Trans. Pattern Anal. Mach. Intel. **27**, 1226–1238 (2005)
14. Randall, R.B., Gao, Y.: Extraction of modal parameters from the response of power cepstrum. J. Sound Vibr. **176**, 179–193 (1994)
15. Spectra Quest: http://www.spectraquest.com (2009)
16. Tandon, N.: A comparision of some vibration parameters for condition monitoring of rolling element bearings. Measurement **12**, 285–286 (1994)
17. Wu, J.D., Liu, C.H.: Investigation of engine fault diagnosis using discrete wavelet transform and neural network. Expert Syst. Appl. **35**, 1200–1213 (2008)
18. Ypma, A.: Learning methods of machine vibration analysis and health monitoring. Ph.D. thesis, Delft University (2001)

Application of Full Spectrum Analysis for Rotor Fault Diagnosis

Tejas H. Patel and Ashish K. Darpe

Abstract Machine vibration signal carries abundant information, including the machine health condition. Reliable and foolproof fault detection needs accurate knowledge of the dynamic response features of the faulty system as well as proper method to extract it. The paper presents experimental investigation of steady state vibration response of the rotor bearing system with rotor faults such as unbalance, crack, rotor-stator rub and misalignment at sub-critical rotational speeds. Test rigs are designed and fabricated for the purpose. The conventional Fourier spectrum (i.e., FFT) has limitations in exhibiting the whirl nature (i.e., forward/backward whirl) of the rotor faults. It has been observed in the past that the several other rotor faults generate higher harmonics in the Fourier spectrum. Hence there is always a level of uncertainty in the diagnosis based on FFT when other faults are also suspected. Present work through the use of full spectra has shown possibility of diagnosing these rotor faults through unique vibration features exhibited in the full spectra. The present investigation focuses on the directional nature of higher harmonics, in particular the 2X component. This provides an important tool to separate rotor faults that generate similar frequency spectra (e.g., crack and misalignment) and lead to a more reliable fault diagnosis. Crack, rub and misalignment fault identification through a full spectrum analysis is verified on a laboratory test rotor set-up.

Keywords Rotor fault diagnosis · Misaligned rotor · Cracked rotor · Rotor-stator rub · Full spectrum · Experimentation

T.H. Patel
Department of Mechanical Engineering, University of Alberta, Edmonton, Alberta T6G 2G8, Canada

A.K. Darpe (✉)
Department of Mechanical Engineering, Indian Institute of Technology, New Delhi 110 016, India
e-mail: akdarpe@mech.iitd.ac.in

K. Gupta (ed.), *IUTAM Symposium on Emerging Trends in Rotor Dynamics*,
IUTAM Bookseries 25, DOI 10.1007/978-94-007-0020-8_45,

1 Introduction

Vibration signal from a machine carries abundant information regarding dynamics and health of the machine components. There has been enormous research [1, 2] on dynamics of rotating machinery and vibration based condition monitoring. Variety of fault features and techniques for processing vibration signal have been proposed that proved effective for condition monitoring and diagnosis of the rotating machines. Shaft crack and rotor-stator rub are two important rotor faults which could result in the catastrophic failure. There has been extensive research on cracked rotors [3, 4]. Researchers mainly studied steady state vibration response at sub critical speeds [5–7], transient response during coast up/down or both [8, 9], and coupled vibrations [10, 11] for the cracked rotor. Higher harmonics at 2X, 3X are widely reported as a crack symptom. During the last two decades, investigations on rotor-stator interaction have gained a lot of importance. Rotor to stator rub interactions is a complex problem and involves phenomena [1] like impacting, friction, stiffening etc. Depending upon the type of rub condition, vibration signals could reveal variety of nonlinear response features [1, 12, 13] like chaos, quasi-periodic motion, sub-synchronous and super-synchronous vibrations.

Misalignment is accepted as the most commonly observed malfunction in rotor system after unbalance. A rotor system is likely to have some residual misalignment or it will develop during service due to variety of reasons. The misalignment condition thus always prevails in a rotor system. Misalignment between drive shafts generates reaction forces and moments (also known as misalignment forces) at coupling location. These forces significantly affect the vibration behaviour of the rotors. Gibbons [14] proposed formulation of misalignment forces for different coupling. Sekhar and Prabhu [15] showed 2X vibration response as the misalignment vibration symptom. Using kinematics of the Hooke's joint, Xu and Marangoni [16] showed even multiples of the shaft rotation frequency as the misalignment excitation frequencies. Al-Hussain and Redmond [17] found 1X bending-torsional coupled vibration response for the rotor with parallel misalignment. It was observed that, there is confusion in harmonic composition of the misalignment fault. Furthermore, most of the past studies on misalignment are analytical ones; experimental investigations are limited.

It may be noted that the rotor faults i.e., crack, rub and misalignment generate higher harmonics, however clear differentiation among these common faults has not been systematically addressed in the past. In practice any signs of 2X frequency component might lead to a confusing picture from the diagnostic point of view. The situation thus suggests need of a well-defined crack/misalignment diagnosis strategy. The present study aims to address this issue from the experimental vibration response analysis. The conventional Fourier spectrum (i.e., FFT) has limitations in exhibiting the whirl nature of the rotor faults. The full spectrum overcomes this limitation and reveals the whirl character (backward/forward) of each of the spectral components. In the experimental results discussed here, full spectrum analysis is employed to reveal the important whirl information about these faults.

2 Experiment Set-up

The experimental work for crack and rotor-stator rub vibration investigation is carried out on a single rotor-bearing set-up, shown in Fig. 1 [7], whereas experimental investigations related to misalignment fault have been carried out on a separate coupled rotor system shown in Fig. 2 [18]. A transverse crack of depth ($a/D = 0.28$) has been created at the mid span of the shaft on a three point bending fatigue testing machine. It can be seen from Fig. 1 that the rub can be conveniently introduced in the system by advancing the bolt in vertical direction. So, the rubbing location would always be at vertical bottom on the rotor disk. Both the set-ups (Figs. 1 and 2) have disks centrally mounted on the rotor shafts supported on ball bearings. An induction motor drives the rotor system. The alignment between inter connecting shafts is done using reverse dial indicator method and misalignment has been brought to a minimum possible level while taking the baseline (aligned rotor case) measurements.

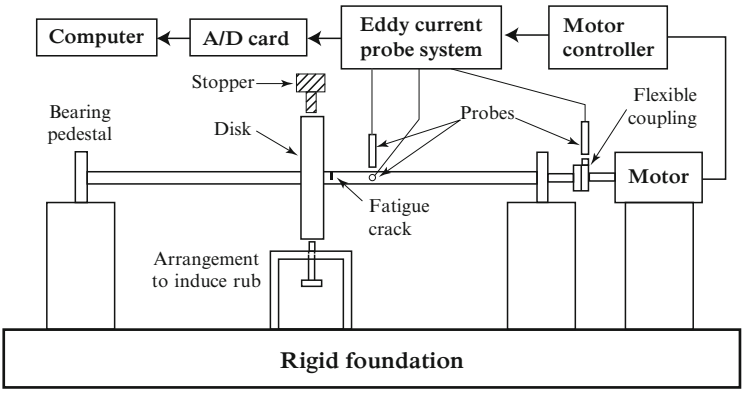

Fig. 1 Schematic of experimental set-up of single rotor system (for rub and crack fault) [7]

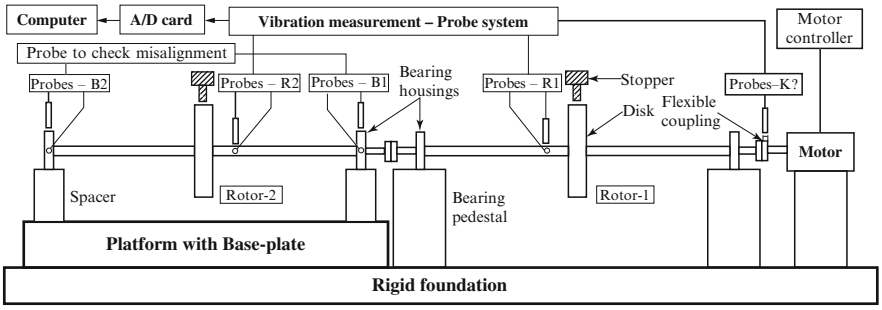

Fig. 2 Schematic of experimental set-up of coupled rotor system (for misalignment fault) [18]

For experimental investigations related to misalignment, provision is made to induce desired amount and type of misalignment (i.e., parallel and angular misalignments) along any of the lateral directions (i.e., horizontal and vertical) between the rotors (i.e., rotor-1 and rotor-2) using a special rotor platform designed for the purpose. A rotor (rotor-2) rests on base plate of the platform through the bearing housings and spacers (Fig. 2). The misalignment can be induced by moving baseplate of rotor-2 relative to rotor-1 along both lateral directions (i.e., horizontal and vertical). Probe systems B1 and B2 are used to gauge the level and type of misalignment introduced between the rotor shafts. The time domain vibration data in vertical and horizontal directions is acquired using Bently Nevada eddy current proximity probes (3,300 series) and processed further for full spectra based on the method discussed in Ref. [19].

3 Results and Discussion

This section presents full spectrum analysis of the experimental vibration response of the unbalance, crack, rotor-stator rub and misalignment faults. The bending natural frequency (ω_o) is found to be 48 Hz, using rap test. The electric motor is operated at constant sub-critical speeds, $p(= \omega/\omega_o) = 1/3$ and 1/2 (i.e., 16 Hz and 24 Hz respectively).

Figure 3 shows the vibration waveform in vertical direction and full spectrum plots of the vibration response of uncracked rotor for $p = 1/3$ and 1/2. Forward whirling 1X component dominates the full spectra. Weak harmonics i.e., 2X, 3X etc. are also present, however, at $p = 1/2$, 2X increases to a noticeable magnitude. Appearance of harmonics in a rotor bearing system, where unbalance is the only applied rotor fault, is due to residual misalignment and other inherent nonlinearity of the rotor bearing system due to support bearings etc.

3.1 Vibration Response of Cracked Rotor

Vertical vibration signals and full spectra of the rotor with a fatigue crack ($a/D = 0.28$) are presented in Fig. 4. It may be noted that the cracked rotor due to stiffness nonlinearity, introduced because of crack breathing; show higher harmonics in the vibration response. The full spectra of the lateral vibration response show that the higher order harmonics are forward whirling. When $p = 1/3, -3$X component of considerable magnitude appears where as at $p = 1/2, -2$X is relatively very weak compared to $+2$X harmonics. This suggests significant forward whirling nature of the 2X component in particular.

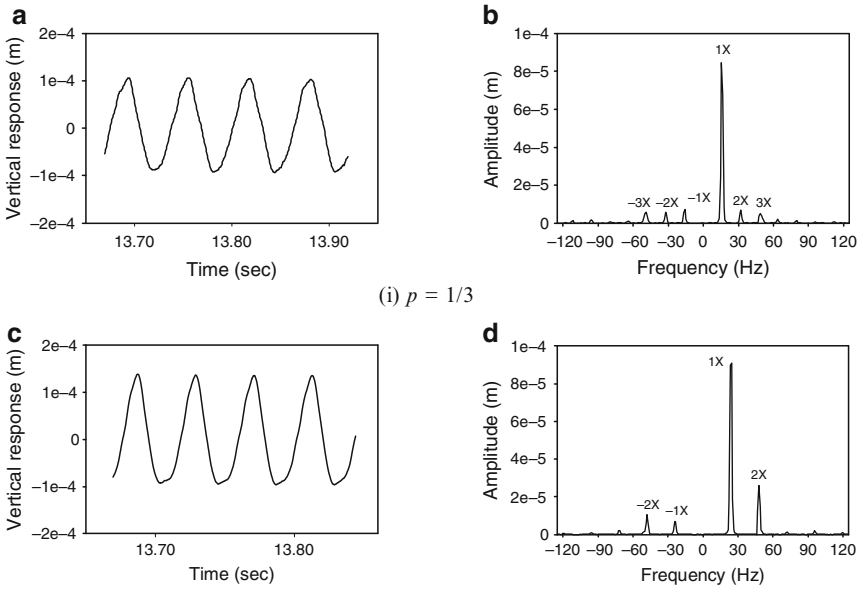

Fig. 3 Vibration response and full spectra of experimental response of uncracked rotor; (**a**) and (**c**) vertical vibration response; (**b**) and (**d**) Full spectra; (i) p = 1/3 and (ii) p = 1/2

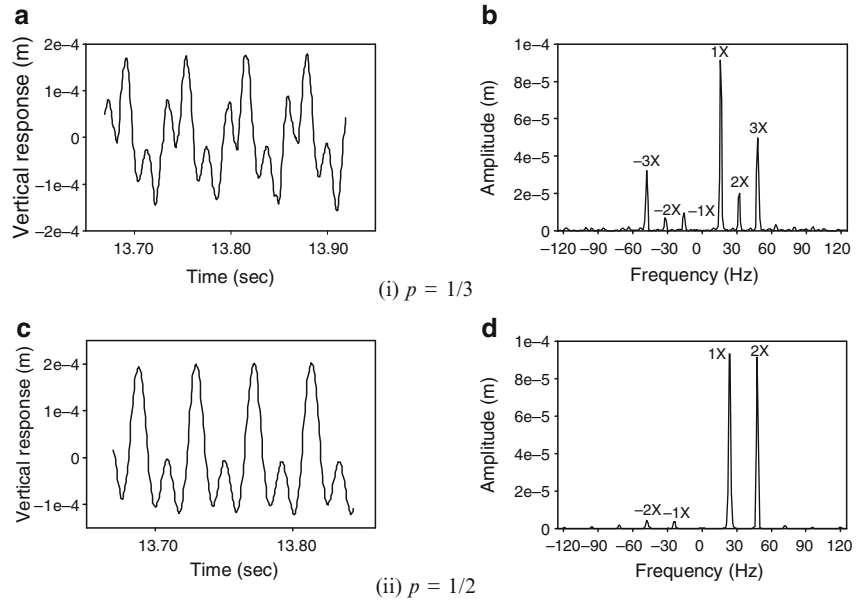

Fig. 4 Vibration response and full spectrum plots of cracked rotor; (**a**) and (**c**) vertical vibration response; (**b**) and (**d**) full spectra; (i) p = 1/3 and (ii) p = 1/2

3.2 Vibration Response of Rotor with rub

The experimental response of rub in uncracked rotor is shown in Fig. 5. Spectra rich in harmonics are observed. Nevertheless, 1X frequency still dominates the spectra. The higher harmonics of almost equal strength appear on both sides of the full spectrum (i.e., along +ve and −ve frequency axis). This feature is typical to a rotor rub and should be used for rub diagnosis. It is important to note that the subharmonic resonances are not observed in this case. It may be noticed that the full spectra of the cracked rotor (Fig. 4b, d) is dominated by forward whirling first three harmonics, however, full spectra for rub in uncracked rotor (Fig. 5b, d) show spectrum rich in harmonics (up to sixth harmonic) with almost equal forward and backward whirl components.

3.3 Vibration Response of Aligned Coupled Rotors

Unbalance response of the uncracked aligned rotors (i.e., rotors with residual misalignment) is obtained on coupled rotor set-up shown in Fig. 2. Figure 6 shows orbit plot and full spectrum of lateral vibration response of rotor-1 at $p = 1/3$. It is apparent that the vibration motion is mainly synchronous and forward whirling with weak harmonics. The orbit is slightly elliptical. Figure 7 shows the orbit and full spectrum

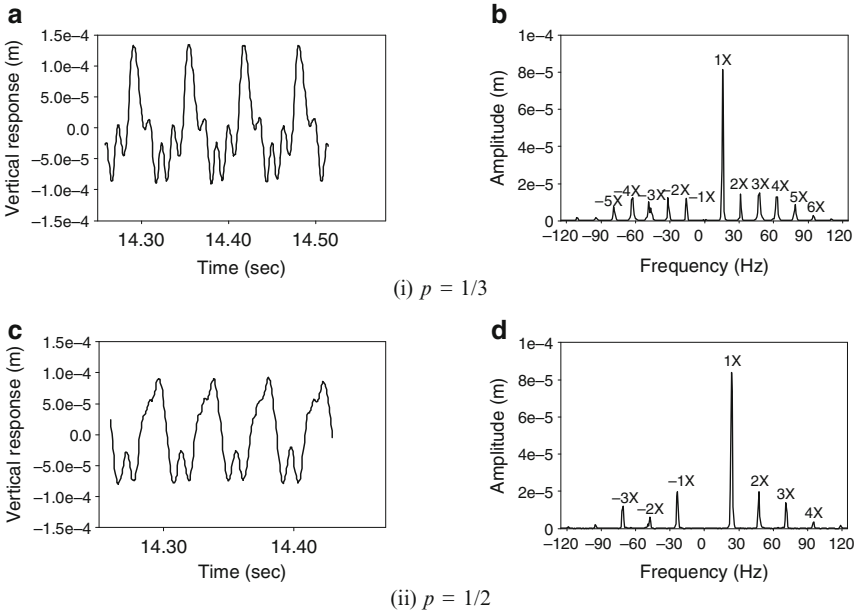

Fig. 5 Vibration response and full spectrum plots of rotor with rub; (**a**) and (**c**) vertical vibration response; (**b**) and (**d**) full spectra; (i) $p = 1/3$ and (ii) $p = 1/2$

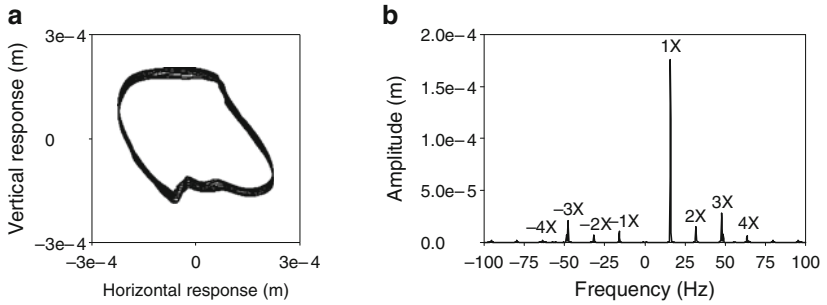

Fig. 6 Unbalance vibration response of aligned rotor at $p = 1/3$, (**a**) orbit plot, (**b**) full spectrum

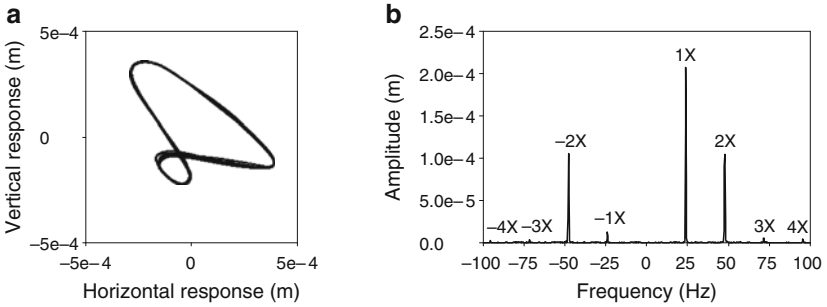

Fig. 7 Unbalance vibration response of aligned rotor at $p = 1/2$, (**a**) orbit plot, (**b**) full spectrum

plots for the rotor speed equal to half the bending critical speed ($p = 1/2$). The orbit of rotor-1 has looped pattern. In this case, along with the strong 1X component, significant 2X component is observed. The synchronous vibrations are strongly forward whirling. The 2X harmonic observes almost equal strength of $-2X$ and $+2X$ spectral components, which explains the reason behind the stretched orbit observed in Fig. 7a. It may be noted that presence of higher harmonics of noticeable magnitude is not expected in a system with unbalance as the only fault. This could be attributed to residual misalignment, bearing nonlinearity, eccentric mounting of coupling, etc.

3.4 Vibration Response of Rotors with Parallel Misalignment

Parallel misalignment of 0.32 mm is introduced in the vertical direction (i.e., in Y coordinate direction). Vibration response for rotor speed $p = 1/3$ is shown in Fig. 8. The horizontal vibration levels are more compared to vibrations in vertical direction due to preload effect along the misalignment direction, i.e., vertical. As a result the orbit of Fig. 9a is stretch along horizontal direction. The 3X is dominant in the horizontal vibration (Fig. 8b). The full spectrum in Fig. 9b shows strong (compared

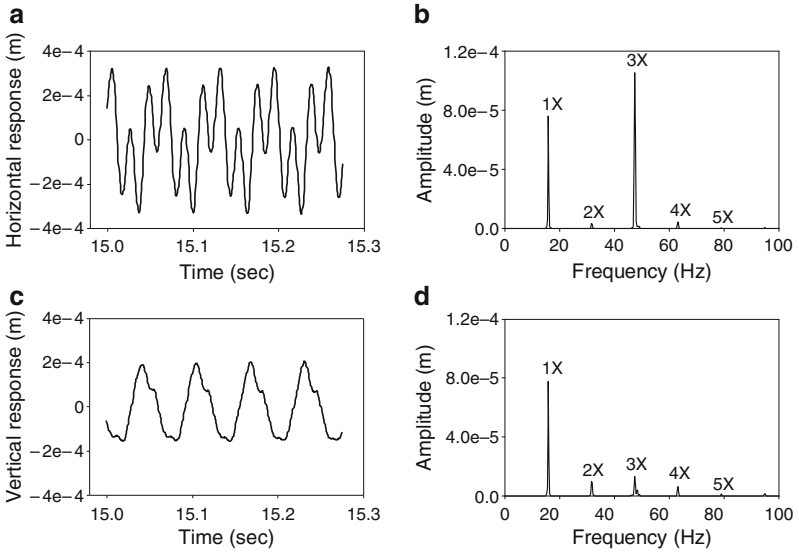

Fig. 8 Vibration response of rotor with misalignment ($dy = 0.32$ mm) at $p = 1/3$, (**a**) and (**c**) vibration waveforms, (**b**) and (**d**) FFT

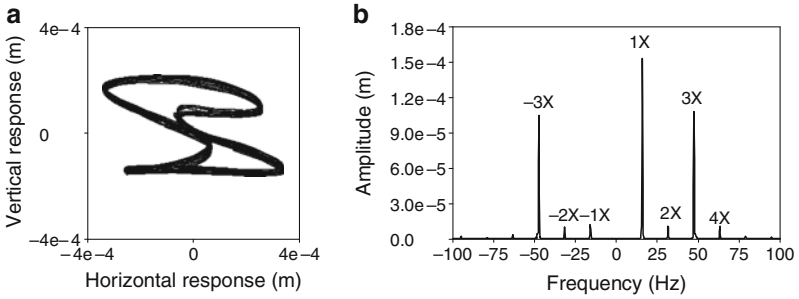

Fig. 9 Vibration response of rotor-1 with misalignment ($dy = 0.32$ mm) at $p = 1/3$, (**a**) orbit plot, (**b**) full spectrum

to 1X) and equal forward and backward whirling 3X frequency components. This is due to the directional nature of misalignment fault as observed in Fig. 8. Similarly at $p = 1/2$ full spectrum (Fig. 10b) shows almost equal $+2$X and -2X components.

3.5 Vibration Response of Rotors with Angular Misalignment

The angular misalignment of 1.6° is induced between the rotor shafts about vertical axis (i.e., 1.6° measured in the horizontal plane). Figure 11 shows the orbit and

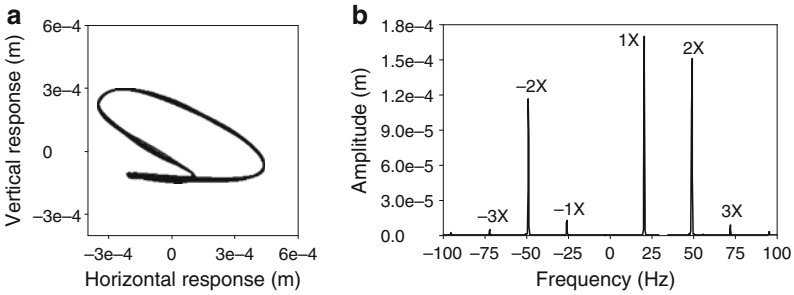

Fig. 10 Vibration response of rotor-1 with misalignment ($dy = 0.32$ mm) at $p = 1/2$, (**a**) orbit plot, (**b**) full spectrum

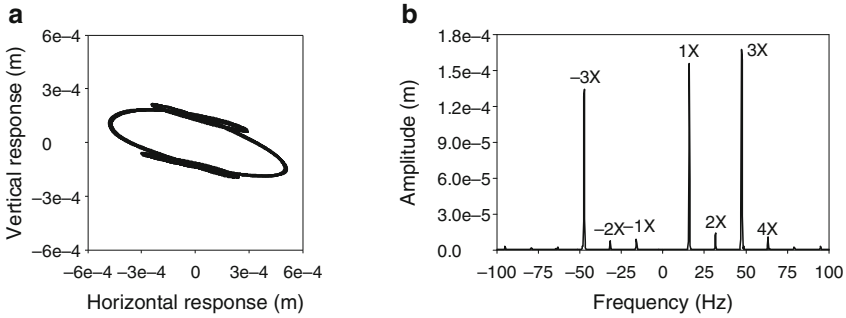

Fig. 11 Vibration response of rotor-1 with misalignment ($\alpha = 1.6°$) at $p = 1/3$, (**a**) orbit plot, (**b**) full spectrum

full spectrum plots of lateral vibration response of rotor at $p = 1/3$. The orbit is stretched along the horizontal direction due to increased vibration level along horizontal direction compared to vertical direction. This is attributed to the increase in rotor's effective stiffness in the direction perpendicular to the plane of misalignment, i.e., vertical direction in this case, due to misalignment. There are outer loops in the orbit. The full spectrum (Fig. 11b) is dominated by 1X and 3X components with amplitude of 3X frequency component more compared to that of 1X due to strong subharmonic resonance condition. The -3X component is comparable with $+1$X and $+3$X components. The orbit of rotor-1 (Fig. 12a) for misaligned rotors at $p = 1/2$, also indicate the stretch along horizontal direction due to misalignment. It is important to note that for angularly misaligned rotors, the orbits are clearly outer looped (Figs. 11a and 12a). The full spectrum (Fig. 12b) reveals the spectral characteristics with strong presence of 2X frequency component and has equal strength for $-$ve and $+$ve frequency components.

The angular misalignment excites almost equal forward and backward whirling higher harmonics, i.e., ± 3X and ± 2X at $p = 1/3$ and 1/2 respectively. From the discussion of previous sub-section 3.3, it may be recalled that parallel misalignment also exhibits this whirl nature. This is very important misalignment spectral

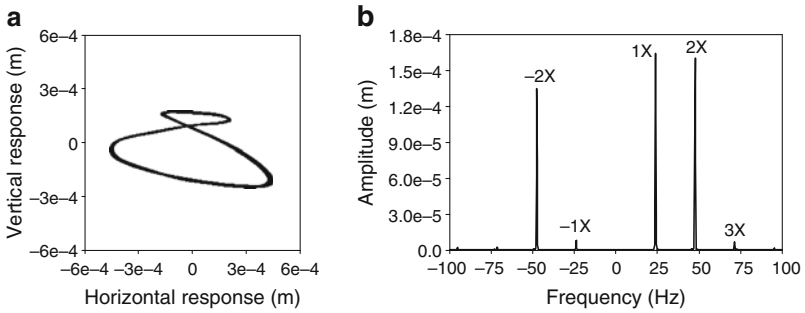

Fig. 12 Vibration response of rotor-1 with misalignment ($\alpha = 1.6°$) at $p = 1/2$, (**a**) orbit plot, (**b**) full spectrum

feature, which separates it from other faults which are known to have the similar spectral symptoms, for example a fatigue crack, rotor-stator rub. As discussed earlier in Sect. 3.1, the crack vibration responses at 3X and 2X spectral components are strongly forward whirling, with weaker -3X and -2X harmonics. The 2X vibration response in particular is strongly forward at $p = 1/2$ (Fig. 4ii) with negligible or almost zero -2X harmonic. The misalignment due to directionality in the strong radial preload forces excites much stronger backward whirling higher harmonics. In particular, the -2X frequency component at one-half the bending critical speed is the most important distinguishing feature to diagnose misalignment when both misalignment and crack are suspects.

4 Conclusions

Research on misalignment fault is limited and sometimes confusing description regarding misalignment spectral components is reported. The 2X spectral component is still a widely used symptom for misalignment diagnosis. However, there are other faults that exhibit strong 2X motion, such as fatigue crack, stiffness asymmetry, etc. The present experimental study is an attempt to address this ambiguity. Steady state lateral vibration response of the cracked rotor, rotor-stator rub and misaligned rotors is obtained at $p = 1/3$ and 1/2 on different experimental set-ups. Full spectrum analysis is presented to reveal the directional nature of these faults. The cracked rotor reveal forward whirling nature of the harmonics (i.e., 3X and 2X) generated due to breathing crack. The 2X response in particular is strongly forward whirling. Misalignment on the other hand is directional and reveal strong $\pm$3X and $\pm$2X at $p = 1/3$ and 1/2 respectively, in full spectra. The orbits are also stretched in the direction orthogonal to the misalignment direction as compared to almost circular inner looped orbit for cracked rotor. This is an important diagnostic feature that should be used to differentiate misalignment from crack, as well as from other rotor faults that generate higher harmonics (in FFT) similar to misalignment. Rotor-stator

rub also generates much low amplitude higher harmonics in the response, but it does not exhibit sub-harmonic resonances. Higher harmonics of the rub signal are almost equal forward and backward whirling amplitudes.

References

1. Muszynska, A.: Rotor-to-Stationary Part Rubbing Contact in Rotating Machinery in Rotordynamics. CRC Press, Taylor and Francis Group, Boca Raton, pp. 555–710 (2005)
2. Rao, J.S.: Vibration Condition Monitoring of Machines. Narosa Publishing House, New Delhi (2000)
3. Dimarogonas, A.D.: Vibration of cracked structures: a state of art review. Eng. Fract. Mech. **55**, 831–857 (1996)
4. Sabnavis, G., Kirk, R.G., Kasarda, M., Quinn, D.: Cracked shaft detection and diagnostics: a literature review. Shock Vib. Dig. **36**, 287–296 (2004)
5. Sinou, J.J., Lees, A.W.: The influence of cracks in rotating shafts. J. Sound Vib. **285**, 1015–1037 (2005)
6. Zhou, T., Sun, Z., Xu, J., Han, W.: Experimental analysis of cracked rotor. J. Dyn. Syst. Meas. Control **127**, 313–320 (2005)
7. Patel, T.H., Darpe, A.K.: Vibration response of a cracked rotor in presence of rotor-stator rub. J. Sound Vib. **317**, 841–865 (2008)
8. Wen, W.C., Wang, Y.C.: Theoretical research, calculation and experiments of cracked shaft dynamic response. Proc. IMechE Conf. London 473–478 (1988)
9. Darpe, A.K., Gupta, K., Chawla, A.: Transient response and breathing behaviour of the cracked Jeffcott rotor. J. Sound Vib. **272**, 207–243 (2004)
10. Papadopoulous, C.A., Dimarogonas, A.D.: Coupled vibrations of a cracked shaft. J. Vib. Acoust. **114**, 461–467 (1992)
11. Darpe, A.K., Gupta, K., Chawla, A.: Coupled bending, longitudinal and torsional vibrations of a cracked rotor. J. Sound Vib. **269**, 33–60 (2004)
12. Chu, F., Zhang, Z.: Periodic, quasi-periodic and chaotic vibrations of a rub impact rotor system supported on oil film bearings. Int. J. Eng. Sci. **35**, 963–973 (1997)
13. Patel, T.H., Darpe, A.K.: Use of full spectrum cascade for rotor rub identification. Adv. Vib. Eng. **8**, 139–151 (2009)
14. Gibbons, C.B.: Coupling misalignment forces. In: Proceedings of the 5th Turbo Machinery Symposium Gas Turbine Laboratory, Texas A & M University, Texas, 111–11306 (1976)
15. Sekhar, A.S., Prabhu, B.S.: Effects of coupling misalignment on vibration of rotating machines. J. Sound Vib. **185**, 655–671 (1995)
16. Xu, M., Marangoni, R.: Vibration analysis of a motor-flexible coupling-rotor system subjected to misalignment and unbalance, part I: theoretical model and analysis. J. Sound Vib. **176**, 663–679 (1994)
17. Al-Hussain, K.M., Redmond, I.: Dynamic response of two rotors connected by rigid mechanical coupling with parallel misalignment. J. Sound Vib. **249**, 483–498 (2002)
18. Patel, T.H., Darpe, A.K.: Experimental investigations on vibration response of misaligned rotors. Mech. Syst. Signal Process. **23**, 2236–2252 (2009)
19. Goldman, P., Muszynska, A.: Application of full spectrum to rotating machinery diagnostics. Orbit First Q. **20**(1), 17–21 (1999)

Author Index